Aus dem Institut für Medizinische Psychologie

der medizinischen Fakultät

der Ludwig-Maximilians-Universität München

Direktorin: Prof. Martha Merrow, PhD

Identification and characterization of N-degron pathways

Identifikation und Charakterisierung von N-Degron Protein-Abbauwegen

Kumulative Habilitationsschrift

Vorgelegt von

Tanja Bange, PhD

2023

Aus dem Institut für Medizinische Psychologie

der medizinischen Fakultät

der Ludwig-Maximilians-Universität München

Direktorin: Prof. Martha Merrow, PhD

Identification and characterization of N-degron pathways

Identifikation und Charakterisierung von N-Degron Protein-Abbauwegen

Kumulative Habilitationsschrift

Vorgelegt von

Tanja Bange, PhD

2023

Summary

Table of contents

1. Background on N-degron pathways

Every protein has a certain lifespan ranging from less than a minute to several days. Regulated protein degradation controls the abundance and activity of all short-lived proteins to ensure cellular homeostasis and also protects cells from accumulating misfolded, aggregated or other abnormal proteins (Varshavsky, 2019). Dysfunctional degradation is implicated in various diseases, including cancer, neurodegenerative disorders and inflammatory diseases (Popovic et al., 2014). Therefore, the identification and understanding of the functional architecture of degradation pathways is of pivotal importance (Mueller and Bange, 2023).

Regulated protein degradation is mostly mediated by the ubiquitin proteasome system (UPS) (Hershko & Ciechanover, 1998). The most important players in this system are E3 ligases which recognize exposed sequence motifs, so-called degrons, of target proteins and conjugate ubiquitin (Ub; an 8 kDa protein) to nearby lysine residues on them (Ravid & Hochstrasser, 2008). Ubiquitinated proteins are subsequently destroyed by a multi-subunit protease, the 26S proteasome. The human proteome predicts the existence of around 700 E3 ligases which provide the UPS with specificity to regulate simultaneously very diverse physiological pathways (Mueller and Bange, 2023)(Zheng & Shabek, 2017).

Degrons can be located anywhere on a protein, but the first degrons, discovered in 1986, are at the very N-terminus (Nt) of proteins, so-called N-degrons (Bachmair et al., 1986). My work is focused on this subset of protein degradation pathways, so called N-degron pathways, in which N-termini of proteins are recognized as degradation signals. N-degrons are very short (~ 1-4 amino acids (aa)) motifs mainly determined by the first N-terminal (Nt-) aa of a protein or the modification of the first aa (e.g. Nt-acetylation) of the protein. On the one hand, N-degrons may be

constitutively exposed from the moment the nascent protein exits the ribosomal tunnel. In this case, N-degrons play a role in maintaining complex stoichiometry or to adopt to environmental changes (Chen et al., 2017; Hwang et al., 2010; Kim et al., 2014; Melnykov et al., 2019; Varshavsky, 2019). On the other hand, N-degrons can be exposed through incorrect or missing co-translational/Nt-modifications or proteolytic cleavage exposing new Nt. The exposed N-degrons are then recognized by E3 ligases, so called N-recognins, and the protein is targeted for proteasomal degradation ensuring protein quality control (Linster et al., 2022; Mueller et al., 2021; Timms et al., 2019)(Mueller and Bange, 2023).

Every protein harbors potential N-degrons and therefore N-degron pathways are involved in a plethora of biological pathways, spanning from regulation of cell cycle progression, heme sensing, response to stress and apoptosis and impairment might lead to human pathologies like e.g. cancer or neurodegeneration (reviewed e.g. in: (Varshavsky, 2011, 2019)).

2. My contribution to the N-degron field

When I started my investigation on N-degron pathways, four N-degron pathways named after the Nt-aa residue or its modification representing the N-degron were described: the Arg/N-degron pathway (Gibbs et al., 2014; Varshavsky, 2011, 2019) and Pro/N-degron pathway (Chen et al., 2017; Lampert et al., 2018; Melnykov et al., 2019) which recognize free Nt; the Ac/N-degron pathway (Hwang et al., 2010; Shemorry et al., 2013) which recognizes acetylated (ac) Nt and the Gly/N-degron pathway which recognize free Nt glycine residues which escaped their correct Nt-myristoylation (Timms et al., 2019).

These studies in the past have mainly focused on characterising systematically the role of the starting amino acid on protein stability and not on the identification of the E3 ligases acting as N-recognins and the characterization of the N-degron pathways. In order to be able to identify new N-degron pathways with their cognate N-recognins, I developed a peptide pull-down workflow combined with mass spectrometry (MS) – based quantitative proteomics. MS-based proteomics is a powerful technique that allows the comprehensive and unbiased characterization of the protein composition of pulled-down complexes. Taking advantage of this technology, I reasoned that peptide pairs only differing in their Nt modification, e.g. free N-terminal sequences versus acetylated N-terminal sequences were part of Nt-degradation signals, they ought to act as determinants of interactions with specialized receptors on E3 ligases or associated proteins which can be identified by MS. To this end, beads exposing synthetic peptide pairs, i.e. acetylated or not, encompassing the Nt-region of proteins (aa 1-10) were incubated with lysates of HeLa cells, followed by MS-based identification and quantification on retained binders (Mueller et al., 2021).

With this work-flow, I was able to identify and characterize a fifth N-degron pathway which has been named nonAc/N-degron pathway (Linster et al., 2022; Mueller et al., 2021)(Mueller and Bange, 2023). The pathway specifically targets proteins lacking their expected, endogenous Nt-acetylation through the Nt-acetyltransferase NatA, rather exposing unmodified alanine, and possibly also serine and threonine (Mueller et al., 2021). I was able to show that residues exposed through omission of their Nt-acetylation represent N-degrons recognized by BIRC2 (Baculoviral IAP repeat-containing protein 2, cIAP1), BIRC3, XIAP (BIRC4), and BIRC6 (also known as APOLLON or BRUCE), four members of an inhibitor of apoptosis protein (IAP) family of E3 ligases that are key regulators of programmed cell death in development, tissue

homeostasis, and tumorigenesis. With this work, I made several major contributions to the Nt-processing and N-degron field, demonstrating that (i) Nt-acetylation of NatA substrates is a protective mark against inhibitor of apoptosis proteins E3-ligases, thus involving Nt-acetylation in protein stabilization; (ii) proteins escaping their natural Nt-modifications can undergo clearance through the Ub system, thus drawing a clear parallel to the Gly/N-degron pathway which proposes that omission of Nt-myristoylation leads to degradation; (iii) IAPs are N-recognins and might serve a more general role in protein quality control and not only in apoptosis as previously thought (Mueller et al., 2021). The results are graphically summarized in **Figure 1**. This publication was the first publication on nonAc/N-degron pathways and paved the way for a series of publications which confirmed the nonAc/N-degron pathway in different species and contexts suggesting that proteins which omit their proper Nt-processing are rapidly removed from the system (Li et al., 2022; Linster et al., 2022)(Varland et al. 2022).

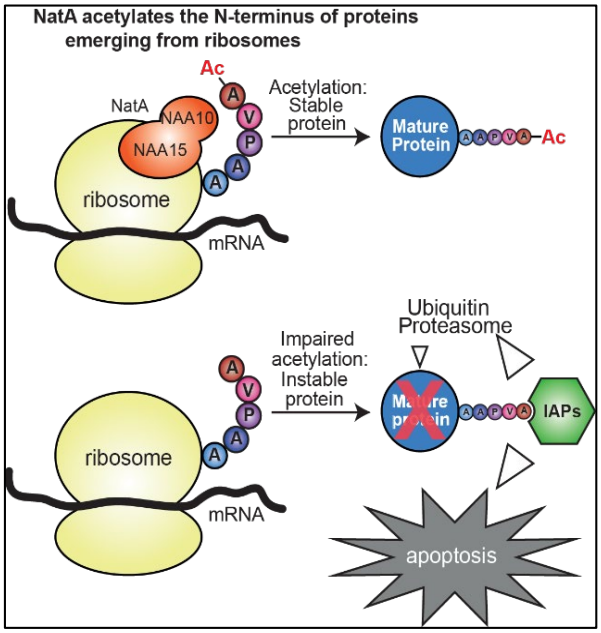

Figure 1. Graphical scheme summarizing the described NatA-IAP pathway (Mueller et al., 2021). NAA10 and NAA15 are the subunits of the N-acetyltransferase NatA. Aa are presented in single letter code.

3. Outlook on future work on N-degron pathways

Our data and recent literature on new N-degron pathways reinforced the assumption that many more E3 ligases act as N-recognins in N-degron pathways and more N-degron pathways exist than hitherto believed. I validated with our published

and preliminary data that peptide pull-downs combined with MS-based proteomics can be applied to identify those E3 ligases and even dissect sequence specificities.

I am using this established pipeline of peptide-pull downs combined with MS-based proteomics to systematically screen for unknown N-degrons and their respective E3 ligases. I already identified three additional E3 ligases (CUKL3-KLHL13/22, CUL4-DDB1-DCAF10, SKP1-MYCBP2-FBXO4) as new N-recognins and confirmed two E3 ligases with an established role (CUL2-ZYG11 and GID/CLTH complex), both showing broader N-degron recognition as known (**Table 1**) (unpublished data).

Table 1: Summary of identified N-degrons and potential N-recognins

E3 ligase	Known N-degron function	N-terminus binding (aa 1-4)	Gene name of target proteins	Omitted modification in cells
CUL2-ZYG11	Gly/N-degron pathway	GCVQ GCIK GAPA	FYN YES TMEM97	Nt-myristoylation
CUL3-KLHL13/KLHL22	No	MDDK VDRE AEDM	EIF2B1 YWHAG COX6B	Nt-acetylation
CUL4-DDB1-DCAF10	No	ac-GCVQ ac-GCIK ac-GAPA	FYN YES TMEM97	Nt-myristoylation
GID/CLTH complex	Pro/N-degron pathway	AVPA MDDK PAYF	COMMD10 EIF2B1 EIF3A	Nt-acetylation

		MAPA VAPV	MTHFD1 ELP2	
SP1-MYCBP2- FBXO45	No	VDRE	YWHAG	Nt-ac (NatA)

Interestingly, literature showed that the identified N-recognin candidates are often overexpressed in cancer and have a role as tumor suppressor or oncogenes depending on the type of cancer. For all candidates the molecular mechanism how they might contribute to malignancy and disease is completely unknown. The E3 ligase adaptor proteins KLHL13 and KLHL22 are not well studied but elevated levels are observed in many types of cancer and roles in mTORC1 signaling and cell cycle progression have been assigned (Beck et al., 2013; Chen et al., 2018; Liu et al., 2020; Maerki et al., 2009; Metzger et al., 2013; Song et al., 2020; Sumara et al., 2007; Xiang et al., 2021; Zhou et al., 2020). CUL4A-DBB1 together with the DDB2 adaptor (CUL4A-DDB1-DDB2) is involved in DNA repair (Groisman et al., 2003), but has never been connected to N-degron pathways. DDB1 and CUL4A may use up to 60 different adaptor proteins, so called DCAFs (DDBA and CUL4-Associated Factors), suggesting a variety of possibilities to target many different pathways (Lee & Zhou, 2007). No function has been assigned so far to the CUL4A-DDB1-DCAF10 complex but CUL4A and DCAFs are as well elevated in many types of cancer (Cui et al., 2019; Jang et al., 2021; Sang et al., 2015). The SKP1-FBXO45-MYCBP2 complex is highly expressed in neuronal cells and has important functions in developmental processes, such as axon determination/degeneration and synapse formation, and it is elevated in different types of cancers (Grill et al., 2016; Lin et al., 2020; Po et al., 2010). Overall, all candidates have been associated to human diseases with unknown mechanisms and

so far, there is no evidence for involvement in N-degron recognition. I am currently validating the identified E3 ligases as N-recognins and investigating the physiological role of the new N-recognin candidates in N-degron pathway. For these experiments, I am using a series of assays which I established to validate the inhibitor of apoptosis proteins as N-recognins (Mueller et al., 2021). This pipeline includes biochemical assays to show a direct interaction between N-degron and N-recognins, *in vitro* and *in vivo* ubiquitination assays and cellular RNA interference (RNAi) or overexpression experiments to investigate the physiological role of the potential new N-degron pathway in healthy and transformed mammalian cells (HeLa, DLD1 and RPM1 cells).

In parallel, we continued and will continue the systematic screening of N-terminal sequences and expect a comprehensive list of potential N-recognin candidates for N-degron pathways in a short period of time. I see the screening for E3 ligases acting as N-recognins as a possibility to develop further long-term projects for my lab.

In sum, emerging data suggest that a complex interplay not unravelled yet of N-recognins and Nt-modifying enzymes, like methionine amino peptidases and e.g. Nt-acetyltransferases or N-myristoyltransferases, exists which ensures protein maturation and quality control of specific subsets of proteins. Thus, improperly modified or unexpectedly unmodified proteins would become rapidly removed through Ub-conjugation after synthesis. My ultimate aim is to contribute to uncover this interplay which ensures protein quality control and to elucidate its role for cellular proteostasis.

The results will be highly relevant for various fields of basic research (Nt-processing, Nt-acetylation, protein quality control and stability, assignment of new roles to E3 ligases) and might shed light on how dysfunctional N-degron pathways

contribute to human diseases like e.g. cancer development and uncover new potential druggable pathways.

4. Summary of my further work on interaction, cross-linking and post-translational modifications experiments using quantitative mass spectrometry-based proteomics

Quantitative MS-based proteomics is not only a powerful technique to study protein interactions (interaction proteomics), but as well to quantify thousands of proteins in a single experiment (expression proteomics), map surface interactions down to the aa level (cross-linking proteomics) and identify post-translational modifications (PTM analysis). The technique is developing at a tremendous speed offering a constantly growing spectrum of methods and a plethora of possibilities to address all kinds of biological questions.

In addition to my biological focus on N-degron pathways, I used my deep technical knowledge of MS techniques acquired in Prof. M. Mann´s lab and my biological background in degradation and signalling pathways, to answer interesting biological questions from different fields, spanning epidermal growth factor receptor (EGFR) signalling and degradation, cell cycle and cell division to the circadian clock field, using quantitative MS-based proteomics. I set-up MS methods and workflows from scratch for data-dependent and independent acquisition, quantitative proteomics, labelling strategies, interaction proteomics, post-translational modification analysis and cross-linking methods which were all successfully applied, as testified by many collaborative papers also in high ranking journals (including Nature (Faesen et al.,

2017) and Science (Bruning et al., 2019)). A summary of my activities is given in the following section.

Work on identification of ubiquitinated proteins using quantitative MS-based proteomics: The epidermal growth factor receptor (EGFR) binds to the EGF family of proteins and activates then several signaling cascades to convert extracellular cues into appropriate cellular responses. I was interested in how poly-ubiquitination of the EGFR affects its internalization, sorting and degradation and in the non-degradative role of mono-ubiquitination of the EGFR and endocytic proteins. Interestingly, cells are able to read monoUb signals through proteins harbouring ubiquitin receptors (e.g., ubiquitin interacting motifs) and then further transmit the signal through their own monoubiquitination analogous to phosphorylation-dependent signaling (Woelk et al., 2006; Woelk et al., 2007). Therefore, we set out to measure ubiquitinated proteins after EGF stimulation for different periods of time. This was the largest ubiquitome at the time and the first time where dynamic changes of ubiquitination in response to signaling were shown (Argenzio et al., 2011).

Work on identification of phosphorylated peptides and phosphorylation sites using quantitative MS-based proteomics: Phosphorylation is a vital reversible (through kinases – phosphatases) post-translational modification in which a phosphate group is attached to serine/threonine or tyrosine residues of proteins. Phosphorylation alters the function and activity of the target proteins and the process plays a crucial role in almost all cellular processes, including cell signaling, metabolism, gene expression, and cell division. Dysregulation of phosphorylation has been linked to many diseases, e.g. cancer, diabetes and neurodegenerative disorders. As such, understanding the complex regulatory mechanisms of phosphorylation is of great interest in basic and clinical research. Phosphorylation sites and changes of

phosphorylation sites can be identified and quantified by MS-based proteomics through an 80 Dalton mass shift introduced on peptides containing phosphorylations.

I applied large scale, proteome-wide phosphopeptide enrichment work-flows to identify changes in phosphorylations to support and answer biological questions from different fields, including topics like meiosis, circadian clock, sleep and DNA repair (Altmannova et al., 2023; Bruning et al., 2019; Harpprecht et al., 2019)(Schmal C. et al., 2023). In addition, I identified and quantified regulatory phosphosites from *in vitro* samples and immunoprecipitations from wild-type and mutant proteins which contributed to decipher regulatory processes in kinetochore assembly and checkpoint signaling (Barbosa et al., 2020; Breit et al., 2015; Cunha-Silva et al., 2020; Faesen et al., 2017; Huis In 't Veld et al., 2016; D. Singh et al., 2021; P. Singh et al., 2021).

Work on cross-linking proteomics: Cross-linking proteomics is a powerful tool to study the structure and intra-/interactions of proteins within a complex or a complex mixture of proteins. In this method, proteins are chemically cross-linked while still in their native state, using e.g. commercially available cross-linker or UV light. Cross-linked proteins are enzymatically digested and then analysed by MS. The technique provides information about the proximity and orientation of protein domains within a complex allowing to reconstruct three-dimensional structures of protein complexes complementing other structural techniques like e.g. electron microscopy. Cross-linking proteomics holds several challenges in sample preparation and data analysis which limits its application mainly to specialized MS labs. I developed a simple single-step purification protocol and easy-to-follow pipeline to make cross-linking MS accessible to non-specialist, structural and biochemistry laboratories which resulted in a last author publication and the protocol is broadly applied (Pan et al., 2018).

In addition, I used UV-light inducible cross-linking of farnesyl-like modifications containing the UV-active compounds (diazirine pyrophosphate, BPP1 and BPP2) to map the interaction site of the farnesylated protein Spindly with the ~800 kDa ROD-Zwilch-ZW10 (RZZ) complex. The RZZ complex builds a fibrous corona that assembles on mitotic kinetochores before microtubule attachment to promote chromosome alignment and robust spindle assembly checkpoint signalling. The cross-linking experiments showed farnesyl-dependent binding of RZZ to Spindly and identified ROD as the Spindly farnesyl receptor. These cross-link MS experiments greatly helped to elucidate the role of RZZ as dynein cargo at human kinetochores (Mosalaganti et al., 2017).

Work on interaction proteomics: Interaction proteomics is a powerful approach to identify and characterize protein-protein, protein-RNA, protein-DNA and protein-small molecule interactions in an unbiased manner. Usually, a bait which can be proteins, peptides, DNA, RNA or as well small molecules is used to affinity/co-purify proteins from complex mixtures like e.g. cellular lysates and potential interaction partners are identified and quantified by MS measurement in un unbiased manner. Interaction proteomics is a powerful technique to discover new interaction partners, dissect binding surfaces of proteins, construct interaction networks and gain insights into the functional roles of proteins in different biological processes. I set up several immunoprecipitation assays combined with labelling strategies (e.g. stable isotope labelling in cell culture (SILAC), tandem mass tag (TMT) to dissect Bub1 and BubR1, two proteins involved in spindle assembly checkpoint signaling and cell cycle progression (Overlack et al., 2017). Furthermore, I performed pull-down experiments using RNA and small molecules as baits to comprehensively identify their interaction partners (Dietrich et al., 2017; Pospiech et al., 2018).

5. References

Publications of the author T.Bange/ maiden name T. Woelk are highlighted in bold.

Altmannova, V., Firlej, M., Muller, F., Janning, P., Rauleder, R., Rousova, D., Schaffler, A., Bange, T., & Weir, J. R. (2023). Biochemical characterisation of Mer3 helicase interactions and the protection of meiotic recombination intermediates. *Nucleic Acids Res*. https://doi.org/10.1093/nar/gkad175

Argenzio, E., Bange, T., Oldrini, B., Bianchi, F., Peesari, R., Mari, S., Di Fiore, P. P., Mann, M., & Polo, S. (2011). Proteomic snapshot of the EGF-induced ubiquitin network. *Mol Syst Biol*, *7*, 462. https://doi.org/10.1038/msb.2010.118

Bachmair, A., Finley, D., & Varshavsky, A. (1986). In vivo half-life of a protein is a function of its amino-terminal residue. *Science*, *234*(4773), 179-186. https://doi.org/10.1126/science.3018930

Barbosa, J., Martins, T., Bange, T., Tao, L., Conde, C., & Sunkel, C. (2020). Polo regulates Spindly to prevent premature stabilization of kinetochore-microtubule attachments. *EMBO J*, *39*(2), e100789. https://doi.org/10.15252/embj.2018100789

Beck, J., Maerki, S., Posch, M., Metzger, T., Persaud, A., Scheel, H., Hofmann, K., Rotin, D., Pedrioli, P., Swedlow, J. R., Peter, M., & Sumara, I. (2013). Ubiquitylation-dependent localization of PLK1 in mitosis. *Nat Cell Biol*, *15*(4), 430-439. https://doi.org/10.1038/ncb2695

Breit, C., Bange, T., Petrovic, A., Weir, J. R., Muller, F., Vogt, D., & Musacchio, A. (2015). Role of Intrinsic and Extrinsic Factors in the Regulation of the Mitotic Checkpoint Kinase Bub1. *PLoS One*, *10*(12), e0144673. https://doi.org/10.1371/journal.pone.0144673

Bruning, F., Noya, S. B., Bange, T., Koutsouli, S., Rudolph, J. D., Tyagarajan, S. K., Cox, J., Mann, M., Brown, S. A., & Robles, M. S. (2019). Sleep-wake cycles drive daily dynamics of synaptic phosphorylation. *Science*, *366*(6462). https://doi.org/10.1126/science.aav3617

Chen, J., Ou, Y., Yang, Y., Li, W., Xu, Y., Xie, Y., & Liu, Y. (2018). KLHL22 activates amino-acid-dependent mTORC1 signalling to promote tumorigenesis and ageing. *Nature*, *557*(7706), 585-589. https://doi.org/10.1038/s41586-018-0128-9

Chen, S. J., Wu, X., Wadas, B., Oh, J. H., & Varshavsky, A. (2017). An N-end rule pathway that recognizes proline and destroys gluconeogenic enzymes. *Science*, *355*(6323). https://doi.org/10.1126/science.aal3655

Cui, H., Wang, Q., Lei, Z., Feng, M., Zhao, Z., Wang, Y., & Wei, G. (2019). DTL promotes cancer progression by PDCD4 ubiquitin-dependent degradation. *J Exp Clin Cancer Res*, *38*(1), 350. https://doi.org/10.1186/s13046-019-1358-x

Cunha-Silva, S., Osswald, M., Goemann, J., Barbosa, J., Santos, L. M., Resende, P., Bange, T., Ferras, C., Sunkel, C. E., & Conde, C. (2020). Mps1-mediated release of Mad1 from nuclear pores ensures the fidelity of chromosome segregation. *J Cell Biol*, *219*(3). https://doi.org/10.1083/jcb.201906039

Dietrich, L., Rathmer, B., Ewan, K., Bange, T., Heinrichs, S., Dale, T. C., Schade, D., & Grossmann, T. N. (2017). Cell Permeable Stapled Peptide Inhibitor of Wnt Signaling that Targets beta-Catenin Protein-Protein Interactions. *Cell Chem Biol*, *24*(8), 958-968 e955. https://doi.org/10.1016/j.chembiol.2017.06.013

Faesen, A. C., Thanasoula, M., Maffini, S., Breit, C., Muller, F., van Gerwen, S., Bange, T., & Musacchio, A. (2017). Basis of catalytic assembly of the mitotic checkpoint complex. *Nature*, *542*(7642), 498-502. https://doi.org/10.1038/nature21384

Gibbs, D. J., Bacardit, J., Bachmair, A., & Holdsworth, M. J. (2014). The eukaryotic N-end rule pathway: conserved mechanisms and diverse functions. *Trends Cell Biol*, *24*(10), 603-611. https://doi.org/10.1016/j.tcb.2014.05.001

Grill, B., Murphey, R. K., & Borgen, M. A. (2016). The PHR proteins: intracellular signaling hubs in neuronal development and axon degeneration. *Neural Dev*, *11*, 8. https://doi.org/10.1186/s13064-016-0063-0

Groisman, R., Polanowska, J., Kuraoka, I., Sawada, J., Saijo, M., Drapkin, R., Kisselev, A. F., Tanaka, K., & Nakatani, Y. (2003). The ubiquitin ligase activity in the DDB2 and CSA complexes is differentially regulated by the COP9 signalosome in response to DNA damage. *Cell*, *113*(3), 357-367. https://doi.org/10.1016/s0092-8674(03)00316-7

Harpprecht, L., Baldi, S., Schauer, T., Schmidt, A., Bange, T., Robles, M. S., Kremmer, E., Imhof, A., & Becker, P. B. (2019). A Drosophila cell-free system that senses DNA breaks and triggers phosphorylation signalling. *Nucleic Acids Res*, *47*(14), 7444-7459. https://doi.org/10.1093/nar/gkz473

Hershko, A., & Ciechanover, A. (1998). The ubiquitin system. *Annu Rev Biochem*, *67*, 425-479. https://doi.org/10.1146/annurev.biochem.67.1.425

Huis In 't Veld, P. J., Jeganathan, S., Petrovic, A., Singh, P., John, J., Krenn, V., Weissmann, F., Bange, T., & Musacchio, A. (2016). Molecular basis of outer kinetochore assembly on CENP-T. *Elife*, *5*. https://doi.org/10.7554/eLife.21007

Hwang, C. S., Shemorry, A., & Varshavsky, A. (2010). N-terminal acetylation of cellular proteins creates specific degradation signals. *Science*, *327*(5968), 973-977. https://doi.org/10.1126/science.1183147

Jang, S. M., Redon, C. E., & Aladjem, M. I. (2021). Switching DCAFs: Beyond substrate receptors. *Bioessays*, *43*(7), e2100057. https://doi.org/10.1002/bies.202100057

Kim, H. K., Kim, R. R., Oh, J. H., Cho, H., Varshavsky, A., & Hwang, C. S. (2014). The N-terminal methionine of cellular proteins as a degradation signal. *Cell*, *156*(1-2), 158-169. https://doi.org/10.1016/j.cell.2013.11.031

Lampert, F., Stafa, D., Goga, A., Soste, M. V., Gilberto, S., Olieric, N., Picotti, P., Stoffel, M., & Peter, M. (2018). The multi-subunit GID/CTLH E3 ubiquitin ligase promotes cell proliferation and targets the transcription factor Hbp1 for degradation. *Elife*, *7*. https://doi.org/10.7554/eLife.35528

Lee, J., & Zhou, P. (2007). DCAFs, the missing link of the CUL4-DDB1 ubiquitin ligase. *Mol Cell*, *26*(6), 775-780. https://doi.org/10.1016/j.molcel.2007.06.001

Li, Y., Zhao, Y., Yan, X., Ye, C., Weirich, S., Zhang, B., Wang, X., Song, L., Jiang, C., Jeltsch, A., Dong, C., & Mi, W. (2022). CRL2(ZER1/ZYG11B) recognizes small N-terminal residues for degradation. *Nat Commun*, *13*(1), 7636. https://doi.org/10.1038/s41467-022-35169-6

Lin, M., Wang, Z. W., & Zhu, X. (2020). FBXO45 is a potential therapeutic target for cancer therapy. *Cell Death Discov*, *6*, 55. https://doi.org/10.1038/s41420-020-0291-2

Linster, E., Forero Ruiz, F. L., Miklankova, P., Ruppert, T., Mueller, J., Armbruster, L., Gong, X., Serino, G., Mann, M., Hell, R., & Wirtz, M. (2022). Cotranslational N-degron masking by acetylation promotes proteome stability in plants. *Nat Commun*, *13*(1), 810. https://doi.org/10.1038/s41467-022-28414-5

Liu, X. R., Wang, W., & Li, H. M. (2020). KLHL22 promotes malignant melanoma growth in vitro and in vivo by activating the PI3K/Akt/mTOR signaling pathway. *Neoplasma*, *67*(5), 1106-1113. https://doi.org/10.4149/neo_2020_190923N954

Maerki, S., Olma, M. H., Staubli, T., Steigemann, P., Gerlich, D. W., Quadroni, M., Sumara, I., & Peter, M. (2009). The Cul3-KLHL21 E3 ubiquitin ligase targets aurora B to midzone microtubules in anaphase and is required for cytokinesis. *J Cell Biol*, *187*(6), 791-800. https://doi.org/10.1083/jcb.200906117

Melnykov, A., Chen, S. J., & Varshavsky, A. (2019). Gid10 as an alternative N-recognin of the Pro/N-degron pathway. *Proc Natl Acad Sci U S A*, *116*(32), 15914-15923. https://doi.org/10.1073/pnas.1908304116

Metzger, T., Kleiss, C., & Sumara, I. (2013). CUL3 and protein kinases: insights from PLK1/KLHL22 interaction. *Cell Cycle*, *12*(14), 2291-2296. https://doi.org/10.4161/cc.25369

Mosalaganti, S., Keller, J., Altenfeld, A., Winzker, M., Rombaut, P., Saur, M., Petrovic, A., Wehenkel, A., Wohlgemuth, S., Muller, F., Maffini, S., Bange, T., Herzog, F., Waldmann, H., Raunser, S., & Musacchio, A. (2017). Structure of the RZZ complex and molecular basis of its interaction with Spindly. *J Cell Biol*, *216*(4), 961-981. https://doi.org/10.1083/jcb.201611060

Mueller F., Bange T. Identification of N-degrons and N-recognins using peptide pull-downs combined with quantitative mass spectrometry (2023) Methods Enzymol., MIE Volume 686; in print; https://authors.elsevier.com/a/1goaSHRzCQBKs

Mueller, F., Friese, A., Pathe, C., da Silva, R. C., Rodriguez, K. B., Musacchio, A., & Bange, T. (2021). Overlap of NatA and IAP substrates implicates N-terminal acetylation in protein stabilization. *Sci Adv*, *7*(3). https://doi.org/10.1126/sciadv.abc8590

Overlack, K., Bange, T., Weissmann, F., Faesen, A. C., Maffini, S., Primorac, I., Muller, F., Peters, J. M., & Musacchio, A. (2017). BubR1 Promotes Bub3-Dependent APC/C Inhibition during Spindle Assembly Checkpoint Signaling. *Curr Biol*, *27*(19), 2915-2927 e2917. https://doi.org/10.1016/j.cub.2017.08.033

Pan, D., Brockmeyer, A., Mueller, F., Musacchio, A., & Bange, T. (2018). Simplified Protocol for Cross-linking Mass Spectrometry Using the MS-Cleavable Cross-linker DSBU with Efficient Cross-link Identification. *Anal Chem*, *90*(18), 10990-10999. https://doi.org/10.1021/acs.analchem.8b02593

Po, M. D., Hwang, C., & Zhen, M. (2010). PHRs: bridging axon guidance, outgrowth and synapse development. *Curr Opin Neurobiol*, *20*(1), 100-107. https://doi.org/10.1016/j.conb.2009.12.007

Popovic, D., Vucic, D., & Dikic, I. (2014). Ubiquitination in disease pathogenesis and treatment. *Nat Med*, *20*(11), 1242-1253. https://doi.org/10.1038/nm.3739

Pospiech, N., Cibis, H., Dietrich, L., Muller, F., Bange, T., & Hennig, S. (2018). Identification of novel PANDAR protein interaction partners involved in splicing regulation. *Sci Rep*, *8*(1), 2798. https://doi.org/10.1038/s41598-018-21105-6

Ravid, T., & Hochstrasser, M. (2008). Diversity of degradation signals in the ubiquitin-proteasome system. *Nat Rev Mol Cell Biol*, *9*(9), 679-690. https://doi.org/10.1038/nrm2468

Sang, Y., Yan, F., & Ren, X. (2015). The role and mechanism of CRL4 E3 ubiquitin ligase in cancer and its potential therapy implications. *Oncotarget*, *6*(40), 42590-42602. https://doi.org/10.18632/oncotarget.6052

Schmal C., Maier B., Ashwal-Fluss R., Bartok O., Finger AM., Bange T., Koutsouli S., Robles MS., Kadener S., Herzel H., Kramer A. An integrative omics approach reveals

posttranscriptional mechanisms underlying circadian temperature compensation. (2023). Under revision; bioRxiv: https://www.biorxiv.org/content/10.1101/2021.10.06.463236v1Shemorry, A., Hwang, C. S., & Varshavsky, A. (2013). Control of protein quality and stoichiometries by N-terminal acetylation and the N-end rule pathway. *Mol Cell*, *50*(4), 540-551. https://doi.org/10.1016/j.molcel.2013.03.018

Singh, D., Schmidt, N., Muller, F., Bange, T., & Bird, A. W. (2021). Destabilization of Long Astral Microtubules via Cdk1-Dependent Removal of GTSE1 from Their Plus Ends Facilitates Prometaphase Spindle Orientation. *Curr Biol*, *31*(4), 766-781 e768. https://doi.org/10.1016/j.cub.2020.11.040

Singh, P., Pesenti, M. E., Maffini, S., Carmignani, S., Hedtfeld, M., Petrovic, A., Srinivasamani, A., Bange, T., & Musacchio, A. (2021). BUB1 and CENP-U, Primed by CDK1, Are the Main PLK1 Kinetochore Receptors in Mitosis. *Mol Cell*, *81*(1), 67-87 e69. https://doi.org/10.1016/j.molcel.2020.10.040

Song, Y., Yuan, H., Wang, J., Wu, Y., Xiao, Y., & Mao, S. (2020). KLHL22 Regulates the EMT and Proliferation in Colorectal Cancer Cells in Part via the Wnt/beta-Catenin Signaling Pathway. *Cancer Manag Res*, *12*, 3981-3993. https://doi.org/10.2147/CMAR.S252232

Sumara, I., Quadroni, M., Frei, C., Olma, M. H., Sumara, G., Ricci, R., & Peter, M. (2007). A Cul3-based E3 ligase removes Aurora B from mitotic chromosomes, regulating mitotic progression and completion of cytokinesis in human cells. *Dev Cell*, *12*(6), 887-900. https://doi.org/10.1016/j.devcel.2007.03.019

Timms, R. T., Zhang, Z., Rhee, D. Y., Harper, J. W., Koren, I., & Elledge, S. J. (2019). A glycine-specific N-degron pathway mediates the quality control of protein N-myristoylation. *Science*, *365*(6448). https://doi.org/10.1126/science.aaw4912

Varshavsky, A. (2011). The N-end rule pathway and regulation by proteolysis. *Protein Sci*, *20*(8), 1298-1345. https://doi.org/10.1002/pro.666

Varshavsky, A. (2019). N-degron and C-degron pathways of protein degradation. *Proc Natl Acad Sci U S A*, *116*(2), 358-366. https://doi.org/10.1073/pnas.1816596116

Varland, S., Duarte Silva, R., Kjosås, I., Faustino A., Bogaert, A., Billmann, M., Boukhatmi, H., Kellen B., Costanzo, M., Drazic A., Osberg C., Chan, K., Zhang, X., HinYan Tong, A., Anreazza S., Lee, JJ., Nedyalkova, L., UŠay, M., Whitworth, AJ., Andrews, BJ., Moffat, J., Myers, CL., Gevaert, K., Boone, C., Gonçalo Martinho, R., Arnesen, T. (2022). N-terminal acetylation shields proteins from degradation and promotes age-dependent motility and longevity. *BioRxiv,* 2022.09.01.505523. https://doi.org/10.1101/2022.09.01.505523

Woelk, T., Oldrini, B., Maspero, E., Confalonieri, S., Cavallaro, E., Di Fiore, P. P., & Polo, S. (2006). Molecular mechanisms of coupled monoubiquitination. *Nat Cell Biol*, *8*(11), 1246-1254. https://doi.org/10.1038/ncb1484

Woelk, T., Sigismund, S., Penengo, L., & Polo, S. (2007). The ubiquitination code: a signalling problem. *Cell Div*, *2*, 11. https://doi.org/10.1186/1747-1028-2-11

Xiang, S., Shi, X., Chen, P., Chen, Y., Bing, S., Jin, X., Cao, J., Wang, J., Yang, B., Shao, X., He, Q., & Ying, M. (2021). Targeting Cul3-scaffold E3 ligase complex via KLHL substrate adaptors for cancer therapy. *Pharmacol Res*, *169*, 105616. https://doi.org/10.1016/j.phrs.2021.105616

Zheng, N., & Shabek, N. (2017). Ubiquitin Ligases: Structure, Function, and Regulation. *Annu Rev Biochem*, *86*, 129-157. https://doi.org/10.1146/annurev-biochem-060815-014922

Zhou, X. A., Zhou, J., Zhao, L., Yu, G., Zhan, J., Shi, C., Yuan, R., Wang, Y., Chen, C., Zhang, W., Xu, D., Ye, Y., Wang, W., Shen, Z., Wang, W., & Wang, J. (2020). KLHL22 maintains PD-1 homeostasis and prevents excessive T cell suppression. *Proc Natl Acad Sci U S A*, *117*(45), 28239-28250. https://doi.org/10.1073/pnas.2004570117

7. Acknowledgments

First, I am grateful to my Fachmentorat, Prof. Martha Merrow, Prof. Maria Robles and Prof. Axel Imhof for their advice and continuous support. In particular, I want to thank here Prof. Maria Robles for the last years, where we set up the laboratory, for her guidance, help and discussions about anything that I was unsure about.

I want to give my deepest appreciation to Franziska Müller for working with me for many years, her tireless effort, commitment and support of our work. A special thanks goes to my former supervisor Prof. Andrea Musacchio for his unlimited support and advice.

I would like to express my gratitude as well to the current and former lab members of the Robles group, Franziska Brüning, Stella Koutsouli, Fatih Aygenli, Fabian Kliem and Lukas Huschet and the more recent members of my group Nora Kremer and Allan Dsilva.

In addition, I would like to mention my former MS support team at the MPI in Dortmund, Andreas Brockmeyer and Malte Metz, and our MS hosting lab in Munich, Ignasi Forné and Teresa Barth, for the nice atmosphere and valuable collaboration.

I would like to extend my sincere thanks to Susanne Ballenweg for all her administrative support, taking time and mentorship.

I want to gratefully acknowledge funding by the Deutsche Forschungsgemeinschaft (DFG).

And finally, I would like to thank my parents, my husband and my children for their immense understanding, support and encouragement in the past years.

7. Versicherung an Eides statt

Hiermit versichere ich an Eides statt, dass ich die schriftliche Habilitationsleistung selbständig verfasst habe. Alle Teile, die ich aus Publikationen entnommen oder zusammengefasst habe, sind ordnungsgemäß kenntlich gemacht.

München, den 6.5.2023

Tanja Bange

8. Erklärung zur Habilitation

Ich bestätige hiermit, dass dies mein erstes Habilitationsverfahren ist, das ich an einer Universität einreiche, dass mir kein akademischer Grad entzogen wurde und auch kein Verfahren anhängig ist.

München, den 6.5.2023

Tanja Bange

10. Bibliography of attached publications

First/ last authorships T. Bange/ maiden name: T.Woelk

Mueller F., **Bange T.** Identification of N-degrons and N-recognins using peptide pull-downs combined with quantitative mass spectrometry (2023) **Methods Enzymol.**, 2023.686:67-97. Doi:10.10

Mueller, F., Friese, A., Pathe, C., Cardoso da Silva, R., Bravo Rodriguez, K., Musacchio A. *, **Bange, T.*** Overlap of NatA and IAP substrates implicates N-terminal acetylation in protein stabilization. (2021). **Sci Adv**, Jan 7;3 doi:10.1126/sciadv.abc8590 *co-corresponding authors

Pan, D., Brockmeyer, A., Mueller, F., Musacchio, A., **Bange, T.** Simplified Protocol for Cross-linking Mass Spectrometry Using the MS-Cleavable Cross-linker DSBU with Efficient Cross-link Identification. (2018) **Anal Chem**, Sep 18;90(18):10990-10999. doi: 10.1021/acs.analchem. 8b02593

Argenzio E.*, **Bange T.***, Oldrini B.*, Bianchi F., Peesari R., Mari S., Di Fiore PP., Mann M., Polo S. Proteomic Snapshot of the EGF-induced ubiquitin network. (2011) **Mol Syst Biol**., Jan 18;7:462. doi: 10.1038/msb.2010.118. *equal contribution

Woelk T.[§], Oldrini B., Maspero E., Confalonieri S., Cavallaro E., Di Fiore PP., Polo S. Molecular mechanisms of coupled monoubiquitination. (2006) **Nat. Cell Biol.**, Nov 8(11), 1246-1254. doi:10.1038/ncb1484. [§]Woelk is the maiden name

Co-authorships T. Bange

Sing D., Schmidt N., Mueller F., **Bange T**., Bird, AW. Destabilization of Long Astral Microtubules via a Cdk1-Dependent Removal of GTSE1 from Their Plus Ends Facilitates Prometaphase Spindle Orientation. (2021) **Curr Biol**, Feb 22; 31(4):766-781.e8. doi: 10.1016/j.cub2020.11.040

Singh, P., Pesenti, M., Maffini, S., Carmignani, S., Hedtfeld, M., Petrovic, A., Srinivasamani, A., **Bange, T**., Musacchio, A., BUB1 and CENP-U primed by CDK1, are the main PLK1 kinetochore receptors in mitosis. (2021) **Mol Cell**, Jan 7;81(1):67-87e9. doi: 10.1016/j.molcel.2020.10.040

Bruening, F., Noya, SB., **Bange, T**., Koutsouli, S., Rudolph, JD., Tyagarajan, SK., Cox, J., Mann, M., Brown, SA, Robles MS. Sleep-wake cycles drive daily dynamics of synaptic phosphorylation. (2019) **Science,** Oct 11;366(6462):eaav3617. Doi: 10.1126 doi: 10.1126/science.aav3617

Overlack K., **Bange T.**, Weissmann F., Faesen A., Maffini S., Primorac I., Mueller F., Peters JM., Musacchio A. BubR1 promotes Bub3-dependent APC/C inhibition during spindle assembly checkpoint signalling. (2017) **Current Biol**, Oct 9;27(19):2915-2927.e7. doi: 10.1016/j.cub.2017.08.033.

Mosalaganti S., Keller J., Altenfeld A., Winzker M., Rombaut P., Saur M., Petrovic A., Wehenkel AM., Wohlgemuth S., Müller F., Maffini S., **Bange T.**, Herzog F., Waldmann

H., Raunser S., Musacchio A. Structure of the RZZ complex and molecular basis of its interaction with Spindly. (2017) **J Cell Biol**, Apr 3;216(4):961-981. doi: 10.1083/jcb.201611060.

Faesen AC., Thanasoula M., Maffini S., Breit C., Müller F., van Gerwen S., **Bange T.**, Musacchio A. Basis of catalytic assembly of the mitotic checkpoint complex. (2017) **Nature,** Feb 23:542(7642):498-502. doi: 10.1038/nature21384.

Identification of N-degrons and N-recognins using peptide pull-downs combined with quantitative mass spectrometry

Franziska Müller[a] **and Tanja Bange**[b,*]

[a]Department of Mechanistic Cell Biology, Max Planck Institute of Molecular Physiology, Dortmund, Germany
[b]Institute of Medical Psychology, Faculty of Medicine, Ludwig-Maximilians University, Munich, Germany
*Corresponding author: e-mail address: tanja.bange@med.uni-muenchen.de

Contents

Methods in Enzymology
ISSN 0076-6879
https://doi.org/10.1016/bs.mie.2023.02.007

Abstract

Regulated protein degradation controls protein levels of all short-lived proteins to ensure cellular homeostasis and also protects cells from misfolded or other abnormal proteins. The most important players in the degradation system are E3 ubiquitin ligases which recognize exposed sequence motifs, so-called degrons, of target proteins and mark them through the attachment of ubiquitin for degradation. N-terminal (Nt) sequences are extensively used as degrons (N-degrons) and all 20 amino acids are able to feed proteins in 1 of the 5 known N-degron pathways. Studies have mainly focused on characterizing systematically the role of the starting amino acid on protein stability and less on the identification of the E3 ligases involved. Recent data from our lab and literature suggest that there is an extensive interplay of N-recognins and Nt-modifying enzymes like Nt-acetyltransferases (NATs) or N-myristoyltransferases which only starts to be elucidated. It suggests that improperly modified or unexpectedly unmodified proteins become rapidly removed after synthesis ensuring protein maturation and quality control of specific subsets of proteins. Here, we describe a peptide pull-down and down-stream bioinformatics workflow conducted in the MaxQuant and Perseus computational environment to identify N-recognin candidates in an unbiased way using quantitative mass spectrometry (MS)-based proteomics. Our workflow allows the identification of N-recognin candidates for specific N-degrons, to determine their sequence specificity and it can be applied as well more general to identify binding partners of N-terminal modifications. This method paves the way to identify pathways involved in protein quality control and stability acting at the N-terminus.

1. Introduction

The lifespan of cellular proteins ranges from less than a minute to several days. Regulated protein degradation controls levels of all short-lived proteins to ensure cellular homeostasis and also protects cells from accumulating misfolded, aggregated or other abnormal proteins (Varshavsky, 2019). Dysfunctional degradation causes multiple pathological processes, spanning

from developmental and neurodegenerative disorders to cancer (Popovic, Vucic, & Dikic, 2014). Therefore, the identification and understanding of the functional architecture of degradation pathways is of pivotal importance.

Regulated protein degradation is mostly mediated by the ubiquitin proteasome system (UPS) (Hershko & Ciechanover, 1998). The most important players in this system are E3 ligases which recognize exposed sequence motifs, so-called degrons, of target proteins and conjugate ubiquitin (Ub; an 8 kDa protein) to nearby lysine residues on them (Ravid & Hochstrasser, 2008). Ubiquitinated proteins are subsequently destroyed by a multi-subunit protease, the 26S proteasome. The human proteome predicts the existence of around 700 E3 ligases which provide the UPS with specificity to regulate simultaneously very diverse physiological pathways (Zheng & Shabek, 2017).

Degrons can be located anywhere on a protein, but the first degrons, discovered in 1986, are at the very N-terminus of proteins, so-called N-degrons (Bachmair, Finley, & Varshavsky, 1986). Five N-degron pathways have been described so far which can be divided in different subtypes based on the type of N-degron recognized (Fig. 1): (i) recognition of free N-termini (Arg/N-degron pathway (Gibbs, Bacardit, Bachmair, & Holdsworth, 2014; Varshavsky, 2011, 2019); Pro/N-degron pathway (Chen, Wu, Wadas, Oh, & Varshavsky, 2017; Lampert et al., 2018; Melnykov, Chen, & Varshavsky, 2019)); (ii) recognition of modified N-termini (Ac/N-degron pathway (Hwang, Shemorry, & Varshavsky, 2010; Shemorry, Hwang, & Varshavsky, 2013)) or (iii) recognition of an omitted Nt-modification (Gly/N-degron pathway (Timms et al., 2019); nonAc/N-degron pathways (Li et al., 2022; Linster et al., 2022; Mueller et al., 2021; Varland et al., 2022)). The fundamental function of N-degron pathway in protein quality control and stability is well established. But studies so far have mainly focused on characterizing systematically the role of the starting amino acid on protein stability and less on the identification of E3 ligases, so-called N-recognins. The recent data on new N-degron pathways reinforce the assumption that many more E3 ligases act as N-recognins in N-degron pathways and more N-degron pathways exist than hitherto believed. Since N-degron pathways are involved in a plethora of pathways and impairment might lead to human pathologies like, e.g., cancer or neurodegeneration (Varshavsky, 2019), the need for methods to uncover the unknown players of these networks grows.

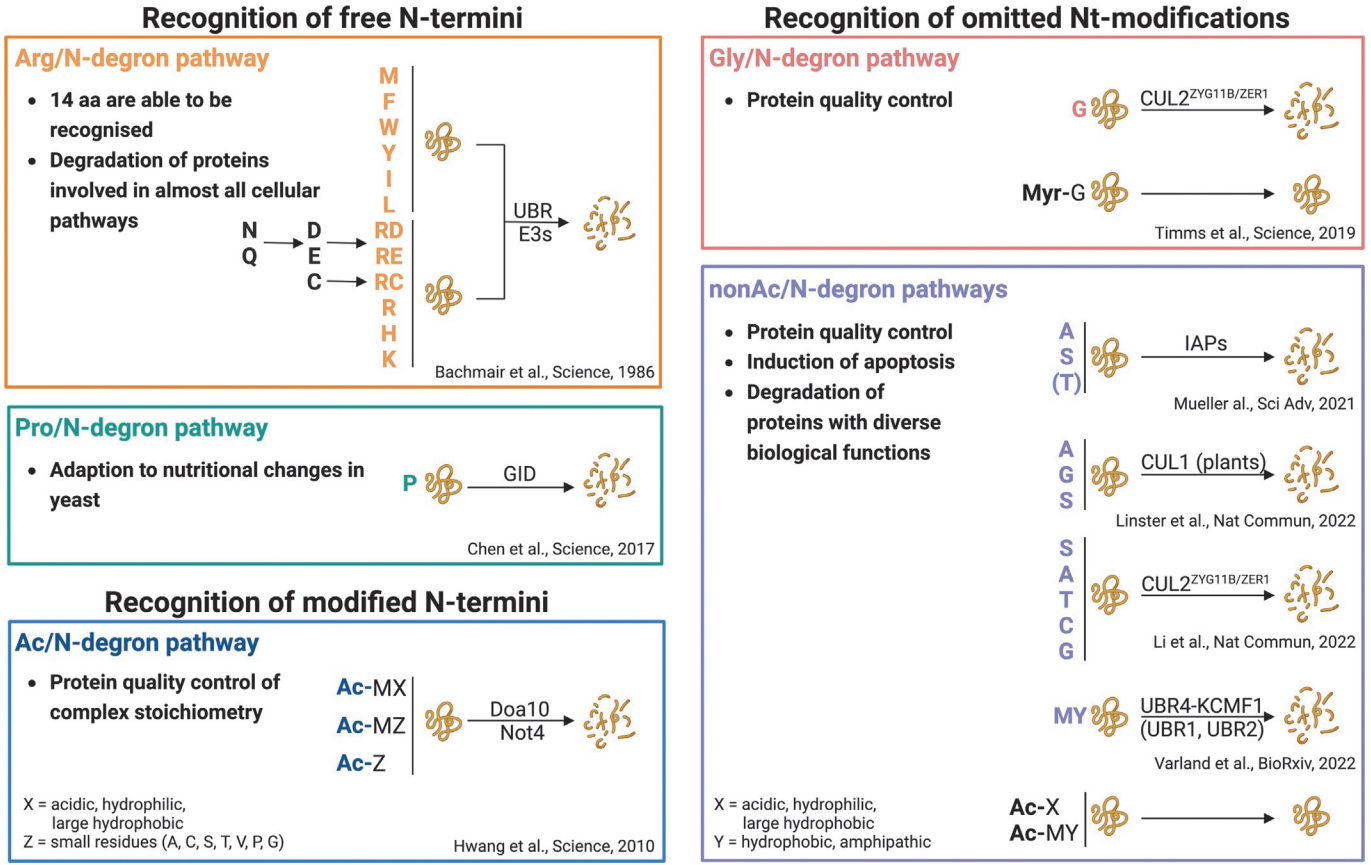

Fig. 1 Overview of the known N-degron pathways. N-degron name, function, recognized amino acids and E3 ligases are indicated. Amino acids are abbreviated with single letter code. The details of the enzymatic reactions for N, Q, D, E and C to feed in the Arg/N-degron pathway are shown only schematically with an arrow. UBR: ubiquitin-protein ligase E3 component N-recognin; X are acidic, hydrophilic and large hydrophobic amino acid residues; Z are small amino acid residues (A, C, S, T, V, P, G); Y are hydrophobic and amphipathic amino acid residues; IAPs: inhibitor of apoptosis E3 ligase proteins; CUL: cullin; GID: glucose induced degradation E3 ligase complex.

This chapter describes a peptide pull-down workflow combined with quantitative mass spectrometry (MS)-based proteomics and downstream bioinformatics analysis to identify N-recognin candidates for specific N-degrons (Mueller et al., 2021). This method has the unique advantage of being able to provide candidates in an unbiased way without prior knowledge and can be applied as well to identify interaction partners dependent on any Nt-modification. We provide detailed protocols for peptide design (Section 3), preparing pull-down input material (Section 4) and peptide pull-down performance (Sections 5 and 6). Sections 7 and 8 contain protocols for the preparation of the samples for MS measurement and a summary of the MS method. Sections 9 and 10 refer to the downstream bioinformatic analysis of the obtained MS raw data using the freely available software MaxQuant and Perseus to obtain a final list of candidate N-recognins and/or Nt-specific interaction partners (Cox & Mann, 2008; Tyanova et al., 2016).

2. Method overview and work flow

MS-based quantitative proteomics is a powerful technique that allows the comprehensive and unbiased analysis of the protein composition of pulled-down complexes. Taking advantage of this technology, we developed a peptide pull-down workflow to identify proteins associated with acetylated (ac) or not acetylated (free) protein N-termini (Mueller et al., 2021). If acetylated N-terminal (ac-Nt) or free N-terminal (free-Nt) sequences are part of N-degrons, they ought to act as determinants of interactions with specialized receptors on E3 ligases or associated proteins, which can be identified by quantitative MS.

To this end, synthetic biotinylated peptide pairs (e.g., ac-Nt or free-Nt) encompassing the Nt-region of proteins are bound to streptavidin beads, then incubated with cellular lysates and binders identified by quantitative MS (see Fig. 2 for a workflow overview). We performed peptide pull-downs with ac-Nt and free-Nt using cellular lysates as input material, but the method can be extended to identify interaction partners of any N-terminal modification pair and other input material like tissue in an unbiased way.

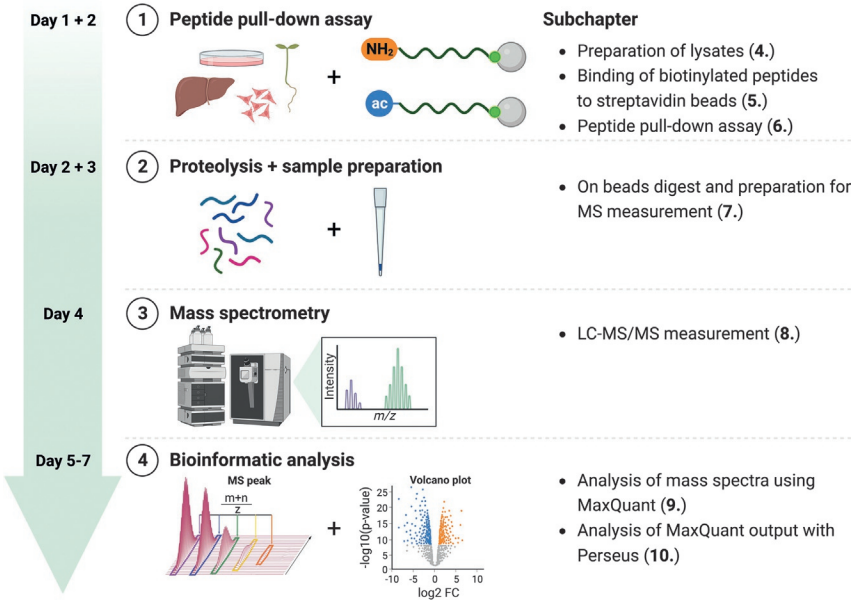

Fig. 2 Workflow overview for the peptide pull-down method combined with quantitative MS described in this chapter. Small green circle: biotin; large gray circle: streptavidin beads; ac: acetyl group; NH_2: free Nt group.

3. General considerations for peptide design

We tested different peptide lengths, linkers (e.g., PEG; Lysine-Lysine (KK); Glycine-Serine-Glycine (GSG)) and linker lengths for optimal pull-down results. We recommend to use the first 10 amino acids (aa) of the N-terminus adding KK to improve general solubility and a final biotinylated lysine to be able to attach the peptide to streptavidin beads. The peptides are usually ordered as pairs (e.g., from GenScript) with a purity of >95% with the sole difference of the Nt-modification. See an example of peptide design in Table 1.

Of note is, that using a KK linker has the disadvantage that the peptide is digested by trypsin and will give a dominant peak in the MS measurement which in some cases might overlay candidates. The problem occurs per se if lysine or arginine are present in the peptide sequence. If MS results do not reveal good candidates, an alternative peptide design with a different linker, i.e., substitution of KK by a GSG linker, should be considered and can help to improve results.

Table 1 Example of peptide pair design using an ac-Nt and free-Nt peptide. **Protein of interest, e.g., COMMD10**

			Modification	
Version	**aa 1–10**	**Linker**	**N-terminal**	**C-terminal**
free-Nt	AVPAALILRE	KK	–	K(Biotin)
ac-Nt	AVPAALILRE	KK	Acetylation	K(Biotin)

4. Preparation of lysates for peptide pull-downs

We describe here the preparation of the biological input material which will be used to identify interaction partners of bait peptides. We focus on cellular lysates, but any other input material, e.g., tissue, plant material, etc. can be used as well.

4.1 Equipment

- Cell culture hood
- Tissue culture dishes or flasks (Sarstedt)
- Water bath at 37 °C
- Sonifier (Branson)

4.2 Reagents

Prepare all solutions using analytical grade reagents and reagents suitable for cell culture. Store all reagents at −20 °C (unless indicated otherwise).

- Dulbecco's modified eagle medium (DMEM, PAN Biotech), store at 4 °C
- Phosphate buffered saline (PBS) pH 7.4, store at room temperature (RT)
- Fetal bovine serum (FBS, Gibco)
- L-Glutamine (Pan Biotech)
- Trypsin-EDTA (Pan Biotech), store at 4 °C
- Lysis buffer: 75 mM HEPES pH 7.5, 150 mM KCl, 1.5 mM EGTA (pH 8.0), 1.5 mM $MgCl_2$, 10% glycerol, store at 4 °C
- Nonidet® P 40 Substitute (NP-40) (Merck)
- Protease inhibitor cocktail (Serva)
- Benzonase® Nuclease (Sigma-Aldrich)
- Dithiothreitol (DTT)
- PhosSTOP phosphatase inhibitors (Roche)

4.3 Procedure

1. Grow HeLa cells in DME medium supplemented with 10% FBS and 2 mM L-glutamine in incubators at 37 °C, 5% CO_2 (see notes 1 and 2).
2. Harvest cells at a confluency of 60–80%. For harvesting, remove media and wash attached cells once with prewarmed PBS.
3. Detach cells with trypsin (in 37 °C incubator) and collect them in DMEM afterwards.
4. Centrifuge at 500×*g* for 5 min at RT.
5. Wash cell pellet once with PBS and centrifuge.
6. Remove supernatant and flash freeze pellet in liquid nitrogen (see note 3).
7. Add lysis buffer supplemented with 0.1% NP-40, protease inhibitor cocktail 1:250, Benzonase® Nuclease 1:5.000–1:10.000, 1× PhosSTOP phosphatase inhibitors and 1 mM DTT to the frozen cell pellet (circa 0.5 mL/10 cm dish).
8. Resuspend cell pellet on ice by pipetting about 50 times up and down using a micropipette.
9. Sonification: Use a sonifier combined with a small sonication tip. Settings are: 2 × 10 pulses, 50% duty cycle, output control 3 (see note 4).
10. Clear lysate by a centrifugation step at ≥20,000×*g*, 4 °C for 30 min.
11. Transfer the supernatant to a new reaction tube and determine the concentration by measuring the absorbance at 280 nm with a NanoDrop spectrophotometer (see note 5).
12. Keep cell lysates on ice until further use in procedure Section 5.3 (peptide pull-down) (see note 6).

4.4 Notes

1. We describe here peptide pull-downs using untreated HeLa cells but the method is as well suited for other primary and transformed cell lines, tissue or material from other species like, for example, plant extracts. Adopt to eventual different media requirements of other cell lines. The requirement for the method is a soluble homogenous protein extract. Cells can be as well treated or synchronized under adaptive conditions likely reflecting broad ongoing generation of targeted protein degradation. For example, in the apoptotic process, a plethora of new N-termini is generated through cleavage and proteins are degraded rapidly. If sample amounts are limiting, peptide pull-downs can be successful as well with lower amounts of starting material.

2. For reliable label-free quantification and statistics after MS measurement, peptide pull-downs have to be performed at least in triplicates for each peptide. Consider for each pull-down replicate 1–3 mg of cell lysate and plate enough 10–15 cm dishes or flasks for the entire experiment (e.g., one confluent 10 cm dish of HeLa cells will yield 4–6 mg of lysate).
3. After flash freezing in liquid nitrogen, cell pellets can be stored in a −80 °C freezer and lysed at a later time point.
4. As alternative to the sonifier and sonication tip, a bioruptor (e.g., Bioruptor Plus; Diagenode) can be used.
5. Any other method to determine protein concentration compatible with reducing reagents (1 mM DTT) and buffer components can be used as well.
6. If not used immediately, cellular lysates can be flash frozen in liquid nitrogen in small aliquots (5–10 mg) and stored at −80 °C.

5. Binding of biotinylated peptides to streptavidin beads

Peptide pull-downs have to be performed at least in triplicates ($n \geq 3$) to obtain a reliable label-free quantification of binding partners and to be able to apply statistical tests to identify suitable N-recognin candidates. Keep this in mind when preparing peptides and solutions. The binding of biotinylated peptides to streptavidin beads consists of: (a) preparation of biotinylated peptides; (b) preparation of Streptavidin Dynabeads; (c) binding of biotinylated peptides to beads. The steps require for one peptide pair in triplicates circa 1.5 h for calculations, pipetting, incubation and washing steps.

In our experience, peptide pull-down assays work optimal when biotinylated peptides are first bound to streptavidin beads and then incubated with lysates. But if no candidate E3 ligases or adaptors are identified, biotinylated peptides can be first incubated with lysates and then bound to streptavidin beads.

Mutations or swaps of amino acids in the Nt-peptide can be used to determine sequence specificities of candidate N-recognins or as well as controls. Pull-downs with beads without conjugated peptide can be performed but are not necessary to identify potential N-recognins because we are interested in different interaction partners between the peptide pair(s) and not in common binding partners.

5.1 Equipment

- 1.5 mL low binding tubes (Eppendorf)
- Magnetic rack (e.g., Eppendorf or PerkinElmer) (see note 1)
- Vortex
- Rotation wheel
- Vacuum pump

5.2 Reagents

Prepare all solutions using ultrapure water and analytical grade reagents. Prepare and store all reagents at RT (unless indicated otherwise).

- Dimethylsulfoxid (DMSO)
- Magnetic beads (Dynabeads™ MyOne™ Streptavidin T1; ThermoFisher), store at 4 °C
- Phosphate buffered saline (PBS) pH 7.4

5.3 Procedure

The subsequent procedures are performed at RT.

(a) Preparation of biotinylated peptides

1. Dissolve lyophilized peptides in DMSO to obtain a stock solution of 10 mM. Aliquot and store at −20 °C.
2. For peptide pull-down assays, dilute peptides in PBS to obtain a concentration of 1 μg/μL.

(b) Preparation of Streptavidin Dynabeads

1. Calculate 50 μL slurry of Dynabeads™ MyOne™ Streptavidin T1 for each peptide pull-down assay. Calculate total amount of slurry required for the experiment (sixfold for one pair of peptides in respective triplicates). Add the amount of one replicate more per peptide pair in the experiment (to account for loss through pipetting) and pipette the total required amount of slurry in a 1.5 mL Eppendorf tube, e.g., for one peptide pair 350 μL (7 × 50 μL) (see note 2–5).
2. Vortex for 5 s, let beads settle down in magnetic rack for 1–2 min, withdraw supernatant with a vacuum pump (see note 6).
3. Wash beads twice with 1 mL of PBS in the same way as in the previous step.
4. Prepare one 1.5 mL tube for each peptide.
5. Put the original calculated slurry volume of PBS on the beads and divide beads in aliquots to bind peptides for triplicate assays. Use 175 μL slurry per peptide (see note 7).

6. Put in magnetic rack, withdraw PBS. Beads are ready for binding to the biotinylated peptide.

(c) Binding of biotinylated peptides to beads

1. Pipette 9–12 μL of 1 μg/μL peptide dilution from above (circa 2 nM peptides) and add PBS to a final volume of 1 mL. 9–12 μL peptides are calculated for assays in triplicates (see note 8).
2. Rotate samples at RT for 30 min.
3. Wash 3× with 1 mL of PBS (vortex, magnetic rack 1–2 min, withdraw liquid) to remove excess of peptides (see note 9).
4. After the last wash, add 175 μL PBS, vortex and divide beads in 3 × 50 μL for three replicates (see note 10).
5. Let beads settle in magnetic rack and withdraw liquid. Beads are ready for the peptide pull-down.

5.4 Notes

1. The use of 96-deep well plates (DPW) is recommended when working with more than 20 samples.
2. Peptide pull-downs can be performed with any kind of streptavidin beads. We adapted the protocol various times and use now magnetic beads for convenience and optimal results. We used as well, for example, Streptavidin Sepharose® High Performance from GE Healthcare with comparable results (the binding buffer changes from PBS to: 50 mM Tris (pH 8), 150 mM NaCl, 0.075% NP-40). In case of sepharose or agarose beads, a table centrifuge is required instead of a magnetic rack. Centrifuge beads according to manufacturer's protocol.
3. The streptavidin bead amount for peptide pull-down assays depends on the binding capacity of the beads. Peptide pull-down assays give the best results with 200–300 pmol of peptide bound to beads. It is very important to saturate beads with biotinylated peptides and thus to calculate and test bead amounts accordingly. For Dynabeads™ MyOne™ Streptavidin T1 the binding capacity for peptides is 400 pmol/mg slurry (beads are provided as 10 mg/mL). 50 μL of slurry are able to bind 200 pmol of peptides (approximately 300–400 ng of peptide depending on the molecular weight) and gave the most reliable quantifications and clearest candidates in a series of tests.
4. When pipetting slurry, we cut pipette tips and vortex briefly before pipetting to ensure a homogenous distribution of beads in the slurry and equal bead amounts in all samples.

5. We do not separate the slurry for single peptide pull-downs as long as possible. This means we wash the total amount of beads for all pull-downs together, then we separate beads in the number of peptides but keep triplicates together and then we pipette the amount for single peptide pull-downs. In our experience this reduces noise in the LC (liquid chromatography)-MS/MS measurements due to unequal peptide-bead amounts in the individual assays and gives clearer results for E3 ligase candidates.
6. The supernatant can be removed as well with a pipette.
7. We need 150 μL (3 × 50 μL) for the triplicates. Since we calculated one sample more per peptide pair than present in the experiment to avoid running out of beads for the last sample(s), we take 175 μL of slurry out of 350 μL for each triplicate.
8. We recommend a 10× excess of peptide over binding capacity of calculated bead amount to ensure saturation of beads with peptide. A 10× excess corresponds to circa 3–4 μg of peptide for each peptide pull-down and 9–12 μg for triplicates depending on the molecular weight. Therefore, we use 9–12 μL of peptide dilution (1 μg/μL) for 175 μL of slurry.
9. It is important to thoroughly remove excess peptides from beads before the pull-down assay to avoid binding of proteins to soluble peptides in the pull-down assay.
10. The additional 25 μL is only to ensure that there is enough slurry for all three pull-downs.

6. Peptide pull-down assay

We use the lysates prepared in Section 4.3 and the peptide-bead conjugates prepared in Section 5.3 to perform the actual peptide pull-down. We describe the workflow for one set of experimental triplicates, but recommend to repeat the peptide pull-downs as well as biological replicates from different lysate preparations.

The procedure takes circa 30 min–1 h for one peptide pair, an overnight incubation and circa 30 min–1 h for washing the pull-downs the next day.

6.1 Equipment

- 1.5 mL low binding tubes (Eppendorf)
- Rotation wheel
- Magnetic rack

6.2 Reagents

Prepare all solutions using ultrapure water and analytical grade reagents. Prepare and store all reagents at 4 °C (unless indicated otherwise).

- Complete lysis buffer: 75 mM HEPES pH 7.5, 150 mM KCl, 1.5 mM EGTA (pH 8.0), 1.5 mM $MgCl_2$, 10% glycerol, 0.075% NP-40 completed with 1 mM DTT, PhosphoStop, Protease Inhibitor Mix (see Section 4.2)
- Lysis buffer without detergent (NP-40) and glycerol

6.3 Procedure

1. Keep lysates always on ice.
2. Use freshly prepared lysates or unfreeze previously prepared lysates on ice (see Section 4.3).
3. Prepare lysates at a concentration of 2 μg/μL. If necessary, dilute with complete lysis buffer. Prepare 1 mg (500 μL) of lysate for each peptide pull-down (see note 1).
4. Add 500 μL of 2 μg/μL lysate to peptide-conjugated beads from Section 5.3. Incubate at 4 °C overnight on a rotation wheel (16–20 h).
5. Next day, wash beads 2× with 1 mL complete lysis buffer and 2× with 1 mL lysis buffer prechilled on ice without detergent and glycerol. Wash by inverting the tubes 10–15 times, then let the beads settle for 1–2 min in a magnetic rack and withdraw supernatant. After removing the supernatant of the 4th wash, proceed directly with the tryptic digest and preparation for MS analysis described in Section 7.3 (see notes 2 and 3).

6.4 Notes

1. We prepare lysates as master-mix for experimental replicates and calculate one sample in excess to avoid reduced lysate amount for the last sample(s). If peptide pull-downs are not successful, we recommend to increase starting material to 3 mg.
2. Avoid vortexing samples after peptide pull-downs, we realized reduced intensities of bound proteins in the MS measurements.
3. Washes with buffer without detergents and glycerol to remove NP-40 and glycerol is critical, since they interfere with down-stream LC-MS/MS analysis.

7. On beads digest and preparation for MS analysis

There is no elution step from the beads required and it can be directly proceeded with the tryptic digest on beads and the preparation for MS measurement. The procedure takes circa 4 h, an overnight incubation and circa another 2 h the next day, then samples are ready for MS measurement.

7.1 Equipment

- 1.5 mL low binding tubes (Eppendorf)
- Thermomixer (Thermoblock plus, Eppendorf)
- Vacuum concentrator (Vacuum concentrator Plus, Eppendorf)
- Blunt-ended syringe
- Sterile filters: 0.22 μm
- Optional: sonication water bath

7.2 Reagents

Prepare all solutions using ultrapure water, analytical grade and LC-MS/MS grade reagents where stated. Prepare and store all reagents at RT (unless indicated otherwise).

- 1 M NH_4HCO_3 (ammonium bicarbonate, ABC): Weigh 4.0 g NH_4HCO_3. Add MS-grade water to a final volume of 50 mL and sterile filter (0.22 μm)
- 1 M dithiothreitol (DTT): Weigh 1.54 g DTT. Add 200 μL of 1 M ABC (final concentration 20 mM ABC). Add sterile water to a volume of 10 mL and sterile filter. Aliquots can be stored at −20 °C
- 0.55 M chloroacetamide (CAA): Weigh 514 mg CAA. Add 200 μL of 1 M ABC (final concentration 20 mM ABC). Add sterile water to a volume of 10 mL and sterile filter. Aliquot and store at −20 °C
- Reduction buffer: 8 M urea in 40 mM Hepes (pH 8.0). Always prepare fresh. Weigh 480 mg urea. Add 40 μL 1 M HEPES (pH 8.0) and 1 μL of 1 M DTT. Fill up to 1 mL with H_2O
- Lysyl endopeptidase (LysC; Wako): Dissolve 1 mg LysC in 2 mL of 20 mM ABC to obtain a stock solution of 0.5 μg/μL. Aliquot and store at −80 °C
- Trypsin endopeptidase (Tryp; Sigma): Dissolve 1 mg Trypsin in 1 mL 10 mM HCl to obtain a stock solution of 1 μg/μL. Aliquot and store at −80 °C

- Trifluoracetic acid (TFA), LC-MS grade
- Stop solution: 10% TFA in LC-MS grade water
- Methanol (MeOH); LC-MS grade
- Formic acid (FA), LC-MS grade
- Buffer A: 0.1% FA in LC-MS grade water. Add 1 mL of 10% FA to 100 mL of LC-MS grade water
- Buffer B: 0.1% TFA in 60% acetonitrile. Add 1 mL of 10% TFA to 40 mL of LC-MS grade water and fill up with acetonitrile (100%) to a final volume of 100 mL
- LC-MS loading buffer: 0.1% TFA in LC-MS grade water
- Octadecyl (C18) solid phase extractions discs (Affinisep)

7.3 Procedure

1. Add 50 μL reduction buffer to the beads and incubate samples at RT for 30 min with rapid agitation (1.000 rpm) (see note 1).
2. Add 5.5 mM CAA at RT for 20 min with rapid agitation (1.000 rpm) (see note 1).
3. Add 50 μL of 20 mM ABC (final urea conc.: 4 M) containing 1 μg LysC and incubate at RT for 1 h with rapid agitation (1.000 rpm). Let beads settle in a magnetic rack. Take supernatant (SN 1) and collect in new 1.5 mL tube (see note 2).
4. Add 50 μL 20 mM ABC containing 1 μg trypsin and incubate at RT for 1 h with rapid agitation (1.000 rpm). Take supernatant (SN 2) and combine with SN1.
5. Add 50 μL 20 mM ABC, pipette beads up and down, let beads settle in a magnetic rack and then take the supernatant (SN 3) and combine with SN 1 and 2.
6. Add again 1 μg trypsin to pooled supernatants (SN 1–3) and continue the digest overnight at RT with rapid agitation (1.000 rpm) (16–20 h) (see note 2).
7. Add 5 μL of 10% TFA to each sample to acidify peptides before desalting and concentration in C18 StageTips. The pH should be below <3 (see note 3).
8. Prepare C18 StageTips (3 layers) as previously described (Rappsilber, Mann, & Ishihama, 2007). In brief: stamp out a small disk from three layers of C18 Solid Phase Extraction Disks with a blunt-ended syringe and plunge into a 200 μL pipette tip.

9. Activate StageTips with 100 µL Methanol and equilibrate with 100 µL buffer A before loading samples. Centrifuge 3–5 min with 200×*g* (see note 4 and 5).
10. Load digested peptides on equilibrated StageTips. Centrifuge 3–5 min with 200×*g*.
11. Wash StageTips with 100 µL Buffer A. Centrifuge 3–5 min with 200×*g*.
12. Place StageTips on top of new 1.5 mL low binding reaction tubes or a 96-well plate. Put 2 × 20 µL Buffer B on StageTips, incubate for 1 min and elute peptides by centrifuging 3–5 min with 200×*g*.
13. Dry in speed vac for circa 20 min at 45 °C (see note 6).
14. Resuspend peptides in 6 µL LC-MS loading buffer for LC-MS/MS analysis (see note 7) and transfer in UHPLC autosampler compatible vials.

7.4 Notes

1. Reduction and alkylation are important sample preparation steps for LC-MS/MS analysis. Low alkylation efficiency of cysteines leads to decreased identification rates, because unmodified cysteines are oxidized in gas phase spontaneously or are not identified with standard search engine settings.
2. We crudely digest the denatured proteins first with LysC because it works at 4 M urea, then add Trypsin in <2 M urea and finally we leave the samples overnight to complete the digest. If increased sequence coverage of proteins is necessary or proteins of interest have only few tryptic MS compatible peptides (<6 aa or >20 aa) consider using other specific proteases (i.e., GluC).
3. It is important that peptides are completely cleared of precipitates to avoid blockage of C18 StageTips. In case precipitates are visible, centrifuge for 10–15 min with max. speed and load supernatant on StageTips.
4. Use either a modified mini centrifuge for stage tipping from Sonation or adaptors to place StageTips on 2 mL reaction tubes.
5. One layer of C18 is able to bind 2–4 µg of peptides (Rappsilber, Ishihama, & Mann, 2003).
6. This step serves the removal of acetonitrile. You can dry samples to complete dryness but do not leave samples for prolonged periods of time in the speed vac otherwise resuspension of peptides gets more difficult.

7. Peptides can be resuspended with the aid of sonication water bath (3–5 min). Resuspended peptides can be stored at −20 °C for months prior to the measurement. In that case, thaw, sonicate a few minutes in a water bath, and briefly spin down peptides prior to injection.

8. LC-MS/MS measurement

We use a 90 min MS method for each peptide pull-down.

8.1 Equipment

- Ultra-high pressure liquid chromatography (UHPLC), e.g., Ultimate 3000 UHPLC or EASY-nLC™ 1200 ultra-high pressure system (Thermo Fisher Scientific) (see note 1)
- Nano-electrospray ion source, e.g., NanoFlex source (Thermo Fisher Scientific)
- Column Oven (sonation)
- High-resolution mass spectrometer, e.g., Orbitrap Exploris™ 480 (Thermo Fisher Scientific) (see note 2)

8.2 Reagents

- Chromatography column: 50 cm, 75 μm inner diameter, ReproSil-Pure C18-AQ 1.9 μm resin (Dr. Maisch GmbH) (see note 3)
- Running buffer A: 0.1% (*v*/v) formic acid in MS grade water (Thermo Fisher Scientific)
- Running buffer B: 0.1% (v/v) formic acid in 80% (v/v) acetonitrile (Thermo Fisher Scientific)

8.3 Procedure

Perform reverse-phase chromatography on a UHPLC coupled to a high-resolution mass spectrometer with a nano electrospray ion source.

1. Load 4 μL out of 6 μL of the digested peptide pull-downs onto a C18 reversed phase column (see note 3).
2. Separate the peptides with a linear gradient of 5%–30% running buffer B for 70 min at a flow rate of 300 nL/min on a 50 cm column with a column oven temperature of 60 °C (gradient is shown in Table 2).
3. Perform LC-MS/MS measurement with a high-resolution mass spectrometer, e.g., Orbitrap Exploris™ 480 (Bekker-Jensen et al., 2020):

Table 2 UHPLC gradient used for the MS measurement of peptide pull-downs.

Time (min)	Duration (min)	Flow (nL/min)	% B
0	0	300	5
70	70	300	30
76	6	300	60
79	3	300	95
84	5	300	95
87	3	300	5
90	3	300	5

Acquire MS data in a data-dependent mode acquiring one survey scan (MS scan) and subsequently 20 MS/MS scans of the most abundant precursor ions from the survey scan (Top20 method). Use a mass range of m/z 300–1650 and set the target value to 3×10^6 precursor ions with 1.4 Th isolation window. Acquire data with a resolution of 60.000 for full scans and 15.000 for MS/MS scans. Exclude unassigned precursor ion charge states and singly charged ions. To avoid repeated sequencing exclude already sequenced ions dynamically for 30 s. The MS method is summarized in Table 3.

8.4 Notes

1. Any UHPLC compatible with the MS and any high-resolution mass spectrometer can be used for the measurement. We currently use an Orbitrap Exploris™ 480, but we analyzed peptide pull-downs already as well on a Q Exactive™ plus, HF and HFX with Top 10–15 methods (Kelstrup et al., 2018; Scheltema et al., 2014).
2. Peptides should elute across the complete gradient and reach a total current (NL) of up to 1-2E10. Q Exactive™ Plus, Q Exactive HF and HFX should reach the same total ion current. Starting material amounts, resuspension or injection volumes can be changed if intensities are too high or low.
3. Commercial (e.g., from Thermo Fisher Scientific or IonOpticks) or self-packed columns between 20 and 50 cm can be used.

Table 3 MS method settings to measure peptide pull-downs.

Method Settings:
Application Mode: **Peptide**
Method Duration (min): **90**
Global Parameters:
Ion Source
Ion Source Type: **NSI**
Spray Voltage: **Static**
Positive Ion (V): **2300**
Negative Ion (V): **600**
Gas Mode: **Static**
Ion Transfer Tube Temp (°C): **275**
Use Ion Source Settings from Tune: **False**
FAIMS Mode: **Not Installed**
MS Global Settings
Infusion Mode: **Liquid Chromatography**
Expected LC Peak Width (s): **15**
Advanced Peak Determination: **True**
Default Charge State: **2**
Internal Mass Calibration: **Off**
Experiment:
Start Time (min): **0**
End Time (min): **90**
Master Scan:
Full Scan
Orbitrap Resolution: **60000**
Scan Range (m/z): **300-1650**
RF Lens (%): **40**
AGC Target: **Custom**
Normalized AGC Target (%): **300**
Maximum Injection Time Mode: **Custom**

Continued

Table 3 MS method settings to measure peptide pull-downs.—cont'd

Maximum Injection Time (ms): **20**
Microscans: **1**
Data Type: **Profile**
Polarity: **Positive**
Source Fragmentation: **Disabled**
Scan Description:
MIPS
Monoisotopic peak determination: **Peptide**
Relax restrictions when too few precursors are found: **True**
Intensity
Filter Type: **Intensity Threshold**
Intensity Threshold: **2.0e4**
Charge State
Include charge state(s): **2-6**
Include undetermined charge states: **False**
Dynamic Exclusion
Dynamic Exclusion Mode: **Custom**
Exclude after n times: **1**
Exclusion duration (s): **30**
Mass Tolerance: **ppm**
Low: **10**
High: **10**
Exclude isotopes: **True**
Perform dependent scan on single charge state per precursor only: **False**
Data Dependent
Data Dependent Mode: **Number of Scans**
Number of Dependent Scans: **20**

Table 3 MS method settings to measure peptide pull-downs.—cont'd

ddMS^2
Multiplex Ions: **False**
Isolation Window (m/z): **1.4**
Isolation Offset: **Off**
Collision Energy Type: **Normalized**
HCD Collision Energies (%): **30**
Orbitrap Resolution: **15000**
TurboTMT: **Off**
Scan Range Mode: **Define First Mass**
First Mass (m/z): **100**
AGC Target: **Custom**
Normalized AGC Target (%): **100**
Maximum Injection Time Mode: **Custom**
Maximum Injection Time (ms): **28**
Microscans: **1**
Data Type: **Profile**
Scan Description:

9. Analysis of mass spectra using MaxQuant

We process MS raw data with MaxQuant to obtain .txt output files of quantified peptides and proteins which can be further bioinformatically analyzed for potential N-recognin candidates. Detailed information about the operation and settings of MaxQuant can be found here: https://www.youtube.com/c/MaxQuantChannel.

9.1 Requirements and equipment

MaxQuant is a freely available software and can be downloaded from https://maxquant.net/maxquant/. Information for the installation and hardware requirements are available at http://coxdocs.org/doku.php?id=maxquant:start.

9.2 Procedure

Use default settings as described to identify proteins and peptides (Cox & Mann, 2008) (see note 1). Important points are briefly described in the following procedure points.

1. Analyze raw data with the MaxQuant software using the integrated search engine Andromeda (Cox et al., 2011). MaxQuant has a common contaminants list included (e.g., BSA, Trypsin, etc.). Use the default settings.
2. Use the latest Uniprot FASTA database of the species used in your experiment for the search with the search engine. You can download the latest Uniprot FASTA files here: https://ftp.uniprot.org/pub/databases/uniprot/current_release/knowledgebase/reference_proteomes/ (see note 2).
3. Use Trypsin as the digestion mode (or change accordingly in case you used other proteases) and allow for a maximum of two missed cleavages. Set N-terminal acetylation and methionine oxidation as variable modification and carbamidomethyl cysteine as a fixed modification. False discovery rate (FDR) should be at 1% on both the peptide and protein levels.
4. Quantify proteins in MaxQuant using the built in XIC-based label-free quantification (LFQ) algorithm (Group-specific parameters → Label-free quantification → select: LFQ) (Cox et al., 2014).
5. Enable "match between runs" to transfer identifications between replicates (Global parameters → Identification → select: Match between runs).
6. Use the experimental design option to ensure LFQ values for all replicates and identification transfer only within replicates (Raw data tab → Write template → open template in Excel, fill in and save under experimentalDesign → return to MaxQuant and load experimentalDesign by clicking on Read from file; see note 3). An example of a typical experimental design for an ac-Nt versus free-Nt peptide pair for MaxQuant analysis is shown in Table 4.
7. MaxQuant output is a folder of .txt files (…combined/txt) which are building up hierarchically form MS/MSscans.txt to proteinGroups.txt files. For the further analysis in Perseus use the proteinGroups.txt file (see note 4).

9.3 Notes

1. Note that default or standard settings are for Orbitrap-based instruments. In case of other high-resolution mass spectrometers, e.g., timsTOF

Table 4 Experimental design for MaxQuant analysis.

Raw file name	Fraction	Experiment
xxx_ac_1	1	ac_1
xxx_ac_2	1	ac_2
xxx_ac_3	1	ac_3
xxx_free_1	10	free_1
xxx_free_2	10	free_2
xxx_free_3	10	free_3

you need to adjust the settings. You find the information on the website indicated above.

2. Download the main and additional FASTA file from your species of interest for your search. The proteomes are coded by numbers. Go to https://www.uniprot.org/proteomes/ to look for the number of your species of interest if not sure.
3. Note that identifications of adjacent numbers in fractions are transferred from one raw file to the others, therefore use numbers apart for different peptides, e.g., 1 and 10).
4. Prior to analysis with Perseus, open the summary.txt file from the MaxQuant output folder to check measurement quality, e.g., in Excel: check if the number of peptides is roughly comparable across samples (in the column Peptides Sequences Identified). The percentage of identified MS/MS should be above 30% in peptide pull-down experiments using Orbitrap equipment. Differing numbers of peptide identifications and low percentage of identified MS/MS indicate experimental, technical or LC-MS/MS instrumentation problems and the experiment has to be repeated.

10. Analysis of MaxQuant output files with Perseus

We analyze the MaxQuant ProteinGroups.txt output file with Perseus. Detailed information about the operation and settings of Perseus can be found here: https://www.youtube.com/c/MaxQuantChannel.

10.1 Requirement and equipment

Perseus is a freely available software and can be downloaded from https://maxquant.net/perseus/. Information for the installation and hardware requirements are available at http://coxdocs.org/doku.php?id=perseus:start.

10.2 Procedure

We describe the data analysis to ensure data quality, to identify potential N-recognins (and/or interaction partners) binding with significant difference to peptides and how data can be visualized (Fig. 3A–D).

1. Upload the proteinGroups.txt file from the MaxQuant output folder (…/combined/txt/proteinGroups) and select LFQ intensities as main columns.
2. Remove contaminant, reverse hits and quantifications based on modified peptides by filtering rows based on categorical column (Filter rows → Filter based on categorical column → select: Only identified by site, Reverse hits and Contaminants; Mode: Remove matching rows; Filter mode: Reduce matrix).
3. Logarithmically transform dataset to obtain normally distributed LFQ intensities (Basic → Transform → Transformation: log2(x)). Check normal distribution by using the histogram function in Perseus (see note 1).
4. Assign replicates of one experiment to one group by appending identical group names; e.g., by removing the replicate number leaving ac and free (Annot. Rows → Categorical annotation rows).
5. Filter out proteins not consistently quantified (Filter rows → Filter rows based on valid values; Min. valids: 2 or 3 (for triplicates); Mode: In at least one group; Filter mode: reduce matrix).
6. Replace missing values (NaN) with values from a normal distribution generated based on the measured data (Imputation → Replace missing values from a normal distribution) leaving the standard settings for Width (0.3) and Downshift (1.8). Check data imputation with the histogram function highlighting the imputed data (Selection from imputed data) (note 2).
7. Check reproducibility between replicates and conditions to assess data quality by calculating the Pearson correlation (Basic → Column correlation) (see note 3).
8. Perform a principal component analysis (Clustering/PCA → Principal component analysis) to evaluate technical and biological variations between replicates and peptide pairs (Fig. 3A) (see note 4).
9. Identify significantly different binding partners for peptide pairs by performing a statistical hypothesis test, e.g., unpaired *t*-test with a permutation-based FDR for peptide pairs (Tests → Two-sample tests) or an ANOVA test if multiple conditions are compared (Tests → Multiple-sample test) (see note 5). Use standard settings in

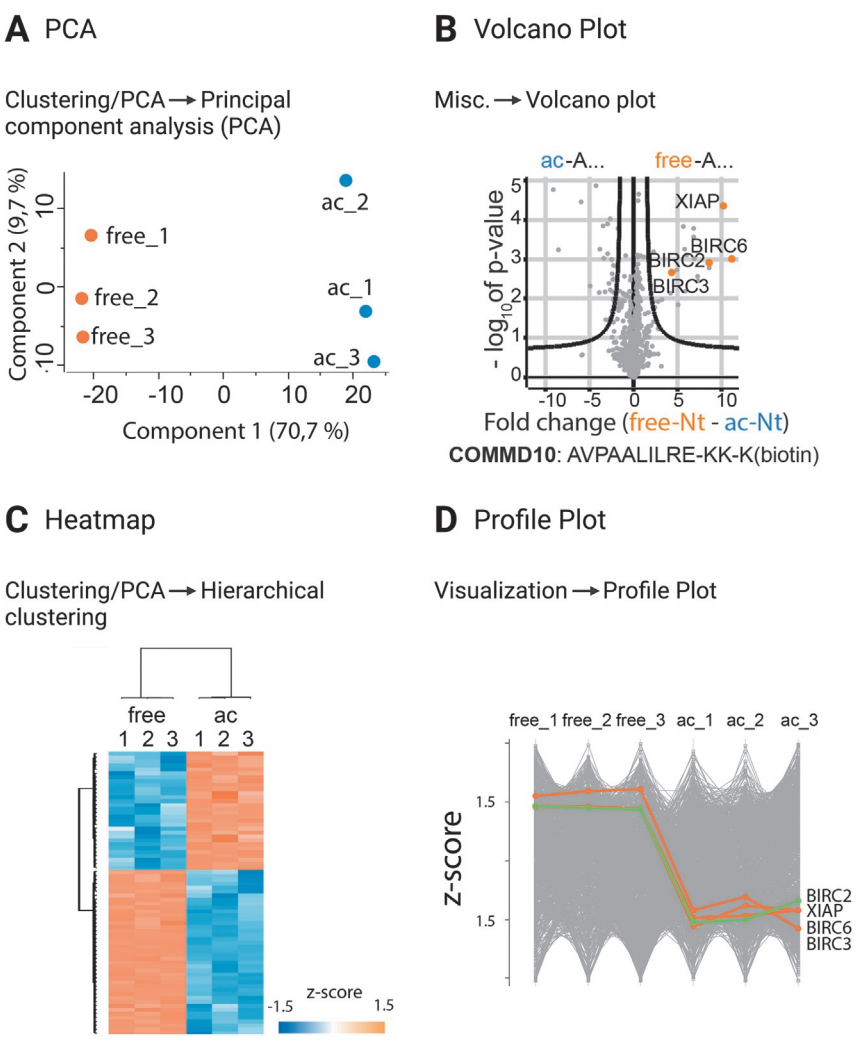

Fig. 3 Examples for the visualization of data analysis of peptide pull-downs using the data from a peptide pull-down ac-Nt vs free-Nt of COMMD10 as example. (A) Principal component analysis (PCA) of the peptide pair replicates to evaluate data quality and differences between replicates and different peptides. (B) Volcano plot based on the *t*-test showing the significance and fold-change difference of all proteins between the two peptides. Outlier significance is controlled by a permutation-based FDR. Cut-off curve: *p*-value <0.01; S0 >2. (C) Heatmap of an unsupervised hierarchical clustering with the significant different proteins from the *t*-test. (D) Profile plot/correlation analysis of binders to visualize different LFQ intensity profiles (z-scored) between different peptides.

Perseus and an FDR between 1% and 5% with S0 between 0.1 and 2 for statistical analysis of peptide pull-downs.

10. Visualize results from the *t*-tests by plotting the $-\log_{10}$ *p*-value against the LFQ intensity fold-change (Misc. → Volcano plot → Grouping, e.g., First group: LFQ intensity free; Second group: LFQ intensity ac). Most promising candidates with a high enrichment fold change and low p-value appear on the upper right and left side of the plot (Fig. 3B) (see note 6).
11. As alternative to volcano plots or when comparing many different peptide pull-downs, generate a heatmap of significantly different proteins between conditions. Filter for the significant different proteins from the *t*-test (Filter row → Filter based on categorical column → Column: Significant *t*-test; Mode: Keep matching rows; Filter mode: Reduce matrix) and plot them in a heat map after having normalized the data by z-score (Normalization → z-score and then Clustering/PCA → Hierarchical clustering) (Fig. 3C).
12. Heatmaps of significant differences can be generated as well when more than two peptides are compared. Use a multiple ANOVA test with default settings to identify significant different binding partners. Select significant proteins (Filter rows/Filter based on categorical column/ANOVA significant, select: Mode: Keep matching rows, Filter mode: Reduce matrix) and plot them in a heat map after having normalized the data by z-score (Normalization → z-score and then Clustering/PCA → Hierarchical clustering).
13. LFQ intensities of individual selected proteins can be as well visualized as profile plots and compared for different peptides (Visualization → Profile plot). To identify proteins with similar profiles across experiments, select a reference protein, e.g., BIRC2 (Visualization → Profile plot → Reference profile → Euclidean → From selected profile: BIRC2 → Refresh). Go back to Profiles section and sort the proteins by Euclidean distance to the selected reference protein. Proteins with distances closest to the selected protein show similar profiles (Fig. 3D).
14. Peptide pull-downs provide a list of potential interaction candidates in an unbiased way, but candidates of interest have to be thoroughly validated by further experiments for a direct interaction and biological function (see Prospects and Conclusions).

10.3 Notes

1. A normally distributed dataset is required for many statistical hypothesis tests. Not normally distributed data indicate problems with the peptide pull-down procedure or with the LC-MS/MS system.
2. Missing values occur if proteins are not present in a peptide pull-down or are only low abundant and are not sequenced by the MS. Proteins which are present specifically only in one peptide pull-down of the peptide pair are the most interesting candidates but if values are missing, they are lost in statistical tests. Therefore, values are imputed by randomly generated values from a Gaussian distribution centered around a down-shifted median. If data imputation should induce a bimodal distribution try to change the standard settings for width and downshift or filter more stringent on valid values to maintain a Gaussian distribution.
3. A correlation <95% is expected for replicates of peptide pull-downs and <75–80% between peptide pairs differing only at the N-terminus (e.g., ac-Nt vs free-Nt) of the peptide.
4. Replicates should cluster together in the PCA and different peptides should separate from each other. If not, biological, experimental or technical problems are likely and the experiment has to be repeated.
5. Even peptide pull-downs consist of thousands of measured data points leading to multiple hypothesis testing problems when performing two-sample *t*-tests. A permutation-based false discovery rate (FDR) can be used to estimate the number of false positive significant hits.
6. For interesting candidates, go back to the unfiltered ProteinGroups.txt table to ensure differences in measured data and avoid following artifacts induced by data imputation. Check filtered but not imputed data as well in a volcano plot.

11. Conclusions and outlook

We describe here a method to identify N-recognin candidates in an unbiased way using quantitative MS-based proteomics. It is important to note that our approach provides a list of candidates which have to be validated as N-recognins in further experiments. Often more than one candidate is identified by MS and it has to be well considered which candidate to follow. We recommend to take the following criteria into consideration:

(i) the involvement of the candidate E3 ligase in N-degron pathways should be novel; (ii) the candidate ligase should demonstrate clear specificity for a particular class of substrate proteins; (iii) sufficient priori literature information on the ligase to be able to plan mechanistic experiments; (iv) some initial reagents for biochemical and cellular experiments, such as antibodies, RNAi tools and/or overexpression constructs should be available, and protein/domain expression in heterologous systems feasible. From the MS data, no direct interaction between candidate N-recognin and N-degron can be concluded. Therefore, the first validation experiments should be in vitro experiments, e.g., fluorescence polarization, to verify a direct interaction between N-degron and potential N-recognin or adaptors of N-recognins avoiding to follow N-degron-independent E3 ligases or interaction partners. Further validation experiments might include in vitro or in vivo ubiquitination assays, cellular overexpression or downregulation (e.g., RNAi experiments) of potential N-recognins combined with proteasome inhibitors. Additionally, depending on the N-degron recognized, experiments can be combined with the downregulation of Nt-modifications, e.g., Nt-acetylation.

We focused so far on Nt-acetylated peptides, but as a protein's nascent chain emerges from a translating ribosome, its N-terminus can undergo various modifications (i.e., Nt-acetylation, Nt-methylation, Nt-myristoylation, and Nt-arginylation (Aksnes, Ree, & Arnesen, 2019; Giglione, Fieulaine, & Meinnel, 2015; Varland, Osberg, & Arnesen, 2015)). Additionally, recent data suggest that N-degron pathways become active after the omission or "wrong" attachment of Nt-modifications to ensure protein quality and to remove potential harmful proteins as fast as possible from the system (Li et al., 2022; Linster et al., 2022; Mueller et al., 2021; Timms et al., 2019; Varland et al., 2022). These data further strengthen the important function of N-degron pathways in protein quality control to maintain cellular proteostasis in health. It suggests as well that a more extensive network of N-recognins and Nt-modifying enzymes exists than previously thought which we only start to discover. In addition, the impairment of N-recognin function or misregulation of Nt-modifications plays a role in various human diseases (impairment of immunity, cancer and neurodegenerative diseases) and disorders (e.g., the Johansen-Blizzard Syndrome or the Naa10-related syndrome) (Hwang et al., 2011; Saunier et al., 2016; Varshavsky, 2019; Wu & Lyon, 2018). Together this reinforces the importance to comprehensively identify N-degron pathways and to study the underlying mechanisms.

We believe that peptide pull-downs combined with quantitative MS-based proteomics will be able to greatly contribute to the elucidation of N-recognins and their interplay with Nt-modifying enzymes.

Acknowledgments

T.B. gratefully acknowledges funding by the Deutsche Forschungsgemeinschaft (DFG) (project number: 5041 140321) and by the Friedrich-Baur Stiftung. We thank Maria Robles and Andrea Musacchio and their group members for their support. Figures were created with BioRender.com.

References

Aksnes, H., Ree, R., & Arnesen, T. (2019). Co-translational, post-translational, and non-catalytic roles of N-terminal acetyltransferases. *Molecular Cell*, *73*(6), 1097–1114. https://doi.org/10.1016/j.molcel.2019.02.007.

Bachmair, A., Finley, D., & Varshavsky, A. (1986). In vivo half-life of a protein is a function of its amino-terminal residue. *Science*, *234*(4773), 179–186. https://doi.org/10.1126/science.3018930.

Bekker-Jensen, D. B., Martinez-Val, A., Steigerwald, S., Ruther, P., Fort, K. L., Arrey, T. N., et al. (2020). A compact quadrupole-orbitrap mass spectrometer with FAIMS interface improves proteome coverage in short LC gradients. *Molecular & Cellular Proteomics*, *19*(4), 716–729. https://doi.org/10.1074/mcp.TIR119.001906.

Chen, S. J., Wu, X., Wadas, B., Oh, J. H., & Varshavsky, A. (2017). An N-end rule pathway that recognizes proline and destroys gluconeogenic enzymes. *Science*, *355*(6323). https://doi.org/10.1126/science.aal3655.

Cox, J., Hein, M. Y., Luber, C. A., Paron, I., Nagaraj, N., & Mann, M. (2014). Accurate proteome-wide label-free quantification by delayed normalization and maximal peptide ratio extraction, termed MaxLFQ. *Molecular & Cellular Proteomics*, *13*(9), 2513–2526. https://doi.org/10.1074/mcp.M113.031591.

Cox, J., & Mann, M. (2008). MaxQuant enables high peptide identification rates, individualized p.p.b.-range mass accuracies and proteome-wide protein quantification. *Nature Biotechnology*, *26*(12), 1367–1372. https://doi.org/10.1038/nbt.1511.

Cox, J., Neuhauser, N., Michalski, A., Scheltema, R. A., Olsen, J. V., & Mann, M. (2011). Andromeda: A peptide search engine integrated into the MaxQuant environment. *Journal of Proteome Research*, *10*(4), 1794–1805. https://doi.org/10.1021/pr101065j.

Gibbs, D. J., Bacardit, J., Bachmair, A., & Holdsworth, M. J. (2014). The eukaryotic N-end rule pathway: Conserved mechanisms and diverse functions. *Trends in Cell Biology*, *24*(10), 603–611. https://doi.org/10.1016/j.tcb.2014.05.001.

Giglione, C., Fieulaine, S., & Meinnel, T. (2015). N-terminal protein modifications: Bringing back into play the ribosome. *Biochimie*, *114*, 134–146. https://doi.org/10.1016/j.biochi.2014.11.008.

Hershko, A., & Ciechanover, A. (1998). The ubiquitin system. *Annual Review of Biochemistry*, *67*, 425–479. https://doi.org/10.1146/annurev.biochem.67.1.425.

Hwang, C. S., Shemorry, A., & Varshavsky, A. (2010). N-terminal acetylation of cellular proteins creates specific degradation signals. *Science*, *327*(5968), 973–977. https://doi.org/10.1126/science.1183147.

Hwang, C. S., Sukalo, M., Batygin, O., Addor, M. C., Brunner, H., Aytes, A. P., et al. (2011). Ubiquitin ligases of the N-end rule pathway: Assessment of mutations in UBR1 that cause the Johanson-Blizzard syndrome. *PLoS One*, *6*(9), e24925. https://doi.org/10.1371/journal.pone.0024925.

Kelstrup, C. D., Bekker-Jensen, D. B., Arrey, T. N., Hogrebe, A., Harder, A., & Olsen, J. V. (2018). Performance evaluation of the Q Exactive HF-X for shotgun proteomics. *Journal of Proteome Research*, *17*(1), 727–738. https://doi.org/10.1021/acs.jproteome.7b00602.

Lampert, F., Stafa, D., Goga, A., Soste, M. V., Gilberto, S., Olieric, N., et al. (2018). The multi-subunit GID/CTLH E3 ubiquitin ligase promotes cell proliferation and targets the transcription factor Hbp1 for degradation. *eLife*, 7. https://doi.org/10.7554/eLife.35528.

Li, Y., Zhao, Y., Yan, X., Ye, C., Weirich, S., Zhang, B., et al. (2022). CRL2(ZER1/ZYG11B) recognizes small N-terminal residues for degradation. *Nature Communications*, *13*(1), 7636. https://doi.org/10.1038/s41467-022-35169-6.

Linster, E., Forero Ruiz, F. L., Miklankova, P., Ruppert, T., Mueller, J., Armbruster, L., et al. (2022). Cotranslational N-degron masking by acetylation promotes proteome stability in plants. *Nature Communications*, *13*(1), 810. https://doi.org/10.1038/s41467-022-28414-5.

Melnykov, A., Chen, S. J., & Varshavsky, A. (2019). Gid10 as an alternative N-recognin of the Pro/N-degron pathway. *Proceedings of the National Academy of Sciences of the United States of America*, *116*(32), 15914–15923. https://doi.org/10.1073/pnas.1908304116.

Mueller, F., Friese, A., Pathe, C., da Silva, R. C., Rodriguez, K. B., Musacchio, A., et al. (2021). Overlap of NatA and IAP substrates implicates N-terminal acetylation in protein stabilization. *Science Advances*, *7*(3). https://doi.org/10.1126/sciadv.abc8590.

Popovic, D., Vucic, D., & Dikic, I. (2014). Ubiquitination in disease pathogenesis and treatment. *Nature Medicine*, *20*(11), 1242–1253. https://doi.org/10.1038/nm.3739.

Rappsilber, J., Ishihama, Y., & Mann, M. (2003). Stop and go extraction tips for matrix-assisted laser desorption/ionization, nanoelectrospray, and LC/MS sample pretreatment in proteomics. *Analytical Chemistry*, *75*(3), 663–670. https://doi.org/10.1021/ac026117i.

Rappsilber, J., Mann, M., & Ishihama, Y. (2007). Protocol for micro-purification, enrichment, pre-fractionation and storage of peptides for proteomics using StageTips. *Nature Protocols*, *2*(8), 1896–1906. https://doi.org/10.1038/nprot.2007.261.

Ravid, T., & Hochstrasser, M. (2008). Diversity of degradation signals in the ubiquitin-proteasome system. *Nature Reviews. Molecular Cell Biology*, *9*(9), 679–690. https://doi.org/10.1038/nrm2468.

Saunier, C., Stove, S. I., Popp, B., Gerard, B., Blenski, M., AhMew, N., et al. (2016). Expanding the phenotype associated with NAA10-related N-terminal acetylation deficiency. *Human Mutation*, *37*(8), 755–764. https://doi.org/10.1002/humu.23001.

Scheltema, R. A., Hauschild, J. P., Lange, O., Hornburg, D., Denisov, E., Damoc, E., et al. (2014). The Q Exactive HF, a benchtop mass spectrometer with a pre-filter, high-performance quadrupole and an ultra-high-field orbitrap analyzer. *Molecular & Cellular Proteomics*, *13*(12), 3698–3708. https://doi.org/10.1074/mcp.M114.043489.

Shemorry, A., Hwang, C. S., & Varshavsky, A. (2013). Control of protein quality and stoichiometries by N-terminal acetylation and the N-end rule pathway. *Molecular Cell*, *50*(4), 540–551. https://doi.org/10.1016/j.molcel.2013.03.018.

Timms, R. T., Zhang, Z., Rhee, D. Y., Harper, J. W., Koren, I., & Elledge, S. J. (2019). A glycine-specific N-degron pathway mediates the quality control of protein N-myristoylation. *Science*, *365*(6448). https://doi.org/10.1126/science.aaw4912.

Tyanova, S., Temu, T., Sinitcyn, P., Carlson, A., Hein, M. Y., Geiger, T., et al. (2016). The Perseus computational platform for comprehensive analysis of (prote)omics data. *Nature Methods*, *13*(9), 731–740. https://doi.org/10.1038/nmeth.3901.

Varland, S., Duarte Silva, R., Kjosås, I., Faustino, A., Bogaert, A., Billmann, M., et al. (2022). N-terminal acetylation shields proteins from degradation and promotes age-dependent motility and longevity. *BioRxiv*. https://doi.org/10.1101/2022.09.01.505523.

Varland, S., Osberg, C., & Arnesen, T. (2015). N-terminal modifications of cellular proteins: The enzymes involved, their substrate specificities and biological effects. *Proteomics*, *15*(14), 2385–2401. https://doi.org/10.1002/pmic.201400619.

Varshavsky, A. (2011). The N-end rule pathway and regulation by proteolysis. *Protein Science*, *20*(8), 1298–1345. https://doi.org/10.1002/pro.666.

Varshavsky, A. (2019). N-degron and C-degron pathways of protein degradation. *Proceedings of the National Academy of Sciences of the United States of America*, *116*(2), 358–366. https://doi.org/10.1073/pnas.1816596116.

Wu, Y., & Lyon, G. J. (2018). NAA10-related syndrome. *Experimental & Molecular Medicine*, *50*(7), 1–10. https://doi.org/10.1038/s12276-018-0098-x.

Zheng, N., & Shabek, N. (2017). Ubiquitin ligases: Structure, function, and regulation. *Annual Review of Biochemistry*, *86*, 129–157. https://doi.org/10.1146/annurev-biochem-060815-014922.

CELL BIOLOGY

Overlap of NatA and IAP substrates implicates N-terminal acetylation in protein stabilization

Franziska Mueller[1], Alexandra Friese[1], Claudio Pathe[1]*, Richard Cardoso da Silva[1], Kenny Bravo Rodriguez[1], Andrea Musacchio[1,2]†, Tanja Bange[1,3]†

SMAC/DIABLO and HTRA2 are mitochondrial proteins whose amino-terminal sequences, known as inhibitor of apoptosis binding motifs (IBMs), bind and activate ubiquitin ligases known as inhibitor of apoptosis proteins (IAPs), unleashing a cell's apoptotic potential. IBMs comprise a four-residue, loose consensus sequence, and binding to IAPs requires an unmodified amino terminus. Closely related, IBM-like N termini are present in approximately 5% of human proteins. We show that suppression of the N-alpha-acetyltransferase NatA turns these cryptic IBM-like sequences into very efficient IAP binders in cell lysates and in vitro and ultimately triggers cellular apoptosis. Thus, amino-terminal acetylation of IBM-like motifs in NatA substrates shields them from IAPs. This previously unrecognized relationship suggests that amino-terminal acetylation is generally protective against protein degradation in human cells. It also identifies IAPs as agents of a general quality control mechanism targeting unacetylated rogues in metazoans.

INTRODUCTION

As a protein's nascent chain emerges from a translating ribosome, its N terminus undergoes various modifications. Common are the acetylation of the initiator N-terminal methionine (Met^i) or its removal by methionine aminopeptidases (MetAPs) (*1*), followed by sequence-specific acetylation of the newly generated N terminus (*2*). N-terminal acetylation (Nt-Ac) may persist for the entire lifetime of the modified protein (*2*).

Nt-Ac requires acetyl–coenzyme A (CoA) as an acetyl donor, and an open question of general interest is the extent to which this modification is interwoven with metabolic regulation in different organisms (*3*, *4*). In a few well-studied cases, Nt-Ac has been implicated in cell physiological functions, including the stabilization of protein complexes, protein subcellular targeting, and protein aggregation (*2*). These functions of Nt-Ac may find an important level of convergence with pathways of regulated protein degradation. Early studies in human cells suggested that Nt-Ac may protect against protein degradation (*5*), and in selected cases, including the Hyx protein in *Drosophila melanogaster* and the THO complex subunit 7 (THOC7) protein in humans (*6*, *7*), a protective function of Nt-Ac has been documented.

More recent work, however, has questioned the role of Nt-Ac as a stabilizing marker. In *Saccharomyces cerevisiae*, acetylated protein N termini starting with methionine (Met or M), serine (Ser or S), alanine (Ala or A), threonine (Thr or T), or valine (Val or V) were proposed to act as potential degradation motifs (Ac-N-degrons). This pathway, which was proposed to predispose proteins for ubiquitin (Ub)–mediated proteolysis through the Doa10 and Not4 Ub-ligases (*8*, *9*), may be especially relevant in the context of protein quality control. A developing paradigm is that improper folding or abnormal stoichiometries of certain protein complex subunits cause exposure of the modified N termini, making them available for the degradation machinery (*8*). The generality of this mechanism, however, remains unclear (*10*).

Our interest in this problem stemmed from the specific question whether Nt-Ac influences processes of protein degradation during cell cycle progression and, more specifically, during mitosis. With an eye to the development of an experimental pipeline that would enable us to analyze variations in Nt-Ac in human cells, we began from a broader perspective and performed an unbiased analysis of the N-terminal proteome (N-terminome) of HeLa cells through mass spectrometry (MS)–based proteomics (*11*, *12*), building on, and extending, previous similar efforts (*12*–*16*). Starting from this dataset, we then developed a biochemical pipeline to identify putative interaction partners of naturally acetylated N-terminal motifs or of their unacetylated counterparts, which led to several unanticipated observations, as will be explained below. Our main general conclusion, corroborated by a remarkably consistent set of observations, is that the unacetylated versions of a large cohort of normally acetylated N termini targeted by the NatA acetyltransferase interact with E3 Ub ligases belonging to a family known as inhibitor of apoptosis proteins (IAPs). Collectively, our results are consistent with a crucial function of Nt-Ac in the control of protein stability. In agreement with previous observations obtained with a restricted number of proteins (*5*, *6*), our results suggest that Nt-Ac may play a general role in protein stabilization in human cells.

RESULTS AND DISCUSSION

The N-terminome of HeLa cells confirms the pervasiveness of Nt-acetylation

As discussed in detail in Methods and illustrated in fig. S1, we developed a pipeline for MS-based N-terminomics. Briefly, we used formaldehyde to dimethylate to completion all susceptible N termini in cleared HeLa cell lysates. The reaction spares preexisting acetylated N termini, on which methylation is ineffective, thus marking specifically unmodified or differently modified (e.g., unmodified or monomethylated) N termini. This allowed us to distinguish the latter

[1]Department of Mechanistic Cell Biology, Max Planck Institute of Molecular Physiology, Otto-Hahn-Str. 11, 44227 Dortmund, Germany. [2]Centre for Medical Biotechnology, Faculty of Biology, University Duisburg-Essen, Universitaetsstrasse, 45141 Essen, Germany. [3]Institute of Medical Psychology, Faculty of Medicine, LMU Munich.
*Present address: MRC Laboratory of Molecular Biology, Division of Protein and Nucleic Acid Chemistry, Francis Crick Avenue, Cambridge CB2 0QH, UK.
†Corresponding author. Email: andrea.musacchio@mpi-dortmund.mpg.de (A.M.); tanja.bange@med.uni-muenchen.de (T.B.)

from internal peptides created artificially by trypsin-mediated endoproteolysis at a later stage of the procedure. Internal peptides with intact N termini were selectively removed, and the resulting enriched preparations of N-terminal peptides were analyzed by high-resolution MS in a Q Exactive Plus Mass Spectrometer.

In line with previous studies (*11*, *13*–*15*, *17*), our results demonstrate the pervasiveness of Nt-Ac. Considering only peptides starting at position 1 (Met^1) or 2 (Met^1 removed) of annotated protein sequences [UniProt (*18*)], we quantified N-terminal peptides in 2876 proteins (Fig. 1A and table S1). A total of 72.3% of these were fully N-terminally acetylated, 9.4% were partially acetylated, and 18.3% were dimethylated. As explained above and summarized in fig. S1, the "dimethylated peptide" group in our experimental setup gathers originally unmodified, monomethylated, and (if at all represented) dimethylated N termini, technically preventing an assessment of the prevalence of cellular N-terminal methylation.

Removal of Nt-acetylation promotes an interaction with IAP baculovirus IAP repeat domains

We reasoned that if Nt-Ac were part of N-terminal degradation signals (Nt-Ac-degrons), it ought to be a determinant of interactions with specialized receptors on Ub ligases or associated proteins. With the possible exception of MARCH6/TEB4 (the Doa10 ortholog), whether such receptors for Nt-Ac-degrons exist in humans is unclear. CDC20 is a well-established cell cycle regulator whose N terminus emerged from our analysis as being thoroughly N terminally acetylated (Fig. 1C). CDC20 is a coactivator of the anaphase-promoting complex/cyclosome (APC/C), an E3 Ub ligase required for the metaphase-anaphase transition (*19*). CDC20 presents the APC/C with two crucial targets, cyclin B and securin, whose degradation is required for eliciting this fundamental cell cycle transition. CDC20 stability is controlled at multiple levels during cell cycle progression (*19*), identifying this protein as a promising entry point in the study of the effects of Nt-Ac.

Because Nt-Ac has been previously shown to contribute directly to the stabilization of intramolecular interactions (*20*–*23*), we reasoned that we could use affinity chromatography to identify putative Nt-Ac-receptor(s) for CDC20. To this end, beads exposing acetylated or unacetylated synthetic peptides encompassing the N-terminal region of CDC20 were incubated with lysates of cycling HeLa cells, followed by MS-based quantification on retained binders (Fig. 1B). Defying our initial goal, no enrichment was observed with the acetylated version of the CDC20 peptide, with the exception of a few nonspecific binders (Fig. 1D and table S2). Conversely, the unmodified version of this peptide showed robust interactions with BIRC2, BIRC3, XIAP (X-linked IAP), and BIRC6 (also known as APOLLON or BRUCE), four members of an IAP family of E3 ubiquitin (Ub)–ligases that are key regulators of programmed cell death in development, tissue homeostasis, and tumorigenesis (*24*, *25*). Thus, our search for potential binding partners of CDC20's acetylated N-terminal region was inconclusive, but it suggested binding to IAPs E3 ligases as a possible outcome of defective acetylation.

To investigate the generality of these observations, we performed the same experiment with two additional peptides identified in our proteomic analysis as being fully acetylated, COMM domain-containing protein 10 (COMMD10) and deaminated glutathione amidase (NIT1). As negative controls, we used the N-terminal peptides from aspartate aminotransferase, cytoplasmic (GOT1) and 40S ribolomal protein S3a (RPS3A), whose sequences are related to those of COMMD10, NIT1, and CDC20 but that were measured as dimethylated (i.e., not acetylated; see above) in our screen (Fig. 1C). As for CDC20, the same four IAPs were strongly enriched in pull-down experiments with the unacetylated versions of the COMMD10 and NIT1 peptides, while no IAP enrichment was observed with the GOT1 or RPS3A control peptides (Fig. 1, E to G, and fig. S2A). Thus, three N-terminal peptides that are normally fully acetylated are also cryptic IAP binders whose IAP binding potential is unleashed when acetylation is missing, whereas the GOT1 and RPS3A peptides, which are not acetylated in vivo, are not cryptic IAP binders either. The glucose-induced degradation-deficient E3 ligase/C-terminal to LisH (hGID/CTLH) complex, a Ub-ligase implicated in the recognition of N-terminal proline (*26*, *27*), a residue that is never acetylated (*2*), was also enriched in pull-downs of the unacetylated COMMD10 peptide (table S2). The reason for this is unclear, but we speculate that it might reflect the unexpected exposure of Pro at position 3 in the COMMD10 peptide.

IAP family members comprise one to three 70-residue baculovirus IAP repeat (BIR) domains, but only BIRC2, BIRC3, and XIAP carry an additional RING domain that confers the Ub-ligase activity (*24*, *28*, *29*). BIRC6 has a Ub-conjugating (UBC) domain rather than a RING but has been shown to act as a chimeric E2/E3 Ub-ligase (*30*). Thus, the unacetylated forms of the COMMD10, NIT1, and CDC20 peptides pull down IAP family members with a proven activity as E3 ligases, whereas they do not pull down IAP family members, such as survivin, that are not associated with Ub-ligase activity (*31*).

The BIR domains of IAP Ub-ligases have been previously implicated in recognition of proteins containing a conserved inhibitor of apoptosis binding motif (IBM) in target proteins such as SMAC/DIABLO, caspase 9 (CASP9), and serine protease HTRA2, mitochondrial (HTRA2) considered crucial determinants of death pathway activation (*32*). Pull-down experiments from HeLa lysates with DIABLO, CASP9, or HTRA2 peptides identified the same four IAPs as preferential binding partners of the unacetylated peptides (Fig. 1, H to I, and fig. S2B), drawing a clear parallel with the COMMD10, NIT1, and CDC20 peptides.

The cryptic IBMs of COMMD10, NIT1, and CDC20 have sequence features that resemble those of the IBMs in SMAC/DIABLO, HTRA2, and CASP9 (Fig. 2A), suggesting that they bind the BIR domains. To test this, we asked whether unacetylated synthetic peptides encompassing the N termini of COMMD10, NIT1, and CDC20 interacted with representative BIR domains (fig. S3A), including the $BIRC3^{BIR3}$ domain and $XIAP^{Linker\text{-}BIR2\text{-}BIR3}$, a tandem BIR construct of XIAP also encompassing the so-called linker region, in a fluorescence polarization assay. The positive controls DIABLO and CASP9 IBM peptides and the COMMD10, NIT1, or CDC20 peptides bound to BIR domains with comparable dissociation constants (K_d), while none of the peptides bound to the $XIAP^{BIR1}$ domain, which does not interact with the IBMs of CASP9 and DIABLO (Fig. 2B, fig. S3B, and table S3) (*24*, *33*). Increasing amounts of DIABLO or COMMD10 peptides in solution competed with similar efficiency the pull-down of IAPs from cellular lysates by an immobilized biotinylated DIABLO peptide (fig. S4 and table S4). As expected on the basis of structural work on IBM:BIR complexes (*34*–*36*) and on our cell lysate pull-down experiments, Nt-Ac abrogated IAP binding by the COMMD10, NIT1, and CDC20 peptides (Fig. 2B and fig. S3B). The IAP-binding N termini of IBMs are generated posttranslationally by endoproteolysis (CASP9) or upon proteolytic processing of signal peptides during mitochondria

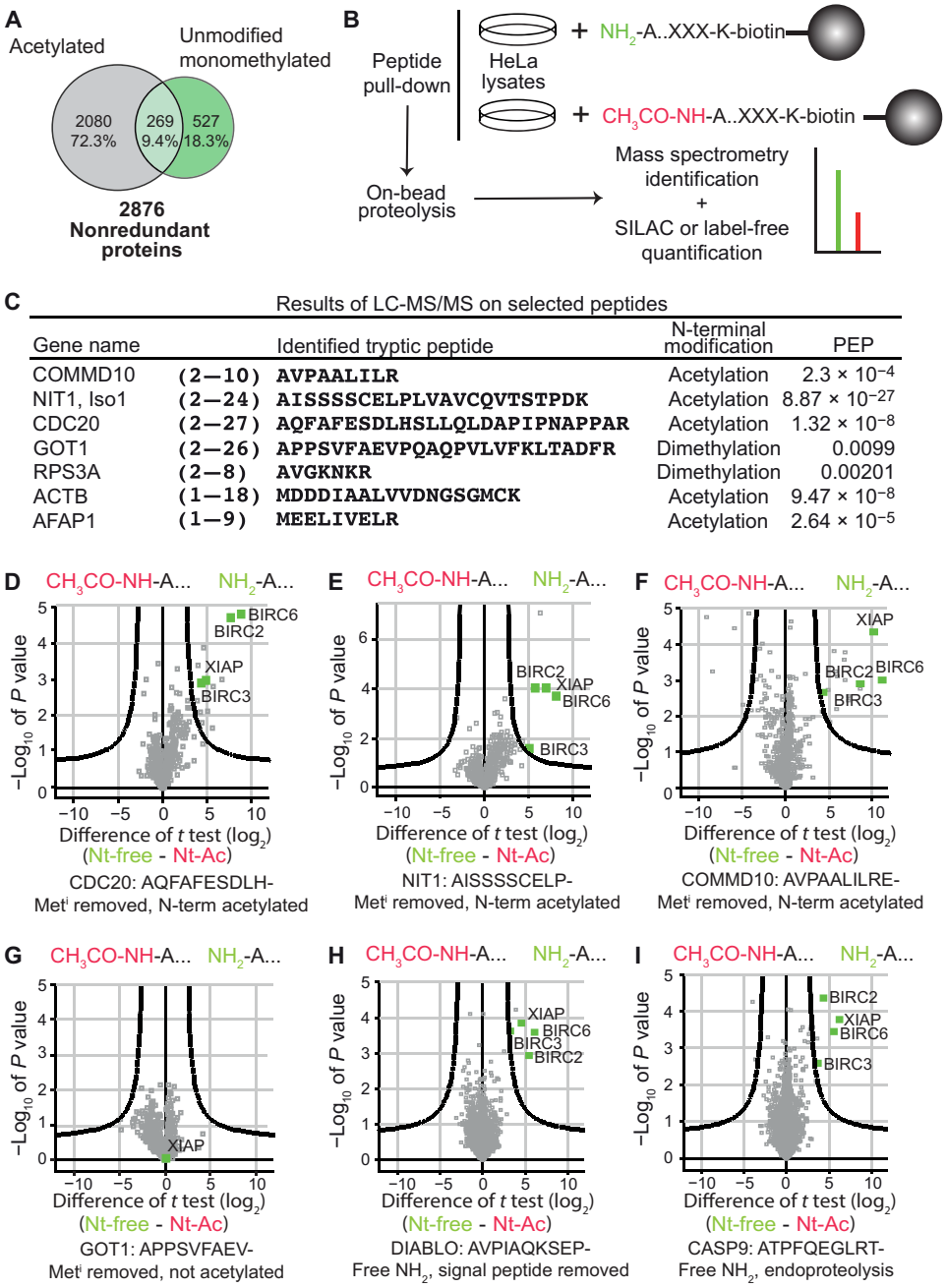

Fig. 1. Free Nt-α-amino forms of Nt-acetylated proteins bind to IAPs in cells. (**A**) Venn diagram summarizing numbers and percentages of all proteins with identified N termini from a large-scale MS experiment using HeLa cells (see experimental scheme in fig. S1). Total numbers and percentage of acetylated, dimethylated (reflecting unmodified, mono, and potentially also dimethylated N termini in cells), and proteins identified with both modifications are shown. All identified N termini are listed in detail in table S1. (**B**) Scheme of the performed peptide pull-down experiments. Nt-Ac or free Nt-α-amino (Nt-free) biotinylated peptides were bound to streptavidin beads. Beads were then incubated with HeLa lysates, washed, and directly digested on beads for MS analysis. Quantification was performed by using label-free intensities (label-free quantitation) or stable isotope labeling by amino acids in cell culture (SILAC). (**C**) Table of examples of N-terminal peptides from the MS dataset (A) used for pull-downs in 1(D to G) and fig. S2. Identified tryptic peptide, its N-terminal modification and posterior error probability (PEP) of the identification are specified. (**D** to **I**) Volcano plots from pull-down experiments comparing binders for free Nt-α-amino and Nt-Ac peptides from CDC20 (D), NIT1 (E), COMMD10 (F), and GOT1 (G) are shown. (**H** and **I**) The positive controls DIABLO and CASP9 are shown in (H) and (I), respectively. For all pull-downs the $-\log_{10}$ of the *t* test values (*y* axis) are plotted against the $\log_2$ of the fold difference of the *t* test (*x* axis) [*t* test, free Nt-α-amino (indicated as Nt-free) versus Nt-Ac; cutoff curve, false discovery rate (FDR) < 0.01, S0 > 2]. IAP family members are highlighted in green. LC-MS/MS, liquid chromatography–tandem MS.

insertion (SMAC/DIABLO and HTRA2), explaining why these sequences are not acetylated (*24*, *37*). Their regulated binding to IAPs results in ubiquitylation and degradation of their carriers (*24*). Collectively, these experiments indicate that IBMs and unacetylated cryptic IBM-like sequences of nuclear or cytosolic proteins bind to BIR domains with similar affinity.

The IBMs' first four residues are crucial for BIR domain binding (*34*–*36*). The first residue is generally alanine (A), but serine (S),

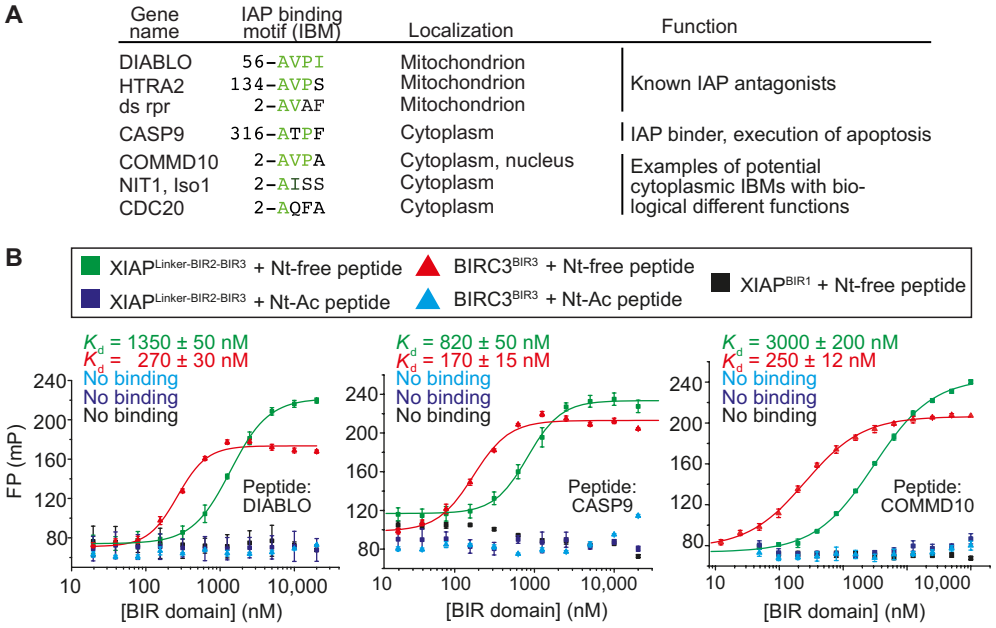

Fig. 2. Free Nt-α-amino peptides of cytosolic proteins bind to IAPs' BIR domains in vitro. (**A**) Table with examples of known IAP antagonists [DIABLO, HTRA2, and dr Reaper (rpr)], IAP binders (CASP9), and cytosolic proteins with potential N-terminal IBM motifs (COMMD10, NIT1 Isoform1, and CDC20). Gene name, (potential) IBM with N-terminal amino acid in processed protein, cellular localization, and function are shown. (**B**) Fluorescein isothiocyanate (FITC)–labeled peptides (free Nt-α-amino, indicated as Nt-free, or Nt-Ac, each used at a concentration of 20 nM) of DIABLO (left), CASP9 (middle), and COMMD10 (right) were incubated for 30 min with increasing concentrations of His-tag BIR domain constructs (XIAP$^{Linker\text{-}BIR2\text{-}BIR3}$, BIRC3^{BIR3}, or XIAP^{BIR1}). Fluorescence polarization (FP) was measured at excitation and emission wavelength of 470 and 525 nm and data (millipolarization units, mP) were plotted as a function of BIR domain concentration and fitted with a logistic fit using Origin7.0. K_d values are summarized in table S3. Measured combinations are shown schematically in the top panel.

valine (V), and threonine (T) are tolerated, and there is relatively modest sequence stringency at subsequent positions, although this may vary for different BIRs (*33*, *38*–*40*). Peptides with sequences retaining Met^i [such as those of actin, cytoplasmic 1 (ACTB) and actin filament-associated protein 1 (AFAP1); Fig. 1C] or encompassing COMMD10 but with an N-terminal methionine that is normally processed did not enrich IAPs when exposed to HeLa lysates (fig. S2, C to F), suggesting that removal of the N-terminal methionine is prerequisite for IAP binding (albeit not sufficient, as shown by the GOT1 and RPS3A peptides). As previously noted (*33*), the incidence of IBM-like sequences in the human proteome is high (4285 sequences of 64,103 complete UniProt annotations were identified with an in-house developed program using the motif [AS]-[EVTQIDSMLFRG]-[PAGVCKMSR]-[VIDEFGLWAY], where square parentheses enclose single-letter codes of allowed residues at positions for residues 2 to 5).

Reduction of Nt-Ac generates new binding partners for IAPs

We asked whether the IAP-binding potential of cryptic IBMs could be unleashed by artificially reducing Nt-Ac in HeLa cells. Mammals have seven N-terminal acetyl transferases (NATs; designated as A to F and H) with different sequence specificities (*41*). NatA, which comprises catalytic NAA10 and regulatory NAA15 subunits, is the only NAT that recognizes peptide sequences starting with A, S, T, V, C, and G after removal of the initiator methionine (*2*, *42*), with the apparent exception of NatD, which is also able to target starting Ser but limited to histone H2A and H4 (*43*, *44*). NatA modifies ~40% of the proteome and is expected to target the majority if not all IBM-like motifs. We therefore targeted NatA by RNA interference (RNAi) for 48 hours (Fig. 3A) and additionally added MG132 for 3 hours before lysis to prevent possible proteasomal degradation of unacetylated targets after their ubiquitination by IAPs, a common fate of BIR domain binders (*28*, *29*). Lysates from RNAi- and mock-treated cells were used for pull-down experiments using His-tagged BIRC3^{BIR3}, XIAP$^{Linker\text{-}BIR2\text{-}BIR3}$, and XIAP^{BIR1} as baits, and interaction partners were identified and quantified by MS. This analysis showed enrichment of several BIRC3^{BIR3} and XIAP$^{Linker\text{-}BIR2\text{-}BIR3}$ binding partners from lysates of NatA RNAi–treated cells in comparison to lysates of mock-treated control cells. In the majority of cases, the enriched targets comprised proteins that (i) are Nt-acetylated under unperturbed conditions in our N-terminome dataset (table S1), (ii) are mainly annotated in UniProt as acetylated, and (iii) carry a cryptic IBM-like motif (fig. S5A and table S5). For a subset of proteins in this enriched set [displayed in green in Fig. 3 (B and C) and fig. S5 (B and C)], it was possible to sequence and quantify the free (i.e., unmodified) N-terminal peptide, thus allowing direct estimation of the enrichment of the non–Nt-acetylated form (free Nt-α-amino) in the BIRC3^{BIR3} and XIAP$^{Linker\text{-}BIR2\text{-}BIR3}$ pull-downs. The enrichment was not caused by major changes in abundance of the target proteins, as no such changes were observed in whole-proteome measurements that readily detected reduced abundance of the NatA subunits caused by RNAi (fig. S5E and table S6). Thus, enrichment of IAP binders upon NatA depletion is likely caused by altered Nt-acetylation.

N-terminal peptides of proteins enriched on the XIAP^{BIR1} pull-downs after NatA depletion, on the other hand, showed no obvious IBM-like motifs (Fig. 3, D and E; fig. S5, D and F to I; and table S5). The reason for their enrichment will therefore require further investigation, but we surmise that these binders represent abundant background proteins [e.g., ACTB/actin, which is known to be regulated by Nt-Ac (*45*–*47*)] whose unacetylated forms accumulate

analytical chemistry

Article

Cite This: *Anal. Chem.* 2018, 90, 10990−10999

pubs.acs.org/ac

Simplified Protocol for Cross-linking Mass Spectrometry Using the MS-Cleavable Cross-linker DSBU with Efficient Cross-link Identification

Dongqing Pan,[*,†,‡] Andreas Brockmeyer,[‡,§] Franziska Mueller,[†] Andrea Musacchio,[†,∥] and Tanja Bange[*,†,⊥]

[†]Department of Mechanistic Cell Biology, Max Planck Institute of Molecular Physiology, Otto-Hahn-Str. 11, 44227 Dortmund, Germany

[§]Department of Chemical Biology, Max Planck Institute of Molecular Physiology, Otto-Hahn-Str. 11, 44227 Dortmund, Germany

[∥]Centre for Medical Biotechnology, Faculty of Biology, University Duisburg-Essen, Universitaetsstrasse, 45141 Essen, Germany

[⊥]Department for Systems Chronobiology, Institute of Medical Psychology, LMU Munich, Goethe-Str. 31, 80336 Munich, Germany

Supporting Information

ABSTRACT: Chemical cross-linking combined with mass spectrometry (MS) is a powerful approach to identify and map protein−protein interactions. Its applications support computational modeling of three-dimensional structures and complement classical structural methodologies such as X-ray crystallography, NMR spectroscopy, and electron microscopy (EM). A plethora of cross-linkers, MS methods, and data analysis programs have been developed, but due to their methodological complexity application is currently reserved for specialized mass spectrometry laboratories. Here, we present a simplified single-step purification protocol that results in improved identifications of cross-linked peptides. We describe an easy-to-follow pipeline that combines the MS-cleavable cross-linker DSBU (disuccinimidyl dibutyric urea), a Q-Exactive mass spectrometer, and the dedicated software MeroX for data analysis to make cross-linking MS accessible to structural biology and biochemistry laboratories. In experiments focusing on kinetochore subcomplexes containing 4−10 subunits (so-called KMN network), one-step peptide purification, and enrichment by size-exclusion chromatography yielded identification of 135−228 non-redundant cross-links (577−820 cross-linked peptides) from each experiment. Notably, half of the non-redundant cross-links identified were not lysine−lysine cross-links and involved side chains with hydroxy groups. The new pipeline has a comparable potential toward the identification of protein−protein interactions as previously used pipelines based on isotope-labeled cross-linkers. A newly identified cross-link enabled us to improve our 3D-model of the KMN, emphasizing the power of cross-linking data for evaluation of low-resolution EM maps. In sum, our optimized experimental scheme represents a viable shortcut toward obtaining reliable cross-link data sets.

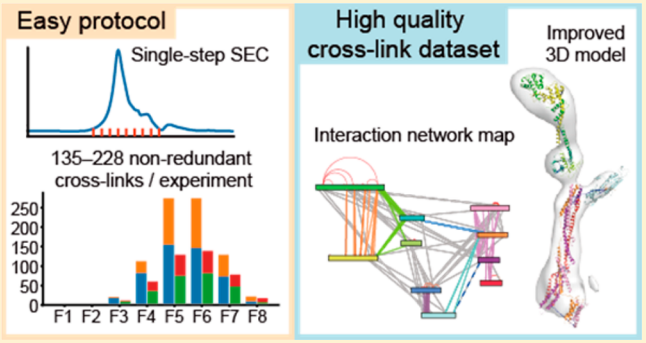

In the past decade, the development of cross-linking mass spectrometry (XL-MS) has progressed at tremendous pace and many ccross-linkers and methods are now available.[1−6] By revealing information on intra- and intermolecular interactions of protein complexes, cross-linking data can provide valuable structural restraints for bioinformatic modeling of 3D-structures or for evaluation and refinement of models obtained through various techniques, including X-ray crystallography, NMR spectroscopy, and single particle cryo-electron microscopy analyses.[6−11]

The very high complexity of the peptide mixtures, which grows with the size of the complexes being studied, represents a major challenge of the XL-MS approach. Many strategies have been developed to facilitate identification of cross-linked peptides.[6,12] The fractionation of digested peptides and the use of mixtures of noncleavable isotope-labeled cross-linkers have emerged as most successful strategies.[2,13] Many noncleavable cross-linkers with and without isotope label have been successfully used, but the identification process using dedicated software for noncleavable cross-linkers is not straightforward for beginners and requires evaluation by XL-MS experts. More recently developed strategies using MS-cleavable cross-linkers made the MS-data analysis more intuitive and automated.[6,14] MS-cleavable cross-linkers can be cleaved in the mass spectrometer, which causes cross-linked peptides to be separated into two linear peptides with easily identifiable

Received: June 8, 2018
Accepted: August 3, 2018
Published: August 3, 2018

DOI: 10.1021/acs.analchem.8b02593
Anal. Chem. 2018, 90, 10990−10999

signature fragments, reducing the search space from n^2 to $2n$ for cross-link identification.[15,16]

The cross-linking reaction and the enrichment of cross-linked peptides are the critical steps of sample preparation.[17−21] Protein concentration should be adjusted so that the reaction mixture contains homogeneous species. The concentration of cross-linkers, reaction temperature, and reaction time should be optimized to obtain sufficient cross-linked products. Peptide enrichment after proteolysis aims to exclude non-cross-linked peptides so to increase the signal of cross-linked products for MS analysis. Size-exclusion chromatography (SEC)[18,20] and strong cation exchange chromatography (SCX)[19,22] have been used after desalting of the digested peptide mixture with C18 columns and shown to improve the final yield of identified cross-links.

Here, we present a simplified protocol of XL-MS for fast and efficient identification of cross-linked peptides (Figure 1A).

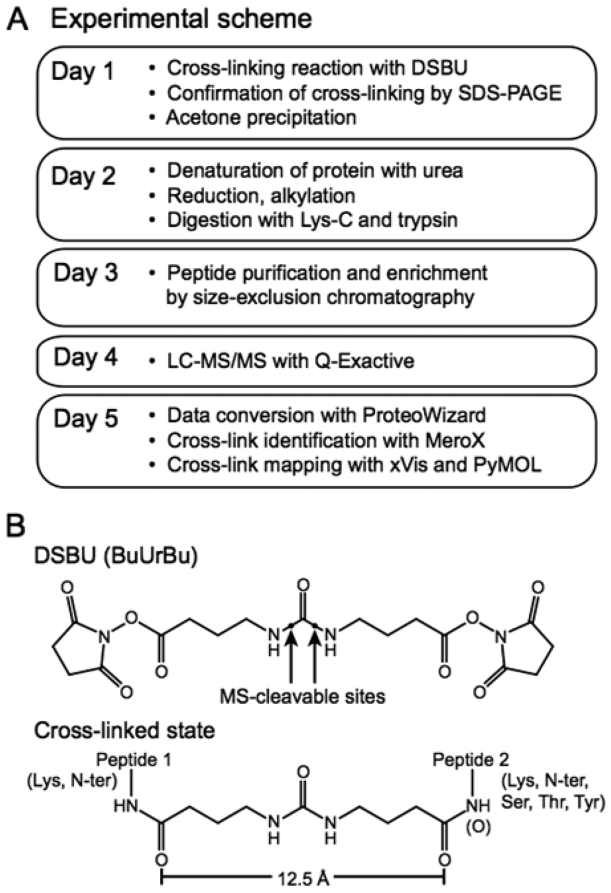

Figure 1. (A) Experimental scheme of the cross-linking MS pipeline described in this study. (B) Chemical structure of DSBU. Side chains of two reactive residues or free N-termini react with NHS esters to obtain the cross-linked state. At least one NHS ester is assumed to react with primary amines for the analysis using MeroX.

The protocol combines existing techniques and has been optimized for researchers with access to high-grade samples for interaction analysis but unfamiliar with XL-MS. Our pipeline uses DSBU (disuccinimidyl dibutyric urea, originally named BuUrBu, for 4-{3-[3-(2,5-dioxo-pyrrolidine-1-yloxycarbonyl)-propyl]ureido}butyric acid 2,5-dioxo-pyrrolidine-1-yl ester) as cross-linking reagent (Figure 1B). DSBU (i) is one of the best characterized MS-cleavable cross-linkers;[14,16,23,24] (ii) can be cleaved with the same energies used for cleaving peptide backbones, avoiding the necessity of using mass spectrometers with MS^3 options; and (iii) has a spacer arm with a length that makes it useful for probing protein interaction interfaces and their boundaries.

DSBU contains *N*-hydroxysuccinimide (NHS) esters at both ends of an 11-atom spacer arm. The central urea moiety in DSBU can be cleaved in the gas phase during tandem mass spectrometry (MS/MS) using various fragmentation methods, such as collision-induced dissociation (CID) and higher-energy collision-induced dissociation (HCD).[16] MS data acquisition was performed with a Q-Exactive Plus, a benchtop quadrupole orbitrap mass spectrometer, because (i) it has a HCD unit for MS/MS allowing DSBU-cleavage; (ii) it can record high resolution MS/MS spectra; and (iii) it is easy to use and maintain for routine assays. For data analysis of MS data obtained using DSBU, we chose MeroX, a multiplatform freeware designed for the identification of cross-linked products.[16,24] MeroX provides an intuitive tool to search and confirm the results by checking the characteristic fragment ion patterns in the MS/MS spectra.

The kinetochore is a large multisubunit protein complex consisting of more than 100 proteins. It mediates physical interaction of chromosomes with the mitotic spindle and ensures faithful chromosome segregation during cell division.[25,26] The KMN network forms the outer layer of the kinetochore and connects its chromosome-proximal part with microtubules. In humans, the KMN consists of 10 subunits: KNL1, ZWINT, the MIS12 complex (MIS12C, containing the four subunits MIS12, PMF1, NSL1, and DSN1), and the NDC80 complex (NDC80C, containing the four subunits NDC80/HEC1, NUF2, SPC24, and SPC25). Previous biochemical, structural, and XL-MS analyses have shed light on many details of the organization of the KMN complex (Figure 2A,B),[27−35] making it an ideal benchmark for our new approach.

Here, we present XL-MS results of three kinetochore protein complexes. Single-step peptide enrichment by SEC enabled us to reduce the loss of peptides and to obtain large numbers of cross-links with high redundancy. We found a large fraction of nonlysine−lysine cross-links in all our cross-linking experiments, owing to the reactivity of NHS groups in DSBU and the functionality of MeroX, expanding the detection of reactive amino-acid residues. A newly identified cross-link enabled us to improve the structural model of the KMN complex.

MATERIALS AND METHODS

Production of Protein Complexes. Protein complexes used in this study were produced using previously published protocols[31,32,34] with minor modifications. NDC80C, consisting of human NDC80, NUF2, SPC25, and SPC24, was coexpressed in insect cells. A 6-His tag was placed at the C-terminus of Spc25 for Ni-affinity chromatography. Insect cells (Tnao38) expressing NDC80C were disrupted by sonication and a cleared lysate was obtained by centrifugation. NDC80C was purified from the lysate by Ni-affinity chromatography with a HisTrap FF column (GE Healthcare) and ion exchange chromatography with a Source 15Q column (GE Healthcare) followed by SEC with a HiPrep 16/60 Sephacryl S-200 HR column (GE Healthcare). Fractions containing NDC80C were pooled and concentrated in buffer containing 50 mM HEPES pH 8.0, 250 mM NaCl, 1 mM TCEP, and 5% glycerol. MIS12C, consisting of human MIS12, DSN1, NSL1, and

DOI: 10.1021/acs.analchem.8b02593
Anal. Chem. 2018, 90, 10990−10999

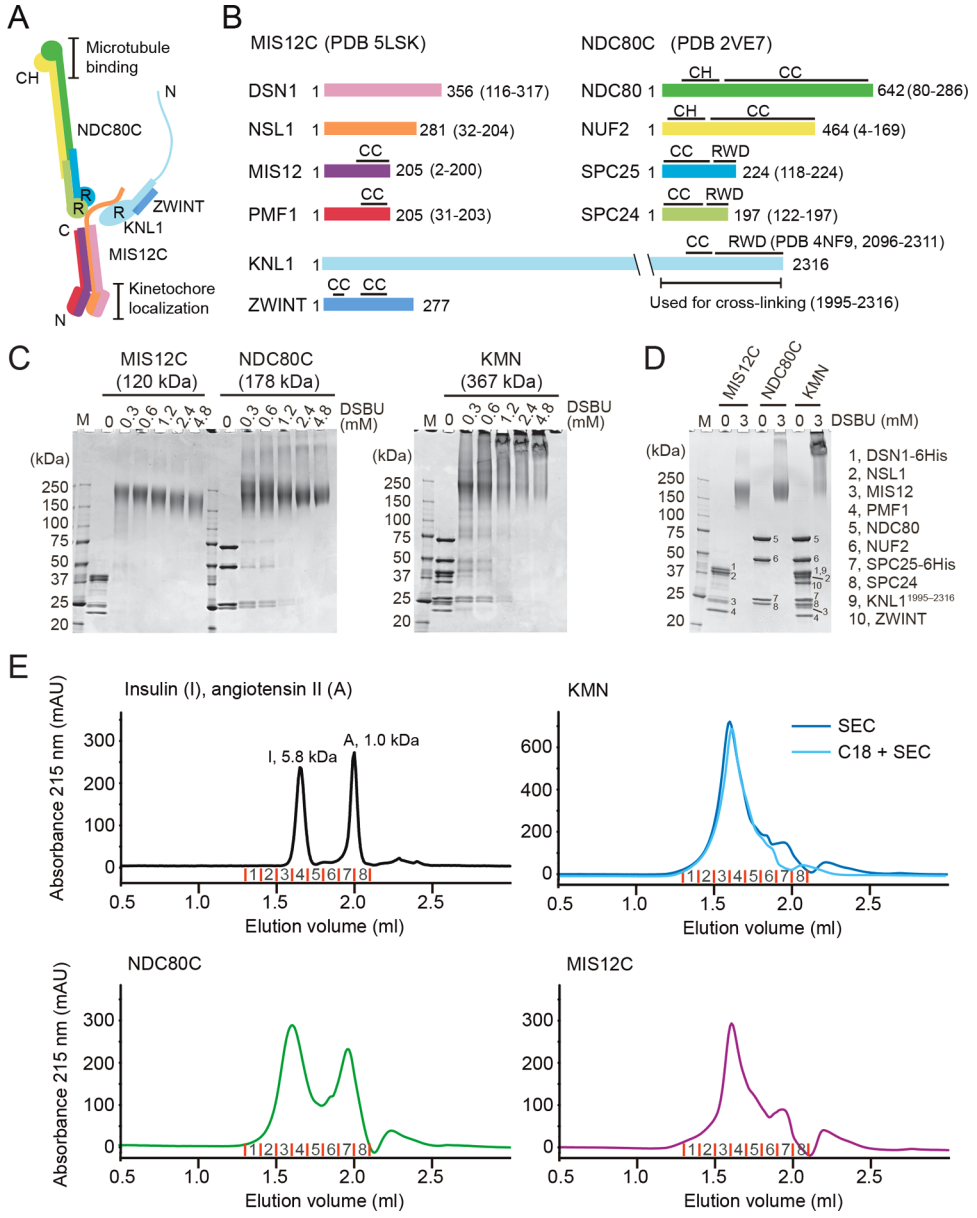

Figure 2. Cross-linking reaction and peptide purification. (A) Schematic of the KMN network. CH, calponin-homology domains; R, RWD domain; N, N-terminus; C, C-terminus. (B) Polypeptides of KMN subunits. The numbers in parentheses indicate the residue ranges of atomic models in the crystal structures used for mapping cross-links. CC, coiled-coil. (C) Optimization of the DSBU concentration for cross-linking. SDS-PAGE gels were stained with CBB. (D) Cross-linking of the samples used for MS analysis was confirmed by SDS-PAGE. (E) Representative SEC profiles of the standard peptides and the KMN complexes. Red lines indicate the borders of the fractions collected for MS analysis.

PMF1, was coexpressed in insect cells and purified in the same way as NDC80C. A 6-His tag was placed at the C-terminus of Dsn1. SEC fractions containing MIS12C were pooled and concentrated in buffer containing 25 mM HEPES pH 8.0, 100 mM NaCl, 2 mM TCEP, and 5% glycerol. Human KNL1$^{1995-2316}$ and ZWINT were expressed in *Escherichia coli* BL21(DE3)Codon+RIL cells using pGEX-6P derived plasmids. GST-tagged KNL1$^{1995-2316}$ and ZWINT were purified from cleared lysate of bacteria cells using a Glutathione Sepharose 4 Fast Flow column (GE Healthcare). After removal of the GST-tag by proteolysis with TEV protease for KNL1$^{1995-2316}$ and PreScission Protease for ZWINT, KNL1$^{1995-2316}$ and ZWINT were purified using a HiLoad 16/600, Superdex 75 pg column (GE Healthcare) with KMN buffer containing 25 mM HEPES pH 8.0, 150 mM NaCl, 2 mM TCEP, and 5% glycerol. KMN was obtained by mixing NDC80C, MIS12C, KNL1$^{1995-2316}$, and ZWINT followed by SEC using a Superose 6 prep grade, XK 16/70 column (GE Healthcare) with KMN buffer.

Chemical Cross-linking with DSBU. Protein samples (222 μg KMN, 107 μg NDC80C, 72 μg Mis12C) were dissolved at 3 μM (0.36 mg/mL MIS12C, 0.53 mg/mL NDC80C, 1.11 mg/mL KMN) in 200 μL of buffer (30 mM HEPES pH 7.5, 300 mM NaCl, 1 mM TCEP). DSBU (200 mM stock solution in DMSO, Alinda Chemical Limited) was added to the protein solution to a final concentration of 3 mM (0.3, 0.6, 1.2, 2.4, and 4.8 mM were used for optimization purposes) and incubated at 25 °C for 1 h. The reaction was stopped by adding Tris-HCl pH 8.0 to a final concentration of 100 mM and incubated at 25 °C for additional 30 min. A total

DOI: 10.1021/acs.analchem.8b02593
Anal. Chem. 2018, 90, 10990−10999

of 10 μL of protein solution were taken before and after the cross-linking reaction and analyzed by SDS-PAGE. SDS-PAGE gels were stained with Coomassie brilliant blue (CBB). Cross-linked proteins were precipitated with 4 volumes of cold acetone (−20 °C). The solution was kept at −20 °C more than 16 h and centrifuged at 15000 rpm for 5 min. The supernatant was removed completely and the pellet was dried by exposing the pellet to air at room temperature for a few minutes until it started to appear transparent. Overdried pellets can be difficult to dissolve in urea.

Lys-C and Trypsin Digestion. Protein pellets obtained from acetone precipitation were dissolved and denatured in 25 μL of denaturation−reduction solution (8 M urea, 1 mM DTT) at 25 °C for 30 min. Alkylation of cysteine residues was done by adding 2-chloroacetamide to a final concentration of 5.5 mM and incubation at 25 °C for 20 min. ABC buffer (20 mM ammonium bicarbonate, pH 8.0, 25 μL) was added to reduce the concentration of urea to 4 M. Lys-C (2 μg) was added to the solution and the mixture was incubated at 25 °C for 3 h. Trypsin (1 μg in 10 μL, 10 mM HCl) was activated in 40 μL of buffer containing 100 mM Tris-HCl pH 8.5, 1 mM $CaCl_2$. The 50 μL of trypsin solution was added to the reaction mixture. Further digestion was done at 25 °C for more than 16 h and stopped by adding TFA to a final concentration of 0.2%. The final volume of the peptide solution was about 105 μL.

Peptide Purification by Size-Exclusion Chromatography (SEC). One third of the peptide solution (35 μL) was mixed with 15 μL of acetonitrile and applied to a Superdex Peptide 3.2/300 column (GE Healthcare) connected to an ÄKTAmicro FPLC system (GE Healthcare). SEC was performed at 0.1 mL/min flow rate with SEC solution containing 30% acetonitrile and 0.1% formic acid in water. Eight fractions (F1−F8, 100 μL each) were collected and the same fractions of three runs were pooled and dried in tubes.

Peptide Purification with C18 Column Followed by SEC. A Sep-Pak tC18 cartridge (50 mg, Waters) was activated with 1 mL of 100% methanol and equilibrated with 1 mL of 2% acetonitrile and 0.1% TFA in water. The solution (105 μL) of digested peptides was loaded onto the column. The C18 column was washed once with 0.5 mL washing solution (2% acetonitrile and 0.5% acetic acid) and twice with 1 mL washing solution. Peptides were eluted from the column with 250 μL elution solution (60% acetonitrile and 0.1% TFA) and dried in the tube. The peptides were dissolved in 150 μL of SEC solution. Three aliquots (50 μL each) of the peptide solution were fractionated by three SEC runs as described above.

LC-MS/MS Analysis. Peptides were dissolved in 25 μL of water containing 0.1% TFA. A total of 5 μL of this peptide solution were separated on an Ultimate 3000 RSLC nano system (precolumn: C18, Acclaim PepMap, 300 μm × 5 mm, 5 μm, 100 Å, separation column: C18, Acclaim PepMap, 75 μm × 500 mm, 2 μm, 100 Å, Thermo Fisher Scientific). After loading the sample on the precolumn, a multistep gradient from 5−40% B (90 min), 40−60% B (5 min), and 60−95% B (5 min) was used with a flow rate of 300 nL/min; solvent A: water + 0.1% formic acid; solvent B: acetonitrile + 0.1% formic acid. The nano-HPLC-system was coupled to a Q-Exactive Plus mass spectrometer (Thermo Fisher Scientific). Data were acquired in data-dependent MS/MS mode. For full scan MS, we used mass range of m/z 300−1800, resolution of R = 140000 at m/z 200, one microscan using an automated gain control (AGC) target of 3e6 and a maximum injection time (IT) of 50 ms. Then, we acquired up to 10 HCD MS/MS scans of the most intense at least doubly charged ions (resolution 17500, AGC target 1e5, IT 100 ms, isolation window 4.0 m/z, normalized collision energy 25.0, intensity threshold 2e4, dynamic exclusion 20.0 s). All spectra were recorded in profile mode.

Data Analysis and Cross-link Identification. Raw data from the Q-Exactive were converted to MGF (Mascot generic files) format with program msConvert GUI from ProteoWizard Toolkit version 3.[36] Program MeroX version 1.6.6.6[16,24] was used for cross-link identification. MS data in MGF format and protein sequences in FASTA format were loaded on the program and the cross-linked residues were searched. In the settings, the precursor precision and the fragment ion precision were changed to 10.0 and 20.0 ppm, respectively. RISE mode was used and the maximum missing ions was set to 1. Cross-links data were exported in CSV (comma-separated values) format. An additional python script (Supporting Information) was used to filter the cross-links with the values of the mass deviation, the false discovery rate (FDR), and the rank. Only cross-links of rank 1 were kept if more than one candidate were found for the same spectrum. Cross-link network maps were generated using cross-link data files exported by MeroX on the xVis[37] web site (https://xvis.genzentrum.lmu.de). Program PyMOL was used to visualize cross-links on the crystal structures (PDB entries: 2VE7, 5LSK, 4NF9) and was used to draw the electron microscopy density map (EMDB entry EMD-2549).

RESULTS

Optimization of Cross-linking Reaction with DSBU. We used three different human protein complexes (MIS12C, NDC80C, and KMN, Figure 2A,B) to establish and evaluate our protocol. First, we tested different concentrations of DSBU to optimize the cross-linking reaction. Protein complexes were diluted in buffer at 3 μM and incubated with different amounts of DSBU. A 1 h incubation at 25 °C with 2.4 mM DSBU (800-fold excess of the cross-linker over the molar concentration of the protein complexes) was sufficient to saturate the reactions of all three protein complexes (Figure 2C). Importantly, we did not observe any precipitation or other changes of the solution after the cross-linking reaction under these conditions. Complete shifts of cross-linked protein bands of MIS12C were observed with lower concentrations of DSBU on the SDS-PAGE gel, reflecting a smaller pool of reactive residues of MIS12C compared to NDC80C and KMN (Table S1 shows the numbers of reactive residues). Since we did not observe significant additional cross-linking of MIS12C and NDC80C at 1600-fold molar concentration of DSBU (Figure 2C), we decided to use 1000-fold molar concentration (3 mM) of DSBU for further cross-linking experiments of all three complexes.

Single-Step SEC Improves Peptide Yield and Subsequent Cross-link Identification. Next, we optimized the protocol of peptide purification and enrichment after proteolysis of the cross-linked proteins. Purification using a C18 reverse phase chromatography column is a common procedure for desalting and concentrating peptides after their proteolytic generation, and prior to further purification steps, most typically SEC or SCX.[18−20,22,38] However, we reasoned that passage on a C18 column might cause a significant loss and a consequent reduction of the pool of cross-linked peptides for subsequent analyses. We therefore asked if this step could be omitted, thus, proceeding directly to SEC. We

DOI: 10.1021/acs.analchem.8b02593
Anal. Chem. 2018, 90, 10990−10999

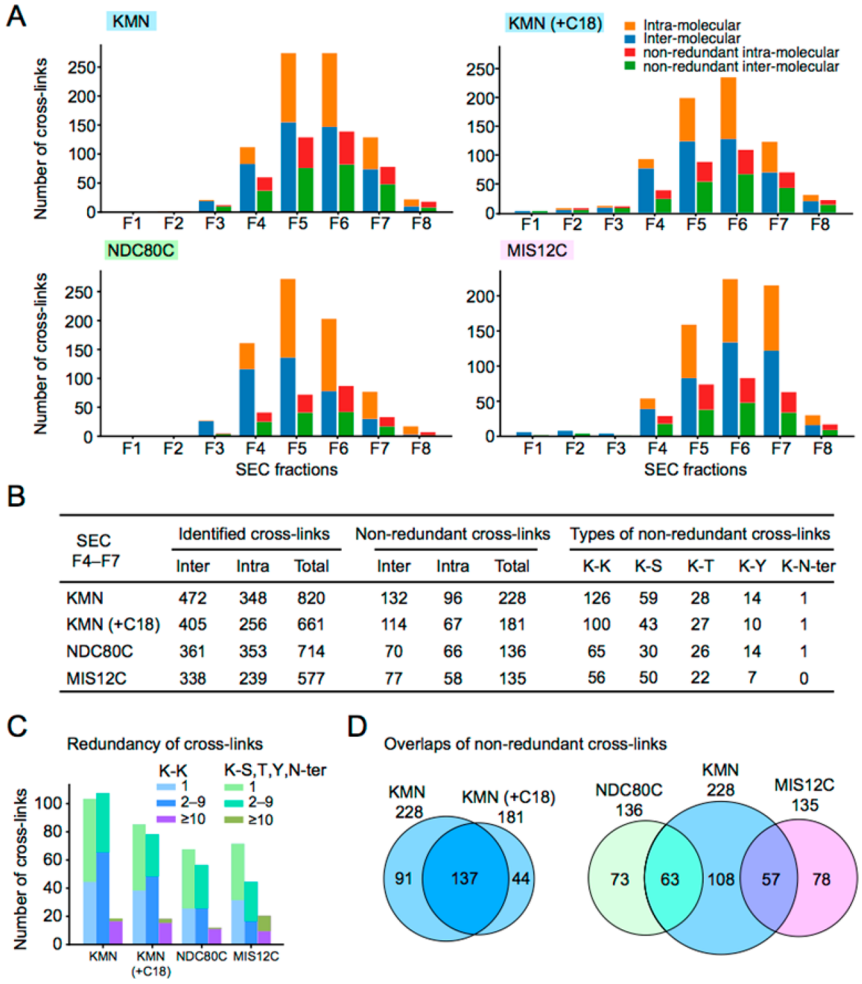

SEC F4–F7	Identified cross-links			Non-redundant cross-links			Types of non-redundant cross-links				
	Inter	Intra	Total	Inter	Intra	Total	K-K	K-S	K-T	K-Y	K-N-ter
KMN	472	348	820	132	96	228	126	59	28	14	1
KMN (+C18)	405	256	661	114	67	181	100	43	27	10	1
NDC80C	361	353	714	70	66	136	65	30	26	14	1
MIS12C	338	239	577	77	58	135	56	50	22	7	0

Figure 3. Representation of identified cross-links. (A) Bar graphs show the distributions of the cross-links identified from the eight SEC fractions of each experiment. Counting the numbers of non-redundant cross-links was limited to each fraction, even if the same cross-links exist in other fractions. (B) The table shows the numbers of cross-link in detailed categories. (C) Bar graphs show the distributions of the redundancy of the non-redundant cross-links in each experiment. (D) Venn diagrams show the overlaps among the cross-link data sets.

compared the results of cross-link identification of cross-linked KMN peptides purified with single-step SEC (on a Superdex Peptide 3.2/300 column on an FPLC system) or with a C18 column followed by SEC. Two pools of KMN (222 μg each) were dissolved at 3 μM in buffer and cross-linked with DSBU as described above (Figure 2D). The excess of DSBU was quenched by Tris-HCl buffer and removed by acetone precipitation of protein content. Cross-linked samples were denatured and digested with Lys-C and trypsin. We kept the final volume of digested peptide solution as low as possible for the subsequent SEC step (105 μL). For single-step SEC, the peptide solutions from each sample were divided into three aliquots for three separate SEC runs to avoid overloading of the column. For the parallel experiment, digested KMN peptides were purified using a 50 mg Sep-Pak tC18 cartridge as reported previously.[18,20] Dried peptides were dissolved in 105 μL of SEC solution and also fractionated in three separate SEC runs. Although the SEC profile of the sample previously purified by reverse phase chromatography was very similar to the profile of the sample directly separated by SEC after proteolytic cleavage (Figure 2E), the number of non-redundant cross-links identified by MeroX was smaller (181 instead of 228) when an additional C18 step was included (Figure 3A,B). Thus, omitting a step of purification on a C18 column simplifies the protocol and increases the yield of cross-linked peptides. We applied the same workflow to the individual MIS12C and NDC80C complexes and performed peptide enrichment with SEC only (Figure 2E, lower panel).

More than 135 Non-redundant Cross-links were Identified from Each Experiment. Peptides in each fraction (F1−F8) were analyzed separately by LC-MS/MS with a Q-Exactive Plus mass spectrometer using HCD for MS/MS acquisition. MeroX was used to identify cross-links and to perform automatic decoy analyses using shuffled sequence databases.[16,24] The FDR cutoff of MeroX at 5% was used to obtain initial cross-link data sets. In experiments with KMN, NDC80C, or MIS12C, most cross-links were found in SEC fractions F4−F7, although the distribution profiles were slightly different from each other (Figure 3A and Table S2). The distributions of non-redundant cross-links found in each SEC fraction were instead very similar in all experiments. Fraction F6 contained the highest number of non-redundant cross-links (Figure 3A). We combined the MS data from the cross-link-enriched fractions (F4−F7) and performed the analysis with MeroX to obtain a combined cross-link data set for each experiment.

We could assign cross-linked peptides to 577−820 spectra in experiments on KMN, NDC80C, and MIS12C with one-step

DOI: 10.1021/acs.analchem.8b02593
Anal. Chem. 2018, 90, 10990−10999

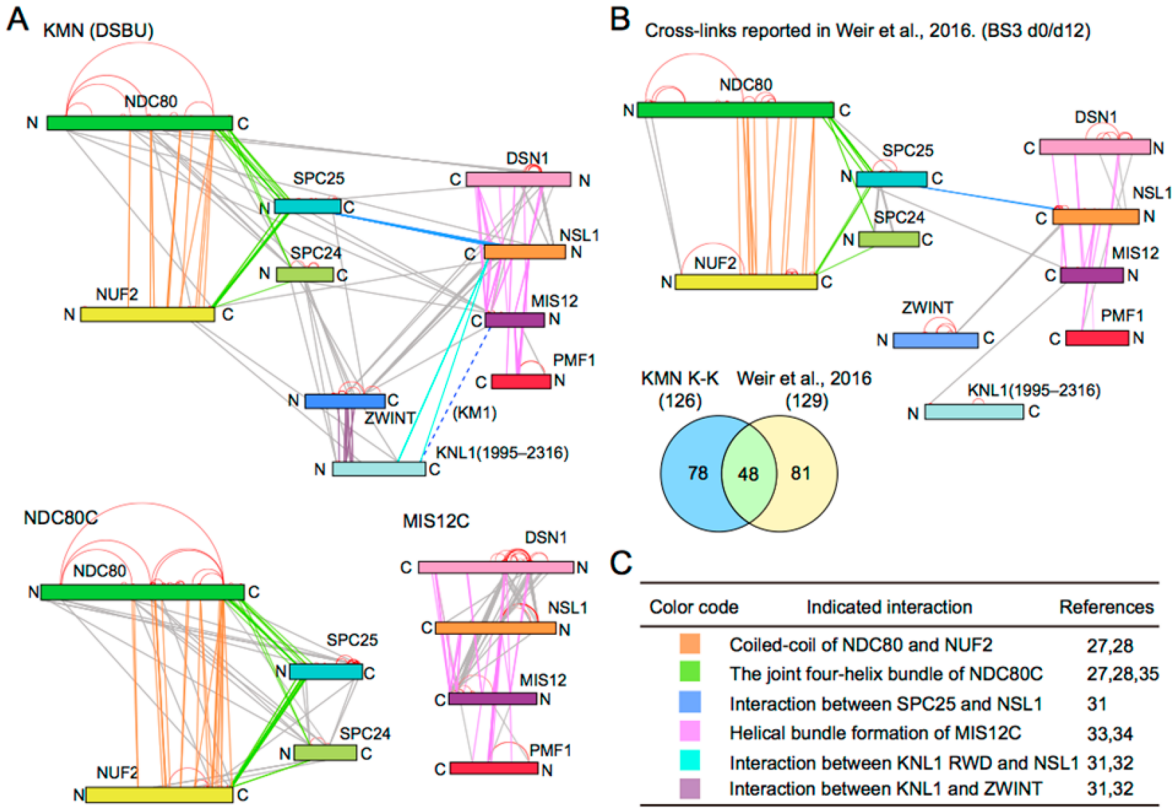

Figure 4. Identified cross-links confirm known interactions for the assembly of the KMN network. (A) Network maps show the cross-links obtained in the experiments of KMN, NDC80C, and MIS12C. Important cross-links were highlighted with colors. (B) The network map shows the previously reported cross-links among KMN subunits obtained with isotope-labeled BS3.[40] Color code as in panel A. Venn diagram shows the overlap between the non-redundant lysine–lysine cross-links of the KMN experiment and the previously reported cross-link data set (lysine–lysine only).[40] (C) Table describes the colored cross-links in (A) and (B) with their corresponding interactions.

SEC purification (Figure 3B and Table S3). Lists of non-redundant cross-links were obtained by removing the redundant entries from the combined cross-link data set (Figure 3B and Table S4). The number of non-redundant cross-links ranged from 135 to 228. About half of the non-redundant cross-links from all experiments were observed at least twice or more (Figure 3C), providing further evidence of their correct identifications. As expected, there were large overlaps between the data sets of non-redundant cross-links of KMN and NDC80C, and between the data sets of KMN and MIS12C, as expected since KMN includes both NDC80C and MIS12C (Figures 3D and 2A,B). At the same time, our analysis also suggests that more non-redundant cross-links can be identified when less complex samples are used (271 in total for NDC80C and MIS12C against 228 for KMN).

Many Nonlysine–Lysine Cross-links Were Identified. NHS-ester cross-linkers also react with serine, threonine, and tyrosine.[17,39] MeroX is programmed to detect nonlysine–lysine cross-links with the default setting, whereas other programs (e.g., xQuest[20] and XlinkX[15]) search exclusively for lysine–lysine cross-links in default mode. Rather unexpectedly, nonlysine–lysine cross-links accounted for 45%, 52%, and 59% of all non-redundant cross-links in the experiments on KMN, NDC80C, and MIS12C, respectively (Figure 3B). Among the nonlysine–lysine cross-links, the number of lysine–serine (K–S) cross-links was the highest and followed by the numbers of lysine–threonine (K–T) and lysine–tyrosine (K–Y) cross-links.

Interaction Networks Among KMN Proteins. In our experiments, we identified many interactions previously shown to be important for KMN formation.[27,28,31–35] Non-redundant cross-links of the three data sets (KMN, NDC80C, MIS12C) obtained in this study were visualized as interaction network maps using the program xVis[37] (Figure 4A,B). Intermolecular cross-links of known interactions were highlighted with different colors according to distinct structural domains (details are described in Figure 4C). In addition, we observed cross-links between ZWINT and NDC80C and cross-links between ZWINT and MIS12C (Figure 4A). Although these interactions have not been identified in previous analytical SEC experiments,[31] we observed cross-links between these components, which is indicative of spatial proximity between ZWINT and cross-linked subunits.

Many of the interactions identified by DSBU cross-linking were observed in previous studies using the noncleavable, isotope-labeled cross-linker BS3.[34,40] For instance, Figure 4B shows cross-links obtained in an experiment with a 21-subunit kinetochore protein complex treated with BS3 cross-linker.[40] For a clearer comparison between the two data sets, the cross-links are shown with the same color code as in Figure 4A. The KMN K–K data set described here and the one described by Weir and co-workers, share more than one-third of lysine–lysine cross-links (Figure 4B).

Newly Identified Cross-link Restricts Orientation of Knl1 RWD Domain. Progress in the determination of the structure of the human KMN network has benefitted from the determination of high-resolution crystal structures of (1) an

DOI: 10.1021/acs.analchem.8b02593
Anal. Chem. 2018, 90, 10990–10999

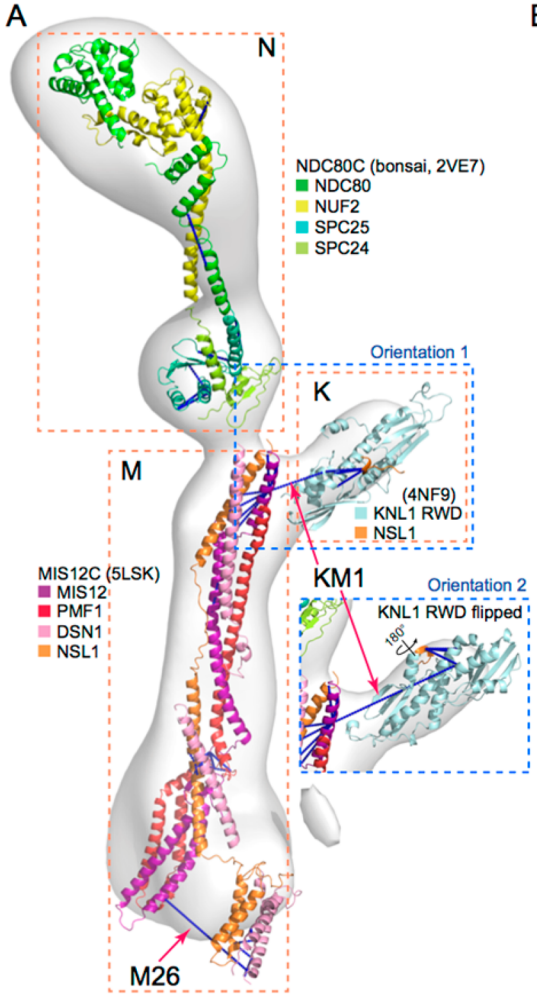

B

Cross-links	Type	Residue 1	Residue 2	Cα-Cα dist. (Å)	Times obs.
N1[a]	Intra	NDC80 Lys271	NDC80 Lys255	21.6	2
N2	Intra	NUF2 Lys21	NUF2 Tyr9	14.3	1
N3[a]	Intra	SPC25 Lys133	SPC25 Lys122	16.4	1
N4[a]	Intra	SPC25 Lys148	SPC25 Lys139	13.6	1
N5	Intra	SPC25 Lys203	SPC25 Lys216	20.0	2
N6	Intra	SPC25 Lys203	SPC25 Thr219	24.1	1
N7	Intra	SPC25 Lys216	SPC25 Ser187	14.3	1
N8	Intra	SPC25 Ser208	SPC25 Lys216	12.4	1
K1[b]	Inter	NSL1 Lys268	KNL1 Lys2221	14.8	7
K2	Inter	NSL1 Lys268	KNL1 Lys2298	21.4	2
K3	Inter	NSL1 Lys268	KNL1 Tyr2219	14.1	1
M1[ac]	Intra	MIS12 Lys146	MIS12 Lys153	10.5	2
M2	Intra	MIS12 Lys146	MIS12 Thr155	14.5	2
M3	Intra	MIS12 Lys187	MIS12 Lys197	15.5	7
M4	Intra	MIS12 Lys187	MIS12 Ser172	23.9	1
M5	Intra	MIS12 Lys187	MIS12 Ser199	18.1	13
M6	Intra	MIS12 Lys187	MIS12 Thr171	21.0	4
M7[ac]	Inter	MIS12 Lys187	NSL1 Lys189	15.1	1
M8	Inter	MIS12 Lys187	NSL1 Ser185	18.1	2
M9[c]	Intra	NSL1 Lys127	NSL1 Lys125	5.4	6
M10	Intra	NSL1 Lys127	NSL1 Thr124	5.0	1
M11	Intra	NSL1 Tyr129	NSL1 Lys125	5.1	2
M12	Intra	NSL1 Tyr129	NSL1 Lys132	5.4	1
M13[abc]	Intra	PMF1 Lys116	PMF1 Lys119	6.7	5
M14[c]	Inter	MIS12 Lys103	PMF1 Lys110	15.6	2
M15[ac]	Inter	NSL1 Lys127	MIS12 Lys103	11.3	16
M16	Inter	NSL1 Lys127	PMF1 Lys110	19.1	1
M17[c]	Inter	NSL1 Lys127	PMF1 Lys116	21.9	3
M18	Inter	NSL1 Tyr129	MIS12 Lys103	14.4	9
M19	Inter	NSL1 Tyr129	PMF1 Lys116	27.1	1
M20[ac]	Inter	PMF1 Lys116	MIS12 Lys103	14.9	13
M21	Inter	PMF1 Lys119	MIS12 Lys103	16.5	1
M22	Intra	DSN1 Lys167	DSN1 Ser160	11.9	1
M23	Intra	DSN1 Ser145	DSN1 Lys148	4.8	1
M24[a]	Inter	DSN1 Lys167	NSL1 Lys59	9.0	7
M25	Inter	DSN1 Ser172	NSL1 Lys59	10.6	1
M26	Inter	MIS12 Lys62	DSN1 Ser163	50.5	1
KM1	Inter	MIS12 Lys187	KNL1 Lys2298	~20 (ori.1) ~50 (ori.2)	2

a, Cross-links reported also in Weir et al., 2016
b, Cross-links reported also in Petrovic et al., 2010
c, Cross-links reported also in Petrovic et al., 2016

Figure 5. Evaluation and comparison of the cross-links with crystal structures. (A) Assembly model of KMN generated by fitting the crystal structures into an EM 3D reconstruction of a negatively stained sample.[34] Cross-links are shown as blue lines. Rectangles with orange-colored dashed line indicate the divided regions of mapped cross-links. Rectangles with blue dashed line indicate the two possible orientations of KNL1 RWD domain for fitting the crystal structure. (B) Table shows the details of the cross-links mapped on the crystal structures in (A). Lysine−lysine cross-links were shaded light blue: dist., distance; obs., observed; ori., orientation.

engineered version of the NDC80C (NDC80^{Bonsai}) lacking most of the coiled-coil region and tetramerization domain and the flexible N-terminal tail of the NDC80 subunit (PDB entry 2VE7); (2) a version of the MIS12C carrying truncation of flexible C-terminal tails involved in interactions with the NDC80C and the KNL1C (PDB entry 5LSK); and (3) the complex of the KNL1 C-terminal domain with its cognate binding site on NSL1 (KNL1$^{2096-2311}$/NSL1$^{266-274}$, PDB entry 4NF9). In a previous study, a composite model of the KMN (lacking ZWINT) was also assembled by fitting these high-resolution structures into a 3D reconstruction obtained from electron micrographs of a negatively stained sample of the KMN network (EMDB entry EMD-2549)[32,34] (Figure 5A). Since this model of the KMN network was obtained with truncated constructs, only 38 cross-links obtained with the full length KMN data set could be mapped onto it. The C_α−C_α distances of cross-linked residues are presented in Figure 5B. The mean value of the C_α−C_α distances was 15.6 Å, with distances distributed in a range of 5−27 Å. The most notable exception was cross-link M26, with a distance, predicted on the basis of the structure, of 50.5 Å. Most likely, the considerable flexibility of the Head2 domain of DSN1, where Ser163 is positioned, enables this cross-link.[34] A total of 13 out of 19 lysine−lysine cross-links were reported in previous studies[31,34,40] (Figure 5B). In many cases, the positions of lysine−lysine cross-links are very close to those of some nonlysine−lysine cross-links. For example, cross-link N5 shares one residue with cross-link N6 and N8. However, we also observed nonlysine−lysine cross-links having no lysine−lysine cross-link close to them, such as cross-link N2 and M23 (Figure 5B).

A new cross-link identified in this study between MIS12 Lys187 and KNL1 Lys2298 (cross-link KM1) was observed twice in the KMN experiment, and the assignment of theoretical masses of fragment ions to the MS/MS spectrum was satisfactory (Figure 6). The crystal structure of KNL1$^{2096-2311}$/NSL1$^{266-274}$ depicts a roughly ellipsoidal structure that can be fitted in the 3D EM reconstruction in two opposite orientations (Figure 5A). In the previous fitting of this model in the 3D reconstruction,[34] the best orientation of the KNL1/NSL1 complex could not be determined due to lack of adequate spatial restrains. We now report that the C_α−C_α distance of the cross-link KM1 in the model positioned in orientation 1 was ∼20 Å, much shorter than the distance of ∼50 Å observed in the model of orientation 2 (Figure 5A). Thus, the availability of cross-link KM1 provided us with a

DOI: 10.1021/acs.analchem.8b02593
Anal. Chem. 2018, 90, 10990−10999

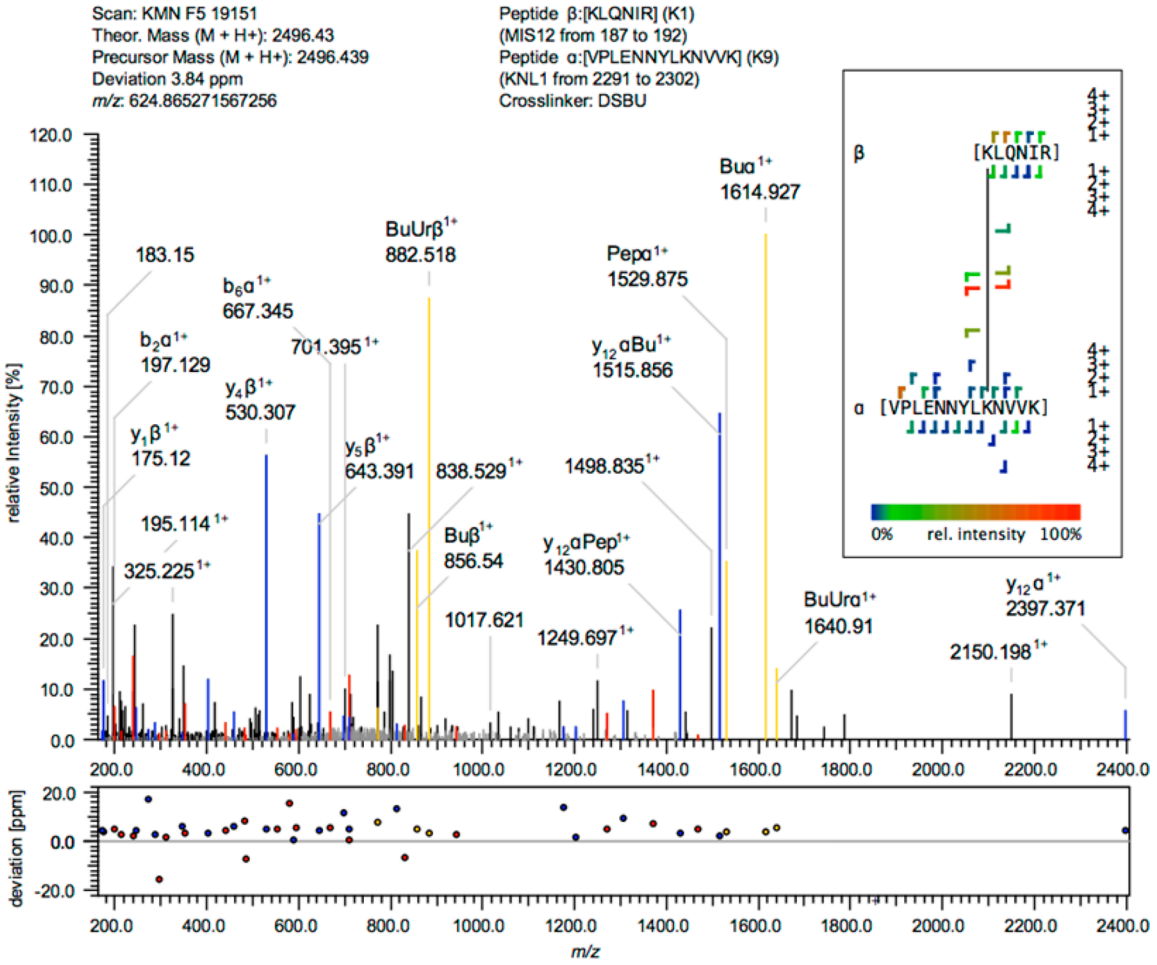

Figure 6. MS/MS spectrum of cross-link KM1. The spectrum was automatically annotated by MeroX. Yellow signals indicate the characteristic ions resulting from the fragmentation of DSBU. Signals for b-type ions are colored in red and y-type ions in blue.

spatial restrain to assess the correct orientation of a domain fitted in a 3D EM reconstruction of the KMN network.

DISCUSSION AND CONCLUSIONS

The MS cleavable cross-linker DSBU is currently less widely used than isotope-labeled noncleavable cross-linkers, but this study confirms its considerable potential for the analysis of protein−protein interactions by cross-linking and MS. After applying DSBU to several multiprotein complexes, we report that 135−228 non-redundant cross-links can be identified from one experiment using 72−222 μg protein samples. A single-step SEC peptide fractionation of the peptide mixture without a prior C18 desalting step was sufficient for desalting and peptide enrichment, resulting in a higher yield of identified cross-links. The high redundancy of cross-links observed in our experiments may reflect the abundance of each cross-linked peptide in the digested peptide mixture. Therefore, redundancy might be used as an additional filter to estimate the true positive cross-links.

Generally, identifying ideal cross-linking conditions requires optimization for each protein sample. Protein concentration of 0.5−2.0 mg/mL and 1 mM cross-linker were previously suggested for an initial trial.[20] The concentration of 2 mM disuccinimidyl sulfoxide (DSSO) has already been used for successful XL-MS analysis of a CRISPR RNA-silencing complex.[9] We used 3 μM protein (0.36−1.1 mg/mL) and 3 mM DSBU and obtained high redundant cross-linking data sets. Under the conditions of our protocol, we did not observe any precipitation after the cross-linking reaction. The resulting network maps of the cross-links are very meaningful (Figure 4A) and are in excellent agreement of the distribution of C_α−C_α distances of cross-links calculated from high-resolution structures (Figure 5B). Thus, our protocol provides a potentially useful starting point for the optimization of cross-linking conditions.

It has been reported previously that NHS esters react not only with lysine, but also with serine, threonine, and tyrosine.[17,39] Identification of a large fraction of nonlysine−lysine cross-links in our experiments (45−59%) is consistent with these previous results. There are several possible reasons why we obtained such a high percentage of nonlysine−lysine cross-links. First, the specificity of NHS esters is pH-dependent.[17,39] We performed the cross-linking reaction at pH 7.5, allowing the formation of nonlysine−lysine cross-links.[17,39] Second, we used higher concentration of DSBU (3 mM) compared to the concentrations (0.5−1 mM) used in previous studies,[16,24] which might increase the overall cross-link formation not only between primary amines but also between primary amines and the hydroxy groups of serine, threonine, and tyrosine. Third, our purification method resulted in high yield of cross-linked peptides and consequently enriched not only lysine−lysine cross-links but also less abundant nonlysine−lysine cross-links.

DOI: 10.1021/acs.analchem.8b02593
Anal. Chem. 2018, 90, 10990−10999

The DSBU cross-linking method we used here is comparable to the cross-linking methods that make use of isotope-labeled cross-linkers such as BS3.[34,40] The pattern of intermolecular cross-links of KMN obtained by DSBU cross-linking was similar to the pattern obtained using isotope-labeled BS3[40] (Figure 4). Both methods produced patterns of cross-links that were fully consistent with KMN subunit interactions previously identified and validated with biochemical and structural approaches.[27,28,31−35,40] Using DSBU we detected a larger set of cross-links between ZWINT or KNL1 and other KMN subunits. However, we cannot conclude that DSBU is superior to isotope-labeled BS3, because the KMN data set obtained with isotope-labeled cross-linkers is a subset of a larger cross-linking data set obtained on a protein complex containing 21 proteins,[40] that is, it was obtained with a more complex sample than the one we have used in the present study. A more systematic comparison goes beyond the scope of the present work, but our analysis clearly indicates that DSBU, combined with data analysis with MeroX, allows reaching results that are at least comparable with those obtained using the isotope-labeled noncleavable BS3.

The newly identified cross-link between MIS12 Lys187 and KNL1 Lys2298 (Figure 6) allowed us to restrain the orientation of the KNL1 C-terminal domain over another possible orientation in the fitting of its crystal structure into an EM 3D reconstruction (Figure 5). Refinement of 3D-models of protein complexes using cross-linking data has been used previously[6,11] and it was recently used to support a 3D-model of the nuclear pore complex.[41] Owing to the rapid development of EM single-particle-analysis, the need for reliable and simple methods to identify protein−protein interactions is increasing. Our simplified DSBU protocol will allow researchers in the field of biochemistry and structural biology to obtain high quality cross-link data sets.

■ ASSOCIATED CONTENT

Supporting Information

The Supporting Information is available free of charge on the ACS Publications website at DOI: 10.1021/acs.analchem.8b02593.

Table S1 and additional information (PDF).

Table S2: distribution of cross-links over SEC fractions (XLSX).

Table S3: all identified cross-links (XLSX).

Table S4: non-redundant cross-links (XLSX).

MeroX results files 1: zhrm and csv files (ZIP).

MeroX result files 2: zhrm and csv files (ZIP).

Python script for analysis (ZIP).

■ AUTHOR INFORMATION

Corresponding Authors

*E-mail: dongqing.pan@mpi-dortmund.mpg.de.

*E-mail: tanja.bange@med.uni-muenchen.de.

ORCID

Tanja Bange: 0000-0002-9680-8586

Author Contributions

‡These authors contributed equally to this work.

Notes

The authors declare no competing financial interest.

■ ACKNOWLEDGMENTS

We thank Arsen Petrovic and Jenny Keller for discussion on the KMN network, Sabine Wohlgemuth, Isabelle Stender, and Annika Take for support with protein production and protocol optimization. We thank Gabriele Stoehr and Petra Janning for critical reading of the manuscript. The mass spectrometry proteomics data have been deposited to the Proteome Xchange Consortium via the PRIDE partner repository (https://www.ebi.ac.uk/pride) with the data set identifier PXD010070.

■ REFERENCES

(1) Sinz, A. *Mass Spectrom. Rev.* **2006**, *25*, 663−682.

(2) Leitner, A.; Walzthoeni, T.; Kahraman, A.; Herzog, F.; Rinner, O.; Beck, M.; Aebersold, R. *Mol. Cell. Proteomics* **2010**, *9*, 1634−1649.

(3) Petrotchenko, E. V.; Borchers, C. H. *Mass Spectrom. Rev.* **2010**, *29*, 862−876.

(4) Rappsilber, J. *J. Struct. Biol.* **2011**, *173*, 530−540.

(5) Herzog, F. *Methods Mol. Biol.* **2014**, *1091*, 259−273.

(6) Yu, C.; Huang, L. *Anal. Chem.* **2018**, *90*, 144−165.

(7) Lasker, K.; Forster, F.; Bohn, S.; Walzthoeni, T.; Villa, E.; Unverdorben, P.; Beck, F.; Aebersold, R.; Sali, A.; Baumeister, W. *Proc. Natl. Acad. Sci. U. S. A.* **2012**, *109*, 1380−1387.

(8) Leitner, A.; Joachimiak, L. A.; Bracher, A.; Monkemeyer, L.; Walzthoeni, T.; Chen, B.; Pechmann, S.; Holmes, S.; Cong, Y.; Ma, B.; Ludtke, S.; Chiu, W.; Hartl, F. U.; Aebersold, R.; Frydman, J. *Structure* **2012**, *20*, 814−825.

(9) Benda, C.; Ebert, J.; Scheltema, R. A.; Schiller, H. B.; Baumgartner, M.; Bonneau, F.; Mann, M.; Conti, E. *Mol. Cell* **2014**, *56*, 43−54.

(10) Shi, Y.; Fernandez-Martinez, J.; Tjioe, E.; Pellarin, R.; Kim, S. J.; Williams, R.; Schneidman-Duhovny, D.; Sali, A.; Rout, M. P.; Chait, B. T. *Mol. Cell. Proteomics* **2014**, *13*, 2927−2943.

(11) Liu, F.; Heck, A. J. *Curr. Opin. Struct. Biol.* **2015**, *35*, 100−108.

(12) Holding, A. N. *Methods* **2015**, *89*, 54−63.

(13) Herzog, F.; Kahraman, A.; Boehringer, D.; Mak, R.; Bracher, A.; Walzthoeni, T.; Leitner, A.; Beck, M.; Hartl, F. U.; Ban, N.; Malmstrom, L.; Aebersold, R. *Science* **2012**, *337*, 1348−1352.

(14) Sinz, A. *Anal. Bioanal. Chem.* **2017**, *409*, 33−44.

(15) Liu, F.; Rijkers, D. T.; Post, H.; Heck, A. J. *Nat. Methods* **2015**, *12*, 1179−1184.

(16) Arlt, C.; Gotze, M.; Ihling, C. H.; Hage, C.; Schafer, M.; Sinz, A. *Anal. Chem.* **2016**, *88*, 7930−7937.

(17) Kalkhof, S.; Sinz, A. *Anal. Bioanal. Chem.* **2008**, *392*, 305−312.

(18) Leitner, A.; Reischl, R.; Walzthoeni, T.; Herzog, F.; Bohn, S.; Forster, F.; Aebersold, R. *Mol. Cell. Proteomics* **2012**, *11*, M111.014126.

(19) Fritzsche, R.; Ihling, C. H.; Gotze, M.; Sinz, A. *Rapid Commun. Mass Spectrom.* **2012**, *26*, 653−658.

(20) Leitner, A.; Walzthoeni, T.; Aebersold, R. *Nat. Protoc.* **2013**, *9*, 120−137.

(21) Schmidt, C.; Robinson, C. V. *Nat. Protoc.* **2014**, *9*, 2224−2236.

(22) Schmidt, R.; Sinz, A. *Anal. Bioanal. Chem.* **2017**, *409*, 2393−2400.

(23) Muller, M. Q.; Dreiocker, F.; Ihling, C. H.; Schafer, M.; Sinz, A. *Anal. Chem.* **2010**, *82*, 6958−6968.

(24) Gotze, M.; Pettelkau, J.; Fritzsche, R.; Ihling, C. H.; Schafer, M.; Sinz, A. *J. Am. Soc. Mass Spectrom.* **2015**, *26*, 83−97.

(25) Pesenti, M. E.; Weir, J. R.; Musacchio, A. *Curr. Opin. Struct. Biol.* **2016**, *37*, 152−163.

(26) Hara, M.; Fukagawa, T. *Curr. Opin. Cell Biol.* **2018**, *52*, 73−81.

(27) Ciferri, C.; De Luca, J.; Monzani, S.; Ferrari, K. J.; Ristic, D.; Wyman, C.; Stark, H.; Kilmartin, J.; Salmon, E. D.; Musacchio, A. *J. Biol. Chem.* **2005**, *280*, 29088−29095.

(28) Wei, R. R.; Sorger, P. K.; Harrison, S. C. *Proc. Natl. Acad. Sci. U. S. A.* **2005**, *102*, 5363−5367.

DOI: 10.1021/acs.analchem.8b02593
Anal. Chem. 2018, 90, 10990−10999

(29) Maiolica, A.; Cittaro, D.; Borsotti, D.; Sennels, L.; Ciferri, C.; Tarricone, C.; Musacchio, A.; Rappsilber, J. *Mol. Cell. Proteomics* **2007**, *6*, 2200−2211.
(30) Ciferri, C.; Pasqualato, S.; Screpanti, E.; Varetti, G.; Santaguida, S.; Dos Reis, G.; Maiolica, A.; Polka, J.; De Luca, J. G.; De Wulf, P.; Salek, M.; Rappsilber, J.; Moores, C. A.; Salmon, E. D.; Musacchio, A. *Cell* **2008**, *133*, 427−439.
(31) Petrovic, A.; Pasqualato, S.; Dube, P.; Krenn, V.; Santaguida, S.; Cittaro, D.; Monzani, S.; Massimiliano, L.; Keller, J.; Tarricone, A.; Maiolica, A.; Stark, H.; Musacchio, A. *J. Cell Biol.* **2010**, *190*, 835−852.
(32) Petrovic, A.; Mosalaganti, S.; Keller, J.; Mattiuzzo, M.; Overlack, K.; Krenn, V.; De Antoni, A.; Wohlgemuth, S.; Cecatiello, V.; Pasqualato, S.; Raunser, S.; Musacchio, A. *Mol. Cell* **2014**, *53*, 591−605.
(33) Dimitrova, Y. N.; Jenni, S.; Valverde, R.; Khin, Y.; Harrison, S. C. *Cell* **2016**, *167*, 1014−1027.
(34) Petrovic, A.; Keller, J.; Liu, Y.; Overlack, K.; John, J.; Dimitrova, Y. N.; Jenni, S.; van Gerwen, S.; Stege, P.; Wohlgemuth, S.; Rombaut, P.; Herzog, F.; Harrison, S. C.; Vetter, I. R.; Musacchio, A. *Cell* **2016**, *167*, 1028−1040.
(35) Valverde, R.; Ingram, J.; Harrison, S. C. *Cell Rep.* **2016**, *17*, 1915−1922.
(36) Chambers, M. C.; Maclean, B.; Burke, R.; Amodei, D.; Ruderman, D. L.; Neumann, S.; Gatto, L.; Fischer, B.; Pratt, B.; Egertson, J.; Hoff, K.; Kessner, D.; Tasman, N.; Shulman, N.; Frewen, B.; Baker, T. A.; Brusniak, M. Y.; Paulse, C.; Creasy, D.; Flashner, L.; et al. *Nat. Biotechnol.* **2012**, *30*, 918−920.
(37) Grimm, M.; Zimniak, T.; Kahraman, A.; Herzog, F. *Nucleic Acids Res.* **2015**, *43*, W362−369.
(38) Rinner, O.; Seebacher, J.; Walzthoeni, T.; Mueller, L. N.; Beck, M.; Schmidt, A.; Mueller, M.; Aebersold, R. *Nat. Methods* **2008**, *5*, 315−318.
(39) Madler, S.; Bich, C.; Touboul, D.; Zenobi, R. *J. Mass Spectrom.* **2009**, *44*, 694−706.
(40) Weir, J. R.; Faesen, A. C.; Klare, K.; Petrovic, A.; Basilico, F.; Fischbock, J.; Pentakota, S.; Keller, J.; Pesenti, M. E.; Pan, D.; Vogt, D.; Wohlgemuth, S.; Herzog, F.; Musacchio, A. *Nature* **2016**, *537*, 249−253.
(41) Kim, S. J.; Fernandez-Martinez, J.; Nudelman, I.; Shi, Y.; Zhang, W.; Raveh, B.; Herricks, T.; Slaughter, B. D.; Hogan, J. A.; Upla, P.; Chemmama, I. E.; Pellarin, R.; Echeverria, I.; Shivaraju, M.; Chaudhury, A. S.; Wang, J.; Williams, R.; Unruh, J. R.; Greenberg, C. H.; Jacobs, E. Y.; et al. *Nature* **2018**, *555*, 475−482.

DOI: 10.1021/acs.analchem.8b02593
Anal. Chem. 2018, 90, 10990−10999

Molecular Systems Biology 7; Article number 462; doi:10.1038/msb.2010.118
Citation: ***Molecular Systems Biology* 7:462**

www.molecularsystemsbiology.com

molecular systems biology

Proteomic snapshot of the EGF-induced ubiquitin network

Elisabetta Argenzio[1,5,7], Tanja Bange[2,7], Barbara Oldrini[1,6,7], Fabrizio Bianchi[1,3], Raghunath Peesari[1], Sara Mari[1], Pier Paolo Di Fiore[1,3,4], Matthias Mann[2] and Simona Polo[1,3,*]

[1] IFOM, Fondazione Istituto FIRC di Oncologia Molecolare, Milan, Italy, [2] Department of Proteomics and Signal Transduction, Max-Planck-Institute of Biochemistry, Martinsried, Germany, [3] Dipartimento di Medicina, Chirurgia ed Odontoiatria, Universita' degli Studi di Milano, Milan, Italy and [4] Dipartimento di Oncologia Sperimentale, Istituto Europeo di Oncologia, Milan, Italy
[5] Present address: The Netherlands Cancer Institute, Amsterdam, The Netherlands
[6] Present address: Memorial Sloan-Kettering, New York, NY, USA
[7] These authors contributed equally to this work
* Corresponding author. IFOM, Fondazione Istituto FIRC di Oncologia Molecolare, Via Adamello 16, Milan 20139, Italy. Tel.: +39 02 57 430 3242; Fax: +39 02 57 430 3231; E-mail: simona.polo@ifom-ieo-campus.it

Received 20.5.10; accepted 9.12.10

The activity, localization and fate of many cellular proteins are regulated through ubiquitination, a process whereby one or more ubiquitin (Ub) monomers or chains are covalently attached to target proteins. While Ub-conjugated and Ub-associated proteomes have been described, we lack a high-resolution picture of the dynamics of ubiquitination in response to signaling. In this study, we describe the epidermal growth factor (EGF)-regulated Ubiproteome, as obtained by two complementary purification strategies coupled to quantitative proteomics. Our results unveil the complex impact of growth factor signaling on Ub-based intracellular networks to levels that extend well beyond what might have been expected. In addition to endocytic proteins, the EGF-regulated Ubiproteome includes a large number of signaling proteins, ubiquitinating and deubiquitinating enzymes, transporters and proteins involved in translation and transcription. The Ub-based signaling network appears to intersect both housekeeping and regulatory circuitries of cellular physiology. Finally, as proof of principle of the biological relevance of the EGF-Ubiproteome, we demonstrated that EphA2 is a novel, downstream ubiquitinated target of epidermal growth factor receptor (EGFR), critically involved in EGFR biological responses.
Molecular Systems Biology **7**: 462; published online 18 January 2011; doi:10.1038/msb.2010.118
Subject Categories: proteomics; signal transduction
Keywords: EGF; network; proteomics; signaling; ubiquitin

Introduction

Post-translational modifications (PTMs) control the function of many proteins and are crucial to the regulation of many cellular processes, as exemplified by the role of phosphorylation in signaling. The reversible addition of a small phosphate group to protein substrates allows the propagation of information through multiple mechanisms, including activation/deactivation of the enzymatic properties of phosphorylated substrates, regulation of their subcellular localization, and their recognition by specific domains present in partner proteins (Seet *et al*, 2006). In another instance of PTM, a more complex molecule, ubiquitin (Ub), is appended by E3 ligases to a multitude of substrates, thereby modulating their function, localization and protein/protein interaction abilities (Mukhopadhyay and Riezman, 2007; Ravid and Hochstrasser, 2008). Deubiquitinating enzymes (DUBs) revert Ub conjugation, thus ensuring a dynamic equilibrium between pools of ubiquitinated and deubiquitinated proteins (Amerik and Hochstrasser, 2004). Particularly relevant to signaling is the ability of the Ub modification to induce *de novo* protein/protein interactions, similarly to phosphorylation, through the recognition of ubiquitinated proteins by proteins harboring Ub-binding domains (Hicke *et al*, 2005; Hurley *et al*, 2006). This mechanism sits at the heart of several signaling cascades (Mukhopadhyay and Riezman, 2007; Woelk *et al*, 2007; Chen and Sun, 2009), and is tightly controlled within the cell by endogenous and exogenous signals, such as DNA damage and growth factor stimulation, respectively (Chen and Sun, 2009).

In this latter instance, one of the best-characterized model systems is represented by the epidermal growth factor (EGF)-induced pathway. Upon EGF stimulation, a variety of proteins

are subject to Ub modification. These include the EGF receptor (EGFR), which undergoes both multiple monoubiquitination (Haglund *et al*, 2003) and K63-linked polyubiquitination (Huang *et al*, 2006), as well as components of the downstream endocytic machinery, which are modified by monoubiquitination (Polo *et al*, 2002; Mukhopadhyay and Riezman, 2007). The impact of ubiquitination on receptor internalization, intracellular sorting and ultimate metabolic fate has been characterized in detail for various receptors, including the EGFR (Acconcia *et al*, 2009).

Little is known, however, about the wider impact of EGF-induced ubiquitination on cellular homeostasis and on the pleiotropic biological functions of the EGFR. A decisive step in this direction would be the acquisition of the repertoire of proteins that are ubiquitinated upon EGF stimulation; i.e., the EGF-Ubiproteome. This study was undertaken to address this issue. Recent advances in quantitative mass spectrometry have allowed the study of PTMs on a global scale (Jensen, 2006; Choudhary *et al*, 2009). In this study, we combined two different purification procedures with high resolution, high accuracy MS, coupled to an efficient quantitation strategy, to obtain the first view of the EGF-induced Ubiproteome.

Results

Purification of Ub-conjugated proteins

Owing to the low abundance and labile nature of ubiquitinated proteins, the most critical step in their identification is the enrichment and purification procedure. This is particularly relevant in our case, as we are interested in the EGF-induced Ubiproteome. Under these conditions, ubiquitination is a rapid, dynamic process, and ubiquitinated substrates are present in the cell at low stoichiometries and in a time-limited manner. To maximize the recovery of ubiquitinated substrates, therefore, we used an integrated approach based on two different purification strategies and two cellular model systems (see schematic representation in Supplementary Figure S1).

In the first purification scheme, a mouse monoclonal antibody (FK2) that recognizes both mono- and polyubiquitinated species, but not free Ub, was used to immunopurify ubiquitinated proteins from HeLa cell lysates. This approach (hereafter, the 'endogenous' approach) allows the purification of proteins modified by endogenous Ub, in the absence of any manipulation of the cellular system (see Supplementary information and legend to Supplementary Figure S1 for details).

In an alternative strategy (hereafter, the tandem affinity purification 'TAP' approach), we exploited TAP. We developed a tandem affinity tag, consisting of a hexahistidine and a FLAG sequence fused to Ub (FLAG-His-Ub). This construct was transfected into B82L-EGFR cells, a mouse fibroblast cell line expressing human EGFR that has been widely used to study EGF-dependent signaling (Chen *et al*, 1989). The TAP method should allow the isolation of highly purified ubiquitinated proteins, as fully denaturing conditions (8M urea) are used, which dissolve most weak protein/protein interactions.

To overcome possible non-physiological and/or toxic effects of the overexpression of Ub (Tagwerker *et al*, 2006), we chose a TET-on inducible system (see Supplementary information for details). The level of expression of tagged Ub at different time points was assessed by immunofluorescence and immunoblot analysis (Figure 1A and B). Detection of high-molecular-weight Ub signals confirmed that the tagged Ub is functional and is conjugated to proteins (Figure 1B). Tagged Ub was expressed at one-tenth of the level of endogenous Ub (Figure 1C), sufficient to maintain the inducibility of the EGF-mediated process, as monitored by monoubiquitination of Eps15 (Figure 1D and Supplementary information). Finally, B82L-EGFR cells overexpressing FLAG-His-Ub displayed the same growth rate as untransfected cells (data not shown), indicating that the expression of the tagged Ub had no major toxic effect. We note that the 'endogenous' approach and the 'TAP' approach are not directly comparable as they are performed in different cellular systems. This was due to our inability to select a stable HeLa cell line expressing this tagged version of Ub. However, we reasoned that the use of a second cellular system, which differs both in terms of species and of tissue origin, might in some respects be advantageous, as it could lead to the identification of a common repertoire of ubiquitinated substrates.

For both approaches, the purification procedure was carefully set up and the yield was calculated to be 8% for the 'endogenous' approach and 20% for the 'TAP' approach (see Supplementary information and legend to Supplementary Figure S1 for details). Representative quality control experiments are presented in Figure 1E–H.

Of note, we performed a mock purification for the 'endogenous' approach by omitting the FK2 Ab in the purification scheme, and an I-DIRT experiment in the case of the 'TAP' approach (see 'control endogenous' and 'I-DIRT TAP' sheets in Supplementary Table S1 and Supplementary Figure S2). These experiments were used to filter out proteins that were non-specifically recovered during the purification procedures (see Supplementary information for details).

Identification of steady-state Ubiproteomes

Our ultimate goal was the identification of the EGF-induced Ubiproteome. Thus, we employed high resolution, high accuracy MS (Olsen *et al*, 2005) combined with stable isotope labeling with amino acids in cell culture (SILAC) (Ong and Mann, 2006) to distinguish the EGF-dependent ubiquitination events from the high background of steady-state ubiquitinated proteins. This strategy allowed the identification and quantitation of the steady-state HeLa and B82L-EGFR Ubiproteomes and the specific EGF-Ubiproteomes in a single experiment. We chose a single time point of EGF stimulation (10 min), and performed three biological replicates of both the 'endogenous' and the 'TAP' purifications. Remarkably, 73.2% (endogenous) and 85.2% (TAP) of proteins were identified in at least two experiments, indicating a high level of reproducibility. Experiment size and features are reported in Supplementary Table S1 and in Supplementary Figure S2.

As an initial step in our analysis, we employed a multi-layered strategy to define the size and specificity of the identified Ubiproteomes (Figure 2A). To obtain 'high-confidence data sets' of quantified proteins, we adopted four filtering criteria described in detail in the Experimental Procedures. By these criteria, from 11 722 non-redundant (NR) peptide sequences (corresponding to 1765 proteins)

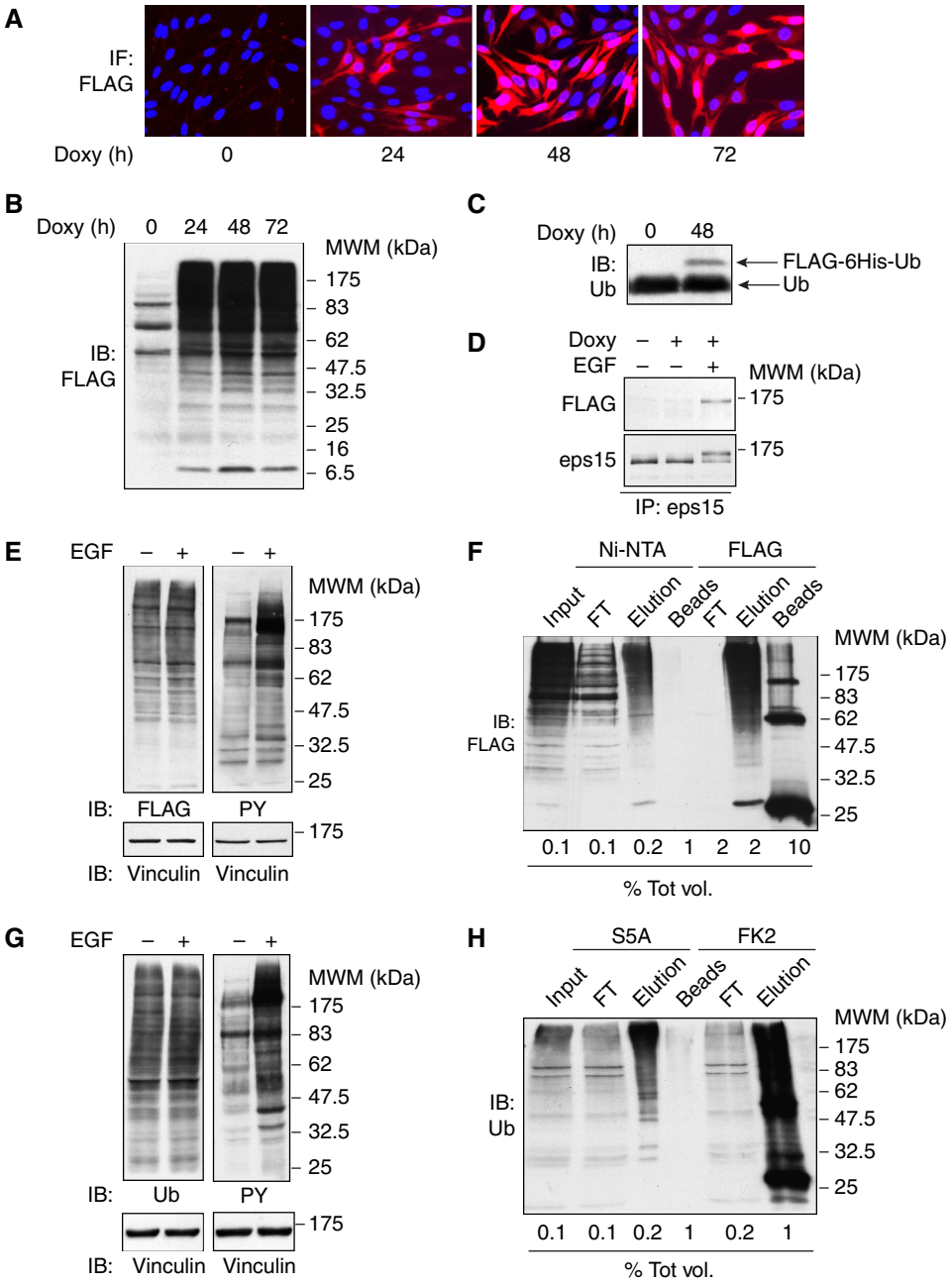

Figure 1 Preparation of samples for MS-based proteomics analysis. (**A**) B82L-EGFR cells stably transfected with FLAG-6His-Ub were fixed at the indicated time points after doxycycline induction (4 μg/ml) and stained with anti-FLAG antibody (red). Nuclei were DAPI stained (blue). (**B**) Parallel samples, treated as in A, were lysed and immunoblotted (IB) as indicated. (**C**) Lysates as in B, were IB with anti-Ub antibody to compare the levels of expression of endogenous and tagged Ub. (**D**) B82L-EGFR cells stably transfected with FLAG-6His-Ub were induced with doxycycline for 48 h and stimulated with EGF or left untreated. Lysates (2 mg) were immunoprecipitated (IP) and IB as indicated. (**E**, **F**) Quality control of a representative 'TAP' purification (experiment FW1, see Experimental Procedures and Results). B82L-EGFR cells induced for 48 h with doxycycline were stimulated with EGF (100 ng/ml) for 10 min or left untreated. Total cell lysates were analyzed by IB with the indicated antibodies before mixing them (1:1) for the purification (E). Aliquots from each step of the purification procedure were analyzed by IB with anti-FLAG antibody. The amount of loaded samples is expressed as % of total sample volume (F). (**G**, **H**) Quality control of a representative 'endogenous' purification (experiment FW2, see Experimental Procedures and Results). Lysates from EGF-treated (100 ng/ml, 10 min) or untreated HeLa cells were analyzed as in E (G). The purification procedure was controlled as in F, except that an anti-Ub antibody (P4D1) was used (H). Note that the EGF-induced increase in the total ubiquitinated protein content is not proportional to the increase in protein tyrosine phosphorylation. This is expected as the vast majority of Ub-modified species in the cell is represented by constitutively ubiquitinated proteins, destined to proteasomal degradation.

identified in the endogenous approach, we assembled a SILAC-based proteome comprising 1175 unambiguously identified and quantified proteins (Figure 2A and Supplementary Table S1). In the case of the TAP approach, we unambiguously identified 582 proteins (from 3173 NR peptides, corresponding to 744 proteins; Figure 2A and Supplementary Table S1). In both cases, the identification of short-lived proteins and monoubiquitinated proteins demonstrates that the two

A

	Endogenous	TAP	NR	Overlap End/TAP	*P* (overlap)
Peptides raw	11 722	3173			
Proteins raw	1765	744	2109	400	2.58×10^{-201}
Proteins after filtering	1175	582	1472	284	2.22×10^{-176}

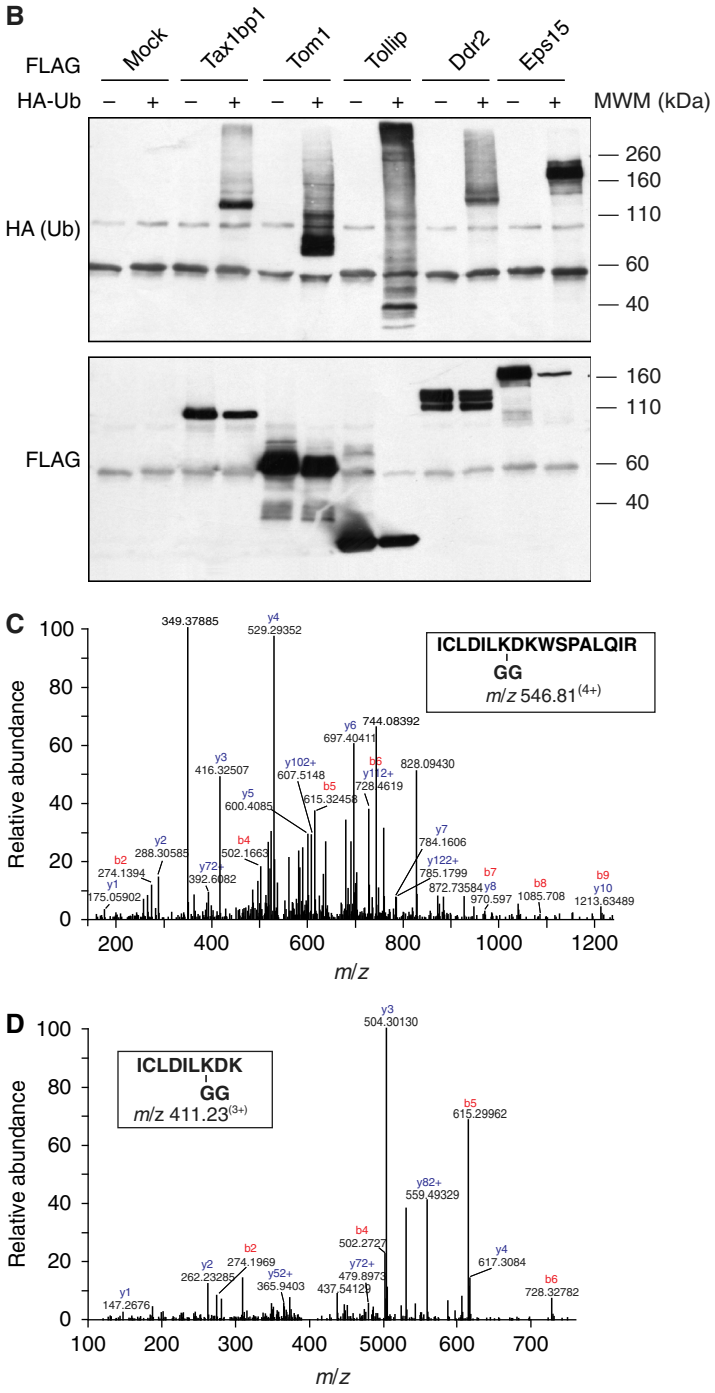

Figure 2 The steady-state Ubiproteome. (**A**) Size and features of steady-state Ubiproteomes identified with the endogenous and TAP approaches. NR, number of non-redundant proteins from the two approaches. Overlap End/TAP, number of proteins identified in common between the two approaches. *P*, significance *P*-value of the overlap (Fisher's exact test). (**B**) Validation of candidates (see also additional examples in Supplementary Figure S3). Cells (293T) were transfected with the indicated constructs and lysed after 24 h. Lysates were IP anti-FLAG (candidates) and IB with anti-HA (Ub) antibody to evaluate the ubiquitination level of the candidates. (**C**, **D**) MS/MS spectra of the identified ubiquitination site of ubiquitin-conjugating enzyme Ube2N (Ubc13). (C) Fragmentation pattern of the quadruple-charged tryptic peptide of Ube2N derived from HeLa cellular extracts. (D) Fragmentation pattern of the triply charged tryptic peptide of Ube2N derived from B82L-EGFR cellular extracts. The y-series of ions (C terminus containing fragments) are labeled in blue and b-series (N terminus containing fragments) are labeled in red.

strategies are effective. In addition, the retrieval of nuclear proteins together with histones argues for the efficiency of the solubilization procedure. This said, we acknowledge that the identified Ubiproteomes are unlikely to represent the full repertoire of ubiquitinated proteins found in mammalian cell, although they are the most complete set of ubiquitinated proteins identified so far (Supplementary Figure S3).

To validate our Ubiproteomes, we tested several candidates by direct immunoprecipitation (IP; Figure 2B and Supplementary Figure S3). On the basis of these results, we estimated a false-positive rate of ~5% for the 'endogenous' approach (2 out of 38 tested candidates were not validated by IP) and ~3% for the TAP approach (1 out of 30 candidates was not validated, see legend to Supplementary Figure S3 for details). The non-validated proteins possibly represent the fraction of Ub-interacting proteins co-purified during the procedure, as they were absent in the control purifications (Supplementary Table S1).

We also analyzed the overlap between the endogenous and the TAP Ubiproteomes. One limitation of our study is that the two approaches were optimized in two different cell types. Nevertheless, 284 proteins were identified in common between the two approaches (P=2.22×10^{-176}, Figure 2A and Supplementary Table S1). This high degree of overlap is remarkable given that the two cellular settings are very different (a human cervical cancer cell line versus a mouse fibroblast cell line).

Of note, we identified 31 ubiquitination sites in 21 target proteins, some of which were previously unknown. The complete list of identified sites is shown in Supplementary Table S1. A representative instance of these findings is the E2-conjugating enzyme Ubc13, for which the same modified K was found in both the human and the mouse cell line (Figure 2C and D, see also legend to Supplementary Table S1 for details).

The EGF-Ubiproteome

We next exploited the quantitative information embedded in the SILAC data to identify the EGF-regulated Ubiproteome. Protein quantitation was performed automatically using MaxQuant, as described previously (Cox and Mann, 2008). Ratios for proteins were determined as the median of all measured peptide ratios for a given protein, to minimize the effect of outliers (Supplementary Figure S4). To identify proteins that were most significantly regulated by EGF, we employed a stringent three-tiered selection process. Starting from the two steady-state Ubiproteomes, we discarded proteins with a P-value >0.1 (Significance B, see Cox and Mann, 2008) and a coefficient of variability >10 (filter A in Figure 3A, see Supplementary information for details). Finally, we applied a manual curation step selecting only those proteins displaying the same trend of regulation in the experimental replicates (filter B, Figure 3A). Additionally, we verified that protein levels did not change upon EGF stimulation in the whole proteomes (Supplementary Figure S5). By these stringent criteria, we concluded that ~15% of the steady-state Ubiproteome was EGF regulated at 10 min after stimulation; 176 of 1175 proteins in the endogenous approach and 105 of 582 proteins in the TAP approach (Figure 3A and Supplementary Table S2). Interestingly, both hyper- and hypoubiquitinated proteins were detected (134 hyper- and 42 hypoubiquitinated in the endogenous approach, 58 hyper- and 47 hypoubiquitinated in the TAP approach; Figure 3B and C and Supplementary Table S2), indicating that EGFR-mediated signaling can modulate the Ub network in both directions. This finding is supported by the presence of both ubiquitinating and deubiquitinating enzymes in the EGF-Ubiproteome (see below).

The major limitation of our study is that our EGF-Ubiproteomes were not time resolved. Indeed, while we identified virtually all proteins known to be ubiquitinated upon EGF stimulation in both Ubiproteomes, only 16 out of 92 proteins were commonly classified as regulated at 10 min of EGF stimulation (when the proteomic analysis was performed). Of these, 14 proteins (10 hyperubiquitinated and 4 hypoubiquitinated) were regulated in the same direction in both approaches (Supplementary Table S1). Twenty-seven additional proteins were found to be regulated only in the endogenous approach (24 hyperubiquitinated and 3 hypoubiquitinated), while 49 additional proteins were identified only in the TAP approach (23 hyperubiquitinated and 26 hypoubiquitinated; see Supplementary Table S1). While cellular specificity may account for some of these variations (Figure 3A), different kinetics of ubiquitination in the two cellular systems might also affect the extent of the overlap. As a case in point, the endocytic adaptor protein Eps15 is ubiquitinated following EGF stimulation (Polo *et al*, 2002). Eps15 was present in the B82L-EGFR (TAP) but not in the HeLa (endogenous) EGF-Ubiproteome (Supplementary Table S2). Immunoblot analysis revealed that the kinetics of Eps15 ubiquitination upon EGF stimulation differed in the two cellular systems: at 10 min Eps15 was ubiquitinated in B82L-EGFR, but not in HeLa, cells (Figure 3D). Similar results were obtained for Rabex-5 and Hgs (data not shown).

The concept that the two EGF-Ubiproteomes might represent different time-resolved snapshots of the same network in two cellular systems is further supported by results derived from protein ontology analysis. We classified the EGF-regulated Ubiproteomes by PANTHER (Protein ANalysis THrough Evolutionary Relationships; Wiesner *et al*, 2007), and analyzed the enrichment of ontology terms. We identified 29 biological process (BP) terms as enriched (P-value <0.05) in the endogenous data set and 17 BP terms in the TAP data set (Figure 3E and F). Nine identical and three closely related BP terms were found in both EGF-Ubiproteomes: 41 and 70% of BP terms in the endogenous and TAP Ubiproteomes, respectively (reported in bold in Figure 3E and F). Therefore, regardless of the different experimental strategies employed and, more importantly, of the different experimental models, the two EGF-regulated Ubiproteomes show a high level of conservation in the cellular mechanisms that they represent.

Chain topology of the EGF-regulated Ubiproteome

To evaluate possible changes in the relative abundance of the different chains upon EGF stimulation, we quantified the Ub 'signature' peptides by SILAC (see Meierhofer *et al*, 2008 and Supplementary Table S3). With the TAP approach, MS analysis revealed an increase in the K63-, K11- and K6-chain modifications after EGF stimulation (Supplementary Table S3 and

Supplementary Figure S6), whereas with the endogenous approach only K63 linkages accumulated, although to a lesser degree (Supplementary Table S3, see its legend for details). A possible explanation for this discrepancy is that the tagged Ub could affect the activity of specific E3s or DUBs, due to the extra N terminus present in the molecule. This would cause indirect changes in the level of specific chain linkages. To evaluate this possibility, we quantified the Ub 'signature' peptides before and after FLAG-His-Ub induction. No significant changes were evident when comparing the two conditions, indicating that, at least in our controlled settings, the expression of tagged Ub *per se* does not change the level of specific Ub chains (Supplementary Figure S7).

These initial, yet not conclusive, results prompted us to validate the MS analysis using the recently developed K48 and K63 linkage-specific antibodies (Newton *et al*, 2008). A strong colocalization of EGFR-containing vesicles and the anti-K63 antibody was observed upon EGF stimulation, whereas no

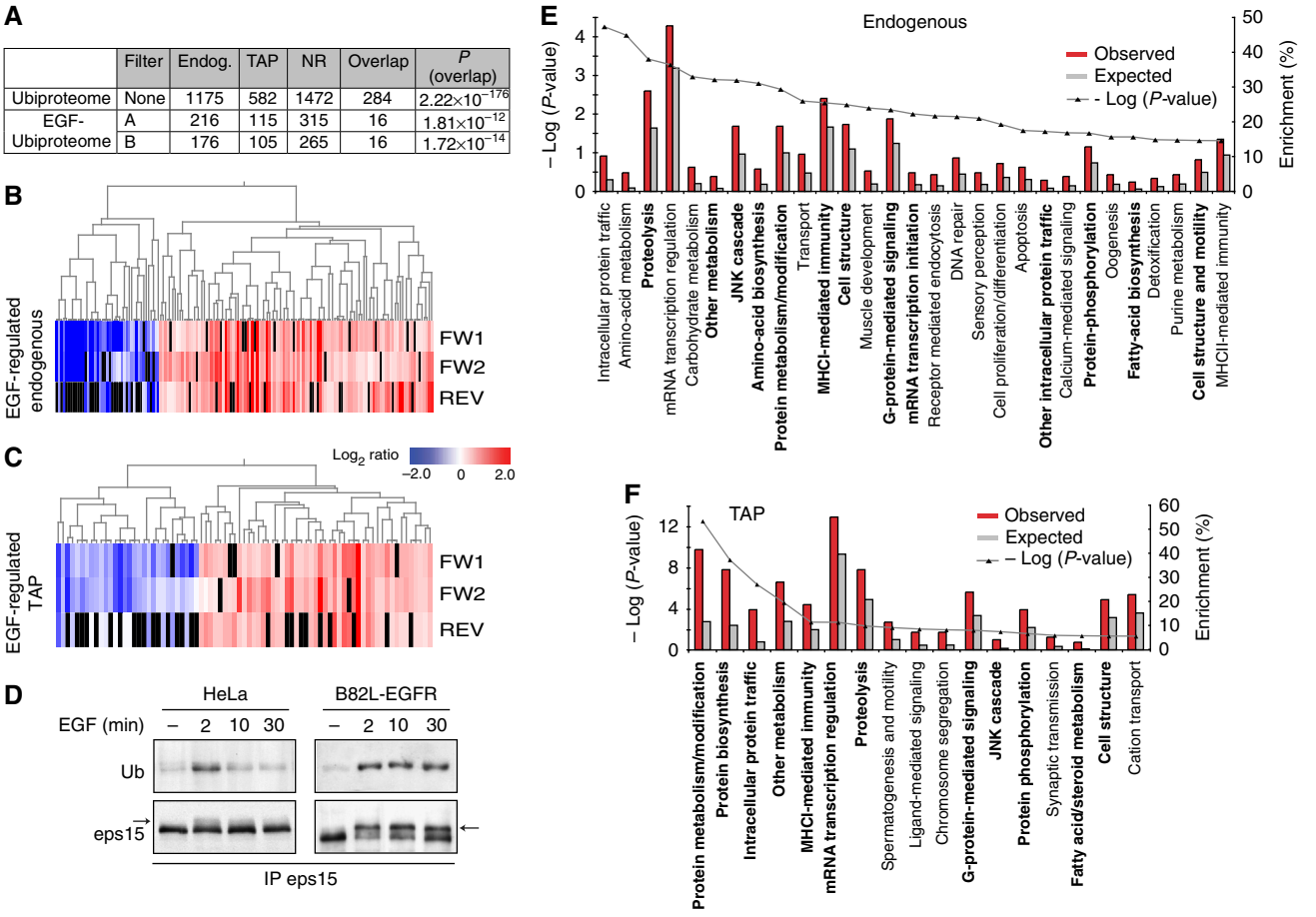

Figure 3 The EGF-regulated Ubiproteome. (**A**) Determination of EGF-regulated ubiquitinated proteins. We discarded from the steady-state Ubiproteomes, proteins with a significance B > 0.1 and a coefficient of variability across replicates > 10 (Filter A), and proteins showing a different trend of regulation in replicate experiments (Filter B). NR, number of non-redundant proteins from the two approaches. Overlap End/TAP, number of proteins identified in common between the two approaches. *P*, significance *P*-value of the overlap (Fisher's exact test). Hyper- and hypoubiquitinated proteins in the EGF-Ubiproteomes. (**B**, **C**) The 176 human (B) and the 105 mouse (C) EGF-regulated proteins were clustered across the three experimental replicates (FW1, FW2, REV). Side color bar represents the $\log_2$ of the normalized protein ratio (H, EGF treated versus L, untreated). Red, positive ratio (hyperubiquitinated); blue, negative ratio (hypoubiquitinated); and Black, missing data. (**D**) Kinetics of Eps15 monoubiquitination in HeLa and B82L-EGFR cells. Serum-starved HeLa (left panel) or B82L-EGFR (right panel) cells were stimulated with EGF (100 ng/ml) for the indicated time points or left untreated. Lysates (1 mg) were IP and IB with the indicated antibodies. Arrows on the lower panels indicate the ubiquitinated form of Eps15. (**E**, **F**) PANTHER analysis of the human (E) and the mouse (F) EGF-Ubiproteomes. Enrichment plots of ontology terms (Biological process, *x* axis) built on the list of EGF-Ubiproteome proteins. The percentage enrichment, based on the ratio between the number of SILAC proteins and the total number of proteins grouped in each term, is plotted on the right *y* axis (red histograms). The expected enrichment (gray histograms) is obtained from the ratio between the total number of genes in the term and the total number of genes in the genome. The statistical significance between observed and expected enrichments (scattered line) was determined by Fisher's exact test and is plotted on the left *y* axis as $-\log_{10}$ of *P*-values; the higher the value, the more significant the enrichment ($-\log_{10}$ of $P=0.05$ is 1.30). In bold, the 12 pathways found in both EGF-Ubiproteomes (three are closely related: protein/amino-acid biosynthesis; intracellular/other intracellular protein traffic; fatty acid biosynthesis/fatty acid and steroid metabolism).

Figure 4 EGF induces K63-specific ubiquitination. (**A**) HeLa cells grown on coverslips were serum-starved for 4 h and treated for 10 min at 37°C with rhodamine-EGF (0.5 μg/ml, red) or left untreated (left panels). Ub (green) was detected with the FK2 antibody that recognizes both mono- and poly-Ub (upper panel) or antibodies that specifically recognize K63- or K48-linked Ub chains (middle and lower panels, respectively). Confocal images are shown. Blue, DAPI staining. Bar, 18 μm. (**B**) Lysates (1 mg) from HeLa cells stimulated with EGF (100 ng/ml) for the indicated times were subjected to IP with K63-Ub or K48-Ub-chain-specific antibodies or the FK2 antibody. IPs and lysates (50 μg/lane) were IB with the indicated antibodies. P4D1 antibody was used for the anti-Ub IB. Asterisk, unspecific band. Note that both spliced forms of Nedd4L appear to be ubiquitinated.

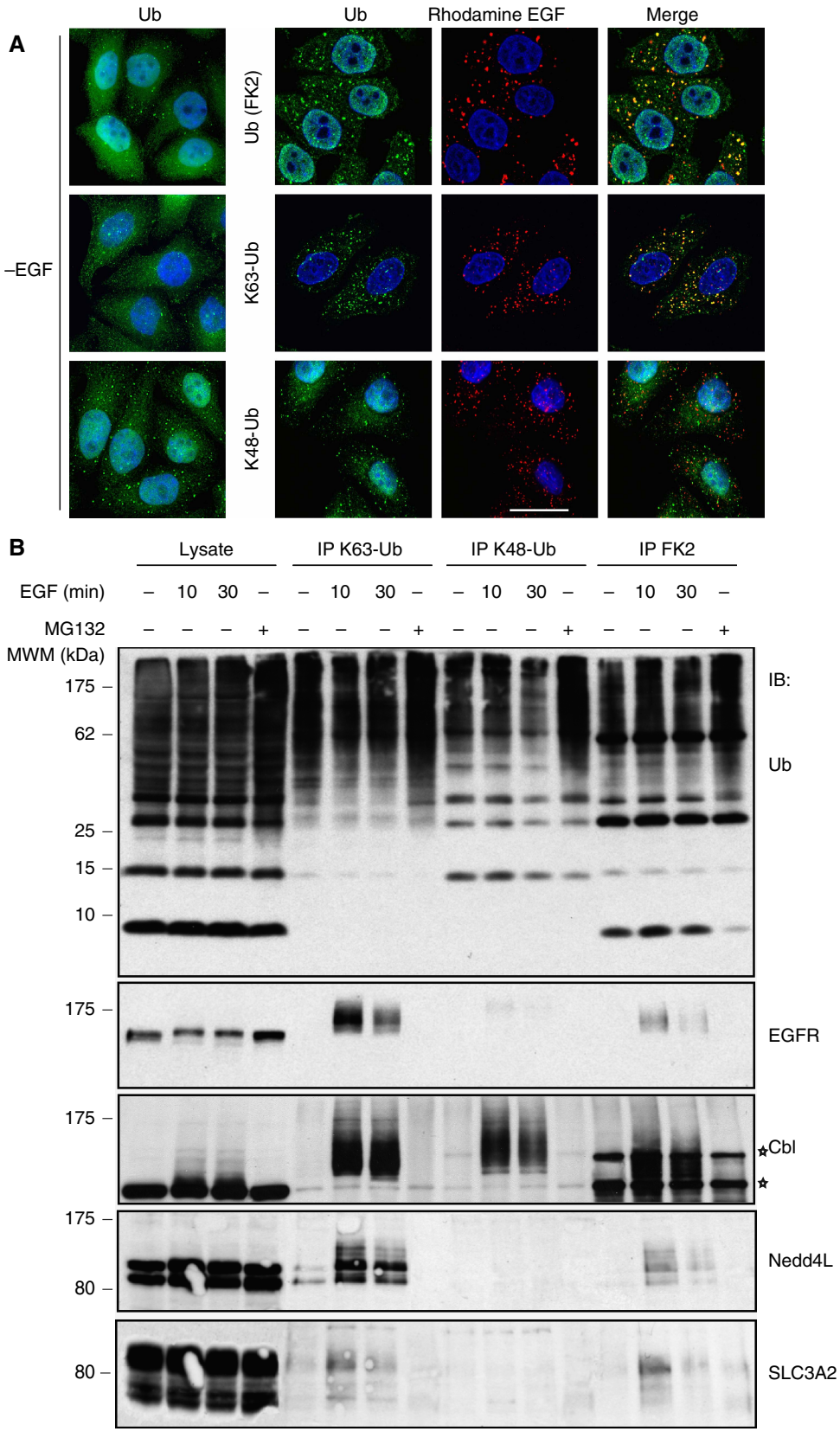

colocalization was visible with the K48-specific antibody (Figure 4A). The FK2 antibody, which recognizes all types of poly-Ub chains equally well (Supplementary Figure S8), displayed an intermediate phenotype (Figure 4A).

We then assessed some validated hits from our EGF-Ubiproteome by IP with linkage-specific antibodies and immunoblot analysis. Upon EGF stimulation, EGFR is almost exclusively modified by K63-linked chains (Figure 4B), in agreement with previous findings (Huang *et al*, 2006). Cbl, which is degraded upon EGF stimulation (Magnifico *et al*, 2003), is also strongly modified by K63 chains (Figure 4B). Notably, we also validated two novel EGF-induced ubiquitinated targets, namely, Nedd4L and SLC3A2, and showed that they carry almost exclusively K63-linked chains (Figure 4B). These results strengthen the idea that K63 might not only be the preferred signal for receptor internalization as previously suggested (Lauwers *et al*, 2010), but also be the major Ub-based signal transmitted by the active EGFR.

Network analysis of the EGF-regulated Ubiproteome

To obtain a higher-resolution molecular picture of the EGF-regulated Ub network, we analyzed the NR-EGF-Ubiproteome (265 proteins, Supplementary Table S2) through the Ingenuity Pathways Knowledge Software (Ingenuity® Systems, http://www.ingenuity.com) and looked for enrichment of canonical pathways. We identified 85 proteins that were significantly enriched in 39 pathways (P-value <0.05, Fisher's exact test), of which 13 pathways (67 proteins) remained significant after multiple test correction (P-value <0.05, Benjamini and Hochberg False Discovery Rate; Figure 5A). In addition to well-established liaisons (such as those with clathrin and caveolar endocytosis, or virus entry pathways), the EGF-Ubiproteome intersects many circuitries of intracellular signaling, suggesting crosstalk between EGFR-activated pathways and other signaling pathways through the Ub network.

We further organized the EGF-Ubiproteome into distinct interaction networks through the Ingenuity Pathways Knowledge Software to predict how the Ub modification might influence the molecular crosstalk between proteins that interact biochemically and/or genetically. The proteins of the EGF-Ubiproteome are grouped into 30 networks, of which 11 reached statistical significance ($P<0.0001$, random permutation test, Figure 5B). Interestingly, unsupervised clustering of these 11 networks, based on the number of common proteins, revealed two main clusters (C1 and C2, Figure 5B). Functional annotation of molecules in these networks through the Molecular Signature Database (MSigDB) (Subramanian *et al*, 2007) revealed that cluster C1 is enriched in proliferation and inflammation signatures, whereas cluster C2 contains networks enriched in apoptosis, adhesion and cell cycle signatures. Interestingly, network 1 does not belong to any cluster (i.e., no proteins are shared with other networks) and is specifically enriched in ribosomal proteins (see Figure 5B and Supplementary information for details).

The ability of EGF-Ubiproteome proteins to nucleate clusters of interactions involved in diverse functions suggests that these proteins might act as organizational 'hubs', proteins that can establish multiple protein/protein interactions and thereby regulate the organization of networks. This is indeed the case, as proteins of the EGF-Ubiproteome displayed significantly higher connectivity than randomly generated lists of proteins (5000 lists were tested; Figure 5C and Supplementary Table S3). In total, 65 hubs (defined as proteins with $\geqslant 5$ interactors) were identified in the EGF-Ubiproteome (Supplementary Table S3). Among them, Hgs and Cbl, which have already been demonstrated to be critical for many intracellular signaling networks (Schmidt and Dikic, 2005; Zwang and Yarden, 2009), displayed the highest connectivity.

Intersection of the EGF-induced Ubi- and phosphotyrosine proteomes

EGF binding to its receptor triggers a series of phosphorylation events that culminates in transcriptional activation and the mitogenic response. Proteins that undergo EGF-triggered phosphorylation have recently been described in three EGF-induced phosphotyrosine (pY) proteomes (Blagoev *et al*, 2004; Oyama *et al*, 2009; Hammond *et al*, 2010). A comparison of our EGF-Ubiproteome with these EGF-pY proteomes, as well as with the phospho.ELM database (Diella *et al*, 2008) that contains experimentally validated pY-containing proteins, revealed a significant overlap between ubiquitinated and pY proteins (Figure 6A, Supplementary Table S3). In total, 23% (61 of 265) of the EGF-Ubiproteome proteins are also tyrosine phosphorylated (Figure 6A, Supplementary Table S3).

Pathway analysis of these 61 Ub/pY-containing proteins revealed a significant enrichment in endocytic and signal-transduction pathways (Figure 6B). Finally, 'hub analysis' revealed that Ub/pY-containing proteins are enriched in highly connected proteins to an even greater extent than Ub-containing proteins alone (Figure 6C). These data point to a complex

Figure 5 Pathway analysis of the EGF-Ubiproteome. (**A**) Ingenuity pathway analysis. Enrichment plots of canonical pathways (*x* axis) built on the list of 265 EGF-regulated proteins Ubiproteome (sum of the endogenous and the TAP approaches). The percentage enrichment, based on the ratio between the number of SILAC regulated proteins and the total number of proteins annotated in each pathway, is plotted on the right *y* axis (black line). The significance of the enrichment (gray bars) was calculated using the Benjiamini Hochberg multiple testing correction and is plotted on the left *y* axis as $-\log_{10}$ of *P*-values; the higher the value, the more significant the enrichment ($-\log_{10}$ of $P=0.05$ is 1.30). (**B**) Network analysis of the EGF-Ubiproteome. Left panel, list of the 11 networks that reach high statistical significance ($P<0.0001$, see Supplementary information). Network, network ID number. Molecules, number of EGF-Ubiproteome proteins/total number of network proteins. Description, functional category based on MSigDB analysis. Relevance, percentage of proteins in functional categories relative to total proteins in the network. Right panel, unsupervised hierarchical clustering of the identified networks. Clusters were generated based on the number of proteins in common between networks divided by the total number of proteins present in each network (Supplementary Table S3). The percentage of shared proteins is indicated by color code (white, 0%; red, $\geqslant$50%). (**C**) Hub analysis. The number of random sets of proteins containing hubs (proteins with more $\geqslant 5$, 10 interactors as annotated in the BioGRID human interaction database (Stark *et al*, 2006)) is displayed. The red dashed line indicates the position in the distribution of the EGF-Ubiproteome (265 proteins). *y* axis, number of random sets containing hubs (defined as above), *x* axis number of proteins defined as hubs. *P*-values indicate significance of the enrichment of hubs in the EGF-Ubiproteome based on this 'null' distribution.

interplay between the Ub and pY networks and suggest that the flow of information from the receptor to downstream signaling molecules is driven by two complementary and interlinked enzymatic cascades: kinases/phosphatases and E3 ligases/DUBs.

Crosstalk between the EGFR and EphA2 signaling receptors

To provide a proof of principle of the biological relevance of our findings, we focused on EphA2, a receptor tyrosine kinase

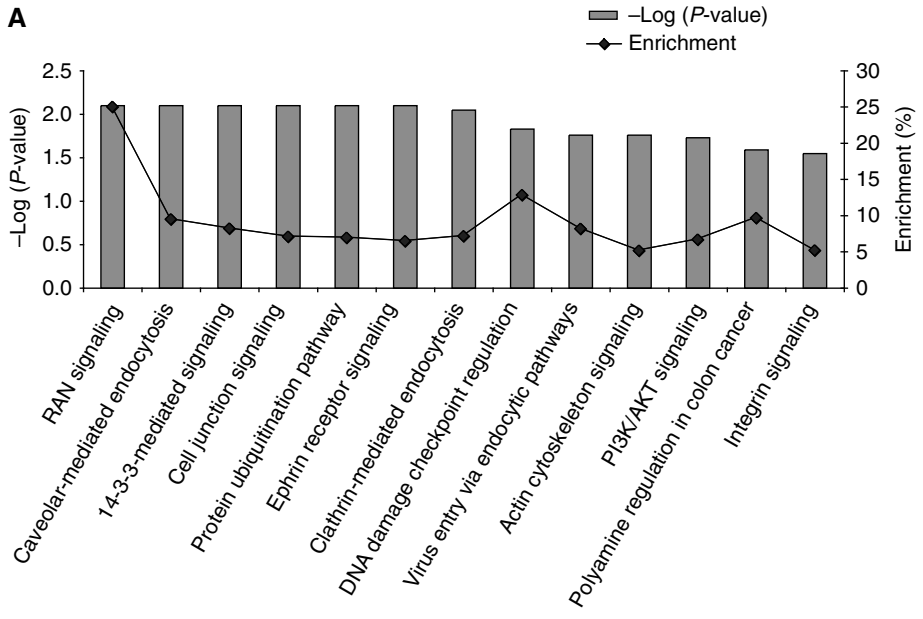

B

NET	Molecules	Description	Relevance
1	17/23	Ribosomes/translation	35%
2	17/35	Toll-like receptor signaling/RAS oncogenic signature/NFKB regulated/Hypoxia	49%
3	15/27	Calpains pathway/TID pathway/p53 signaling/HIF targets/Myc targets	41%
4	15/35	ERK pathway/EGFR signaling/IL6 pathway/focal adhesion/proliferation	51%
5	14/35	Insulin signaling/adipocytokine siganling/GCR signaling	34%
6	14/35	TGFb regulated/calcineurin signaling/inflammation	37%
7	14/35	Adherens junction/cell cycle	31%
8	13/35	Cytokine-cytokine receptor interaction/RAS oncogenic signature/NFKB regulated	34%
9	13/35	Adherens junction/ERBB signaling pathway/focal adhesion/CXCR4 pathway	49%
10	12/35	p53 signaling/apoptosis/cell cycle/drug resistance and metabolism	51%
11	12/35	Proliferation cell cycle/calcineurin -NF AT signaling/DNA damage	60%

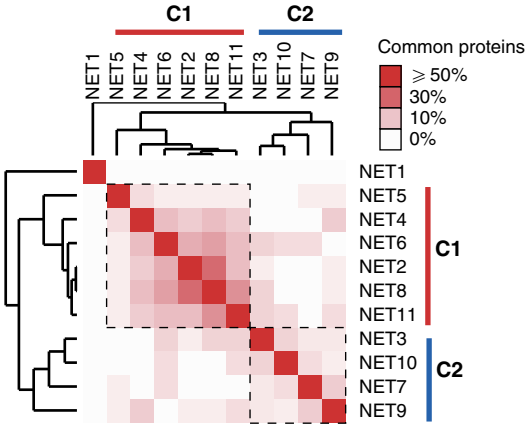

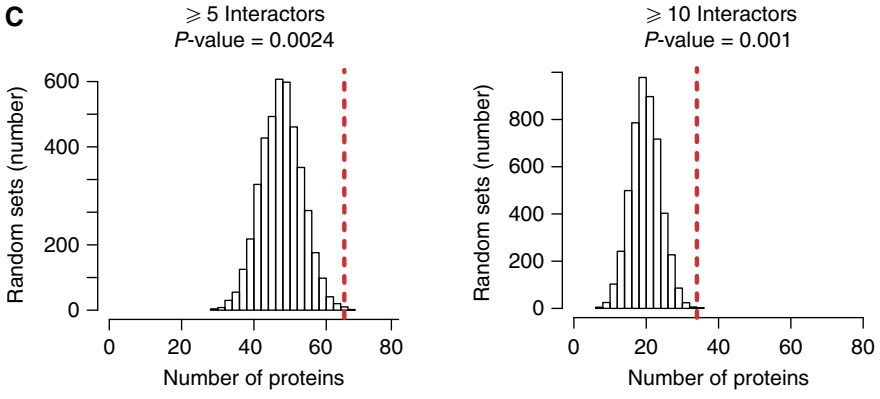

A

	EGF-Ubiproteome (265 proteins)	
	Overlap (*N*)	*P*
EGF-pY Blagoev (*N*=81)	18	4.6×10^{-16}
EGF-pY Oyama (*N*=136)	25	1.0×10^{-19}
EGF-pY Hammond (*N*=93)	18	6.2×10^{-15}
Phospho.ELM (*N*=687)	38	1.9×10^{-11}
All (*N*=900)	61	1.5×10^{-22}

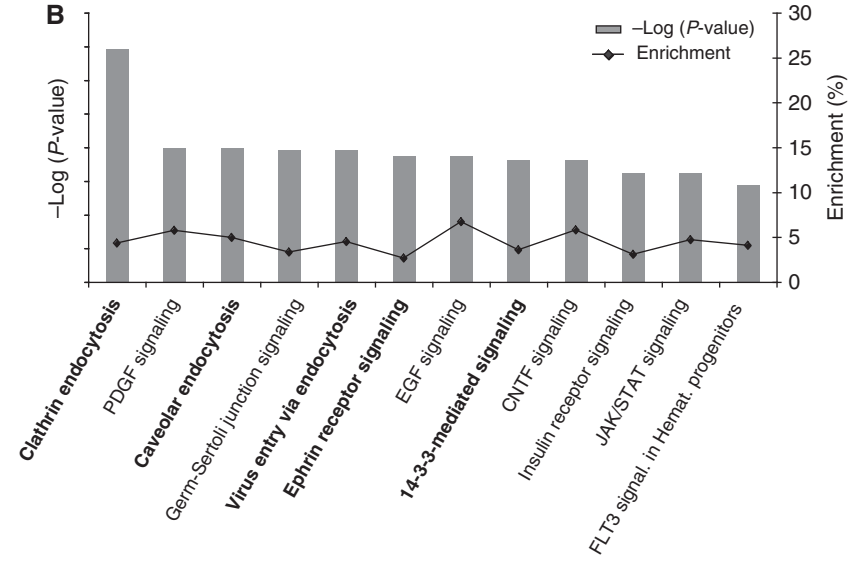

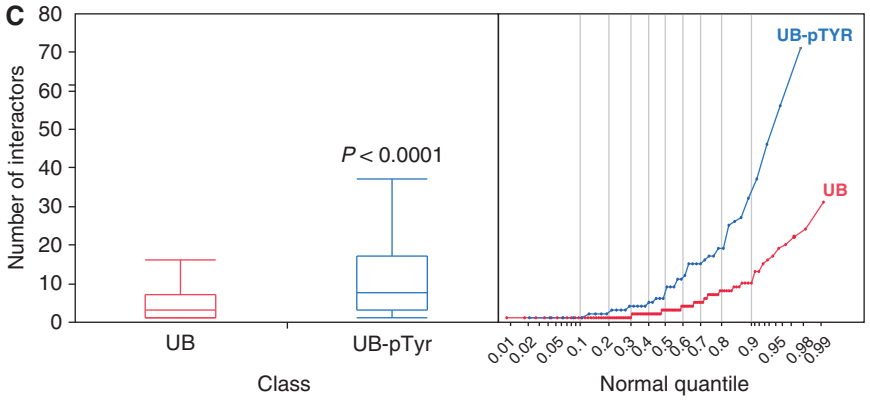

Figure 6 EGF-Ubiproteome and EGF-pYproteome. Comparison of the EGF-Ubiproteome (265 proteins) with two EGF-induced phosphotyrosine (pY) proteomes (Blagoev *et al*, 2004; Oyama *et al*, 2009; Hammond *et al*, 2010), and a pY-proteome database, phosho.ELM database (Diella *et al*, 2008). (**A**) The number of overlapping proteins (*N*) and the significance of the overlap (*P*: *P*-values calculated by Fisher's exact test) are shown. List of overlapping proteins is reported in Supplementary Table S3. (**B**) Ingenuity pathway analysis. Enrichment plots of canonical pathways (*x* axis) built on the list of 55 EGF-induced Ub and pY-modified proteins. The percentage of enrichment (black line) is plotted on the right *y* axis. The significance of the enrichment (gray bars) was calculated using the Benjiamini Hochberg multiple testing correction and is plotted on the left *y* axis as the $-\log_{10}$ of *P*-values. In bold, enriched pathways found also in the list of 265 EGF-Ubiproteome (Figure 5). (**C**) Enrichment of hubs in the list of 55 EGF-induced Ub and pY-modified proteins, or 265 EGF-induced Ub proteins. Only proteins with five interactors or more, as annotated in the BioGRID human interaction database (Stark *et al*, 2006), were considered for the analysis. Box plots and normal quantile plots are shown. Statistical significance of the difference in enrichment was calculated using Wilcoxon–Kruskal Wallis tests, one-way χ^2-approximation (JMP 5.1 software, SAS).

involved in development and often overexpressed in cancer (Pasquale, 2008). We started from the observation that proteins of the EGF-Ubiproteome are indeed enriched in the Ephrin receptor signaling pathway(s) (Figure 5A) and that EphA2 displayed a ratio of 2.67 (Supplementary Table S2).

As an initial step, we validated the MS data. Upon EGF stimulation, we observed an increase in both the tyrosine phosphorylation and ubiquitination of EphA2, indicating a crosstalk between the two receptors (Figure 7A and Supplementary Figure S9A). Interestingly, the crosstalk was unidir-

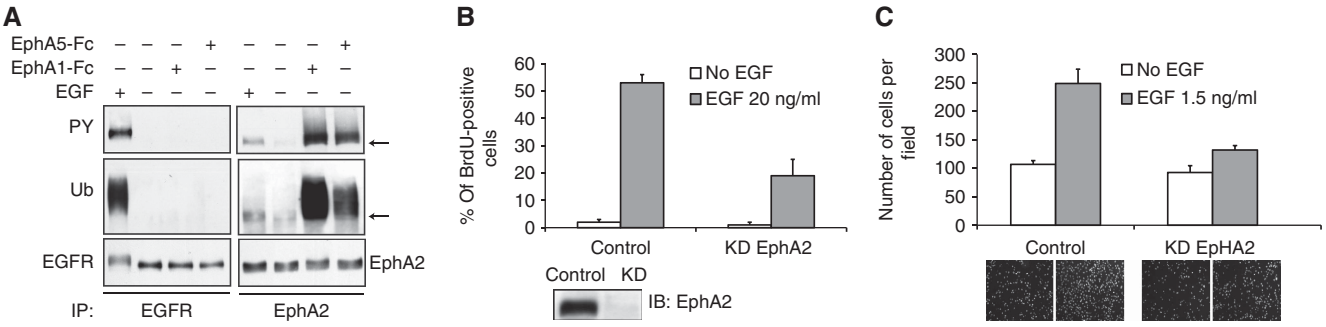

Figure 7 EphA2 is a novel EGF-induced ubiquitinated target. (**A**) EphA2 validation. Serum-starved B82L-EGFR cells were stimulated with EGF (100 ng/ml), ephrinA1-Fc (1 μg/ml) or ephrinA5–Fc (1 μg/ml) for 10 min or left untreated. Lysates (1 mg) were IP and IB with the indicated antibodies. (**B**) Quantification of cell proliferation assessed by BrdU incorporation in control and EphA2 KD cells. Data are expressed as the mean ± s.e.m. of three independent experiments. Lower blot shows the efficiency of RNAi in EphA2 KD cells. (**C**) EphA2 KD reduces cell migration. The lower panels show DAPI-stained representative fields for each sample. Data are expressed as the mean ± s.e.m. of three independent experiments.

ectional, as stimulation with ephrin-A1 or -A5/Fc did not lead to EGFR activation (Figure 7A).

We then assessed how the signal is transmitted from EGFR to EphA2. The two receptors do not appear to stably physically interact, as determined by co-IP (data not shown). However, the kinase activity, but not the cytoplasmic tail of the EGFR, is required for both modifications of EphA2 (Supplementary Figure S9A). One possibility is that EphA2 phosphorylation might be a prerequisite for Cbl recruitment, as this E3 ligase has previously been shown to be involved in ligand-mediated EphA2 degradation (Walker-Daniels *et al*, 2002; Wang *et al*, 2002). While this hypothesis deserves further investigation, we observed that prolonged EGF stimulation did not result in EphA2 degradation, indicating that EGF-induced EphA2 ubiquitination does not signal for degradation (Supplementary Figure S9C and data not shown).

What is then the functional consequence of EphA2 ubiquitination? One obvious possibility is internalization. Thus, we investigated the effect of EGF stimulation on the localization of EphA2 by confocal microscopy. No strong changes were visible on the total level or distribution of EphA2, although a partial co-internalization with EGFR upon EGF activation was clearly detectable (Supplementary Figure S9B).

While these data clearly demonstrate that EphA2 is a novel, downstream ubiquitinated target of EGFR, the role exerted by EphA2 ubiquitination on EGF signaling remains to be established. To start to assess the relevance of EphA2 to EGFR biology, we turned to the normal human breast epithelial cell line MCF10A that expresses both EphA2 and EGFR at significant levels (Supplementary Figure S9C). siRNA knock-down (KD) of EphA2 resulted in reduced EGF-induced proliferation (Figure 7B) and migration (Figure 7C), indicating that this receptor is critically involved in these EGFR biological readout. These results, although preliminary, set the stage for future 'in depth' molecular studies and highlight the 'resource' feature of our EGF-Ubiproteome.

Discussion

Although the Ub system has been intensively investigated in the past two decades, its impact on cellular homeostasis remains largely unexplored. This is particularly true for the signaling functions of ubiquitination, which have emerged as a major regulatory mechanism of signal transduction (Chen and Sun, 2009). Here, we report the first analysis of the EGF-Ubiproteome, which reveals an unexpected degree of pervasiveness of growth factor-induced ubiquitination across several signaling pathways, and a similarly unanticipated level of integration between two distinct types of PTM-based signaling.

The steady-state Ubiproteome

We initially defined the steady-state Ubiproteomes in HeLa and B82-EGFR cells. By combining the two, we defined a list of 1472 NR proteins, which constitutes the largest collection of ubiquitinated proteins reported so far in mammals (Figure 2A and Supplementary Figure S3). The comparison with previously published Ubiproteomes shows a significant overlap, ranging from ~60% for data sets obtained in non-stringent conditions to ~75% for those obtained under stringent denaturing conditions (Supplementary Figure S3). A distinct feature of our Ubiproteome is that it has been extensively validated. The effectiveness of our strategy is underscored by the fact that >95% of the tested candidates were shown to be *bona fide* ubiquitinated proteins (see Supplementary Figure S3 and its legend). In addition, there is a substantial overlap between the HeLa (endogenous) and B83L-EGFR (TAP) Ubiproteomes, with ~50% of 'mouse proteins' being present in the list of 'human proteins'.

The EGF-Ubiproteome

We used a stringent statistical analysis to identify 265 proteins, whose ubiquitination was regulated by activated EGFR. Thus, ~18% of the steady-state Ubiproteome (265 of 1472) is modulated by an exogenous signal. As a kinetic analysis of the EGF-Ubiproteome was not performed, the above percentage likely underestimates the impact of EGFR on the Ub network.

A first obvious question is how EGFR, a receptor tyrosine kinase, transmits signals to the ubiquitination machinery to execute the modification of such a vast number of proteins. There is scarce literature on this topic. One known circuitry involves the E3 ligase Cbl, which binds to pY-sites on the EGFR

(Levkowitz *et al*, 1999) and is then phosphorylated and activated (Kassenbrock and Anderson, 2004). This leads to EGFR ubiquitination and might also facilitate ubiquitination of other receptor-associated molecules, among which Cbl itself (Magnifico *et al*, 2003). Of note, the presence of non-proteolytic Ub chains on this E3 ligase (Figure 4B) suggests the existence of additional modes of regulation for this key Ub network player. Other effector enzymes (E2s, E3s, DUBs) might also be regulated though EGFR-mediated tyrosine phosphorylation. However, only three E3s (Cbl, Cbl-b and Huwe-1) and no E2s or DUBs have been identified in EGFR pY proteomes (Blagoev *et al*, 2004; Oyama *et al*, 2009). Conversely, we identified scores of Ub machinery enzymes in the EGF-Ubiproteome. These include E3s (Cbl, Cbl-b, Nedd4-2, RNF149, Rnf25, Huwe1, ZNF207, Znf319, Hectd1 and HERC4), E2s (Ube2O, UBE2Z, UBA2) and DUBs (JOSD1, USP15, ATXN3, USP11, USP5, USP34). The involvement of such a large number of effectors was unexpected. It appears, therefore, that regardless of the initial triggering mechanism (which must necessarily involve the kinase activity of the EGFR), the Ub signal is rapidly transmitted to, and amplified through, the Ub machinery. Similar to the phosphorylation cascade, in which critical enzymes such as kinases and phosphatases are often activated by phosphorylation, Ub enzymes may be regulated by ubiquitination (see for example Woelk *et al*, 2006; Ring1B (Ben-Saadon *et al*, 2006)). The impact of EGFR-mediated ubiquitination on the activity of E3s, E2s and DUBs warrants further investigation.

A second line of EGF-regulated ubiquitination events impinges on endocytic and signaling proteins. While these pathways are known factors in the Ub network, the magnitude of their involvement is somewhat surprising. EGF-regulated ubiquitination is involved in both clathrin-dependent and -independent endocytosis, in dozens of intracellular signaling circuitries, in cell-to-cell and cell-to-substrate adhesion mechanisms, and in actin remodeling. It seems, therefore, that EGFR-dependent ubiquitination intersects all aspects of signaling; the biochemical circuitries (such as PI3K-, 14-3-3-, JAK/STAT- and PTEN-related); the components that confer spatial and temporal dimensions to signaling (endocytosis); the coordinated modifications in cyto-architecture and relationships with the external milieu (actin, integrins, ephrins) that are necessary for the execution of complex signaling programs. As a proof of principle we investigated the functional link between EGFR and EphA2 and we demonstrated that activation of this signaling receptor is indeed required for EGF-mediated proliferation and migration (Figure 7). This result is particularly relevant considering that downregulation of EphA2 has been shown to decrease malignant phenotypes of cancer cells *in vitro* and to inhibit tumor growth in several mouse cancer models (Pasquale, 2008 and references therein). How this and other crosstalk are achieved, in mechanistic terms, remains to be elucidated. The emerging picture, however, is that the impact of ubiquitination on receptor-activated pathways might be as profound and as vast as the canonical pY-based network.

Finally, a third line of ubiquitinated proteins connects EGFR activity to many other aspects of cellular physiology, including DNA repair, nuclear transport, mRNA processing, various metabolic pathways and ribosome biogenesis. In the latter case, recent literature suggests that ubiquitination and degradation of ribosomal proteins might be a general mechanism adopted by mammalian cells to control ribosome production that can be adjusted according to cellular needs (Caldarola *et al*, 2009 and references therein). It remains to be established whether the EGFR-dependent ubiquitination of ribosomal proteins, uncovered herein, serves to regulate their degradation or has other, yet to be discovered, non-proteolytic functions.

One intriguing connection concerns EGF regulation of the solute carriers (SLCs)/transporters (validation of SLC3A2 is reported in Figure 4). These molecules are gatekeepers for cells and organelles, and control the uptake and efflux of important metabolites such as sugars, amino acids, nucleotides and inorganic ions. Almost all categories of SLCs are represented in our EGF-induced Ubiproteome, and all are hyperubiquitinated upon EGF stimulation (Supplementary Table S2). A growing body of biochemical and biophysical evidence suggests that these transporters are modulated by trafficking, and that the Ub modification is the signal for their internalization and/or lysosomal degradation (Miranda and Sorkin, 2007). Moreover, while transactivation of EGFR elicited by activation of the Na(+)/K(+)-ATPase has been described (Xie, 2003), our data demonstrate, for the first time, the EGF-induced regulation of SLC proteins. In this context, it is worth mentioning that EGFR is able to interact directly with SLC5A1/SGLT1, stabilizing the sodium/glucose cotransporter and facilitating glucose transport into cells (Weihua *et al*, 2008). The mechanisms through which EGFR can trigger the ubiquitination of SLCs, and the ultimate functional significance of the modification remain to be elucidated: a line of investigation that may have important implications also for neurological diseases (Tzingounis and Wadiche, 2007) and cancer (Engelman and Cantley, 2008; Nicklin *et al*, 2009), where alterations of SLCs have an important pathogenetic role.

Connectivity of the EGF-Ubiproteome

The EGF-Ubiproteome displayed remarkable connectivity—a possible indication of a wide pervasiveness of this network in cell regulation—organized into three levels. The first level is represented by intra-network connectivity. Indeed, the proteins of the EGF-Ubiproteome grouped into two major clusters, enriched in proliferation/inflammation and apoptosis/adhesion/cell cycle signatures (Figure 5). This result suggests that the EGF-regulated Ub network is a rather compact infrastructure, which allows coordinated control by EGFR of a multiplicity of signaling mechanisms. This 'core' regulatory network then reaches out to intersect (level 2 of connectivity) virtually every aspect of intracellular signaling, as discussed in the previous section.

Finally, a third level of connectivity is represented by the considerable overlap between the EGF-induced Ubiproteome and pY proteome. These two PTM-based networks can be conceptualized as two overlapping, diffusely interconnected, matrices through which the EGFR transduces signals to make them readable to the cell. How this is achieved remains to be established and will require high-resolution studies, probably on a protein-by-protein basis. In principle, ubiquitination might control the stability and/or degradation of

pY-containing proteins (Hunter, 2007). In this context, the EGFR might exert dual control on the activation (through pY) and deactivation (through Ub) of signaling pathways. We note, however, that the EGFR mostly induces K63-linked ubiquitination (Figure 4). This modification has been linked to the signaling ability of Ub, rather than to its degradation properties (Woelk *et al*, 2007). It is thus possible that EGFR-induced ubiquitination adds a layer of signaling complexity to the canonical pY-based circuitry of EGFR signaling.

The ability of the proteins of the EGF-Ubiproteome to nucleate clusters of interactions was mirrored by their enrichment in 'hubs', which became even more evident when dually modified (pY and Ub) proteins were considered. Hubs are proteins that form critical interconnections between signaling pathways and are points of fragility of signaling networks (Amit *et al*, 2007). As such, they represent ideal targets for pharmacological intervention. However, detailed molecular knowledge of the mechanisms of interconnectivity of hubs is indispensable to predict the results of 'hub interference'. Our results might thus be relevant for the identification of therapeutic targets, and to determine appropriate strategies of intervention in pathological conditions in which subversion of signaling by EGFR (and other receptor tyrosine kinases) is relevant, such as cancer.

Materials and methods

Reagents, constructs and cell culture

EGF was purchased from Intergen (Oxford, UK), rhodamine-EGF was from Molecular Probes. Puromycin, doxycyline, FLAG peptide, trypsin (proteomic grade), DTT, iodacetamide, chloroacetamide and N-ethylmaleimide, ephrinA1/A5 extracellular domain/Fc chimera, L-Arg $^{12}C_6$, $^{14}N_4$-HCl, L-Arg $^{13}C_6$, $^{15}N_4$-HCl, L-Lys $^{12}C_6$, $^{14}N_2$-HCl and L-Lys $^{13}C_6$, $^{15}N_2$-HCl were from Sigma. Imidazole and urea were from Carlo Erba. EDTA-free protease inhibitor cocktail tablets were from Roche. Ni-NTA agarose beads were from Qiagen. (K specific only)Ub_n chains were from ENZO Life Sciences. Antibodies used were as follows: monoclonal anti-FLAG (M2, Sigma), M2-agarose affinity gel (Sigma), monoclonal anti-HA (clone 16B12, Babco), anti-vinculin (Sigma), monoclonal anti-Ub (P4D1, Santa Cruz and FK2, ENZO Life Sciences), anti-K63 and K48 Ub-chain-specific antibodies (Genentech), polyclonal anti-EGFR (directed against aa 1172–1186 of human EGFR, produced in-house), anti-eps15 (monoclonal, produced in-house), monoclonal anti-EphA2 (clone D7, Upstate) polyclonal anti-EphA2 (clone C-20, Santa Cruz), polyclonal anti-SLC3A2 (H-300, Santa Cruz), monoclonal anti-Cbl (BD), anti-phospho-ERK (Cell Signaling), anti-phospho-AKT (Cell Signaling) and anti-pY (Clone 4G10, Upstate Biotechnology).

The engineering of FLAG-6His-Ub and GST-S5a is reported in Supplementary information.

GST–S5a fusion protein and FK2 antibody were crosslinked using AminoLink® and CarboLink™ Coupling Gel (Pierce Biotechnology), respectively, according to the manufacturer's instructions. Avidin-agarose beads used in the control purification were from Pierce Biotechnology.

B82L fibroblasts expressing the human wild-type EGFR (B82L-wt), kinase-defective EGFR (B82L-Kin$^-$) and the COOH terminally truncated EGFR at Tyr-958 (B82L-958) have been described previously (Welsh *et al*, 1994). B82L-EGFR cells stably expressing FLAG-6His-Ub were obtained by transfecting pSG213-FLAG-6His-Ub using LipofectAMINE™ (Invitrogen). Cells were selected in medium containing 5 μg/ml puromycine. Expression of FLAG-6His-Ub was induced by adding doxycycline to the culture medium at a final concentration of 4 μg/ml. MCF10A cells were cultured in Dulbecco's modified Eagle's medium and F12 medium (DMEM-F12) supplemented with 5% horse serum, hydrocortisone (0.5 μg/ml), insulin (10 μg/ml), cholera toxin (50 ng/ml), EGF (20 ng/ml) and penicillin-streptomycin (100 μg/ml each). When serum-starved, cells were cultured in the same medium devoid of serum and EGF.

Cell lysis and IP were performed as previously described (Penengo *et al*, 2006). For the IPs with the anti-Ub antibodies, 500 μg of HeLa lysate was subjected to IP either with 20 μg of FK2 antibody or 5 μg of K63 Ub-chain-specific antibody for 2 h at 4°C, followed by 1 h incubation with Protein G-conjugated sepharose beads (Zymed). Soluble EphrinA1 and A5 fusion proteins (EphrinA1-, EphrinA5–Fc) were obtained by mixing EphrinA1/5 with the Fc portion of human IgG in a molar ratio 1:10. Preclustering was performed on ice for 1 h. Immunofluorescence procedures, ablation of EphA2, BrdU incorporation and migration assays are in the Supplementary information.

The procedures for SILAC labeling and for the TAP and endogenous (FK2) purifications are described in the Supplementary information.

LC-MS/MS analysis

Peptides were separated on a 15 cm C18-reversed phase column (75 μm inner diameter) packed in-house with Reprosil (ReproSil-Pur C18-AQ 3-μm resin, Dr Maisch), using a nanoflow HPLC system (Agilent Technologies, Waldbronn, Germany or Proxeon, Proxeon Biosystems, Odense, Denmark). The HPLC was coupled online via a nanoelectrospray ion source (Proxeon Biosystems) to an LTQ-Orbitrap mass spectrometer (Thermo Scientific). We used a 140 min gradient from 2 to 60% acetonitrile in 0.5% acetic acid at a flow of 250 nl/min. The LTQ-Orbitrap was operated in the positive ion mode, with the following acquisition cycle: a full scan (from m/z 300–2000) recorded in the orbitrap analyzer at resolution R=60 000 followed by sequential isolation and fragmentation of the five most-intense peptide ions in the LTQ analyzer by collisionally induced dissociation. The 'lock mass' option was enabled in all full scans to improve mass accuracy of precursor ions (Olsen *et al*, 2005). Up to 500 sequenced ions were dynamically excluded for 60 s after sequencing. The maximum allowed fill time for an Orbitrap survey scan (ion target 1 000 000) was 1 s, and for an LTQ MS/MS scan (ion target 5000), 150 ms.

Data analysis

The raw data files were analyzed with the in-house developed quantitative proteomics software MaxQuant, version 1.0.11.5 (see Cox and Mann (2008) for details), which was used for peak list generation, identification and quantitation of SILAC pairs, and filtering. The software is supported by Mascot (version 2.2, Matrix Science) as the database search engine for peptide identification (Perkins *et al*, 1999). MS/MS spectra were searched against the human (endogenous Ub, HeLa cells) or mouse (FLAG-6His-Ub, B82L-EGFR cells) International Protein Index (IPI) databases (versions 3.37). False discovery rates (FDR) were controlled by searching in a concatenated database consisting of the original protein sequences plus their reversed versions, in which all Ks and Rs have been exchanged with each other. Protein sequences of common contaminants, e.g., human keratins and proteases used, were added to the database. Proteins and peptides with an FDR > 1% were discarded. Posterior error probability for peptides were calculated as described previously (Cox and Mann, 2008) and set to 1%. The initial mass tolerance in MS mode was set to 7 p.p.m. and MS/MS mass tolerance was 0.5 Da. For the Mascot search, cysteine carbamidomethylation was searched as a fixed modification, whereas N-acetyl (Protein), Oxidation (M) and GlyGly (K) were searched as variable modifications. Labeled arginine ($^{13}C_6$, $^{15}N4$) and lysine ($^{13}C_6$, $^{15}N_2$) were specified as fixed or variable modifications, depending on prior knowledge of the parent ion for the Mascot searches. Full tryptic specificity with up to two missed cleavages was required and only peptides of at least six amino acids were considered. By default, it was required that each protein group was identified by at least one peptide unique to the assigned protein group.

Three independent biological replicates were measured for the endogenous Ub and the overexpressed FLAG-6His-Ub experiments. Two experiments were identical (forward: FW1, FW2) and one was with swapped labels (reverse: REV). Raw files of technical and biological replicates were analyzed together, whereas the ratios of the REV experiments were inverted (1/ratio) in order to have a median

ratio over all three experiments. To obtain 'high-confidence data sets' of quantified proteins, we adopted four filtering criteria, according to which proteins should (i) be represented by at least two peptides, one of which should be unique for the protein sequence; (ii) be identified in at least two of the three biological replicates; (iii) be quantified on at least three peptide pairs (heavy and light versions of the same peptide), referred to as ratio counts; (iv) not be present to a similar degree in the control purification (see Supplementary Table S1 and its legend for list of contaminants present in the control purification).

The filtering procedure to define potential regulated proteins, the identification of ubiquitination sites and the quantitation of the 'signature peptides' are described in the Supplementary information.

Clustering and functional analysis

Bioinformatics analyses were performed with online tools or tools available in-house, as described in the Supplementary information.

Supplementary information

Supplementary information is available at the *Molecular Systems Biology* website (www.nature.com/msb).

Acknowledgements

We thank Rosalind Gunby for critically reading the manuscript. Andrea Cocito and Giovanni d'Ario for statistical analysis. Pietro De Camilli for generously providing anti-Nedd4L antibody. This work was supported by grants from AIRC (Italian Association for Cancer Research) and The European Community (VI Framework, Rubicon) to SP, PPDF and MM. TB is a recipient of a European Molecular Biology Organization fellowship.

Author contributions: EA and BO set up and performed the biochemical purifications, TB carried out the mass spectrometry analysis, FB performed the statistical analysis and the meta-analysis, RP and SM carried out the validation experiments. PPDF participated in the initial design of the study and helped to draft the manuscript, MM provided the logistic support for the mass spectrometry analysis. SP designed the experiments, analyzed the data and wrote the paper.

Conflict of interest

The authors declare that they have no conflict of interest.

References

Acconcia F, Sigismund S, Polo S (2009) Ubiquitin in trafficking: the network at work. *Exp Cell Res* **315:** 1610–1618

Amerik AY, Hochstrasser M (2004) Mechanism and function of deubiquitinating enzymes. *Biochim Biophys Acta* **1695:** 189–207

Amit I, Wides R, Yarden Y (2007) Evolvable signaling networks of receptor tyrosine kinases: relevance of robustness to malignancy and to cancer therapy. *Mol Syst Biol* **3:** 151

Ben-Saadon R, Zaaroor D, Ziv T, Ciechanover A (2006) The polycomb protein Ring1B generates self atypical mixed ubiquitin chains required for its *in vitro* histone H2A ligase activity. *Mol Cell* **24:** 701–711

Blagoev B, Ong SE, Kratchmarova I, Mann M (2004) Temporal analysis of phosphotyrosine-dependent signaling networks by quantitative proteomics. *Nat Biotechnol* **22:** 1139–1145

Caldarola S, De Stefano MC, Amaldi F, Loreni F (2009) Synthesis and function of ribosomal proteins—fading models and new perspectives. *FEBS J* **276:** 3199–3210

Chen WS, Lazar CS, Lund KA, Welsh JB, Chang CP, Walton GM, Der CJ, Wiley HS, Gill GN, Rosenfeld MG (1989) Functional independence of the epidermal growth factor receptor from a domain required for ligand-induced internalization and calcium regulation. *Cell* **59:** 33–43

Chen ZJ, Sun LJ (2009) Nonproteolytic functions of ubiquitin in cell signaling. *Mol Cell* **33:** 275–286

Choudhary C, Kumar C, Gnad F, Nielsen ML, Rehman M, Walther TC, Olsen JV, Mann M (2009) Lysine acetylation targets protein complexes and co-regulates major cellular functions. *Science* **325:** 834–840

Cox J, Mann M (2008) MaxQuant enables high peptide identification rates, individualized p.p.b.-range mass accuracies and proteome-wide protein quantification. *Nat Biotechnol* **26:** 1367–1372

Diella F, Gould CM, Chica C, Via A, Gibson TJ (2008) Phospho.ELM: a database of phosphorylation sites—update 2008. *Nucleic Acids Res* **36:** D240–D244

Engelman JA, Cantley LC (2008) A sweet new role for EGFR in cancer. *Cancer Cell* **13:** 375–376

Haglund K, Sigismund S, Polo S, Szymkiewicz I, Di Fiore PP, Dikic I (2003) Multiple monoubiquitination of RTKs is sufficient for their endocytosis and degradation. *Nat Cell Biol* **5:** 461–466

Hammond DE, Hyde R, Kratchmarova I, Beynon RJ, Blagoev B, Clague MJ (2010) Quantitative analysis of HGF and EGF-dependent phosphotyrosine signaling networks. *J Proteome Res* **5:** 2734–2742

Hicke L, Schubert HL, Hill CP (2005) Ubiquitin-binding domains. *Nat Rev Mol Cell Biol* **6:** 610–621

Huang F, Kirkpatrick D, Jiang X, Gygi S, Sorkin A (2006) Differential regulation of EGF receptor internalization and degradation by multiubiquitination within the kinase domain. *Mol Cell* **21:** 737–748

Hunter T (2007) The age of crosstalk: phosphorylation, ubiquitination, and beyond. *Mol Cell* **28:** 730–738

Hurley JH, Lee S, Prag G (2006) Ubiquitin-binding domains. *Biochem J* **399:** 361–372

Jensen ON (2006) Interpreting the protein language using proteomics. *Nat Rev Mol Cell Biol* **7:** 391–403

Kassenbrock CK, Anderson SM (2004) Regulation of ubiquitin protein ligase activity in c-Cbl by phosphorylation-induced conformational change and constitutive activation by tyrosine to glutamate point mutations. *J Biol Chem* **279:** 28017–28027

Lauwers E, Erpapazoglou Z, Haguenauer-Tsapis R, Andre B (2010) The ubiquitin xcode of yeast permease trafficking. *Trends Cell Biol* **20:** 196–204

Levkowitz G, Waterman H, Ettenberg SA, Katz M, Tsygankov AY, Alroy I, Lavi S, Iwai K, Reiss Y, Ciechanover A, Lipkowitz S, Yarden Y (1999) Ubiquitin ligase activity and tyrosine phosphorylation underlie suppression of growth factor signaling by c-Cbl/Sli-1. *Mol Cell* **4:** 1029–1040

Magnifico A, Ettenberg S, Yang C, Mariano J, Tiwari S, Fang S, Lipkowitz S, Weissman AM (2003) WW domain HECT E3s target Cbl RING finger E3s for proteasomal degradation. *J Biol Chem* **278:** 43169–43177

Meierhofer D, Wang X, Huang L, Kaiser P (2008) Quantitative analysis of global ubiquitination in HeLa cells by mass spectrometry. *J Proteome Res* **7:** 4566–4576

Miranda M, Sorkin A (2007) Regulation of receptors and transporters by ubiquitination: new insights into surprisingly similar mechanisms. *Mol Interv* **7:** 157–167

Mukhopadhyay D, Riezman H (2007) Proteasome-independent functions of ubiquitin in endocytosis and signaling. *Science* **315:** 201–205

Newton K, Matsumoto ML, Wertz IE, Kirkpatrick DS, Lill JR, Tan J, Dugger D, Gordon N, Sidhu SS, Fellouse FA, Komuves L, French DM, Ferrando RE, Lam C, Compaan D, Yu C, Bosanac I, Hymowitz SG, Kelley RF, Dixit VM (2008) Ubiquitin chain editing revealed by polyubiquitin linkage-specific antibodies. *Cell* **134:** 668–678

Nicklin P, Bergman P, Zhang B, Triantafellow E, Wang H, Nyfeler B, Yang H, Hild M, Kung C, Wilson C, Myer VE, MacKeigan JP, Porter JA, Wang YK, Cantley LC, Finan PM, Murphy LO (2009) Bidirectional transport of amino acids regulates mTOR and autophagy. *Cell* **136:** 521–534

Olsen JV, de Godoy LM, Li G, Macek B, Mortensen P, Pesch R, Makarov A, Lange O, Horning S, Mann M (2005) Parts per million mass accuracy on an Orbitrap mass spectrometer via lock mass injection into a C-trap. *Mol Cell Proteomics* **4:** 2010–2021

Ong SE, Mann M (2006) A practical recipe for stable isotope labeling by amino acids in cell culture (SILAC). *Nat Protoc* **1:** 2650–2660

Oyama M, Kozuka-Hata H, Tasaki S, Semba K, Hattori S, Sugano S, Inoue J, Yamamoto T (2009) Temporal perturbation of tyrosine phosphoproteome dynamics reveals the system-wide regulatory networks. *Mol Cell Proteomics* **8:** 226–231

Pasquale EB (2008) Eph-ephrin bidirectional signaling in physiology and disease. *Cell* **133:** 38–52

Penengo L, Mapelli M, Murachelli AG, Confalonieri S, Magri L, Musacchio A, Di Fiore PP, Polo S, Schneider TR (2006) Crystal structure of the ubiquitin binding domains of rabex-5 reveals two modes of interaction with ubiquitin. *Cell* **124:** 1183–1195

Perkins DN, Pappin DJ, Creasy DM, Cottrell JS (1999) Probability-based protein identification by searching sequence databases using mass spectrometry data. *Electrophoresis* **20:** 3551–3567

Polo S, Sigismund S, Faretta M, Guidi M, Capua MR, Bossi G, Chen H, De Camilli P, Di Fiore PP (2002) A single motif responsible for ubiquitin recognition and monoubiquitination in endocytic proteins. *Nature* **416:** 451–455

Ravid T, Hochstrasser M (2008) Diversity of degradation signals in the ubiquitin-proteasome system. *Nat Rev Mol Cell Biol* **9:** 679–690

Schmidt MH, Dikic I (2005) The Cbl interactome and its functions. *Nat Rev Mol Cell Biol* **6:** 907–918

Seet BT, Dikic I, Zhou MM, Pawson T (2006) Reading protein modifications with interaction domains. *Nat Rev Mol Cell Biol* **7:** 473–483

Stark C, Breitkreutz BJ, Reguly T, Boucher L, Breitkreutz A, Tyers M (2006) BioGRID: a general repository for interaction datasets. *Nucleic Acids Res* **34:** D535–D539

Subramanian A, Kuehn H, Gould J, Tamayo P, Mesirov JP (2007) GSEA-P: a desktop application for gene set enrichment analysis. *Bioinformatics* **23:** 3251–3253

Tagwerker C, Flick K, Cui M, Guerrero C, Dou Y, Auer B, Baldi P, Huang L, Kaiser P (2006) A tandem affinity tag for two-step purification under fully denaturing conditions: application in ubiquitin profiling and protein complex identification combined with *in vivo* cross-linking. *Mol Cell Proteomics* **5:** 737–748

Tzingounis AV, Wadiche JI (2007) Glutamate transporters: confining runaway excitation by shaping synaptic transmission. *Nat Rev Neurosci* **8:** 935–947

Walker-Daniels J, Riese II DJ, Kinch MS (2002) c-Cbl-dependent EphA2 protein degradation is induced by ligand binding. *Mol Cancer Res* **1:** 79–87

Wang Y, Ota S, Kataoka H, Kanamori M, Li Z, Band H, Tanaka M, Sugimura H (2002) Negative regulation of EphA2 receptor by Cbl. *Biochem Biophys Res Commun* **296:** 214–220

Weihua Z, Tsan R, Huang WC, Wu Q, Chiu CH, Fidler IJ, Hung MC (2008) Survival of cancer cells is maintained by EGFR independent of its kinase activity. *Cancer Cell* **13:** 385–393

Welsh JB, Worthylake R, Wiley HS, Gill GN (1994) Specific factors are required for kinase-dependent endocytosis of insulin receptors. *Mol Biol Cell* **5:** 539–547

Wiesner S, Ogunjimi AA, Wang HR, Rotin D, Sicheri F, Wrana JL, Forman-Kay JD (2007) Autoinhibition of the HECT-type ubiquitin ligase Smurf2 through its C2 domain. *Cell* **130:** 651–662

Woelk T, Oldrini B, Maspero E, Confalonieri S, Cavallaro E, Di Fiore PP, Polo S (2006) Molecular mechanisms of coupled monoubiquitination. *Nat Cell Biol* **8:** 1246–1254

Woelk T, Sigismund S, Penengo L, Polo S (2007) The ubiquitination code: a signalling problem. *Cell Div* **2:** 11

Xie Z (2003) Molecular mechanisms of Na/K-ATPase-mediated signal transduction. *Ann N Y Acad Sci* **986:** 497–503

Zwang Y, Yarden Y (2009) Systems biology of growth factor-induced receptor endocytosis. *Traffic* **10:** 349–363

nature cell biology

Molecular mechanisms of coupled monoubiquitination

Tanja Woelk[1], Barbara Oldrini[1,4], Elena Maspero[1,4], Stefano Confalonieri[1], Elena Cavallaro[1], Pier Paolo Di Fiore[1,2,3,5] and Simona Polo[1,2,5]

Many proteins contain ubiquitin-binding domains or motifs (UBDs), such as the UIM (ubiquitin-interacting motif) and are referred to as ubiquitin receptors. Ubiquitin receptors themselves are frequently monoubiquitinated by a process that requires the presence of a UBD and is referred to as coupled monoubiquitination. Using a UIM-containing protein, eps15, as a model, we show here that coupled monoubiquitination strictly depends on the ability of the UIM to bind to monoubiquitin (mUb). We found that the underlying molecular mechanism is based on interaction between the UIM and a ubiquitin ligase (E3), which has itself been modified by ubiquitination. Furthermore, we demonstrate that the *in vivo* ubiquitination of members of the Nedd4 family of E3 ligases correlates with their ability to monoubiquitinate eps15. Thus, our results clarify the mechanism of coupled monoubiquitination and identify the ubiquitination of E3 ligases as a critical determinant in this process.

Ubiquitination is a versatile posttranslational modification involved in various cellular functions, including endocytic trafficking[1], NF-κB signalling[2], histone activity[3], DNA repair[4] and virus budding[5], in addition to its established role in protein degradation[6]. Ubiquitination is executed by a hierarchical cascade of three types of enzymes: ubiquitin-activating (E1), ubiquitin-conjugating (E2) and ubiquitin ligase (E3) enzymes[6]. E3 ligases, the final effectors of the cascade, can append ubiquitin to intracellular targets either as a single moiety (monoubiquitination), or as chains of ubiquitin (polyubiquitination) branching from various lysines within the ubiquitin moiety[7].

Recent studies have begun to determine how the cell interprets ubiquitin modification. Several families of UBDs have been identified that confer the ability to bind molecules modified by mUb or by ubiquitin chains (polyubiquitin, pUb) to ubiquitin receptors[8]. There is evidence that different UBDs display a range of mUb or pUb binding abilities. In general, although most UBDs seem to bind to pUb, only a subset display detectable binding to mUb[8]. The structural basis for this specificity remains unclear. Also, it is not clear whether and how UBD-mediated differential recognition of mUb, with respect to pUb, impacts on ubiquitin-dependent signalling within the cell.

Another feature of ubiquitin receptors is their ability to undergo monoubiquitination by a process that requires the integrity of the UBD (referred to as coupled monoubiquitination)[8]. Seven classes of UBDs (UIM, UBA, CUE, MIU, GAT, UBM and UBZ) are known to sustain this process[8–10]. Importantly, in those cases analysed, the UBDs do not contain lysine residues that function as acceptors of ubiquitin, therefore their requirement for monoubiquitination must relate to different aspects of the process — most probably the recognition of ubiquitin ligases[11,12].

A number of endocytic proteins, including eps15, epsin and Hrs, represent well-characterised examples of ubiquitin receptors that undergo coupled monoubiquitination[11–14]. There is evidence that members of the Rsp5p–Nedd4 HECT-family are the E3s responsible, at least in part, for this event[11,14–16]. Rsp5p is the sole member of this family in yeast, whereas in mammals, the family has expanded to at least nine members displaying both redundant and specialised functions[17]. In mammals, proteins ubiquitinated by this family of E3s usually contain a conserved PPxY motif, which interacts with trypthophan–tryptophan (WW) domains[17]. The observation that members of the Rsp5p–Nedd4 HECT-family of E3s contain WW domains suggests an immediate mechanism for enzyme–substrate recognition[17]. However, endocytic proteins seemingly do not bind to Rsp5p–Nedd4 HECT-family members through WW-mediated interaction[11,18]. In particular, no stable interaction could be detected between Nedd4 and the UIM-containing protein eps15 (ref. 11, suggesting a new mode of interaction between this E3 and its substrate(s) that may lie at the heart of the process of coupled monoubiquitination.

Here, using eps15 as a model, we demonstrate that selective binding to mUb, but not to pUb, is responsible for its coupled monoubiquitination and provide initial insights into how the differential recognition of mUb may participate in biochemical pathways *in vivo*. In addition, we show that monoubiquitination of E3s of the Rsp5p–Nedd4 HECT-family renders them competent to ubiquitinate eps15 *in vitro* and *in vivo*. Our results, therefore, establish that, at least in the cases analysed, coupled monoubiquitination is caused by the interaction between a ubiquitinated E3 enzyme and a mUb-binding ubiquitin receptor.

[1]IFOM, The FIRC Institute for Molecular Oncology, Via Adamello 16, 20139, Milan, Italy. [2]European Institute of Oncology, Via Ripamonti 435, 20141 Milan, Italy.
[3]University of Milan, 20122, Milan, Italy. [4]These authors contributed equally to this work.
[5]Correspondence should be addressed to S.P. or P.P.D.F. (e-mail: simona.polo@ifom-ieo-campus.it; pierpaolo.difiore@ifom-ieo-campus.it)

Received 21 June 2006; accepted 5 September 2006; published online 1 October 2006; DOI: 10.1038/ncb1484

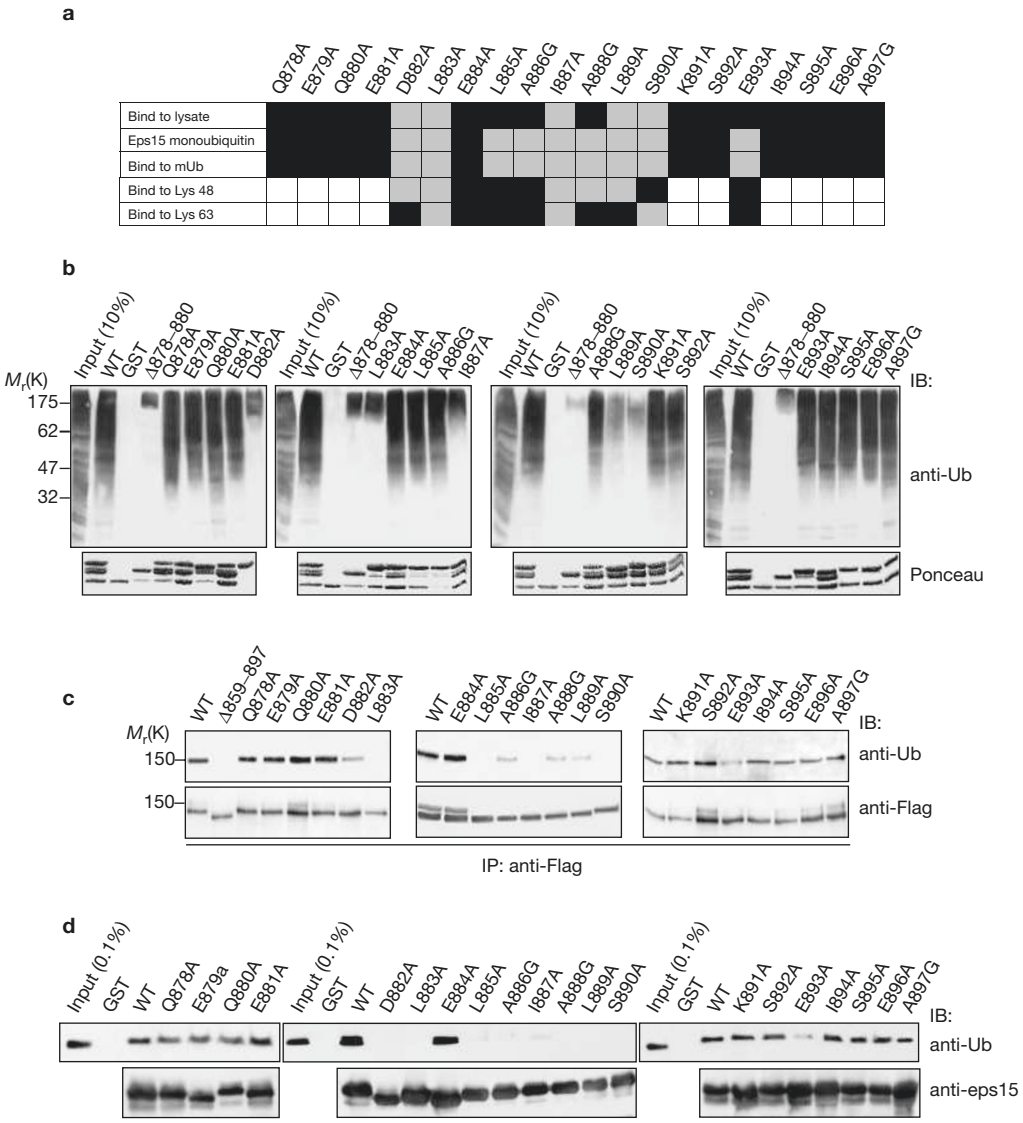

Figure 1 Analysis of eps15-UIM mutants. (**a**) The engineered mutations are shown, together with a summary of their characterisation. 'Bind to lysate' and 'Eps15 monoubiquitin' summarize the results in **b** and **c**, respectively; 'Bind to mUb' summarizes results in **d**; 'Bind to Lys 48 and 'Bind to Lys 63' summarize results shown in the Supplementary Information, Fig. S1. Results represent the average of three independent experiments and are expressed with a colour code: black, ≥70% of wild type; grey, ≤30% of wild type. Empty, not tested. Representative experiments are shown in **b**–**d**. (**b**) GST-fusion proteins containing the last 55 amino acid of eps15 (amino acids 842–897) and the mutations indicated were used in pulldown experiments with lysates from MG132-treated B82L cells. Detection was by immunoblotting with anti-ubiquitin (anti-Ub). Comparable loading of the GST proteins is indicated by Ponceau staining. (**c**) B82L cells were transfected with the indicated constructs (all engineered in Flag-tagged full-length eps15), serum-starved and treated with EGF. Immunoprecipitation (1.5 mg of lysates) and immunoblotting were as indicated. (**d**) The GST fusions described in **b** were used to pulldown monomeric ubiquitin and detection was by immunoblotting as indicated.

RESULTS

Coupled monoubiquitination of eps15 is a function of binding of its UIM to monoubiquitin.

The endocytic protein eps15 contains two copies of a ubiquitin-binding motif, the UIM, in its carboxy terminus. However, functional studies revealed that only the second UIM (henceforth referred to simply as UIM) determines coupled ubiquitination[11]. Thus, we focused on the properties of this UIM, with the goal of elucidating the molecular mechanisms leading to coupled monoubiquitination. Initially, scanning mutagenesis of the eps15-UIM (amino acids 878–897) was performed by mutating each residue individually to alanine, or to glycine if alanine was already present (Fig. 1a).

The ubiquitin binding properties of the various UIM mutants were tested by pulldown assays, using MG132-treated cellular lysates as a source of ubiquitinated proteins. The mutants fell into two classes: those showing binding that was either comparable to wild type (≥70% of wild type), or considerably impaired (≤30% of wid type, mutants 882, 883, 887, 889 and 890; Fig. 1a, b). Next, the mutations were introduced in the context of full-length eps15, to analyse epidermal growth factor (EGF)-induced monoubiquitination[11]. B82L or COS7 (data not shown) cells were transiently transfected with Flag-tagged eps15, or its mutants, and stimulated for 10 min with EGF (Fig. 1c). Again, mutants behaved either comparably with wild type (≥70% of wild type), or were significantly impaired (≤30% of wild type, mutants 882, 883,

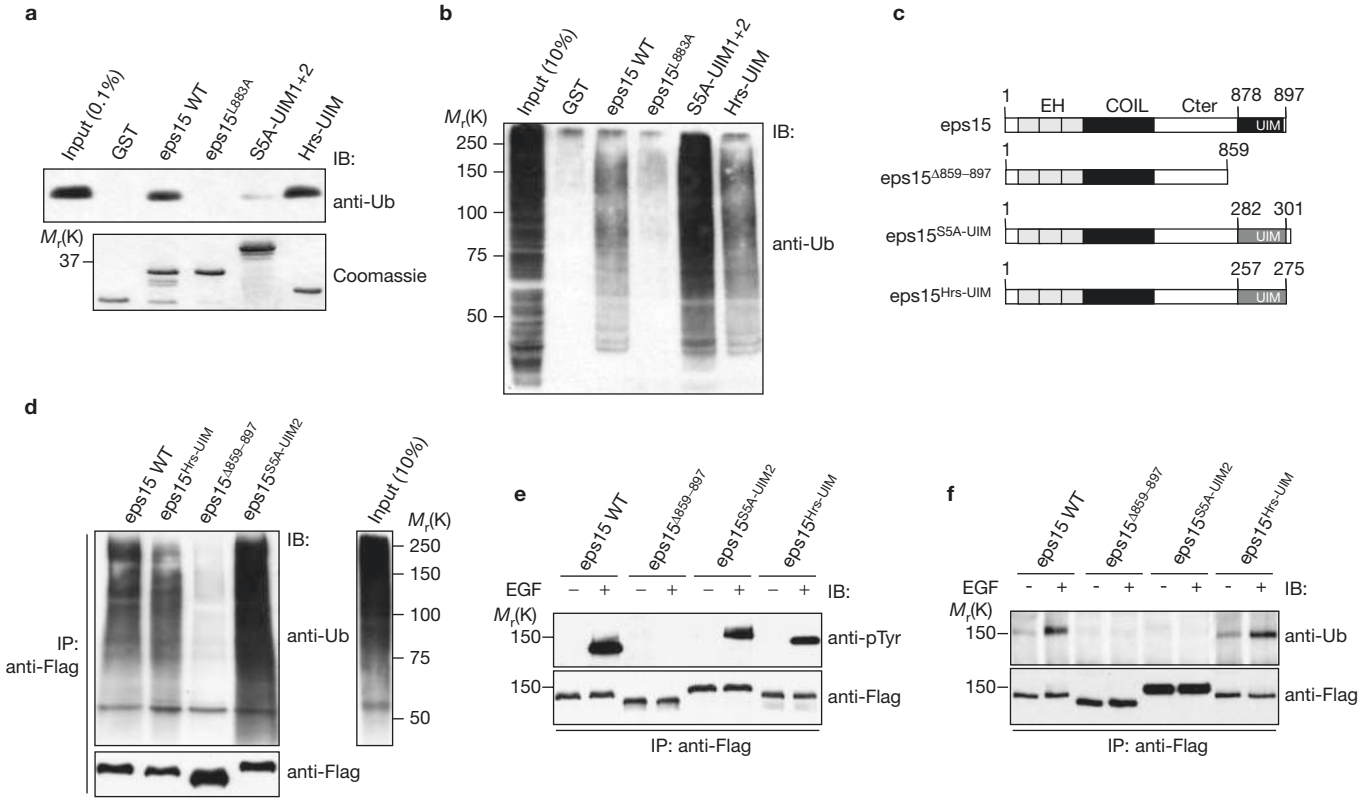

Figure 2 Analysis of chimeric eps15-UIM proteins. (**a**, **b**) GST-fusion proteins containing the indicated UIMs were used in pulldown assays with monomeric ubiquitin (**a**), or with lysates from MG132-treated B82L cells (**b**). (**c**) Schematic representation of the eps15 chimerae used in this study. Replaced UIMs are numbered according to the amino acid position in the protein of origin. (**d**) HeLa cells were transfected with the chimeric proteins shown in **c** (all Flag-tagged) and treated with MG132. Total cellular proteins (800 μg) were immunoprecipitated and immunoblotted as indicated. (**e**, **f**) HeLa cells (**e**) or B82L cells (**f**) were transfected with the chimeric proteins shown in **c** and treated or not (+ or –) with EGF. Total cellular proteins: 0.8 mg in **e**; 2.5 mg in **f**. A second chimeric eps15-S5a molecule containing the first UIM of S5a (amino acids 211–230) was also used (in experiments as in **e** and **f**) with results comparable to those shown for the eps15-UIM2-S5a (data not shown).

885-890 and 893; Fig. 1a, c). All mutants that retained the ability to be monoubiquitinated were also able to bind to ubiquitinated proteins; however, mutants 885, 886, 888 and 893 displayed an impairment in coupled monoubiquitination, although they retained unaltered binding to ubiquitinated proteins (Fig. 1a, d).

These data indicate that the ability of eps15-UIM to cause eps15 monoubiquitination is not a function of its 'general' ubiquitin binding properties. However, different forms of ubiquitin modification exist in the cell. In addition, recent studies revealed that ubiquitin chains, linked through different lysines, can adopt different conformations[19,20]. For instance, although Lys 48-linked chains are in a closed conformation due to stable inter-unit interactions, the Lys 63-linked structure is characterised by an extended conformation, where the ubiquitin subunits are arranged like "beads on a string". These findings led to the hypothesis that there are specific modes of interaction between different ubiquitin-binding modules and different forms of ubiquitin[8,21]. Therefore, we tested the ability of our UIM mutants to bind to different ubiquitin isoforms — Lys 48- or Lys 63-linked chains and mUb. The mutants showed various degrees of interaction with Lys 48- or Lys 63-linked chains (Fig. 1a and see Supplementary Information, Fig. S1); however, no straightforward correlation with monoubiquitination was found. Conversely, binding to mUb, albeit at low affinity as previously reported[11], correlated perfectly with coupled monoubiquitination (Fig. 1a, d).

Taken together, these results indicate that the presence of a functional UIM, capable of binding to mUb, is required for ubiquitination of eps15. We went on to examine this observation further. For a subset of UIM-containing proteins, such as the endocytic proteins eps15, Hrs or epsin[11–14], the phenomenon of coupled ubiquitination has previously been described. In other cases, UIM-containing proteins, are not monoubiquitinated, as in the case of the proteasome subunit S5a[22]. Using pulldown assays, we found that the UIMs of eps15 and Hrs were considerably more efficient than the S5a-UIMs at interacting with mUb (Fig. 2a), whereas all UIMs could bind to polyubiquitinated proteins (Fig. 2b). Therefore, chimeric molecules were engineered in which the eps15-UIM was substituted by either one of the S5a-UIMs, or by the UIM of Hrs (Fig. 2c). The eps15-based chimerae did not show grossly altered biochemical properties *in vivo*, as evident from their ability to coimmunoprecipitate polyubiquitinated proteins (Fig. 2d), and to undergo EGF-stimulated tyrosine phosphorylation — a hallmark of wild-type eps15 (ref. 23; Fig. 2e). However, eps15$^{Hrs\text{-}UIM}$ was monoubiquitinated as efficiently as wild-type eps15, whereas eps15$^{S5a\text{-}UIM}$ was not (Fig. 2f).

Monoubiquitination of the E3 ligase is responsible for coupled monoubiquitination of eps15 *in vitro*.

Although our results indicate that monoubiquitination of eps15 is a function of the ability of its UIM to bind to mUb, the molecular mechanisms through which this happens are not immediately obvious.

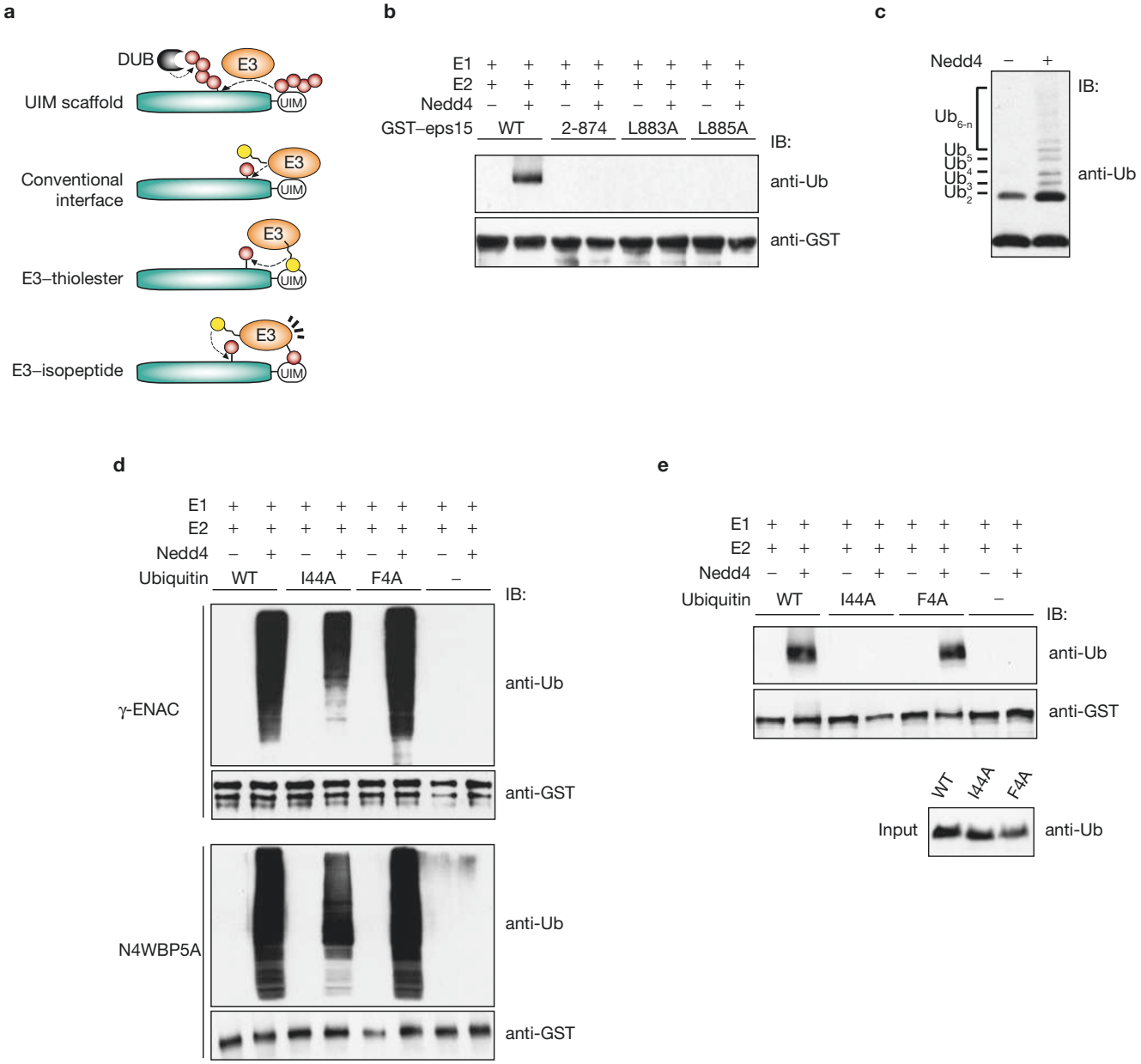

Figure 3 Coupled monoubiquitination in an *in vitro* ubiquitination assay. (**a**) Schematic representation of models to explain coupled monoubiquitination: UIM scaffold, the UIM recruits free polyUb chains, thus facilitating their ligation *en bloc*, followed by trimming of the chain by deubiquitinating enzymes[22]; Conventional interface, the UIM serves as a conventional protein–protein interaction surface to contact an E3; E3–thiol ester, the UIM binds to the thiol ester-conjugated ubiquitin in the E3 (ref. 40) and the ubiquitin is then transferred to the substrate; E3–isopeptide, the E3 modified by ubiquitin–isopeptide conjugation, or by other ubiquitin-like modifiers (such as Nedd8), interacts with the UIM and transfers the thiol ester-conjugated ubiquitin to the ubiquitin receptor. Isopeptide-ubiquitin, red. Thiol ester–ubiquitin, yellow. (**b**) GST-fusions containing full-length eps15 or the indicated mutants were subjected to *in vitro* ubiquitination assays. (**c**) Free polyubiquitin chains are produced in the *in vitro* ubiquitination assays. One tenth of the supernatants from reactions with wild-type eps15 were loaded onto the Tricine–PAGE (11%) gel. (**d**, **e**) GST-fusions containing full-length γ-ENAC or N4WBP5A (**d**) or full-length eps15 (**e**) were subjected to *in vitro* ubiquitination assays using various wild-type ubiquitin, UB^{I44A} or Ub^{F4A}, as indicated. 0.1% of the ubiquitin input is shown at the bottom of **e**.

Several models have been put forward to explain the phenomenon of coupled monoubiquitination[8] (Fig. 3a). These models are variously supported and/or argued against by published evidence[8] (mostly obtained in living cells), but their formal verification is difficult because of the complexity of the molecular pathways involved *in vivo*. We reasoned that a highly controlled *in vitro* system may be adequate to compare these models to each other. It is worth noting that all models contain precise predictions that can be verified in an *in vitro* ubiquitination assay (see below). To set up such a system, we started from the observation that Nedd4 is an E3 ligase capable of ubiquitinating eps15 *in vivo* and *in vitro*[11]. Therefore, an *in vitro* system containing solely the enzymatic machinery (E1 + E2 + E3–Nedd4), plus ubiquitin and substrates, was used.

Initially, wild-type eps15 and two mutants, $eps15^{L883A}$ and $eps15^{L885A}$, were selected as substrates. These mutants do not bind to mUb and are not ubiquitinated *in vivo*, but they display different binding properties to polyUb. Neither $eps15^{L883A}$ nor $eps15^{L885A}$ (nor a UIM-deleted eps15)

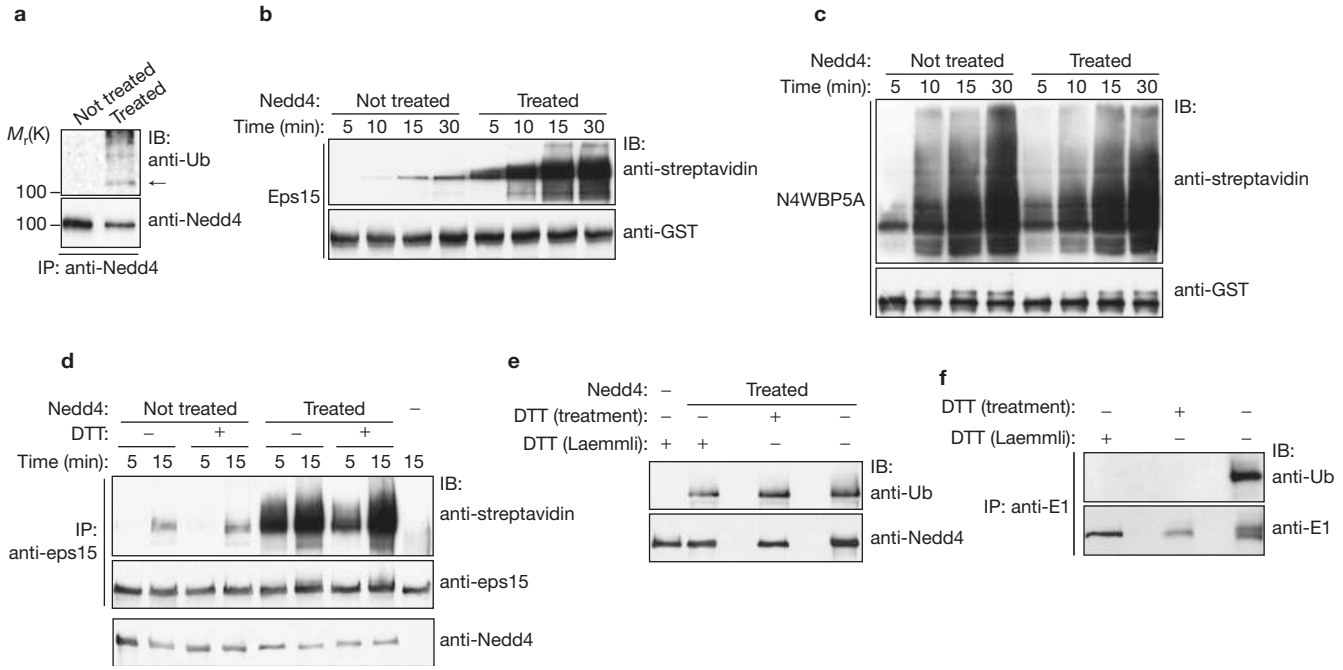

Figure 4 *In vitro* ubiquitination assays with pretreated Nedd4. (**a**–**c**) Nedd4 was pretreated or not with ubiquitin as described in the Methods. Nedd4 was immunoprecipitated from aliquots (0.5 μg) of the reactions to control its ubiquitination state (**a**). The arrow indicates the monoubiquitinated form of Nedd4. After pretreatment, biotinylated ubiquitin and either GST–eps15 (**b**), or GST–N4WBP5A (**c**) were added for the indicated times. (**d**) GST–Nedd4 attached to GSH-beads was pretreated or not with ubiquitin. Beads were then incubated (+) or not (–) with 100 mM DTT in ubiquitin buffer for 15 min at room temperature and extensively washed in YY buffer. Next, biotinylated ubiquitin and recombinantly produced and purified eps15 were added for the indicated times. To assess eps15 ubiquitination, the supernatant of the reactions (containing eps15) was immunoprecipiated and immunoblotted as indicated. Nedd4 was eluted from the beads (in Laemmli buffer) and analysed to show equal amounts of Nedd4. (**e**, **f**) GST–Nedd4 was pretreated as in **d**, then reactions were treated or not with DTT. Beads were recovered and washed in YY buffer and finally eluted in Laemmli buffer with or without DTT (**e**). The supernatant of the reactions (containing E1) was diluted 20 times in ubiquitin buffer and immunoprecipitated with an anti-E1 antibody (**f**) before immunoblotting. An uncropped image of **d** is shown in the Supplementary Information, Fig. S4.

could be monoubiquitinated (Fig. 3b). This result argues against the "UIM scaffold" model (Fig. 3a) given that pUb chains can form in the reaction (Fig. 3c), as this model would predict polyubiquitination of wild-type eps15 and of the L885A mutant.

A modified ubiquitin that cannot bind to UBDs (Ub^{I44A}) was then used, with another ubiquitin mutant Ub^{F4A}, which is capable of interaction with UBDs, as a control. Nedd4 was able to use either wild-type ubiquitin, Ub^{F4A} or Ub^{I44A} to polyubiquitinate γ-ENAC (epithelial sodium channel) and N4WBP5A (Nedd4 WW-domain-binding protein 5a); the ubiquitination of these two substrates depends on the interaction between the WW domain of Nedd4 and a conserved PPxY motif on the substrate[24–26], and does not require the presence in *cis* of a UBD (Fig. 3d). Although Ub^{I44A} was attached less efficiently than wild-type ubiquitin to γ-ENAC and N4WBP5A (approximately threefold; see Supplementary Information, Fig. S2), its incorporation into these substrates was readily detectable (Fig. 3d). Conversely, Ub^{I44A} could not be incorporated into eps15 in the *in vitro* assay (Fig. 3e), even if the reaction was carried out for longer times and detected with maximal exposure of the film (data not shown). These results formally negate the "conventional interface" model (Fig. 3a), which does not predict any relevance for the binding surface of ubiquitin.

The models compatible with the data are, therefore, those relying on ubiquitin modification of the E3 ligase, that is, the "E3–thiol ester model" and the "E3–isopeptide model" (Fig. 3a). Both models are compatible with present knowledge, in that E3 ligases form thiol ester bonds with ubiquitin, but they can also be ubiquitinated[8]. *In vitro*, Nedd4 is capable of self-ubiquitination, thus fulfilling the requirements of the E3–isopeptide model. According to this, increasing the amount of covalently ubiquitinated Nedd4 in the reaction should lead to increased monoubiquitination of eps15. Conversely, in the E3–thiol ester model, the reaction should be indifferent to the state of ubiquitin–isopeptide modification of Nedd4. Therefore, we pretreated Nedd4 with ubiquitin for 20 min in a ubiquitination reaction without the eps15 substrate. This resulted in an increase in ubiquitin–isopeptide–Nedd4, with respect to a control reaction (Fig. 4a) and in a dramatic increase in eps15 monoubiquitination (Fig. 4b). This was not due to an enhancement of the intrinsic catalytic activity of Nedd4, as both pretreated and non-pretreated Nedd4 were able to polyubiquitinate N4WBP5A with comparable efficiency and time kinetics (Fig. 4c).

To exclude the possibility that the observed effects depended on the accumulation of thiol-ester bound Nedd4, the ubiquitinated Nedd4 was treated with the reducing agent, DTT — a condition that reduces thiol esters, but not isopeptide, bonds and that has been already used to reduce thiol ester bound ubiquitin in other HECT-E3 ligases, such as E6-AP[27]. No difference in the ability of Nedd4 to monoubiquitinate eps15 was detected between the reduced and non-reduced conditions (Fig. 4d). Notably, in reducing conditions most of Nedd4 seemed to be covalently linked to ubiquitin through an isopeptide bond (DTT resistant; Fig. 4e), whereas thiol ester bonds were efficiently reduced, as evident by the disappearance of ubiquitin–thiol ester–E1 (Fig. 4f).

As monoubiquitination of eps15 correlates exclusively with the ability to bind to mUb, we examined whether a monoubiquitinated Nedd4 was sufficient to exert its function. The pretreatment experiment was

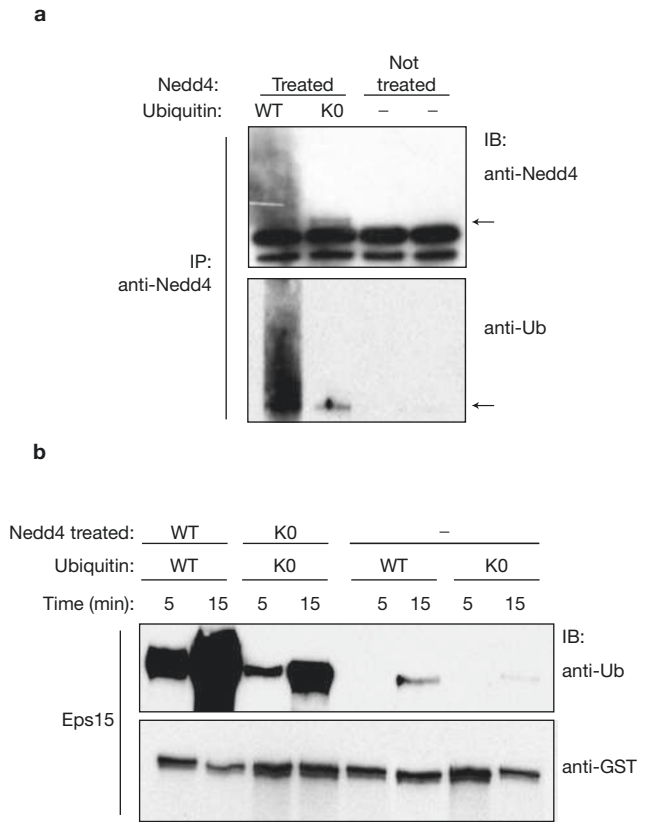

Figure 5 Monoubiquitination is sufficient to render Nedd4 competent for coupled monoubiquitination. (**a**, **b**) Nedd4 was pretreated or not using either wild-type ubiquiting or lysine-less Ub (Ub–KO). Aliquots were immunoprecipitated with an anti-Nedd4 antibody, to assess its ubiquitination state (**a**). Arrows indicate the monoubiquitinated form of Nedd4. After pretreatment, GST–eps15 (2.5 μg) and 2.5 μg of either wild-type ubiquitin or lysine-less ubiquitin were added for the indicated times (**b**). Detection was as indicated.

performed using a lysine-less ubiquitin (KO), which cannot form ubiquitin chains. The use of this mutant led to an overall decrease in the efficiency of the *in vitro* reaction (Fig. 5a), most likely because the lysine-less ubiquitin is used less efficiently by the enzymes (E1, E2 and E3) of the ubiquitination cascade[28]. However, the pretreatment of Nedd4 led to a substantial increase in its ability to monoubiquitinate eps15, even when the E3 is modified with a lysine-less ubiquitin (Fig. 5a, b). Thus, monoubiquitination, as opposed to polyubiquitination, of Nedd4 is sufficient to ubiquitinate eps15.

In the E3–isopeptide model, substrate recognition is mediated by the interaction between the UIM and the isopeptide–ubiquitin attached to the E3. The model predicts that, once modified with wild-type ubiquitin, Nedd4 should be able to transfer Ub^{I44A} to eps15. This prediction was confirmed by experiments illustrated in Fig. 6: when pretreated with wild-type ubiquitin, Nedd4 could transfer Ub^{I44A} or wild-type ubiquitin to eps15 with comparable efficiency (Fig. 6a). Conversely, modification with Ub^{I44A} essentially abolished the differences in efficiency and time kinetics observed between pretreated and not pretreated enzymes (Fig. 6b).

Taken together, our results clearly show that the E3–isopeptide model is the only one that withstands experimental scrutiny, at least under our experimental conditions.

In vivo ubiquitination of Nedd4-family members correlates with their ability to monoubiquitinate eps15.

Nedd4 is a prototypical member of a large HECT family with a common modular architecture and possible redundant functions[17]. Prompted by our findings, we analysed a subset of these HECT ligases *in vivo*. In agreement with *in vitro* results, monoubiquitinated and, possibly multi- or polyubiquitined forms of Nedd4 family members were easily detectable, the sole exception being WWP2 (Fig. 7a). The same E3 ligases were tested for their ability to induce monoubiquitination of eps15. Although overexpression of Nedd4, Nedd4L, AIP4–ITCH and WWP1 promoted eps15 monoubiquitination, even in the absence of EGF stimulation, WWP2 was not able to do so (Fig. 7b).

These results indicate that there is a correlation between the ubiquitination of Nedd4-family ligases and their capacity to execute ubiquitination of eps15 *in vivo*, strongly arguing in favour of the physiological relevance of E3 ubiquitination in the process of coupled monoubiquitination. In addition, they provided us with the opportunity of comparing the efficiency of WWP2 and Nedd4 in the *in vitro* ubiquitination assay. In agreement with the *in vivo* studies, WWP2 could not undergo ubiquitination (Fig. 7c) or monoubiquitinate eps15 (Fig. 7d). However, WWP2 was competent as an E3, as shown by ubiquitination of its *bona fide* substrate, Oct-4 (ref. 29; Fig. 7d).

Altogether, these data provide a strong argument for an *in vivo* requirement for E3 ubiquitination to perform coupled monoubiquitination of UIM-containing substrates, at least in the context of the Nedd4-family and eps15 system.

DISCUSSION

UBDs vary wildly in their affinity for ubiquitin, in the type of ubiquitin modification that they preferentially recognise and in their ability to sustain coupled monoubiquitination. Here, we provide insights into how this surprising variety of biochemical properties contributes to the cellular interpretation of ubiquitin-dependent signals, with particular regard to monoubiquitination and coupled monobiquitination.

First, we showed that monoubiquitination of eps15 depends on the intrinsic property of its UIM (or of surrogate UIMs) to interact with monomeric ubiquitin. It will be interesting to observe whether these conclusions can be extended to other ubiquitin receptors, carrying different UIMs or UBDs. In this regard we would caution that coupled ubiquitination may not be the sole mechanism leading to monoubiquitination, as monoubiquitinated proteins are known that seemingly do not contain UBDs[30]. At the biological level, however, our results present a number of interesting implications. In cellular processes relying on mUb-based transfer of information (such as internalisation and trafficking[1,31]), the presence of UIMs, and possibly of other UBDs that are capable of binding mUb, may enable ubiquitin receptors to recognise monoubiquitinated cargoes and to further transmit the signal through their own monoubiquitination. This, in turn, may help to distinguish particular pathways among the plethora of ubiquitin-based signals, to maintain the 'purity' of the signal in the signalling route.

Second, we uncovered an unexpected function for ubiquitin in the regulation of substrate recognition by E3 ligases, by showing that ubiquitination of an E3 ligase confers the ability to the enzyme to execute coupled monoubiquitination. E3 ligases are responsible for the spatial and temporal selection of substrates, providing specificity to the ubiquitination process[32]. In addition, several ubiquitination

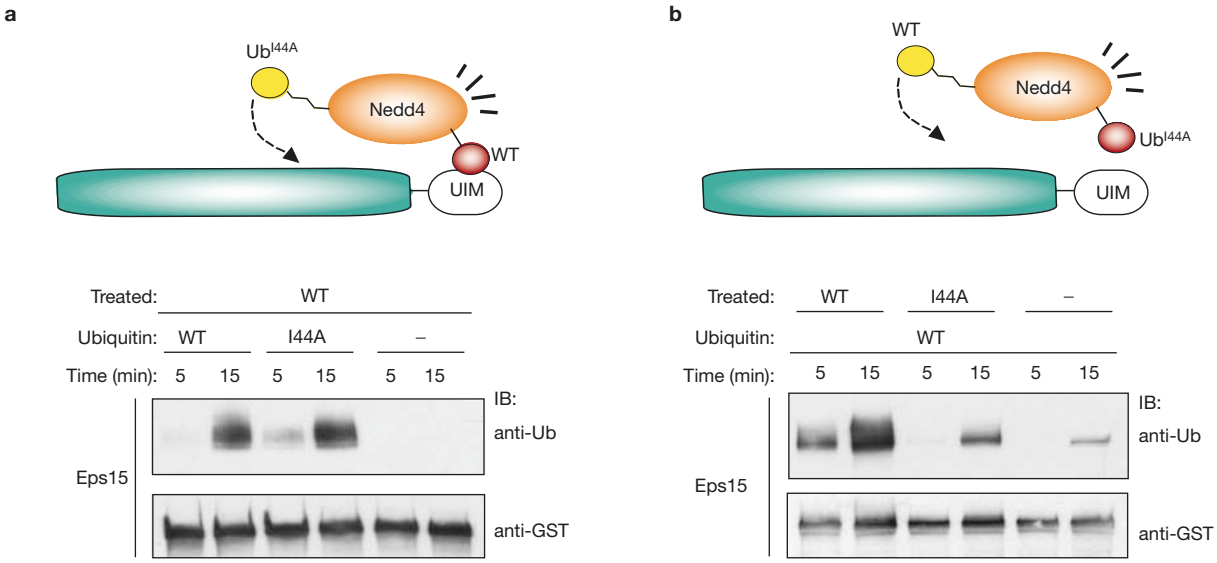

Figure 6 Challenging the E3–isopeptide model. (**a**) Nedd4 was pretreated using limiting doses of wild-type ubiquitin (200 ng). After preloading, GST–eps15 (2.5 μg) and wild-type ubiquitin or Ub^{I44A} (2.5 μg) or no ubiquitin were added for the indicated times. Detection was as indicated. (**b**) Nedd4 was pretreated with the indicated ubiquitin (200 ng) and then GST–eps15 (2.5 μg) and wild-type ubiquitin (2.5 μg) were added for the indicated times. Detection was as indicated. Note that the last sample is underloaded. Densitometric scans and normalisation for loaded proteins revealed comparable levels of eps15 monoubiquitination in the reactions performed with non-pretreated Nedd4 and Nedd4 pretreated with Ub^{I44A}.

events are induced by signalling cascades[2,4,33], therefore, the regulation of E3 enzymes is an important issue. Recent findings indicated that protein phosphorylation can directly regulate the activity of E3 ligases (reviewed in ref. 32). The regulation of E3s by ubiquitination reported here, unveils another mechanism for "regulating the regulators", allowing a greater degree of selectivity in substrate recognition. Whether the ubiquitination of E3 ligases is regulated *in vivo* and in what manner, has yet to be established. Our findings may help to rationalise why, in some cases, different E3 ligases are found in complexes (such as Cbl with Nedd4 or with AIP4; refs 34, 35), as one ligase may ubiquitinate the other.

Finally, among the many outstanding questions, one begs to be addressed: what regulates mono- versus polyubiquitination in E3 ligases that are equally competent for both types of reaction? As we have shown, Nedd4 is capable of catalysing both monoubiquitination of eps15 and polyubiquitination of γ-ENAC and N4WBP5A (see also refs 24, 25). Our *in vitro* data were obtained under conditions in which only E1, E2, Nedd4, ubiquitin and substrates were present, thus excluding the contribution of other cellular components (for example, deubiquitinating enzymes or putative E4-type molecules). Hence, the decision to mono- or polyubiquitinate must depend solely on the components present in the reaction mixture. One possible explanation is that when the E3 ubiquitinates a ubiquitin receptor, the UBD may fold back on the ubiquitin attached *in cis*, thus preventing elongation of the ubiquitin chain[36] (see Supplementary Information, Fig. S3). However, this model is not completely compatible with the data showing that, when it is conjugated with wild-type ubiquitin, Nedd4 can efficiently monoubiquitinate eps15 with Ub^{I44A} (Fig. 6a). Under these conditions, the "fold back" model would more readily predict polyubiquitination of eps15, as Ub^{I44A} would not be expected to efficiently bind the folded back UIM.

Alternative explanations are possible (see Supplementary Information, Fig. S3) that would be more directly compatible with our results. In particular, we note that the UIM–ubiquitin interaction is of low affinity and that, therefore, a stable ubiquitinated E3–substrate complex is not predicted to form, and it is not detected[11]. Therefore, after catalysis, the contact between enzyme and substrate is rapidly lost. In subsequent cycles, a monoubiquitinated or a naïve substrate moiety would have equal probabilities of undergoing modification. Under rate-limiting conditions this should result almost exclusively in monoubiquitination. Clearly, the question of what directs the catalytic activity of an E3 ligase towards mono- or polyubiquitination warrants further investigation. □

METHODS

Reagents, constructs and cellular biochemical studies. EGF was purchased from Intergen (Oxford, UK). Lys 48- and Lys 63-linked pUb chains (2–7 ubiquitin moieties), ubiquitin, ubiquitin-KO, biotinylated ubiquitin and E1, and UbcH6 were from BostonBiochem (Cambridge, MA). ATP and DTT were from Sigma (St Louis, MO); MG132 was from Affiniti Research Products (Exeter, UK). Antibodies and their suppliers were: anti-Ub (P4G7, Babco; Covance Research Products (Berkeley, CA): anti-Flag (M2, Sigma); anti-Flagaffinity gel (M2, Sigma); anti-GFP agarose beads (RQ2; MBL, Woburn, MA); streptavidin–HRP (Pierce, Rockford, IL); anti-phospho-Tyr (4G10, Upstate Biotechnology, Lake Placid, NY); anti-HA (16B12, Babco); anti-Nedd4 (BD Transduction Laboratories, San Diego, CA); and anti-E1 (05-624, Upstate Biotechnlogy).

Point mutations and deletions in all eps15-based constructs were generated by site-directed mutagenesis. Constructs containing the UIMs of S5a (amino acids 196–306) were engineered by PCR. GST–Oct4 was generated by PCR starting from clone IRAKp961K04111Q (RZPD, Berlin, Germany). YFP–Nedd4L was purchased from RZPD (NM_015277). All constructs were sequence verified and details are available on request. All other constructs were previously described[11,37–39].

Transfections were performed using Lipofectamine (Invitrogen). Cells were serum starved for 24 h and then stimulated with EGF (100 ng ml^{-1}) at 37 °C for 10 min, where indicated. Lysis was performed in JS buffer (50 mM HEPES at pH 7.5, 1% glycerol, 50 mM NaCl, 1% Triton X-100, 1.5 mM $MgCl_2$, 5 mM EGTA) plus protease inhibitors. Immunoprecipitation and immunoblotting were performed as p reviously described[10,11,23]. In the experiment in Fig. 2d, immunoprecipitation was performed using fresh (non-frozen) lysates to maximise detection of polyUb-containing proteins with the various eps15-based constructs. In the experiment in Fig. 7a, lysis was performed in JS buffer plus 0.2% SDS, then lysates were frozen and

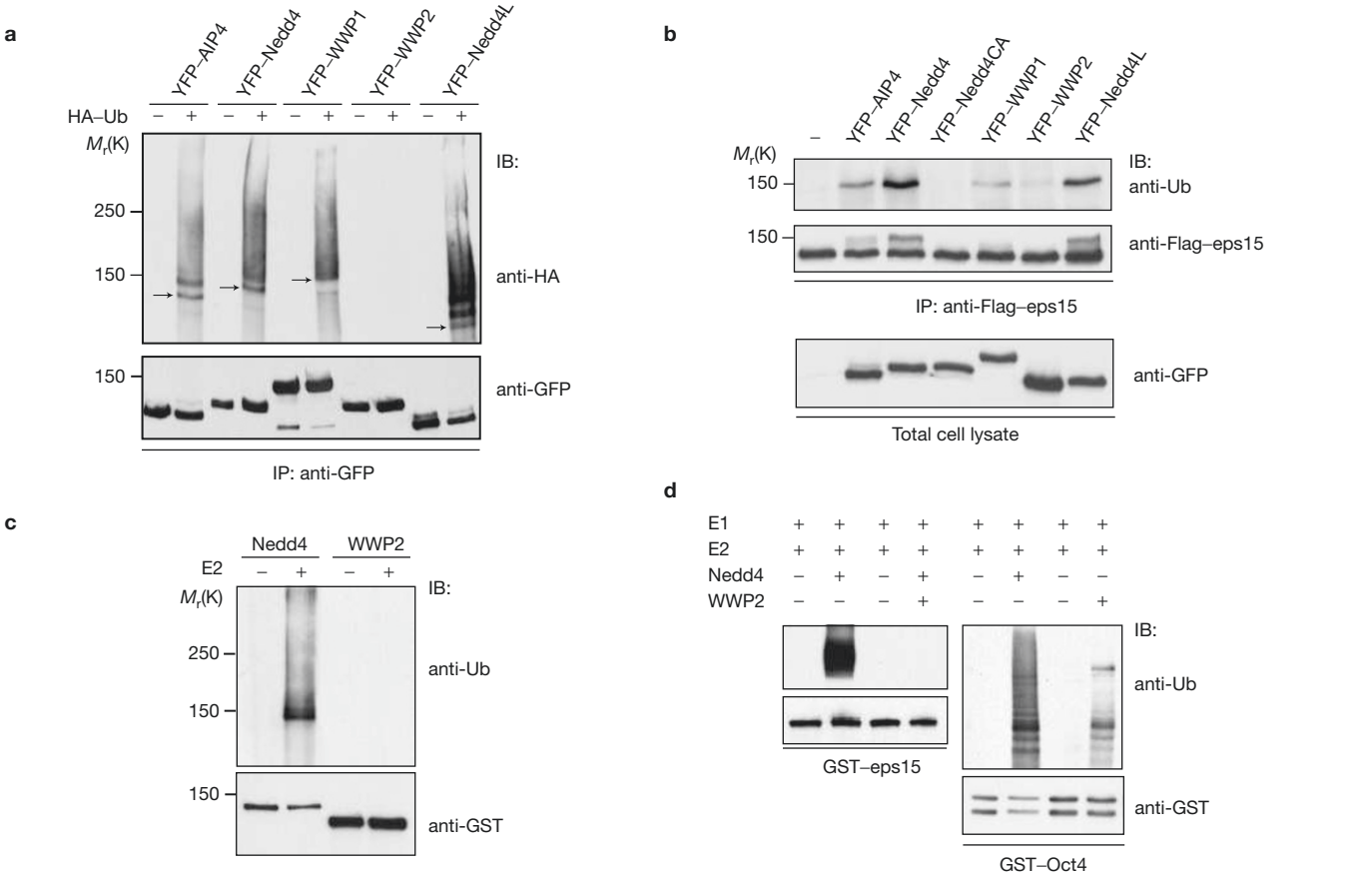

Figure 7 *In vivo* ubiquitination assays with Nedd4-family members. (**a**) HeLa cells were transfected with the indicated YFP-based constructs together with HA–Ub or empty vector. Immunoprecipitation (from 300 μg of lysates) and immunoblotting were as indicated. Arrows indicate the monoubiquitinated form of the E3 ligases. (**b**) HeLa cells were transfected with Flag-tagged eps15 and the indicated constructs Immunoprecipitation (from 750 μg of lysates) and immunoblotting were as indicated. Nedd4CA is the catalytically inactive mutant C867A. (**c**) GST-fusions containing full-length Nedd4 or WWP2 were subjected to *in vitro* self-ubiquitination assays using wild-type ubiquitin. The E2's used were His-tagged UbcH5B for Nedd4 and Ubc6 for WWP2. Detection was as indicated. (**d**) GST-fusions containing full-length eps15 or Oct-4 were subjected to *in vitro* ubiquitination assays using either Nedd4 or WWP2, as indicated. Detection was as indicated. An uncropped image of **a** is shown in the Supplementary Information, Fig. S4.

diluted four times in JS buffer before immunoprecipitation. Washes were performed in the presence of 0.1% SDS to avoid detection of ubiquitinated interacting proteins.

Ubiquitin-binding assays. For assays with cellular lysates, B82L or HeLa cells were treated for 6 h with MG132 (5 μm) and lysed in JS buffer. Total cellular protein (500 μg) was then incubated with GST fusion proteins (15 μg) at 4 °C for 2 h, washed four times with JS buffer and analysed by immunoblot.

For assays with synthetic ubiquitins, Lys 48- or Lys 63-linked polyUb chains (400 ng) or ubiquitin (4 μg) were incubated at 4 °C for 2 h with 15 μg of GST-fusion proteins in 100 μl of YY buffer (50 mM HEPES at pH 7.5, 10% glycerol, 150 mM NaCl, 1% Triton X-100, 1 mM EDTA, 1 mM EGTA), followed by four washes with YY buffer and analysis by immunoblot.

Ubiquitination assays. Nedd4, WWP2, wild-type ubiquitin, Ub^{I44A} and Ub^{F4A} were produced as GST-fusion proteins, cleaved and purified with the thrombin cleavage capture kit (Novagen, Darmstadt, Germany). Reaction mixtures contained purified enzymes (100 ng E1, 100 ng purified His-tagged UbcH5B or UbcH6, 0.5 μg of Nedd4 or WWP2), 2.5 μg of the substrate (either full-length eps15 or mutants, or γ-ENAC, N4WBP5A or Oct-4, all produced as GST fusion proteins) and 2.5 μg of either wild-type ubiquitin, Ub^{I44A} or Ub^{F4A} or lysine-less ubiquitn in ubiquitination buffer (25 mM Tris–HCl at pH 7.6, 5 mM $MgCl_2$, 100 mM NaCl, 1 μm DTT, 2 mM ATP). Reactions were incubated at 30 °C for 1 h, followed by four washes in YY buffer and detection by immunoblotting.

For assays with pretreated E3, 0.5 μg of Nedd4 was incubated with 100 ng E1, 100 ng UbcH5B and 200 ng wild-type ubiquitin or various mutant at 30 °C for 20 min. Subsequently, 2.5 μg of the substrate (either full-length GST–eps15 or GST–N4WBP5A) and 2.5 μg biotinylated ubiquitin were added. Reactions were incubated for different time periods, washed four times in YY buffer and detected using streptavidin–HRP.

For self-ubiquitination assays using GST–Nedd4 or WWP2, reaction mixtures contained 100 ng E1, 0.5 μg Nedd4 or WWP2, 250 ng biotinylated ubiquitin and 100 ng His-tagged UbcH5B as E2 for Nedd4, or His-tagged UbcH6 as E2 for WWP2. Reactions were incubated at 30 °C for 30 min, followed by four washes in YY buffer and detection by immunoblotting.

Note: Supplementary Information is available on the Nature Cell Biology website.

ACKNOWLEDGEMENTS

We thank: L. Hicke for providing GST–ubiquitin (wild type), Ub^{I44A} and Ub^{F4A} constructs; S. Kumar for N4WBP5A construct; M. Sudol for γ-ENAC construct; P. Bienias for AIP4, WWP1 and WWP2 constructs. We thank I. Dikic for critical review of the manuscript. The authors' work is supported by grants from AIRC (Italian Association for Cancer Research) and The European Community (RUBICON, VI Framework) to S.P. and P.P.D.F.; AICR (Association for International Cancer Research) to S.P.; Human Science Frontier Program, the Italian Ministries of Health and of Education and University (MIUR), and the Monzino Foundation to P.P.D.F. B.O. is recipient of a fellowship from RUBICON.

COMPETING FINANCIAL INTERESTS

The authors declare that they have no competing financial interests.

Published online at http://www.nature.com/naturecellbiology/
Reprints and permissions information is available online at http://npg.nature.com/reprintsandpermissions/

1. Hicke, L. & Dunn, R. Regulation of membrane protein transport by ubiquitin and ubiquitin-binding proteins. *Annu. Rev. Cell Dev. Biol.* **19,** 141–172 (2003).
2. Chen, Z. J. Ubiquitin signalling in the NF-κB pathway. *Nature Cell Biol.* **7,** 758–765 (2005).
3. Zhang, Y. Transcriptional regulation by histone ubiquitination and deubiquitination. *Genes Dev* **17,** 2733–2740 (2003).
4. Huang, T. T. & D'Andrea, A. D. Regulation of DNA repair by ubiquitylation. *Nature Rev. Mol. Cell Biol.* **7,** 323–334 (2006).
5. Morita, E. & Sundquist, W. I. Retrovirus budding. *Annu. Rev. Cell Dev. Biol.* **20,** 395–425 (2004).
6. Pickart, C. M. Mechanisms underlying ubiquitination. *Annu. Rev. Biochem.* **70,** 503–533 (2001).
7. Hochstrasser, M. Lingering mysteries of ubiquitin-chain assembly. *Cell* **124,** 27–34 (2006).
8. Hicke, L., Schubert, H. L. & Hill, C. P. Ubiquitin-binding domains. *Nature Rev. Mol. Cell Biol.* **6,** 610–621 (2005).
9. Bienko, M. *et al.* Ubiquitin-binding domains in Y-family polymerases regulate translesion synthesis. *Science* **310,** 1821–1824 (2005).
10. Penengo, L. *et al.* Crystal structure of the ubiquitin binding domains of rabex-5 reveals two modes of interaction with ubiquitin. *Cell* **124,** 1183–1195 (2006).
11. Polo, S. *et al.* A single motif responsible for ubiquitin recognition and monoubiquitination in endocytic proteins. *Nature* **416,** 451–455 (2002).
12. Oldham, C. E., Mohney, R. P., Miller, S. L., Hanes, R. N. & O'Bryan, J. P. The ubiquitin-interacting motifs target the endocytic adaptor protein epsin for ubiquitination. *Curr. Biol.* **12,** 1112–1116 (2002).
13. Klapisz, E. *et al.* A ubiquitin-interacting motif (UIM) is essential for Eps15 and Eps15R ubiquitination. *J. Biol. Chem.* **277,** 30746–30753 (2002).
14. Katz, M. *et al.* Ligand-independent degradation of epidermal growth factor receptor involves receptor ubiquitylation and Hgs, an adaptor whose ubiquitin- interacting motif targets ubiquitylation by Nedd4. *Traffic* **3,** 740–751 (2002).
15. Shih, S. C. *et al.* A ubiquitin-binding motif required for intramolecular monoubiquitylation, the CUE domain. *EMBO J.* **22,** 1273–1281 (2003).
16. Stamenova, S. D., Dunn, R., Adler, A. S. & Hicke, L. The Rsp5 ubiquitin ligase binds to and ubiquitinates members of the yeast CIN85-endophilin complex, Sla1-Rvs167. *J. Biol. Chem.* **279,** 16017–16025 (2004).
17. Ingham, R. J., Gish, G. & Pawson, T. The Nedd4 family of E3 ubiquitin ligases: functional diversity within a common modular architecture. *Oncogene* **23,** 1972–1984 (2004).
18. Murillas, R., Simms, K. S., Hatakeyama, S., Weissman, A. M. & Kuehn, M. R. Identification of developmentally expressed proteins that functionally interact with Nedd4 ubiquitin ligase. *J. Biol. Chem.* **277,** 2897–2907 (2002).
19. Tenno, T. *et al.* Structural basis for distinct roles of Lys63- and Lys48-linked polyubiquitin chains. *Genes Cells* **9,** 865–875 (2004).
20. Varadan, R. *et al.* Solution conformation of Lys63-linked di-ubiquitin chain provides clues to functional diversity of polyubiquitin signaling. *J. Biol. Chem.* **279,** 7055–7063 (2004).
21. Raasi, S., Varadan, R., Fushman, D. & Pickart, C. M. Diverse polyubiquitin interaction properties of ubiquitin-associated domains. *Nature Struct. Mol. Biol.* **12,** 708–714 (2005).
22. Miller, S. L., Malotky, E. & O'Bryan, J. P. Analysis of the role of ubiquitin-interacting motifs in ubiquitin binding and ubiquitylation. *J. Biol. Chem.* **279,** 33528–33537 (2004).
23. Fazioli, F. *et al.* Identification and biochemical characterization of novel putative substrates for the epidermal growth factor receptor kinase. *J. Biol. Chem.* **267,** 5155–5161 (1992).
24. Staub, O. *et al.* WW domains of Nedd4 bind to the proline-rich PY motifs in the epithelial Na^+ channel deleted in Liddle's syndrome. *EMBO J.* **15,** 2371–2380 (1996).
25. Harvey, K. F., Shearwin-Whyatt, L. M., Fotia, A., Parton, R. G. & Kumar, S. N4WBP5, a potential target for ubiquitination by the Nedd4 family of proteins, is a novel Golgi-associated protein. *J. Biol. Chem.* **277,** 9307–9317 (2002).
26. Shearwin-Whyatt, L. M., Brown, D. L., Wylie, F. G., Stow, J. L. & Kumar, S. N4WBP5A (Ndfip2), a Nedd4-interacting protein, localizes to multivesicular bodies and the Golgi, and has a potential role in protein trafficking. *J. Cell Sci.* **117,** 3679–3689 (2004).
27. Huibregtse, J. M., Scheffner, M., Beaudenon, S. & Howley, P. M. A family of proteins structurally and functionally related to the E6-AP ubiquitin-protein ligase. *Proc. Natl Acad. Sci. USA* **92,** 2563–2567 (1995).
28. Wang, M., Cheng, D., Peng, J. & Pickart, C. M. Molecular determinants of polyubiquitin linkage selection by an HECT ubiquitin ligase. *EMBO J.* **25,** 1710–1719 (2006).
29. Xu, H. M. *et al.* Wwp2, an E3 ubiquitin ligase that targets transcription factor Oct-4 for ubiquitination. *J. Biol. Chem.* **279,** 23495–23503 (2004).
30. Polo, S., Confalonieri, S., Salcini, A. E. & Di Fiore, P. P. EH and UIM: endocytosis and more. *Sci. STKE* **213**, re17 (2003).
31. Haglund, K., Di Fiore, P. P. & Dikic, I. Distinct monoubiquitin signals in receptor endocytosis. *Trends Biochem. Sci.* **28,** 598–603 (2003).
32. Gao, M. & Karin, M. Regulating the regulators: control of protein ubiquitination and ubiquitin-like modifications by extracellular stimuli. *Mol. Cell* **19,** 581–593 (2005).
33. Haglund, K. & Dikic, I. Ubiquitylation and cell signaling. *EMBO J.* **24,** 3353–3359 (2005).
34. Courbard, J. R. *et al.* Interaction between two ubiquitin-protein isopeptide ligases of different classes, CBLC and AIP4/ITCH. *J. Biol. Chem.* **277,** 45267–45275 (2002).
35. Magnifico, A. *et al.* WW domain HECT E3s target Cbl RING finger E3s for proteasomal degradation. *J. Biol. Chem.* **278,** 43169–74317 (2003).
36. Hoeller, D. *et al.* Regulation of ubiquitin-binding proteins by monoubiquitination. *Nature Cell Biol.* **8,** 163–169 (2006).
37. Confalonieri, S., Salcini, A. E., Puri, C., Tacchetti, C. & Di Fiore, P. P. Tyrosine phosphorylation of Eps15 is required for ligand-regulated, but not constitutive, endocytosis. *J. Cell Biol.* **150,** 905–912 (2000).
38. Haglund, K. *et al.* Multiple monoubiquitination of RTKs is sufficient for their endocytosis and degradation. *Nature Cell Biol.* **5,** 461–466 (2003).
39. Sigismund, S. *et al.* Clathrin-independent endocytosis of ubiquitinated cargos. *Proc. Natl Acad. Sci. USA* **102,** 2760–2765 (2005).
40. Di Fiore, P. P., Polo, S. & Hofmann, K. When ubiquitin meets ubiquitin receptors: a signalling connection. *Nature Rev. Mol. Cell Biol.* **4,** 491–497 (2003).

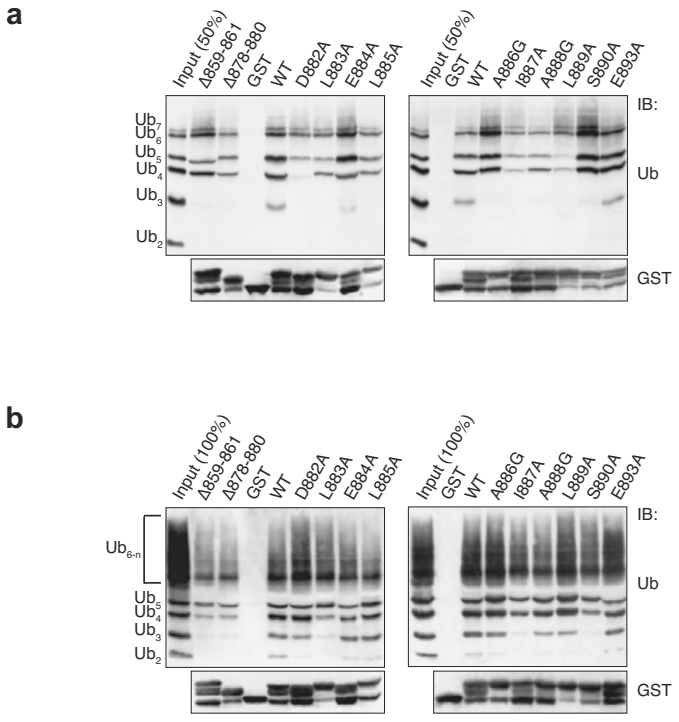

Figure S1 Binding of UIM mutants to synthetic polyUb K48- or K63-linked chains. The indicated GST-eps15 fusion proteins (aa 842-897) were incubated with polyUb chains (2 to 7 ubiquitin moieties) linked by K48 (**a**) or K63 (**b**). Binding was assessed in IB with anti-Ub. The same blot was redecorated with an anti-GST antibody to show comparable loading. As evidenced, the various mutations had different impacts on binding to individual forms of polyUb (Ub_2, Ub_3, Ub_4 etc.), which also varied for K48- or K63-linked chains. While the molecular bases for this phenomenon are unclear, we never detected 100% correlation between coupled monoubiquitination and ability to bind to a particular isoform of polyUb (not shown). Quantitation of binding to different forms of Ub (as summarized in Fig. 1a) was obtained by scanning/densitometry of the blots at two different exposures, followed by normalization for loaded proteins. In the case of data in Fig. 1b (reported in Fig. 1a as "bind. to lysate"), the intensity of the top band of the GST-fusion proteins (as obtained by Ponceau staining, and representing the not degraded full length GST fusion, in each case) was used for normalization. Absolute data were then converted to% of wt, for each individual protein. Experiments were repeated three times, and the final values (average of 3 independent experiments) were expressed as indicated in the legend to Fig. 1a.

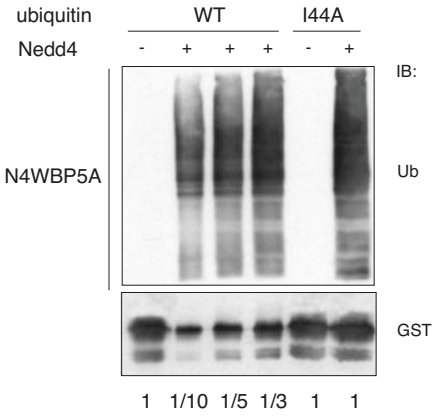

Figure S2 In vitro ubiquitination of N4WBP5A with Ub-wt or Ub-I44A. A GST-fusion protein, encoding full-length N4WBP5A was subjected to in vitro ubiquitination using Ub-wt or Ub-I44A (as in Fig. 3d of the main text). To better appreciate differences in the incorporation of Ub, 1/10, 1/5 and 1/3 of the reaction performed with Ub-wt was loaded on the gel, as indicated at the bottom. The reaction performed with Ub-I44A was loaded entirely (indicated at bottom as "1"). Detection was as indicated. Quantitation of the signals revealed a three-fold reduction in the polyubiquitination of N4WBP5A when the reaction was performed in the presence of Ub-I44A, with respect to Ub-wt.

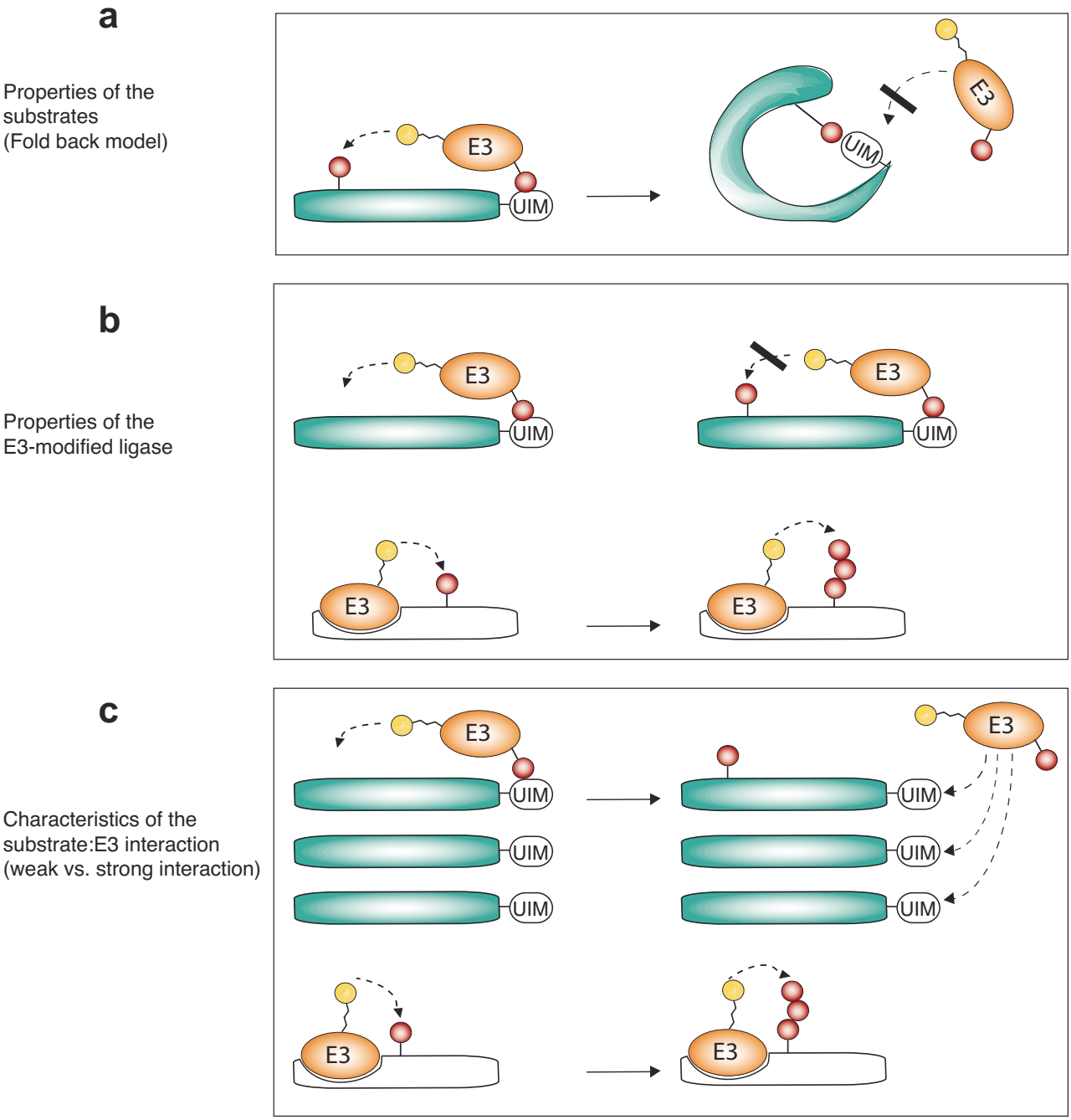

Figure S3 Models for mono- vs. poly-ubiquitination by the same E3 ligase. An E3 ligase, such as Nedd4, capable of catalysing polyubiquitination, might in some cases catalyse monoubiquitination, due to several possible molecular mechanisms, that are not necessarily mutually exclusive. Here, some possibilities are depicted. (**a**) Properties of the substrates (fold-back model). As proposed[1], the UIM might fold back on the Ub appended *in cis*, preventing elongation of the Ub chain (interactions *in trans* are also possible). (**b**) Properties of the Ub-modified E3 ligase. The Ub-modified E3 ligase might not be "processive", thus leading to monoubiquitination. This might happen, for instance, because the E3 bound to a UIM-protein (shown in green) cannot be properly re-loaded by the E2 enzyme; or because, after the first cycle of catalysis, the substrate:E3 complex is in a conformation that prevents access of the thiol-ester Ub to the "branching" lysines on the Ub that is already appended to the substrate. When the E3 binds to a substrate (shown in white) with modalities different from a Ub:UIM interaction, the described constraints would not apply, thus leading to polyubiquitination. (**c**) Characteristics of the substrate:E3 interaction (weak vs. strong interaction model). The interaction between the UIM-protein (shown in green) and the Ub(isopeptide)-E3 is of low affinity, and a stable enzyme:substrate complex is not predicted to form (and indeed it is not detectable[2]). Thus, after the first cycle of catalysis, contact between enzyme and substrate is rapidly lost. In subsequent cycles, a monoubiquitinated or a unmodified substrate will have the same probability of undergoing modification. This should result, under rate-limiting conditions, almost exclusively in monoubiquitination. Conversely, if a stable enzyme:substrate complex forms (as in the case of the Nedd4:γ-ENAC or Nedd4:N4WBP5A complexes, which are mediated by WW domains, shown here in white), processive catalysis, leading to polyubiquitination can take place.

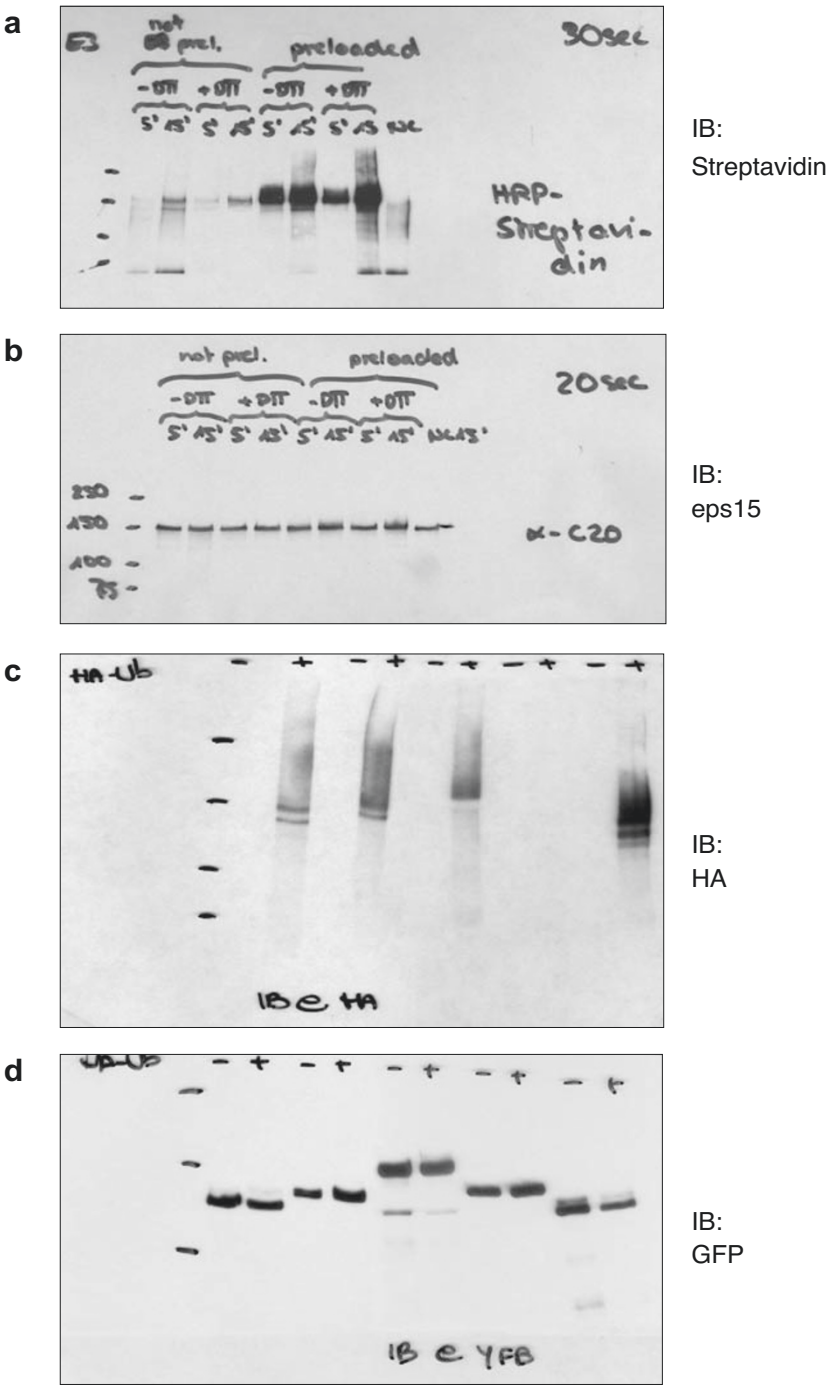

Figure S4 Original scans. **a** full scan of Fig. 4d, upper panel. **b** full scan of Fig. 4d, middle panel. **c** full scan of Fig. 7a, upper panel. **d** full scan of Fig. 7a, lower panel.

References to Supplemental Figures

1. Hoeller, D. *et al.* Regulation of ubiquitin-binding proteins by monoubiquitination. *Nat Cell Biol* **8**, 163-9 (2006).
2. Polo, S. *et al.* A single motif responsible for ubiquitin recognition and monoubiquitination in endocytic proteins. *Nature* **416**, 451-5. (2002).

Molecular Cell

Article

BUB1 and CENP-U, Primed by CDK1, Are the Main PLK1 Kinetochore Receptors in Mitosis

Graphical Abstract

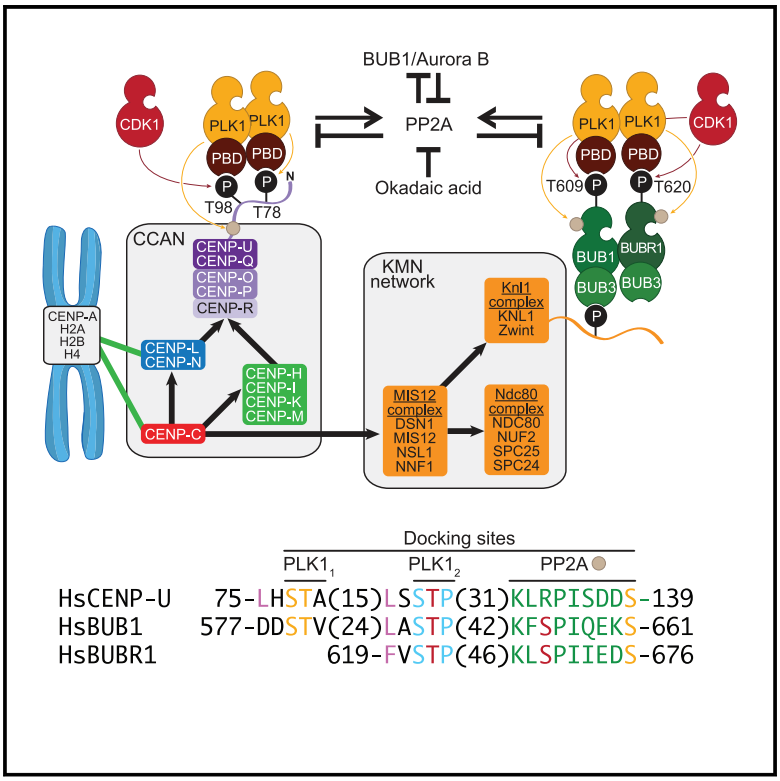

Highlights

- Recruitment of PLK1 to BUB1 and to the core kinetochore is reconstituted *in vitro*
- The CENP-U N-terminal region exposes the only PLK1 receptor in the core kinetochore
- CDK1 and PLK1 promote PLK1 recruitment on BUB1 and CENP-U and PLK1 dimerization
- Like BUB1, CENP-U contains a previously unnoticed PP2A-phosphatase-binding motifs

Authors

Priyanka Singh, Marion E. Pesenti, Stefano Maffini, ..., Anupallavi Srinivasamani, Tanja Bange, Andrea Musacchio

Correspondence

andrea.musacchio@mpi-dortmund.mpg.de

In Brief

Polo-like kinase 1 (PLK1) targets kinetochores to regulate microtubule attachment and mitotic checkpoint signaling. Singh et al. show how CDK1 and PLK1 promote kinetochore recruitment and dimerization of PLK1 onto BUB1 and CENP-U, probably the only PLK1 receptors in the core kinetochore. A conserved constellation of docking sites in BUB1 and CENP-U, including one for PP2A phosphatase, suggests a common regulatory switch.

Singh et al., 2021, Molecular Cell *81*, 67–87
January 7, 2021
https://doi.org/10.1016/j.molcel.2020.10.040

CellPress

Molecular Cell

CellPress
OPEN ACCESS

Article

BUB1 and CENP-U, Primed by CDK1, Are the Main PLK1 Kinetochore Receptors in Mitosis

Priyanka Singh,[1,3,7] Marion E. Pesenti,[1,7] Stefano Maffini,[1] Sara Carmignani,[1] Marius Hedtfeld,[1] Arsen Petrovic,[1,4] Anupallavi Srinivasamani,[1,5] Tanja Bange,[1,6] and Andrea Musacchio[1,2,8,*]

[1]Department of Mechanistic Cell Biology, Max Planck Institute of Molecular Physiology, Otto-Hahn-Straße 11, 44227 Dortmund, Germany
[2]Centre for Medical Biotechnology, Faculty of Biology, University Duisburg-Essen, Universitätsstrasse, 45141 Essen, Germany
[3]Present address: Department of Bioscience & Bioengineering, Indian Institute of Technology Jodhpur, NH65, Nagaur Road, Karwar 342037, Jodhpur, Rajasthan, India
[4]Present address: Department of Molecular Structural Biology, Max Planck Institute of Biochemistry, Am Klopferspitz 18, 82152 Martinsried, Germany
[5]Present address: Department of Immunology, University of Texas MD Anderson Cancer Center, 1515 Holcombe Boulevard, Unit 901, Houston, TX 77054, USA
[6]Present address: Department for Systems Chronobiology, Institute of Medical Psychology, LMU Munich, Goethe-Str. 31, 80336 Munich, Germany
[7]These authors contributed equally
[8]Lead Contact
*Correspondence: andrea.musacchio@mpi-dortmund.mpg.de
https://doi.org/10.1016/j.molcel.2020.10.040

SUMMARY

Reflecting its pleiotropic functions, Polo-like kinase 1 (PLK1) localizes to various sub-cellular structures during mitosis. At kinetochores, PLK1 contributes to microtubule attachments and mitotic checkpoint signaling. Previous studies identified a wealth of potential PLK1 receptors at kinetochores, as well as requirements for various mitotic kinases, including BUB1, Aurora B, and PLK1 itself. Here, we combine ectopic localization, *in vitro* reconstitution, and kinetochore localization studies to demonstrate that most and likely all of the PLK1 is recruited through BUB1 in the outer kinetochore and centromeric protein U (CENP-U) in the inner kinetochore. BUB1 and CENP-U share a constellation of sequence motifs consisting of a putative PP2A-docking motif and two neighboring PLK1-docking sites, which, contingent on priming phosphorylation by cyclin-dependent kinase 1 and PLK1 itself, bind PLK1 and promote its dimerization. Our results rationalize previous observations and describe a unifying mechanism for recruitment of PLK1 to human kinetochores.

INTRODUCTION

By catalyzing the post-translation phosphorylation of consensus motifs on their targets, protein kinases regulate, in space and time, countless biological processes (Ubersax and Ferrell, 2007). In the cell division cycle of eukaryotes, which ultimately results in cell duplication, several protein kinases have essential regulatory roles (Novak et al., 2010). In single-celled eukaryotes, including for *Saccharomyces cerevisiae* and *Schizosaccharomyces pombe*, a single member of the cyclin-dependent kinase family (CDK) is the "engine" of cell division. Progressive, controlled activation of this CDK orders in time the duplication of chromosomes during the S phase and their segregation during mitosis (Novak et al., 2010). This general scheme is conserved in multicellular eukaryotes, where additional CDKs with partly redundant functions exist (Novak et al., 2010).

Although CDK activity directs the cell cycle, it also regulates the activation of various other protein kinases that execute the multitude of events required for cell division (Saurin, 2018). Among them, Polo-like kinases represent a conserved family of effector kinases that orchestrate key functions in mitosis and cytokinesis (Archambault and Glover, 2009; Combes et al., 2017; Zitouni et al., 2014). Genes encoding members of this kinase family, *cdc5* and *polo*, were first identified in genetic screens in *S. cerevisiae* and *Drosophila melanogaster*, respectively (Hartwell et al., 1973; Llamazares et al., 1991; Sunkel and Glover, 1988). Polo orthologs were later identified in *S. pombe*, *Xenopus laevis*, and mammals, where they were named, respectively, Plo1, Plx1, and PLK1 (Clay et al., 1993; Golsteyn et al., 1994; Holtrich et al., 1994; Kumagai and Dunphy, 1996; Mulvihill et al., 1999; Ohkura et al., 1995). A requirement for Polo in mitotic progression and bipolar spindle formation was first identified in flies (Llamazares et al., 1991; Sunkel and Glover, 1988). In humans, PLK1 peaks between the G2 and M phases of the cell cycle, when PLK1 occupies sub-cellular locations that include centrosomes, kinetochores, microtubules, the central spindle, and the midbody (Ahonen et al., 2005; Arnaud et al., 1998; De Luca et al., 2006; Golsteyn et al., 1994, 1995; Goto et al., 2006; Lane

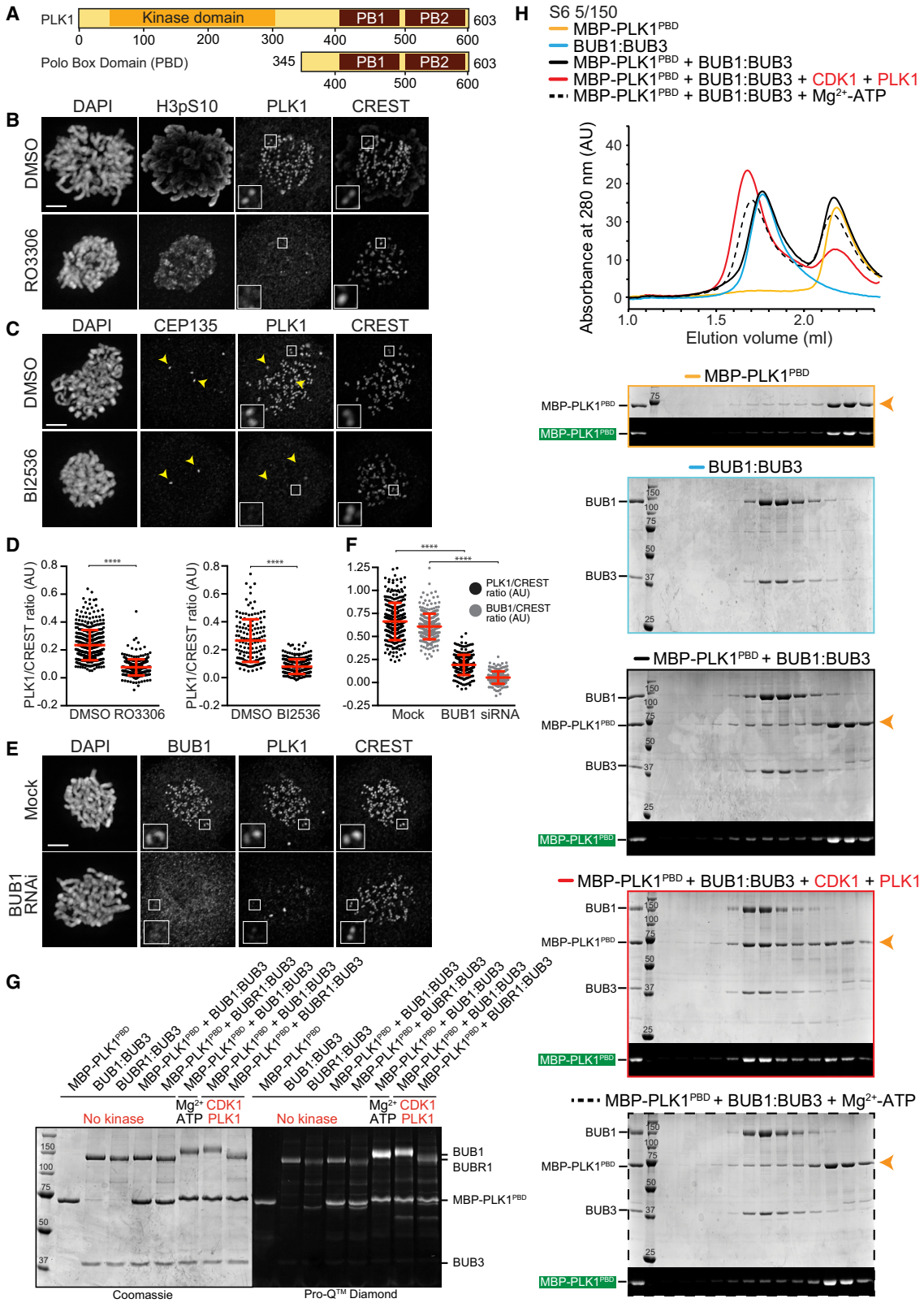

(legend on next page)

and Nigg, 1996; Lénárt et al., 2007; Liu et al., 2004; Neef et al., 2003). At these locations, PLK1 participates in functions that include mitotic entry, centrosome separation and maturation, chromosome alignment, spindle checkpoint signaling, and cytokinesis (Combes et al., 2017; Saurin, 2018).

PLK1 has an N-terminal catalytic Ser/Thr kinase domain and a C-terminal Polo-box domain (PBD; Figure 1A). The kinase domain phosphorylates target proteins on Ser or Thr within the consensus motif [**D**/**N**/**E**/Y]-X-S/T-[**F**/Φ; no P]-[Φ/X], where Φ and X indicate hydrophobic and any amino acid, respectively, and residues in bold indicate strong preference (Alexander et al., 2011; Dou et al., 2011; Hegemann et al., 2011; Heinrich et al., 2013; Kettenbach et al., 2011; Nakajima et al., 2003). The PBD (comprising residues 345–603 in human PLK1) includes two polo box (PB) motifs (residues 411–489 and 511–592), intervening residues, and part of the linker between the kinase domain and PB1 (residues 373–410) (Cheng et al., 2003; Elia et al., 2003b). The PBD mediates PLK1 localization and activation (Elia et al., 2003b; Hanisch et al., 2006; Jang et al., 2002a; Lee et al., 1998; Lowery et al., 2007; Seong et al., 2002). It docks onto a motif of binding partners characterized by the sequence Ser-[pSer/pThr]-[Pro/X], where pSer and pThr indicate phosphorylated serine and threonine, respectively, and X can be any residue (Elia et al., 2003a, 2003b). When X is proline (Pro), the PBD-binding motif embeds the core phosphorylation target of proline-directed kinases, such as CDK1, the main mitotic kinase, which target Ser/Thr-Pro motifs. Thus, CDK1 phosphorylation of these motifs generates binding sites for PLK1 (Elowe et al., 2007; Lowery et al., 2007; Moshe et al., 2004; Watanabe et al., 2004; Wong and Fang, 2007; Xu et al., 2013; Yamaguchi et al., 2005; Yamashiro et al., 2008; Yoo et al., 2004). In addition, the PBD may interact with non-phosphorylated motifs or with motifs phosphorylated by PLK1 itself (self-priming). Self-priming may become especially relevant after the decline of CDK activity at anaphase (Burkard et al., 2009; García-Alvarez et al., 2007; Kang et al., 2006; Lee et al., 2014; McKinley and Cheeseman, 2014; Neef et al., 2003, 2007; Park et al., 2010; Wolfe et al., 2009). Collectively, these interactions mediate the recruitment of PLK1 to various subcellular locations (Archambault and Glover, 2009; Combes et al., 2017; Zitouni et al., 2014) and, in addition, contribute to stimulate its kinase activity by relieving an intra-molecular interaction of the PBD and kinase domain that stabilizes an inactive conformation of PLK1 (Mundt et al., 1997; Xu et al., 2013). Activation of PLK1 also requires phosphorylation by Aurora A or Aurora B, related kinases localizing, respectively, at spindle poles and centromeres-kinetochores on Thr210 of the PLK1 activation loop (Carmena et al., 2012; Jang et al., 2002b; Johnson et al., 2008; Kelm et al., 2002; Kothe et al., 2007; Macůrek et al., 2008; Seki et al., 2008; Xu et al., 2013).

Centromeres are chromosome *loci* that provide a foundation for the kinetochore, a multi-subunit complex whose primary function is the capture, through specialized machinery that includes the NDC80 complex (Cheeseman et al., 2006; DeLuca et al., 2006; Pesenti et al., 2018). Microtubule binding to kinetochores is necessary but not sufficient for chromosome bi-orientation and segregation. The latter requires a local, kinetochore- and centromere-confined regulatory network of several mitotic kinases, including CDK1, Aurora B, BUB1, MPS1, PLK1, their many substrates, and counteracting protein phosphatases, including PP1 and PP2A (Saurin, 2018). Treatments that interfere with these regulators expose dramatic defects in chromosome alignment. The network modulates the stability of kinetochore-microtubule attachments, most notably, but not exclusively, through multisite phosphorylation of NDC80 (Monda and Cheeseman, 2018; Musacchio and Desai, 2017) and is thought to respond to different levels of microtubule-generated forces on mono-oriented (and incorrectly oriented) or bi-oriented chromosomes, respectively (Nezi and Musacchio, 2009; Rago and Cheeseman, 2013). How the force-sensing mechanism operates is obscure, but Aurora B and PLK1 appear to oppose each other, acting, respectively, to destabilize and stabilize the kinetochore-microtubule interface (Foley et al., 2011; Liu et al., 2012).

Studying bi-orientation and its feedback control is enormously challenging, not least because it is accomplished within the very restricted volume of the kinetochore-centromere region, whose

Figure 1. BUB1 Is a Prominent Kinetochore Receptor of PLK1

(A) Scheme of human PLK1.

(B) HeLa cells were released from double-thymidine block into nocodazole (3.3 μM) to synchronize in prometaphase. Cells were exposed to DMSO or RO3306 for 10 min in the presence of MG132 before fixation. Representative cells for DMSO and RO3306 were immunostained for DAPI (DNA marker), H3pS10 (Aurora B activity marker), PLK1, and CREST (kinetochore marker). Intensities from 436 kinetochores for DMSO-treated cells and 289 for RO3306 in five to six cells were scored. Scale bar, 5 μm.

(C) HeLa cells, synchronized as in (B), were exposed to DMSO or BI2536 for 90 min in the presence of MG132 before fixation. Cells were immunostained for DAPI, CEP135 (centrosome marker), PLK1, and CREST. Yellow arrowheads highlight centrosomes. Intensities from 143 kinetochore for DMSO-treated and 291 for BI-2536 treatment in four to five cells were scored.

(D) Dot plots representing PLK1/CREST intensity ratios for individual kinetochores. Statistical significance in all figures reflects Mann-Whitney test (see Method Details). Error bars represent means ± standard errors of the mean.

(E) Representative images showing mock and BUB1-depleted HeLa cell immunostained for DAPI, BUB1, PLK1, and CREST.

(F) Dot plots representing PLK1/CREST kinetochore intensity ratio (black bars) and mean BUB1/CREST kinetochore ratio (gray bars) in the case of BUB1 RNAi. Error bars represent means ± standard errors of the mean; 303 kinetochores for mock and 232 kinetochores for BUB1 RNAi in four to five different cells were scored.

(G) Phosphorylation of input proteins of SEC experiment in (H) and Figure S3B were assessed by SDS-PAGE, followed by Coomassie or Pro-Q Diamond staining. The same gels are also displayed in Figure S2A.

(H) Elution profile and SDS-PAGE analysis of an SEC run on a Superose6 5/150 column (S6 5/150) of the interaction of Alexa-488-labeled MBP-PLK1^{PBD} with the BUB1:BUB3 complex (5 μM each) in the presence of the indicated priming kinases (marked in red; used at 1/20 ratio). In-gel fluorescence of Alexa-488-labeled MBP-PLK1^{PBD} in the SEC fractions analyzed by SDS-PAGE is also shown. The orange arrows highlight MBP-PLK1^{PBD} in each gel. The MBP-PLK1^{PDB} control elution profile and SDS-PAGE are also displayed in Figure S3A.

nanoscale organization is incompletely understood. Specific sub-localizations of the regulators within this restricted volume establish short-range (tens or hundreds of nanometer) and dynamic spatial activity gradients that are likely to be crucial for the tension-sensing mechanism (Krenn and Musacchio, 2015; Lampson and Grishchuk, 2017). Before mechanistic insight into these dynamics can be gained, how and where, in kinetochores, the different mitotic kinases and phosphatases are recruited must be understood. Here, we elucidate kinetochore recruitment of PLK1 in mitotic human cells. Previous work suggested that this recruitment depends on a remarkably long list of docking partners, including BUB1 and its paralog BUBR1, CLASP2, INCENP, and survivin (subunits of the Aurora-B-containing chromosome passenger complex [CPC]), SGO1 (a CPC-, PP2A-, and cohesin-associated protein), dynactin, NUDC (a regulator of dynein and LIS1), CLIP 170 (a microtubule-binding protein), NCAPG2 (a condensin subunit), Meikin (a meiotic protein), RSF1 (a chromatin remodeler), CENP-U (also named CENP-50 or PBIP1, an inner kinetochore protein), and USP16 (a deubiquitinase) (Amin et al., 2014; Goto et al., 2006; Ikeda and Tanaka, 2017; Kang et al., 2006, 2011; Kim et al., 2014, 2015; Lee et al., 2015; Maia et al., 2012; Matsumura et al., 2007; Nishino et al., 2006; Pouwels et al., 2007; Qi et al., 2006; Sun et al., 2012; Yeh et al., 2013; Zhuo et al., 2015). It is unclear whether these proteins, individually, are bona fide receptors of PLK1 or are, rather, part of a hierarchical regulatory network that eventually converges on PLK1 recruitment to only one or a few of them. In favor of the latter, although the receptors listed above are scattered through the entire centromere and kinetochore, PLK1 occupies a smaller, focused region of the kinetochore (Lénárt et al., 2007; Lera et al., 2016), suggesting a specific interaction with one or a few confined receptors. Even within this confined localization, regulation of PLK1 binding may be complex. For instance, although a role of CDK1 in the recruitment of PLK1 to BUB1 and BUBR1 is well established, PLK1 has also been proposed to bind CENP-U in mitosis simply through self-priming (Kang et al., 2006, 2011).

Here, we demonstrate physical interactions of PLK1 with BUB1, BUBR1, and CENP-U and show that CENP-U may be the sole, prominent PLK1 receptor within the kinetochore core. Aurora B and BUB1 promote PLK1 binding to CENP-U, but their requirement is indirect and can be bypassed. Importantly, binding of PLK1 to CENP-U is strictly dependent on priming CDK1 activity, which promotes robust PLK1 docking through PLK1 dimerization on Thr78 (T78), previously identified as the PLK1 self-priming site (Kang et al., 2006, 2011), and Thr98. A conserved and unique constellation of binding motifs in BUB1, BUBR1, and CENP-U suggests a unifying view of the PLK1 kinetochore recruitment mechanism.

RESULTS

Role of PLK1, CDK1, and BUB1 in Kinetochore Recruitment of PLK1

PLK1 interacts with binding partners through self-priming or through CDK1 priming activity (Lowery et al., 2005). To test whether PLK1 or CDK1 promote kinetochore recruitment of PLK1 in HeLa cells, we individually inhibited them in mitotically arrested cells (nocodazole, 3.3 μM) with highly selective small-molecule inhibitors of PLK1 (BI2536, used at 100 nM) or CDK1 (RO3306, 9 μM) (Lénárt et al., 2007; Vassilev et al., 2006) and analyzed kinetochore localization at 10, 30, and 90 min in the presence of the proteasome inhibitor MG132 (10 μM) to prevent mitotic exit (Figures S1A–S1G). Both inhibitors caused a very prominent reduction of kinetochore PLK1, as assessed by immunofluorescence (Figures 1B–1D). BI2536 depleted PLK1 not only from kinetochores but also from mitotic centrosomes, as described (Lénárt et al., 2007).

Kinetochore recruitment of PLK1 requires at least two additional kinases, BUB1 and Aurora B (subunit of the CPC) (Goto et al., 2006; Qi et al., 2006; Sun et al., 2012). Indeed, depletion of BUB1 by small interfering RNA (siRNA) interference (Figure S1H; validated by disappearance of the H2A-pT120 mark in Figure S1I) largely depleted PLK1 from kinetochores (Figures 1E and 1F). Thus, recruitment of PLK1 to kinetochores requires the kinase activity of CDK1 and PLK1 and at least the presence of BUB1. Phosphorylation of BUB1 and BUBR1 by CDK1 kinase, respectively, on Thr609 and Thr620, which lie within Ser-Thr-Pro (STP) motifs, preludes PLK1 recruitment (Elowe et al., 2007; Huang et al., 2008; Qi et al., 2006; Wong and Fang, 2007). In kinase assays *in vitro*, recombinant BUB1:BUB3 incubated with Mg^{2+}-ATP only strongly auto-phosphorylated, as revealed by shifts in the electrophoretic mobility in SDS-PAGE and staining of phosphorylated proteins with Pro-Q Diamond (Figures 1G and S2A). BUB1 became even more strongly phosphorylated in the presence of sub-stoichiometric concentrations of priming CDK1 and PLK1 (in this and other experiments, priming kinases were used at 1/10 to 1/30 ratio to their substrate; in figures, priming kinases are marked in red). BUBR1:BUB3, which does not auto-phosphorylate (unpublished data; Breit et al., 2015; Suijkerbuijk et al., 2012a), also became phosphorylated with priming CDK1 and PLK1, albeit less than BUB1:BUB3 (Figures 1G and S2A).

Next, we combined primed BUB1:BUB3 or BUBR1:BUB3 with a fluorescently labeled fusion of maltose-binding protein (MBP) and the PLK1 Polo-box domain (MBP-PLK1^{PBD}; Figure 1A), which is sufficient for kinetochore targeting. To detect binding, the mix was analyzed by size-exclusion chromatography (SEC). Both BUB1:BUB3 and BUBR1:BUB3 formed stoichiometric complexes with Alexa-488-labeled MBP-PLK1^{PBD}, but only after treatment with priming CDK1 and PLK1 (Figures 1H and S3A). Without priming kinases, addition of Mg^{2+}-ATP did not promote binding to MBP-PLK1^{PBD}, indicating that despite considerable auto-phosphorylation BUB1 kinase activity is not required for binding to MBP-PLK1^{PBD}. These observations are in line with previous work on the role of BUB1 and BUBR1 as PLK1 receptors (Cordeiro et al., 2020; Elowe et al., 2007; Qi et al., 2006) and show that CDK1 and PLK1 prime BUB1 and BUBR1 to become direct binding partners of PLK1^{PBD}.

Aurora B and BUB1 Contribute Indirectly to PLK1 Recruitment

MPS1 phosphorylates KNL1 to generate binding sites for BUB1 (and, indirectly, through the latter for BUBR1) (Krenn et al., 2014; Overlack et al., 2015; Vleugel et al., 2013). In agreement with those previous studies, inhibition of MPS1 with Reversine

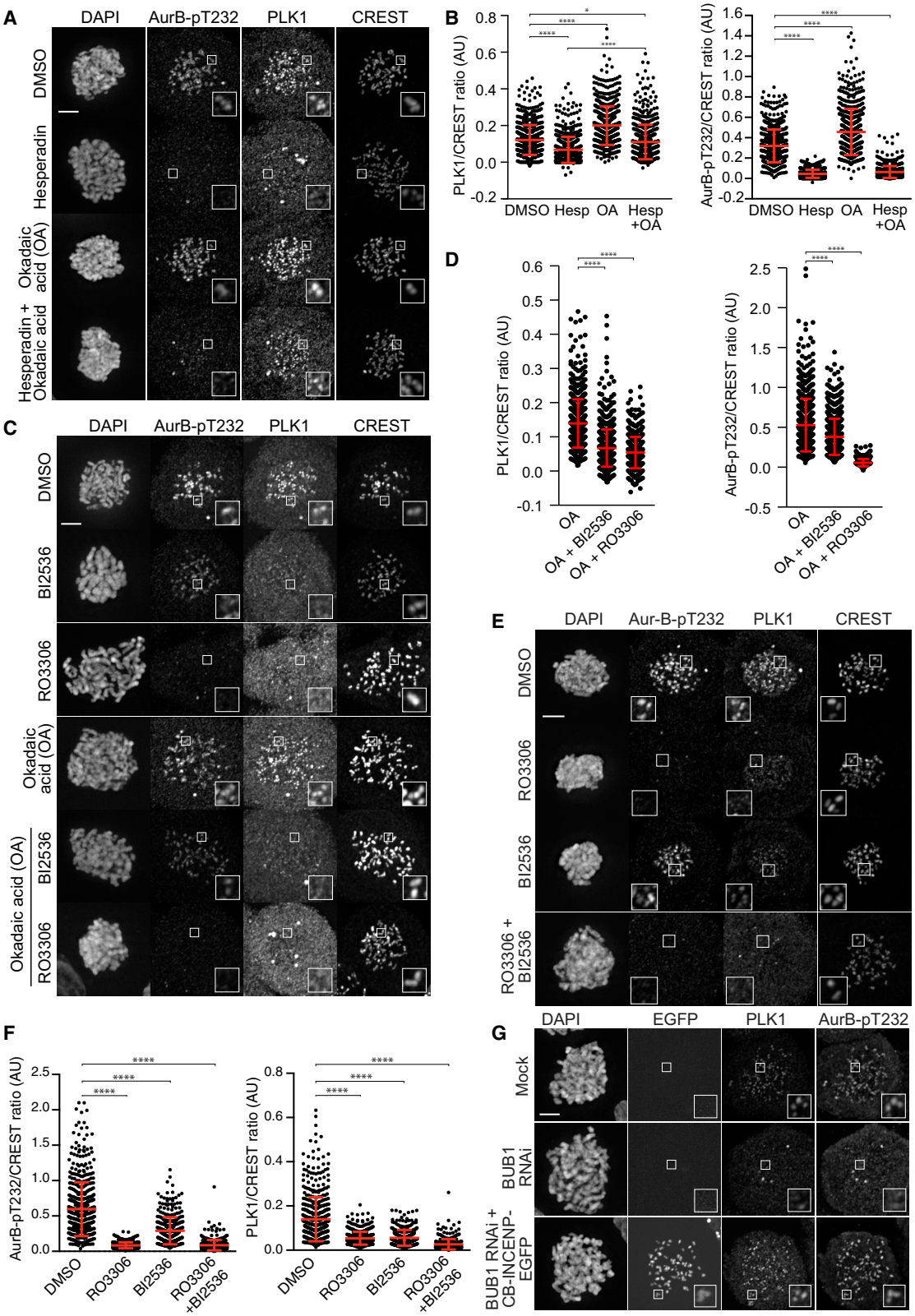

(legend on next page)

(Santaguida et al., 2010) led to a strong decrease of BUB1 kinetochore levels (Figures S4A and S4B), concomitant with the previously reported increase of MPS1 kinetochore levels (Santaguida et al., 2010) (Figures S4C and S4D). The kinetochore levels of PLK1 correlated with those of BUB1, with reduced but residual kinetochore localization (Figures S4E and S4F).

Next, we tested a requirement for Aurora B in PLK1 kinetochore recruitment. The selective Aurora B inhibitor hesperadin (500 nM) (Hauf et al., 2003) ablated H3-pS10 (phosphorylated Ser10 of Histone H3, a mitotic substrate of Aurora B [Hsu et al., 2000]). PLK1 levels were significantly reduced in comparison to DMSO-treated control cells, indicating that Aurora B is also required for kinetochore recruitment of PLK1 (Figures S2B and S2C). Aurora B may control PLK1 recruitment in various ways. First, Aurora B is required for kinetochore recruitment of BUB1 (Morrow et al., 2005), which, in turn, recruits PLK1. Second, Aurora B exercises homeostatic control of the levels of kinetochore phosphorylation by controlling the major human mitotic phosphatases PP1 and PP2A (reviewed in Joukov and De Nicolo, 2018, and Saurin, 2018). Interference with Aurora B activity might, therefore, cause ectopic activation of phosphatases that counteract PLK1 kinetochore recruitment through hydrolysis of phosphosites required for PLK1 docking. Third, Aurora B phosphorylates the activation loop of PLK1, activating it (Carmena et al., 2012; Shao et al., 2015).

To dissect these complex interdependencies, we focused on PP1 and PP2A, both of which are inhibited by okadaic acid (OA) (Bialojan and Takai, 1988). We treated mitotic HeLa cells with hesperadin, OA (100 nM), or their combination in nocodazole and MG132. After 90 min, cells were fixed and processed for immunofluorescence. In isolation, OA caused a marked increase of kinetochore PLK1 and AurB-pT232 (an Aurora B auto-phosphorylation site (Sessa et al., 2005)). OA also rescued the detrimental effects of Aurora B inhibition, allowing kinetochore accumulation of PLK1 in hesperadin-treated cells to levels almost comparable to those in DMSO-treated cells (Figures 2A and 2B). This was not due to re-activation of Aurora B because the levels of AurB-pT232 remained low (Figures 2A and 2B). Similarly, and in agreement with previous studies (De Antoni et al., 2012), Aurora B kinetochore levels were not affected by hesperadin, OA, or their combination (Figures S4G and S4H). Thus, PLK1 can be recruited to kinetochores when Aurora B is inhibited, if the phosphatase activity is also suppressed. This suggests that Aurora B is not directly required for PLK1 kinetochore recruitment. Rather, its requirement may reflect regulation of phosphatases that control the abundance of phospho-epitopes directly or indirectly involved in PLK1 recruitment.

We addressed the role of CDK1 and PLK1 using the same assay. As already shown (Figures 1B–1D), BI2536 or RO3306 strongly counteracted kinetochore recruitment of PLK1 (Figures 2C, 2D, and S1A–S1F). In addition, RO3306 strongly inhibited the accumulation of AurB-pT232, probably because CDK1 activity is required for efficient CPC recruitment to centromeres and kinetochores (Krenn and Musacchio, 2015). Importantly, OA did not promote re-accumulation of PLK1 at kinetochores in the presence of BI2536 or RO3306, suggesting that the activity of both CDK1 and PLK1 is directly required for PLK1 kinetochore recruitment (Figures 2C, 2D, and S1J). Indeed, PLK1 almost disappeared from mitotic kinetochores in HeLa cells co-treated with BI2536 or RO3306 (Figures 2E and 2F).

Another Kinetochore Binding Site for PLK1

BUB1 is required for kinetochore localization of BUBR1 (Overlack et al., 2015), possibly explaining why BUBR1 depletion has no major consequences on kinetochore PLK1 (Cordeiro et al., 2020; Elowe et al., 2007). BUB1 also contributes to a positive feedback loop that promotes localized accumulation and activation of Aurora B (Baron et al., 2016; Caldas et al., 2013; Hindriksen et al., 2017; Liu et al., 2013; van der Waal et al., 2012; Wang et al., 2011). Indeed, depletion of BUB1 by RNAi prevented accumulation of the active form of Aurora B (Figure 2G, middle). This raises a conundrum because it implies that depletion of BUB1, in addition to removing binding sites for PLK1 on BUB1 and BUBR1, may also interfere with other Aurora-B-dependent interactions of PLK1, even if only indirectly through control of protein phosphatases. To test that, we resorted to a CENP-B-INCENP-EGFP chimera (CB-INCENP-EGFP; Figure S2D) (Liu et al., 2009), in which the centromere-targeting domain of CB is fused to INCENP, a CPC subunit required for Aurora B localization and activation (Adams et al., 2000; Kaitna et al., 2000). Expression of CB-INCENP-EGFP in BUB1-depleted cells largely restored the levels of AurB-pT232 (Figures S2E–S2G). Remarkably, it also promoted kinetochore localization of PLK1 to levels almost comparable to control cells (Figures 2G, bottom, S2F, and S2G), revealing that another kinetochore receptor for PLK1 must exist, in addition to BUB1 and BUBR1.

Figure 2. PLK1 and CDK1 Activity Is Required for Kinetochore Recruitment of PLK1

(A) Representative images of pro-metaphase-synchronized HeLa cells treated with DMSO, hesperadin (500 nM, here and elsewhere), okadaic acid (100 nM, here and elsewhere), or hesperadin plus okadaic acid for 90 min with MG132. Cells were immunostained for DAPI, Aur-pT232, PLK1, and CREST.

(B) Dot plots of PLK1/CREST (left) or AurB-pT232/CREST (right) intensity ratio for individual kinetochores; 734 kinetochores for DMSO, 689 for hesperadin, 684 for okadaic acid and 650 for hesperadin + okadaic acid-treated cells in eight to 12 different cells were scored. Error bars, means ± standard errors of the mean.

(C) Representative pro-metaphase-synchronized HeLa cells treated with DMSO, BI 2536, RO3306, okadaic acid, and RO3306 or BI 2536 plus okadaic acid for 90 min (10 min in the case of RO3306) in the presence of MG132. Cells were immunostained for DAPI, AurB-pT232, PLK1, and CREST. Scale bar, 5 μm.

(D) Dot plots representing PLK1/CREST (left) and AurB-pT232 over CREST (right) intensity ratios for individual kinetochores; 382 to 1,298 individual kinetochores in seven to 17 different cells were scored. The red line indicates means ± standard deviation. Additional controls in Figure S1J.

(E) Representative images of prometaphase synchronized HeLa cells treated with DMSO (control), RO3306, BI2536, or RO3306 + BI2536, stained with DAPI, AurB-pT232, PLK1, and CREST. Scale bar, 5 μm.

(F) Dot plots of AurB-pT232/CREST (left) or PLK1/CREST (right) intensity ratios for individual kinetochores. Error bars represent means ± standard errors of the mean; 426–541 individual kinetochores in seven to 11 different cells were scored.

(G) Representative images showing mock, BUB1-RNAi alone, or concomitantly expressing doxycycline-inducible CB-INCENP-EGFP in HeLa cells. Cells were immunostained for DAPI, PLK1, and phosphorylated T232 residue of Aurora B (AurB-pT232). EGFP reflects CB-INCENP expression. Scale bar, 5 μm.

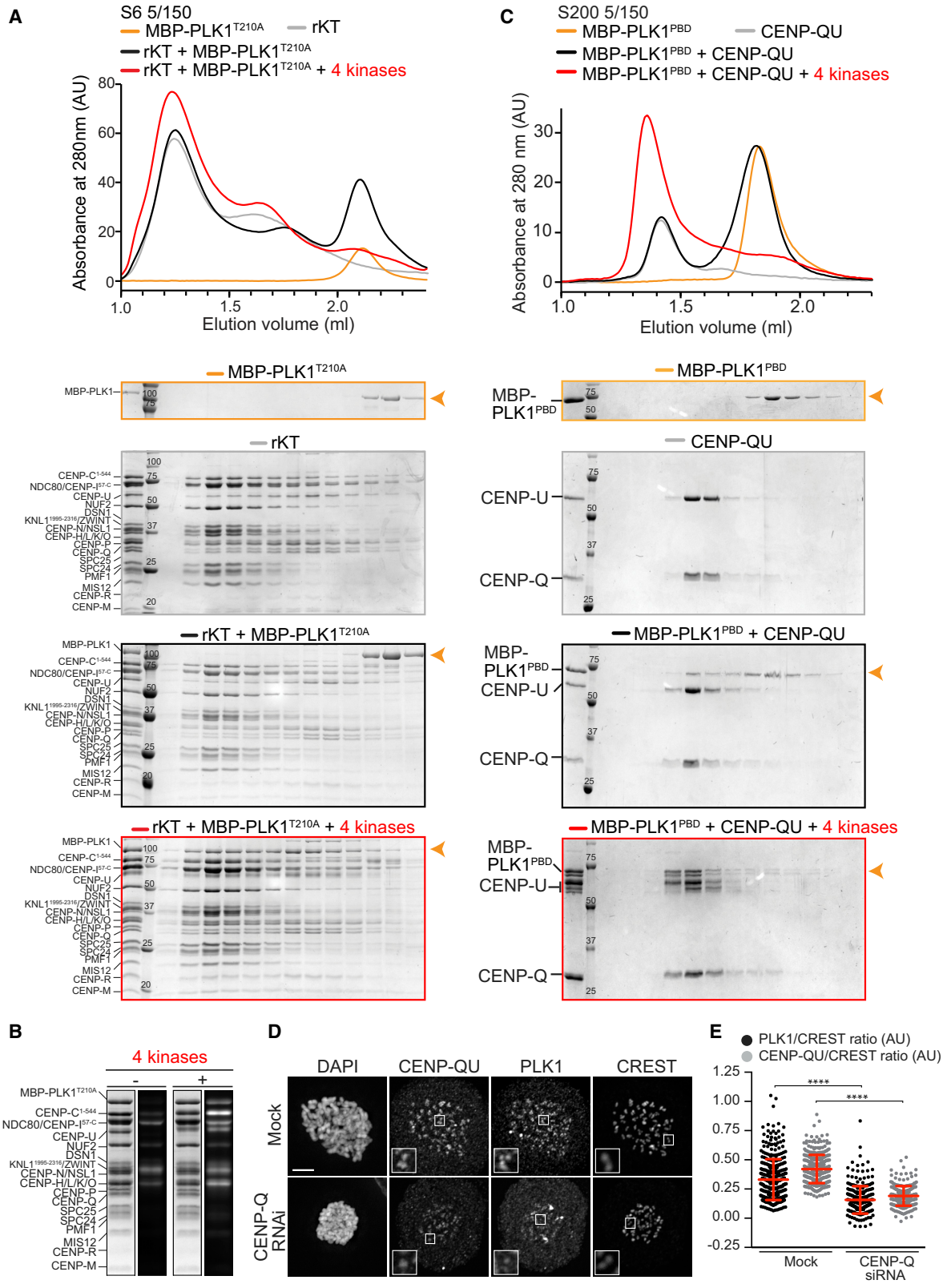

(legend on next page)

PLK1 recruitment to this additional receptor(s) was strictly dependent on Aurora B activity because it was strongly inhibited by hesperadin (Figure S2H).

PLK1 Binds to the Core Kinetochore

To identify the additional PLK1 receptor(s), we reconstituted recombinant kinetochore particles (rKTs) containing 22 subunits, most of inner and outer kinetochore proteins (Figure S5A; note that, for these reconstitutions, we used a C-terminal fragment of KNL1 devoid of BUB1 or BUBR1 binding sites) (Pesenti et al., 2018; Weir et al., 2016). We combined the rKT with MBP-PLK1^{T210A}, a recombinant fusion of MBP with an inactive (or very poorly active) mutant of PLK1 (Jang et al., 2002b; Kelm et al., 2002). Aurora B, BUB1, PLK1, and CDK1 were then incubated with rKTs as putative priming kinases, and the resulting mixes were analyzed by SEC. When MBP-PLK1^{T210A} was combined with rKTs without priming kinases, its elution volume did not shift (Figure 3A). Conversely, a complete shift in elution volume was observed with priming kinases, indicating that they generate binding sites for MBP-PLK1^{T210A} on the rKT. Pro-Q Diamond staining revealed background levels of phosphorylation on some rKT subunits, which are generated in insect cells (Figure 3B). Priming kinases caused prominent increases in phosphorylation on only a few rKT subunits, most notably CENP-C (represented by its first 544 residues, CENP-C$^{1–544}$), CENP-U, and the MBP-PLK1^{T210A} fusion itself (Figures 3B and S5B).

With the exception of BUB1:BUB3, the other kinases phosphorylated the rKT individually (Figure S5B). To bypass the confounding factor that PLK1^{T210A} may deliver residual kinase activity at stoichiometric concentrations, we repeated the binding experiments with fluorescent MBP-PLK1^{PBD}, testing its interaction with rKT in the presence of individual priming kinases (Figure S3B). Occasionally, the CENP-OPQUR sub-complex detaches from the rKTs in SEC runs and elutes in a separate peak of larger elution volume. Remarkably, priming phosphorylation by PLK1 or CDK1, but not by Aurora B or BUB1:BUB3, promoted co-elution of MBP-PLK1^{PBD} with this CENP-OPQUR peak (Figure S3B). Thus, we asked whether PLK1 also interacts with the CENP-OPQUR complex in the absence of other rKT subunits. At equimolar concentrations (5 μM), the MBP-PLK1^{PBD} and the 5-subunit CENP-OPQUR complex (Pesenti et al., 2018) did not co-elute from a SEC column, whereas a stoichiometric complex was assembled after pre-incubation with priming kinases (Figure S3C). Further SEC analyses demonstrated that the CENP-QU sub-complex was sufficient for a phosphorylation-dependent interaction with MBP-PLK1^{PBD} (Figure 3C), whereas MBP-PLK1^{PBD} did not bind the CENP-OP sub-complex (Figure S3D). Individual CENP-OPQUR subunits are unstable and could not be tested (Pesenti et al., 2018).

Within CENP-OPQUR, CENP-U is a target of priming PLK1, CDK1, or Aurora B (but not BUB1) and is even more pervasively phosphorylated after their combination (Figures 3B, S5B, and S5C). When we pre-incubated the CENP-OPQUR complex with individual priming kinases, only PLK1 (mildly) or CDK1 (strongly) stimulated binding of MBP-PLK1^{PBD} to CENP-OPQUR, whereas Aurora B and BUB1 did not (Figure S5D). Thus, CDK1, and to a lesser extent PLK1, create binding sites for the MBP-PLK1^{PBD} on CENP-QU *in vitro*.

RNAi-based depletion of CENP-Q prevents kinetochore recruitment of the entire CENP-OPQUR without affecting other kinetochore subunits (Pesenti et al., 2018). It also caused a strong reduction of PLK1 kinetochore levels (Figures 3D and 3E). RNAi-based depletion of CENP-Q was not uniform in the cell population, but there was good correlation between residual CENP-Q and PLK1 levels at kinetochores (Figures S6A and S6B). We surmise, however, that in addition to possible variations in individual cells, residual kinetochore PLK1 under these conditions is recruited by BUB1 (and BUBR1), whose levels are unaffected by CENP-OPQUR depletion (Figures S2I–S2L).

Recruitment of PLK1 to CENP-U at an Ectopic Site

Thr78 of CENP-U^{PBIP1} has been previously identified as a PLK1 target and docking site (Kang et al., 2011; Kang et al., 2006; Kettenbach et al., 2011). Thus, we initially focused on CENP-U to investigate the molecular basis of PLK1 docking. Human CENP-U consists of 418 residues (Figure S6C). Its N-terminal ~115 residues, which have a high-disorder probability and may be unstructured, are not required for kinetochore localization, because a chimeric CENP-U construct encompassing residues 115–418 fused to eGFP was sufficient for kinetochore recruitment. Conversely, a GFP chimera encompassing CENP-U$^{1–114}$ failed to reach kinetochores (Figure 4A).

We asked whether chimeric constructs containing CENP-U or its fragments fused with the LacI repressor were sufficient for targeting PLK1 to an ectopic array of LacO operator sites in an engineered U2OS cell line (Janicki et al., 2004). Full-length (FL) CENP-U or deletion constructs of CENP-U tagged with LacI-EGFP were transiently expressed in these cells for 48 h. Nocodazole (330 nM) was then added for 15–16 h to synchronize cells in mitosis. All LacI-EGFP-CENP-U constructs localized to the ectopic LacO array (Figure 4B). LacI-EGFP-CENP-U$^{1–418}$

Figure 3. PLK1 Binds CENP-U in the Core Kinetochore

(A) Elution profile and SDS-PAGE analysis of analytical SEC runs on a Superose 6 increase 5/150 (S6 5/150) column. A mixture of rKT (5 μM) and MBP-PLK1^{T210A} (5 μM) was treated without or without CDK1:cyclin-B, PLK1, Aurora B, and BUB1 (used at 1/20 ratio to target proteins). The orange arrows indicate MBP-PLK1^{T210A}.

(B) Phosphorylation of input proteins of the SEC experiment in (A) was assessed by SDS-PAGE, followed by Coomassie or Pro-Q Diamond staining.

(C) Elution profile and SDS-PAGE analysis of analytical SEC runs on a Superdex 200 increase 5/150 (S200 5/150) column of a mixture of CENP-QU subcomplex (5 μM) and MBP-PLK1^{PBD} (5 μM) with or without the same kinases used in (B). Orange arrows highlight MBP-PLK1^{PBD}. The MBP-PLK1^{PDB} control is also displayed in Figure S3C.

(D) Representative cells of mock and CENP-Q depleted (using RNAi) HeLa cells immunostained for DAPI, CENP-QU complex, PLK1, and CREST. Scale bar, 5 μm. Small insets frame kinetochores in individual channels.

(E) Dot plots representing PLK1/CREST (black bars) or CENP-QU/CREST (gray bars) kinetochore intensity ratios. Error bars represent means ± standard errors of the mean. A total of 377 kinetochores for mock and 257 kinetochores for CENP-QU-depleted cells in five to six cells were scored.

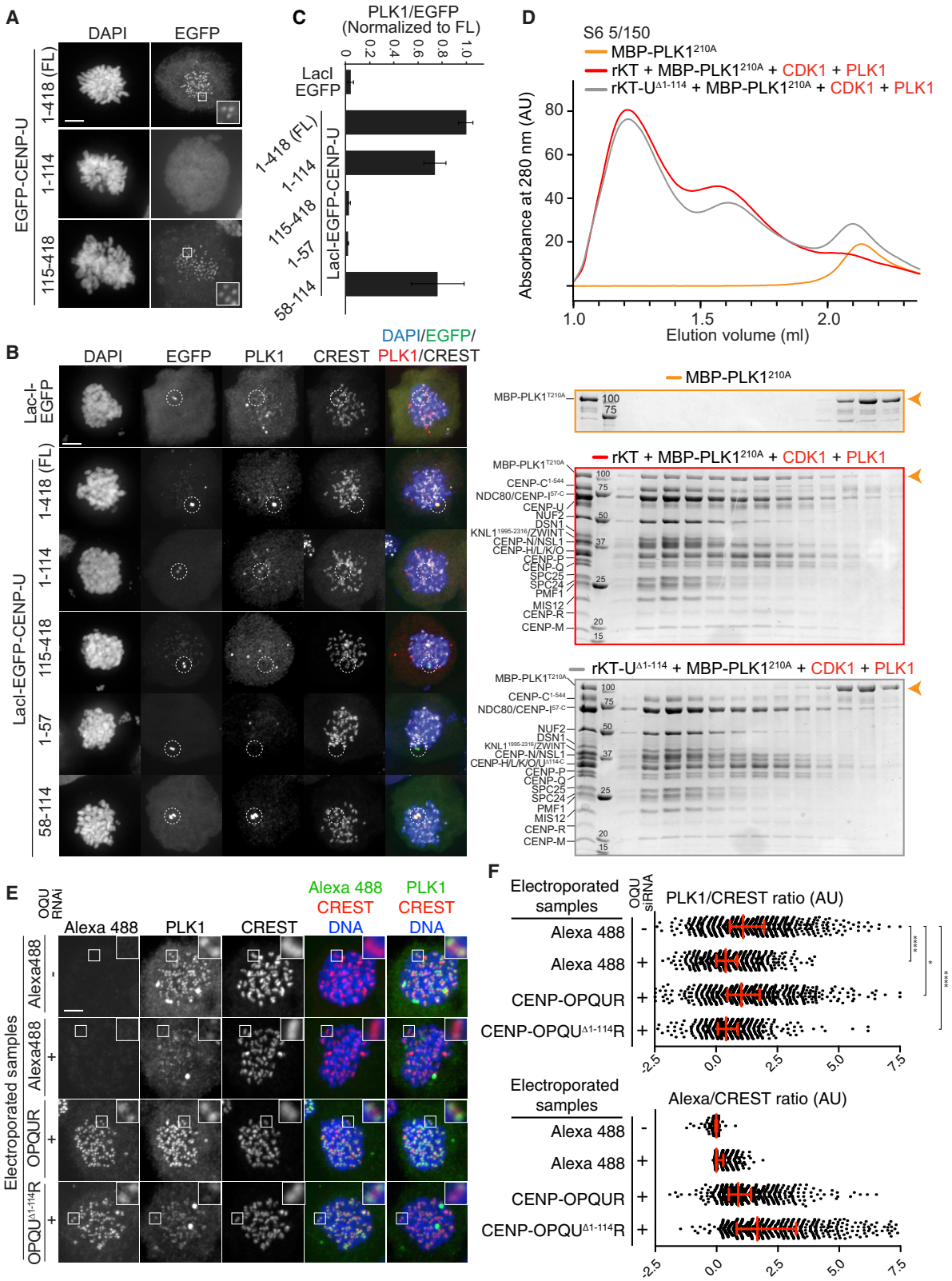

(legend on next page)

promoted effective recruitment of PLK1 to the ectopic site, whereas LacI-EGFP-CENP-U$^{115–418}$ did not (Figures 4B, 4C, and S6D). Conversely, LacI-EGFP-CENP-U$^{1–114}$ was sufficient for ectopic localization of PLK1 (Figures 4B and 4C). To map the PLK1 binding site even more precisely, we trimmed CENP-U$^{1–114}$ into two segments, CENP-U$^{1–57}$ and CENP-U$^{58–114}$. CENP-U$^{58–114}$ was sufficient to recruit PLK1 to the ectopic LacO array (Figures 4B, 4C, and S6E). Further trimming resulted in two segments, CENP-U$^{58–85}$ and CENP-U$^{86–114}$, which were unable to recruit PLK1 (Figure S6F). Thus, CENP-U$^{58–114}$ is necessary and sufficient for the interaction of PLK1 to an ectopic chromosome site (Figure S6G).

CENP-U Is the Sole PLK1 Receptor of Reconstituted Kinetochores

In SEC experiments, recombinant CENP-OPQUR lacking the CENP-U N-terminal region (CENP-OPQU$^{\Delta1–114}$R) did not co-elute with MBP-PLK1^{PBD} in the presence of priming kinases (Figure S7A). As in Figure 3A, MBP-PLK1^{T210A} co-eluted with rKTs phosphorylated by mitotic kinases but failed to co-elute with rKTs reconstituted with CENP-OPQU$^{\Delta1–114}$R (Figure 4D). Thus, the N-terminal region of CENP-U contains the only prominent binding site for PLK1 within rKTs. The phosphorylation pattern of wild-type (WT) and mutant rKTs showed that wild-type CENP-U was effectively phosphorylated, whereas CENP-U$^{\Delta1–114}$ was not (Figure S7B), suggesting that MBP-PLK1^{T210A} interacts directly with the N-terminal fragment of CENP-U after its phosphorylation by CDK1 and PLK1. Thus, we depleted the CENP-OPQUR complex by RNAi (Method Details; Figures S6H–S6J) and replaced it with electroporated recombinant Alexa-488-labeled CENP-OPQUR complexes containing CENP-U^{WT} or CENP-U$^{\Delta1–114}$ (Figures 4E and 4F). As expected, the CENP-U^{WT}-containing complex, but not the CENP-U$^{\Delta1–114}$-containing complex, restored high PLK1 kinetochore levels.

BUB1, BUBR1, and CENP-U as the Only PLK1 Receptors in the Core Kinetochore

Forced kinetochore localization of the CPC restores high kinetochore levels of PLK1 in the absence of BUB1 (Figure 2). A rescue of PLK1 levels in BUB1-depleted cells was also observed upon addition of OA (Figures 5A and 5B), linking PLK1 depletion to dysregulation of phosphatase activity when the BUB1-Aurora B axis is perturbed. Thus, BUB1 has a dual role as a direct PLK1 receptor and as a fulcrum of a confined, but poorly understood, homeostatic phosphorylation network whose abrogation enhances phosphatase activity. Counteracting the latter with OA exposes additional kinetochore receptors of PLK1, at least one of which is CENP-U (Figures 3D, 3E, 5A, and 5B). If CENP-U were the only remaining PLK1 receptor at kinetochores, then, its depletion when the BUB1 axis is disrupted in the presence of OA ought to ablate PLK1 recruitment entirely. In agreement with that, double-depletion of BUB1 and of the CENP-OPQUR complex resulted in complete loss of the kinetochore PLK1. The kinetochore levels of PLK1 under those conditions were comparable to those observed when only BUB1 had been depleted. In contrast with the latter condition, however, no rescue of PLK1 was observed in the double depletion of BUB1 and CENP-OPQUR after addition of OA, indicating that there are no additional major PLK1 receptors (Figures 5A, 5B, and S6K). Conversely, depletion of BUBR1 led to an only marginal co-depletion of kinetochore PLK1, in agreement with previous studies (Cordeiro et al., 2020; Elowe et al., 2007; Ikeda and Tanaka, 2017). We conclude that BUB1 and CENP-U represent the two main kinetochore recruitment axes for PLK1 in nocodazole-arrested cells.

Role of Thr78 and Thr98 in Kinetochore Recruitment of PLK1

No binding of MBP-CENP-U$^{58-114}$ to PLK1^{PBD} was observed in SEC experiments in the absence of priming kinases (Figure S7C), but pre-phosphorylation of MBP-CENP-U$^{58-114}$ with CDK1 led to complex assembly. Addition of PLK1 promoted a more modest shift in the elution profile of MBP-CENP-U$^{58-114}$ and PLK1^{PBD}, suggesting a weak interaction, whereas combination of priming PLK1 and CDK1 caused a robust shift (Figure S7C). Thus, residues 58–114 of CENP-U are sufficient to bind the PBD of PLK1 through CDK1 priming. Although MPS1 and PLK1 share similar target sequences (Dou et al., 2011), MPS1 did not phosphorylate MBP-CENP-U$^{58–114}$ (Figure S4I) and did not promote binding of PLK1^{PBD} to MBP-CENP-U$^{58–114}$ (Figure S4J).

We phosphorylated MBP-CENP-U$^{58–114}$ with PLK1 or CDK1 and analyzed the products by mass spectrometry. CDK1 and

Figure 4. The CENP-U N Terminus Recruits PLK1

(A) Representative images of HeLa cells stably expressing doxycycline-inducible constructs of EGFP-CENP-U. Cells were stained with DAPI. EGFP signal is also shown.

(B) Representative images showing U2OS-LacO cells, transiently expressing LacI-EGFP or LacI-EGFP-CENP-U (full-length or deletions). Cells were immunostained for DAPI, PLK1, and CREST. EGFP represent ectopic chromatin location of LacI-EGFP-CENP-U (white circles). Scale bar, 5 μm.

(C) Bar graph shows mean PLK1/CREST intensity at an ectopic location after background subtraction. Each condition was normalized to the signal of the full-length construct. Error bars represent means ± standard errors of the mean. Six to 17 cells were used for quantification, and the experiment was repeated at least three times.

(D) Elution profile and SDS-PAGE analysis of SEC runs of a mixture of rKT and MBP-PLK1^{T210A} (both at 5 μM, red curve) or rKT containing N-terminally deleted CENP-U (rKT-U$^{\Delta1–114}$) and MBP-PLK1^{T210A} (both at 5 μM, gray curve) in the presence of the priming kinases CDK1:cyclin-B and PLK1. Orange arrows highlight MBP-PLK1^{T210A} in each gel.

(E) Representative images of HeLa cells electroporated with CENP-OPQRU^{WT} or CENP-OPQRU$^{\Delta1–114}$ and depleted of endogenous CENP-OPQRU complex by RNAi depletion of CENP-Q, O, U (see Method Details). After siRNA transfection, cells were electroporated with recombinant Alexa-488-labeled CENP-OPQUR complexes, arrested in mitosis with nocodazole and prepared for immunofluorescence. Scale bar, 5 μm.

(F) Dot plots of control normalized PLK1/CREST (top) or Alexa/CREST kinetochore intensity ratio (bottom). Red lines indicate median with interquartile range; 961 kinetochores were scored for mock cells. For CENP-OQU-depleted cells, 782 kinetochores were scored for control Alexa 488 electroporation, 972 for OPQRU^{WT} and 806 for CENP-OPQRU$^{\Delta1–114}$ in 11 to 12 cells per condition.

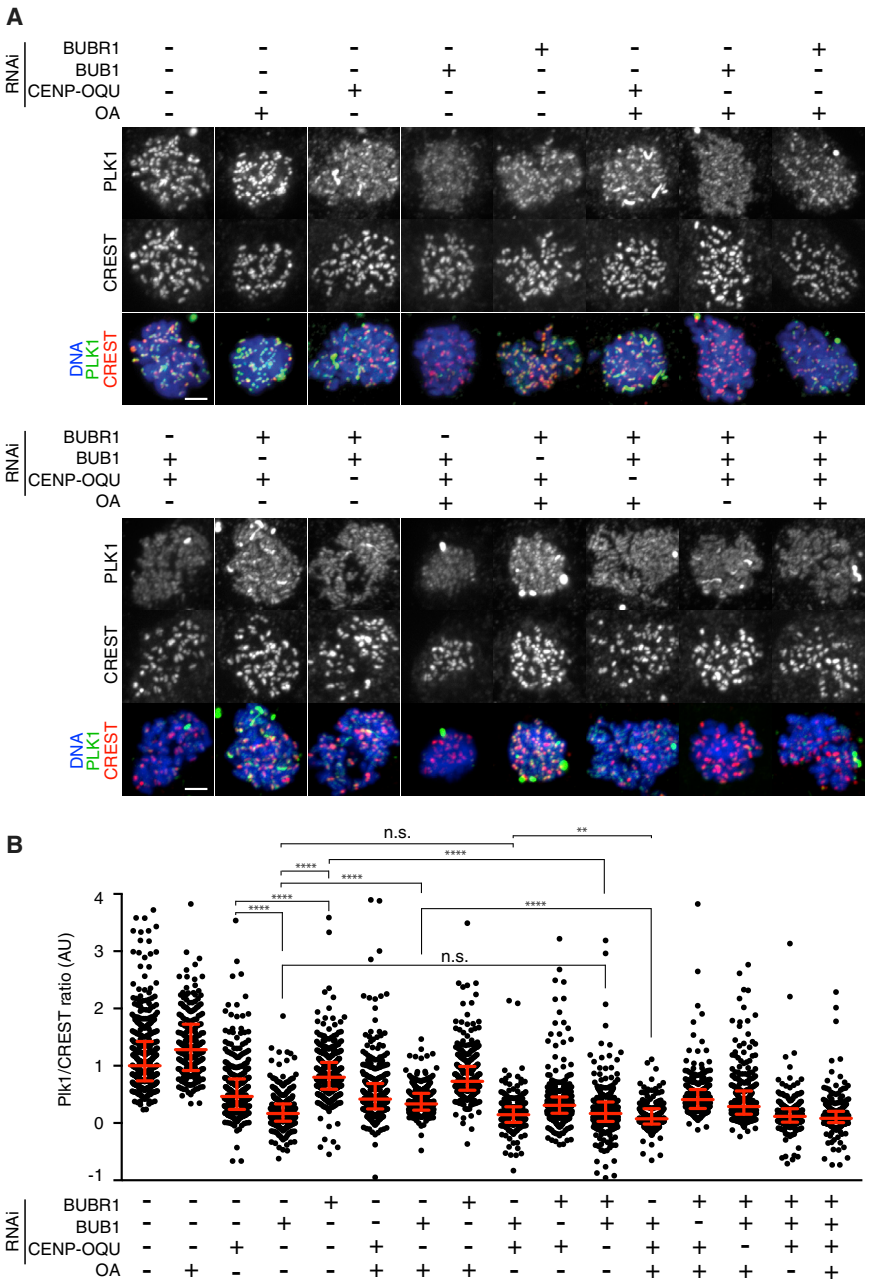

Figure 5. BUB1/BUBR1 and CENP-U Are the Main PLK1 Kinetochore Recruitment Axes

(A) Representative images of mitotic HeLa cells depleted for the indicated endogenous proteins and treated with okadaic acid (OA) are indicated. Scale bar, 5 μm.

(B) Dot plots show individual kinetochore quantification of control-normalized PLK1/CREST intensity ratios for cells in (A). Red lines represent median and interquartile range, respectively. Between 233 and 482 kinetochores in 5 to 15 cells were scored for each condition.

PLK1 phosphorylated Thr98 and Thr78, respectively (Figure 6A). Thr98 sits within a classic Ser-Thr-Pro CDK1 consensus site and an ideal recognition motif for the PBD (Elia et al., 2003a) and has been previously identified in a large-scale proteomic analysis (Zhou et al., 2013). Co-incubation with CDK1 and PLK1 did not alter the intensity of the pThr98 signal but led to a significant increase in the stoichiometry of the previously identified PLK1 site Thr78 (Kang et al., 2011; Kang et al., 2006), suggesting that Thr98, after CDK1 phosphorylation, promotes PLK1 binding and, in turn, enhances phosphorylation of Thr78 (Figure 6A). Alanine mutants at Thr78 or Thr98 within MBP-CENP-U$^{58–114}$ demonstrated exquisite specificity of PLK1 and CDK1 for Thr78 and Thr98, respectively (Figure 6B).

To investigate how Thr78 and Thr98 influence PLK1 binding to CENP-U, we phosphorylated MBP-CENP-U$^{58–114}$-S77A/T78A or MBP-CENP-U$^{58–114}$-T98A in subsequent steps with priming CDK1 and PLK1. Pre-treated with CDK1 and PLK1, MBP-CENP-U$^{58–114}$ co-eluted in a stoichiometric complex with MBP-PLK1^{PBD} from a SEC column (Figure 6C). MBP-CENP-U$^{58–114}$-T98A or MBP-CENP-U$^{58–114}$-S77A/T78A, similarly pre-treated, also interacted with MBP-PLK1^{PBD} but eluted with greater elution volume, indicative of a weaker, rapidly dissociating interaction and/or of a different complex stoichiometry. We expressed wild-type EGFP-CENP-U, EGFP-CENP-U-T98A, or EGFP-CENP-U-S77A/T78A in HeLa cells and measured the kinetochore levels of PLK1 (Figures 6D, 6E, and S6L). Both mutants caused a significant reduction in kinetochore PLK1 levels in comparison to wild-type CENP-U, providing evidence for a cellular role of Thr78 and Thr98 in PLK1 recruitment. Thus, CDK1 primes binding of PLK1 to CENP-U through phosphorylation of Thr98, which PLK1 may then use as an initial binding platform to create a stable docking configuration. As a side note, PLK1 recruitment to the ectopic LacO site was independent of cell-cycle stage (Figures S6D–S6F). This may seem inconsistent with a crucial role of CDK1, but we note that this assay may not faithfully recapitulate the conditions of kinetochores in which counteracting phosphatases are enriched.

PLK1 Dimerization on CENP-U

Finally, we investigated whether the requirement for PLK1 and CDK1 for robust recruitment of PLK1 to T78 and T98 reflected binding of distinct PLK1 molecules to the two sites. To assess that, we incubated, in 3-fold excess to saturate binding sites,

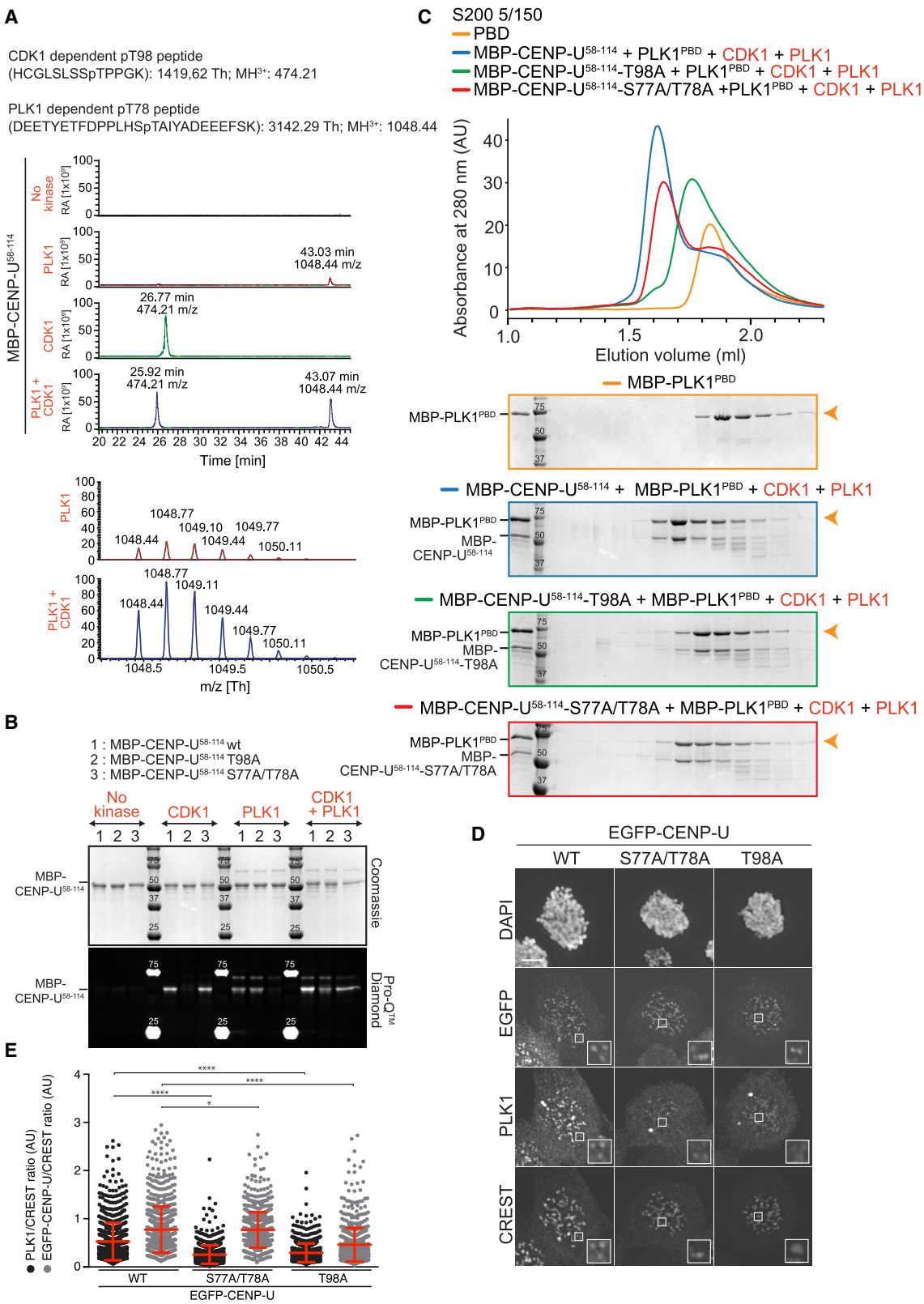

(legend on next page)

fluorescently labeled MBP-PLK1^{T210A} and CENP-OPQUR in the presence of CDK1 and PLK1 as priming kinases. We then isolated the resulting complex by SEC and estimated its mass by sedimentation velocity analytical ultracentrifugation (AUC; Figures 7A and S7D). The MBP-PLK1^{210A}:CENP-OPQUR complex had a sedimentation coefficient of 7.6 S and an apparent molecular mass of 387.6 kDa, in excellent agreement with the predicted molecular mass for a complex of two MBP-PLK1^{210A} molecules and one CENP-OPQUR (385.1 kDa). These results indicate that two molecules of PLK1 bind phosphorylated CENP-U.

DISCUSSION

Here, we answer a long-standing question on the molecular mechanism of PLK1 recruitment to kinetochores. Through a combination of *in vitro* reconstitution and cellular work, we corroborate previous evidence that PLK1 interacts with BUB1 and BUBR1 and demonstrate that the N-terminal region of CENP-U is the sole robust binding site for PLK1 within the core kinetochore (Figure 7B). The reconstituted kinetochores used in our studies incorporate most kinetochore subunits, generally in full-length form. Some segments, however, have been removed because of poor expression or instability of the full-length proteins. The largest single missing segment is the N-terminal region of KNL1, a protein that is only represented in our reconstitutions by the C-terminal 1995 to 2316 residues. Residues 1–56 of CENP-I and 545–943 of CENP-C are also missing (Pesenti et al., 2018; Weir et al., 2016). Because depletion of the CENP-OPQUR complex in human cells does not affect the localization of CENP-C and CENP-I (Pesenti et al., 2018), whereas it leads to complete disappearance of PLK1 from kinetochores when BUB1 is co-depleted (this study), we conclude that most PLK1 in the core kinetochore is recruited to CENP-U. The proposed localization of PLK1 at a defined location internal (i.e., more chromatin proximal) to CENP-I (Lera et al., 2016) is indeed consistent with the expected position of the CENP-QU subcomplex revealed by recent structural work (Hinshaw and Harrison, 2019; Pesenti et al., 2018; Yan et al., 2019). We cannot exclude the possibility that PLK1 recruitment to BUB1 and CENP-U activates downstream phosphorylation events that promote hierarchical recruitment of PLK1 to additional receptors, thus explaining the plethora of different potential PLK1 kinetochore receptors previously identified (see Introduction). Because our PLK1 localization experiments were performed in nocodazole, i.e., in the absence of microtubules, they do not exclude recruitment of PLK1 to additional receptors generated after recruitment of "late" kinetochore residents, such as the SKA and SKAP complexes (Wimbish and DeLuca, 2020).

We show that CDK activity is required for PLK1 recruitment to mitotic kinetochores, extending a previous proposal that PLK1's binding to CENP-U is exclusively primed by PLK1 itself (Kang et al., 2006, 2011). The self-priming model proposed that PLK1 phosphorylates Thr78 of CENP-U and subsequently docks onto that site (Kang et al., 2011; Kang et al., 2006). Importantly, our observations are not inconsistent with self-priming because we confirm that PLK1 phosphorylates, and docks onto, Thr78. However, we show that kinetochore recruitment of PLK1 is, in addition, also CDK1 dependent. Combining PLK1 and CDK1 inhibitors essentially eliminated kinetochore PLK1 (Figures 2E and 2F).

As already observed, self-priming may be the prevalent mechanism of PLK1 interaction with its targets in anaphase, such as PRC1, a key regulator of cytokinesis that cross-links anti-parallel microtubules. Dissection of the mechanism of PLK1 binding to PRC1 in anaphase has focused on two closely spaced Ser-Thr-X (with X ≠ proline) PLK1 target motifs on PRC1 (Neef et al., 2007) (Figure 7C). Lacking negative charges at position −2 relative to the phosphorylated Thr, these sites are non-ideal PLK1 substrates (Alexander et al., 2011; Hegemann et al., 2011; Kettenbach et al., 2011; Nakajima et al., 2003). However, they are predicted to be good PBD docking sites in view of the hydrophobic residue (Φ) at position −3 (in magenta in Figures 7C and 7D), which has been shown to increase binding affinity for the PBD (Zhu et al., 2016). After recruitment of the first PLK1 molecule (arbitrarily depicted at the PLK1$_2$ site in Figure 7D, top), stable binding may be achieved after local phosphorylation of the neighboring PLK1$_1$ site, recruitment there of the second PLK1 molecule, and dimerization. There is evidence that the hydrophobic residue at −3 facilitates PBD domain dimerization, further leading to activation of PLK1 kinase activity (Zhu et al., 2016). Similarly spaced, tandem Ser-Thr-X strings are also present in MKLP2, another self-primed anaphase binding partner of PLK1 (Neef et al., 2003), but it is unclear whether this constellation is required for PLK1 localization. Nothing prevents this mechanism from working during mitosis as well. Indeed, pre-anaphase binding of PLK1 to PRC1 is only hindered by CDK1 itself through inhibitory phosphorylation (Neef et al., 2007).

The interdependence of CDK1 and PLK1 kinase activity for PLK1 kinetochore recruitment to its mitotic receptors needs to

Figure 6. CDK1 and PLK1 Prime PLK1 Interaction with the CENP-U N-Terminal Region

(A) Profiles of consecutive MS runs of the pT98 and pT78 containing CENP-U peptides. The relative abundance (RA, y axis) was set for all runs to 1 × 10E^9 (top). Isotopic pattern of the MS1 spectra of the pT78 containing peptide incubated only with PLK1 (upper spectrum) and incubated with PLK1 and CDK1 (lower spectrum). MS1 spectra were taken from eluted peaks. The highest peak from both spectra was set to 100%. Data were directly extracted from Xcalibur (bottom).

(B) Phosphorylation state of CENP-U$^{58-114}$ wild-type, S77A/T78A, or T98A upon phosphorylation by CDK1:cyclin B and/or PLK1 kinases was assessed using SDS-PAGE followed by Pro-Q Diamond and Coomassie staining.

(C) Elution profile and SDS-PAGE of analytical SEC runs of MBP-PLK1^{PBD} alone (orange) and of mixtures of CENP-U$^{58-114}$ wild-type, S77A/T78A, or T98A (5 μM) with MBP-PLK1^{PBD} (5 μM) in the presence of PLK1 and/or CDK1:cyclinB (blue, green, and red curves, respectively). The SDS-PAGE and elution profile for the CDK1+PLK1 condition are also displayed in Figure S7C.

(D) Representative images of HeLa cells stably expressing doxycycline-inducible wild-type, S77/T78A, or T98A EGFP-CENP-U, immunostained for DAPI, PLK1, and CREST. Scale bar, 5 μm.

(E) Dot plot of PLK1/CREST (black dots) or EGFP-CENP-U (WT or mutant, gray dots) kinetochore intensity ratios. Error bars represent means ± standard errors of the mean; 910 kinetochores for WT, 791 for S77/T78A, and 797 for T98A mutant, belonging to 14–17 different cells, were scored.

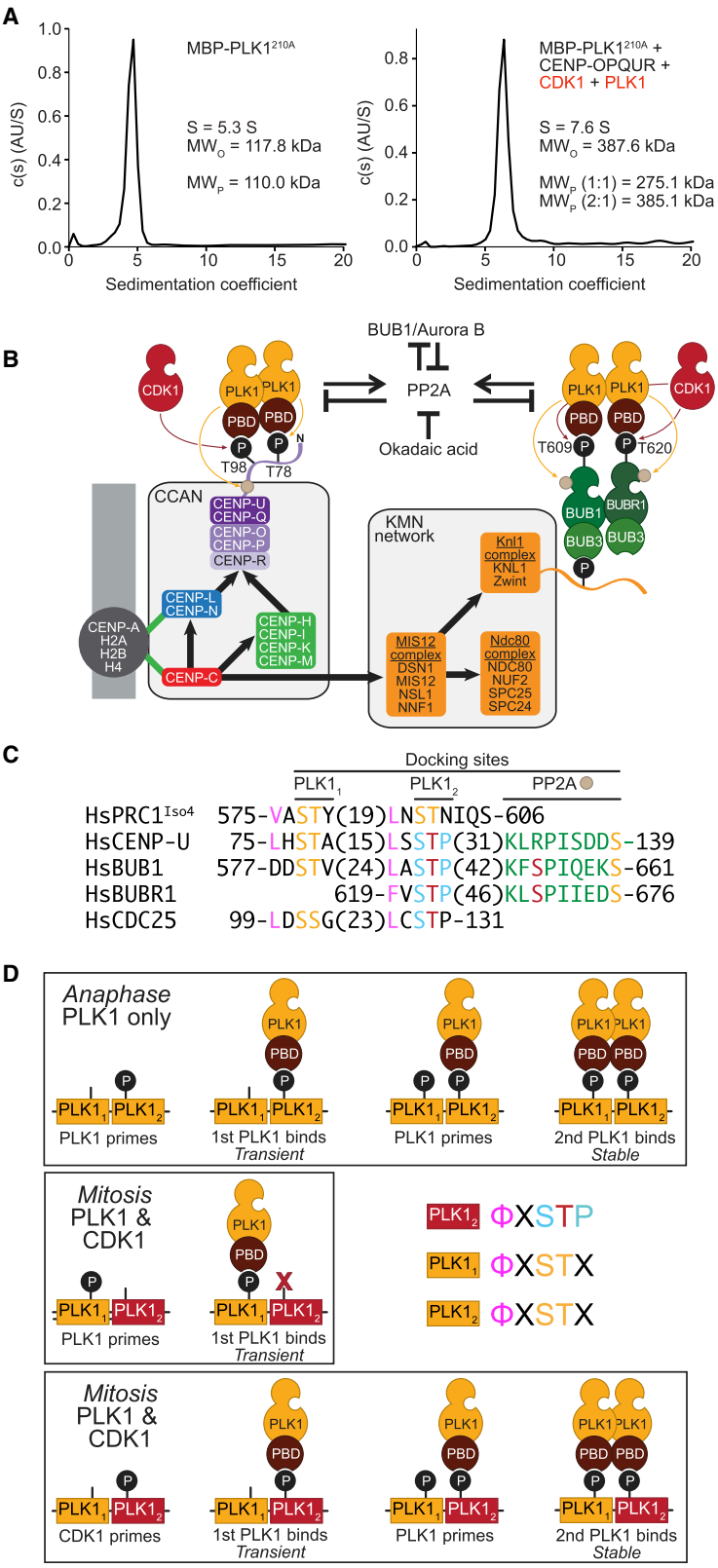

Figure 7. Docking and Dimerization of PLK1 on Target Proteins

(A) Sedimentation velocity AUC monitoring absorbance of fluorescent MBP-PLK1^{T210A}. MBP-PLK1^{T210A} bound to CENP-OPQUR complex in 2:1 ratio in the presence of catalytic amounts of PLK1, CDK1, and ATP-Mg^{2+}.

(B) Scheme of main findings on the mechanism of kinetochore recruitment of PLK1.

(C) Sequence alignment of various mitotic and post-anaphase receptors of PLK1. PLK1 substrate sites or motifs are in yellow; CDK target sites in red within a blue motif; a hydrophobic residue enhancing target binding and dimerization is in magenta; PP2A-B56 docking motif is in green. Numbers in parentheses indicate residues in sequence gaps.

(D) Models for kinetochore recruitment of PLK1 at anaphase and mitosis.

explain (1) the requirement for CDK1, and (2) why PLK1 is insufficient to self-prime its own recruitment to these proteins. The PLK1 recruitment sites on BUB1 and CENP-U resemble the PRC1 constellation (Figure 7B), suggesting that the CDK1-PLK1 interdependence may be achieved through a variation on the theme of the PRC1 recruitment model. The most notable difference is that, in BUB1 and CENP-U, there are Ser-Thr-Pro sites at the $PLK1_2$ position, whereas a Ser-Thr-X sequence remains at the $PLK1_1$ site (not in BUBR1, however). Because proline versus non-proline specificity in the P+1 position of protein kinases are mutually exclusive properties (Canagarajah et al., 1997; Songgyang et al., 1996), initial docking of PLK1 to the Ser-Thr-X $PLK1_1$ site will fail to lead to phosphorylation of the Ser-Thr-Pro $PLK1_2$ site. This will prevent recruitment of a second molecule of PLK1 and stabilization of binding, thus explaining why self-priming does not work with this constellation (Figure 7D, middle). Conversely, initial phosphorylation by CDK1 of the Ser-Thr-Pro site at $PLK1_2$ will ignite recruitment of PLK1, followed by successful phosphorylation of the Ser-Thr-X site at $PLK1_1$, recruitment of a second PLK1 molecule, and stabilization by dimerization, explaining the requirement for CDK1 (Figure 7D, bottom). Indeed, CDK1 phosphorylation at Thr98 facilitates the phosphorylation of the non-ideal substrate Thr78 (Figure 6A). Furthermore, dimerization of PLK1 (presumably through the PBDs) explains why both CDK1 and PLK1 are necessary for a full shift of the PBDs with CENP-U (Figure 6C). This recruitment model for PLK1 involves motifs predicted not to be ideal targets of the catalytic domain, thus predicting that strong physical interactions with PLK1 are limited to proteins that provide a defined constellation of PBD binding sites, but also that the range of PLK1 kinase substrates may be significantly larger.

Sequential CDK1-PLK1 phosphorylation has been observed with various PLK1 substrates, including NEK9, NEDD1, Caspase8, and CDC25 (Bertran et al., 2011; Lobjois et al., 2011; Matthess et al., 2014; O'Donovan et al., 2013; Zhang et al., 2009). The model we are proposing does not require a specific order for the $PLK1_1$ and $PLK1_2$ motifs, but only that they are spatially adjacent to permit dimerization. We note, however, that several other known or potential PLK1-binding partners, including Meikin and BuGZ (Jiang et al., 2014; Kim et al., 2015), have constellations of CDK1 and PLK1 that closely resemble those of BUB1 and CENP-U (unpublished data).

Aurora B is crucial for kinetochore-microtubule attachment and mitotic checkpoint signaling, and it is important to address whether INCENP and other subunits of the CPC contribute to PLK1 recruitment as proposed (Goto et al., 2006; Sun et al., 2012). The CPC is predominantly centromeric and, therefore, extends into a domain that is precluded to PLK1, whose microscopic distribution is limited to kinetochores (this study and many others, including, for instance, Lénárt et al. [2007] and Lera et al. [2016]). It is possible, however, that the interaction is limited to kinetochore-confined pools of these proteins. Arguing against that idea, in the presence of priming kinases and under conditions similar to those that promote robust interactions of PLK1 with BUB1 or CENP-U, we failed to observe direct binding of the CPC and PLK1 (M.P. and A.M., unpublished data). Thus, the CPC may contribute to the recruitment of BUB1 through the kinase activity of Aurora B, as previously proposed (Qi et al., 2006) and confirmed here (Figure S2H). The requirement for Aurora B was bypassed by inhibition of protein phosphatases (Figure 2A), suggesting that Aurora B regulates the balance of kinase and phosphatase activity required for optimal PLK1 recruitment.

Dynamic regulation of kinase-phosphatase switches within kinetochores, including those involving PLK1, is crucial for kinetochore-microtubule attachment and spindle assembly checkpoint but remains very poorly understood (Cordeiro et al., 2020; Elowe et al., 2007, 2010; Ikeda and Tanaka, 2017; Jia et al., 2016; Kaisari et al., 2019; Lénárt et al., 2007; Liu et al., 2012; Maia et al., 2012; Moutinho-Santos et al., 2012; O'Connor et al., 2015; Peters et al., 2006; von Schubert et al., 2015). High PLK1 activity at kinetochores in prometaphase stabilizes kinetochore microtubules and balances a destabilizing activity attributed to Aurora B (Foley et al., 2011; Liu et al., 2012). PLK1 has been previously implicated in the control of PP2A activity (Joukov and De Nicolo, 2018; Saurin, 2018) through the creation of docking sites for the B56 regulatory subunit on BUB1 and BUBR1 (Cordeiro et al., 2020; Elowe et al., 2007; Hertz et al., 2016; Kruse et al., 2013; Suijkerbuijk et al., 2012b). MYPT1, a PP1 regulator and a CDK1:cyclin A substrate, has instead emerged as a potential negative regulator of PLK1 (Dumitru et al., 2017; Yamashiro et al., 2008).

When we were scanning the sequence of human CENP-U, we realized that it encompasses the same constellation of PLK1 and PP2A-B56 docking sites observed in BUB1 and BUBR1 (Figure 7B). This new observation strongly suggests that CENP-U, like BUB1 and BUBR1, provides a PLK1-regulated docking site for the B56 regulatory subunit, a hypothesis that we are currently testing. We note that, in a previous study, the PP2A regulator BOD1 was implicated in kinetochore recruitment of PLK1 (Porter et al., 2013). We speculate that the CENP-U-associated pool of PP2A-B56 may be directed to two crucial functions of the CENP-OPQUR complex. First, CENP-Q has been implicated in microtubule depolymerization-coupled pulling on kinetochores, (Bancroft et al., 2015). In a previous study, we identified a microtubule binding site in the N-terminal region of CENP-Q, a direct binding partner of CENP-U (Pesenti et al., 2018). As evinced from the structure of their orthologs in *S. cerevisiae*, CENP-Q and CENP-U are predicted to form a parallel coiled-coil structure (Hinshaw and Harrison, 2019; Yan et al., 2019), predicting close proximity of their N-termini and supporting speculations of crosstalk between the microtubule-binding site of CENP-Q and PLK1 activity from the CENP-U docking site. Thus, it will be crucial to assess whether microtubule binding by CENP-Q affects PLK1 recruitment or activity, and if so, how. Second, the CENP-OPQUR complex promotes cohesin recruitment and loading at the centromere in *S. cerevisiae*, and CENP-U has been shown to contain a sequence motif, preceding the PLK1 binding sites, for interaction with the SA2 subunit of cohesin (Fernius and Marston, 2009; Hinshaw et al., 2017; Li et al., 2020; Natsume et al., 2013). PP2A bound to CENP-U may contribute to protect cohesin at centromeres from the so-called prophase pathway that removes cohesin from chromosome arms concomitantly with the individualization of sister chromatids (Haarhuis et al., 2014).

In conclusion, we present a comprehensive analysis of the mechanism of PLK1 recruitment to kinetochores (Figure 7B). We are still far from understanding how the complex interaction of Aurora B and PLK1 kinases and of the PP1, PP2A, and possibly other phosphatases leads to bi-orientation, the stabilization of kinetochore-microtubule attachment, satisfaction of the mitotic checkpoint, and centromere organization. Our attempts to reconstitute *in vitro* these dependencies lay the foundations for surgical molecular manipulations required to dissect their mechanistic basis.

STAR★METHODS

Detailed methods are provided in the online version of this paper and include the following:

- KEY RESOURCES TABLE
- RESOURCE AVAILABILITY
  - Lead Contact
  - Materials Availability
  - Data and Code Availability
- EXPERIMENTAL MODEL AND SUBJECT DETAILS
  - Cells lines and Expression strains
- METHOD DETAILS
  - Cell transfection and electroporation
  - Plasmids
  - Cell synchronization
  - Immunofluorescence
  - Western blotting
  - Cell imaging
  - Protein expression and purification
  - *In vitro* assembly of rKT and rKT containing CENP-U$^{\Delta 1\text{-}114}$
  - Recombinant proteins fluorescence labeling
  - *In vitro* phosphorylation of rKT, rKT containing CENP-U$^{\Delta 1\text{-}114}$, CENP-OPQUR, -OPQU$^{\Delta 1\text{-}114}$R, -OP, -QU, 6His-MBP-CENP-U$^{58\text{-}114}$-WT and mutants, BUB1:-BUB3 and BUBR1:BUB3
  - Phosphostaining of recombinant proteins
  - Analytical SEC
  - Analytical ultracentrifugation (AUC)
  - Mass spectrometry and phosphorylation site analysis
- QUANTIFICATION AND STATISTICAL ANALYSIS
  - Cell image analysis
  - AUC analysis
  - Mass Spectrometry analysis

SUPPLEMENTAL INFORMATION

Supplemental Information can be found online at https://doi.org/10.1016/j.molcel.2020.10.040.

ACKNOWLEDGMENTS

We are grateful to Geert Kops and Andrew McAinsh for sharing tools and reagents; Charlotte M. Smith for sharing oligos for CENP-QU RNAi; Hendrik Hausmann, Ingrid Hoffmann, Carolin Koerner, Lisa Schulze, Isabelle Stender, Doro Vogt, Beate Voss, and Sabine Wohlgemuth for general technical assistance; Valentina Piano and Suruchi Sethi for sharing BUB1:BUB3 and BUBR1:BUB3; Raphael Gasper-Schonenbrucher for help with biophysical experiments; and Adrian Saurin for helpful discussions. A.M. gratefully acknowledges funding by the Max Planck Society, the European Research Council (ERC) Advanced Investigator Grant RECEPIANCE (proposal 669686), and the DFG's Collaborative Research Centre (CRC) 1093. P.S. gratefully acknowledges the support of the Alexander von Humboldt Foundation through a postdoctoral fellowship and is thankful to IIT Jodhpur for the present infrastructure support. P.S. also acknowledges the Science and Engineering Research Board (ECR/2017/001001410) and the Har Gobind Khorana-Innovative Young Biotechnologist Award (BT/12/IYBA/2019/02) for current support.

AUTHOR CONTRIBUTIONS

P.S., M.E.P., and A.M. conceptualized the study. P.S. and M.E.P. conducted most of the experiments and analyzed data for the work. S.C. and A.P. (biochemistry); A.S., S.M., and M.H. (cell biology); and T.B. (mass spectrometry) assisted P.S. and M.E.P. in experiments and data analysis. P.S. and M.E.P., with help from the other authors, compiled the data for the manuscript. A.M. wrote the manuscript with contributions from all authors.

DECLARATION OF INTERESTS

The authors declare no competing interests

Received: April 10, 2020
Revised: September 8, 2020
Accepted: October 28, 2020
Published: November 27, 2020

REFERENCES

Adams, R.R., Wheatley, S.P., Gouldsworthy, A.M., Kandels-Lewis, S.E., Carmena, M., Smythe, C., Gerloff, D.L., and Earnshaw, W.C. (2000). INCENP binds the Aurora-related kinase AIRK2 and is required to target it to chromosomes, the central spindle and cleavage furrow. Curr. Biol. *10*, 1075–1078.

Ahonen, L.J., Kallio, M.J., Daum, J.R., Bolton, M., Manke, I.A., Yaffe, M.B., Stukenberg, P.T., and Gorbsky, G.J. (2005). Polo-like kinase 1 creates the tension-sensing 3F3/2 phosphoepitope and modulates the association of spindle-checkpoint proteins at kinetochores. Curr. Biol. *15*, 1078–1089.

Alex, A., Piano, V., Polley, S., Stuiver, M., Voss, S., Ciossani, G., Overlack, K., Voss, B., Wohlgemuth, S., Petrovic, A., et al. (2019). Electroporated recombinant proteins as tools for in vivo functional complementation, imaging and chemical biology. eLife *8*, e48287.

Alexander, J., Lim, D., Joughin, B.A., Hegemann, B., Hutchins, J.R., Ehrenberger, T., Ivins, F., Sessa, F., Hudecz, O., Nigg, E.A., et al. (2011). Spatial exclusivity combined with positive and negative selection of phosphorylation motifs is the basis for context-dependent mitotic signaling. Sci. Signal. *4*, ra42.

Amaro, A.C., Samora, C.P., Holtackers, R., Wang, E., Kingston, I.J., Alonso, M., Lampson, M., McAinsh, A.D., and Meraldi, P. (2010). Molecular control of kinetochore-microtubule dynamics and chromosome oscillations. Nat. Cell Biol. *12*, 319–329.

Amin, M.A., Itoh, G., Iemura, K., Ikeda, M., and Tanaka, K. (2014). CLIP-170 recruits PLK1 to kinetochores during early mitosis for chromosome alignment. J. Cell Sci. *127*, 2818–2824.

Archambault, V., and Glover, D.M. (2009). Polo-like kinases: conservation and divergence in their functions and regulation. Nat. Rev. Mol. Cell Biol. *10*, 265–275.

Arnaud, L., Pines, J., and Nigg, E.A. (1998). GFP tagging reveals human Polo-like kinase 1 at the kinetochore/centromere region of mitotic chromosomes. Chromosoma *107*, 424–429.

Bancroft, J., Auckland, P., Samora, C.P., and McAinsh, A.D. (2015). Chromosome congression is promoted by CENP-Q- and CENP-E-dependent pathways. J. Cell Sci. *128*, 171–184.

Baron, A.P., von Schubert, C., Cubizolles, F., Siemeister, G., Hitchcock, M., Mengel, A., Schröder, J., Fernández-Montalván, A., von Nussbaum, F.,

Mumberg, D., and Nigg, E.A. (2016). Probing the catalytic functions of Bub1 kinase using the small molecule inhibitors BAY-320 and BAY-524. eLife *5*, e12187.

Bertran, M.T., Sdelci, S., Regué, L., Avruch, J., Caelles, C., and Roig, J. (2011). Nek9 is a Plk1-activated kinase that controls early centrosome separation through Nek6/7 and Eg5. EMBO J. *30*, 2634–2647.

Bialojan, C., and Takai, A. (1988). Inhibitory effect of a marine-sponge toxin, okadaic acid, on protein phosphatases. Specificity and kinetics. Biochem. J. *256*, 283–290.

Bird, A.W., and Hyman, A.A. (2008). Building a spindle of the correct length in human cells requires the interaction between TPX2 and Aurora A. J. Cell Biol. *182*, 289–300.

Breit, C., Bange, T., Petrovic, A., Weir, J.R., Müller, F., Vogt, D., and Musacchio, A. (2015). Role of Intrinsic and Extrinsic Factors in the Regulation of the Mitotic Checkpoint Kinase Bub1. PLoS ONE *10*, e0144673.

Burkard, M.E., Maciejowski, J., Rodriguez-Bravo, V., Repka, M., Lowery, D.M., Clauser, K.R., Zhang, C., Shokat, K.M., Carr, S.A., Yaffe, M.B., and Jallepalli, P.V. (2009). Plk1 self-organization and priming phosphorylation of HsCYK-4 at the spindle midzone regulate the onset of division in human cells. PLoS Biol. *7*, e1000111.

Caldas, G.V., DeLuca, K.F., and DeLuca, J.G. (2013). KNL1 facilitates phosphorylation of outer kinetochore proteins by promoting Aurora B kinase activity. J. Cell Biol. *203*, 957–969.

Canagarajah, B.J., Khokhlatchev, A., Cobb, M.H., and Goldsmith, E.J. (1997). Activation mechanism of the MAP kinase ERK2 by dual phosphorylation. Cell *90*, 859–869.

Carmena, M., Pinson, X., Platani, M., Salloum, Z., Xu, Z., Clark, A., Macisaac, F., Ogawa, H., Eggert, U., Glover, D.M., et al. (2012). The chromosomal passenger complex activates Polo kinase at centromeres. PLoS Biol. *10*, e1001250.

Cheeseman, I.M., Chappie, J.S., Wilson-Kubalek, E.M., and Desai, A. (2006). The conserved KMN network constitutes the core microtubule-binding site of the kinetochore. Cell *127*, 983–997.

Cheng, K.-Y., Lowe, E.D., Sinclair, J., Nigg, E.A., and Johnson, L.N. (2003). The crystal structure of the human polo-like kinase-1 polo box domain and its phospho-peptide complex. EMBO J. *22*, 5757–5768.

Clay, F.J., McEwen, S.J., Bertoncello, I., Wilks, A.F., and Dunn, A.R. (1993). Identification and cloning of a protein kinase-encoding mouse gene, Plk, related to the polo gene of Drosophila. Proc. Natl. Acad. Sci. USA *90*, 4882–4886.

Combes, G., Alharbi, I., Braga, L.G., and Elowe, S. (2017). Playing polo during mitosis: PLK1 takes the lead. Oncogene *36*, 4819–4827.

Cordeiro, M.H., Smith, R.J., and Saurin, A.T. (2020). Kinetochore phosphatases suppress autonomous kinase activity to control the spindle assembly checkpoint. J. Cell Biol. *219*, e202002020.

Cox, J., and Mann, M. (2008). MaxQuant enables high peptide identification rates, individualized p.p.b.-range mass accuracies and proteome-wide protein quantification. Nat. Biotechnol. *26*, 1367–1372.

De Antoni, A., Maffini, S., Knapp, S., Musacchio, A., and Santaguida, S. (2012). A small-molecule inhibitor of Haspin alters the kinetochore functions of Aurora B. J. Cell Biol. *199*, 269–284.

De Luca, M., Lavia, P., and Guarguaglini, G. (2006). A functional interplay between Aurora-A, Plk1 and TPX2 at spindle poles: Plk1 controls centrosomal localization of Aurora-A and TPX2 spindle association. Cell Cycle *5*, 296–303.

DeLuca, J.G., Gall, W.E., Ciferri, C., Cimini, D., Musacchio, A., and Salmon, E.D. (2006). Kinetochore microtubule dynamics and attachment stability are regulated by Hec1. Cell *127*, 969–982.

Dou, Z., von Schubert, C., Körner, R., Santamaria, A., Elowe, S., and Nigg, E.A. (2011). Quantitative mass spectrometry analysis reveals similar substrate consensus motif for human Mps1 kinase and Plk1. PLoS ONE *6*, e18793.

Dumitru, A.M.G., Rusin, S.F., Clark, A.E.M., Kettenbach, A.N., and Compton, D.A. (2017). Cyclin A/Cdk1 modulates Plk1 activity in prometaphase to regulate kinetochore-microtubule attachment stability. eLife *6*, e29303.

Elia, A.E., Cantley, L.C., and Yaffe, M.B. (2003a). Proteomic screen finds pSer/pThr-binding domain localizing Plk1 to mitotic substrates. Science *299*, 1228–1231.

Elia, A.E., Rellos, P., Haire, L.F., Chao, J.W., Ivins, F.J., Hoepker, K., Mohammad, D., Cantley, L.C., Smerdon, S.J., and Yaffe, M.B. (2003b). The molecular basis for phosphodependent substrate targeting and regulation of Plks by the Polo-box domain. Cell *115*, 83–95.

Elowe, S., Hümmer, S., Uldschmid, A., Li, X., and Nigg, E.A. (2007). Tension-sensitive Plk1 phosphorylation on BubR1 regulates the stability of kinetochore microtubule interactions. Genes Dev. *21*, 2205–2219.

Elowe, S., Dulla, K., Uldschmid, A., Li, X., Dou, Z., and Nigg, E.A. (2010). Uncoupling of the spindle-checkpoint and chromosome-congression functions of BubR1. J. Cell Sci. *123*, 84–94.

Fernius, J., and Marston, A.L. (2009). Establishment of cohesion at the pericentromere by the Ctf19 kinetochore subcomplex and the replication fork-associated factor, Csm3. PLoS Genet. *5*, e1000629.

Foley, E.A., Maldonado, M., and Kapoor, T.M. (2011). Formation of stable attachments between kinetochores and microtubules depends on the B56-PP2A phosphatase. Nat. Cell Biol. *13*, 1265–1271.

García-Alvarez, B., de Cárcer, G., Ibañez, S., Bragado-Nilsson, E., and Montoya, G. (2007). Molecular and structural basis of polo-like kinase 1 substrate recognition: Implications in centrosomal localization. Proc. Natl. Acad. Sci. USA *104*, 3107–3112.

Golsteyn, R.M., Schultz, S.J., Bartek, J., Ziemiecki, A., Ried, T., and Nigg, E.A. (1994). Cell cycle analysis and chromosomal localization of human Plk1, a putative homologue of the mitotic kinases Drosophila polo and Saccharomyces cerevisiae Cdc5. J. Cell Sci. *107*, 1509–1517.

Girdler, F., Sessa, F., Patercoli, S., Villa, F., Musacchio, A., and Taylor, S. (2008). Molecular basis of drug resistance in aurora kinases. Chem. Biol. *15*, 552–562.

Golsteyn, R.M., Mundt, K.E., Fry, A.M., and Nigg, E.A. (1995). Cell cycle regulation of the activity and subcellular localization of Plk1, a human protein kinase implicated in mitotic spindle function. J. Cell Biol. *129*, 1617–1628.

Goto, H., Kiyono, T., Tomono, Y., Kawajiri, A., Urano, T., Furukawa, K., Nigg, E.A., and Inagaki, M. (2006). Complex formation of Plk1 and INCENP required for metaphase-anaphase transition. Nat. Cell Biol. *8*, 180–187.

Haarhuis, J.H., Elbatsh, A.M., and Rowland, B.D. (2014). Cohesin and its regulation: on the logic of X-shaped chromosomes. Dev. Cell *31*, 7–18.

Hanisch, A., Wehner, A., Nigg, E.A., and Silljé, H.H. (2006). Different Plk1 functions show distinct dependencies on Polo-Box domain-mediated targeting. Mol. Biol. Cell *17*, 448–459.

Hartwell, L.H., Mortimer, R.K., Culotti, J., and Culotti, M. (1973). Genetic control of the cell division cycle in yeast: V. genetic analysis of cdc mutants. Genetics *74*, 267–286.

Hauf, S., Cole, R.W., LaTerra, S., Zimmer, C., Schnapp, G., Walter, R., Heckel, A., van Meel, J., Rieder, C.L., and Peters, J.M. (2003). The small molecule Hesperadin reveals a role for Aurora B in correcting kinetochore-microtubule attachment and in maintaining the spindle assembly checkpoint. J. Cell Biol. *161*, 281–294.

Hegemann, B., Hutchins, J.R., Hudecz, O., Novatchkova, M., Rameseder, J., Sykora, M.M., Liu, S., Mazanek, M., Lénárt, P., Hériché, J.K., et al. (2011). Systematic phosphorylation analysis of human mitotic protein complexes. Sci. Signal. *4*, rs12.

Heinrich, S., Geissen, E.M., Kamenz, J., Trautmann, S., Widmer, C., Drewe, P., Knop, M., Radde, N., Hasenauer, J., and Hauf, S. (2013). Determinants of robustness in spindle assembly checkpoint signalling. Nat. Cell Biol. *15*, 1328–1339.

Hertz, E.P.T., Kruse, T., Davey, N.E., López-Méndez, B., Sigurðsson, J.O., Montoya, G., Olsen, J.V., and Nilsson, J. (2016). A conserved motif provides binding specificity to the PP2A-B56 phosphatase. Mol. Cell *63*, 686–695.

Hindriksen, S., Lens, S.M.A., and Hadders, M.A. (2017). The ins and outs of aurora B inner centromere localization. Front. Cell Dev. Biol. *5*, 112.

Hinshaw, S.M., and Harrison, S.C. (2019). The structure of the Ctf19c/CCAN from budding yeast. eLife *8*, e44239.

Hinshaw, S.M., Makrantoni, V., Harrison, S.C., and Marston, A.L. (2017). The kinetochore receptor for the cohesin loading complex. Cell *171*, 72–84.e13.

Holtrich, U., Wolf, G., Bräuninger, A., Karn, T., Böhme, B., Rübsamen-Waigmann, H., and Strebhardt, K. (1994). Induction and down-regulation of PLK, a human serine/threonine kinase expressed in proliferating cells and tumors. Proc. Natl. Acad. Sci. USA *91*, 1736–1740.

Hsu, J.Y., Sun, Z.W., Li, X., Reuben, M., Tatchell, K., Bishop, D.K., Grushcow, J.M., Brame, C.J., Caldwell, J.A., Hunt, D.F., et al. (2000). Mitotic phosphorylation of histone H3 is governed by Ipl1/aurora kinase and Glc7/PP1 phosphatase in budding yeast and nematodes. Cell *102*, 279–291.

Huang, H., Hittle, J., Zappacosta, F., Annan, R.S., Hershko, A., and Yen, T.J. (2008). Phosphorylation sites in BubR1 that regulate kinetochore attachment, tension, and mitotic exit. J. Cell Biol. *183*, 667–680.

Huis In 't Veld, P.J., Jeganathan, S., Petrovic, A., Singh, P., John, J., Krenn, V., Weissmann, F., Bange, T., and Musacchio, A. (2016). Molecular basis of outer kinetochore assembly on CENP-T. eLife *5*, e21007.

Ikeda, M., and Tanaka, K. (2017). Plk1 bound to Bub1 contributes to spindle assembly checkpoint activity during mitosis. Sci. Rep. *7*, 8794.

Ishida, T., and Kinoshita, K. (2007). PrDOS: prediction of disordered protein regions from amino acid sequence. Nucleic. Acids Res. W460–W464.

Jang, Y.J., Lin, C.Y., Ma, S., and Erikson, R.L. (2002a). Functional studies on the role of the C-terminal domain of mammalian polo-like kinase. Proc. Natl. Acad. Sci. USA *99*, 1984–1989.

Jang, Y.J., Ma, S., Terada, Y., and Erikson, R.L. (2002b). Phosphorylation of threonine 210 and the role of serine 137 in the regulation of mammalian polo-like kinase. J. Biol. Chem. *277*, 44115–44120.

Janicki, S.M., Tsukamoto, T., Salghetti, S.E., Tansey, W.P., Sachidanandam, R., Prasanth, K.V., Ried, T., Shav-Tal, Y., Bertrand, E., Singer, R.H., and Spector, D.L. (2004). From silencing to gene expression: real-time analysis in single cells. Cell *116*, 683–698.

Jia, L., Li, B., and Yu, H. (2016). The Bub1-Plk1 kinase complex promotes spindle checkpoint signalling through Cdc20 phosphorylation. Nat. Commun. *7*, 10818.

Jiang, H., He, X., Wang, S., Jia, J., Wan, Y., Wang, Y., Zeng, R., Yates, J., 3rd, Zhu, X., and Zheng, Y. (2014). A microtubule-associated zinc finger protein, BuGZ, regulates mitotic chromosome alignment by ensuring Bub3 stability and kinetochore targeting. Dev. Cell *28*, 268–281.

Johnson, T.M., Antrobus, R., and Johnson, L.N. (2008). Plk1 activation by Ste20-like kinase (Slk) phosphorylation and polo-box phosphopeptide binding assayed with the substrate translationally controlled tumor protein (TCTP). Biochemistry *47*, 3688–3696.

Joukov, V., and De Nicolo, A. (2018). Aurora-PLK1 cascades as key signaling modules in the regulation of mitosis. Sci. Signal. *11*, eaar4195.

Kaisari, S., Shomer, P., Ziv, T., Sitry-Shevah, D., Miniowitz-Shemtov, S., Teichner, A., and Hershko, A. (2019). Role of Polo-like kinase 1 in the regulation of the action of $p31^{comet}$ in the disassembly of mitotic checkpoint complexes. Proc. Natl. Acad. Sci. USA *116*, 11725–11730.

Kaitna, S., Mendoza, M., Jantsch-Plunger, V., and Glotzer, M. (2000). Incenp and an aurora-like kinase form a complex essential for chromosome segregation and efficient completion of cytokinesis. Curr. Biol. *10*, 1172–1181.

Kang, Y.H., Park, J.-E., Yu, L.-R., Soung, N.-K., Yun, S.-M., Bang, J.K., Seong, Y.-S., Yu, H., Garfield, S., Veenstra, T.D., and Lee, K.S. (2006). Self-regulated Plk1 recruitment to kinetochores by the Plk1-PBIP1 interaction is critical for proper chromosome segregation. Mol. Cell *24*, 409–422.

Kang, Y.H., Park, C.-H., Kim, T.-S., Soung, N.-K., Bang, J.K., Kim, B.Y., Park, J.-E., and Lee, K.S. (2011). Mammalian polo-like kinase 1-dependent regulation of the PBIP1-CENP-Q complex at kinetochores. J. Biol. Chem. *286*, 19744–19757.

Kelm, O., Wind, M., Lehmann, W.D., and Nigg, E.A. (2002). Cell cycle-regulated phosphorylation of the *Xenopus polo*-like kinase Plx1. J. Biol. Chem. *277*, 25247–25256.

Kettenbach, A.N., Schweppe, D.K., Faherty, B.K., Pechenick, D., Pletnev, A.A., and Gerber, S.A. (2011). Quantitative phosphoproteomics identifies substrates and functional modules of *Aurora* and *Polo*-like kinase activities in mitotic cells. Sci. Signal. *4*, rs5.

Kim, J.H., Shim, J., Ji, M.-J., Jung, Y., Bong, S.M., Jang, Y.-J., Yoon, E.K., Lee, S.J., Kim, K.G., Kim, Y.H., et al. (2014). The condensin component NCAPG2 regulates microtubule-kinetochore attachment through recruitment of Polo-like kinase 1 to kinetochores. Nat. Commun. *5*, 4588.

Kim, J., Ishiguro, K., Nambu, A., Akiyoshi, B., Yokobayashi, S., Kagami, A., Ishiguro, T., Pendas, A.M., Takeda, N., Sakakibara, Y., et al. (2015). Meikin is a conserved regulator of meiosis-I-specific kinetochore function. Nature *517*, 466–471.

Klare, K., Weir, J.R., Basilico, F., Zimniak, T., Massimiliano, L., Ludwigs, N., Herzog, F., and Musacchio, A. (2015). CENP-C is a blueprint for constitutive centromere-associated network assembly within human kinetochores. J. Cell Biol. *210*, 11–22.

Kothe, M., Kohls, D., Low, S., Coli, R., Cheng, A.C., Jacques, S.L., Johnson, T.L., Lewis, C., Loh, C., Nonomiya, J., et al. (2007). Structure of the catalytic domain of human polo-like kinase 1. Biochemistry *46*, 5960–5971.

Krenn, V., and Musacchio, A. (2015). The Aurora B kinase in chromosome bi-orientation and spindle checkpoint signaling. Front. Oncol. *5*, 225.

Krenn, V., Overlack, K., Primorac, I., van Gerwen, S., and Musacchio, A. (2014). KI motifs of human Knl1 enhance assembly of comprehensive spindle checkpoint complexes around MELT repeats. Curr. Biol. *24*, 29–39.

Kruse, T., Zhang, G., Larsen, M.S., Lischetti, T., Streicher, W., Kragh Nielsen, T., Bjørn, S.P., and Nilsson, J. (2013). Direct binding between BubR1 and B56-PP2A phosphatase complexes regulate mitotic progression. J. Cell Sci. *126*, 1086–1092.

Kumagai, A., and Dunphy, W.G. (1996). Purification and molecular cloning of Plx1, a Cdc25-regulatory kinase from Xenopus egg extracts. Science *273*, 1377–1380.

Lampson, M.A., and Grishchuk, E.L. (2017). Mechanisms to Avoid and Correct Erroneous Kinetochore-Microtubule Attachments. Biology (Basel) *6*, 1.

Lane, H.A., and Nigg, E.A. (1996). Antibody microinjection reveals an essential role for human polo-like kinase 1 (Plk1) in the functional maturation of mitotic centrosomes. J. Cell Biol. *135*, 1701–1713.

Laue, T.M., Shah, B.D., Ridgeway, T.M., and Pelletier, S.L. (1992). Analytical Ultracentrifugation in Biochemistry and Polymer Science (Royal Society of Chemistry), pp. 90–125.

Lee, K.S., Grenfell, T.Z., Yarm, F.R., and Erikson, R.L. (1998). Mutation of the polo-box disrupts localization and mitotic functions of the mammalian polo kinase Plk. Proc. Natl. Acad. Sci. USA *95*, 9301–9306.

Lee, K.S., Park, J.E., Kang, Y.H., Kim, T.S., and Bang, J.K. (2014). Mechanisms underlying Plk1 polo-box domain-mediated biological processes and their physiological significance. Mol. Cells *37*, 286–294.

Lee, H.-S., Park, Y.-Y., Cho, M.-Y., Chae, S., Yoo, Y.-S., Kwon, M.-H., Lee, C.-W., and Cho, H. (2015). The chromatin remodeller RSF1 is essential for PLK1 deposition and function at mitotic kinetochores. Nat. Commun. *6*, 7904.

Lénárt, P., Petronczki, M., Steegmaier, M., Di Fiore, B., Lipp, J.J., Hoffmann, M., Rettig, W.J., Kraut, N., and Peters, J.-M. (2007). The small-molecule inhibitor BI 2536 reveals novel insights into mitotic roles of polo-like kinase 1. Curr. Biol. *17*, 304–315.

Lera, R.F., Potts, G.K., Suzuki, A., Johnson, J.M., Salmon, E.D., Coon, J.J., and Burkard, M.E. (2016). Decoding Polo-like kinase 1 signaling along the kinetochore-centromere axis. Nat. Chem. Biol. *12*, 411–418.

Li, Y., Haarhuis, J.H.I., Sedeño Cacciatore, Á., Oldenkamp, R., van Ruiten, M.S., Willems, L., Teunissen, H., Muir, K.W., de Wit, E., Rowland, B.D., and Panne, D. (2020). The structural basis for cohesin-CTCF-anchored loops. Nature *578*, 472–476.

Liu, J., Lewellyn, A.L., Chen, L.G., and Maller, J.L. (2004). The polo box is required for multiple functions of Plx1 in mitosis. J. Biol. Chem. *279*, 21367–21373.

Liu, D., Vader, G., Vromans, M.J., Lampson, M.A., and Lens, S.M. (2009). Sensing chromosome bi-orientation by spatial separation of aurora B kinase from kinetochore substrates. Science *323*, 1350–1353.

Liu, D., Davydenko, O., and Lampson, M.A. (2012). Polo-like kinase-1 regulates kinetochore-microtubule dynamics and spindle checkpoint silencing. J. Cell Biol. *198*, 491–499.

Liu, H., Jia, L., and Yu, H. (2013). Phospho-H2A and cohesin specify distinct tension-regulated Sgo1 pools at kinetochores and inner centromeres. Curr. Biol. *23*, 1927–1933.

Llamazares, S., Moreira, A., Tavares, A., Girdham, C., Spruce, B.A., Gonzalez, C., Karess, R.E., Glover, D.M., and Sunkel, C.E. (1991). polo encodes a protein kinase homolog required for mitosis in Drosophila. Genes Dev. *5* (12A), 2153–2165.

Lobjois, V., Froment, C., Braud, E., Grimal, F., Burlet-Schiltz, O., Ducommun, B., and Bouche, J.P. (2011). Study of the docking-dependent PLK1 phosphorylation of the CDC25B phosphatase. Biochem. Biophys. Res. Commun. *410*, 87–90.

Lowery, D.M., Lim, D., and Yaffe, M.B. (2005). Structure and function of Polo-like kinases. Oncogene *24*, 248–259.

Lowery, D.M., Clauser, K.R., Hjerrild, M., Lim, D., Alexander, J., Kishi, K., Ong, S.E., Gammeltoft, S., Carr, S.A., and Yaffe, M.B. (2007). Proteomic screen defines the Polo-box domain interactome and identifies Rock2 as a Plk1 substrate. EMBO J. *26*, 2262–2273.

Lupas, A., Van Dyke, M., and Stock, J. (1991). Predicting coiled coils from protein sequences. Science *252*, 1162–1164.

Macůrek, L., Lindqvist, A., Lim, D., Lampson, M.A., Klompmaker, R., Freire, R., Clouin, C., Taylor, S.S., Yaffe, M.B., and Medema, R.H. (2008). Polo-like kinase-1 is activated by aurora A to promote checkpoint recovery. Nature *455*, 119–123.

Maia, A.R.R., Garcia, Z., Kabeche, L., Barisic, M., Maffini, S., Macedo-Ribeiro, S., Cheeseman, I.M., Compton, D.A., Kaverina, I., and Maiato, H. (2012). Cdk1 and Plk1 mediate a CLASP2 phospho-switch that stabilizes kinetochore-microtubule attachments. J. Cell Biol. *199*, 285–301.

Matsumura, S., Toyoshima, F., and Nishida, E. (2007). Polo-like kinase 1 facilitates chromosome alignment during prometaphase through BubR1. J. Biol. Chem. *282*, 15217–15227.

Matthess, Y., Raab, M., Knecht, R., Becker, S., and Strebhardt, K. (2014). Sequential Cdk1 and Plk1 phosphorylation of caspase-8 triggers apoptotic cell death during mitosis. Mol. Oncol. *8*, 596–608.

McKinley, K.L., and Cheeseman, I.M. (2014). Polo-like kinase 1 licenses CENP-A deposition at centromeres. Cell *158*, 397–411.

Michalski, A., Damoc, E., Hauschild, J.P., Lange, O., Wieghaus, A., Makarov, A., Nagaraj, N., Cox, J., Mann, M., and Horning, S. (2011). Mass spectrometry-based proteomics using Q Exactive, a high-performance benchtop quadrupole Orbitrap mass spectrometer. Mol. Cell Proteomics, 10, M111.011015.

Monda, J.K., and Cheeseman, I.M. (2018). The kinetochore-microtubule interface at a glance. J. Cell Sci. *131*, jcs214577.

Moriya, T., Saur, M., Stabrin, M., Merino, F., Voicu, H., Huang, Z., Penczek, P.A., Raunser, S., and Gatsogiannis, C. (2017). High-resolution Single Particle Analysis from Electron Cryo-microscopy Images Using SPHIRE. J. Vis. Exp. *123*, 55448.

Morrow, C.J., Tighe, A., Johnson, V.L., Scott, M.I., Ditchfield, C., and Taylor, S.S. (2005). Bub1 and aurora B cooperate to maintain BubR1-mediated inhibition of APC/CCdc20. J. Cell Sci. *118*, 3639–3652.

Moshe, Y., Boulaire, J., Pagano, M., and Hershko, A. (2004). Role of Polo-like kinase in the degradation of early mitotic inhibitor 1, a regulator of the anaphase promoting complex/cyclosome. Proc. Natl. Acad. Sci. USA *101*, 7937–7942.

Moutinho-Santos, T., Conde, C., and Sunkel, C.E. (2012). POLO ensures chromosome bi-orientation by preventing and correcting erroneous chromosome-spindle attachments. J. Cell Sci. *125*, 576–583.

Mulvihill, D.P., Petersen, J., Ohkura, H., Glover, D.M., and Hagan, I.M. (1999). Plo1 kinase recruitment to the spindle pole body and its role in cell division in Schizosaccharomyces pombe. Mol. Biol. Cell *10*, 2771–2785.

Mundt, K.E., Golsteyn, R.M., Lane, H.A., and Nigg, E.A. (1997). On the regulation and function of human polo-like kinase 1 (PLK1): effects of overexpression on cell cycle progression. Biochem. Biophys. Res. Commun. *239*, 377–385.

Musacchio, A., and Desai, A. (2017). A molecular view of kinetochore assembly and function. Biology (Basel) *6*, 5.

Nakajima, H., Toyoshima-Morimoto, F., Taniguchi, E., and Nishida, E. (2003). Identification of a consensus motif for Plk (Polo-like kinase) phosphorylation reveals Myt1 as a Plk1 substrate. J. Biol. Chem. *278*, 25277–25280.

Natsume, T., Müller, C.A., Katou, Y., Retkute, R., Gierliński, M., Araki, H., Blow, J.J., Shirahige, K., Nieduszynski, C.A., and Tanaka, T.U. (2013). Kinetochores coordinate pericentromeric cohesion and early DNA replication by Cdc7-Dbf4 kinase recruitment. Mol. Cell *50*, 661–674.

Neef, R., Preisinger, C., Sutcliffe, J., Kopajtich, R., Nigg, E.A., Mayer, T.U., and Barr, F.A. (2003). Phosphorylation of mitotic kinesin-like protein 2 by polo-like kinase 1 is required for cytokinesis. J. Cell Biol. *162*, 863–875.

Neef, R., Gruneberg, U., Kopajtich, R., Li, X., Nigg, E.A., Sillje, H., and Barr, F.A. (2007). Choice of Plk1 docking partners during mitosis and cytokinesis is controlled by the activation state of Cdk1. Nat. Cell Biol. *9*, 436–444.

Nezi, L., and Musacchio, A. (2009). Sister chromatid tension and the spindle assembly checkpoint. Curr. Opin. Cell Biol. *21*, 785–795.

Nishino, M., Kurasawa, Y., Evans, R., Lin, S.-H., Brinkley, B.R., and Yu-Lee, L.Y. (2006). NudC is required for Plk1 targeting to the kinetochore and chromosome congression. Curr. Biol. *16*, 1414–1421.

Novak, B., Kapuy, O., Domingo-Sananes, M.R., and Tyson, J.J. (2010). Regulated protein kinases and phosphatases in cell cycle decisions. Curr. Opin. Cell Biol. *22*, 801–808.

O'Connor, A., Maffini, S., Rainey, M.D., Kaczmarczyk, A., Gaboriau, D., Musacchio, A., and Santocanale, C. (2015). Requirement for PLK1 kinase activity in the maintenance of a robust spindle assembly checkpoint. Biol. Open *5*, 11–19.

O'Donovan, D.S., MacFhearraigh, S., Whitfield, J., Swigart, L.B., Evan, G.I., and Mc Gee, M.M. (2013). Sequential Cdk1 and Plk1 phosphorylation of protein tyrosine phosphatase 1B promotes mitotic cell death. Cell Death Dis. *4*, e468.

Ohkura, H., Hagan, I.M., and Glover, D.M. (1995). The conserved Schizosaccharomyces pombe kinase plo1, required to form a bipolar spindle, the actin ring, and septum, can drive septum formation in G1 and G2 cells. Genes Dev. *9*, 1059–1073.

Olsen, J.V., Macek, B., Lange, O., Makarov, A., Horning, S., and Mann, M. (2007). Higher-energy C-trap dissociation for peptide modification analysis. Nat. Methods *4*, 709–712.

Overlack, K., Primorac, I., Vleugel, M., Krenn, V., Maffini, S., Hoffmann, I., Kops, G.J., and Musacchio, A. (2015). A molecular basis for the differential roles of Bub1 and BubR1 in the spindle assembly checkpoint. eLife *4*, e05269.

Pan, D., Klare, K., Petrovic, A., Take, A., Walstein, K., Singh, P., Rondelet, A., Bird, A.W., and Musacchio, A. (2017). CDK-regulated dimerization of M18BP1 on a Mis18 hexamer is necessary for CENP-A loading. eLife *6*, e23352.

Park, J.E., Soung, N.K., Johmura, Y., Kang, Y.H., Liao, C., Lee, K.H., Park, C.H., Nicklaus, M.C., and Lee, K.S. (2010). Polo-box domain: a versatile mediator of polo-like kinase function. Cell. Mol. Life Sci. *67*, 1957–1970.

Pentakota, S., Zhou, K., Smith, C., Maffini, S., Petrovic, A., Morgan, G.P., Weir, J.R., Vetter, I.R., Musacchio, A., and Luger, K. (2017). Decoding the centromeric nucleosome through CENP-N. eLife *6*, e33442.

Pesenti, M.E., Prumbaum, D., Auckland, P., Smith, C.M., Faesen, A.C., Petrovic, A., Erent, M., Maffini, S., Pentakota, S., Weir, J.R., et al. (2018). Reconstitution of a 26-subunit human kinetochore reveals cooperative microtubule binding by CENP-OPQUR and NDC80. Mol. Cell *71*, 923–939.e910.

Peters, U., Cherian, J., Kim, J.H., Kwok, B.H., and Kapoor, T.M. (2006). Probing cell-division phenotype space and Polo-like kinase function using small molecules. Nat. Chem. Biol. *2*, 618–626.

Petrovic, A., Pasqualato, S., Dube, P., Krenn, V., Santaguida, S., Cittaro, D., Monzani, S., Massimiliano, L., Keller, J., Tarricone, A., et al. (2010). The MIS12 complex is a protein interaction hub for outer kinetochore assembly. J. Cell Biol. *190*, 835–852.

Petrovic, A., Mosalaganti, S., Keller, J., Mattiuzzo, M., Overlack, K., Krenn, V., De Antoni, A., Wohlgemuth, S., Cecatiello, V., Pasqualato, S., et al. (2014). Modular assembly of RWD domains on the Mis12 complex underlies outer kinetochore organization. Mol. Cell *53*, 591–605.

Pettersen, E.F., Goddard, T.D., Huang, C.C., Couch, G.S., Greenblatt, D.M., Meng, E.C., and Ferrin, T.E. (2004). UCSF Chimera--a visualization system for exploratory research and analysis. J. Comput. Chem. *25*, 1605–1612.

Porter, I.M., Schleicher, K., Porter, M., and Swedlow, J.R. (2013). Bod1 regulates protein phosphatase 2A at mitotic kinetochores. Nat. Commun. *4*, 2677.

Pouwels, J., Kukkonen, A.M., Lan, W., Daum, J.R., Gorbsky, G.J., Stukenberg, T., and Kallio, M.J. (2007). Shugoshin 1 plays a central role in kinetochore assembly and is required for kinetochore targeting of Plk1. Cell Cycle *6*, 1579–1585.

Qi, W., Tang, Z., and Yu, H. (2006). Phosphorylation- and polo-box-dependent binding of Plk1 to Bub1 is required for the kinetochore localization of Plk1. Mol. Biol. Cell *17*, 3705–3716.

Rago, F., and Cheeseman, I.M. (2013). Review series: the functions and consequences of force at kinetochores. J. Cell Biol. *200*, 557–565.

Rappsilber, J., Mann, M., and Ishihama, Y. (2007). Protocol for micro-purification, enrichment, pre-fractionation and storage of peptides for proteomics using StageTips. Nat. Protoc. *2*, 1896–1906.

Santaguida, S., Tighe, A., D'Alise, A.M., Taylor, S.S., and Musacchio, A. (2010). Dissecting the role of MPS1 in chromosome biorientation and the spindle checkpoint through the small molecule inhibitor reversine. J. Cell Biol. *190*, 73–87.

Saurin, A.T. (2018). Kinase and phosphatase cross-talk at the kinetochore. Front. Cell Dev. Biol. *6*, 62.

Schindelin, J., Arganda-Carreras, I., Frise, E., Kaynig, V., Longair, M., Pietzsch, T., Preibisch, S., Rueden, C., Saalfeld, S., Schmid, B., et al. (2012). Fiji: an open-source platform for biological-image analysis. Nat. Methods *9*, 676–682.

Schuck, P. (2000). Size-distribution analysis of macromolecules by sedimentation velocity ultracentrifugation and lamm equation modeling. Biophys. J. *78*, 1606–1619.

Seki, A., Coppinger, J.A., Jang, C.Y., Yates, J.R., and Fang, G. (2008). Bora and the kinase Aurora a cooperatively activate the kinase Plk1 and control mitotic entry. Science *320*, 1655–1658.

Seong, Y.S., Kamijo, K., Lee, J.S., Fernandez, E., Kuriyama, R., Miki, T., and Lee, K.S. (2002). A spindle checkpoint arrest and a cytokinesis failure by the dominant-negative polo-box domain of Plk1 in U-2 OS cells. J. Biol. Chem. *277*, 32282–32293.

Sessa, F., Mapelli, M., Ciferri, C., Tarricone, C., Areces, L.B., Schneider, T.R., Stukenberg, P.T., and Musacchio, A. (2005). Mechanism of Aurora B activation by INCENP and inhibition by hesperadin. Mol. Cell *18*, 379–391.

Shao, H., Huang, Y., Zhang, L., Yuan, K., Chu, Y., Dou, Z., Jin, C., Garcia-Barrio, M., Liu, X., and Yao, X. (2015). Spatiotemporal dynamics of Aurora B-PLK1-MCAK signaling axis orchestrates kinetochore bi-orientation and faithful chromosome segregation. Sci. Rep. *5*, 12204.

Songyang, Z., Lu, K.P., Kwon, Y.T., Tsai, L.H., Filhol, O., Cochet, C., Brickey, D.A., Soderling, T.R., Bartleson, C., Graves, D.J., et al. (1996). A structural basis for substrate specificities of protein Ser/Thr kinases: primary sequence preference of casein kinases I and II, NIMA, phosphorylase kinase, calmodulin-dependent kinase II, CDK5, and Erk1. Mol. Cell. Biol. *16*, 6486–6493.

Suijkerbuijk, S.J., van Dam, T.J., Karagöz, G.E., von Castelmur, E., Hubner, N.C., Duarte, A.M., Vleugel, M., Perrakis, A., Rüdiger, S.G., Snel, B., and Kops, G.J. (2012a). The vertebrate mitotic checkpoint protein BUBR1 is an unusual pseudokinase. Dev. Cell *22*, 1321–1329.

Suijkerbuijk, S.J., Vleugel, M., Teixeira, A., and Kops, G.J. (2012b). Integration of kinase and phosphatase activities by BUBR1 ensures formation of stable kinetochore-microtubule attachments. Dev. Cell *23*, 745–755.

Sun, S.-C., Liu, H.-L., and Sun, Q.-Y. (2012). Survivin regulates Plk1 localization to kinetochore in mouse oocyte meiosis. Biochem. Biophys. Res. Commun. *421*, 797–800.

Sunkel, C.E., and Glover, D.M. (1988). polo, a mitotic mutant of *Drosophila* displaying abnormal spindle poles. J. Cell Sci. *89*, 25–38.

Tighe, A., Staples, O., and Taylor, S. (2008). Mps1 kinase activity restrains anaphase during an unperturbed mitosis and targets Mad2 to kinetochores. J. Cell Biol. *181*, 893–901.

Ubersax, J.A., and Ferrell, J.E., Jr. (2007). Mechanisms of specificity in protein phosphorylation. Nat. Rev. Mol. Cell Biol. *8*, 530–541.

van der Waal, M.S., Saurin, A.T., Vromans, M.J., Vleugel, M., Wurzenberger, C., Gerlich, D.W., Medema, R.H., Kops, G.J., and Lens, S.M. (2012). Mps1 promotes rapid centromere accumulation of Aurora B. EMBO Rep. *13*, 847–854.

Vassilev, L.T., Tovar, C., Chen, S., Knezevic, D., Zhao, X., Sun, H., Heimbrook, D.C., and Chen, L. (2006). Selective small-molecule inhibitor reveals critical mitotic functions of human CDK1. Proc. Natl. Acad. Sci. USA *103*, 10660–10665.

Vleugel, M., Tromer, E., Omerzu, M., Groenewold, V., Nijenhuis, W., Snel, B., and Kops, G.J. (2013). Arrayed BUB recruitment modules in the kinetochore scaffold KNL1 promote accurate chromosome segregation. J. Cell Biol. *203*, 943–955.

von Schubert, C., Cubizolles, F., Bracher, J.M., Sliedrecht, T., Kops, G.J.P.L., and Nigg, E.A. (2015). Plk1 and Mps1 cooperatively regulate the spindle assembly checkpoint in human cells. Cell Rep. *12*, 66–78.

Wang, F., Ulyanova, N.P., van der Waal, M.S., Patnaik, D., Lens, S.M.A., and Higgins, J.M.G. (2011). A positive feedback loop involving Haspin and Aurora B promotes CPC accumulation at centromeres in mitosis. Curr. Biol. *21*, 1061–1069.

Watanabe, N., Arai, H., Nishihara, Y., Taniguchi, M., Watanabe, N., Hunter, T., and Osada, H. (2004). M-phase kinases induce phospho-dependent ubiquitination of somatic Wee1 by SCFbeta-TrCP. Proc. Natl. Acad. Sci. USA *101*, 4419–4424.

Weir, J.R., Faesen, A.C., Klare, K., Petrovic, A., Basilico, F., Fischböck, J., Pentakota, S., Keller, J., Pesenti, M.E., Pan, D., et al. (2016). Insights from biochemical reconstitution into the architecture of human kinetochores. Nature *537*, 249–253.

Weissmann, F., Petzold, G., VanderLinden, R., Huis In 't Veld, P.J., Brown, N.G., Lampert, F., Westermann, S., Stark, H., Schulman, B.A., and Peters, J.M. (2016). biGBac enables rapid gene assembly for the expression of large multisubunit protein complexes. Proc. Natl. Acad. Sci. USA *113*, E2564–E2569.

Wimbish, R.T., and DeLuca, J.G. (2020). Hec1/Ndc80 tail domain function at the kinetochore-microtubule interface. Front. Cell Dev. Biol. *8*, 43.

Wolfe, B.A., Takaki, T., Petronczki, M., and Glotzer, M. (2009). Polo-like kinase 1 directs assembly of the HsCyk-4 RhoGAP/Ect2 RhoGEF complex to initiate cleavage furrow formation. PLoS Biol. *7*, e1000110.

Wong, O.K., and Fang, G. (2007). Cdk1 phosphorylation of BubR1 controls spindle checkpoint arrest and Plk1-mediated formation of the 3F3/2 epitope. J. Cell Biol. *179*, 611–617.

Xu, J., Shen, C., Wang, T., and Quan, J. (2013). Structural basis for the inhibition of Polo-like kinase 1. Nat. Struct. Mol. Biol. *20*, 1047–1053.

Yamaguchi, T., Goto, H., Yokoyama, T., Silljé, H., Hanisch, A., Uldschmid, A., Takai, Y., Oguri, T., Nigg, E.A., and Inagaki, M. (2005). Phosphorylation by Cdk1 induces Plk1-mediated vimentin phosphorylation during mitosis. J. Cell Biol. *171*, 431–436.

Yamashiro, S., Yamakita, Y., Totsukawa, G., Goto, H., Kaibuchi, K., Ito, M., Hartshorne, D.J., and Matsumura, F. (2008). Myosin phosphatase-targeting subunit 1 regulates mitosis by antagonizing polo-like kinase 1. Dev. Cell *14*, 787–797.

Yan, K., Yang, J., Zhang, Z., McLaughlin, S.H., Chang, L., Fasci, D., Ehrenhofer-Murray, A.E., Heck, A.J.R., and Barford, D. (2019). Structure of the inner kinetochore CCAN complex assembled onto a centromeric nucleosome. Nature *574*, 278–282.

Yeh, T.Y., Kowalska, A.K., Scipioni, B.R., Cheong, F.K., Zheng, M., Derewenda, U., Derewenda, Z.S., and Schroer, T.A. (2013). Dynactin helps target Polo-like kinase 1 to kinetochores via its left-handed beta-helical p27 subunit. EMBO J. *32*, 1023–1035.

Yoo, H.Y., Kumagai, A., Shevchenko, A., Shevchenko, A., and Dunphy, W.G. (2004). Adaptation of a DNA replication checkpoint response depends upon inactivation of Claspin by the Polo-like kinase. Cell *117*, 575–588.

Zhang, X., Chen, Q., Feng, J., Hou, J., Yang, F., Liu, J., Jiang, Q., and Zhang, C. (2009). Sequential phosphorylation of Nedd1 by Cdk1 and Plk1 is required for targeting of the gammaTuRC to the centrosome. J. Cell Sci. *122*, 2240–2251.

Zhou, H., Di Palma, S., Preisinger, C., Peng, M., Polat, A.N., Heck, A.J., and Mohammed, S. (2013). Toward a comprehensive characterization of a human cancer cell phosphoproteome. J. Proteome Res. *12*, 260–271.

Zhu, K., Shan, Z., Zhang, L., and Wen, W. (2016). Phospho-pon binding-mediated fine-tuning of Plk1 activity. Structure *24*, 1110–1119.

Zhuo, X., Guo, X., Zhang, X., Jing, G., Wang, Y., Chen, Q., Jiang, Q., Liu, J., and Zhang, C. (2015). Usp16 regulates kinetochore localization of Plk1 to promote proper chromosome alignment in mitosis. J. Cell Biol. *210*, 727–735.

Zitouni, S., Nabais, C., Jana, S.C., Guerrero, A., and Bettencourt-Dias, M. (2014). Polo-like kinases: structural variations lead to multiple functions. Nat. Rev. Mol. Cell Biol. *15*, 433–452.

STAR★METHODS

KEY RESOURCES TABLE

REAGENT or RESOURCE	SOURCE	IDENTIFIER
Antibodies		
anti-Mps1 rabbit polyclonal	This study	933 Affinity purified
anti-CENP-O rabbit polyclonal	Amaro et al., 2010	NA
anti-Tubulin mouse monoclonal	Sigma	Cat#T9026; RRID: AB_477593
anti-GFP rabbit polyclonal	Abcam	Cat#ab190584
anti-BubR1 mouse monoclonal	BD	Cat#612503; RRID: AB_2066085
anti-Incenp rabbit polyclonal	Cell Signaling	Cat#2807; RRID: AB_2127513
anti-Plk1 mouse monoclonal	Abcam	Cat#ab17057; RRID: AB_443613
anti-Cyclin B mouse monoclonal	Santa Cruz	Cat#Sc-245; RRID: AB_627338
anti-Vinculin mouse monoclonal	Sigma	Cat#V9131; RRID: AB_477629
anti-Aurora B mouse monoclonal	Abcam	Cat#ab3609; RRID: AB_449204
anti-BUB1 rabbit polyclonal	Abcam	Cat#ab9000; RRID: AB_449765
anti-BUBR1 rabbit polyclonal	Abcam	Cat#ab70544; RRID: AB_1209397
anti-mouse IgG-Alexa 488 secondary	Invitrogen	Cat#A11001; RRID: AB_2534069
anti-rabbit IgG-Alexa 488 secondary	Invitrogen	Cat#A21206; RRID: AB_2535792
anti-mouse IgG-Rhodamine secondary	Jackson Imm.Res	Cat#115-295-003; RRID: AB_2338756
anti-rabbit IgG- Rhodamine secondary	Jackson Imm.Res	Cat#111-295-003; RRID: AB_2338022
anti-human IgG-Alexa 647 secondary	Invitrogen	Cat#A21445; RRID: AB_2535862
Human anti-centromere (CREST)	Antibodies Inc.	Cat#15-234-0001; RRID: AB_2687472
anti-H3pS10 rabbit polyclonal	Abcam	Cat#ab5176; RRID: AB_304763
anti-Cep135 rabbit	Bird and Hyman, 2008	N/A
anti-CENP-QU goat polyclonal	Pesenti et al., 2018	N/A
anti-pT232 Aurora B rabbit polyclonal	Rockland	Cat#660-401-677; RRID: AB_2061641
anti-H2ApT120 rabbit polyclonal	Active Motif	Cat#39391; RRID: AB_2744670
Goat anti-rabbit DyLight 405	Jackson Immuno Research	Cat#111-475-003; RRID: AB_2338035
Donkey anti-goat 488	Invitrogen	Cat#A11055; RRID: AB_2534102
Chicken anti-rabbit Alexa Fluor 647	Invitrogen	Cat#A11046; RRID: AB_142716
Bacterial and Virus Strains		
E.coli: BL21(DE3)-RIL strain	Agilent Technologies	Cat#230240
E.coli: BL21CodonPlus(DE3)-RIL strain	Agilent Technologies	Cat#230280
E. coli BL21 (DH5α)	ThermoFisher	Cat#18265017
Insect Cells		
S.frugiperda:Sf9 cells	ThermoFisher	Cat#12659017
Trichoplusia ni:BTI-Tnao38	Garry W Blissard Lab	N/A
Chemicals, Peptides, and Recombinant Proteins		
Okadaic Acid	Merck	Cat#04906845001
RO-3306	Millipore	Cat#217699
MG-132	Calbiochem	CAS 133407-82-6
Reversine	Cayman Chemical	Cat#10004412
Hesperadin	Merck	Cat#375680-5MG
Fetal bovine serum (FBS)	Clonetech	Cat#631107
Zeocin	Invitrogen	Cat#R25001
L-glutamine	PAN Biotech	Cat#P04-80100
Nocodazole	Sigma	Cat#M1404

(*Continued on next page*)

Continued

REAGENT or RESOURCE	SOURCE	IDENTIFIER
RNAiMAX	Invitrogen	Cat#13778100
DAPI	Sigma	Cat#D9542
PenStrep	GIBCO	Cat#15-140
Oligofectamine	Invitrogen	Cat#12252011
Thymidine	Sigma	Cat#T9250
Trypsin EDTA	PAN	Cat#P10-027100
Doxycycline	Sigma	Cat#D9891
Triton-100	Sigma	Cat#T8787
Paraformaldehyde	VWR	Cat#100503-914
NEON transfection Kit (includes buffers)	Invitrogen	Cat#MPK10096
PhosSTOP phosphatase inhibitor	Roche	Cat#4906845001
Alexa Fluor 488 C5 maleimide Protein labeling kit	ThermoFisher	Cat#A10254
Blasticidin	Invitrogen	Cat#A1113902
Hygromycin B	Invitrogen	Cat#10687010
DMEM	PAN Biotech	Cat#P0403609
Fetal Bovine Serum (FBS)	PAN Biotech	Cat#P303031
Penicillin/Streptomycin	PAN Biotech	Cat#P0607300
Lipofectamine 2000	Invitrogen	Cat#11668019
Oligofectamine	Thermo Fischer	Cat#12252011
X-tremeGENE	Roche	Cat#4476093001
BI2536	Selleck	Cat#S1109
Poly-D-Lysine	Sigma-Aldrich	Cat#A003E
PIPES	Sigma-Aldrich	Cat#P6757
HEPES	Sigma-Aldrich	Cat#H3375
EGTA	Sigma-Aldrich	Cat#324626
$MgCl_2$	Sigma-Aldrich	Cat#M8266
BSA	Sigma-Aldrich	Cat#B6917
Mowiol	Calbiochem	Cat#475904
IPTG	Sigma-Aldrich	Cat#I6758
NaCl	Sigma-Aldrich	Cat#S9888
Glycerol	Sigma-Aldrich	Cat#G5516
Imidazole	Sigma-Aldrich	Cat#I5513
TCEP	Sigma-Aldrich	Cat#75259
Protease Inhibitor Cocktail	Serva	Cat#39107
HiTrap TALON crude	GE Healthcare	Cat#45-002-386
Glutathione Sepharose 4 Fast Flow beads	GE Healthcare	Cat#17-5132-01
Resource Q anion exchange chromatography column	GE Healthcare	Cat#17-1179-01
L-reduced Glutathione	Sigma-Aldrich	Cat#G6529
Pro-Q Diamond phosphoprotein stain	Thermo Fischer	Cat#P33300
Coomassie Brilliant Blue R-250 dye	Thermo Fischer	Cat#20278
Alexa Fluor 488 C5 maleimide Protein labeling kit	Thermo Fischer	Cat#A10254
CENP-OPQUR complex	Pesenti et al., 2018	N/A
CENP-QU complex	Pesenti et al., 2018	N/A
CENP-OP complex	Pesenti et al., 2018	N/A
CENP-LN complex	Pentakota et al., 2017	N/A
CENP-CHKIM complex	Weir et al., 2016	N/A
MIS12 complex	Petrovic et al., 2014	N/A
NDC80 complex	Huis In 't Veld et al., 2016	N/A

(*Continued on next page*)

Continued

REAGENT or RESOURCE	SOURCE	IDENTIFIER
KNL1 complex	Petrovic et al., 2014	N/A
BUB1:BUB3 complex	Breit et al., 2015	N/A
BUBR1:BUB3 complex	Breit et al., 2015	N/A
BUB1 kinase (BUB1$^{705-1050}$)	Breit et al., 2015	N/A
Aurora B kinase (Aurora B$^{45-344}$:INCENP$^{835-903}$)	Girdler et al., 2008	N/A
PLK1 kinase	Pan et al., 2017	N/A
CDK1 kinase (CDK1:CyclinB complex)	This study	N/A
MPS1 kinase	This study	N/A
CENP-OPQU$^{114-418}$R	This study	N/A
PLK1^{210A}	This study	N/A
PLK1^{PBD}	This study	N/A
CENP-U$^{58-114}$	This study	N/A
CENP-U$^{58-114}$T98A	This study	N/A
CENP-U$^{58-114}$S77A/T78A	This study	N/A
Deposited Data		
Proteomics data	This study	PXD: 022033
Unprocessed images	This study	https://doi.org/10.17632/rhgb7xcv5c.1
Experimental Models: Cell Lines		
HeLa cells	IEO Milan	N/A
U2OS-LacO	Janicki et al., 2004	N/A
HeLa Flp-In T-REx	Tighe et al., 2008	N/A
HeLa Flp-In T-REx_CENP-B-INCENP-EGFP	This study	N/A
HeLa Flp-In T-REx_EGFP-CENP-U_1-418	This study	N/A
HeLa Flp-In T-REx_EGFP-CENP-U_1-114	This study	N/A
HeLa Flp-In T-REx _EGFP-CENP-U_115-418	This study	N/A
HeLa Flp-In T-REx_EGFP-CENP-U_S77/78A	This study	N/A
HeLa Flp-In T-REx_EGFP-CENP-U_T98A	This study	N/A
Oligonucleotides		
CENP-Q smart pool	Dharmacon/Horizon	Cat#L-020768-02
CENP-Q	Amaro et al., 2010	N/A
CENP-U smart pool	Dharmacon/Horizon	Cat#L-004988-00
CENP-O	Dharmacon/Horizon	Cat#L-014339-02-0005
CENP-P	Amaro et al., 2010	N/A
Bub1 #2	Overlack et al., 2015	N/A
BubR1_NEW176-196	Overlack et al., 2015	N/A
Recombinant DNA		
pCDNA5/FRT/TO	Invitrogen	Cat#V601020
pCDNA5/FRT/TO-EGFP-IRES	Petrovic et al., 2010	N/A
pCDNA5/FRT/TO-EGFP-IRES_EGFP-CENP-U_1-418	This study	N/A
pCDNA5/FRT/TO-EGFP-IRES_EGFP-CENP-U_1-114	This study	N/A
pCDNA5/FRT/TO-EGFP-IRES_EGFP-CENP-U_115-418	This study	N/A
pCDNA5/FRT/TO-EGFP-IRES_EGFP-CENP-U_S77/78A	This study	N/A
pCDNA5/FRT/TO-EGFP-IRES_EGFP-CENP-U_T98A	This study	N/A
LacI-EGFP	This study	N/A
Lac-I-EGFP-CENP-U_1-418	This study	N/A
Lac-I-EGFP-CENP-U_1-114	This study	N/A
Lac-I-EGFP-CENP-U_115-418	This study	N/A
Lac-I-EGFP-CENP-U_1-57	This study	N/A

(*Continued on next page*)

Continued

REAGENT or RESOURCE	SOURCE	IDENTIFIER
Lac-I-EGFP-CENP-U_58-114	This study	N/A
Lac-I-EGFP-CENP-U_86-114	This study	N/A
Lac-I-EGFP-CENP-U_58-85	This study	N/A
pCDNA5/FRT/TO-EGFP-IRES_CENP-B-INCENP-EGFP	De Antoni et al., 2012	N/A
pETDuet-1	Novagen	Cat#71146
pETDuet-1_6xHis-MBP-PLK1_PBD	This study	N/A
pETDuet-1_6xHis-MBP-PLK1_T210A	This study	N/A
pETDuet-1_6xHis-MBP-CENP-U$^{58-114}$	This study	N/A
pETDuet-1_6xHis-MBP-CENP- U$^{58-114}$_S77A/T78A	This study	N/A
pETDuet-1_6xHis-MBP-CENP- U$^{58-114}$_T98A	This study	N/A
pLIB	Addgene	Cat#80610
pLIB_6xHis_PLK1	Pan et al., 2017	N/A
pLIB_GST-CDK1	This study	N/A
pLIB_6xHis-Cyclin B1	This study	N/A
pBIGa	Addgene	Cat#80611
pBIGa_GST-CDK1_6xHis-CyclinB1	This study	N/A
pBIGa_CENP-O_P_6xHisQ_U_R	Pesenti et al., 2018	N/A
pBIGa_CENP-O_P_6xHisQ_U$^{114-418}$_R	This study	N/A
pBIGa_6xHis-CENP-C$^{1-544}$_H_K_I^{57-C}_M	Weir et al., 2016	N/A
pBIGa_NDC80_NUF2_6xHis-SPC25_SPC24	Huis In 't Veld et al., 2016	N/A
pLIB_GST-MPS1	This study	N/A
pFL Multibac	Geneva Biotech	N/A
pFL_6xHis-BUB1$^{705-1050}$	Breit et al., 2015	N/A
pFL_6xHis-BUB1_BUB3	Breit et al., 2015	N/A
pFL_6xHis-BUBR1_BUB3	Breit et al., 2015	N/A
pFL_6xHis-CENP-Q-U	Pesenti et al., 2018	N/A
pFL_6xHis-CENP-O-P	Pesenti et al., 2018	N/A
pFL_GST-CENP-L_CENP-N	Pentakota et al., 2017	N/A
pFL_DSN1-6xHis_NSL1	Petrovic et al., 2014	N/A
pFL_NNF1-MIS12	Petrovic et al., 2014	N/A
pGEX-6P	GE Healthcare	Cat#27-4598-01
pGEX-6P-2rbs_GST-Aurora B$^{45-344}$:INCENP$^{835-903}$	Girdler et al., 2008	N/A
pGEX-6P-2rbs_GST-KNL1$^{1995-2316}$	Petrovic et al., 2010	N/A
pGEX-6P-2rbs-GST-ZWINT	Petrovic et al., 2010	N/A
Software and Algorithms		
GraphPad Prism 6.0	GraphPad software	https://www.graphpad.com
Imaris 9.2	Bitplane	https://imaris.oxinst.com/packages
ImageJ 1.46/ Fiji	NIH	https://imageJ.nih.gov/ij/
SoftWorx	Applied Precision	N/A
Slidebook 6.0	3i	N/A
Image Lab	Bio-rad	https://www.bio-rad.com/de-de/product/image-lab-software?ID=KRE6P5E8Z
UCSF Chimera	Pettersen et al., 2004	http://www.cgl.ucsf.edu/chimera
SPHIRE suit	Moriya et al., 2017	http://www.sphire.mpg.de
SEDFIT	Schuck, 2000	http://www.analyticalultracentrifugation.com/default.htm
SEDNTERP	Laue et al., 1992	http://bitcwiki.sr.unh.edu/index.php/Main_Page

(*Continued on next page*)

Continued

REAGENT or RESOURCE	SOURCE	IDENTIFIER
GUSSI	Chad Brautigam	https://www.utsouthwestern.edu/labs/mbr/software/
PrDOS	Ishida and Kinoshita, 2007	http://prdos.hgc.jp/cgi-bin/top.cgi
COILS	Lupas et al., 1991	https://embnet.vital-it.ch/software/COILS_form.html
Image Lab software Version 5.2	Biorad	https://www.bio-rad.com/de-de/product/image-lab-software?ID=KRE6P5E8Z

RESOURCE AVAILABILITY

Lead Contact

Requests for resources and reagents should be directed to the Lead Contact, Andrea Musacchio (andrea.musacchio@mpi-dortmund.mpg.de).

Materials Availability

The plasmids and cell lines generated in this study are available on request to the Lead Contact.

Data and Code Availability

Proteomics data have been deposited to the ProteomeXchange Consortium via the PRIDE partner repository with dataset identifier PXD: 022033. All the original/source data for Figures 1, 2, 3, 4, 5, 6, and S1–S7 are available on Mendeley (Mendeley Data: https://doi.org/10.17632/rhgb7xcv5c.1).

EXPERIMENTAL MODEL AND SUBJECT DETAILS

Cells lines and Expression strains

HeLa and U2OS-LacO (a gift by Geert Kops, UMC, Utrecht, Netherlands; (Janicki et al., 2004)) cell lines were maintained in DMEM (PAN Biotech, Aidenbach, Germany) supplemented with 10% FBS (PAN Biotech), 50 μg/ml Penicillin/Streptomycin (PAN Biotech), and 2 mM L-glutamine (PAN Biotech). HeLa Flp-In T-REx host cell lines (Tighe et al., 2008) were maintained in complete DMEM media as described above, but containing 10% tetracycline-free FBS (PAN Biotech) instead and supplemented with 50 μg/ml Zeocin (Invitrogen, Carlsbad, California, United States). Flp-In T-REx HeLa cells expressing GFP-fusions were generated as previously described (Tighe et al., 2008), maintained in DMEM with 10% tetracycline-free FBS supplemented with 250 μg/ml hygromycin and 4 μg/ml blastidicin (Invitrogen, Carlsbad, CA) and gene expression was induced by addition of 100 ng/ml doxycycline (Sigma, St. Louis, Missouri, United States) for 12-24 hr. *E. coli* BL21 (DH5a) (ThermoFisher Scientific, Waltham, Massachusetts, United States), BL21(DE3)-RIL and BL21CodonPlus(DE3)-RIL (Agilent Technologies, Santa Clara, California, United States) strains were cultured on LB agar or liquid media at 37°C. LB supplemented with ampicillin (50 μg/ml) to maintain the pETDuet plasmids and with chloramphenicol (34 μg/ml) to maintain the extra copies of tRNA Genes in CodonPlus strain. SF9 (ThermoFisher Scientific, Waltham, Massachusetts, United States) and Tnao38 (gift from Garry W Blissard) cells were maintain in Sf-900 II medium (ThermoFisher Scientific, Waltham, Massachusetts, United States) supplemented with 10% (v/v) fetal bovine serum, at 27°C and 110 rpm orbital rotation.

METHOD DETAILS

Cell transfection and electroporation

CENP-B-INCENP-EGFP gene expression was induced by addition of 10 ng/ml doxycycline (Sigma, St. Louis, Missouri, United States) for 12-24 hours. To achieve single depletion of either Bub1 or CENP-Q, cells were transfected with either Lipofectamine 2000 or RNAiMAX(Invitrogen, Carlsbad, California, United States) and Bub1 siRNA (Dharmacon, part of GE Healthcare, Piscataway, NJ; 5′-GUUGCCAACACAAGUUCU-3′) or CENP-Q siRNA (CENP-Q (GAGUUAAUGACUGGGAAUA; AUGGAAAGGGCACGAAGACA; ACAAAGCACACUAACCUAA; UGUCAGAGAAUAAGGUUAG;) at 50 nM for respectively 24 and 48 hours using manufacturer's protocol. Depletion of endogenous CENP-OQU was achieved with two rounds of Lipofectamine RNAiMAX transfection, for a total of 72 hours, with the following siRNA oligos at a total concentration of 100 nM: CENP-Q (GAGUUAAUGACUGGGAAUA; AUGGAAAGGGCACGAAGACA; ACAAAGCACACUAACCUAA; UGUCAGAGAAUAAGGUUAG; GGUCUGGCAUUACUACAGGAAGAAA), CENP-U: (GAAAGCCAUCUGCGAAAUA; GAAAAUAAGUACACAACGU; GGGAAGAUAUCUCAUGACA; GCGCAAGACGUUCAAAGAA) and CENP-O (GUACGAAGCCCUUGCAUCA; AAGCCAUUCUGCAGGCAUA; GCUCACACAAUCCACGAACA; CUAGAUUGCUGUAUAAGGA). For rescue experiments, 48 hours into the siRNA depletion of endogenous OQU, we performed electroporation of Alexa488 labeled recombinant CENP-OPQUR at a concentration of 4 μM as previously described (Alex et al., 2019; Pesenti et al.,

2018)(Neon Transfection System, Thermo Fisher). As control we used Alexa488. Following recovery from electroporation, cells were arrested in mitosis with a 3.3 μm nocodazole (Sigma-Aldrich, Missouri, USA) treatment for 16 hours and then prepared for immunofluorescence analysis. For co-depletion of endogenous OQU with either Bub1 or BubR1, cells were treated with 100 nM of siBUB1 or siBUBR1 RNA duplexes as previously described (Overlack et al., 2015) for the last 24 hours of the experiment, where 4 hours before fixation cells were treated with 3.3 μM nocodazole followed by 2 hours treatment with 100 nM Okadaic acid. U2OS-lacO cells were transfected with the LacI-EGFP-CENP-U full length or deletion/mutant constructs using X-tremeGENE (Roche, Basel, Switzerland) transfection reagent (3:1 ratio) for 48 hours using manufacturer's protocol.

Plasmids

To generate plasmids for expressing N terminus tagged Lac-I-EGFP-CENP-U full length or deletion proteins in U2OS-lacO cells, CENP-U gene was PCR amplified from the codon optimized CENP-U cDNA (GeneArt, Life Technologies, Carlsbad, California, United States) and cloned into the pCDNA5/FRT/TO-EGFP-IRES (Petrovic et al., 2010), a modified form of pCDNA5/FRT/TO vector (Invitrogen, Carlsbad, California, United States)) between the BamHI and *Xho*I restriction sites. LacI gene was PCR-amplified and inserted in the same reading frame between the *Pme*I restriction sites using the Gibson cloning compatible primers. To generate a plasmid for expressing CENP-B (2-164)-INCENP (48-918)-EGFP, the gene sequences were sub-cloned from the SL417 vector (Liu et al., 2009) into pCDNA5/FRT/TO-EGFP-IRES between BamHI and *Not*I restriction sites (De Antoni et al., 2012). To generate a plasmid for expressing N terminus 6xHis tagged PLK1 recombinant protein in insect cells, codon optimized PLK1 cDNA (GeneArt, Life Technologies) was sub-cloned between the BamHI and SalI restriction sites of a modified pLIB (Clontech, now TAKARA Bio USA, Kyoto, Kyoto, Japan) vector already containing 6xHis followed by TEV protease sequences (as described in Pan et al. [2017]). Plasmids to express 6xHis-MBP-PBD and 6xHis-MBP-PLK1^{T210A} in bacterial cells were generated by cloning the PCR amplified sequences for the polo-box-domain (PBD; amino acids 345-603) of PLK1 and full length PLK1 (T210 residue was mutated to alanine using site-directed mutagenesis), respectively, between the BamHI and SalI restriction sites of a modified pETDuet-1 (Novagen) vector, already containing 6xHis followed by PreScission Protease-MBP-TEV protease sequences. HsMPS1 was PCR-amplified from a human cDNA library and sub-cloned in a modified pLIB vector in frame with the sequence encoding GST and a PreScission protease cleavage site. Plasmids to express N terminus tagged GST-CDK1 and 6xHis tagged Cyclin B1 were generated by sub-cloning, codon optimized cDNA of CDK1 and Cyclin B1 (GeneArt, Life Technologies) between the BamHI and SalI restriction sites of a modified pLIB vectors containing sequences for the GST followed by PreScission protease and 6xHis followed by TEV protease, respectively. These pLIB plasmids generated so-forth were used to insert the GST-CDK1 and His-Cyclin B1 sequences into a baculovirus-based multigene-expressing vector, pBIGa (Weissmann et al., 2016) by Gibson cloning method. CENP-OP and CENP-QU plasmids were published previously (Pesenti et al., 2018). To generate plasmids for expressing CENP-OPQUR and CENP-OPQU$^{\Delta1\text{-}114}$R complexes in insect cells, plasmid to express N terminus 6xHis tagged CENP-Q were generated by Gibson cloning method, codon optimized cDNA of CENP-Q (GeneArt, Life Technologies) was inserted in a modified pLIB vectors containing sequences for the 6xHis followed by TEV protease. The codon optimized cDNA of CENP-O, -P, -U- U$^{\Delta1\text{-}114}$, and -R were inserted by Gibson cloning method in to unmodified pLIB plasmids. These pLIB plasmids generated so-forth were used to insert the CENP-O, -P, -U, -U$^{\Delta1\text{-}114}$, -R and 6His-CENP-Q sequences into two baculovirus-based multigene-expressing vectors, pBIGa (Weissmann et al., 2016) by Gibson assembly, one containing CENP-O, -P, -U, -R and −6His-CENP-Q, and one containing CENP-O, -P, -U$^{\Delta1\text{-}114}$, -R and 6His-CENP-Q. CENP-LN, CENP-C$^{1\text{-}544}$HKI$^{57\text{-}C}$M, Mis12, NDC80, KNL1, BUB1:BUB3, and BUBR1:BUB3 complexes were previously published (Breit et al., 2015; Huis In 't Veld et al., 2016; Klare et al., 2015; Pentakota et al., 2017; Petrovic et al., 2014). Plasmids to express 6xHis-MBP-CENP-U$^{58\text{-}114}$ wild-type, S77A/T78A and T98A, in bacterial cells were generated by cloning the PCR amplified sequences for CENP-U$^{58\text{-}114}$ (amino acids 58-114) of codon-optimized CENP-U cDNA, between the BamHI and *Hind*III restriction sites of a modified pETDuet-1 (Novagen) vector, already containing 6xHis followed by PreScission Protease-MBP-TEV protease sequences. The MBP-CENP-U$^{58\text{-}114}$S77A/T78A and T98A mutants were generated by mutating S77/T78 and T98 residues in alanine using site-directed mutagenesis.

Cell synchronization

To test the effect of various kinases and phosphatases on the localization of kinetochore proteins cells were synchronized using double thymidine arrest. Cells were released from 18 hours thymidine (2 mM; Sigma–Aldrich) block by washing them with the fresh media several times. After releasing them for the next 9 hours, second exposure to thymidine (2 mM) was continued for another 15 hours. Cells were released into the S phase for 4 hours and then nocodazole (3.3 μM) was added to the media for the next 3-4 hours to enrich the mitotic cell population. Kinase activity inhibitors, RO-3306 (9 μM), BI 2536 (100 nM), hesperadin (500 nM), reversine (500 nM)(Calbiochem) and/or phosphatase inhibitor, okadaic acid (100 nM; Calbiochem) were added in presence of MG132 proteasome inhibitor (10 μM; Calbiochem) to the cells for 10, 30, or 90 minutes before fixing for immunofluorescence or harvesting for western blotting analysis. H3-pS10 staining was used to indicate the potency of hesperadin directly and RO-3306 indirectly, whereas, Cep135, a centrosome marker was used to indicate the absence of PLK1 from centrosome as well, when BI-2536 was used, thus indicating its potency. CREST was used as kinetochore marker and DAPI indicates mitotic cells.

Immunofluorescence

Cells were grown on coverslips pre-coated with 0.01% poly-D-lysine (Sigma-Aldrich). Cells were pre-permealized with 0.5% Triton X-100 solution in PHEM (Pipes, HEPES, EGTA, $MgCl_2$) buffer for 2-5 minutes before fixing with 4% PFA in PHEM for 15-20 minutes.

After blocking the cells with either 3% BSAor 5% boiled goat serum in PHEM buffer supplemented with 0.1% Triton X-100 (PHEM-T), they were incubated at room temperature for 1-2 or 16 hours at 4°C with the following primary antibodies: anti-CENP-QU (in-house generated; goat 1:100), anti CENP-O (rabbit; 1:500) (Amaro et al., 2010), anti-PLK1 (Abcam #ab17057, mouse monoclonal antibody; 1:300), anti-H3-pS10 (Abcam # ab5176, rabbit polyclonal antibody, 1:2000), rabbit anti-CEP135 (gift from Alex Bird [Bird and Hyman, 2008], 1:3000), anti-BUB1 (Abcam #ab9000, rabbit polyclonal antibody, 1:1000), anti-BubR1 (rabbit polyclonal, Abcam, ab70544, 1:500), anti-Aurora B (mouse monoclonal, Abcam, ab3609, 1:500), anti-Mps1 (rabbit polyclonal affinity purified, #933, produced in house, 1:500), anti-AurB-pT232 (Rockland #660-401-667, rabbit polyclonal antibody, 1:2000), anti-H2ApT120 (Active Motif #39391, rabbit polyclonal antibody, 1:2000), CREST/anticentromere antibody (human autoimmune serum, Antibodies, Inc., 1:100) diluted in the blocking buffer. Washings were done in PHEM-T buffer. Donkey anti-rabbit Alexa Fluor 488 (Invitrogn A21206), Goat anti-rabbit DyLight 405 (Jackson Immuno Research 111-475-003), Donkey anti-goat 488 (Invitrogen, Carlsbad, California, United States), Goat anti-human Alexa Fluor 647 (Invitrogen, Carlsbad, California, United States), Chicken anti-rabbit Alexa Fluor 647 (Invitrogen, Carlsbad, California, United States A11046) and goat anti-mouse Rhodamine Red (Jackson Immuno Research) were used as secondary antibodies. DNA was stained with 0.5 μg/ml DAPI (Serva) and Mowiol (Calbiochem) was used as mounting media.

Western blotting

Cell pellets were resuspended in sample buffer, boiled and analyzed by western blotting. Membranes were probed with the following antibodies: anti-GFP (rabbit polyclonal, Abcam, ab190584, 1:10000), anti-Bub1 (rabbit polyclonal; Abcam, Cambridge, UK; 1:5000), anti-BubR1 (mouse monoclonal; BD #612503, 1:1000) and anti-Tubulin (mouse monoclonal; Sigma; 1:8000), anti-Incenp (rabbit polyclonal, Cell Signaling #2807, 1:500), anti-Cyclin B (mouse monoclonal, Santa Cruz, sc-245, 1:1000), anti-PLK1 (mouse monoclonal; Abcam #ab17057, 1:1000), anti-Vinculin (mouse monoclonal, Sigma, V9131, 1:10000).

Cell imaging

Cells were imaged at room temperature using a spinning disk confocal device on the 3i Marianas system equipped with an Axio Observer Z1 microscope (Zeiss), a CSU-X1 confocal scanner unit (Yokogawa Electric Corporation, Tokyo, Japan), 100 × /1.4NA Oil Objectives (Zeiss), and Orca Flash 4.0 sCMOS Camera (Hamamatsu). Images were acquired as z sections at 0.25 μm. Images were converted into maximal intensity projections, exported, and converted into 8-bit using ImageJ. Images were cropped and merged in ImageJ. The figures were arranged using Adobe Illustrator software. either Imaris 7.3.4 and 9.2 software (Bitplane, Zurich, Switzerland) or with ImageJ/Fiji (Schindelin et al., 2012).

Protein expression and purification

6xHis-PLK1, GST-CDK1/Cyclin B1 complex, and GST-MPS1 were expressed in insect cells. High-titer virus (V2) produced in Sf9 cells was used to express protein in Tnao38 insect cells (72 hours, 27°C). 6xHis-MBP-PBD and 6xHis-MBP-PLK1^{T210A} were expressed in *E. coli* BL21 (DE3) cells using 0.2 mM IPTG for approximately 15 hours at 18°C. To purify 6xHis-PLK1, 6xHis-MBP-PBD or 6xHis-MBP-PLK1^{T210A}, cells were pelleted down and re-suspended in His-lysis buffer (50 mM HEPES pH 7.5, 500 mM NaCl, 5% (v/v) Glycerol, 10 mM Imidazole and 2 mM TCEP) supplemented with protease inhibitor cocktail (Serva). In case of GST-Cdk1/His-Cyclin B1 complex, cell pellet was re-suspended in GST-lysis buffer (50 mM HEPES pH 7.5, 300 mM NaCl, 5% (v/v) Glycerol, 2 mM TCEP) and in case of GST-MPS1 in GST-lysis buffer (50 mM HEPES pH 7.5, 500 mM NaCl, 5% (v/v) glycerol, 1 mM TCEP). After sonication, cell suspension was clarified and applied to a pre-equilibrated, 5 mL HisTALON Cartridge pre-packed TALON Superflow Resin (Clontech) or Glutathione Sepharose 4 Fast Flow beads (GE Healthcare), respectively. Column or beads were washed with at least 10 volumes of respective lysis buffer and protein was eluted using either His-lysis buffer supplemented with 250 mM imidazole or GST-lysis buffer supplemented with 20 mM reduced Glutathione, respectively. Protein fractions were pooled and concentrated in order to load on a Superdex 200 16/60 size exclusion chromatography (SEC) column, pre-equilibrated with SEC buffer (20 mM HEPES pH 7.5, 200 mM NaCl, 5% (v/v) Glycerol and 1 mM TCEP), and in case of GST-MPS1 with SEC buffer (25 mM HEPES pH 7.5, 150 mM NaCl, 5% (v/v) glycerol, 1 mM TCEP). Fractions containing protein of interest, as analyzed by 12.5% SDS-PAGE, were pooled, concentrated, flash frozen in liquid nitrogen and stored at – 80°C. CENP-OPQUR, CENP-QU and CENP-OP has been purified as described previously (Pesenti et al., 2018). CENP-OPQU$^{\Delta 1\text{-}114}$R was purified using the previously described protocol for CENP-OPQUR wild-type (Pesenti et al., 2018). *Escherichia coli* BL21 (DE3) cells harboring vectors expressing 6His-MBP-CENP-U58-114 wt and mutants were grown in Terrific Broth at 37°C to an OD600 of 0.6 - 0.8, when 0.2 mM IPTG was added and the culture was grown at 18°C for ~15 hours. Cell pellets were resuspended in lysis buffer (20 mM Tris/HCl pH 6.8, 300 mM NaCl, 7 mM imidazole, 5% (v/v) glycerol and 1 mM TCEP) supplemented with protease inhibitor cocktail, lysed by sonication and cleared by centrifugation at 108,000 g at 4°C for 1 hour. The cleared lysate was applied to 5 mL HisTALON Cartridges pre-packed with TALON Superflow Resin (Clontech) pre-equilibrated in lysis buffer, washed with 10 volumes of lysis buffer. Bound proteins were eluted with lysis buffer supplemented with 250 mM imidazole. The fractions containing the 6His-MBP-CENP-$^{U58\text{-}114}$wt and mutants were then diluted in 10 volumes of 20 mM Tris/HCl pH 6.8, 5% glycerol, 1 mM TCEP. Resource Q anion exchange chromatography column (GE Healthcare) was pre-equilibrated in 20 mM Tris/HCl pH 6.8, 30 mM NaCl, 5% (v/v) glycerol, 1 mM TCEP. The sample now adjusted to a salt concentration of 30 mM was loaded onto the Resource Q column and eluted with a linear gradient of 30 - 1000 mM NaCl in 15 bed column volumes. Fractions containing 6His-MBP-CENP-$^{U58\text{-}114}$wt and mutants complex were pooled and concentrated and loaded onto a Superdex 75 16/60 SEC column (GE Healthcare) pre-equilibrated in SEC buffer (20 mM Tris pH 6.8, 300 mM NaCl,

5% (v/v) glycerol and 1 mM TCEP). Fractions containing 6His-MBP-CENP-$^{U58-114}$wt and mutants were concentrated, flash-frozen in liquid nitrogen and stored at −80°C. CENP-LN, CENP-C$^{1-544}$HKI^{57-C}M, Mis12, NDC80, KNL1, BUB1:BUB3 and BUBR1:BUB3 complexes, BUB1 kinase (BUB1$^{705-1050}$) and Aurora B kinase (Aurora B$^{45-344}$:INCENP$^{835-903}$) were expressed and purified according to previously published protocols (Breit et al., 2015; Huis In 't Veld et al., 2016; Klare et al., 2015; Pentakota et al., 2017; Petrovic et al., 2014; Sessa et al., 2005)

In vitro assembly of rKT and rKT containing CENP-U$^{\Delta 1-114}$

Reconstitution of rKT and rKT containing CENP-U$^{\Delta 1-114}$ particles was performed as previously published in Pesenti et al., 2018. In brief, a stoichiometric amount of purified CENP-LN, CENP-CHKIM, CENP-OPQUR, Mis12, Ndc80 and KNL1 complexes were incubated at 4°C for minimum 1 hour and purified by SEC using a buffer containing 20 mM Tris pH 6.8, 300 mM NaCl, 5% (v/v) glycerol and 1 mM TCEP.

Recombinant proteins fluorescence labeling

MBP-PLK1^{PBD}, MBP-PLK1^{201A}, CENP-OPQUR and CENP-OPQU$^{\Delta 1-114}$R were labeled using Alexa Fluor 488 Protein Labeling Kit (ThermoFisher Scientific, Waltham, Massachusetts, United States) according to the manufacturer instructions.

In vitro phosphorylation of rKT, rKT containing CENP-U$^{\Delta 1-114}$, CENP-OPQUR, -OPQU$^{\Delta 1-114}$R, -OP, -QU, 6His-MBP-CENP-U$^{58-114}$-WT and mutants, BUB1:BUB3 and BUBR1:BUB3

CENP-OPQUR, -OPQU$^{\Delta 1-114}$R, CENP-QU and CENP-OP purified from insect cell were carefully de-phosphorylated by treatment with lambda phosphatase (produced in house) as described previously (Pesenti et al., 2018). The phosphorylation of these recombinant proteins was performed in SEC buffer supplemented by 2 mM of ATP and 10 mM of $MgCl_2$. A ratio kinase/protein of 1/25 for CDK1 (in house production), Aurora B (in house production), MPS1 (in house production) and BUB1 (in house production), and 1/20 to 1/10 for PLK1 (in house production) depending of the activity of the recombinant kinase. If the proteins used in the reaction were previously treated with lambda phosphatase 1mM of sodium orthovanadate and 5μM of okadaic acid were added to the reaction. The reactions were incubated at 4 or 10°C for 16h and submitted to analyze by mass spectrometry and phosphostaining.

Phosphostaining of recombinant proteins

Samples containing equal amount of un-phosphorylated and phosphorylated proteins were separated by 12.5% SDS-PAGE and stained by Pro-Q Diamond phosphoprotein stain (Invitrogen, Carlsbad, California, United States) according to the manufacturer instruction. Images were acquired using a BioRAD chemiDoc MP Imaging System (BioRAD). Images were adjusted using Image Lab software Version 5.2 (BioRAD). The same gel was subsequently stained with Coomassie stain.

Analytical SEC

Analytical size exclusion chromatography was carried out on a Superdex 200 5/150 or Superose 6 5/150 in a buffer containing 20 mM Tris or HEPES pH 6.8, 300 mM NaCl, 2,5% (v/v) glycerol and 1 mM TCEP on an ÄKTA micro system. All samples were eluted under isocratic conditions at 4°C in SEC buffer (20 mM Tris or HEPES pH 6.8, 300 mM NaCl, 5% (v/v) glycerol and 1 mM TCEP) at a flow rate of 0.15 ml/min. Elution of proteins was monitored at 280 nm and 488 nm in case of MBP-PLK1^{210A} and MBP-PLK1^{PBD} labeled with Alexa488. 100 μL fractions were collected and analyzed by SDS-PAGE and Coomassie blue staining. In experiments were MBP-PLK1^{210A} and MBP-PLK1^{PBD} labeled with Alexa488 were used, the in-gel detection of the fluorescence was detected using a BioRAD chemiDoc MP Imaging System (BioRAD). To detect the formation of a complex, proteins were mixed at the concentrations of 5 μM in 50 μl, incubated for at least 1 hour on ice, subjected to SEC then analyzed by SDS-PAGE.

Analytical ultracentrifugation (AUC)

Sedimentation velocity experiments were performed in an Optima XL-A analytical ultracentrifuge (Beckman Coulter, Palo Alto, US-CA) with Epon charcoal-filled double-sector quartz cells and an An-60 Ti rotor (Beckman Coulter, Palo Alto, US-CA). Samples were centrifuged at 203,000xg at 20°C and 500 radial absorbance scans at 488 nm and collected with a time interval of 1 min. Analysis of MBP-PLK1^{210A} and MBP-PLK1^{210A}:CENP-OPQUR complex were carried out at 20°C in 20 mM HEPES pH 7.5, 2.5% (v/v) glycerol, 300 mM NaCl and 1 mM TCEP.

Mass spectrometry and phosphorylation site analysis

Liquid chromatography coupled with mass spectrometry was used to assess the phosphorylation status of CenpU. CENP-QU or CENP-OPQUR FL were *in vitro* phosphorylated by CDK1 or PLK1 alone or in combination. Mutants (S77A/T78A or 98A) were phosphorylated in the context of MBP-CENP-U$^{58-114}$. Controls by omitting the kinase(s) were performed for all samples. Samples were reduced, alkylated and digested with LysC/Trypsin and prepared for mass spectrometry as previously described (Rappsilber et al., 2007). 100 ng of obtained peptides were separated on a ThermoFisher Scientific EASY-nLC 1000 HPLC system (ThermoFisher Scientific, Waltham, Massachusetts, United States) using an 45 min gradient from 5%–60% acetonitrile with 0.1% formic acid and directly sprayed via a nano-electrospray source in a Q Exactive (ThermoFisher Scientific, Waltham, Massachusetts, United States)

(Michalski et al., 2011). The Q Exactive was operated in data-dependent mode acquiring one survey scan and subsequently ten MS/MS scans (Olsen et al., 2007). Samples were measured at least three times.

QUANTIFICATION AND STATISTICAL ANALYSIS

Cell image analysis

For Imaris quantifications, CREST signal was used as reference channel and spots were placed on kinetochores using automatic setting in Imaris. Four spots of same size were placed manually in cytoplasm and their average was used as background for respective channel. After background subtraction, ratio of intensity mean signal of the protein of interest versus CREST was used to plot the graphs. In case of U2OS lacO-lacI experiments, GFP channel was used as a reference channel to put a surface manually on ectopic foci. A spot was placed manually in the cytoplasm and the value was used as background for respective channel. After background subtraction, intensity mean of PLK1 versus GFP was used to plot the graphs. ImageJ/Fiji quantifications were performed using a semi-automated script (Pan et al., 2017). Intensity measurements were exported to Excel (Microsoft) and graphs were plotted using Prism software. Sample size is indicated for each figure. Statistical analysis was performed with a rank sum, nonparametric test comparing two unpaired groups (Mann-Whitney test). Symbols indicates: n.s = $p > 0.05$, * = $p \leq 0.05$, ** = $p \leq 0.01$, *** = $p \leq 0.001$, **** = $p \leq 0.0001$.

AUC analysis

Data was analyzed using the SEDFIT software (Schuck, 2000) in terms of continuous distribution function of sedimentation coefficients (c(S)). The protein partial specific volume was estimated from the amino acid sequence using the program SEDNTERP. Data were plotted using the program GUSSI, which is freely available from https://www.utsouthwestern.edu/labs/mbr/software/. The calculated values for the buffer density and the viscosity are 1.01928 g/ml and 1.1190 cP respectively. The calculated values of the partial specific volume [V(bar), inverse of density] at 20°C for MBP-PLK1^{210A} is 0.7424 ml/g and for MBP-PLK1^{210A}:CENP-OP-QUR complex is 0.7404 ml/g.

Mass Spectrometry analysis

Mass spectrometry raw files were processed with the MaxQuant software (version 1.5.2.18) using a reduced database containing only the proteins present in the samples for the search giving deamidation (NQ), oxidation (M) and phosphorylation (STY) as variable modifications and carbamidomethylation (C) as fixed modification (Cox and Mann, 2008). A false discovery rate cut-off of 1% was applied at the peptide and protein levels and as well on the phosphorylation site table (Cox and Mann, 2008). Identified phosphorylation sites were further analyzed for their localization probability and only unambiguous identified sites were kept. MS/MS spectra were additionally manually inspected. Peptide peaks and isotope patterns from MS scans containing Thr78 or Thr98 were directly extracted from Xcalibur (ThermoFisher Scientific, Waltham, Massachusetts, United States).

Article

Current Biology

Destabilization of Long Astral Microtubules via Cdk1-Dependent Removal of GTSE1 from Their Plus Ends Facilitates Prometaphase Spindle Orientation

Graphical Abstract

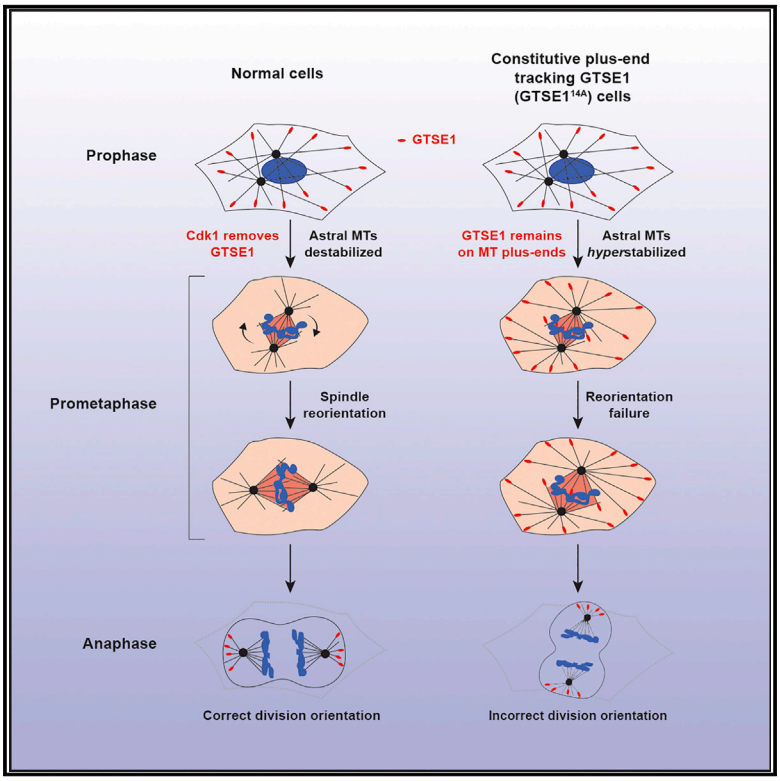

Highlights

- Cdk1 activity disrupts GTSE1 interaction with EB1 and MT plus-end tracking in mitosis
- The regulated loss of GTSE1 from MT plus ends destabilizes long astral MTs
- Destabilization of long astral MTs facilitates spindle reorientation in prometaphase

Authors

Divya Singh, Nadine Schmidt, Franziska Müller, Tanja Bange, Alexander W. Bird

Correspondence

alex.bird@mpi-dortmund.mpg.de

In Brief

Singh et al. show that Cdk1 negatively regulates astral microtubule length in prometaphase by disrupting the interaction between the plus-end tracking proteins EB1 and GTSE1. This disruption preferentially destabilizes long astral microtubules, which facilitates cells' ability to reorient their spindles in response to cell-shape/adhesion cues.

Singh et al., 2021, Current Biology *31*, 766–781
February 22, 2021
https://doi.org/10.1016/j.cub.2020.11.040

CellPress

CellPress

Current Biology

Article

Destabilization of Long Astral Microtubules via Cdk1-Dependent Removal of GTSE1 from Their Plus Ends Facilitates Prometaphase Spindle Orientation

Divya Singh,[1] Nadine Schmidt,[1] Franziska Müller,[1] Tanja Bange,[2] and Alexander W. Bird[1,3,*]
[1]Max Planck Institute of Molecular Physiology, Otto-Hahn-Strasse 11, 44227 Dortmund, Germany
[2]Department for Systems Chronobiology, Institute of Medical Psychology, LMU Munich, Goethestrasse 31/ I, 80336 Munich, Germany
[3]Lead Contact
*Correspondence: alex.bird@mpi-dortmund.mpg.de
https://doi.org/10.1016/j.cub.2020.11.040

SUMMARY

The precise regulation of microtubule dynamics over time and space in dividing cells is critical for several mitotic mechanisms that ultimately enable cell proliferation, tissue organization, and development. Astral microtubules, which extend from the centrosome toward the cell cortex, must be present for the mitotic spindle to properly orient, as well as for the faithful execution of anaphase and cytokinesis. However, little is understood about how the dynamic properties of astral microtubules are regulated spatiotemporally, or the contribution of astral microtubule dynamics to spindle positioning. The mitotic regulator Cdk1-CyclinB promotes destabilization of centrosomal microtubules and increased microtubule dynamics as cells enter mitosis, but how Cdk1 activity modulates astral microtubule stability, and whether it impacts spindle positioning, is unknown. Here, we uncover a mechanism revealing that Cdk1 destabilizes astral microtubules in prometaphase and thereby influences spindle reorientation. Phosphorylation of the EB1-dependent microtubule plus-end tracking protein GTSE1 by Cdk1 in early mitosis abolishes its interaction with EB1 and recruitment to microtubule plus ends. Loss of Cdk1 activity, or mutation of phosphorylation sites in GTSE1, induces recruitment of GTSE1 to growing microtubule plus ends in mitosis. This decreases the catastrophe frequency of astral microtubules and causes an increase in the number of long astral microtubules reaching the cell cortex, which restrains the ability of cells to reorient spindles along the long cellular axis in early mitosis. Astral microtubules thus must not only be present but also dynamic to allow the spindle to reorient, a state assisted by selective destabilization of long astral microtubules via Cdk1.

INTRODUCTION

Astral microtubules are essential for several aspects of cell division. For example, early in mitosis they guide orientation of the spindle in response to cell-shape and adhesion cues, and later in mitosis they guide anaphase-specific spindle positioning and cleavage furrow ingression.[1–6] The formation of astral microtubules at the transition from interphase to mitosis, when the large interphase microtubule array is reorganized into a more compact mitotic structure, is accompanied by a dramatic increase in global microtubule dynamics (i.e., shorter half-lives, increased catastrophes, and reduced rescues).[7–9] This global increase in microtubule dynamics has been linked to activation of the Cdk1 kinase by Cyclin B, a major regulator of entry into mitosis,[10–12] and is typically considered necessary for disassembling large interphase arrays, assembling the mitotic spindle, and aiding in search and capture of chromosomes. Less attention has been focused on how Cdk1-Cyclin B activity specifically modulates the properties of astral microtubules to facilitate early mitotic processes such as spindle positioning.[13]

Astral microtubule dynamics can be controlled by modulating microtubule nucleation and stability at the centrosome[14–17] and by impacting their dynamic plus ends.[18–20] Major regulators of microtubule plus-end dynamics are the EB family of proteins, which are directly recruited to the growing plus ends of microtubules.[21] EB1 is required for astral microtubule stability and spindle orientation, including spindle positioning in response to cell-shape and adhesion cues.[18,22–26] EB1 itself impacts microtubule dynamics but can also directly recruit to the microtubule plus ends a large number of microtubule plus-end tracking proteins ("+TIPS"), themselves necessary for several microtubule-dependent functions.[21] How distinct compositions of +TIPs are differentially recruited to EB proteins, to tune the dynamics and interactions of different microtubule populations for specific functions, including spindle orientation, is not well understood.[22,23] Many +TIPs interact with EB1 via short conserved peptide motifs (SxIP) surrounded by basic, serine, and proline residues.[27] Phosphorylation of +TIPs close to these motifs appears to be a common mechanism to modulate their association with growing microtubule plus ends, by abolishing their interaction with EB1.[27] However, Cdk1 phosphorylation has not been directly linked to its role in modulating microtubule dynamics at mitotic onset via a such a mechanism.

A critical role of astral microtubules is to facilitate the positioning of the mitotic spindle within the cell. This not only ensures accurate segregation of genetic material but also facilitates embryogenesis, cell-fate determination, and tissue organization.[22,28] Depending on the cell type and environment, multiple intrinsic and extrinsic determinants (e.g., localization of polarity factors, or cell-cell contacts and other external mechanical cues) cooperate with astral microtubules to determine the positioning of the spindle.[4,29,30] One of the first elements described to guide positioning of the spindle, during embryogenesis in amphibians, was cell shape.[31] Cell shape is also frequently observed to correlate with spindle orientation in a microtubule-dependent fashion in cell lines plated as monolayers in tissue culture, where, as observed earlier in embryos, spindles are positioned during mitosis with respect to the long axis of the cell established prior to mitotic onset.[1,29,30] In these single-cell systems, it was later shown that extracellular adhesion forces from retraction fibers, which also contribute to cell shape, are transduced to the spindle to guide orientation.[32,33] It has recently become clear, however, that both cell shape and mechanical forces can separately provide cues for spindle orientation, and that spindle positioning in response to cell shape per se plays an important role in tissue and developmental contexts.[34,35] Because centrosomes are not always aligned with respect to the long cell-shape axis (and retraction fiber forces) prior to mitosis, the spindle may need to "reorient," or rotate by as much as 90 degrees in early mitosis in order to align with shape and adhesion cues.[36]

Astral microtubules function in spindle orientation by physically coupling the spindle to the cell cortex, where protein complexes interact with microtubules and provide the cues and forces required for positioning the spindle. The best characterized of these complexes contains the LGN, NuMA, and $G\alpha_i$ proteins and cooperates with the microtubule motor dynein to link microtubules to the cell cortex and exert a pulling force.[4,37] The specific localization of such proteins can dictate spindle positioning, for example, in polarized systems or in response to adhesion patterns, as well as dynamically respond to the position of the spindle and chromosomes.[38–40] Given the central role of astral microtubules in spindle orientation, it is not surprising that many factors identified as important for spindle orientation promote the formation of astral microtubules, and when perturbed thus compromise the ability of astral microtubules to reach the cell cortex.[16,18,23,41–46,47]

While the precise regulation of microtubule dynamics has been shown to be critical for processes such as chromosome capture and alignment, or microtubule-kinetochore error correction,[48] less is clear about the importance of astral microtubule dynamics to spindle positioning, or its precise regulation mechanisms. A few studies suggest that indeed more than the presence of astral microtubules at the cell cortex is required for spindle positioning. Depletion of Kinesin-13 or Kinesin-8 microtubule destabilizing kinesins, which results in longer, stabilized astral microtubules, has been shown to negatively impact spindle positioning.[39,41,42,49–51] Second, depolymerization of astral microtubules engaged with cortical NuMA/dynein complexes has been theorized to provide forces required for spindle positioning.[22,52,53] Pathways specifically regulating astral microtubule dynamics in time and space, however, remain unclear.

We previously found that a +TIP, GTSE1, is important for astral microtubule stability and spindle orientation.[41,54] During mitosis GTSE1 inhibits the ability of the microtubule depolymerase MCAK to depolymerize microtubules, thus stabilizing them.[41] However, while GTSE1 interacts with microtubules and tracks microtubule plus ends through interaction with EB1 in interphase, during mitosis it does neither.[54] Instead, it is recruited to the mitotic spindle by direct interaction with spindle-associated clathrin heavy chain (CHC).[55] GTSE1 is thus restricted to the inner spindle and spindle poles, where it controls astral microtubule length, likely via inhibition of centrosomal MCAK. This raises the question of why GTSE1 would be removed from all microtubules and EB1 at plus ends in mitosis, only to be recruited back to inner spindles via a different mechanism. Here, we show that loss of the microtubule stabilizing protein GTSE1 from microtubule plus ends at the onset of prometaphase is regulated by Cdk1. This is important to destabilize long astral microtubules, which allows spindles to more efficiently react to cell cues and reorient in prometaphase.

RESULTS

Cdk1-Dependent Phosphorylation of GTSE1 Abolishes Its Interaction with EB1 and Plus-End Tracking during Mitosis

GTSE1 associates with the microtubule lattice and growing microtubule plus ends in interphase, but this localization is reduced during mitosis.[54] To characterize the association of GTSE1 with growing microtubule plus ends as cells enter mitosis, we imaged U2OS cells expressing GTSE1-GFP from a bacterial artificial chromosome (BAC) and a marker for microtubule plus ends (EB3-mCherry) and quantified the relative intensities of both proteins at individual microtubule ends (Figure 1A; Figure S1A). GTSE1 accumulated at EB3-positive microtubule plus ends in interphase but was rapidly displaced from plus ends in mitosis, coincident with nuclear envelope breakdown (NEBD) (Figure 1A). We also observed these GTSE1-GFP dynamics in the non-transformed cell line RPE-1, indicating it is a typical behavior of the protein (Video S1). In prometaphase and metaphase, GTSE1 localized to the inner spindle, which we previously reported is via interaction with spindle-associated clathrin.[55] Upon anaphase onset, GTSE1 resumed its localization at growing microtubule plus ends (Figure S1A). To establish whether the loss of GTSE1 plus-end tracking during mitosis was due to loss of interaction with EB1, we used purified EB1-GST to pull down GTSE1 from U2OS cell extracts arrested in either the S-phase or prometaphase. GTSE1 from the S-phase, but not prometaphase, extract interacted with EB1-GST, confirming the loss of this interaction in mitosis (Figure S1B).

We next sought the mechanism by which cells control the dissociation of GTSE1 from EB1 in mitosis. We first confirmed that GTSE1 is hyperphosphorylated during mitosis in human cells, as has been shown in mouse and *Xenopus* (Figure S1C).[54,56] We next asked whether this affected the GTSE1-EB1 interaction by performing an EB1-GST pull-down as above using mitotic lysates, but after treatment with λ-phosphatase to dephosphorylate mitotic proteins. GTSE1 from dephosphorylated mitotic lysate could be pulled down by EB1, suggesting that this interaction is regulated by mitotic-specific

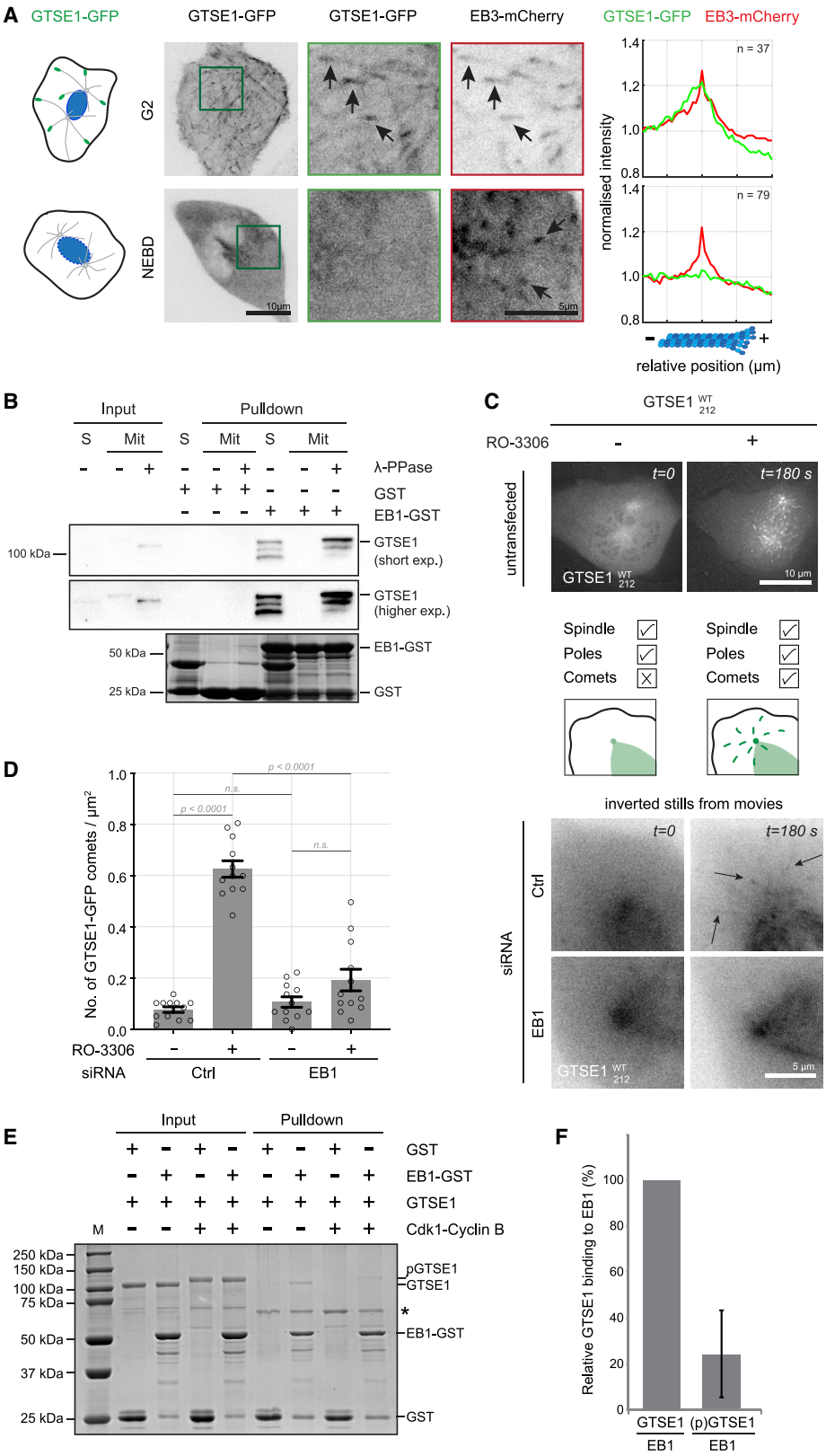

(legend on next page)

phosphorylation (Figure 1B). To identify the kinase(s) responsible for disrupting the GTSE1 interaction with EB1 in mitosis, we asked whether inhibition of different mitotic kinases with small molecular inhibitors could force GTSE1 to localize to growing microtubule plus ends in mitosis. U2OS cells expressing GTSE1-GFP from a BAC transgene ($GTSE1^{WT}_{212}$)[54] were thus imaged in mitosis after treatment with inhibitors against Aurora A (MLN8054), Aurora B (ZM447439), Plk1 (BI 2536), or Cdk1 (RO-3306).[57–60] No discernable plus-end tracking of GTSE1-GFP was observed in mitosis in untreated cells (Figure 1C; Figure S1D) nor after inhibition of Aurora A, Aurora B, or Plk1 (Figure S1D). Inhibition of Aurora A did cause complete displacement of GTSE1 from the mitotic spindle, as previously reported.[61] In contrast, inhibition of Cdk1 shortly after NEBD led to the appearance of moving comet-like structures of GTSE1-GFP, similar to that seen in interphase (Figure 1C; Video S2). Quantification of the number of detectable GTSE1-GFP comets in mitosis indicated an approximately 6-fold increase after Cdk1 inhibition (Figure 1D). Washing out the Cdk1 inhibitor 30 s later caused these comets to rapidly disappear again (Video S3). Quantification of GTSE1-GFP levels at EB3-mCherry-labeled plus ends in a dual-labeled cell line indicated that 90% of these plus ends now accumulated GTSE1 after Cdk1 inhibition (Figures S1E and S1F). We further confirmed the Cdk1-dependent delocalization of GTSE1 from plus ends in RPE-1 cells (Video S4). All Cdk1-inhibition experiments were performed within a few minutes of NEBD to avoid cells exiting mitosis during analysis. To confirm that the relocalization of GTSE1 to growing microtubule plus ends was dependent on EB1, we repeated these experiments after EB1 depletion (Figures 1C and D; Figure S1G; Video S5). Following RNAi of EB1, we no longer observed an increase in the number of GTSE1-GFP-positive comets after Cdk1 inhibition. To test whether phosphorylation of GTSE1 by Cdk1 directly disrupts its interaction with EB1 *in vitro*, we performed pull-down experiments with purified proteins after phosphorylation by Cdk1-CyclinB. EB1-GST was incubated with either unphosphorylated or Cdk1-phosphorylated GTSE1. Phosphorylation of GTSE1 reduced its interaction with EB1 by 80% (Figures 1E and 1F). In contrast, phosphorylation of EB1 by Cdk1 did not affect its interaction with GST-GTSE1, demonstrating that this interaction is regulated by the action of Cdk1 on GTSE1 (Figures S1H and S1I). Thus, Cdk1 removes GTSE1 from growing microtubule plus ends during mitosis by disrupting its interaction with EB1, constraining GTSE1 to the clathrin-associated inner spindle.

Mutating Cdk1- and Mitosis-Dependent Phosphorylation Sites around Its EB1-Interaction Motifs Causes GTSE1 to Plus End Track in Mitosis

We next aimed to identify the phosphorylation sites on GTSE1 that regulate the interaction with EB1. First, we identified mitosis-specific phosphorylation sites on GTSE1 by immunoprecipitating it from U2OS cells arrested in either the S-phase or prometaphase and subjecting it to mass spectrometry analysis. This revealed a total of 29 mitosis-specific phosphosites on GTSE1 from a total peptide coverage of 70% (Figure 2A; Table S1). 27 of these 29 sites were previously identified in large-scale proteomic studies in mitotic cells (Figure 2A; Table S1).[62–64] Many of the mitosis-specific phosphorylation sites identified by us and others were concentrated in a region 20 residues before and after the two SxIP motifs, suggesting that phosphorylation at these sites could potentially hinder electrostatic interactions between GTSE1 and EB1 (Figure 2A). We next purified His-tagged GTSE1, phosphorylated it *in vitro* with recombinant Cdk1-Cyclin B (Figure S2A), and analyzed phosphorylated residues by mass spectrometry (Table S1). 55 sites on GTSE1 were phosphorylated by Cdk1 *in vitro*. Combining all mitotic and Cdk1-dependent phosphorylation data, we identified 14 phosphorylation sites within a 58-amino-acid stretch surrounding the two SxIP sites on GTSE1 (Figure 2A).

To evaluate which phosphorylation sites in the proximity of the EB1-interaction motifs in GTSE1 disrupted EB1-interaction during mitosis, we generated a series of GTSE1-GFP mutants with these phosphorylation sites mutated to alanine (Figure S2B). The mutants were then transiently transfected into GTSE1 knockout cells ($GTSE1^{KO}$),[41] and their ability to plus end track in mitotic cells was evaluated by live microscopy. We initially mutated two conserved Cdk1 consensus sites located directly adjacent to the SxIP motifs ($GTSE1^{TP/AA}$). This mutant, however, displayed no apparent plus-end tracking in mitosis (Figure S2B).

Figure 1. Cdk1 Phosphorylates GTSE1 and Prevents Its Interaction with EB1 and Microtubule Plus-End Tracking in Mitosis

(A) Schematic depicting GTSE1 localization at microtubule plus ends in G2 and at nuclear envelope breakdown (NEBD). Live-cell images of U2OS cells stably expressing GTSE1-GFP from a BAC (green) and EB3-mCherry from a plasmid (red). Scale bar, 10 μm. Magnified insets show GTSE1 (middle) and EB3 (right) with arrows indicating comets. Scale bar, 5 μm. Averaged line-scan intensity profiles of microtubule plus ends show relative intensities of GTSE1-GFP (green) and EB3-mCherry (red), centered at the maximum EB3 intensity. Line-scan insets indicate the number of microtubule plus ends from 2 cells in 2 experiments expressing comparable levels of both transgenes.

(B) Disruption of the EB1-GTSE1 interaction during mitosis requires phosphorylation. Immunoblot (anti-GTSE1) of an EB1-GST pull-down using U2OS cells arrested in S-phase or prometaphase; the latter was also treated (or not) with λ-phosphatase (λ-PPase). Below is Coomassie Blue staining of GST and EB1-GST pulled down in all three conditions.

(C) Inhibition of Cdk1 restores EB1-dependent GTSE1 plus-end tracking in mitosis. Top: stills from live-cell microscopy of U2OS cells stably expressing GTSE1-GFP ($U2OS^{WT}_{212}$) before and after addition of RO-3306. Scale bar, 10 μm. Middle: schematic depicting GTSE1 localization (in green) on the spindle, poles, and comets in early prometaphase before and after addition of Cdk1 inhibitor (RO-3306). Bottom: $U2OS^{WT}_{212}$ cells were transfected with control (Ctrl) or EB1 siRNA for 48 h. Cells were imaged at 1-s intervals for 20 s in prometaphase and then treated with RO-3306 and imaged similarly for 3 min. Arrows indicate comets. Scale bar, 5 μm. See Videos S2 and S5.

(D) Quantification of the number of GTSE1-GFP comets per unit area in the four conditions shown in (C). n = 12 cells per condition over 2 experiments. p values are from an unpaired two-tailed t test using Welch's correction. Error bars indicate SEM.

(E) Cdk1 phosphorylation of GTSE1 reduces interaction with EB1 *in vitro*. Coomassie Blue stained gel of a GST pull-down assay using EB1-GST as bait to pull down purified GTSE1 phosphorylated (or not) with Cdk1-Cyclin B. *GSH beads blocked using BSA.

(F) Quantification of relative GTSE1 binding to EB1 before and after phosphorylation of GTSE1 by Cdk1. n = 3 experiments. Error bars represent SD.

See also Figure S1 and Videos S1, S2, S3, S4, and S5.

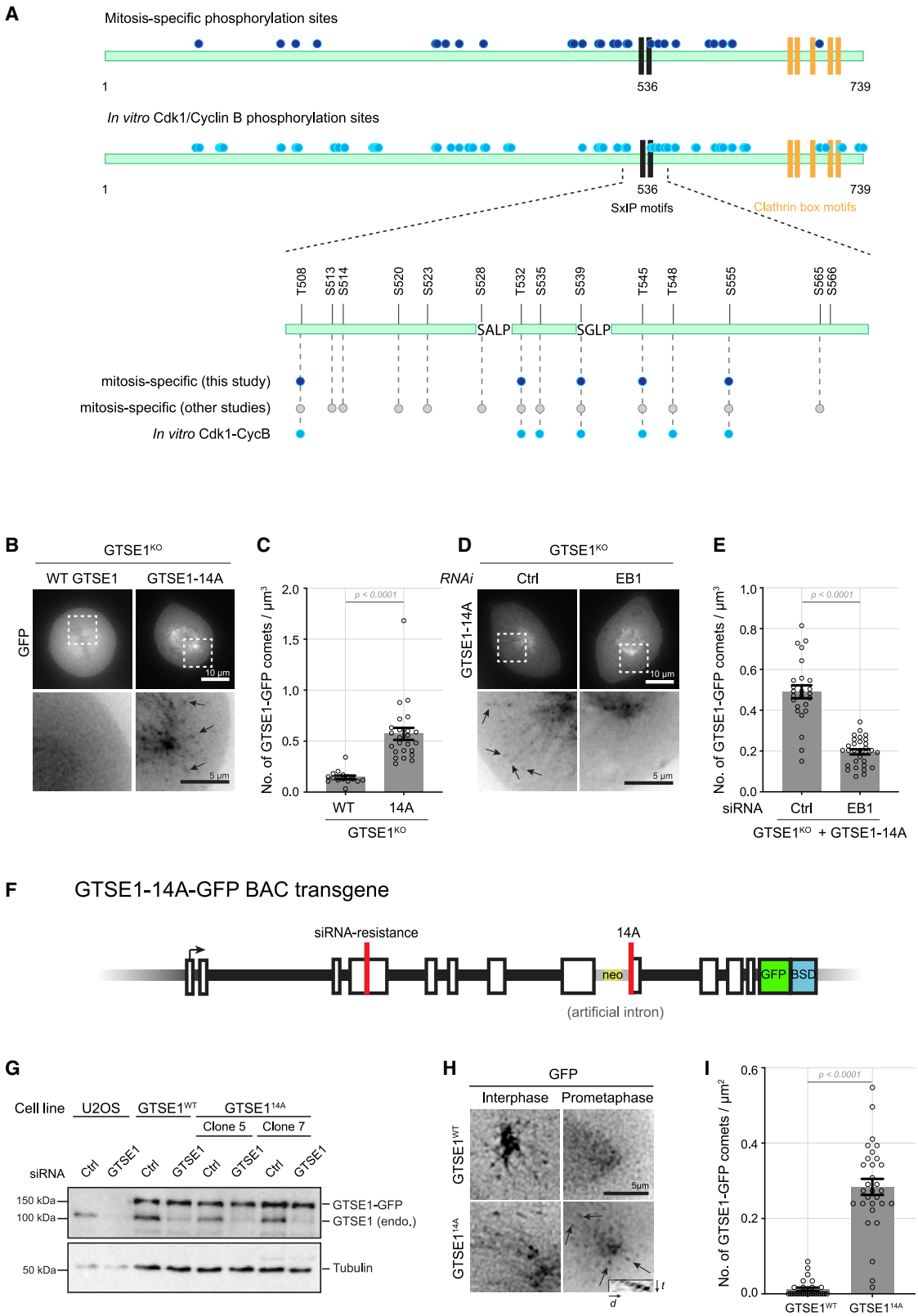

Figure 2. A Phospho-mutant of GTSE1 Plus-End Tracks in Mitosis in an EB1-Dependent Manner

(A) Mitotic and Cdk1 phosphorylation sites identified in this study in GTSE1. Schematic representation of GTSE1, with two SxIP motifs shown in black and clathrin box motifs in yellow. Mitosis-specific (dark-blue circles) and *in vitro* Cdk1-Cyclin B (light blue circles) phosphosites are shown. The 58 amino acid region between

(legend continued on next page)

We then constructed several mutants with increasing numbers of mutated phosphorylation sites. While all mutants plus end tracked in interphase, we could only observe weak tip-tracking in mitosis after mutating 7 phosphosites and found that mutation of all 14 phosphosites resulted in the most robust plus-end tracking (Figures 2B and 2C; Figure S2B; Video S6). To confirm this mutant was plus-end tracking via EB1 interaction, we depleted EB1 in the presence of the mutant, which indeed abolished the increased plus-end tracking (Figures 2D and 2E; Figure S2C; Video S6). Thus, disrupting mitotic phosphorylation of GTSE1 prevents removal of GTSE1 from microtubule plus ends at mitosis.

To study the importance of the disruption of the EB1-GTSE1 interaction for mitotic function, we generated the 14 phosphosite mutations in an RNAi-resistant BAC harboring GTSE1-GFP in a single step via ESI mutagenesis (Figure 2F).[65] We then generated stable and clonal cell lines expressing RNAi-resistant versions of either wild-type (WT) GTSE1-GFP or the GTSE1-14A-GFP mutant ($GTSE1^{WT}$ and $GTSE1^{14A}$) (Figure 2G). Both transgenes exhibited plus-end tracking in interphase (Video S7). Additionally, GTSE1-14A-GFP expressed at near endogenous levels was clearly recruited to growing microtubule plus ends in mitosis, unlike WT GTSE1-GFP (Figures 2H and 2I; Video S7).

Phosphoregulated Removal of GTSE1 from Microtubule Plus Ends Restricts Astral Microtubule Length, in Cooperation with the Destabilizing Kinesin Kif18B

In interphase, GTSE1 tracks microtubule plus ends and stabilizes microtubule growth duration.[54] We thus analyzed whether microtubule stability in mitotic $GTSE1^{14A}$ cells was changed as compared to WT cells. Fixed imaging of metaphase $GTSE1^{14A}$ cells revealed an increased abundance of astral microtubules, that appeared to often reach the cell cortex (Figure 3A). We then used EB1 comet signals and their distances from the centrosome to quantify the number and individual lengths of astral microtubules.[19,55] As previously shown, depletion of GTSE1 reduces both the number and length of metaphase astral microtubules, and an RNAi-resistant GTSE1-GFP transgene ($GTSE1^{WT}$) rescues these defects (Figures 3A–3C).[41,55] Cells expressing equivalent protein levels of GTSE1-14A, however, displayed significantly longer and more abundant astral microtubules in metaphase, even before RNAi-depletion of endogenous GTSE1 (Figures 3A–3C). We verified this effect with an independently isolated cell line generated with the same mutant BAC (Figures S3A and S3B). This indicated a dominant effect of the mutant, which was expected given the gain of function of EB1-dependent microtubule plus-end localization. This stabilization effect of the mutant appeared specific to astral microtubules, as there was not a significant change in the number of EB1 comets within the spindle as compared to U2OS or $GTSE1^{WT}$ cells (Figure 3D), and the total tubulin intensity within the inner spindle was not affected (Figures 3E and S3C). Plotting the distribution of metaphase astral microtubule lengths among cell lines suggested that, in the $GTSE1^{14A}$ mutant, there was a selective increase in the number of longer (6–10 μm) astral microtubules (Figure 3C). Indeed, plotting the fold difference in astral microtubule numbers at different lengths showed no significant difference of microtubules less than 6 μm long, nearly 2-fold as many microtubules 6–9 μm long, and over 3-fold more microtubules longer than 9 μm in $GTSE1^{14A}$ cells (Figure S3D).

GTSE1-mediated stabilization of astral microtubules in WT cells is clathrin dependent, requiring clathrin-mediated recruitment of GTSE1 to the spindle poles and inner spindle.[55] Due to the localization of GTSE1-14A protein to astral microtubule plus ends (where clathrin is absent) and the dominant impact on astral length, we hypothesized the gain of function of this mutant would be clathrin independent. To test this, we depleted CHC in $GTSE1^{WT}$ and $GTSE1^{14A}$ cells (Figure S3E). Indeed, even after removal of CHC, the GTSE1-14A mutations remained able to induce longer astral microtubules, supporting a clathrin-independent gain of GTSE1 function at astral microtubule plus ends (Figures 4A–4C). Furthermore, CHC still contributed to astral microtubule length in $GTSE1^{14A}$ cells (Figure 4C), cf. dark-green and light-green traces), again indicating separate pathways.

To determine whether GTSE1-14A was impacting a known astral microtubule (de)stabilization pathway, we performed a genetic analysis of our mutant with Kif18B, a kinesin that localizes specifically to astral microtubule plus ends and promotes astral

508 and 566 on GTSE1 is shown in more detail, with mitosis-specific phosphorylation sites identified by others in high throughput MS studies (gray circles) additionally represented.

(B) Single frames from live imaging in mitosis of U2OS cells knocked out for GTSE1 ($GTSE1^{KO}$). Cells were transiently transfected with plasmids expressing WT GTSE1-GFP or GTSE1-14A-GFP. Scale bar, 10 μm. Magnified insets show comets indicated by arrows in cell expressing GTSE1-14A. Scale bar, 5 μm. See Video S6.

(C) Quantification of number of GFP comets per unit volume from experiment shown in (B). n = 16–24 cells from 3 independent experiments. p value from unpaired t test with Welch's correction.

(D) Single frames from live imaging in mitosis of $GTSE1^{KO}$ cells treated with control (Ctrl) or EB1 siRNA for 48 h followed by transient transfection of plasmids expressing GTSE1-14A-GFP. Scale bar, 10 μm. Magnified insets show comets indicated by arrows. Scale bar, 5 μm. See Video S7.

(E) Quantification of number of GTSE1-14A-GFP comets per unit volume in presence and absence of EB1 from experiment shown in (D). n = 25–30 cells from 3 independent experiments. p value from unpaired t test with Welch's correction.

(F) A schematic showing the design of the GTSE1-14A-GFP BAC containing exons and introns and mutations for resistance to siRNA. The intron between exons 8 and 9 and the WT exon 9 was replaced with an artificial intron that confers neomycin resistance and the mutated exon 9 with 14 Ser/Thr residues mutated to alanine.

(G) Western blot showing comparable levels of BAC-expressed GFP tagged WT ($GTSE1^{WT}$) or two independent clones expressing GTSE1-14A transgene ($GTSE1^{14A}$), before and after depletion of endogenous GTSE1 for 48 h using siRNA. Immunoblot using anti-GTSE1 and anti-tubulin antibodies.

(H) Stills from live microscopy of U2OS cells stably expressing WT GTSE1 ($GTSE1^{WT}$) or GTSE1-14A ($GTSE1^{14A}$) in interphase and prometaphase. Arrows indicate comets in mitosis in $GTSE1^{14A}$ and the inset shows a kymograph of a GTSE1-14A labeled microtubule plus end. Scale bar, 5 μm.

(I) Quantification of number of GTSE1-GFP comets per unit area in prometaphase from experiment shown in (H). At least 28 cells of $GTSE1^{WT}$ and $GTSE1^{14A}$ were analyzed from 3 independent experiments. p value from unpaired t test with Welch's correction. Error bars indicate SEM unless otherwise indicated.

See also Figure S2, Table S1, and Videos S6 and S7.

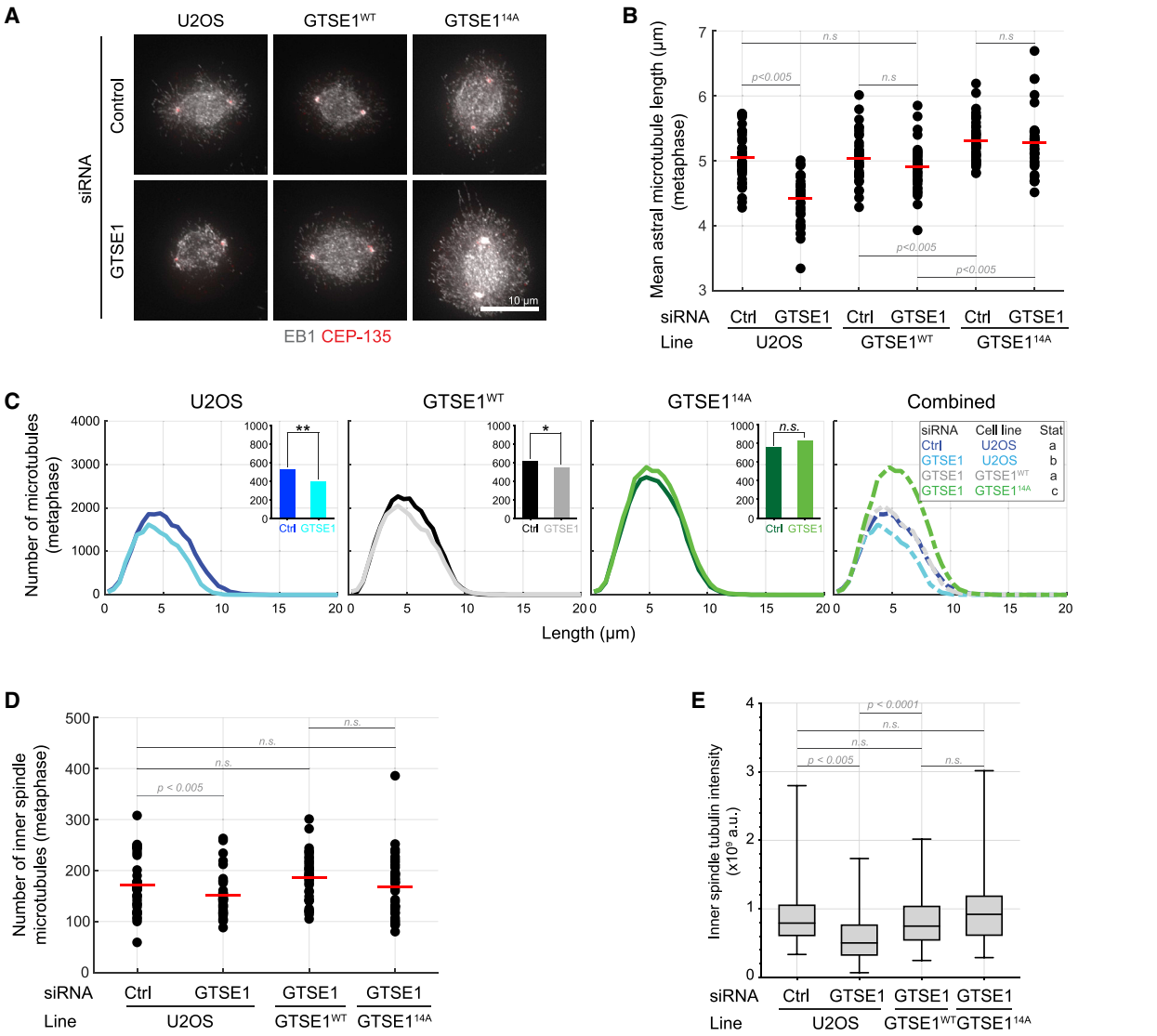

Figure 3. Restoring GTSE1 to Growing Microtubule Plus Ends in Mitosis Stabilizes Astral Microtubules

(A) Immunofluorescence images in metaphase of U2OS, GTSE1^{WT}, and GTSE1^{14A} cells treated with control (Ctrl) or GTSE1 siRNA. Cells were fixed and stained with antibodies against EB1 (in gray) and CEP-135 (in red). Scale bar, 10 μm.

(B) Quantification of mean astral microtubule length from experiment shown in (A). The red horizontal line indicates mean. n = 37 cells from 3 independent experiments, pooled for representation. p values are from an unpaired two-tailed Student's t test.

(C) Distributions of astral microtubule numbers as a function of their lengths. n = 37 cells from 3 independent experiments, pooled for representation. The mean number of astral microtubules is presented as histograms in insets. *p < 0.05, **p < 0.01, unpaired two-tailed Student's t test. The inset in "Combined" shows the significances (different letters indicate groups differing significantly).

(D) Quantification of number of EB1 labeled microtubules in the inner spindle in metaphase U2OS, GTSE1^{WT}, and GTSE1^{14A} cells after control (Ctrl) or GTSE1 RNAi. The mean is shown in red. p values are from an unpaired two-tailed Student's t test.

(E) Boxplot showing intensity of tubulin in the inner spindle from experiment shown in (C). n = 55–76 cells, from 3 independent experiments. p values are from an unpaired t test with Welch's correction.

See also Figure S3.

microtubule destabilization via cooperation with MCAK.[19,66] Depletion of Kif18B in U2OS cells, similar to the GTSE1-14A mutant, increased astral microtubule length and abundance, consistent with previous reports[19] (Figure 4D; Figures S3F and S3G). Combining these two perturbations, however, did not further stabilize astral microtubules, suggesting that both hyper-stabilization phenotypes are caused by disruption of the same pathway. Furthermore, when Kif18B is depleted, loss of GTSE1 (which normally leads to a dramatic destabilization of microtubules), has little effect on astral microtubule stability (Figure 4D; Figure S3G). Together, these results suggest that both the removal of GTSE1 and the presence of Kif18B at astral microtubule plus ends is required for destabilization of astral microtubules.

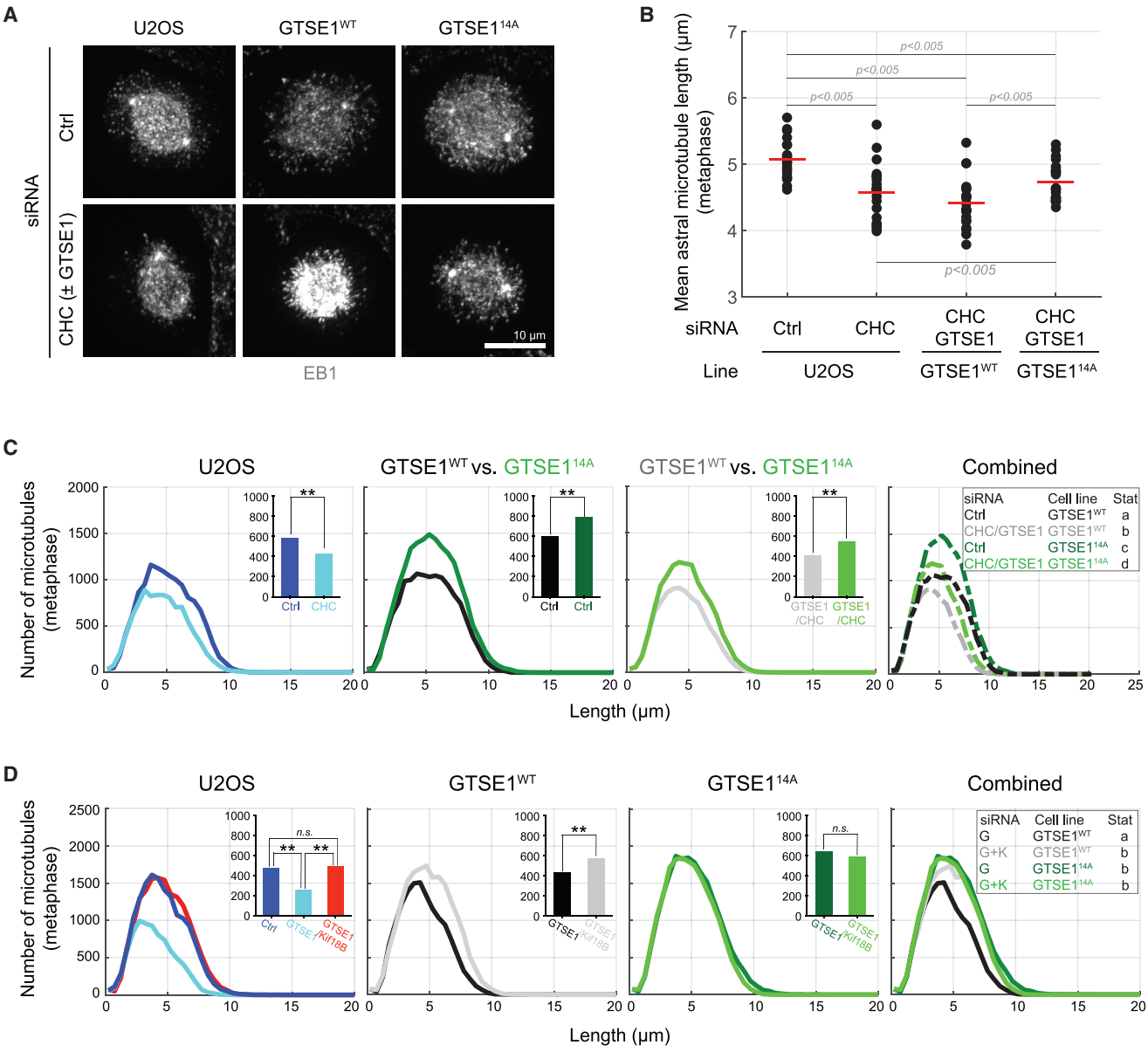

Figure 4. Phosphoregulated Removal of GTSE1 from Microtubule Plus Ends Restricts Astral Microtubule Length in Cooperation with the Destabilizing Kinesin Kif18B

(A) Immunofluorescence images in metaphase of U2OS, GTSE1^{WT}and GTSE1^{14A} cells treated with control (Ctrl), CHC siRNA alone (U2OS), or a combination of CHC and GTSE1 siRNA (in GTSE1^{WT}and GTSE1^{14A}). Cells were fixed and stained with antibodies against EB1. Scale bar, 10 µm.

(B) Quantification of mean astral microtubule lengths from 3D reconstructions of images of cells in metaphase of U2OS, GTSE1^{WT}, and GTSE1^{14A} cells treated with control (Ctrl), CHC siRNA alone (U2OS), or a combination of CHC and GTSE1 siRNA (in GTSE1^{WT} and GTSE1^{14A}). The mean is marked in red. n = 22–43 cells from 3 independent experiments, pooled for representation. p values are from an unpaired two-tailed Student's t test.

(C) Distributions of astral microtubule numbers in metaphase of U2OS, GTSE1^{WT}, and GTSE1^{14A} cells treated with control (Ctrl), CHC siRNA alone (U2OS), or a combination of CHC and GTSE1 siRNA (in GTSE1^{WT} and GTSE1^{14A}) as a function of their lengths. n = 22 cells from 3 independent experiments, pooled for representation. The mean number of astral microtubules is presented as histograms in insets. **p < 0.01, unpaired two-tailed Student's t test. The inset in "Combined" shows the significances (different letters indicate groups differing significantly).

(D) Distributions of astral microtubule numbers in metaphase of U2OS, GTSE1^{WT}, and GTSE1^{14A} cells treated with control (Ctrl), GTSE1 siRNA alone, or in combination with Kif18B siRNA (in U2OS) and GTSE1 alone or a combination of GTSE1 and Kif18B siRNA (in GTSE1^{WT} and GTSE1^{14A}) as a function of their lengths. n = 33 cells from 3 independent experiments, pooled for representation. The mean number of astral microtubules is presented as histograms in insets. **p < 0.01, unpaired two-tailed Student's t test. The inset in "Combined" shows the significances (different letters indicate groups differing significantly).

See also Figure S3.

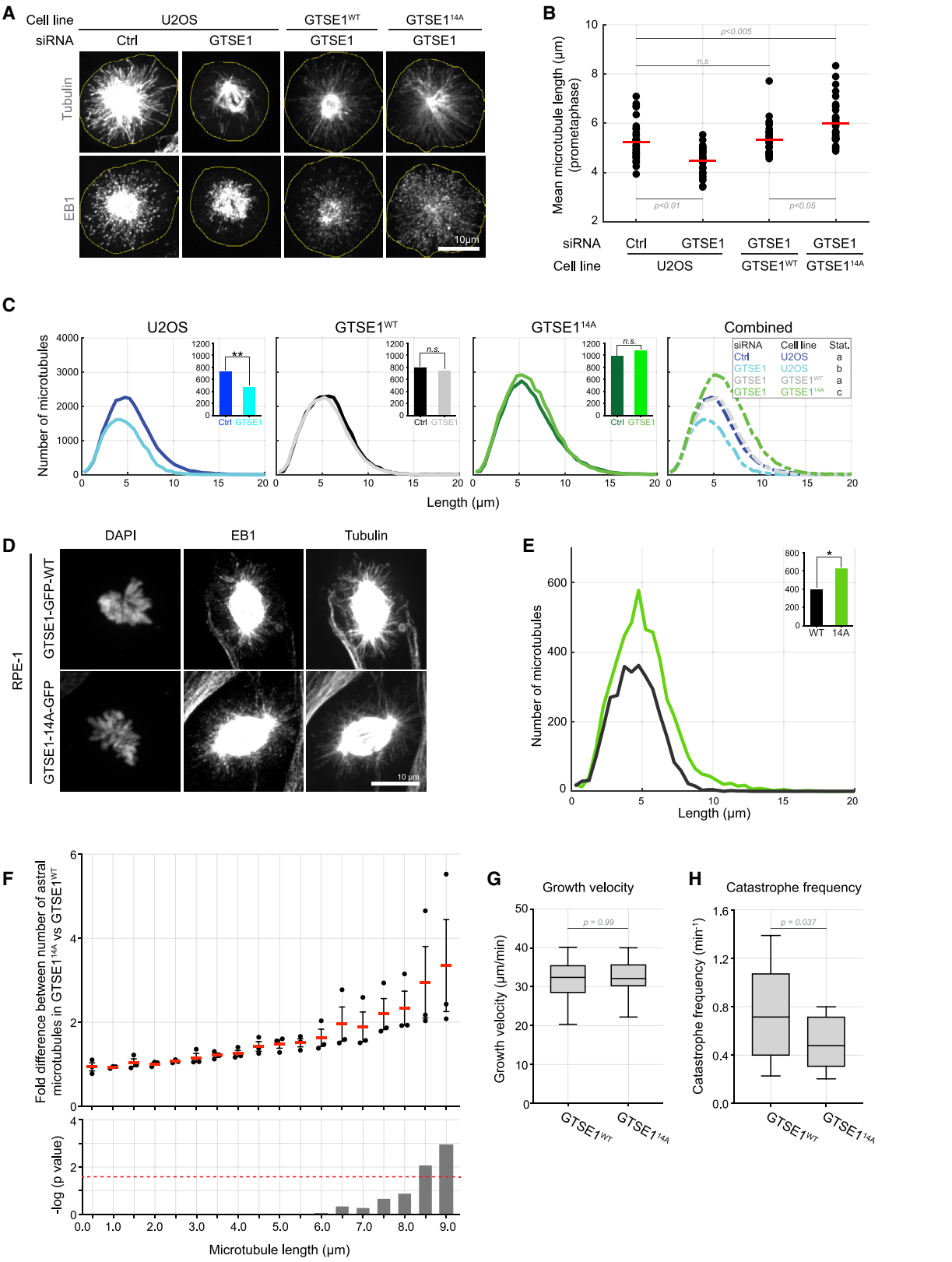

(legend on next page)

Restoring GTSE1 Plus-End Tracking in Prometaphase Selectively Stabilizes Long Astral Microtubules

As Cdk1-mediated removal of GTSE1 from growing microtubule plus ends occurs at NEBD, we next asked whether the defect in the ability of the mitotic GTSE1^{14A} cells to control astral microtubule length also manifested in prometaphase. Quantification of microtubule lengths and abundance from asters in early prometaphase cells, both in U2OS and RPE-1 cells, revealed a significantly increased number of astral microtubules, which was again characterized by an apparent increase in the number of longer astral microtubules (Figures 5A–5E). Plotting the fold difference in astral microtubule numbers of different lengths in prometaphase cells showed no significant difference of microtubules less than 8.5 μm long, yet over 3-fold more microtubules longer than 8.5 μm in GTSE1^{14A} cells compared to GTSE1^{WT} (Figure 5F). For insight into the underlying changes leading to longer astral microtubules, we analyzed microtubule dynamics in prometaphase cells additionally expressing mCherry-EB3. While we did not observe any change in microtubule growth rates in GTSE1^{14A} cells compared to GTSE1^{WT}, the average catastrophe frequency reduced (Figures 5G and 5H). Thus, the GTSE1-EB1 interaction is negatively regulated by phosphorylation in early mitosis to confine the number of long astral microtubules, likely by increasing the chance of microtubule catastrophe.

Normally, GTSE1 localization to microtubule plus ends is restored at anaphase onset, consistent with a decline in Cdk1 activity at this time[54] (Figure S1A). As both regulation of EB1 interaction with +TIPs and astral microtubule length are important for anaphase spindle functions,[5,67,68] we asked whether preventing GTSE1 from relocalizing to microtubule plus ends at this stage would destabilize microtubules or impact anaphase progression. A cell line containing GTSE1 mutated at its two SxIP motifs (GTSE1$^{SK}{}_{202}$) no longer interacts with EB1 nor plus end tracks and is proficient for metaphase astral microtubule length and chromosome alignment but fails to restore GTSE1 plus-end tracking at anaphase onset.[41,54] These cells did not display any major defects in anaphase astral microtubule stability (Figure S4A). We quantified anaphase function by live-cell imaging to monitor the timing from anaphase onset to initiation of cytokinesis furrow ingression. While depleting cells of GTSE1 indicated a role for GTSE1 in anaphase progression, the GTSE1$^{SK}{}_{202}$ mutant showed no changes, suggesting that regulation of the EB1-GTSE1 interaction is not functionally important to these processes (Figure S4B).

Phospho-Dependent Displacement of GTSE1 from Microtubule Plus Ends in Prometaphase Is Required for Spindle Reorientation via Astral Microtubule Destabilization

Given the importance of astral microtubules for spindle reorientation, we asked whether restoring the mitotic EB1-GTSE1 interaction and subsequent hyperstabilization of astral microtubules led to a defect in spindle orientation that could explain the need to disrupt this interaction. We previously reported that cells depleted of GTSE1 are defective in metaphase spindle orientation with respect to the substrate due to shorter astral microtubules.[41] We thus asked whether the longer metaphase astral microtubules observed in GTSE1^{14A} cells also perturbed this type of orientation. While the defect after GTSE1 depletion was restored in GTSE1^{WT} cells, GTSE1^{14A} cells were defective, suggesting the failure of these cells to destabilize long astral microtubules compromised spindle orientation in metaphase (Figure S4C). Loss of GTSE1 causes an increased mitotic duration due to chromosome congression defects.[41,55,69] As chromosome congression defects can perturb spindle orientation,[40] we analyzed mitotic timing in GTSE1^{14A} cells. We did not observe any defect, suggesting they are proficient for chromosome alignment and that this could not explain the spindle orientation defects (Figure S4D).

We next assayed the ability of the prometaphase spindles in GTSE1^{14A} cells to orient their axis relative to cell-shape/adhesion cues by imaging cells with microtubules labeled entering and proceeding through mitosis. The initial cell-shape axis was determined 8 min prior to NEBD, and the orientation of spindles was tracked over time with respect to this axis (Figure 6A). For analysis, we considered cells in which the centrosome-centrosome axis at NEBD was more than 30 degrees deviated from the cell-shape axis (and thus would require active repositioning).

Figure 5. CDK1-Mediated Removal of GTSE1 from Microtubule Plus Ends Destabilizes Long Astral Microtubules and Promotes Microtubule Catastrophe in Prometaphase

(A) Immunofluorescence images in prometaphase of U2OS, GTSE1^{WT}, and GTSE1^{14A} cells treated with control (Ctrl) or GTSE1 siRNA. Cells were fixed and stained with anti-tubulin and anti-EB1 antibodies. Scale bar, 10 μm.

(B) Quantification of mean microtubule lengths from experiment shown in (A). Red line indicates mean. n = 43 cells over 3 independent experiments. p values are from an unpaired two-tailed Student's t test.

(C) Distributions of microtubule numbers as a function of their lengths. n = 43 cells from 3 independent experiments, pooled for representation. The mean number of microtubules is presented as histograms in insets. **$p < 0.01$, unpaired two-tailed Student's t test. The inset in "Combined" shows the significances (different letters indicate groups differing significantly).

(D) Immunofluorescence images in prometaphase of RPE-1 cells transiently transfected with plasmids expressing WT GTSE1-GFP or GTSE1-14A-GFP. Cells were fixed and stained with anti-tubulin and anti-EB1 antibodies. Scale bar, 10 μm.

(E) Distributions of number of microtubules from experiment shown in (D) as a function of their lengths. n = 8 equally transfected cells from 1 experiment. The mean number of microtubules is presented as histograms in insets. *$p < 0.05$, unpaired two-tailed Student's t test.

(F) Quantification of the fold difference in the number of microtubules of different lengths in prometaphase between GTSE1^{WT} and GTSE1^{14A}. p values are from a one-way ANOVA. The horizontal red dashed line indicates a p value of 0.05.

(G) Mean microtubule growth velocity in mitosis in GTSE1^{WT} and GTSE1^{14A} cells, obtained from videos of cells co-expressing EB3-mCherry, analyzed with plusTipTracker software. n = 17–19 cells from one experiment. p values are from an unpaired t test with Welch's correction.

(H) Mean catastrophe frequency in GTSE1^{WT} and GTSE1^{14A} cells co-expressing EB3-mCherry calculated using plusTipTracker software. n = 10–14 cells from one experiment, and only values lying between 10th and 90th percentiles were considered. p values are from an unpaired t test with Welch's correction. Error bars represent SEM unless otherwise indicated.

See also Figure S4.

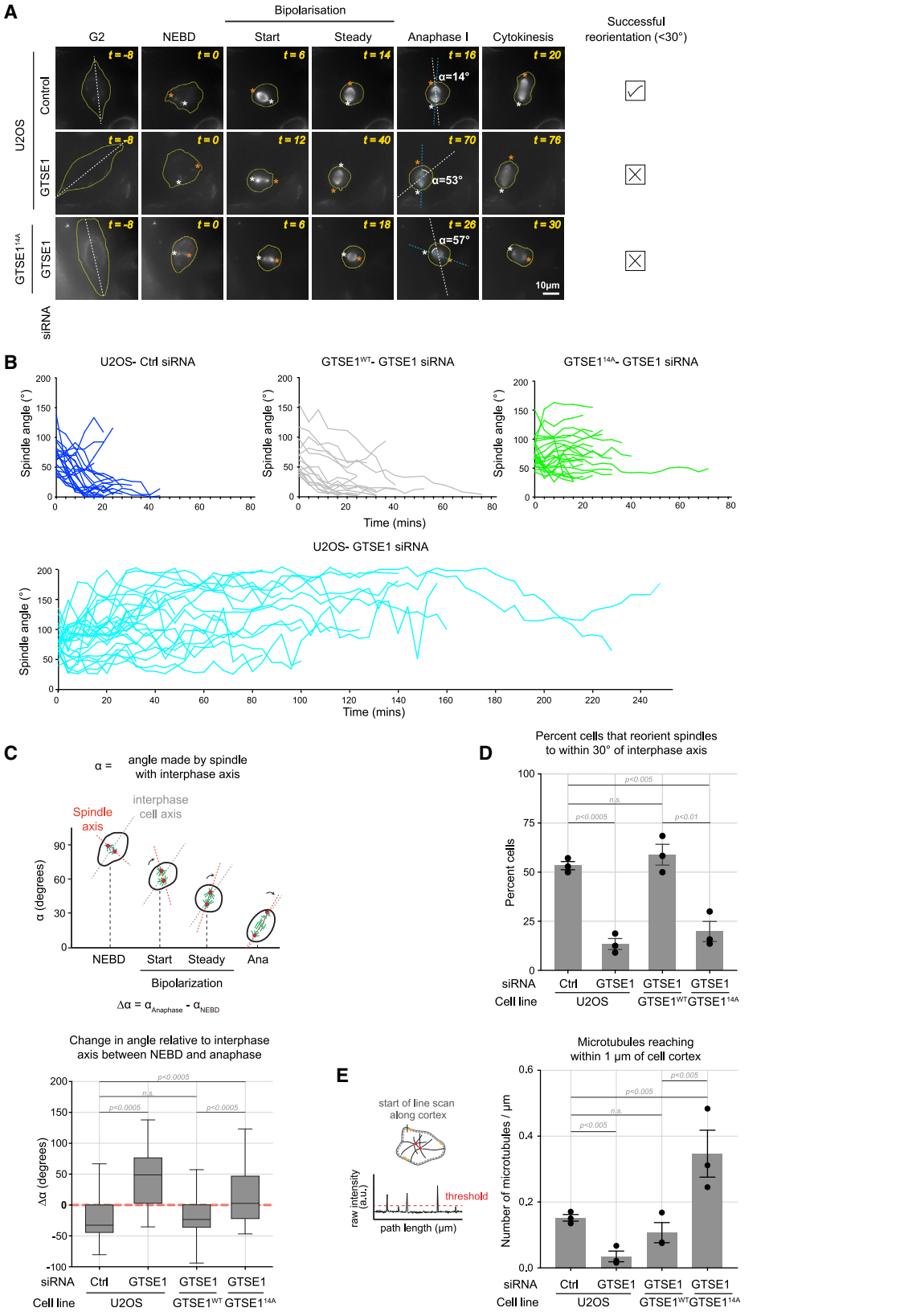

(legend on next page)

As is shown in Figure 6B, control cells rapidly oriented their spindles to align with the cell-shape axis. After depletion of GTSE1, which destabilizes astral microtubules and has previously been shown to disrupt spindle positioning, spindles no longer align efficiently but appear to display random and rapid movements (Figure 6B, bottom panel). The presence of a WT copy of GTSE1 rescues this defect, but the GTSE1-14A mutant, which stabilizes astral microtubules, displays spindle behavior distinct from WT or GTSE1-depleted cells. Namely, the spindles appear to resist rotation, mostly maintaining their position established at NEBD.

To quantify the differences in rotation behavior of these spindles, we determined the difference between the final orientation of the spindle (i.e., at the metaphase-anaphase transition; $\alpha_{Anaphase}$) and the initial orientation of the spindle (α_{NEBD}), relative to the interphase shape axis (again in cells with an initial α_{NEBD} of more than 30 degrees; Figure 6C). As expected, spindles in both control cells and GTSE1^{WT} cells corrected their orientation, indicated by the angle becoming smaller (Figure 6C). In cells depleted of GTSE1, spindle orientation angles actually became more deviant than they started, consistent with a lack of microtubules resulting in a complete failure to sense cell-shape/adhesion cues. In contrast, spindles in GTSE1^{14A} cells on average did not change from their initial, off-axis position, reflected by their traces and suggesting that they resisted rotation during prometaphase. Quantification of the final position of spindles at anaphase onset relative to the shape axis revealed that, although the rotation behavior of spindles of GTSE1-depleted cells and GTSE1-14A cells contrasted (reflecting the opposite impacts on microtubule dynamics), both led to a similar failure to efficiently align spindles prior to anaphase (Figure 6D). As the orientation defect in GTSE1-14A cells could arise from excessive and/or stabilized engagement of cortical astral microtubule-interacting complexes, we measured the number of astral microtubules reaching the cell cortex in prometaphase (Figure 6E). Consistently, cells expressing GTSE1-14A contained more than 3 times the number of astral microtubules reaching the cortex than under WT conditions. Together, these results indicate that mitotic phosphorylation of GTSE1, which disrupts the interaction with EB1 and microtubule plus-end tracking, is required for spindle orientation. Cells containing mutations disrupting this regulation are unable to reorient the mitotic spindle in response to cell-shape and adhesion cues, which we attribute to the coincident stabilization of long astral microtubules reaching the cell cortex.

DISCUSSION

Despite the importance of astral microtubules to cell division, little is known about how their dynamics and stability are specifically controlled, and how this may affect their functions. Here, we show that astral microtubule destabilization is controlled at NEBD by Cdk1 phosphorylation of GTSE1, which disrupts the recruitment of GTSE1 to growing microtubule plus ends by abolishing its interaction with EB1. Loss of GTSE1 from microtubule plus ends in mitosis promotes astral microtubule instability by raising their catastrophe frequency. We find that this destabilization of long astral microtubules in prometaphase is required for spindle orientation in response to cell-shape and adhesion cues.

While Cdk1 activity has been previously linked to spindle orientation via negatively regulating the cortical localization of NuMA,[70] we show the first link via regulation of microtubule stability. Cdk1 activity has long been known to promote increased microtubule dynamics as cells transition to mitosis[10–12]; to our knowledge, this is the first example of a mechanism linking Cdk1 phosphorylation of a target protein to specifically control astral microtubule stability in metazoans. Targeting an EB1-+TIP interaction may be a repeated mechanism for the Cdk1-dependent regulation of microtubule dynamics that happens in mitosis. Although only a few +TIPs have been reported to be removed from microtubules in mitosis,[71–73] we have identified via quantitative mass spectrometry more than 10 SxIP-containing proteins that interact with EB1 in interphase but not mitosis (unpublished data). Some have likely been previously overlooked due to commonly used overexpressing GFP-transgene constructs. Indeed, when dramatically overexpressed, GTSE1-GFP plus end tracks during mitosis (unpublished observation), probably due in part to overwhelming the cellular phosphorylation machinery.

While loss of EB1 (and thus the associated array of +TIPs from growing ends) has been documented to inhibit microtubule dynamics and destabilize astral microtubules,[18,23,74] our work here highlights that there is a dynamic and precise tuning of astral microtubule length and dynamics mediated by the

Figure 6. Restoring GTSE1 to Growing Microtubule Plus Ends in Mitosis Inhibits the Ability of Cells to Reorient Spindles in Response to Cell-Shape Cues

(A) Stills from live-cell imaging of U2OS and GTSE1^{14A} cells treated with control (Ctrl) or GTSE1 siRNA for 48 h and imaged in presence of the cell-permeable siR-Tubulin dye. Individual centrosomes are labeled with * in white and orange. Dashed white lines indicate the cell-shape axis; dashed blue lines indicate the spindle axis. Scale bar, 10 μm.

(B) Traces of spindle angles relative to the interphase axis after NEBD till anaphase onset in individual cells in different conditions from experiment shown in (A). n = 21–26 cells are shown from 1 experiment.

(C) Top panel: schematic illustrating the change in angle α made by the spindle with the interphase axis at different phases as indicated on the graph. An example illustrating progressive spindle rotation to eventually align along the interphase axis is shown. A negative value for Δα indicates spindle movement toward long axis, while a positive value indicates spindle movement away from the long axis. Right panel: boxplot of Δα values in U2OS, GTSE1^{WT}, and GTSE1^{14A} cells. p values are from an unpaired t test with Welch's correction.

(D) Quantification of spindle positioning defect in experiment shown in (A). Only cells that have their spindle axis more than 30° away from the interphase axis at NEBD are considered for analysis. Percentage of cells that are able to align their spindles to within 30° of their interphase axis is shown (with individual experimental means displayed). n = 39–51 cells over 3 experiments. p values are from an unpaired t test.

(E) Left panel: schematic illustrating the method for semi-automatic detection of microtubules reaching the cortex. Right panel: quantification of the number of microtubules reaching within 1 μm of the cell cortex, per μm of cortex in 2-dimensions in U2OS, GTSE1^{WT}, and GTSE1^{14A} prometaphase cells (with individual experimental means displayed). n = 30–37 cells over 3 independent experiments. p values are from an unpaired t test. All error bars represent SEM unless otherwise indicated.

See also Figure S4.

spatiotemporal regulation of +TIP interactions. Perturbations causing dramatic global hyperstabilization of microtubules throughout the cell, such as treatment with Taxol, are known to affect spindle positioning.[75,76] What we show here is that even relatively subtle changes to astral microtubule stability nevertheless have a quite dramatic impact on spindle repositioning in prometaphase and thus must be precisely controlled. Our results suggest that the spindle orientation defect exhibited by GTSE1^{14A} cells arises from hyperstabilization of long astral microtubules in prometaphase. This is consistent with the observation that perturbation of the microtubule destabilizing kinesin Kif18B, which also results in longer astral microtubules, leads to spindle orientation defects.[19,39,50,66,77] The coincident removal of GTSE1 and recruitment of Kif18B to astral microtubule plus ends by EB1 at the onset of mitosis highlights the importance of regulating astral microtubule length and dynamics via modulation of +TIP-EB1 interactions.[19,66] In fact, our results indicate that the microtubule stabilization phenotypes of GTSE1-14A are due to disruption of the same pathway as depletion of Kif18B.

Why must long astral microtubules be destabilized in prometaphase? We show that, in stark contrast to cells lacking astral microtubules, which display exaggerated and random spindle movements, cells with hyperstabilized long astral microtubules resist spindle rotation in response to cell shape. Under these conditions, a combination of excessive engagement of cortical microtubule-interaction sites and a reduced likelihood of a catastrophe/depolymerization event could pose a significant barrier to reorientation of a spindle.[78] Excessive longer astral microtubules may establish too many cortical interactions early in prometaphase and, in combination with a lack of microtubule dynamicity, inhibit the ability of spindles to dynamically react to cell shape. This is consistent with a simple model from Minc et al.[22] of how microtubules can position nuclei by sensing cell geometry, which was also applied to spindle reorientation in response to cell shape.[2] In this model, microtubules "probe" the cell shape and exert length-dependent pulling when engaged with force generators at the cell cortex. Consistently, increasing the numbers of microtubules reaching the cortex in the first division of *C. elegans* embryos increases the "centering stiffness" of the spindle or force required to displace the spindle within the cell.[49] Additionally, evidence suggests that microtubules may need to be dynamic at the cell cortex in order to generate depolymerization-coupled force generation, for example, via NuMA, to position spindles.[52,53,76,79]

We show that Cdk1 destabilizes long astral microtubules by removing the microtubule-stabilizing protein GTSE1 from growing microtubule plus ends. GTSE1 stabilizes microtubules by inhibiting the microtubule depolymerization activity of MCAK, which localizes to both astral microtubule plus ends as well as centrosomes during mitosis.[41,80,81] During mitosis, GTSE1 is normally only present at spindle poles and the inner spindle, through recruitment by clathrin.[55] Clathrin is thus required for GTSE1's normal microtubule stabilization ability and likely stabilizes astral microtubules by inhibition of centrosomal MCAK.[55] However, we have shown here that the ability of GTSE1-14A mutant to stabilize astral microtubules is independent of clathrin, consistent with it inhibiting a distinct pool of MCAK at growing microtubule plus ends. Thus, the control of astral microtubule (in)stability requires the concerted removal of an MCAK inhibitor (GTSE1) and recruitment of an MCAK potentiator (Kif18b) at astral microtubule plus ends.

The decreased catastrophe frequency and longer lengths of microtubules observed when GTSE1 is not removed from astral microtubule plus ends (i.e., in GTSE1^{14A} cells) thus likely reflects inhibition of the microtubule plus-end-associated pool of MCAK. Indeed, the reduction in catastrophe frequency we observe in GTSE1^{14A} mutant cells is similar to that observed when MCAK is inhibited in PtK2 cells.[82] Consistently, inhibition of MCAK by RNAi leads to longer astral microtubules and spindle positioning defects.[41,42] In the future, molecular definition of the MCAK inhibition mechanism of GTSE1 will allow point mutation of GTSE1-14A to test this directly.

In summary, we have provided evidence here that astral microtubule dynamics must be precisely regulated to ensure spindle orientation mechanisms, in particular, that long astral microtubules must be selectively destabilized. We further have elucidated a molecular pathway by which these changes are both spatially and temporally regulated by Cdk1 activity at the onset of prometaphase: by disrupting recruitment of the microtubule stabilizing protein GTSE1 to microtubule plus ends via EB1. Regulation of EB1-+TIP complexes may be a common theme by which Cdk1 induces the substantial changes in microtubule dynamics accompanying mitosis.

STAR★METHODS

Detailed methods are provided in the online version of this paper and include the following:

- KEY RESOURCES TABLE
- RESOURCE AVAILABILITY
  - Lead Contact
  - Materials Availability
  - Data and Code Availability
- EXPERIMENTAL MODEL AND SUBJECT DETAILS
- METHOD DETAILS
  - Cloning and plasmids
  - Construction of stable cell lines and transient transfection
  - RNAi
  - Live cell imaging
  - Immunofluorescence (IF)
  - Microtubule dynamics
  - Immunoprecipitation (IPs)
  - Western blot (WB)
  - Antibodies
  - Mass spectrometry
  - Protein purification
  - *In vitro* protein phosphorylation
  - GST Pulldowns
- QUANTIFICATION AND STATISTICAL ANALYSIS
  - Image analysis and quantification
  - Statistical analysis

SUPPLEMENTAL INFORMATION

Supplemental Information can be found online at https://doi.org/10.1016/j.cub.2020.11.040.

ACKNOWLEDGMENTS

We thank Andrea Musacchio, Priyanka Singh, and Carolin Körner for purified Cdk1-Cyclin B and other reagents. We thank Makarand Tapaswi for help with MATLAB analyses. We thank members of the Bird and Vader labs for helpful discussions. We thank Gerben Vader, Arnaud Rondelet, Harish Thakur, and Marina Mapelli for comments on the manuscript. The authors declare no competing financial interests. This work was supported by the Max Planck Institute of Molecular Physiology.

AUTHOR CONTRIBUTIONS

Conceptualization, D.S. and A.W.B.; Methodology, D.S. and A.W.B.; Software, D.S.; Formal Analysis, D.S.; Investigation, D.S., N.S., F.M., T.B., and A.W.B.; Resources, A.W.B.; Writing – Original Draft, D.S. and A.W.B.; Writing – Review and Editing, D.S. and A.W.B.; Visualization, D.S.; Supervision, A.W.B.; Project Administration, A.W.B.

DECLARATION OF INTERESTS

The authors declare no competing interests.

Received: May 26, 2020
Revised: September 25, 2020
Accepted: November 16, 2020
Published: December 16, 2020

REFERENCES

1. O'Connell, C.B., and Wang, Y.L. (2000). Mammalian spindle orientation and position respond to changes in cell shape in a dynein-dependent fashion. Mol. Biol. Cell *11*, 1765–1774.
2. Minc, N., Burgess, D., and Chang, F. (2011). Influence of cell geometry on division-plane positioning. Cell *144*, 414–426.
3. Palmer, R.E., Sullivan, D.S., Huffaker, T., and Koshland, D. (1992). Role of astral microtubules and actin in spindle orientation and migration in the budding yeast, Saccharomyces cerevisiae. J. Cell Biol. *119*, 583–593.
4. di Pietro, F., Echard, A., and Morin, X. (2016). Regulation of mitotic spindle orientation: an integrated view. EMBO Rep. *17*, 1106–1130.
5. Kiyomitsu, T., and Cheeseman, I.M. (2013). Cortical dynein and asymmetric membrane elongation coordinately position the spindle in anaphase. Cell *154*, 391–402.
6. D'Avino, P.P., Savoian, M.S., and Glover, D.M. (2005). Cleavage furrow formation and ingression during animal cytokinesis: a microtubule legacy. J. Cell Sci. *118*, 1549–1558.
7. Zhai, Y., Kronebusch, P.J., Simon, P.M., and Borisy, G.G. (1996). Microtubule dynamics at the G2/M transition: abrupt breakdown of cytoplasmic microtubules at nuclear envelope breakdown and implications for spindle morphogenesis. J. Cell Biol. *135*, 201–214.
8. Belmont, L.D., Hyman, A.A., Sawin, K.E., and Mitchison, T.J. (1990). Real-time visualization of cell cycle-dependent changes in microtubule dynamics in cytoplasmic extracts. Cell *62*, 579–589.
9. Rusan, N.M., Fagerstrom, C.J., Yvon, A.M., and Wadsworth, P. (2001). Cell cycle-dependent changes in microtubule dynamics in living cells expressing green fluorescent protein-alpha tubulin. Mol. Biol. Cell *12*, 971–980.
10. Verde, F., Labbé, J.C., Dorée, M., and Karsenti, E. (1990). Regulation of microtubule dynamics by cdc2 protein kinase in cell-free extracts of Xenopus eggs. Nature *343*, 233–238.
11. Verde, F., Dogterom, M., Stelzer, E., Karsenti, E., and Leibler, S. (1992). Control of microtubule dynamics and length by cyclin A- and cyclin B-dependent kinases in Xenopus egg extracts. J. Cell Biol. *118*, 1097–1108.
12. Stiffler, L.A., Ji, J.Y., Trautmann, S., Trusty, C., and Schubiger, G. (1999). Cyclin A and B functions in the early Drosophila embryo. Development *126*, 5505–5513.
13. Huisman, S.M., and Segal, M. (2005). Cortical capture of microtubules and spindle polarity in budding yeast - where's the catch? J. Cell Sci. *118*, 463–471.
14. Stearns, T., and Kirschner, M. (1994). In vitro reconstitution of centrosome assembly and function: the central role of gamma-tubulin. Cell *76*, 623–637.
15. Young, A., Dictenberg, J.B., Purohit, A., Tuft, R., and Doxsey, S.J. (2000). Cytoplasmic dynein-mediated assembly of pericentrin and gamma tubulin onto centrosomes. Mol. Biol. Cell *11*, 2047–2056.
16. Chen, C.-T., Hehnly, H., Yu, Q., Farkas, D., Zheng, G., Redick, S.D., Hung, H.F., Samtani, R., Jurczyk, A., Akbarian, S., et al. (2014). A unique set of centrosome proteins requires pericentrin for spindle-pole localization and spindle orientation. Curr. Biol. *24*, 2327–2334.
17. Kinoshita, K., Noetzel, T.L., Pelletier, L., Mechtler, K., Drechsel, D.N., Schwager, A., Lee, M., Raff, J.W., and Hyman, A.A. (2005). Aurora A phosphorylation of TACC3/maskin is required for centrosome-dependent microtubule assembly in mitosis. J. Cell Biol. *170*, 1047–1055.
18. Rogers, S.L., Rogers, G.C., Sharp, D.J., and Vale, R.D. (2002). Drosophila EB1 is important for proper assembly, dynamics, and positioning of the mitotic spindle. J. Cell Biol. *158*, 873–884.
19. Stout, J.R., Yount, A.L., Powers, J.A., Leblanc, C., Ems-McClung, S.C., and Walczak, C.E. (2011). Kif18B interacts with EB1 and controls astral microtubule length during mitosis. Mol. Biol. Cell *22*, 3070–3080.
20. Green, R.A., Wollman, R., and Kaplan, K.B. (2005). APC and EB1 function together in mitosis to regulate spindle dynamics and chromosome alignment. Mol. Biol. Cell *16*, 4609–4622.
21. Akhmanova, A., and Steinmetz, M.O. (2015). Control of microtubule organization and dynamics: two ends in the limelight. Nat. Rev. Mol. Cell Biol. *16*, 711–726.
22. Lu, M.S., and Johnston, C.A. (2013). Molecular pathways regulating mitotic spindle orientation in animal cells. Development *140*, 1843–1856.
23. Toyoshima, F., and Nishida, E. (2007). Integrin-mediated adhesion orients the spindle parallel to the substratum in an EB1- and myosin X-dependent manner. EMBO J. *26*, 1487–1498.
24. Korinek, W.S., Copeland, M.J., Chaudhuri, A., and Chant, J. (2000). Molecular linkage underlying microtubule orientation toward cortical sites in yeast. Science *287*, 2257–2259.
25. Lu, B., Roegiers, F., Jan, L.Y., and Jan, Y.N. (2001). Adherens junctions inhibit asymmetric division in the Drosophila epithelium. Nature *409*, 522–525.
26. Luo, Y., Ran, J., Xie, S., Yang, Y., Chen, J., Li, S., Shui, W., Li, D., Liu, M., and Zhou, J. (2016). ASK1 controls spindle orientation and positioning by phosphorylating EB1 and stabilizing astral microtubules. Cell Discov. *2*, 16033–13.
27. Honnappa, S., Gouveia, S.M., Weisbrich, A., Damberger, F.F., Bhavesh, N.S., Jawhari, H., Grigoriev, I., van Rijssel, F.J., Buey, R.M., Lawera, A., et al. (2009). An EB1-binding motif acts as a microtubule tip localization signal. Cell *138*, 366–376.
28. Morin, X., and Bellaïche, Y. (2011). Mitotic spindle orientation in asymmetric and symmetric cell divisions during animal development. Dev. Cell *21*, 102–119.
29. Nestor-Bergmann, A., Goddard, G., and Woolner, S. (2014). Force and the spindle: mechanical cues in mitotic spindle orientation. Semin. Cell Dev. Biol. *34*, 133–139.
30. Finegan, T.M., and Bergstralh, D.T. (2019). Division orientation: disentangling shape and mechanical forces. Cell Cycle *18*, 1187–1198.
31. Hertwig, O. (1884). Das Problem der Befruchtung und der Isotropie des Eies, eine Theorie der Vererbung. Jenaische Zeitschrift Fur Naturwissenschaft *18*, 276–318.
32. Théry, M., Racine, V., Pépin, A., Piel, M., Chen, Y., Sibarita, J.-B., and Bornens, M. (2005). The extracellular matrix guides the orientation of the cell division axis. Nat. Cell Biol. *7*, 947–953.

33. Fink, J., Carpi, N., Betz, T., Bétard, A., Chebah, M., Azioune, A., Bornens, M., Sykes, C., Fetler, L., Cuvelier, D., and Piel, M. (2011). External forces control mitotic spindle positioning. Nat. Cell Biol. *13*, 771–778.

34. Nestor-Bergmann, A., Stooke-Vaughan, G.A., Goddard, G.K., Starborg, T., Jensen, O.E., and Woolner, S. (2019). Decoupling the Roles of Cell Shape and Mechanical Stress in Orienting and Cueing Epithelial Mitosis. Cell Rep. *26*, 2088–2100.

35. Li, J., Cheng, L., and Jiang, H. (2019). Cell shape and intercellular adhesion regulate mitotic spindle orientation. Mol. Biol. Cell *30*, 2458–2468.

36. Peyre, E., Jaouen, F., Saadaoui, M., Haren, L., Merdes, A., Durbec, P., and Morin, X. (2011). A lateral belt of cortical LGN and NuMA guides mitotic spindle movements and planar division in neuroepithelial cells. J. Cell Biol. *193*, 141–154.

37. Kiyomitsu, T. (2019). The cortical force-generating machinery: how cortical spindle-pulling forces are generated. Curr. Opin. Cell Biol. *60*, 1–8.

38. Kiyomitsu, T., and Cheeseman, I.M. (2012). Chromosome- and spindle-pole-derived signals generate an intrinsic code for spindle position and orientation. Nat. Cell Biol. *14*, 311–317.

39. Tame, M.A., Raaijmakers, J.A., van den Broek, B., Lindqvist, A., Jalink, K., and Medema, R.H. (2014). Astral microtubules control redistribution of dynein at the cell cortex to facilitate spindle positioning. Cell Cycle *13*, 1162–1170.

40. Tame, M.A., Raaijmakers, J.A., Afanasyev, P., and Medema, R.H. (2016). Chromosome misalignments induce spindle-positioning defects. EMBO Rep. *17*, 317–325.

41. Bendre, S., Rondelet, A., Hall, C., Schmidt, N., Lin, Y.-C., Brouhard, G.J., and Bird, A.W. (2016). GTSE1 tunes microtubule stability for chromosome alignment and segregation by inhibiting the microtubule depolymerase MCAK. J. Cell Biol. *215*, 631–647.

42. Wolf, B., Busso, C., and Gönczy, P. (2019). Live imaging screen reveals that TYRO3 and GAK ensure accurate spindle positioning in human cells. Nat. Commun. *10*, 2859.

43. Thoma, C.R., Toso, A., Gutbrodt, K.L., Reggi, S.P., Frew, I.J., Schraml, P., Hergovich, A., Moch, H., Meraldi, P., and Krek, W. (2009). VHL loss causes spindle misorientation and chromosome instability. Nat. Cell Biol. *11*, 994–1001.

44. Hanafusa, H., Kedashiro, S., Tezuka, M., Funatsu, M., Usami, S., Toyoshima, F., and Matsumoto, K. (2015). PLK1-dependent activation of LRRK1 regulates spindle orientation by phosphorylating CDK5RAP2. Nat. Cell Biol. *17*, 1024–1035.

45. Gai, M., Bianchi, F.T., Vagnoni, C., Vernì, F., Bonaccorsi, S., Pasquero, S., Berto, G.E., Sgrò, F., Chiotto, A.M., Annaratone, L., et al. (2016). ASPM and CITK regulate spindle orientation by affecting the dynamics of astral microtubules. EMBO Rep. *17*, 1396–1409.

46. Kitagawa, D., Kohlmaier, G., Keller, D., Strnad, P., Balestra, F.R., Flückiger, I., and Gönczy, P. (2011). Spindle positioning in human cells relies on proper centriole formation and on the microcephaly proteins CPAP and STIL. J. Cell Sci. *124*, 3884–3893.

47. Delaval, B., Bright, A., Lawson, N.D., and Doxsey, S. (2011). The cilia protein IFT88 is required for spindle orientation in mitosis. Nat. Cell Biol. *13*, 461–468.

48. Heald, R., and Khodjakov, A. (2015). Thirty years of search and capture: The complex simplicity of mitotic spindle assembly. J. Cell Biol. *211*, 1103–1111.

49. Garzon-Coral, C., Fantana, H.A., and Howard, J. (2016). A force-generating machinery maintains the spindle at the cell center during mitosis. Science *352*, 1124–1127.

50. McHugh, T., Gluszek, A.A., and Welburn, J.P.I. (2018). Microtubule end tethering of a processive kinesin-8 motor Kif18b is required for spindle positioning. J. Cell Biol *217*, 2403–2416.

51. Gupta, M.L., Jr., Carvalho, P., Roof, D.M., and Pellman, D. (2006). Plus end-specific depolymerase activity of Kip3, a kinesin-8 protein, explains its role in positioning the yeast mitotic spindle. Nat. Cell Biol. *8*, 913–923.

52. Laan, L., Pavin, N., Husson, J., Romet-Lemonne, G., van Duijn, M., López, M.P., Vale, R.D., Jülicher, F., Reck-Peterson, S.L., and Dogterom, M. (2012). Cortical dynein controls microtubule dynamics to generate pulling forces that position microtubule asters. Cell *148*, 502–514.

53. Seldin, L., Muroyama, A., and Lechler, T. (2016). NuMA-microtubule interactions are critical for spindle orientation and the morphogenesis of diverse epidermal structures. eLife *5*, 2257.

54. Scolz, M., Widlund, P.O., Piazza, S., Bublik, D.R., Reber, S., Peche, L.Y., Ciani, Y., Hubner, N., Isokane, M., Monte, M., et al. (2012). GTSE1 is a microtubule plus-end tracking protein that regulates EB1-dependent cell migration. PLoS ONE *7*, e51259.

55. Rondelet, A., Lin, Y.-C., Singh, D., Porfetye, A.T., Thakur, H.C., Hecker, A., Brinkert, P., Schmidt, N., Bendre, S., Müller, F., et al. (2020). Clathrin's adaptor interaction sites are repurposed to stabilize microtubules during mitosis. J. Cell Biol. *219*, 213–229.

56. Collavin, L., Monte, M., Verardo, R., Pfleger, C., and Schneider, C. (2000). Cell-cycle regulation of the p53-inducible gene B99. FEBS Lett. *481*, 57–62.

57. Manfredi, M.G., Ecsedy, J.A., Meetze, K.A., Balani, S.K., Burenkova, O., Chen, W., Galvin, K.M., Hoar, K.M., Huck, J.C., LeRoy, P.J., et al. (2007). Antitumor activity of MLN8054, an orally active small-molecule inhibitor of Aurora A kinase. Proc. Natl. Acad. Sci. USA *104*, 4106–4111.

58. Steegmaier, M., Hoffmann, M., Baum, A., Lénárt, P., Petronczki, M., Krssák, M., Gürtler, U., Garin-Chesa, P., Lieb, S., Quant, J., et al. (2007). BI 2536, a potent and selective inhibitor of polo-like kinase 1, inhibits tumor growth in vivo. Curr. Biol. *17*, 316–322.

59. Ditchfield, C., Johnson, V.L., Tighe, A., Ellston, R., Haworth, C., Johnson, T., Mortlock, A., Keen, N., and Taylor, S.S. (2003). Aurora B couples chromosome alignment with anaphase by targeting BubR1, Mad2, and Cenp-E to kinetochores. J. Cell Biol. *161*, 267–280.

60. Vassilev, L.T., Tovar, C., Chen, S., Knezevic, D., Zhao, X., Sun, H., Heimbrook, D.C., and Chen, L. (2006). Selective small-molecule inhibitor reveals critical mitotic functions of human CDK1. Proc. Natl. Acad. Sci. USA *103*, 10660–10665.

61. Hubner, N.C., Bird, A.W., Cox, J., Splettstoesser, B., Bandilla, P., Poser, I., Hyman, A., and Mann, M. (2010). Quantitative proteomics combined with BAC TransgeneOmics reveals in vivo protein interactions. J. Cell Biol. *189*, 739–754.

62. Olsen, J.V., Vermeulen, M., Santamaria, A., Kumar, C., Miller, M.L., Jensen, L.J., Gnad, F., Cox, J., Jensen, T.S., Nigg, E.A., et al. (2010). Quantitative phosphoproteomics reveals widespread full phosphorylation site occupancy during mitosis. Sci. Signal. *3*, ra3–ra3.

63. Gnad, F., Gunawardena, J., and Mann, M. (2011). PHOSIDA 2011: the posttranslational modification database. Nucleic Acids Res. *39*, D253–D260.

64. Hornbeck, P.V., Zhang, B., Murray, B., Kornhauser, J.M., Latham, V., and Skrzypek, E. (2015). PhosphoSitePlus, 2014: mutations, PTMs and recalibrations. Nucleic Acids Res. *43*, D512–D520.

65. Rondelet, A., Pozniakovsky, A., Leuschner, M., Poser, I., Ssykor, A., Berlitz, J., et al. (2020). ESI mutagenesis: A one-step method for introducing point mutations into bacterial artificial chromosome transgenes. Life Science Alliance.

66. Tanenbaum, M.E., Macůrek, L., van der Vaart, B., Galli, M., Akhmanova, A., and Medema, R.H. (2011). A complex of Kif18b and MCAK promotes microtubule depolymerization and is negatively regulated by Aurora kinases. Curr. Biol. *21*, 1356–1365.

67. Tamura, N., Simon, J.E., Nayak, A., Shenoy, R.T., Hiroi, N., Boilot, V., Funahashi, A., and Draviam, V.M. (2015). A proteomic study of mitotic phase-specific interactors of EB1 reveals a role for SXIP-mediated protein interactions in anaphase onset. Biol. Open *4*, 155–169.

68. Collins, E.S., Balchand, S.K., Faraci, J.L., Wadsworth, P., and Lee, W.L. (2012). Cell cycle-regulated cortical dynein/dynactin promotes symmetric cell division by differential pole motion in anaphase. Mol. Biol. Cell *23*, 3380–3390.

69. Tipton, A.R., Wren, J.D., Daum, J.R., Siefert, J.C., and Gorbsky, G.J. (2017). GTSE1 regulates spindle microtubule dynamics to control Aurora B kinase and Kif4A chromokinesin on chromosome arms. J. Cell Biol. *216*, 3117–3132.

70. Kotak, S., Busso, C., and Gönczy, P. (2013). NuMA phosphorylation by CDK1 couples mitotic progression with cortical dynein function. EMBO J. *32*, 2517–2529.

71. Smyth, J.T., Beg, A.M., Wu, S., Putney, J.W., Jr., and Rusan, N.M. (2012). Phosphoregulation of STIM1 leads to exclusion of the endoplasmic reticulum from the mitotic spindle. Curr. Biol. *22*, 1487–1493.

72. van der Vaart, B., Manatschal, C., Grigoriev, I., Olieric, V., Gouveia, S.M., Bjelic, S., Demmers, J., Vorobjev, I., Hoogenraad, C.C., Steinmetz, M.O., and Akhmanova, A. (2011). SLAIN2 links microtubule plus end-tracking proteins and controls microtubule growth in interphase. J. Cell Biol. *193*, 1083–1099.

73. Liakopoulos, D., Kusch, J., Grava, S., Vogel, J., and Barral, Y. (2003). Asymmetric loading of Kar9 onto spindle poles and microtubules ensures proper spindle alignment. Cell *112*, 561–574.

74. Tirnauer, J.S., Grego, S., Salmon, E.D., and Mitchison, T.J. (2002). EB1-microtubule interactions in Xenopus egg extracts: role of EB1 in microtubule stabilization and mechanisms of targeting to microtubules. Mol. Biol. Cell *13*, 3614–3626.

75. Rankin, K.E., and Wordeman, L. (2010). Long astral microtubules uncouple mitotic spindles from the cytokinetic furrow. Proc. Natl. Acad. Sci. USA *190*, 35–43.

76. Nguyen-Ngoc, T., Afshar, K., and Gönczy, P. (2007). Coupling of cortical dynein and G α proteins mediates spindle positioning in Caenorhabditis elegans. Nat. Cell Biol. *9*, 1294–1302.

77. Walczak, C.E., Zong, H., Jain, S., and Stout, J.R. (2016). Spatial regulation of astral microtubule dynamics by Kif18B in PtK cells. Mol. Biol. Cell *27*, 3021–3030.

78. Kern, D.M., Nicholls, P.K., Page, D.C., and Cheeseman, I.M. (2016). A mitotic SKAP isoform regulates spindle positioning at astral microtubule plus ends. J. Cell Biol. *213*, 315–328.

79. Bergstralh, D.T., Dawney, N.S., and St Johnston, D. (2017). Spindle orientation: a question of complex positioning. Development *144*, 1137–1145.

80. Moore, A.T., Rankin, K.E., von Dassow, G., Peris, L., Wagenbach, M., Ovechkina, Y., Andrieux, A., Job, D., and Wordeman, L. (2005). MCAK associates with the tips of polymerizing microtubules. J. Cell Biol. *169*, 391–397.

81. Walczak, C.E., Mitchison, T.J., and Desai, A. (1996). XKCM1: a Xenopus kinesin-related protein that regulates microtubule dynamics during mitotic spindle assembly. Cell *84*, 37–47.

82. Kline-Smith, S.L., and Walczak, C.E. (2002). The microtubule-destabilizing kinesin XKCM1 regulates microtubule dynamic instability in cells. Mol. Biol. Cell *13*, 2718–2731.

83. Poser, I., Sarov, M., Hutchins, J.R.A., Hériché, J.-K., Toyoda, Y., Pozniakovsky, A., Weigl, D., Nitzsche, A., Hegemann, B., Bird, A.W., et al. (2008). BAC TransgeneOmics: a high-throughput method for exploration of protein function in mammals. Nat. Methods, 409–415.

84. Applegate, K.T., Besson, S., Matov, A., Bagonis, M.H., Jaqaman, K., and Danuser, G. (2011). plusTipTracker: Quantitative image analysis software for the measurement of microtubule dynamics. J. Struct. Biol. *176*, 168–184.

85. Rappsilber, J., Mann, M., and Ishihama, Y. (2007). Protocol for micro-purification, enrichment, pre-fractionation and storage of peptides for proteomics using StageTips. Nat. Protoc. *2*, 1896–1906.

86. Michalski, A., Damoc, E., Hauschild, J.-P., Lange, O., Wieghaus, A., Makarov, A., Nagaraj, N., Cox, J., Mann, M., and Horning, S. (2011). Mass spectrometry-based proteomics using Q Exactive, a high-performance benchtop quadrupole Orbitrap mass spectrometer. Mol. Cell. Proteomics *10*, M111.011015.

87. Olsen, J.V., Macek, B., Lange, O., Makarov, A., Horning, S., and Mann, M. (2007). Higher-energy C-trap dissociation for peptide modification analysis. Nat. Methods *4*, 709–712.

88. Cox, J., and Mann, M. (2008). MaxQuant enables high peptide identification rates, individualized p.p.b.-range mass accuracies and proteome-wide protein quantification. Nat. Biotechnol. *26*, 1367–1372.

89. Klare, K., Weir, J.R., Basilico, F., Zimniak, T., Massimiliano, L., Ludwigs, N., Herzog, F., and Musacchio, A. (2015). CENP-C is a blueprint for constitutive centromere-associated network assembly within human kinetochores. J. Cell Biol. *210*, 11–22.

STAR★METHODS

KEY RESOURCES TABLE

REAGENT or RESOURCE	SOURCE	IDENTIFIER
Antibodies		
Goat polyclonal anti-GFP	MPI-CBG, Dresden;[83]	N/A
Rabbit polyclonal anti-GTSE1	MPI-CBG, Dresden;[54]	N/A
Mouse monoclonal anti- α-tubulin (DM1α)	Sigma Aldrich	Cat#T6199; RRID:AB_477583
Goat anti-clathrin heavy chain	LSBio	LS-C348290; RRID:AB_2313773
Rabbit polyclonal anti-Kif18B	Bethyl Laboratories	Cat# A303-982A-T; RRID:AB_2620331
Rat polyclonal anti-EB1	Absea Biotechnology	Cat#010811b11; RRID: AB_2313773
Rabbit polyclonal anti-CEP135	MPI-CBG, Dresden	N/A
Donkey anti-rat Alexa594	Bethyl Laboratories	Cat#A110-337D4; RRID:AB_10681669
Donkey anti-rat Alexa488	Bethyl Laboratories	Cat#A110-337D2; RRID:AB_10682975
Donkey anti-rabbit Alexa650	Bethyl Laboratories	Cat#A120-208D5; RRID:AB_10630867
Donkey anti-mouse Alexa488	Bethyl Laboratories	Cat#A90-337D2; RRID:AB_10632009
Donkey anti-mouse Alexa594	Bethyl Laboratories	Cat#A90-337D4; RRID:AB_10630877
Donkey anti-mouse Alexa647	Invitrogen	Cat#A31571; RRID:AB_162542
Donkey anti-goat Alexa488	Jackson Immunoresearch	Cat#705-545-147; RRID:AB_2336933
HRP-conjugated Sheep anti-mouse	GE-Amersham	Cat# NA931; RRID: AB_772210
HRP-conjugated donkey anti-rabbit	GE-Amersham	Cat# NA934; RRID: AB_772206
HRP-conjugated goat anti-rat	GE-Amersham	Cat# NA935; RRID:AB_772207
Bacterial and Virus Strains		
E. coli Rosetta 2 (DE3)	Agilent Technologies	Cat#230240
E. coli DH10β		N/A
Max Efficiency DH10Bac™ Chemically competent cells (EMBacY)	MPI-Dortmund, DPF	N/A
Chemicals, Peptides, and Recombinant Proteins		
Blasticidin	Corning	Cat# 3513-03-9
Puromycin	GIBCO	Cat#A11138-03
NotI-HF	New England Biolabs	Cat#R3189S
L-Glutamine	PAN Biotech	Cat#P04-80100
PenStrep	PAN Biotech	Cat#P06-07100
OptiMEM	Invitrogen	Cat#31985-054
RO-3306	Millipore	Cat#217699
RO-3306	Calbiochem	Cat#217699-5mg
ZM447439	EMD Millipore Corp.	Cat#189410
BI 2536	Enzo Life Sciences	Cat#ENZ-CHM160-0005
MLN8054-004-H	Millenium Pharmaceuticals, Cambridge, MA;	NA
siR-DNA	Spirochrome	Cat# SC007
siR-tubulin	Spirochrome	Cat# SC002
Methanol	Sigma-Aldrich	Cat#32213-2.5L-M
Fetal Bovine Serum	Sigma-Aldrich	Cat#f7524 Batch:111M3395
Prolong Gold containing DAPI	Invitrogen	Cat# P36941
DAPI	Sigma	Cat#D9542
Mowiol 4-88 Reagent	Calbiochem	Cat#475904
(+)S-trityl-L-Cysteine (STLC)	Sigma-Aldrich	Cat#164739
MG-132	Calbiochem	Cat#CAS 133407-82-6

(*Continued on next page*)

Continued

REAGENT or RESOURCE	SOURCE	IDENTIFIER
Protease-Inhibitor Mix HP plus	Serva	Cat#39107
PhosStop phosphatase inhibitor	EASY Pack, Roche	Cat#04906845001
Dynabeads coupled to protein G	Invitrogen	Cat#10004D
ECL Prime Western Blotting Detection Reagent^{TM}	GE Healthcare	Cat#RPN2232
GST-GTSE1 FL	This paper	N/A
GTSE1 FL- 6xHis	This paper	N/A
GTSE1 1-460- 6xHis	This paper	N/A
GTSE1 381-739- 6xHis	This paper	N/A
EB1-GST	This paper	N/A
Histone H1	Musacchio Lab	N/A
Cdk1-Cyclin B	Musacchio Lab	N/A
GST Precission protease	Musacchio Lab	N/A
λ-phosphatase	Musacchio Lab	N/A
ATP	Carl Roth GmbH + Co	Cat#HN35.4
Sodium orthovanadate	Sigma	Cat#S6508-10G
ProQ-Diamond^{R}	Invitrogen	Cat#P33300
Glutathione beads	Serva	Cat#42172.01
Glutathione	BIORoxx GmbH	Cat#CAS 70-18-8
IPTG	Carl Roth GmbH + Co	Cat#CAS 367-93-1
Critical Commercial Assays		
Nucleobond^{R} xtra bac kit	Macherey-Nagel	Cat#747436.25
Effectene	QIAGEN	Cat#301425
Lipofectamine-2000	Invitrogen	Cat#11668-019
Oligofectamine	Invitrogen	Cat#12252011
Experimental Models: Cell Lines		
Human: U2OS (epithelial osteosarcoma cells)	MPI-CBG	N/A
Human: U2OS GTSE1^{WT}	This paper	N/A
Human: U2OS GTSE1$^{WT}{}_{212}$	Bird Lab;[54]	N/A
Human: U2OS GTSE1$^{WT(303)}$	Bird Lab;[55]	N/A
Human: U2OS GTSE1^{14A}	This paper	N/A
Human: U2OS GTSE1^{14A} EB3-mCherry	This paper	N/A
Human: U2OS GTSE1$^{WT}{}_{212}$ EB3-mCherry$_{109}$	Bird Lab	N/A
Human: U2OS GTSE1$^{TP/AA}$	This paper	N/A
Human: U2OS GTSE1^{KO}	Bird Lab;[41]	N/A
Human: U2OS GTSE1^{WT} EB3-mCherry$_4$	Bird Lab	N/A
Human: U2OS GTSE1$^{Sk(202)}$	Bird Lab;[54]	N/A
Human: RPE-1	ATCC	N/A
Trichoplusia ni: BTI-Tnao38	Gary W. Blissard Lab	N/A
S.frugiperda: Sf9	Thermo Fischer	Cat#12659017
Oligonucleotides		
siRNA targeting hGTSE1: 5′-GAUUCAUACAGGAGUCAAA-3′	Ambion;[54]	N/A
siRNA targeting hEB1: 5′-UUCGUUCAGUGGUUCAAGA-3′	Ambion;[54]	N/A
siRNA targeting clathrin heavy chain (CHC): 5′-GGUUGCUCUUGUUACGGAUTT-3′	Ambion;[55]	N/A
siRNA targeting Kif18B: 5′-UAUUUGAGGGUGUUGUACG-3′	Sigma-Aldrich;[66]	N/A
Silencer Select Negative Control #2 siRNA	Ambion	Cat#4390847

(*Continued on next page*)

Continued

REAGENT or RESOURCE	SOURCE	IDENTIFIER
Fwd_AI-14A (forward recombineering primer for amplifying the artificial intron fused to the mutant exon 9): 5′- CCAAAGCTTTCGCGGGCACAGCGGCCGCAGTCG TGCACGTCAGTTGGCAGGTAAGTGTGTACGGTG GGAT −3′	Sigma-Aldrich	N/A
Rev_AI-14A (reverse recombineering primer for amplifying the artificial intron fused to the mutant exon 9): 5′- CAGCAAGCCTAGGAATTTGAGACCAATTTATTA CCACCTTCGTGTCTTACCTCATTGCAGAGTTCTT GCG −3′	Sigma-Aldrich	N/A
Recombinant DNA		
pEGFP-N2-GTSE1-14A-GFP-T2A-Bsd	This paper	N/A
pEGFP-N2-GTSE1-GFP-T2A-Bsd	Bird Lab;[41]	N/A
pEGFP-N2-GTSE1-3A-GFP-T2A-Bsd	This paper	N/A
pEGFP-N2-GTSE1-4A-GFP-T2A-Bsd	This paper	N/A
pEGFP-N2-GTSE1-5A-GFP-T2A-Bsd	This paper	N/A
pEGFP-N2-GTSE1-7A-GFP-T2A-Bsd	This paper	N/A
pEGFP-N2-GTSE1-10A-GFP-T2A-Bsd	This paper	N/A
pEGFP-N2-GTSE1-12A-GFP-T2A-Bsd	This paper	N/A
hGTSE1$^{TP/AA}$ Bacterial Artificial Chromosome	This paper	N/A
hGTSE1-14A Bacterial Artificial Chromosome	This paper	N/A
pEB3-mCherry (puro)	Bird Lab;[54]	N/A
pGEX-6p1-EB1-GST	This paper	N/A
pET28a-GTSE1 FL	Bird Lab;[55]	N/A
pET28a-GTSE1 1-460	Bird Lab;[55]	N/A
pET28a-GTSE1 381-739	Bird Lab;[55]	N/A
MultiBac	Geneva Biotech	N/A
pFG-GTSE1 FL	Bird Lab;[41,55]	N/A
Software and Algorithms		
FIJI/ImageJ	National Insititutes of Health (Public Domain)	https://imagej.net/Fiji/Downloads
ImageLab	BioRad	https://www.bio-rad.com
Prism 7	Graphpad	https://www.graphpad.com/scientific-software/prism/
Slidebook Software 6.0	Intelligent Imaging Innovations Inc.	https://www.intelligent-imaging.com/slidebook
SoftWorX 6.1.1	GE Healthcare Life Sciences	http://incelldownload.gehealthcare.com/bin/download_data/SoftWoRx/7.0.0/SoftWoRx.htm
plusTipTracker	Danuser Lab[84]	
Imaris 7.6.4	Oxford Instruments	https://imaris.oxinst.com/
MaxQuant software 1.5.2.18	MPI-Biochem	https://www.maxquant.org/
MATLAB R2018a	Mathworks	https://www.mathworks.com/products/matlab.html
Other		
Deltavision Imaging System	GE Healthcare	
3i Marianas^{TM} spinning disc confocal system	Intelligent Imaging Innovations Inc.	
8-well ibidi chambers	ibidi	Cat# 80827

RESOURCE AVAILABILITY

Lead Contact

Further information and requests for resources and reagents should be directed to and will be fulfilled by the Lead Contact, Alexander W. Bird (alex.bird@mpi-dortmund.mpg.de).

Materials Availability

Plasmids and cell lines generated for this study are available upon request.

Data and Code Availability

The code supporting the analyses of astral microtubule parameters in this study are available at https://github.com/divyarfrn/GTSE1_14A_CurrBiol

EXPERIMENTAL MODEL AND SUBJECT DETAILS

The parental U2OS and RPE-1 cells were maintained in DMEM (PAN Biotech) containing 10% FBS (GIBCO), 2mM L-glutamine (PAN Biotech), 100 U/mL penicillin, and 0.1 mg/ml streptomycin (PAN Biotech) at 37°C in 5% CO_2. Parental U2OS cells stably-integrated with the Bacterial Artificial Chromosome (BAC) encoding RNAi-resistant *wild-type* GTSE1-GFP or GTSE1-14A-GFP were maintained in the same media supplemented with 4 μg/mL blasticidin. All BACs integrated into the parental cell line were verified by DNA sequencing, and stably integrated cells were authenticated by selection for blasticidin resistance. The $GTSE1^{WT}$ and $GTSE1^{14A}$ clones expressing the GTSE1-GFP and GTSE1-14A-GFP BAC transgenes close to endogenous level, respectively, were selected for phenotypic analysis. U2OS cells stably expressing RNAi-resistant wild-type GTSE1-LAP ($GTSE1^{WT}_{212,}$ $GTSE1^{303}$) were described previously[52,53]. Dual cell lines expressing BAC-based GTSE1-14A and plasmid-encoded EB3-mCherry were made by selecting for stable integration of EB3-mCherry using media supplemented with 1 μg/mL puromycin, and subsequent fluorescence microscopy analysis to detect EB3 comets.

METHOD DETAILS

Cloning and plasmids

Plasmids for mammalian expression were derived from the pEGFP-N2 GTSE1-GFP-T2A-Bsd, a previously modified version[41] of the pEGFP-N2 vector (Addgene). Mutations were introduced into the GTSE1 cDNA by either site-directed mutagenesis or Gibson cloning, with the exception of the $GTSE1^{TP/AA}$ BAC that was previously generated in the laboratory. The GST-hGTSE1 construct used for protein purification from insect cells was also described in the study mentioned above. The GTSE1-14A BAC carrying point mutations at T508, S513, S514, S520, S523, S523, S528, T532, S535, S539, T545, T548, T555, S565, S566 was generated through recombineering by ESI mutagenesis based on Redβ and Redγ expression[65]. Briefly, a cassette was first created that contains mutated exon 9 linked via a T2A peptide to neomycin resistance gene flanked by splice sites at both ends. This cassette was amplified by PCR using primers that provide 50 bp long homology arms to specify the site of recombination on the GTSE1 WT BAC. Standard recombination based on inducible Redβ and Redγ expression was carried out and positive clones were tested for the correct recombination event. Correctly modified BACs were verified by DNA sequencing. The integrity of GTSE1-14A BAC was checked by performing restriction digestion with NotI (New England Biolabs) and comparing the obtained profile with that of the GTSE1 WT BAC.

Construction of stable cell lines and transient transfection

To obtain U2OS cells expressing the GTSE1-GFP or GTSE1-14A-GFP transgenes, the corresponding BACs were transfected into U2OS cells using the Effectene kit (QIAGEN) following the manufacturer's instruction and selected using blasticidin supplemented media. To make EB3 expressing cell lines, the appropriate plasmid was transfected into $GTSE1^{14A}$ using Lipofectamine-2000 (Invitrogen) according to manufacturer's instructions and stably integrated colonies were selected using puromycin. Transient transfections of GTSE1 point mutants in U2OS and RPE-1 cells were performed in ibidi chambers using 750 ng DNA and 0.75 μL Lipofectamine 2000 (Invitrogen) according to the manufacturer's protocol.

RNAi

siRNA against hGTSE1 (Ambion; 5′-GAUUCAUACAGGAGUCAAA-3′), EB1 (Ambion; 5′-UUCGUUCAGUGGUUCAAGA-3′), Kif18B (Sigma-Aldrich;) and control siRNA (Ambion; Silencer negative control 2; AM4637) were used. Approximately 35,000 U2OS cells were added to prewarmed media in 24-well plates or 8-well imaging chambers (ibidi), and transfection complexes containing 2.5 μL Oligofectamine and siRNA were added immediately afterward. Media was changed after 6–8 hours. Final concentrations of 80 nM RNAi for GTSE1 and 100nM each for EB1 and Kif18B were used.

For depleting endogenous GTSE1, EB1 and Kif18B in U2OS cells, reverse transfection was performed using Oligofectamine (Invitrogen). Briefly, transfection complexes consisting of siRNA and Oligofectamine were prepared by mixing 2.5 μL Oligofectamine with siRNA in OptiMEM (Invitrogen) at room temperature for 20 min. This was added to roughly 35000-40000 cells in prewarmed medium in 24-well plates (Sarstedt) containing glass coverslips, or 8-well imaging chambers (ibidi), and the volume made up to 500 μL.

The cells were left in the humidified incubator at 37°C for 8 hours after which the media was replaced. All experiments were performed 48 hours after transfection.

Clathrin depletion in human cells was performed using a forward transfection approach. Cells were seeded into a 3.5 cm dish with coverslips and grown until 75% confluent. Prior to transfection, medium was exchanged for 1.8 mL OptiMEM supplemented with 100 U/mL penicillin and 0.1 mg/mL streptomycin (PAN Biotech, Pen/Strep mix). A 200 μL transfection mix containing 3 μL Lipofectamine RNAi Max (Invitrogen) and the siRNA was prepared in OptiMEM (Invitrogen), and incubated for 25 min at RT before addition to the cells. Experiments were performed 66 hours after transfection. Clathrin heavy chain (CHC) siRNA (5′-GGUUGCUCUUGUUACG GAUTT-3′) was used at 50 nM final concentration. When necessary, cells transfected with Control or CHC siRNA for 66 hours using the forward transfection approach were submitted to a second round of reverse transfection with Control, GTSE1 (100 nM), or CHC (100 nM) siRNAs for an extra 48 hours.

Live cell imaging

For identifying kinase dependency on phosphorylation of GTSE1 in mitosis, GTSE1^{WT} cells were treated with appropriate dilutions of specific kinase inhibitors in CO_2-independent visualization medium (GIBCO) supplemented with 10% FBS, 2mM L-glutamine and penicillin/streptomycin as mentioned earlier. Aurora A inhibitor (MLN8054; Sigma-Aldrich) and Aurora B inhibitor (ZM447439; EMD Millipore Corp.) were added at 500 nM and 2 μM respectively for 90 min while 100 nM of Plk1 inhibitor (BI 2536; Enzo Life Sciences) was added for one hour prior to imaging. For inhibiting Cdk1, 9 μM RO-3306 (Calbiochem) was used. Cells were imaged in prometaphase first for 20 s followed by replacing the media with fresh visualization medium containing RO-3306 and imaging for 180 s. A z stack consisting of 3 sections at intervals of 0.4 μm was acquired every 1 s. Cells transfected with phosphonull GTSE1 mutants were imaged using similar parameters.

To visualize DNA for measuring the time from NEBD to anaphase, 1 hour prior to imaging, 500 nM of the cell permeable DNA dye called siR-DNA (Spirochrome) and 1 μM Verapamil, a sodium channel efflux inhibitor, were added to the visualization media. Serial z stacks of 2 μm were acquired every 2 min for 12 hours in a heated chamber (37°C). For visualizing microtubules for analyzing spindle positioning defects and studying anaphase timing, 1 hour prior to imaging, 125 nM of siR-tubulin (Spirochrome) and 1 μM Verapamil were added to the visualization media. All live cell imaging was performed on the DeltaVision Imaging System (GE Healthcare) using the 40 × /1.3 NA UPLFLN Oil Objective.

For studying microtubule dynamics in mitosis, GTSE1^{WT} and GTSE1^{14A} cells dually expressing EB3-mCherry were used and imaged using the 60 × Oil Objective on the 3i Marianas spinning disk confocal system. Three serial z stacks of 0.4 μm were acquired every second for two min at 37°C.

Immunofluorescence (IF)

Cells grown on coverslips were fixed using pre-cooled methanol (Sigma-Aldrich) for 10 min at −20°C, followed by washing and rehydration in PBS for 10 min. Next, the cells were blocked for 1 hour in 5% BSA prepared in PBS followed by incubation for 1 hour in the dark with appropriate dilutions of primary antibodies (prepared in 5% BSA) in a humidified chamber at 37°C. After washing the coverslips thrice in PBS to remove excess primary antibody, they were similarly incubated with corresponding secondary antibodies, and washed thrice to remove excess antibody. Coverslips were either mounted on glass slides using Prolong Gold containing DAPI (Invitrogen) or stained separately with DAPI (Sigma; diluted 1:10000) before mounting using Mowiol (Calbiochem).

Images used for quantifying astral microtubule lengths in metaphase were acquired using the 60 × /1.4 NA Plan-Apochromat Oil Objective (Zeiss) on the DeltaVision Imaging System (GE Healthcare) equipped with an sCMOS camera (PCO edge 5.5). Serial Z stacks of 0.25 μm thickness were acquired and then deconvolved using SoftWoRx 6.1.1 software. All other images for quantifying inner spindle intensity, microtubule lengths in prometaphase and spindle tilt were taken using the 3i Marianas spinning disk confocal system (Intelligent Imaging Innovations Inc.) equipped with Axio Observer Z1 microscope (Zeiss), Plan-Apochromat 60 × /1.4 NA Oil Objective, M27 with DIC III Prism (Zeiss), Orca Flash 4.0 sCMOS Camera (Hamamatsu Photonics) and controlled by Slidebook Software 6.0 (Intelligent Imaging Innovations Inc.).

Microtubule dynamics

Microtubule dynamics were analyzed from EB3-mCherry movies using the software plusTipTracker that has been made publicly available by the Danuser laboratory[84]. The same parameters were used for all movies: maximum gap length, fifteen frames; minimum track length, three frames; search radius range, 5-25 pixels; maximum forward angle, 60° maximum reverse angle, 15° maximum shrinkage factor, 1.0; fluctuation radius, 1.5 pixels; and time-interval 1 s. Data collected from the analysis included mean microtubule growth velocity, mean microtubule growth-track lifetime, number of bgaps and the growth time before bgap. Catastrophe frequency was calculated as the number of bgaps (corresponding to shrinkage events) divided by the growth time before bgap.

Immunoprecipitation (IPs)

Cells at ~70% confluency were arrested in prometaphase using 10 μM S-trityl-L-Cysteine (STLC; Sigma-Aldrich) for 16 hours and collected using mitotic shake off. They were then pelleted down by centrifuging at 1000 rpm for 5 min and then washed with PBS supplemented with 10 μM MG-132 (Calbiochem). After centrifugation, the cells were resuspended in complete DMEM medium supplemented with 10 μM MG-132 and incubated in an incubator maintained at 37°C and 5% CO_2 for 90 min to allow the cells to reach metaphase. Following this, the cells were once again washed, lysed in cell lysis buffer (50 mM Na_2HPO_4, 150 mM NaCl, 10% glycerol,

1% Triton X-100, 1 mM EGTA, 1.5 mM $MgCl_2$, 50 mM HEPES pH 7.2, 1 mM DTE) supplemented with 2 × protease inhibitor mix (SERVA), and PhosStop (EASY Pack, Roche) and incubated on ice for 15 min. The cell suspension was then clarified by centrifuging at 13000 rpm at 4°C for 15 min. Total protein concentration of the cell extract was calculated using Bradford reagent. For performing immunoprecipitation, 1 mg total protein in a volume of 1 mL was used. A 4% sample was taken out as input. To the remaining cell lysate, 1-2 μg of indicated antibodies were added and the mixture incubated at 4°C for 90 min. Subsequently, pre-washed dynabeads coupled to protein G (Invitrogen) were added to the lysate and the mixture incubated at 4°C for 4 hours. The beads were then washed thrice with 1 mL of the appropriate lysis buffer, resuspended in SDS-loading buffer and boiled at 95°C for 5 min before analyzing by SDS-PAGE and western blotting.

Western blot (WB)

For western blotting after RNAi, cells were harvested by directly adding hot Lamelli buffer in 24-well plates or ibidi chambers as required. The proteins were separated on SDS-PAGE gels and transferred onto nitrocellulose membranes. Membranes were blocked using either 5% milk prepared in PBS containing 0.1% Tween (PBS-T) or in the case of CHC, using 5% bovine serum albumin (BSA) in PBS-T for 1 hour at room temperature. The membrane was incubated with the indicated primary antibodies, followed by secondary antibodies coupled to horseradish peroxidase. Protein signal was detected using chemiluminescence with the ECL Prime Western Blotting Detection Reagent (GE Healthcare) according to manufacturer's instructions. After incubation with the ECL blotting reagent, images were acquired using the ChemiDoc MP Imaging System (BioRad).

Antibodies

Primary antibodies used: goat anti-GFP (MPI Dresden; described in[80]; diluted 1:5000 for IF), rabbit anti-GTSE1 (custom generated; described in[52]; diluted 1:5000 for WB), mouse anti-α-tubulin (DM1α, Sigma-Aldrich; diluted 1:400 for IF and 1:5000 for WB), mouse anti-CHC (X22, ab2731, Abcam; diluted 1:300 for WB), rat anti-EB1 (KT-51, Absea Biotechnology, diluted 1:1000 for IF and WB), rabbit anti-Kif18B (A303-982A-T, Bethyl Laboratories; diluted 1:100 for WB), rabbit anti-CEP135 (MPI Dresden, described in[81]; diluted 1:5000 for IF). Secondary antibodies used: donkey anti-human antibodies conjugated to Cy5 or Texas red (Jackson ImmunoResearch Laboratories; #709-175-149 and #709-075-149), donkey anti-rat Alexa488 (Bethyl Laboratories; A110-337D2, donkey anti-rat Alexa594 (Bethyl Laboratories; A110-337D4), donkey anti-rabbit Alexa488 (Thermofisher; A-21206), donkey anti-rabbit Alexa594 (Bethyl Laboratories; A120-208D4), donkey anti-rabbit Alexa650 (Bethyl Laboratories; A120-208D5), donkey anti-mouse Alexa488 (Bethy Laboratories l; A90-337D2), donkey anti-mouse Alexa594 (Bethyl Laboratories; A90-337D4), donkey anti-mouse Alexa647 (Invitrogen; A31571), donkey anti-goat Alexa488 (Jackson Immunoresearch; 705 545 147), donkey anti-goat HRP (Santa Cruz; SC-2020), sheep anti-mouse HRP (Amersham; NXA931-1ml), donkey anti-rat HRP (Amersham; NA935) donkey anti-rabbit HRP (Amersham; NXA934-1ml).

Mass spectrometry

For MS analysis, IPs and *in vitro* phosphorylation reactions were performed in triplicates to obtain reliable label-free data. Liquid chromatography coupled with mass spectrometry was used to assess the phosphorylation status of GTSE1. *In vitro* phosphorylated His-tagged GTSE1 (full-length, 1-460 or 381-739) using Cdk1 as kinase and its unphosphorylated controls were reduced, alkylated and digested with LysC/Trypsin and prepared for mass spectrometry as previously described[85]. Obtained peptides were separated on a Thermo Scientific EASY-nLC 1000 HPLC system (Thermo Fisher Scientific, Odense, Denmark) using a 45 min gradient from 5%–60% acetonitrile with 0.1% formic acid and directly sprayed via a nano-electrospray source in a quadrupole Orbitrap mass spectrometer (Q ExactiveTM, Thermo Fisher Scientific)[86]. The Q Exactive was operated in data-dependent mode acquiring one survey scan and subsequently ten MS/MS scans[87]. Resulting raw files were processed with the MaxQuant software (version 1.5.2.18) using GTSE1 and Cdk1 for the database search. Deamidation (NQ), oxidation (M) and phosphorylation (STY) were given as variable modifications and carbamidomethylation (C) as fixed modification[88]. A false discovery rate cut off of 1% was applied at the peptide and protein levels and as well on the site decoy fraction[88]. Identified phospho peptides were further separated in class I sites where the calculated localization probability on a specific residue was > 75% and class II sites with localization probabilities < 75%. Immunopreciptiated GTSE1 was directly digested on beads[61] and peptides subsequently treated as described above using a 90 min gradient (5%–60% acetonitrile with 0.1% formic acid) instead of 45 min.

Protein purification

Full length GTSE1 was purified from insect cells using the protocol described in[41]. Briefly, insect cells expressing recombinant protein were harvested by centrifuging at 1800 rpm for 15 min and resuspended in 100mL ice-cold Buffer A (50 mM HEPES, pH 8.0, 300 mM NaCl, 5% glycerol supplemented with 2 mM TCEP and 1 × protease inhibitor) followed by lysing the cells by sonication (Sonifier Cell Disruptor, Branson Ultrasonics Corp.) and then centrifuging at 30000 rpm for 30 min at 4°C. For the first step of affinity purification, the clarified supernatant was incubated with 1mL glutathione beads (Amintra) in a rolling shaker for 1 hour. The glutathione beads were then passed over gravity flow columns and washed in 3 iterations with 150 mL of Buffer A. An overnight incubation with GST Precission protease (purified in-house) in a volume of 5mL was performed to cleave off the GST tag. After eluting and concentrating the cleaved protein in Amicon Ultra-15 Centrifugal Filters 50K MWCO (Merck Millipore), size exclusion chromatography (SEC) was performed in a Superdex 200 10/300 column using gel filtration buffer (30 mM HEPES pH 8.0, 300 mM NaCl, 5% glycerol supplemented with 2 mM TCEP). The appropriate fractions were collected, concentrated to 5-10 μM and stored at −80°C.

For purification of GST-tagged EB1, *E. coli* Rosetta cells expressing GST-EB1 were grown to $O.D._{600}$ of 0.7 and expression of recombinant protein was induced using 1 mM IPTG (Carl Roth) at 18°C overnight. Cells were harvested by centrifuging at 4000 rpm for 20 min and the pellet washed once with sterile PBS followed by resuspending and sonicating in 100 mL ice-cold GST binding buffer (25 mM HEPES pH 7.5, 300 mM NaCl, 1 mM EDTA, 5% glycerol) supplemented with 1% Triton X-100, 2 mM TCEP and protease inhibitor. The cell lysate was clarified by centrifuging at 30000 rpm for 30 min at 4°C. Affinity purification was carried out by passing the clarified lysate over a GSH column (GE Healthcare) using the ÄKTA Prime Plus system (GE Healthcare). After washing with GST binding buffer, the bound protein was eluted in GST binding buffer containing 20 mM Glutathione and concentrated to a volume of 2 mL in Falcon^{BD} concentrators with a 30000 MWDa cutoff at 3000 rpm. This was followed by performing SEC using GST binding buffer supplemented with 0.5 mM TCEP on a Superdex 200 10/300 column using an ÄKTA purifier (GE Healthcare). The fractions corresponding to the peak were pooled, concentrated and stored at −80°C.

His-tagged variants of GTSE1 (full length, 1-460 and 381-739) were used for *in vitro* phosphorylation reactions for identification of Cdk1 phosphosites on GTSE1. All expression constructs were cloned into *E. coli* Rosetta cells and purified as described in[55]. Briefly, bacteria expressing target protein were harvested and lysed by sonicating in ice-cold His binding buffer (20 mM Tris-HCl pH 8.0, 300 mM NaCl, 5% glycerol, 1 mM EDTA) supplemented with 10 mM Imidazole, 1% Triton X-100, 1 mM TCEP, DNase and 1 × protease inhibitor. The cell lysate was clarified by centrifugation at 30000 rpm and the clarified supernatant was passed through a gravimetric filter column to remove particulate matter, and then incubated for 3 hours with His beads (GE Healthcare) prewashed in His binding buffer. The beads were washed with 300 mL His washing buffer (20 mM Tris-HCl pH 8.0, 500 mM NaCl, 5% glycerol, 1 mM EDTA) supplemented with 30 mM Imidazole and 0.5 mM TCEP in three iterations, before being resuspended in His binding buffer, flash frozen and stored at −80°C.

In vitro protein phosphorylation

For identification of phosphorylation sites on GTSE1, on-bead phosphorylation of full length GTSE1, 1-460 GTSE1 and 381-739 GTSE1 was performed using His-tagged protein purified from bacteria. Cdk1-cyclinB was a kind gift from Dr. Priyanka Singh and Dr. Andrea Musacchio (MPI Dortmund). Purified proteins were phosphorylated by Cdk1 at 4°C overnight, at a molar ratio of 1:100 (kinase:protein) in kinase buffer (20 mM HEPES pH 7.8, 150 mM NaCl, 5% glycerol supplemented with 2 mM $MgCl_2$, 2 mM sodium orthovanadate and 10 mM ATP). Phosphorylation was confirmed by ProQ-Diamond® staining of the protein. For using the phosphorylated protein for pulldown experiments, the kinase was first inactivated by adding 5 μM of Cdk1 inhibitor (RO-3306; Calbiochem) and 500 nM of Aurora A inhibitor (MLN8054; Sigma-Aldrich) followed by incubation for 10 min on ice. In case of phosphorylation of EB1-GST using Cdk1, the kinase was removed after phosphorylated EB1-GST was bound to beads.

GST Pulldowns

GSH beads (Amintra) were preblocked overnight in BSA blocking buffer (20 mM HEPES pH 7.5, 500 mM NaCl, 500 μg/mL BSA) as described earlier[89]. For the pulldown, 3 μM of the prey (phosphorylated or unphosphorylated protein) was mixed with 1 μM of the GST-tagged protein or the 'bait' and 5 μL of GSH beads in a total volume of 25 μL of the kinase buffer (20 mM HEPES pH 7.8, 150 mM NaCl, 5% glycerol). A sample (25%) was taken out as input before incubating the protein mixture on ice for 1 hour for the pulldown. The beads were then washed thrice with 250 μL of wash buffer (20 mM HEPES pH 7.0, 500 mM NaCl, 5% glycerol, 0.1% Triton X-100, 1 mM TCEP) and the protein was denatured by adding 20 μL 1 × SDS-loading buffer before loading the samples on SDS gels. Pulldowns were quantified by calculating band intensities corrected for background using ImageJ.

QUANTIFICATION AND STATISTICAL ANALYSIS

Image analysis and quantification

Image quantification was performed on unmodified 16-bit z series images using ImageJ and Imaris 7.6.4 32-bit software (Bitplane). On Imaris, all images were opened and analyzed in the 'Surpass' mode in the software.

For determining colocalization between GTSE1 and EB3, the 'Spots' function with a diameter threshold of 0.5 μm was applied to the EB3 channel to identify comets, and the intensities of EB3 and GTSE1 at identified comets was extracted. An average value of background intensity for both channels was obtained by placing three points on the microtubule lattice (identified from faint EB3 signal). Background subtracted intensities of EB3 were thresholded based on a value determined by visually confirming correct annotation of 'faint' EB3 comets. GTSE1 intensities at corresponding spots was calculated in the same manner, without thresholding. For colocalization analysis during mitosis, a region of interest lying outside the spindle, over astral microtubules, was chosen.

For making line scans to compare GTSE1 and EB3 localization at microtubule plus ends across the cell cycle, maximum projection images of cells expressing GTSE1-GFP and EB3-mCherry were opened on ImageJ, and ~4 μm long lines were manually drawn along EB3 labeled microtubule ends. All lines began on the microtubule lattice and terminated outside the comet. The absolute intensities of EB3 and GTSE1 were extracted using the Plot Profile plugin of ImageJ. All line scan intensity profiles were aligned to the position of the peak intensity of the EB3 channel and normalized before plotting using MATLAB scripts.

To calculate the number of GTSE1 comets after transient transfection, stills from live-cell imaging of equally transfected cells were opened on Imaris. A ROI of fixed dimensions was placed over astral microtubules. The 'Spots' function with a diameter threshold of

0.5 μm was used to identify GTSE1 comets. The average background GFP intensity was calculated from three randomly placed points in the cytoplasm. Background corrected intensities were thresholded using a value 1.5 × greater than the average background.

Raw images of cells stained for EB1, tubulin and CEP-135 were used for calculating microtubule lengths by adapting the protocol outlined in[19] and writing MATLAB functions and scripts. The 3D position of the spindle poles (P_x, P_y, P_z) was determined by using the 'Measurement' function on the CEP-135 signal. The 'Spots' function was used to determine spherical coordinates of all EB1 comets (C_x, C_y, C_z) using the spot diameter thresholded at 0.5 μm with application of occasional manual filtering to eliminate spots not also visibly associated with tubulin. These coordinates were extracted using the 'Statistics' function on Imaris. MATLAB scripts were used to calculate distances between all comets to both spindle poles using the formula $PC = \sqrt{(Px - Cx)^2 + (Py - Cy)^2 + (Pz - Cz)^2}$. The shorter of the two distances was used as a proxy for microtubule length. The spindle length '*l*' was determined by calculating the distance between the two poles according to the equation written above. The spindle width '*w*' was defined as the distance between the outermost kinetochore fibers on opposite ends of the spindle attached to DNA and was manually determined using the tubulin channel. This was used to determine the spindle angle θ, defined as $\tan^{-1}(w/l)$. Next, the angle φ between the line formed by a comet and its closest pole, and the line formed by the two spindle poles, was calculated using the cosine law. An EB1 comet was associated with an astral microtubule if φ was greater than θ. The mean length of astral microtubules per cell and the total number of astral microtubules per cell were calculated. For cells in prometaphase, owing to cytoskeleton and spindle morphology, there is no defined spindle angle. Therefore, the lengths of all microtubules were calculated as described above. All analyses were performed in Microsoft Excel and MATLAB R2019a.

For calculating the intensity of tubulin in the inner spindle, the spindle was detected using the 'Surface' module on Imaris using a surface detail value of 1.0 on the tubulin channel. The total fluorescence intensity of tubulin in a manually placed ROI over the spindle was obtained through the 'Statistics' option. The volume corrected background intensity was calculated by multiplying the spindle volume with the average tubulin intensity of four manually placed spots in the cytoplasm that lacked polymerized tubulin. The tubulin intensity in the inner spindle corrected for the background was calculated.

For semi-automatic detection of number of microtubules reaching the cortex, maximum projections of 16-bit raw images were used to determine the outline of cells using the cytoplasmic intensity of the CEP-135 fluorescence. A line of 1.05 μm thickness was drawn toward the inside of the cell boundary and the corresponding intensities of tubulin across that line were extracted using the Plot Profile plugin on ImageJ. A background value obtained by averaging the intensities at 3 random points lacking tubulin along the cortex-adjacent line was subtracted from absolute intensities at all points. Background corrected tubulin intensities were subjected to a threshold value, determined from visual inspection of correctly annotated microtubules in at least eight cells per experiment. The number of microtubules thus obtained was divided by the length of the cortex of the corresponding cell.

For calculating the angle α made between the spindle and the long cell axis at different time points, unmodified 16-bit videos were opened on ImageJ and the long cell axis was defined 8 min prior to NEBD. The angle α was measured using the Angle tool of ImageJ software.

Statistical analysis

Statistical significances were determined by performing unpaired, (non-)parametric two-tailed Student's t tests, and Welch's correction was applied if the standard deviation of the distributions under comparison were more than 2 × different from each other. Significances were calculated using Microsoft Excel, Graphpad Prism 7 and MATLAB 2019a. Details of statistical analyses performed in this study are provided in the Figure legends.

RESEARCH ARTICLE SUMMARY

NEUROSCIENCE

Sleep-wake cycles drive daily dynamics of synaptic phosphorylation

Franziska Brüning*, Sara B. Noya*, Tanja Bange, Stella Koutsouli, Jan D. Rudolph, Shiva K. Tyagarajan, Jürgen Cox, Matthias Mann, Steven A. Brown†, Maria S. Robles†

INTRODUCTION: Globally, circadian clock–driven protein phosphorylation is a key mechanism to temporally compartmentalize biological processes across the day in peripheral tissues. In the brain, phosphorylation of several proteins has been reported to correlate with sleep pressure, itself regulated in a circadian fashion. Locally in neurons, phosphorylation plays a critical role in the regulation of synaptic function by allowing rapid modulation of protein activity and could thus dynamically scale synaptic strength in response to circadian or sleep-driven cues. Understanding the magnitude and origin of phosphorylation dynamics within synaptic proteins on a system level would be of great value to mechanistically assess synaptic function deficiencies and to understand temporal contributions to brain pathologies.

RATIONALE: Little is known about whether and how global phosphorylation signaling in synapses is shaped in a time-dependent manner. To comprehensively characterize phosphorylation rhythms in the synaptic compartment driven by circadian and sleep-wake–dependent cues, we biochemically isolated synaptoneurosomes from mouse forebrain and analyzed them with advanced mass spectrometry–based proteomics.

RESULTS: Of more than 8000 phosphopeptides in almost 2000 proteins accurately quantified in the synaptoneurosome compartment across 24 hours, 30% oscillated in abundance. The phases of rhythmic phosphopeptides were distributed in two major clusters, corresponding to the transition from wake to sleep at dawn and sleep to wake at dusk. In addition to important synaptic constituents such as ion channels, receptors, and scaffolds, a large number of kinases were among the synaptic proteins modulated by phosphorylation in a time-dependent manner. More than half of the detected phosphorylated kinases in synapses show rhythmic phosphorylation at one or more residues. Predictive and experimental data demonstrate that widespread dynamic regulation of kinase activity is a core phospho-dependent functional process at synapses. Together, our data uncover molecular processes in synapses whose activity is temporally gated by phosphorylation, such as synaptic inhibition at dawn and excitation at dusk. We further assessed circadian- and sleep-driven signals by interfering with the sleep-wake cycle by applying 4 hours of sleep deprivation at different times of the day. Sleep deprivation resulted in the loss of 98% of rhythmic phosphorylation in forebrain synapses but left circadian cycles unaffected in a core of 41 phosphoproteins that function in synaptic transport and scaffolding.

ON OUR WEBSITE

Read the full article at http://dx.doi.org/10.1126/science.aav3617

CONCLUSION: This global rhythmic phosphoproteome of isolated synaptoneurosomes reveals a major reorganization of the synaptic molecular compartment concomitant with changes in activity. Our results indicate that phospho-dependent activation of kinases in response to sleep and wake is a core driver of these synaptic phosphorylation dynamics. Together, our data point toward an association of synaptic potentiation with wakefulness (activity) and down-scaling with sleep (rest). High sleep pressure induced through sleep deprivation almost completely abrogates both peaks of daily phosphorylation cycles in synapses. We thus hypothesize that modulation of phosphorylation-mediated synaptic signaling could be a key driver underlying sleep- and wake-dependent mechanisms to regulate synaptic homeostasis and function. ■

The list of author affiliations is available in the full article online.
*These authors contributed equally to this work.
†Corresponding author. Email: charo.robles@med.uni-muenchen.de (M.S.R.); steven.brown@pharma.uzh.ch (S.A.B.)
Cite this article as F. Brüning *et al.*, *Science* **366**, eaav3617 (2019). DOI: 10.1126/science.aav3617

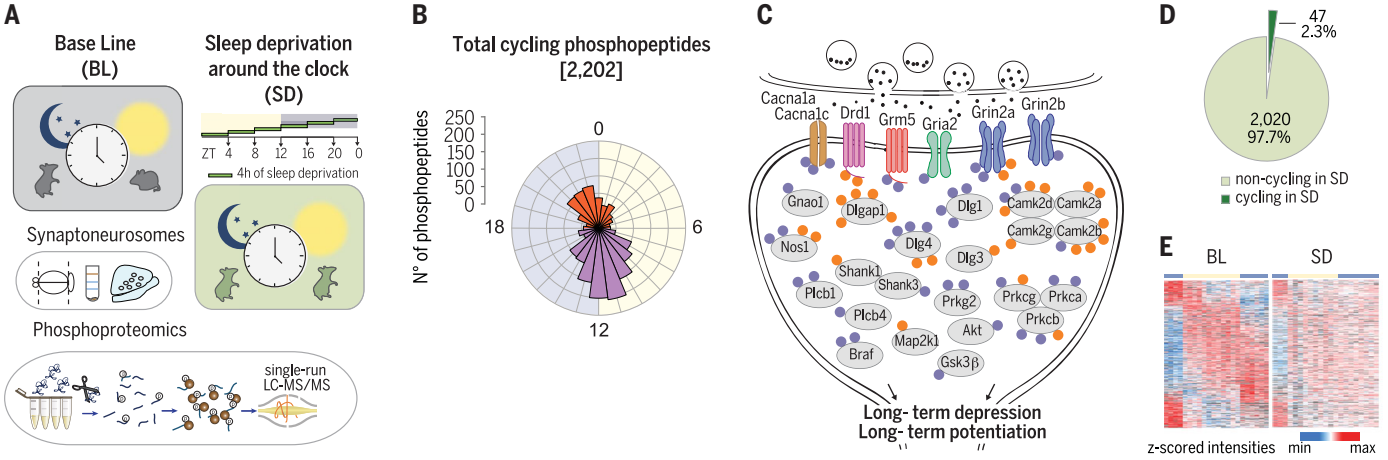

Daily dynamics of global phosphorylation in forebrain synaptoneurosomes under basal and sleep-deprived conditions. (**A**) Quantitative phosphoproteomics analyses of isolated synaptoneurosomes from rested and sleep-deprived mice around the clock. (**B** and **C**) More than 30% of phosphorylations in many synaptic components and numerous kinases cycle daily with peaks at the sleep-wake-sleep transitions. (**D** and **E**) Sleep deprivation abolished 98% of all phosphorylation cycles in synaptoneurosomes.

RESEARCH ARTICLE

NEUROSCIENCE

Sleep-wake cycles drive daily dynamics of synaptic phosphorylation

Franziska Brüning[1,2]*, Sara B. Noya[3]*, Tanja Bange[1], Stella Koutsouli[1], Jan D. Rudolph[4], Shiva K. Tyagarajan[3], Jürgen Cox[4], Matthias Mann[2,5], Steven A. Brown[3]†, Maria S. Robles[1]†

The circadian clock drives daily changes of physiology, including sleep-wake cycles, through regulation of transcription, protein abundance, and function. Circadian phosphorylation controls cellular processes in peripheral organs, but little is known about its role in brain function and synaptic activity. We applied advanced quantitative phosphoproteomics to mouse forebrain synaptoneurosomes isolated across 24 hours, accurately quantifying almost 8000 phosphopeptides. Half of the synaptic phosphoproteins, including numerous kinases, had large-amplitude rhythms peaking at rest-activity and activity-rest transitions. Bioinformatic analyses revealed global temporal control of synaptic function through phosphorylation, including synaptic transmission, cytoskeleton reorganization, and excitatory/inhibitory balance. Sleep deprivation abolished 98% of all phosphorylation cycles in synaptoneurosomes, indicating that sleep-wake cycles rather than circadian signals are main drivers of synaptic phosphorylation, responding to both sleep and wake pressures.

Circadian clocks are endogenous oscillators present in virtually every mammalian cell. The molecular mechanism of the clock drives cycles of transcription, translation, and protein activity to regulate daily changes in physiology and behavior. Mass spectrometry (MS)–based quantitative proteomics has contributed substantially to our understanding of how circadian posttranscriptional mechanisms temporally shape metabolic processes in peripheral tissues (*1*, *2*). Circadian phosphorylation changes by far eclipse the regulation at the transcriptional and proteome levels in amplitude (*3*). Temporal characterization of proteome and phosphoproteome changes in the central nervous system, by contrast, has been challenging because of the sensitivity, dynamic range, and throughput required to capture the regional, cellular, and synaptic heterogeneity. However, recent advances in MS in combination with spatial isolation methods allow the deep characterization of proteomes from different brain regions and cell populations (*4*, *5*). In addition, high-throughput phosphoproteomic technologies are now suitable for the global characterization of phosphorylation signaling dynamics in different brain areas (*6*).

Numerous synaptic features—such as diffusion of receptors in membranes, channel conductance, or cytoskeleton remodeling—depend on fast phosphorylation-based control mechanisms. In particular, synaptic plasticity and scaling have been linked to phosphorylation of receptor, scaffolding, cytoskeletal, and other synaptic proteins (*7*, *8*). Although quantitative phosphoproteomics has been applied to the synaptic compartment, technical limitations have so far precluded accurate quantification that would allow the precise characterization of global phosphorylation dynamics associated with synaptic function (*7*). It is thus unknown whether daily changes in synaptic activity are coupled to global dynamics of phosphorylation in synapses or, moreover, whether daily rhythms of phosphorylation temporally segregate synaptic processes. Two recent reports have addressed these technical limitations by either fractionating postsynaptic density (*9*) or by mapping whole-brain phosphoproteomics to synaptic protein annotations (*10*). They highlight a role for sleep pressure in driving synaptic phosphorylation changes associated with the kinase SIK3 (*10*) and downstream effectors of plasticity such as HOMER1a (*9*).

We applied state-of-the-art quantitative MS-based proteomics to characterize in vivo phosphorylation dynamics across the day in isolated synaptoneurosomes from mouse forebrain, resulting in the most comprehensive time-resolved phosphoproteome of synapses to date. In combination with in-depth proteomics (*11*), we found that more than one-fourth of the individual phosphorylation sites in synaptic proteins oscillate daily and independently of protein abundance. Temporally modulated phosphorylation networks gate synaptic processes at both dawn and dusk, primarily dependent on sleep-wake cycles. Thus, maintaining sleep pressure approximately constant across the day leads to a dramatic ablation of global phosphorylation cycles, suggesting a dominant role of both sleep and wake pressure in synaptic phosphorylation dynamics. In turn, our analyses suggest that these dynamics profoundly shape both synaptic function and downstream regulatory networks.

Results

In-depth phosphoproteomic profiling of synaptoneurosomes

To characterize daily dynamics of phosphorylation abundance specifically in synapses, we biochemically isolated synaptoneurosomes from mouse forebrains (*11*). Mice were kept in 12-hour:12-hour (light:dark) schedules and then euthanized in biological quadruplicates at six time points, every 4 hours, across 24 hours (n = 24 mice). We used a rapid method based on Percoll gradients to prepare synaptoneurosomes from forebrains, containing both pre- and postsynaptic components (*12*), and immediately flash-froze them to prevent dephosphorylation. To achieve sufficient throughput for our time-dependent experiments, we used the EasyPhos method (*13*) to enrich phosphopeptides from only 1 mg of protein homogenate for each synaptoneurosome preparation. The MS-based quantitative phosphoproteomics workflow, consisting of single runs on a high-resolution, high-sensitivity quadrupole-Orbitrap HF-X mass spectrometer, is shown in Fig. 1A. Across all samples, this resulted in a total of 10,439 unique phosphosites identified in 14,462 phosphopeptides, mapping to more than 2000 proteins (Fig. 1B and table S1). Comparing phosphorylated amino acids in synapses with our previous circadian study in the liver (*3*) revealed similar proportions [83.6% phosphoserine (pS), 15.7% phosphothreonine (pT), 0.6% phosphotyrosine (pY)] (Fig. 1B). Phosphopeptide intensities between measurements were highly reproducible in both biological replicates and time points [mean Pearson correlation coefficient (r) = 0.88 and 0.83, respectively] (fig. S1A). The intensities of phosphopeptides in synaptoneurosomes ranged over five orders of magnitude (fig. S1B), similar to what we found in liver, indicating that the synaptic compartment still has a wide quantitative range of phosphorylation levels. To indirectly evaluate our isolation method, we performed a Fisher's exact test on the total phosphoproteome dataset. Of all annotated protein keywords, the top two most significant are "synapse" and "cell junction" ($P < 10^{-40}$ for both), and the other highly enriched ones are also relevant to synaptic function, even when analyzing every time point separately (fig. S1, C to E, and materials and methods). Our data

[1]Institute of Medical Psychology, Faculty of Medicine, LMU Munich, Germany. [2]Department of Proteomics and Signal Transduction, Max-Planck Institute of Biochemistry, 82152 Martinsried, Germany. [3]Institute of Pharmacology and Toxicology, University of Zurich, Zurich, Switzerland. [4]Computational Systems Biochemistry, Max-Planck Institute of Biochemistry, Martinsried, Germany. [5]Novo Nordisk Foundation Center for Protein Research, Faculty of Health Science, University of Copenhagen, Copenhagen, Denmark.
*These authors contributed equally to this work.
†Corresponding author. Email: charo.robles@med.uni-muenchen.de (M.S.R.); steven.brown@pharma.uzh.ch (S.A.B.)

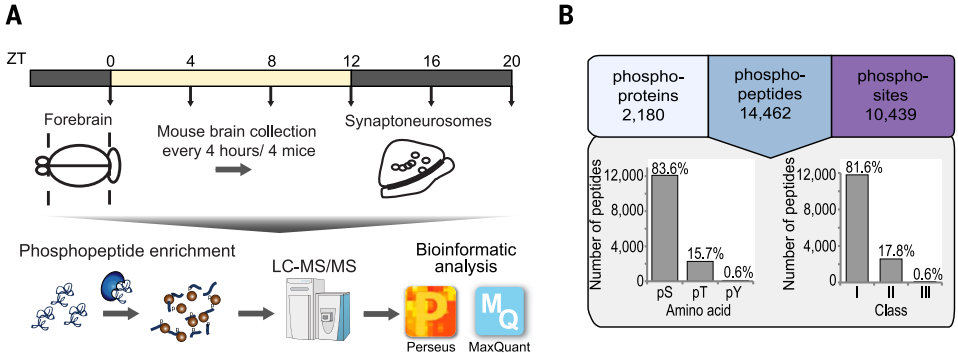

Fig. 1. Phosphoproteome characterization of synaptoneurosomes isolated across the day from mouse forebrains. (**A**) Experimental workflow. (**B**) Number of identified phosphoproteins, phosphopeptides, and phosphosites in all measured samples. (Bottom left) Distribution of phosphorylated amino acids [serine (pS), threonine (pT), and tyrosine (pY)]. (Bottom right) Number of phosphorylated residues from different classes according to localization probability: class I (probability > 75%), class II (probability = 50 to 75%), and class III (probability < 50%).

show the power of combining high-throughput phosphoproteomics with biochemical isolation of synaptoneurosomes to deeply profile phosphorylation in this discrete neuronal compartment.

Daily rhythms of the synaptic phosphoproteome

Next, we performed statistical cycling analysis in the circadian module of the Perseus software (*2*, *3*, *14*) to filter and cosine-fit the phosphopeptide intensities. A total of 2202 (30.4%) of the 7257 phosphopeptides accurately quantified in at least 50% of the samples oscillate in abundance with a rhythm of 24 hours (q < 0.05) (Fig. 2, A and B; table S2; and materials and methods). We detected rhythmic phosphorylations in more than half of the synaptic phosphoproteins (838 out of the total 1655) (Fig. 2C). These cycling sites were localized with high probability to a single residue (mean 0.97), and their amino acid distribution was similar to that of the total dataset (Fig. 1B and fig. S2A). Cycling phosphopeptides had an intensity distribution similar to that of the total phosphoproteome (fig. S2B), implying that circadian phosphoregulation is not biased by abundance. Little is known about the magnitude of dynamic phosphorylation changes in the synaptic compartment, and our data revealed that these changes are substantial: The mean amplitude changes are more than threefold, with hundreds of sites at more than 10-fold (Fig. 2D).

To assess the extent to which these phosphorylation dynamics depend on protein abundance changes, we quantitatively compared the levels of phosphopeptides with the abundance of the corresponding protein. Almost 90% of proteins with cycling phosphopeptides were quantified at the protein level in our companion study (*11*), and of these, only 5% significantly oscillate in abundance (q < 0.05, period = 24 hours) (Fig. 2E). Even the small fraction of rhythmic proteins with oscillating phosphorylation displays different phases across the day, and furthermore, multiple sites in the same protein generally behaved differently (Fig. 2F and fig. S2C). In the minor population of rhythmic proteins carrying cycling phosphorylation, the mean amplitudes at the phosphorylation level were 10-fold larger than those at the protein level (Fig. 2G). Our data clearly establish that protein phosphorylation in forebrain synaptoneurosomes is highly dynamic across the day and almost completely independent of protein abundance, suggesting another layer of synaptic functional regulation.

Temporal compartmentalization of synaptic protein phosphorylation

Our previous study in liver revealed that dynamic phosphorylation drives daily organ functions to a previously unappreciated degree (*3*). Examining the phosphorylation rhythms in the synaptic compartment showed that the phases of rhythmic phosphopeptides gathered in two distinct clusters. The larger one, at the light-to-dark transition when mice start to be active, contains two-thirds of the phosphopeptides, whereas the remaining ones peak at the end of the night, preceding the sleep phase (Fig. 3A). This phase distribution indicates a major rewiring of protein phosphorylation and presumably synaptic function at the wake-to-sleep and sleep-to-wake transitions. In order to identify synaptic functions that are temporally compartmentalized by protein phosphorylation, we searched for statistically enriched protein annotations in each of the two defined phase clusters (Fisher's exact test, P < 0.05) (materials and methods). At the end of the resting phase, our analysis found keywords corresponding to "cell adhesion" and "cell junction" as well as "ion channels," "ion transporters," "hydrolases," and "kinases highly enriched." By contrast, "cell projection," "cytoskeleton," and "ubiquitin conjugation protein" annotations are overrepresented in the phosphopeptide cluster at the end of the activity phase (Fig. 3, B and C, and table S3). Proteins involved in cell division and mitosis were also enriched in the phosphorylation cluster at the end of the activity phase, likely because several cell cycle kinases, such as CDK5, are also important for synaptic activity (*15*). Thus, our results imply that different remodeling processes that are known to occur at synapses (*16*) might occur separately in temporally distinct nodes.

Synapses are hubs of kinases

We next focused our attention on the major and specific enrichment of kinases, key regulators of almost all cellular processes, in the phosphopeptide cluster that peaks at the end of the resting phase. We identified almost 500 phosphorylated peptides from a total of 128 kinases from all major families in mammals. Thus, a fifth of the total mouse kinome is not only present in the synaptic compartment but also detectable in a phosphorylated form (fig. S3A). More than half of these kinases show at least one rhythmic phosphorylation (q < 0.05) (Fig. 4, A and B, and table S4), and these belong to all major kinase families, with a higher representation of AGC threonine/serine kinases (Fig. 4, C and D). All of the 66 kinases with rhythmic phosphorylation were also quantified at the protein level in the synaptic compartment (*11*); however, only four of them cycled in protein abundance (fig. S3B). Therefore, phosphorylation, rather than protein abundance, likely regulates temporal kinase function at synapses across the day. Our analyses also detected cycles of phosphorylation and protein abundance in several phosphatases at the synapses but in a lesser extent compared with kinases. Out of the 77 phosphatases detected in synapses, only three cycle at the protein level, and 10 out of 20 phosphorylated phosphatases showed rhythms of phosphorylation (fig. S4, A to D).

The overall phase distribution of rhythmic phosphopeptides from kinases resembles the total cycling synaptic phosphoproteome (Figs. 3A and 5A), suggesting that phosphorylation-dependent temporal activation of kinases contributes to the global phosphorylation rhythms in synapses. However, because site-specific phosphorylation does not always imply changes in kinase activity, we next set out to identify temporally activated kinases with an unbiased workflow that uses high-confidence protein-

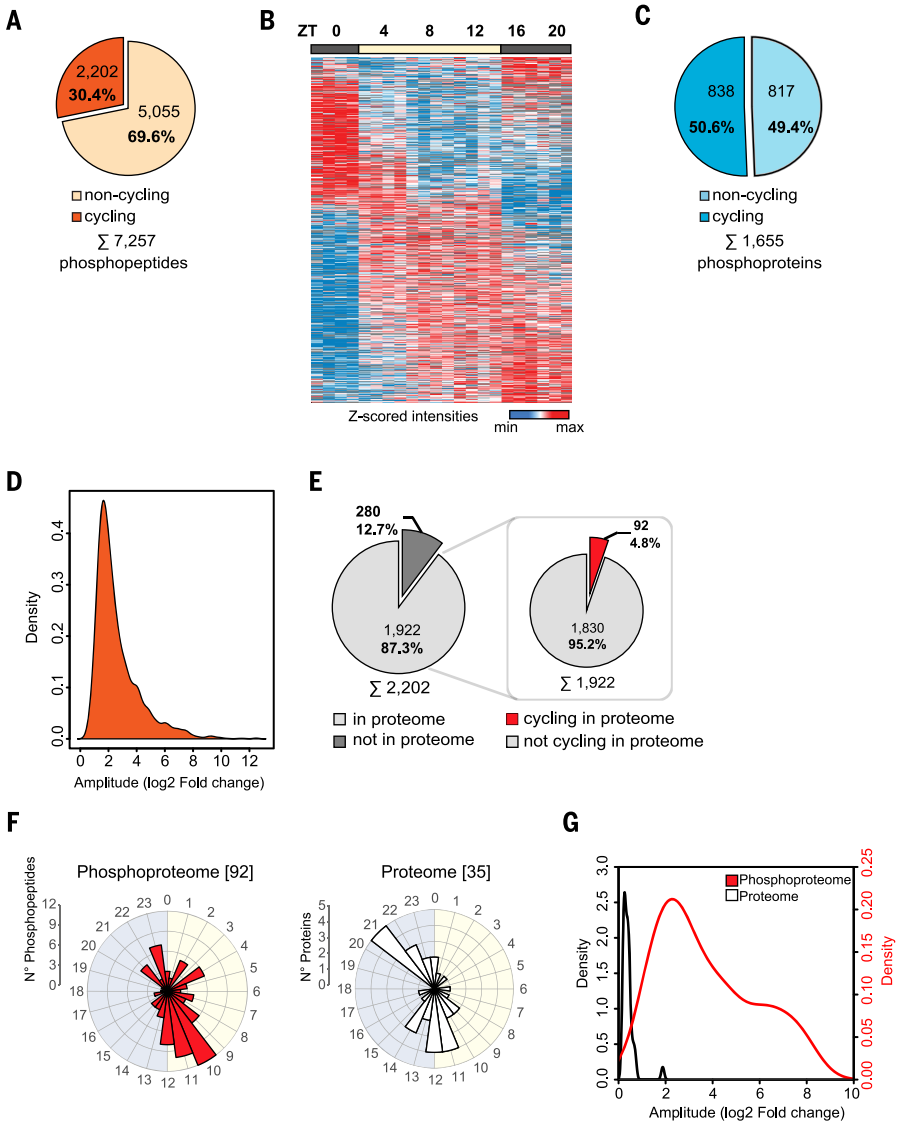

Fig. 2. Daily rhythms of the synaptic phosphoproteome. (**A**) Pie chart showing the percentage of phosphopeptides oscillating (q < 0.05, period = 24 hours) in synaptoneurosomes. (**B**) Heat map with the intensities (log2 z-scored normalized) of each cycling phosphopeptide (rows) across the measure samples (columns) ordered by peak of abundance. (**C**) Pie chart with the percentage of proteins carrying at least one cycling phosphorylation in synaptoneurosomes. (**D**) Density plot showing the calculated amplitudes of rhythmic phosphopeptides in synaptoneurosomes. (**E**) Pie charts showing (left) the percentage of cycling phosphopeptides from proteins quantified in our proteome study and (right) the fraction of cycling phosphopeptides in proteins that are also rhythmic at the protein level. (**F**) Rose plots representing the phase distribution of rhythmic phosphopeptides (left) and their corresponding oscillating proteins (right). (**G**) Density plots comparing the amplitudes of the rhythmic phosphopeptides and the corresponding oscillating proteins.

protein interaction networks and large-scale phosphorylation data to retrieve protein signaling functionality. This PHOTON pipeline assigns a score to each protein according to the phosphorylation status of their interacting proteins (*17*). Because these scores reflect the changes in phosphorylation levels of their substrates and interactors, kinases that are activated rather than only phosphorylated should have PHOTON scores that cycle across the 24 hours, with the maximum score indicating the peak of kinase activity. From the 66 synaptic kinases with rhythmic phosphorylation, this analysis resulted in rhythmic activity patterns for 13 of them (materials and methods). Of these, 11 are active at the sleep-wake transition, including protein kinase C (PRKCA, PRKCB, and PRKCG) and Ca^{2+}/calmodulin-dependent kinase 2 (CAMK2B and CAMK2G). Conversely, the tyrosine-protein kinase ABL2 and the serine/threonine-protein kinase DCLK1 showed the opposite behavior, peaking in activity at the wake-sleep transition (Fig. 5, B and C).

To substantiate the PHOTON prediction data, we used a second computational method [kinase substrate enrichment analysis (KSEA)] that infers kinase activity by using curated kinase-substrate relationships (*18*). This second method estimated, very similarly to PHOTON, the activation of PKC and CAMK2 at the sleep-wake transition (fig. S5 and materials and methods). We verified these kinase activity patterns by immunoblotting using phospho-specific antibodies against phosphorylated residues known to regulate the activity of these two kinases (fig. S6, A and B) (*19*, *20*). The KSEA algorithm also identified additional putative temporally activated kinases with rhythms of phosphorylation (fig. S5). For example, this method predicted that GSK3β, a molecular switch in synaptic activation and plasticity (*21*), is active during the sleep stage. Such predicted activation would be in antiphase to the phosphorylation cycle of two residues known to inhibit its kinase activity, S389 and S9 (*22*, *23*). The former was detected in our data with a peak at ZT11, and the latter was further confirmed by means of immunoblotting (fig. S6C).

Considering the published literature about rhythmically regulated kinases predicted by PHOTON and KSEA, the kinases activated at the transition to the wake phase (CAMK and PKC) are associated with excitatory synaptic activity (*8*), whereas those activated at the transition to and during the sleep phase (ABL2, DCLK1, and GSK3β) are associated with inhibitory synaptic activity (*24*, *25*). An identical temporal compartmentalization of synaptic function was independently predicted by PHOTON by means of phosphorylation dynamics of Gene Ontology (GO) molecular functions (materials and methods); it inferred that the triggering of inhibitory synaptic mechanism, involving γ-aminobutyric acid (GABA), occurs at the end of the wake period, whereas glutamate-mediated synaptic excitatory activity was predominantly associated to the sleep-wake transition (fig. S7). These data are consistent with the roles of these synaptic types in sleep and wake, respectively (*26*, *27*).

Sleep deprivation abrogates synaptic phosphorylation rhythms

We hypothesized that the sharp biphasic distribution of synaptic phosphorylation patterns at the wake-sleep and sleep-wake transitions might reflect either buildup and dissipation of sleep pressure (a sleep homeostat), or alternatively a circadian (time-of-day) mechanism, or a combination of the two. To test their relative contributions, we subjected mice to 4 hours of sleep deprivation (SD) by means of gentle handling (*28*) before each time point

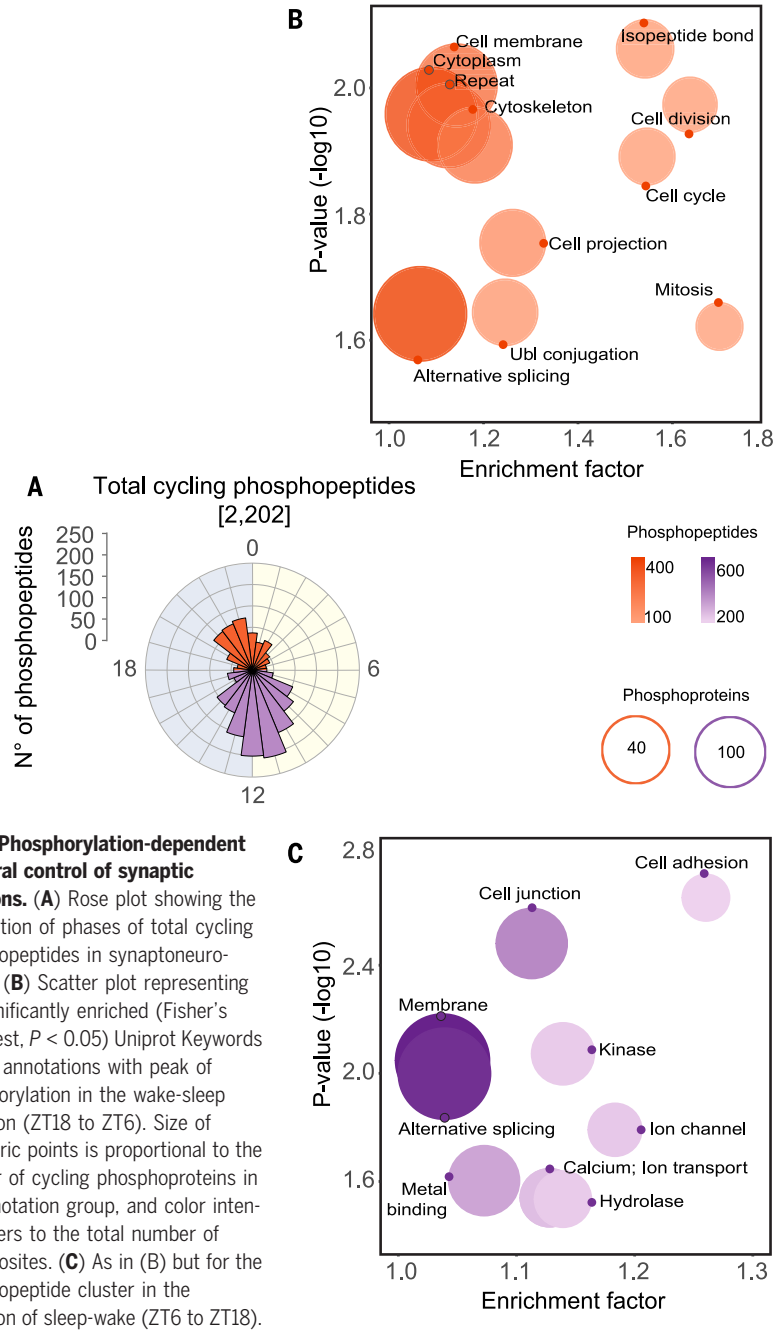

Fig. 3. Phosphorylation-dependent temporal control of synaptic functions. (**A**) Rose plot showing the distribution of phases of total cycling phosphopeptides in synaptoneurosomes. (**B**) Scatter plot representing the significantly enriched (Fisher's exact test, $P < 0.05$) Uniprot Keywords protein annotations with peak of phosphorylation in the wake-sleep transition (ZT18 to ZT6). Size of geometric points is proportional to the number of cycling phosphoproteins in the annotation group, and color intensity refers to the total number of phosphosites. (**C**) As in (B) but for the phosphopeptide cluster in the transition of sleep-wake (ZT6 to ZT18).

and collected brains every 4 hours in 24 hours ($n = 4$ brains per time point) (Fig. 6A). A similar protocol of SD across the 24-hour time course equalizes sleep pressure to keep it constantly high (*29*). First, we empirically verified that this was the case by measuring the amplitude of electroencephalogram (EEG) oscillations during sleep (0.5 to 4 Hz, the "delta" range proportional to sleep pressure) (*30*) and demonstrating that this was similar at each time point to that maximally observed spontaneously in the day before the manipulation. Although some fluctuation in delta power across time points was still observed, we estimated it to be less than a fifth of what is observed under the same conditions across the normal circadian day. We also demonstrated that the pattern and timing of sleep and activity in the subsequent day were not altered by this protocol—that the protocol was not shifting the phase of the circadian clock (Fig. 6B and figs. S8, A and B, and S9). Next, we prepared synaptoneurosomes from forebrains of SD mice, and as in baseline (BL) conditions, we enriched phosphopeptides before MS analysis (Fig. 6A and materials and methods). We accurately quantified 7021 phosphopeptides in at least 50% of the samples, which are very similar values to those in the BL experiment, with more than 90% (6526 phosphopeptides) overlap between them (fig. S10A). Cycling analysis of the 6526 phosphopeptides revealed almost complete abrogation of rhythmic phosphorylation in the synaptic compartment of SD mice. Only 2.3% (47 phosphopeptides corresponding to 41 proteins) of the phosphopeptides rhythmic in BL maintained the cycle in SD (period = 24 hours, $q < 0.05$) (Fig. 6, C and D; table S5; and materials and methods). These few remaining cycling phosphopeptides oscillated with similar amplitudes and with comparable phases in both conditions (Fig. 7, A to C, and table S6), suggesting that they might be driven primarily by the circadian clock. Of the corresponding 41 synaptic phosphoproteins, 31 belong to interconnected cellular structures such as cytoskeleton, synaptic scaffolding, membrane, vesicle trafficking, and ubiquitin mechanisms, all of which are important for synaptic integrity and function (fig. S11) (*31*–*33*). Aside from this small fraction, the remaining 98% of phosphorylations, affecting all aspects of synaptic biology, were severely affected by SD across the day, leading to a dramatic loss in rhythmicity (fig. S10, B to D).

Discussion

Synaptic plasticity and function dynamically change across the day (*34*). It is already known that changes in synaptic activity are associated with the phosphorylation of several signaling proteins (*8*, *33*). However, our large-scale quantitative phosphoproteome of isolated synaptoneurosomes resulted in a comprehensive time-resolved map of synaptic phosphorylation across the entire wake and sleep phases. The phosphoproteome is much more dynamic than the proteome (50% of synaptic proteins showing cyclic phosphorylation at one or more sites versus only 12% of synaptic proteins whose abundance oscillates). Moreover, similar to our previous finding in the liver (*3*), mean fold-changes of the phosphoproteome are more than threefold higher than in the proteome. At 7000 accurately quantified phosphopeptides, our analysis allowed in-depth bioinformatic analysis, retrieving both known and unknown temporally regulated processes at synapses. Overall, the phases of cycling phosphorylation fall into two main clusters just preceding daily activity-rest transitions, when the mouse typically wakes up or falls asleep, implying a major role of synaptic phosphorylation in regulating these transitions. This pattern contrasts markedly with that of the rhythmic phosphoproteome of total forebrain (including entire cells, not just synapses), where phosphorylation peaks gather at the wake and sleep periods (fig. S12), similarly to what we observed for the total rhythmic forebrain proteome described in (*11*).

Numerous kinases are expressed in the brain, and some of them also have been localized

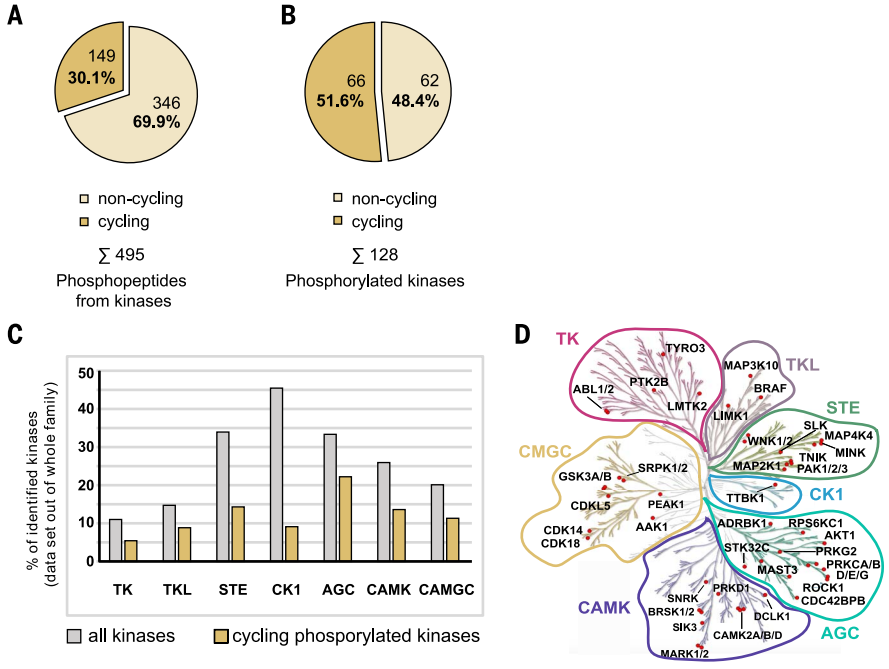

Fig. 4. Synapses are hubs of kinases. (**A**) Pie chart showing the percentage of cycling and not cycling phosphopeptides from kinases. (**B**) Pie chart showing the percentage of kinases with at least one cycling and noncycling phosphorylation. (**C**) Bar plot representing the percentage of all (gray) and cycling (orange) phosphorylated kinases quantified in synaptoneurosomes from each of the major mammalian kinase families. (**D**) Kinases with at least one cycling phosphorylation annotated to the major kinase families (52 out of the total 66 cycling) using www.kinhub.org. TK, tyrosine kinases; TKL, tyrosine kinase-like; STE, homologs of the yeast *STE7*, *STE11*, and *STE20* genes; CK1, casein/cell kinase 1 family; AGC, protein kinase A, G, C families; CAMK, calmodulin/calcium-regulated kinases and some non–calcium-regulated families; and CMGC is CDK, MAPK, GSK3, and CLK kinase families. Atypical kinases are not shown.

to the synaptic compartment (*35*). However, our study clearly identifies the synapse as a major kinase hub. We detected more than 100 phosphorylated kinases (20% of the total kinome) and found that 50% show daily rhythmic phosphorylation of least one residue. Combining protein interaction network data with our quantitative phosphoproteome revealed that these phosphorylation changes regulate the activity of at least a subset of them, predictions that we verified through immunoblotting of known activating and inhibiting phosphoresidues for some kinases. Prediction and empirical validation of kinase activities notably matched to the phosphorylation profiles of known substrates detected in our dataset (fig. S6). Although the existing network data are sufficient to associate rhythmic activity with a substantial subset of the kinases, more complete networks and meta-analyses will likely establish activity changes for a much larger fraction of the cycling synaptic phosphoproteome in the future. Together, the combination of predictive and experimental data places extensive temporal regulation of kinase activity as a core phospho-dependent functional process at the synapse.

An obvious question leading from these data concerns the regulatory target of this control. Considering our predictive and experimental data, we speculate that one possible consequence could be temporally distinct windows for promotion of synaptic long-term potentiation (LTP) and long-term depression (LTD). Kinases with higher activity in anticipation of the wake period are involved in LTP, such as CAMK2 and PRKC, which function directly downstream of *N*-methyl-D-aspartate receptor (NMDAR) Ca^{2+} signaling (*8*). By contrast, ABL2 and DCLK1, two kinases that modulate structural synaptic plasticity (*24*, *25*), peak in activity in anticipation of sleep. Lack of ABL2 leads to elevated NMDAR synaptic currents (*25*); therefore, ABL2 activation at the beginning of the resting phase may mediate synaptic down-scaling. Moreover, phospho-dependent activation of GSK3β during sleep regulates LTD and GABA receptor (GABAR) trafficking (*21*), and its activity is in turn blocked at the wake transition by LTP-mediated phosphorylation of its inhibitory site S9 (*36*) and S389. This mechanistic speculation is further supported by the extensive overlap of phosphorylated residues increased by LTP induction in mouse hippocampus (*33*) with those peaking at the transition to the wake phase in our dataset (fig. S13). Together, our data point toward an association of synaptic potentiation with wakefulness (activity) and synaptic down-scaling with sleep (rest). This supports the general synaptic homeostasis hypothesis for sleep—that synaptic down-scaling is a key function of sleep (*37*) at the molecular level—and provides starting points for a multitude of mechanistic investigations.

Critically, this functional support is created both by phosphorylation rhythms dependent on the sleep-wake cycle and their peaks clustering at the wake-sleep-wake transitions. Thus, an experimental protocol to produce constant sleep pressure across the 24-hour day almost entirely abrogates global diurnal oscillation of phosphorylation in the synaptic compartment. This discovery establishes the importance of the homeostatic regulation of sleep over any other mechanism in generating daily rhythms of phosphorylation to modulate synaptic function. However, these phosphorylation changes are governed both by wake and by sleep. A recent analysis of wake-dependent protein phosphorylation in total mouse brain showed that increasing hours of SD resulted in increasing average phosphorylation levels of 80 synaptic proteins (*10*). We examined our data and found phosphorylations in all of those 80 proteins, with sites showing increased phosphorylation at times of high sleep pressure in 69 of them. However, our amino acid–resolution data reveal a more nuanced picture than a simple overall increase in phosphorylation, with both sleep- and wake-dependent phosphorylation at different residues in these proteins. Another recent phosphoproteomics study in the synaptic compartment showed that sleep regulates dephosphorylation of AMPA receptors in response to HOMER1a-dependent immediate early transcriptional signaling (*9*). Our data independently support these findings, extend them to several other neurotransmitter receptors, and supply their diurnal rhythms of phosphorylation in response to sleep and wake pressure. Globally across the entire phosphoproteome, we found about one-third of cycling phosphorylations to be maximal at the end of the wake phase when sleep pressure is highest and two-thirds to peak at the end of the sleep phase before waking.

Although the vast majority of protein phosphorylation appears to be regulated by sleep or wake states, a small number of rhythmic phosphorylations remain unchanged in amplitude and phase under SD. These phosphorylations occur in a highly connected node of proteins involved in both synaptic vesicle trafficking (molecular motors and microtubule-associated proteins) and synaptic scaffold (SHANK3, PICCOLO, and BASSOON). Circadian regulation of cortical function is already well documented at both behavioral and molecular levels (*38*). Our data imply that even as sleep-wake pressures dynamically reconfigure

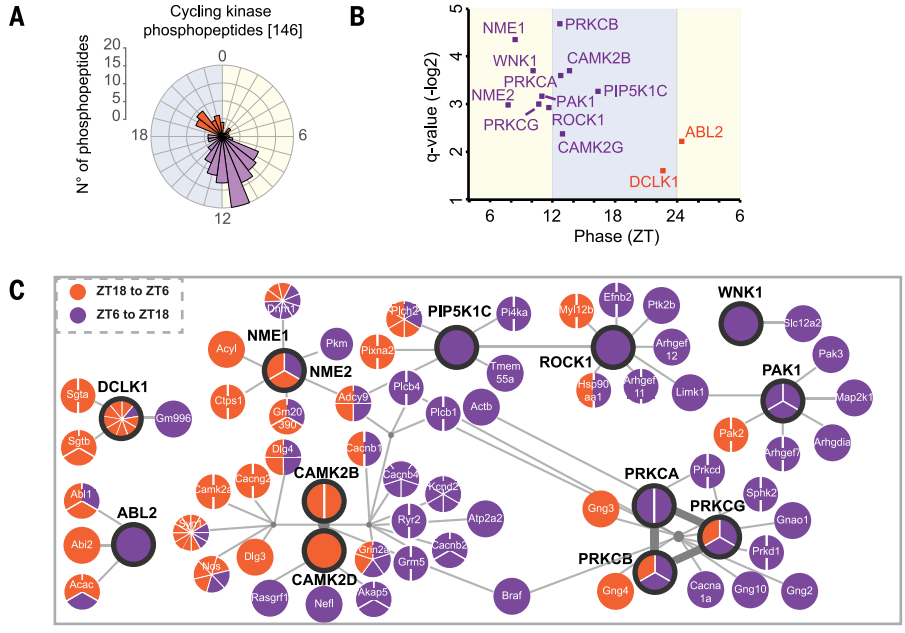

Fig. 5. Rhythmic phosphorylation and activation of synaptic kinases. (**A**) Rose plot with the phases of cycling phosphopeptides from kinases detected in synaptoneurosomes. Colors denote the clusters of wake-sleep transition (ZT18-ZT6, orange) and sleep-wake transition (ZT6-ZT18, purple). (**B**) Scatter plot showing kinases temporally activated predicted by PHOTON. The *x* axis indicates the phase of activation, and the *y* axis indicates the *q* value of the cycling analysis by using PHOTON scores. Kinase names are color-coded according to the two phosphopeptide clusters shown in (A). (**C**) Protein interaction network of PHOTON predicted cycling active kinases ($q < 0.05$) with rhythmic phosphorylations with their cycling phosphorylated interactors. Nodes are divided on the basis of the number of cycling phosphorylations identified in each protein and color-coded according to the clusters in (A). Nodes with thick lines denote those kinases with rhythmic phosphorylated residues that are also predicted to be temporally activated by PHOTON.

synaptic structure and function, circadian control—or at least circadian clock-sleep interactions—continue to influence cortical function. For example, in our accompanying manuscript, we show that synaptic provisioning of RNA can be independently controlled by the circadian clock or by sleep-circadian interactions (*11*). For both synaptic protein abundance and synaptic protein phosphorylation, however, by far the major diurnal influence is that of daily sleep and wake. The mechanism of this influence remains unknown and could include not only direct signaling (such as receptor-driven kinase cascades) but also indirect effects such as light-dark cycles or changes in cortisol or body temperature, which have been shown to play roles in sleep-wake–dependent gene expression (*39*) and in circadian entrainment (*40*, *41*).

This study presents in vivo proof of rhythmic orchestration for thousands of phosphorylation events in synapses across the day. Our study demonstrates a central role for sleep-wake cycles in phosphorylation-dependent regulation of many aspects of synaptic function in response to both sleep and wake pressure, potentially modulating processes that range from plasticity to cellular housekeeping. Interfering with rest-activity cycles almost completely abolished rhythms of phosphorylation in synaptic proteins. Our findings may thus contribute to understanding the molecular basis of mental dysfunction frequently associated with SD.

Materials and methods

Animals and tissue collection

All experiments were performed in accordance with the Animal Welfare Officer of the University of Zürich and the veterinary authorities of the Canton of Zürich. For the circadian base line (BL) experiments, 10-week-old male C57BL/6 mice were housed with free access to food and water and entrained to a 12-hour/12-hour light-dark schedule for 14 days. Mice were sacrificed at 4-hour intervals over 1 day. At the time points overlapping with light transitions (ZT0 and ZT12), euthanasia was performed by cervical dislocation before the light change. For the around-the-clock SD, mice were allowed to acclimatize to a 12-hour light/12-hour dark cycle for 14 days. Six groups of mice were sleep deprived for 4 hours by gentle handling (cage exchange and introduction of novel objects) before being sacrificed at different times of day (ZT0, ZT4, ZT8, ZT12, ZT16, and ZT20). Animals were sacrificed by cervical dislocation avoiding anesthetics, which are potent inhibitors of synaptic transmission. In addition, to boost preservation of phosphorylation, total preparation time was minimized, and samples were kept cooled at every step of the protocol.

Electroencephalogram (EEG) recording and sleep data analysis

Adult wild-type (WT) mice were used for surgery (8 to 10 weeks old at surgery). Mice were implanted epidurally under isoflurane anesthesia for EEG recording. Right before and 24 hours after surgery mice were treated with an analgesic (Temgesic, 0.1 mg/kg, intraperitoneal). Gold-plated miniature screws (0.9 mm diameter) were used as EEG electrodes and positioned on the left hemisphere above the frontal cortex (1.5 mm anterior to bregma, 1.5 mm lateral to the midline) and the parietal cortex (2 mm posterior to bregma and 2 mm lateral to the midline). The reference electrode was placed above the cerebellum (2 mm posterior to lambda, 0 mm lateral to the midline). Screws were connected to copper wires and fixed to the skull with dental cement (Paladur 2-component system). Electromyography (EMG) was recorded using two gold wires (0.2 mm diameter) inserted bilaterally in the neck muscle. After 1 week of recovery EEG-EMG was recorded continuously for 7 days. 2 cohorts of 6 and 8 mice, respectively, underwent a BL days recording and 3 SD days with 48 hours of recovery in between. Cohort 1 underwent SD at ZT4-8, ZT12-16 and ZT 16-20. Cohort 2 underwent SD at ZT0-4, ZT8-12 and ZT20-24. SD was performed by gentle handling as described by (*42*). Both EEG and EMG signals were amplified (factor 2000), analog filtered (high-pass filter: –3 dB at 0.016 Hz; low-pass filter: –3 dB at 40 Hz, less than –35 dB at 128 Hz), sampled with 512 Hz, digitally filtered (EEG: low-pass FIR filter 25 Hz; EMG: band-pass FIR 20-50 Hz) and stored with a 128 Hz resolution. EEG power spectra were computed for 4-s epochs by a Fast Fourier Transform routine within the frequency range of 0.5 to 25 Hz. Between 0.5 Hz and 5 Hz, 0.5 Hz bins were used, and between 5 and 25 Hz 1 Hz bins were used. The corresponding slow-wave-activity (SWA) was calculated using the raw parietal and frontal EEG, as well as the raw and integrated EMG to visually score three vigilance states [non–rapid eye-movement sleep (NREM) sleep, rapid eye-movement sleep (REM), and wake] for 4-s epochs. Epochs containing artifacts were identified and excluded from the spectral analysis. Data analysis was carried out using MATLAB version R2015a (The Math Works, Natick, MA, USA). Relative frontal SWA was calculated relative to the mean SWA at ZT8-12 during the BL day. Sleep loss was calculated

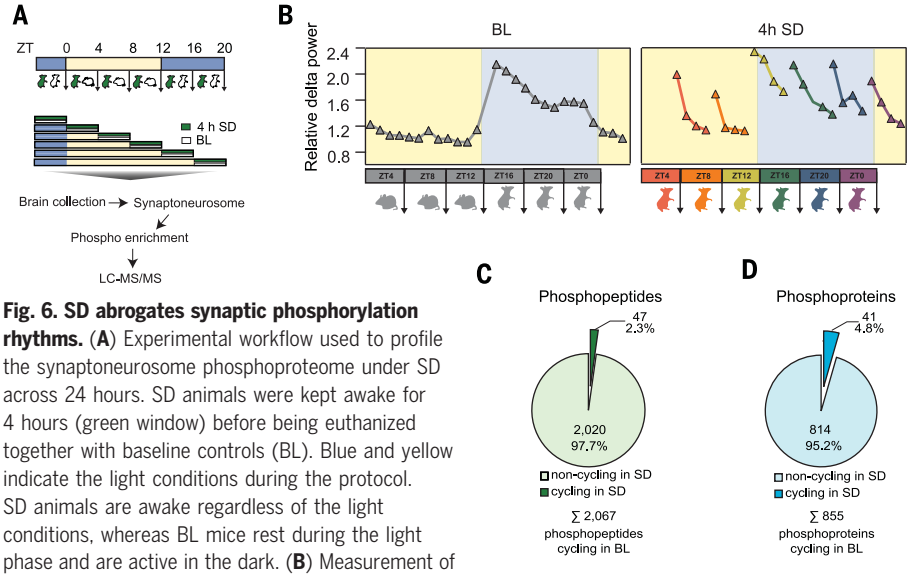

Fig. 6. SD abrogates synaptic phosphorylation rhythms. (**A**) Experimental workflow used to profile the synaptoneurosome phosphoproteome under SD across 24 hours. SD animals were kept awake for 4 hours (green window) before being euthanized together with baseline controls (BL). Blue and yellow indicate the light conditions during the protocol. SD animals are awake regardless of the light conditions, whereas BL mice rest during the light phase and are active in the dark. (**B**) Measurement of the EEG of relative frontal delta power during NREM sleep (triangles, percent of the last 4 hours of the baseline light periods) for the same time courses in BL (left) and SD (right). (**C**) Pie chart indicates the fraction of cycling phosphopeptides (period = 24 hours, $q < 0.05$) in forebrain synaptoneurosomes from SD mice out of the 2067 rhythmic in BL mice. (**D**) Pie chart shows the fraction of proteins with at least one cycling (period = 24 hours, $q < 0.05$) phosphopeptide in synaptoneurosomes of SD mice out of the 855 oscillating under BL conditions.

by comparing NREM sleep amount in each 4h SD slot to the sleep amount in the same time of day of the corresponding BL day [1-way analysis of variance (ANOVA), $P < 0.05$). Sleep latency was analyzed by measuring the time each mouse stayed awake after the end of each 4 hours SD until it slept for more than 1 min (1-way ANOVA, $P < 0.05$).

Purification of synaptoneurosomes

Synaptoneurosomes and total mouse forebrain samples were prepared as described previously (*12*). In brief, brain was isolated and rapidly cooled to 4°C, washed in ice-cooled sucrose buffer (320 mM Sucrose, 5 mM HEPES, pH 7.4) followed by homogenization with a Teflon-glass tissue grinder using a motor-driven pestle keeping samples cooled. To isolate synaptoneurosomes, each forebrain homogenate was centrifuged at 1000 g for 10 min. 2 ml of the supernatant were loaded over discontinuous Percoll gradients (3%, 10%, and 23% Percoll in sucrose buffer) and centrifuged at 31,000 g for 5 min. The fraction at the interfaces between 3-10% and 10 to 23% were collected and further centrifuged at 20,000 g to pellet synaptoneurosomes. All centrifugation steps were performed at 4°C. All solutions were supplemented with complete protease inhibitor cocktail (Roche), 0.05 mM DTT, 0.1 mM PMSF and RNaseOUT 20 U/10 µl (Invitrogen).

Sample preparation and phosphopeptides enrichment

Isolated synaptoneurosome and total forebrain samples were lysed [0.1 M Tris-HCl (pH 7.6) and 4% SDS], sonicated in a bioruptor (4°C for 15 min or until homogenous suspension was formed) and boiled at 95°C for 5 min. A total of 1 mg protein lysate was treated first with 1 µl DTT (1 M) followed by 10 µl 2-Chloroacetamide (0.5 M). Each treatment was performed at room temperature (RT; 22°C) for 20 min. The lysates were precipitated with acetone and phosphopeptides were enriched using the EasyPhos method as described (*3*). In detail, pellets were resuspended in 500 µl trifluoroethanol (TFE) buffer prior to the addition of digestion enzymes (trypsin and LysC) 1:100 (protein:enzyme). After overnight incubation at 37°C with rapid agitation (1500 rpm) 150 µl 3.2 M KCl, 55 µl of 150 mM KH_2PO_4, 800 µl 100% acetonitrile (ACN), and 95 µl 100% trifluoroacetic acid (TFA) were added to the peptides and incubated at RT for 5 min at 1600 rpm prior to centrifugation. The peptide supernatant was transferred to a clean 2 ml tube, TiO_2 beads subsequently added at a ratio of 10:1 beads/protein, and incubated at 40°C for 5 min at 2000 rpm. Beads with bound phosphopeptides were pelleted by centrifugation for 1 min at 3500 g and the supernatant was discarded. Beads were then resuspended in wash buffer (60% ACN and 1% TFA) and transferred to a clean 2 ml tube, and washed further four times with 1 ml of washing buffer. After the last wash, beads were resuspended in transfer buffer (80% ACN and 0.5% acetic acid) and transferred on top of C8 (3M Empore) StageTips. Phosphopeptides were eluted with 60 µl elution buffer [40% ACN and 15% NH4OH (25%, HPLC grade)] and collected in clean PCR tubes, concentrated in a SpeedVac for 15 min at 45°C, and acidified with 10 µl of 10% TFA. Peptides were then desalted using StageTips with two layers of styrenedivinylbenzene–reversed phase sulfonated (SDB-RPS; 3M Empore), washed twice with wash buffer (0.2% TFA) and once with isopropanol containing 1% TFA. Peptides were eluted by adding 60 µl SDB-RPS elution buffer [80% ACN, 1.25% NH_4OH (25%, HPLC grade)] and immediately concentrated in a SpeedVac for 30 min at 45°C. Concentrated peptides were then resuspended in a buffer containing 2% ACN and 0.1% TFA prior to LC-MS/MS analysis.

LC-MS/MS analysis and data processing

Phosphopeptides were loaded onto a 50 cm reversed-phase column (diameter 75 µM; packed in-house with 1.9 µM C18 ReproSil particles [Dr. Maisch GmbH]). The temperature of the column oven was maintained at 60°C. The column was mounted to an EASY-nLC 1200 system (Thermo Fisher Scientific). The peptides were eluted with a binary buffer system consisting of buffer A (0.1% formic acid) and buffer B (80% ACN and 0.1% formic acid). A gradient length of 140 min was chosen (5 to 65% buffer B for 130 min followed by 10 min 80% buffer B) with a flow rate of 300 nl/min. Peptides were analyzed in a Q Exactive HF (synaptoneurosomes) and Q Exactive HF-X (total forebrain) mass spectrometer (MS) (Thermo Fisher Scientific) coupled to the nLC. Full scans [300 to 1600 mass/charge ratio (m/z), R = 60,000 at 200 m/z] were obtained at a target of 3e6 ions. The 10 most abundant ions were selected and fragmented with higher-energy collisional dissociation (HCD) (target 1e5 ions, maximum injection time 120 ms, isolation window 1.6 m/z, normalized collision energy 25% underfill ratio 40%) followed by the detection in the Orbitrap (R = 15,000 at 200 m/z). Raw MS data files were processed using MaxQuant [version 1.5.5.6 and 1.5.5.12 (*43*)] with the Andromeda search engine using false discovery rate (FDR) < 0.01 at protein, peptide, and modification level. The default settings were used with the following modifications: (i) the variable modification methionine (M), acetylation (protein N-term), as well as phosphorylation (STY) and the fixed modification carbamidomethyl (C) were selected, (ii) only peptides with a minimal length of seven amino acids were considered, and (iii) the "match between run" option was enabled with a matching time window of 0.7 min. For protein and peptide identification we used the UniProt database from mouse (September 2014) containing 51,210 entries. Each raw file was treated as one experiment. The following samples were not considered for the final analysis due to low identification number and outlier clustering within the replicates: replicate 4 of ZT16, 3 of ZT20 of the base line group and

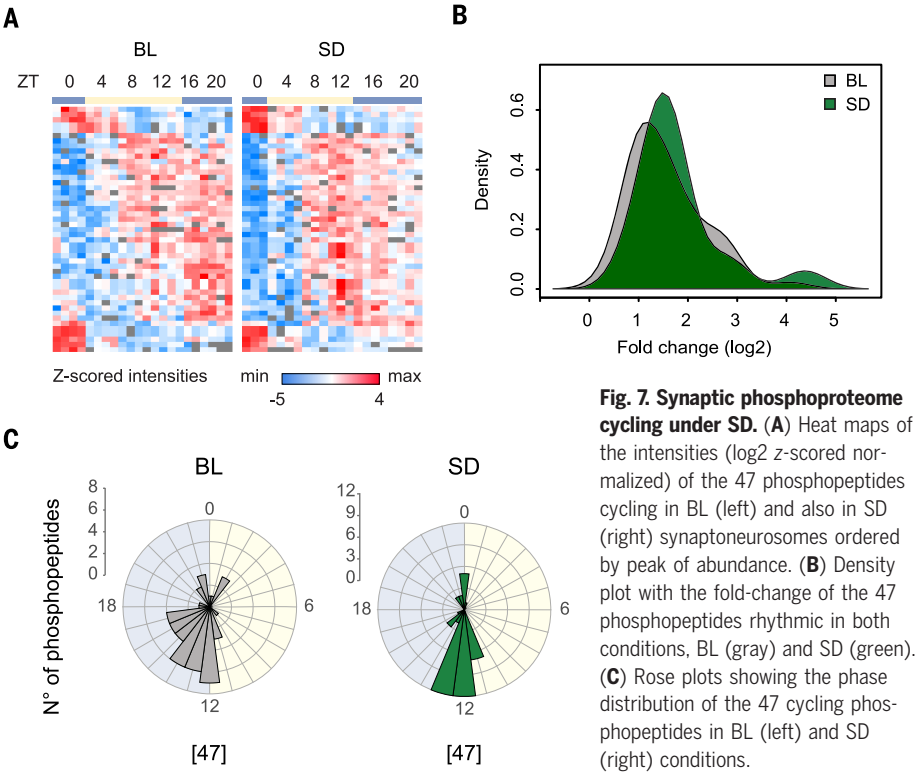

Fig. 7. Synaptic phosphoproteome cycling under SD. (**A**) Heat maps of the intensities (log2 *z*-scored normalized) of the 47 phosphopeptides cycling in BL (left) and also in SD (right) synaptoneurosomes ordered by peak of abundance. (**B**) Density plot with the fold-change of the 47 phosphopeptides rhythmic in both conditions, BL (gray) and SD (green). (**C**) Rose plots showing the phase distribution of the 47 cycling phosphopeptides in BL (left) and SD (right) conditions.

replicate 1 of ZT0, 4 of ZT8, and 2 of ZT12 of the sleep deprived group.

Bioinformatic and statistical analyses

Processed data was uploaded in the Perseus software (*14*) to perform bioinformatical analyses. First, reverse sequences and potential contaminants were removed from the total matrix. Then phosphopeptides intensities were log2 transformed and after expanding the site table, phosphopeptide entries without intensities in <12 samples independently in each data set (SD/BL) were removed. Following this, a normalization was applied to each sample individually: the intensity of every phosphopeptide was divided by the median intensity of all phosphopeptides in the same sample. Relative enrichment of UniProt KB -Keywords annotations in the total BL phosphoproteome dataset was achieved using Fisher's exact test enrichment analyses (FDR < 0.02) comparing to a total in silico mouse gene list generated by Perseus, both datasets were matched using gene names. Cycling analyses were performed as described using the computational platform Perseus (*2*, *14*). Phosphopeptides with a q < 0.05 were classified as "cycling." Hierarchical clustering was performed in a phase preserving-manner by which the order of elements is restricted to that determined by the output of the periodicity analysis. The proteome and the phosphoproteome data were matched using Uniprot ID. Amplitudes were calculated as the difference between maximum and minimum values across all the time points using the mean of log2 intensities for the biological replicates. Cycling phosphopeptides were divided in two groups depending on their peak of phosphorylation ("phase"): one group containing phosphopeptides which peak between ZT18 to ZT6 and the other group comprising phosphopeptides which peak between ZT6 to ZT18. Relative enrichment of UniProt KB -Keywords annotations for both groups was individually performed using Fisher's exact test enrichment analyses (P < 0.05) comparing the protein annotations of both groups to the protein annotations of the total cycling phosphopeptides.

Phosphopeptides belonging to kinases and phosphatases (using Keyword and manual annotations) were extracted from the total list of phosphopeptides and collapsed to protein entries (kinases). Kinases and phosphatases with at least one cycling phosphopeptide (cycling analysis, q < 0.05) were defined as "cycling." Gene name lists of all quantified kinases and of cycling kinases were submitted to www.kinhub.org to annotate kinases to the major families and to generate the kinase trees. Percentages of total quantified and cycling kinases in each family were calculated based on the entries for each family designated in www.kinhub.org.

Integrated analysis and visualization of phosphoproteomic data and protein-protein interaction network

Interactions for mouse were downloaded from STRING (v10.5) and filtered for high-confidence edges with scores of at least 0.9. Since the node identifiers in the network are Ensemble protein IDs (ENSP), the protein groups in the phosphoproteomics data were mapped ENSP IDs using the UniProt annotations in Perseus. After annotating the nodes of the network with the data, signaling functionality scores were calculated using PHOTON. In brief, for each protein in the network a moderated t test was performed on the phosphorylation found on its neighbors in the network. Using a permutation-based FDR approach the resulting P value was corrected for multiple testing and transformed into a final score. Intuitively, proteins with high/low scores pro-/demote the phosphorylation of their neighbors. Cycling analysis was performed on the PHOTON scores to identify kinases with an oscillatory signaling functionality score (q < 0.05, period 24 hours). For the visualization, all cycling kinases and their interactions were extracted from the network. The subnetwork was overlaid with phosphorylation data from cycling sites and plotted using the d3.js library and manual layouting.

For the KSEA prediction, 1,664 site-specific mouse kinase substrate interactions were downloaded from phosphosite.org (*44*). The 7257 phosphopeptides could be mapped to 84 distinct kinase-substrate interactions. KSEA z-scores were calculated for all kinases in the network (*17*, *18*), resulting in 37 kinase activity profiles with at least 3 valid values. After z-scoring the profiles, periodicity analysis was performed and cycling (q < 0.05, period 24 hours) kinase activity profiles were visualized in a scatter plot.

Western blotting and antibodies

Synaptoneurosome lysates were loaded onto 4 to 12% Bis-Tris NuPAGE gels (Thermo Fisher Scientific). After electrophoreses proteins were transferred to a nitrocellulose membrane and blocked in 5% BSA in TBS with 0.1% Tween-20 for 1 hour at room temperature. The incubation with the primary antibody was done overnight at 4°C following supplier instructions. Antibodies were obtained from Cell Signaling: CAMKII pT286 (12716), GSK3β pS9 (5558), and PKC pS660 (9371). The same secondary antibody against rabbit was used for all phospho-specific antibodies (GE Healthcare, NA934V) and was incubated for 1 hour at RT. Loading control was done with an antibody against glyceraldehyde-3-phosphate dehydrogenase (GAPDH) conjugated with horseradish peroxidase from ThermoFisher Scientific (MA5-15738-HRP). Densitometric quantification was performed using the ImageJ software.

REFERENCES AND NOTES

1. D. Mauvoisin *et al.*, Circadian clock-dependent and -independent rhythmic proteomes implement distinct diurnal functions in mouse liver. *Proc. Natl. Acad. Sci. U.S.A.* **111**, 167–172 (2014). doi: 10.1073/pnas.1314066111; pmid: 24344304

2. M. S. Robles, J. Cox, M. Mann, In-vivo quantitative proteomics reveals a key contribution of post-transcriptional mechanisms to the circadian regulation of liver metabolism. *PLOS Genet.* **10**, e1004047 (2014). doi: 10.1371/journal.pgen.1004047; pmid: 24391516
3. M. S. Robles, S. J. Humphrey, M. Mann, Phosphorylation is a central mechanism for circadian control of metabolism and physiology. *Cell Metab.* **25**, 118–127 (2017). doi: 10.1016/j.cmet.2016.10.004; pmid: 27818261
4. F. Hosp, M. Mann, A primer on concepts and applications of proteomics in neuroscience. *Neuron* **96**, 558–571 (2017). doi: 10.1016/j.neuron.2017.09.025; pmid: 29096073
5. K. Sharma *et al*., Cell type- and brain region-resolved mouse brain proteome. *Nat. Neurosci.* **18**, 1819–1831 (2015). doi: 10.1038/nn.4160; pmid: 26523646
6. J. J. Liu *et al*., In vivo brain GPCR signaling elucidated by phosphoproteomics. *Science* **360**, eaao4927 (2018). doi: 10.1126/science.aao4927; pmid: 29930108
7. D. C. Dieterich, M. R. Kreutz, Proteomics of the synapse–A quantitative approach to neuronal plasticity. *Mol. Cell. Proteomics* **15**, 368–381 (2016). doi: 10.1074/mcp.R115.051482; pmid: 26307175
8. K. M. Woolfrey, M. L. Dell'Acqua, Coordination of protein phosphorylation and dephosphorylation in synaptic plasticity. *J. Biol. Chem.* **290**, 28604–28612 (2015). doi: 10.1074/jbc.R115.657262; pmid: 26453308
9. G. H. Diering *et al*., Homer1a drives homeostatic scaling-down of excitatory synapses during sleep. *Science* **355**, 511–515 (2017). doi: 10.1126/science.aai8355; pmid: 28154077
10. Z. Wang *et al*., Quantitative phosphoproteomic analysis of the molecular substrates of sleep need. *Nature* **558**, 435–439 (2018). doi: 10.1038/s41586-018-0218-8; pmid: 29899451
11. S. B. Noya *et al*., The forebrain synaptic transcriptome is organized by clocks, but its proteome is driven by sleep. *Science* **366**, eaav2642 (2019).
12. P. R. Dunkley, P. E. Jarvie, P. J. Robinson, A rapid Percoll gradient procedure for preparation of synaptosomes. *Nat. Protoc.* **3**, 1718–1728 (2008). doi: 10.1038/nprot.2008.171; pmid: 18927557
13. S. J. Humphrey, S. B. Azimifar, M. Mann, High-throughput phosphoproteomics reveals in vivo insulin signaling dynamics. *Nat. Biotechnol.* **33**, 990–995 (2015). doi: 10.1038/nbt.3327; pmid: 26280412
14. S. Tyanova *et al*., The Perseus computational platform for comprehensive analysis of (prote)omics data. *Nat. Methods* **13**, 731–740 (2016). doi: 10.1038/nmeth.3901; pmid: 27348712
15. K. O. Lai, Z. Liang, E. Fei, H. Huang, N. Y. Ip, Cyclin-dependent kinase 5 (Cdk5)-dependent phosphorylation of p70 ribosomal S6 kinase 1 (S6K) is required for dendritic spine morphogenesis. *J. Biol. Chem.* **290**, 14637–14646 (2015). doi: 10.1074/jbc.M114.627117; pmid: 25903132
16. V. M. Ho, J. A. Lee, K. C. Martin, The cell biology of synaptic plasticity. *Science* **334**, 623–628 (2011). doi: 10.1126/science.1209236; pmid: 22053042
17. J. D. Rudolph, M. de Graauw, B. van de Water, T. Geiger, R. Sharan, Elucidation of signaling pathways from large-scale phosphoproteomic data using protein interaction networks. *Cell Syst.* **3**, 585–593.e3 (2016). doi: 10.1016/j.cels.2016.11.005; pmid: 28009266
18. P. Casado *et al*., Kinase-substrate enrichment analysis provides insights into the heterogeneity of signaling pathway activation in leukemia cells. *Sci. Signal.* **6**, rs6 (2013). doi: 10.1126/scisignal.2003573; pmid: 23532336
19. L. M. Keranen, E. M. Dutil, A. C. Newton, Protein kinase C is regulated in vivo by three functionally distinct phosphorylations. *Curr. Biol.* **5**, 1394–1403 (1995). doi: 10.1016/S0960-9822(95)00277-6; pmid: 8749392
20. J. Lisman, R. Yasuda, S. Raghavachari, Mechanisms of CaMKII action in long-term potentiation. *Nat. Rev. Neurosci.* **13**, 169–182 (2012). doi: 10.1038/nrn3192; pmid: 22334212
21. C. A. Bradley *et al*., A pivotal role of GSK-3 in synaptic plasticity. *Front. Mol. Neurosci.* **5**, 13 (2012). doi: 10.3389/fnmol.2012.00013; pmid: 22363262
22. D. A. Cross, D. R. Alessi, P. Cohen, M. Andjelkovich, B. A. Hemmings, Inhibition of glycogen synthase kinase-3 by insulin mediated by protein kinase B. *Nature* **378**, 785–789 (1995). doi: 10.1038/378785a0; pmid: 8524413
23. T. M. Thornton *et al*., Phosphorylation by p38 MAPK as an alternative pathway for GSK3beta inactivation. *Science* **320**, 667–670 (2008). doi: 10.1126/science.1156037; pmid: 18451303
24. E. Shin *et al*., Doublecortin-like kinase enhances dendritic remodelling and negatively regulates synapse maturation. *Nat. Commun.* **4**, 1440 (2013). doi: 10.1038/ncomms2443; pmid: 23385585
25. X. Xiao, A. D. Levy, B. J. Rosenberg, M. J. Higley, A. J. Koleske, Disruption of coordinated presynaptic and postsynaptic maturation underlies the defects in hippocampal synapse stability and plasticity in Abl2/Arg-deficient mice. *J. Neurosci.* **36**, 6778–6791 (2016). doi: 10.1523/JNEUROSCI.4092-15.2016; pmid: 27335408
26. C. Cirelli, C. M. Gutierrez, G. Tononi, Extensive and divergent effects of sleep and wakefulness on brain gene expression. *Neuron* **41**, 35–43 (2004). doi: 10.1016/S0896-6273(03)00814-6; pmid: 14715133
27. V. V. Vyazovskiy, C. Cirelli, M. Pfister-Genskow, U. Faraguna, G. Tononi, Molecular and electrophysiological evidence for net synaptic potentiation in wake and depression in sleep. *Nat. Neurosci.* **11**, 200–208 (2008). doi: 10.1038/nn2035; pmid: 18204445
28. I. Tobler, T. Deboer, M. Fischer, Sleep and sleep regulation in normal and prion protein-deficient mice. *J. Neurosci.* **17**, 1869–1879 (1997). doi: 10.1523/JNEUROSCI.17-05-01869.1997; pmid: 9030645
29. S. Maret *et al*., Homer1a is a core brain molecular correlate of sleep loss. *Proc. Natl. Acad. Sci. U.S.A.* **104**, 20090–20095 (2007). doi: 10.1073/pnas.0710131104; pmid: 18077435
30. P. Franken, D. Chollet, M. Tafti, The homeostatic regulation of sleep need is under genetic control. *J. Neurosci.* **21**, 2610–2621 (2001). doi: 10.1523/JNEUROSCI.21-08-02610.2001; pmid: 11306614
31. N. Z. Gerges *et al*., Independent functions of hsp90 in neurotransmitter release and in the continuous synaptic cycling of AMPA receptors. *J. Neurosci.* **24**, 4758–4766 (2004). doi: 10.1523/JNEUROSCI.0594-04.2004; pmid: 15152036
32. D. Ivanova, A. Dirks, A. Fejtova, Bassoon and piccolo regulate ubiquitination and link presynaptic molecular dynamics with activity-regulated gene expression. *J. Physiol.* **594**, 5441–5448 (2016). doi: 10.1113/JP271826; pmid: 26915533
33. J. Li *et al*., Long-term potentiation modulates synaptic phosphorylation networks and reshapes the structure of the postsynaptic interactome. *Sci. Signal.* **9**, rs8 (2016). doi: 10.1126/scisignal.aaf6716; pmid: 27507650
34. G. Tononi, C. Cirelli, Sleep and the price of plasticity: From synaptic and cellular homeostasis to memory consolidation and integration. *Neuron* **81**, 12–34 (2014). doi: 10.1016/j.neuron.2013.12.025; pmid: 24411729
35. L. L. Baltussen, F. Rosianu, S. K. Ultanir, Kinases in synaptic development and neurological diseases. *Prog. Neuropsychopharmacol. Biol. Psychiatry* **84**, 343–352 (2018). doi: 10.1016/j.pnpbp.2017.12.006; pmid: 29241837
36. C. Hooper *et al*., Glycogen synthase kinase-3 inhibition is integral to long-term potentiation. *Eur. J. Neurosci.* **25**, 81–86 (2007). doi: 10.1111/j.1460-9568.2006.05245.x; pmid: 17241269
37. G. Tononi, C. Cirelli, Sleep function and synaptic homeostasis. *Sleep Med. Rev.* **10**, 49–62 (2006). doi: 10.1016/j.smrv.2005.05.002; pmid: 16376591
38. R. Iyer, T. A. Wang, M. U. Gillette, Circadian gating of neuronal functionality: A basis for iterative metaplasticity. *Front. Syst. Neurosci.* **8**, 164 (2014). doi: 10.3389/fnsys.2014.00164; pmid: 25285070
39. V. Mongrain *et al*., Separating the contribution of glucocorticoids and wakefulness to the molecular and electrophysiological correlates of sleep homeostasis. *Sleep* **33**, 1147–1157 (2010). doi: 10.1093/sleep/33.9.1147; pmid: 20857860
40. A. Balsalobre *et al*., Resetting of circadian time in peripheral tissues by glucocorticoid signaling. *Science* **289**, 2344–2347 (2000). doi: 10.1126/science.289.5488.2344; pmid: 11009419
41. S. A. Brown, G. Zumbrunn, F. Fleury-Olela, N. Preitner, U. Schibler, Rhythms of mammalian body temperature can sustain peripheral circadian clocks. *Curr. Biol.* **12**, 1574–1583 (2002). doi: 10.1016/S0960-9822(02)01145-4; pmid: 12372249
42. I. Tobler, K. Jaggi, Sleep and EEG spectra in the Syrian hamster (*Mesocricetus auratus*) under baseline conditions and following sleep deprivation. *J. Comp. Physiol. A* **161**, 449–459 (1987). doi: 10.1007/BF00603970; pmid: 3668881
43. S. Tyanova, T. Temu, J. Cox, The MaxQuant computational platform for mass spectrometry-based shotgun proteomics. *Nat. Protoc.* **11**, 2301–2319 (2016). doi: 10.1038/nprot.2016.136; pmid: 27809316
44. P. V. Hornbeck *et al*., PhosphoSitePlus, 2014: Mutations, PTMs and recalibrations. *Nucleic Acids Res.* **43**, D512–D520 (2015). doi: 10.1093/nar/gku1267; pmid: 25514926
45. J. A. Vizcaíno *et al*., 2016 update of the PRIDE database and its related tools. *Nucleic Acids Res.* **44**, D447–D456 (2016). doi: 10.1093/nar/gkv1145; pmid: 26527722

ACKNOWLEDGMENTS

We thank K. Mayr, I. Paron, and G. Sowa for technical assistance with the MS measurements; B. Collins for critical reading of the manuscript; and B. Splettstößer for technical help with experimental workflow. **Funding:** M.S.R., F.B., and M.M. were supported by the Max Planck Society for the Advancement of Sciences and the German Research Foundation (DFG/Gottfried Wilhelm Leibniz Prize) and the Volkswagen Foundation (93 071); M.S.R. and S.K. received funding from by the DFG (Projektnummer 329628492 – SFB 1321 and INST 86/1800-1 FUGG). S.A.B. and S.B.N. were supported by the Swiss National Science Foundation, the Velux Foundation, the Human Frontier Science Program, and the Zürich Clinical Research Priority Project "Sleep and Health," and both are members of the Neurosciences program within the Life Sciences Zürich Graduate School; J.C. and J.D.R. have received funding from the European Union Horizon (2020 research and innovation program) under grant agreement 686547 and from the FP7 grant agreement GA ERC-2012-SyG 318987 CToPAG (to J.C., J.D.R, and F.B.). **Author contributions:** S.B.N., M.S.R., and S.A.B. conceived and initiated the project and designed experiments; S.B.N., M.S.R., and F.B. performed sample preparation and mass spectrometry experiments; M.S.R., F.B., and S.B.N. performed bioinformatic and data analysis with help from T.B. and S.K.T.; J.D.R. performed PHOTON analysis under supervision of J.C.; S.B.N., F.B., M.S.R., S.A.B., and M.M. wrote the manuscript with editing and input from T.B., S.K., and J.D.R. **Data and materials availability:** The mass spectrometry proteomics data have been deposited to the ProteomeXchange Consortium via the PRIDE (45) partner repository with the dataset identifier PXD010697.

SUPPLEMENTARY MATERIALS

science.sciencemag.org/content/366/6462/eaav3617/suppl/DC1
Figures S1 to S13
Tables S1 to S6
View/request a protocol for this paper from *Bio-protocol*.

9 September 2018; accepted 4 September 2019
10.1126/science.aav3617

Sleep-wake cycles drive daily dynamics of synaptic phosphorylation

Franziska Brning, Sara B. Noya, Tanja Bange, Stella Koutsouli, Jan D. Rudolph, Shiva K. Tyagarajan, Jrgen Cox, Matthias Mann, Steven A. Brown, and Maria S. Robles

Science, **366** (6462), eaav3617.
DOI: 10.1126/science.aav3617

Sleep-wake cycles at mouse synapses

Analysis of the transcriptome, proteome, and phosphoproteome at synapses in the mouse brain during daily sleep-wake cycles reveals large dynamic changes (see the Perspective by Cirelli and Tononi). Noya *et al.* found that almost 70% of transcripts showed changes in abundance during daily circadian cycles. Transcripts and proteins associated with synaptic signaling accumulated before the active phase (dusk for these nocturnal animals), whereas messenger RNAs and protein associated with metabolism and translation accumulated before the resting phase. Brüning *et al.* found that half of the 2000 synaptic phosphoproteins quantified showed changes with daily activity-rest cycles. Sleep deprivation abolished nearly all (98%) of these phosphorylation cycles at synapses.

Science, this issue p. eaav2642, p. eaav3617; see also p. 189

LETTER

doi:10.1038/nature21384

Basis of catalytic assembly of the mitotic checkpoint complex

Alex C. Faesen[1], Maria Thanasoula[1], Stefano Maffini[1], Claudia Breit[1], Franziska Müller[1], Suzan van Gerwen[1], Tanja Bange[1] & Andrea Musacchio[1,2]

In mitosis, for each daughter cell to inherit an accurate copy of the genome from the mother cell, sister chromatids in the mother cell must attach to microtubules emanating from opposite poles of the mitotic spindle, a process known as bi-orientation. A surveillance mechanism, termed the spindle assembly checkpoint (SAC), monitors the microtubule attachment process and can temporarily halt the separation of sister chromatids and the completion of mitosis until bi-orientation is complete[1]. SAC failure results in abnormal chromosome numbers, termed aneuploidy, in the daughter cells, a hallmark of many tumours. The HORMA-domain-containing protein mitotic arrest deficient 2 (MAD2) is a subunit of the SAC effector mitotic checkpoint complex (MCC). Structural conversion from the open to the closed conformation of MAD2 is required for MAD2 to be incorporated into the MCC[1]. *In vitro*, MAD2 conversion and MCC assembly take several hours[2–4], but in cells the SAC response is established in a few minutes[5–7]. Here, to address this discrepancy, we reconstituted a near-complete SAC signalling system with purified components and monitored assembly of the MCC in real time. A marked acceleration in MAD2 conversion and MCC assembly was observed when monopolar spindle 1 (MPS1) kinase phosphorylated the MAD1–MAD2 complex, triggering it to act as the template for MAD2 conversion and therefore contributing to the establishment of a physical platform for MCC assembly. Thus, catalytic activation of the SAC depends on regulated protein–protein interactions that accelerate the spontaneous but rate-limiting conversion of MAD2 required for MCC assembly.

The SAC temporarily targets the activity of the E3 ubiquitin ligase anaphase promoting complex/cyclosome (APC/C), which is required for mitotic exit (Fig. 1a). Two SAC proteins, MAD2 and BUBR1 (the latter of which forms a constitutive complex with BUB3), interact directly with cell-division cycle protein 20 (CDC20), an APC/C co-activator. The resulting quaternary complex, comprising MAD2, BUBR1–BUB3 and CDC20, represents the core of the mitotic checkpoint complex (MCC^{core}), which is the SAC effector[8–11] (Fig. 1a and Extended Data Fig. 1a, b). MCC^{core} binds APC/C, which is already bound to a second CDC20 molecule, inhibiting its activity[12–14]. Thus, CDC20, an APC/C co-activator when devoid of SAC proteins, becomes an APC/C inhibitor when bound to SAC proteins in the MCC.

MAD2 binds the MAD2-interacting motif (MIM) of CDC20. This promotes a topological remodelling of MAD2 in which its 'safety belt', a structurally mobile element comprising around the last 45 residues of MAD2, changes from an open (O-MAD2) to a closed conformation (C-MAD2)[15,16] (Extended Data Fig. 1c). Direct measurements have indicated that O-MAD2 binds to the CDC20 MIM with a dissociation constant (K_d) of approximately 10^{-7} M (refs 15,16). However, when measured *in vitro*, the reaction appeared to have a remarkably small on-rate constant[2–4], probably because structural remodelling of MAD2 requires a large activation energy. Thus, binding of MAD2 to CDC20 may be rate-limiting for SAC activation; because SAC reactivation takes only minutes in cells[5–7], this binding reaction is likely to be catalysed.

To identify this catalyst, we tagged recombinant human O-MAD2, CDC20, and BUBR1 with fluorophores, creating Förster resonance energy transfer (FRET) sensors for MCC assembly. MCC sensor 1 (MCC^{S1}) monitors the binding of cyan fluorescent protein (CFP)-tagged CDC20 (CFP–CDC20) and O-MAD2–TAMRA (Fig. 1b and Extended Data Fig. 2a–c); MCC sensor 2 (MCC^{S2}) monitors the binding of CFP–BUBR1 and O-MAD2–TAMRA (Fig. 1b and Extended Data Fig. 2a, d, e). When injected into mitotic HeLa cells, the fluorescent proteins localized to kinetochores, which is where SAC proteins normally reside during mitosis, showing that the fluorescent proteins retain functionality (Extended Data Fig. 3).

We measured the FRET-acceptor fluorescence of MCC^{S1} at different concentrations of O-MAD2 after a 15-h pre-incubation, which allowed the system to reach equilibrium (Fig. 1c, red curve). The dissociation constant of the CDC20–C-MAD2 interaction ($K_d = 150$ nM) was similar to that previously measured using CDC20 peptides that contain the MIM motif[3,15,16]. When we titrated O-MAD2 in the presence of dark (that is, non-fluorescently labelled) BUBR1, 3 nM O-MAD2 was sufficient to obtain half-maximal saturation of MCC^{S1} (the apparent K_d ($K_{d,app}$); defined in Supplementary Information Section A), indicating a strongly augmented (by approximately 50-fold) binding affinity (Fig. 1c, blue curve).

There was no FRET signal from MCC^{S2} in the absence of CDC20, indicating that CDC20 is necessary for the high-affinity binding of BUBR1 and O-MAD2 (Extended Data Fig. 2d). As for MCC^{S1}, the $K_{d,app}$ for the binding of O-MAD2 to BUBR1 in the presence of CDC20 was 3 nM (Fig. 1c, green curve), indicating that the chosen position of the fluorophores does not interfere with MCC assembly. Co-elution of the four subunits of MCC^{S1} from a size-exclusion chromatography column further supports this conclusion (Extended Data Fig. 2f).

Removal of BUB3 did not affect the stability of MCC (Extended Data Fig. 2g). BUBR1 binds CDC20 in the MCC^{core} through its first KEN-box (KEN1) motif[12] (Extended Data Fig. 1a); however, binding of the second CDC20 subunit requires KEN2 (ref. 12). The CDC20-dependent FRET signal of MCC^{S2} requires KEN1, but not KEN2 (Fig. 1d; blue and green curves, respectively), showing that MCC^{S2} monitors the assembly of the MCC^{core}. The apparent binding affinity did not change in the presence of the KEN2 mutant, suggesting that binding of a second CDC20 protein does not stabilize the MCC^{core}. These studies at equilibrium support two notable conclusions: (1) MCC^{core} assembly is high-affinity, so BUBR1, CDC20, and O-MAD2, whose cellular concentrations are at least ten times higher than the $K_{d,app}$ values that we measured (Supplementary Information Section B), are expected to associate spontaneously; and (2) interactions that engage two MCC subunits are strongly augmented upon addition of the third subunit (for example, BUBR1 augments the CDC20–MAD2 interaction).

[1]Department of Mechanistic Cell Biology, Max-Planck Institute of Molecular Physiology, Otto-Hahn-Straße 11, 44227 Dortmund, Germany. [2]Centre for Medical Biotechnology, Faculty of Biology, University Duisburg-Essen, Universitätsstraße, 45141 Essen, Germany.

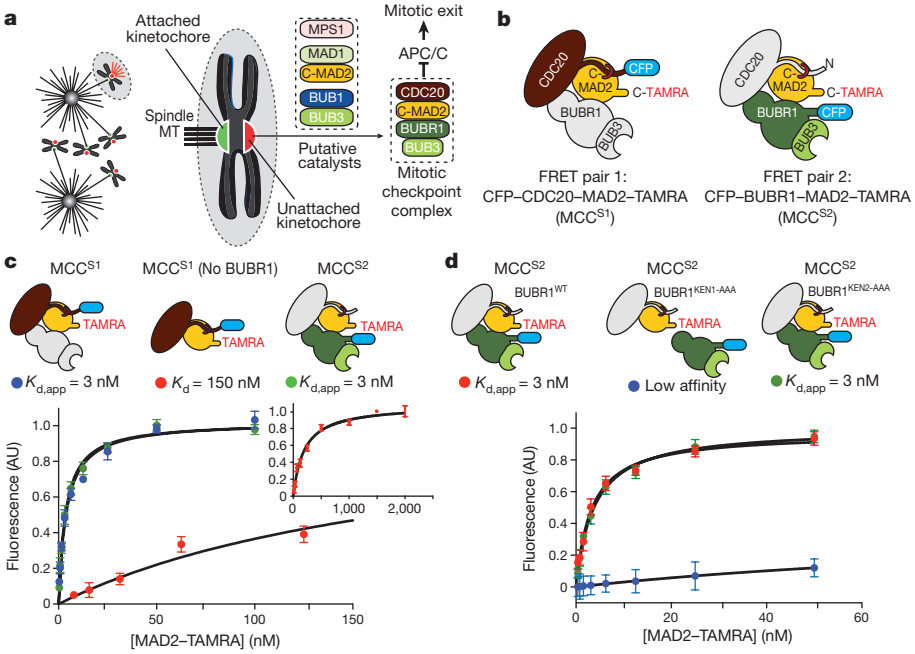

Figure 1 | Stability of MCC. a, Putative SAC catalysts at unattached kinetochores promote MCC assembly to inhibit APC/C, preventing mitotic exit. MT, microtubule. **b**, Schematic of the two MCC FRET sensors used. **c**, Inter-subunit interactions in the MCC augment binding affinity. Responses of MCC^{S1} and MCC^{S2} to the indicated MAD2–TAMRA concentrations (red, MCC^{S1}, no BUBR1; blue, MCC^{S1}, with BUBR1; green, MCC^{S2}). BUBR1 augments the stability of MCC^{S1}. For MCC^{S1}, 1 nM CFP–CDC20 and 500 nM BUBR1 were used; for MCC^{S2}, 1 nM CFP–BUBR1 and 500 nM CDC20 were used. The 'Fluorescence' label on the *y*-axis indicates FRET acceptor fluorescence at the indicated MAD2 concentration, normalized to the maximum FRET-acceptor fluorescence at saturating MAD2 concentrations (measured at 583 nm). AU, arbitrary units. Inset, full curve of MCC^{S1} without BUBR1. **d**, Titration experiment with wild-type BUBR1 (red) or Ala-Ala-Ala (AAA) mutants of KEN-box 1 (blue) or KEN-box 2 (green). Data are mean ± s.e.m. of three independent technical replicates (**c**, **d**).

We used MCC^{S2} to measure MCC assembly by FRET in real time. The time-dependence of the FRET signal could be fitted with a single exponential function to yield an apparent reaction rate (k_{obs}) that increased linearly with the concentration of MAD2 (Extended Data Fig. 4a, b), indicative of pseudo-first-order kinetics. At a near-physiological concentration of MCC components (100 nM), MCC assembly, as measured with MCC^{S2}, was very slow, with a half-life ($t_{1/2}$) of approximately 220 min (or 13,200 s; Fig. 2a). MCC^{S1} displayed precisely the same slow rates as MCC^{S2} (Extended Data Fig. 4d, red curve) and omission of BUBR1 did not change the rate of activation of MCC^{S1} (Extended Data Fig. 4d, red and blue curves). Instead, when O-MAD2–TAMRA and CDC20 were pre-incubated, and CFP–BUBR1 was added to pre-formed CDC20–C-MAD2–TAMRA, MCC formation was practically instantaneous (Fig. 2a). Thus, reorganization of the MAD2 safety belt upon binding of O-MAD2–TAMRA and CFP–CDC20 may limit the rate of MCC^{core} assembly[3] and, as such, it is the likely target of the catalytic apparatus of the SAC (Fig. 1a).

The MAD1–C-MAD2 complex forms the kinetochore receptor of O-MAD2 and has been proposed to accelerate its conversion, which is required for CDC20 to bind via a template-directed mechanism[17,18] (the MAD2 template model, see Supplementary Information Section C). Previous studies, however, detected only modest effects of MAD1–C-MAD2 on MCC assembly *in vitro*, which were clearly insufficient to account for the rapid accumulation of the MCC in living cells[3,4,17]. MAD1–C-MAD2 might therefore require an activator. In looking for this activator, we focused on the protein kinases BUB1–BUB3 and MPS1, owing to their role in the regulation of MAD1–C-MAD2 (ref. 1).

We pre-incubated recombinant MAD1–C-MAD2, BUB1–BUB3, and MPS1 at a concentration of 1 μM for 30 min at 30 °C with ATP and Mg^{2+}, before diluting them at different concentrations into solutions containing MCC^{S2} (Fig. 2b). Even at low-nanomolar concentrations, pre-incubated MAD1–C-MAD2, BUB1–BUB3 and MPS1 strongly increased the rate of MCC assembly (Fig. 2b). The initial velocity of MCC formation increased linearly as a function of catalyst concentration (Extended Data Fig. 4e). At concentrations (25–50 nM) comparable to those reported to exist in cells, pre-incubated MAD1–C-MAD2, BUB1–BUB3 and MPS1 caused the MCC-binding reaction to equilibrate in minutes ($t_{1/2}$ = 165 and 82 s for 25 and 50 nM, respectively; Fig. 2b), in line with signalling dynamics *in vivo*[5,6]. At equivalent concentrations of MCC subunits and catalytic activators, the behaviour of MCC^{S1} was essentially indistinguishable from that of MCC^{S2} (Extended Data Fig. 4f). Thus, our *in vitro* assay captures a crucial catalytic activation step of the SAC.

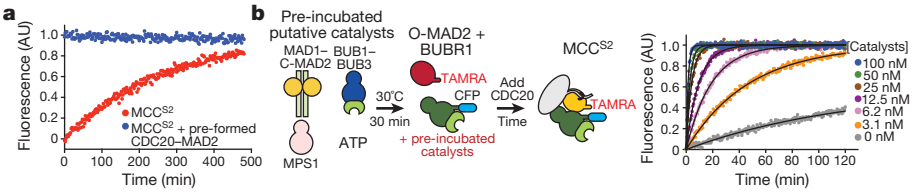

Figure 2 | Catalytic assembly of MCC. a, Binding of CDC20 to MAD2 is rate-limiting for MCC formation. Zero minutes is the first time point after mixing 100 nM CFP–BUBR1–BUB3 either with CDC20 and O-MAD2–TAMRA (red) or with CDC20–C-MAD2–TAMRA, allowed to form by overnight pre-incubation at 4 °C (blue). **b**, MAD1–C-MAD2, BUB1–BUB3 and MPS1 catalyse MCC assembly. After pre-incubation at 30 °C for 30 min, MAD1–C-MAD2, BUB1–BUB3 and MPS1 were diluted at indicated concentrations into 100 nM MCC^{S2} (with 500 nM CDC20). Data are single measurements representative of at least three independent technical replicates of the experiment (**a**, **b**).

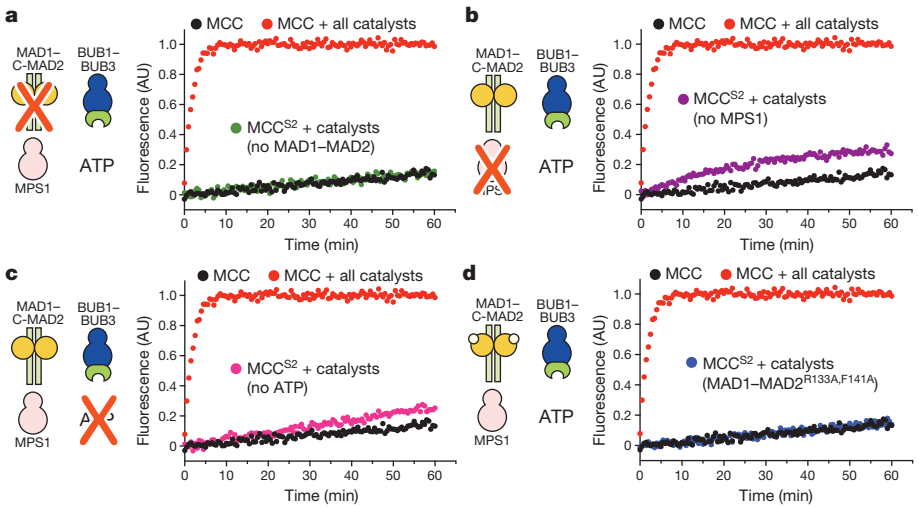

Figure 3 | Molecular requirements of catalytic MCC assembly. a–c, Catalytic MCC assembly requires MAD1–C-MAD2, MPS1, ATP and BUB1–BUB3. MCC assembly was monitored with MCC^{S2} as described in Fig. 2b using 100 nM catalysts. Individual components were omitted as indicated. The same control profiles (black and red curves) are shown in all panels. **d**, Mutations in C-MAD2 bound to MAD1 that prevent its interaction with O-MAD2 of MCC^{S2} abrogate catalysis. Control profiles (black and red curves) are as shown in **a–c** and Extended Data Fig. 5a. Assay performed with MCC^{S2} as described in Fig. 2b using 100 nM catalysts.

To identify the factors necessary for rapid accumulation of the MCC, we omitted individual components from the pre-incubation step (catalyst concentrations in these experiments are discussed in Supplementary Information Section D). Removing MAD1–C-MAD2 prevented any acceleration of MCC formation (Fig. 3a). Removing MPS1 (Fig. 3b) or ATP (Fig. 3c) resulted in a strong reduction in the rate of MCC assembly. Removing BUB1–BUB3 still had a large effect but it was less substantial (Extended Data Fig. 5a).

Asymmetrical dimerization of O-MAD2 and C-MAD2 has previously been identified as part of the mechanism of MAD2 activation in the SAC[3,17,18]. We investigated whether mutations to MAD2 in the MAD1–C-MAD2 complex (the mutation of residues 133 and 141 to alanine), which prevent dimerization with O-MAD2 (refs 18,19), would ablate the catalytic role of MAD1–C-MAD2. Indeed, MAD1–C-$MAD2^{R133A–F141A}$ was inert, confirming that MAD2 dimerization is a crucial component of the catalytic mechanism (Fig. 3d). N-terminal truncations of MAD1 (Extended Data Figs 1d, 2a) showed that residues 1–419 of MAD1 are dispensable for catalysis, whereas deletions affecting residues 420–485 decreased the catalytic function of MAD1–C-MAD2 (Extended Data Fig. 5b).

MPS1 and BUB1 are protein kinases. We studied the relevance of kinase activity on the catalytic reaction with the small-molecule kinase inhibitors Reversine and BAY-320, which target MPS1 and BUB1, respectively[20,21] (Extended Data Fig. 6a). Addition of Reversine during pre-incubation had substantial negative consequences for the catalytic activation of MCC assembly, but its addition at the end of pre-incubation was fully compatible with catalysis. Thus, MPS1 activity is required only during pre-incubation (Fig. 4a). Much milder effects were observed with BAY-320, suggesting that the kinase activity of BUB1 makes a relatively modest contribution to the catalytic activation of MCC (Extended Data Fig. 6b).

We dissected the requirements for kinase activity by performing two separate pre-incubation reactions (with ATP): one with MPS1 and MAD1–C-MAD2 and the other with BUB1–BUB3. Catalysis was fully reconstituted when the two pre-incubation reactions were added to MCC^{S2} and CDC20 (Extended Data Fig. 6c). Addition of Reversine to MPS1 and MAD1–C-MAD2 during pre-incubation strongly reduced the rate of MCC assembly (Extended Data Fig. 6d), suggesting that MPS1 phosphorylates and activates MAD1–C-MAD2.

Using mass spectrometry, we identified several phosphorylation sites on the MAD1–MAD2 complex after *in vitro* phosphorylation with MPS1 (Extended Data Fig. 7a). On the basis of sequence conservation, previous phosphoproteomic analyses (as summarized in the PHOSIDA (http://141.61.102.18/phosida/index.aspx) and Phosphosite Plus (http://www.phosphosite.org/homeAction.action) websites) and previous functional analyses, we prioritized four MPS1 phosphorylation sites located in two distinct regions: Ser428 of MAD1 (in the coiled-coil region of MAD1, upstream of the MIM), and Ser699, Ser713 and Thr716 (in the RWD domain)[15,16,22] (Extended Data Figs 1d and 7a). An alanine point mutation in Ser428 (S428A) had no effect on the catalytic activity of MAD1–C-MAD2 (Fig. 4b). Conversely, a triple-alanine mutant of Ser699, Ser713 and Thr716 (S699A/S713A/T716A, hereafter $MAD1^{RWD-A}$) abrogated the catalytic role of MAD1 in MCC assembly. The residual response of $MAD1^{RWD-A}$ was ascribed to BUB1, because when that was omitted, catalysis was completely abrogated. Our attempts to generate phospho-mimetic mutants of MAD1–C-MAD2 were frustrated by instability of the protein products (A.C.F. and A.M., unpublished data).

Removal of MAD1–C-MAD2 from the kinetochores following microtubule attachment is required to suppress SAC signalling. A chimeric fusion protein of wild-type MAD1 ($MAD1^{WT}$) and MIS12 (which stably binds kinetochores) prevents MAD1 release and arrests mitosis at metaphase[23]. When expressed in HeLa cells, the MIS12–$MAD1^{WT}$ chimaera created a durable checkpoint arrest in mitosis, which was suppressed by the inhibition of MPS1 with Reversine (Fig. 4c and Extended Data Fig. 7b–d). MIS12–$MAD1^{S428A}$ behaved like MIS12–$MAD1^{WT}$, whereas MIS12–$MAD1^{RWD-A}$ failed to arrest mitosis at metaphase, indicating that the $MAD1^{RWD-A}$ mutant impairs the SAC response caused by fusing MAD1 to MIS12 (Fig. 4c). Thus, preventing MPS1 phosphorylation with the $MAD1^{RWD-A}$ mutant abrogates the catalytic role of MAD1–C-MAD2 both *in vitro* and in an established SAC assay in human cells.

A tenfold reduction in the concentration of MPS1 during pre-incubation had little effect on the half-life of MCC assembly, suggesting that MPS1 can perform multiple rounds of MAD1–C-MAD2 phosphorylation (Extended Data Fig. 8a, conditions 1 and 4). Conversely, a tenfold reduction in the concentration of either MAD1–C-MAD2 or BUB1–BUB3 (Extended Data Fig. 8a) resulted in an approximately threefold increase in the half-life of MCC accumulation. A tenfold reduction in the concentrations of both MAD1–C-MAD2 and BUB1–BUB3 compounded the individual effects, causing a tenfold reduction in the half-life of MCC accumulation.

These observations suggest that MAD1–C-MAD2 and BUB1–BUB3 may both act as physical constituents of the catalyst of MCC assembly, in line with evidence that these proteins might interact physically (Supplementary Information Section E). To assess this theory, we used MCC^{S1} to measure the influence of BUB1–BUB3 on the binding of CDC20 and MAD2. When BUB1–BUB3 was omitted, a strong reduction in the formation of the CDC20–C-MAD2 complex was observed (Extended Data Fig. 8b). This effect did not involve BUBR1–BUB3 (which binds directly to BUB1–BUB3)[24], because omission of BUBR1–BUB3 did not influence the rate of FRET accumulation from MCC^{S1} (Extended Data Fig. 8b).

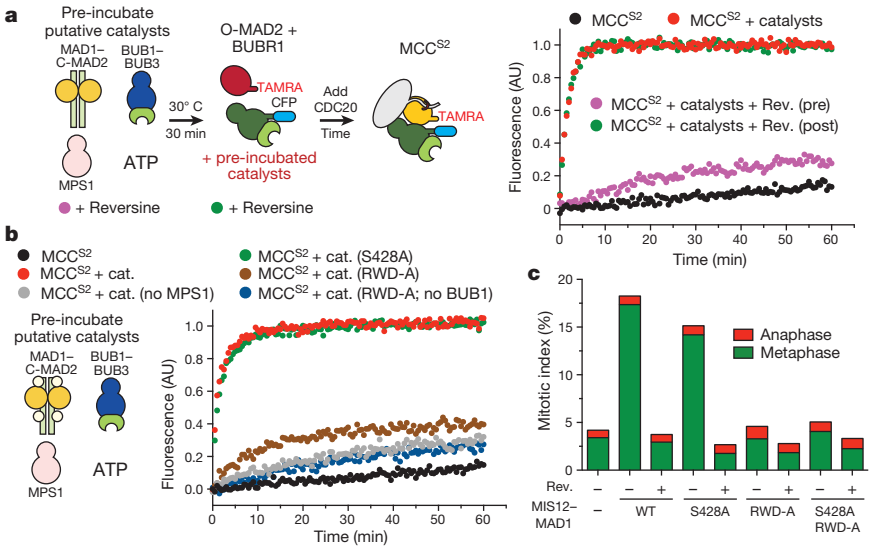

Figure 4 | MPS1 activates MAD1. a, Reversine (Rev.) added during pre-incubation of catalysts (pre, purple points) or during MCC^{S2} assembly phase (post, green points). Concentration of inhibitor was 5 μM in FRET assay and 50 μM in pre-incubation. Assay was performed as described in Fig. 2b using 100 nM catalysts. **b**, Phosphorylation sites in $MAD1^{RWD\text{-}A}$ are required for MCC catalysis (brown). Limited residual catalysis is due to BUB1 (compare brown and blue). Experiments conducted with $MAD1^{420\text{-}C}$ as described in Fig. 2b using 100 nM catalysts (cat.). **c**, HeLa cells in the presence or absence of Reversine were transfected with mCherry (−; 1,471 cells), mCherry–MIS12–$MAD1^{WT}$ (WT; 1,451 (left) and 1,224 (right) cells), mCherry–MIS12–$MAD1^{S428A}$ (S428A; 1,309 (left) and 1,198 (right) cells), mCherry–MIS12–$MAD1^{RWD\text{-}A}$ (RWD-A; 1,838 (left) and 1,138 (right) cells), or mCherry–MIS12–$MAD1^{S428A,RWD\text{-}A}$ (S428A-RWD-A; 1,657 (left) and 1,289 (right) cells). After 30 h, mitotic indexes of mCherry-positive cells (Extended Data Fig. 6b) were scored by visualization of DNA, CREST (kinetochores), and α-tubulin (not shown). Cells were also treated with 500 nM Reversine for 2 h before fixation. Graphs show the mean of at least two technically independent experiments; the number of cells used for each quantification is listed above.

We next investigated whether BUB1 exercises its functions through CDC20. When using a BUB1 construct with mutations in the CDC20-binding motif (the KEN1-ABBA motif[25–27]), we observed that the rate of assembly of CDC20–C-MAD2 was reduced to levels similar to those observed after removal of BUB1–BUB3 (Extended Data Fig. 8c). Thus, the contribution of BUB1 to MCC assembly appears to require an interaction with CDC20, and we surmise that the kinase activity of BUB1 mildly stimulates this interaction.

MAD1 and BUB1 have previously been shown to interact[28–30]. We therefore investigated whether human MAD1–C-MAD2 and BUB1 form a complex by performing pull-down experiments in which MAD1 tagged with maltose-binding protein (MBP) and bound to C-MAD2 (MBP–MAD1–C-MAD2) was immobilized on amylose beads (Extended Data Fig. 8d). We observed binding of BUB1–BUB3 to MBP–MAD1–C-MAD2 only in the presence of MPS1 kinase activity, suggesting that MPS1 triggers the interaction, as in *Saccharomyces cerevisiae*[28]. The interaction between MAD1–C-MAD2 and BUB1–BUB3 is transient and low affinity, as the proteins did not co-elute from a size-exclusion chromatography column (A.C.F., M.T., C.B. and A.M., unpublished results).

Our data indicate that BUB1–BUB3 and MAD1–C-MAD2 (the latter after appropriate modification by MPS1) accelerate the conversion of O-MAD2 to C-MAD2 that is required to bind CDC20. We propose that MPS1, MAD1–C-MAD2, and BUB1–BUB3 act strictly catalytically; that is, they do not effect changes in the free energy of association of the MCC subunits. To test this idea, we investigated whether the K_d of MCC^{S2} (Fig. 1c) changed when measured in the presence of catalysts (at 25 nM) at equilibrium. In agreement with our hypothesis, the presence of catalysts did not change the apparent binding affinity of MCC^{S2} (Extended Data Fig. 8e). The Michaelis–Menten parameters K_M and k_{cat}, calculated by fitting initial velocities at varying concentrations of MAD2, indicated considerable efficiency of the SAC catalyst (k_{cat}/K_M in excess of $10^5\ s^{-1}\ M^{-1}$; Fig. 5a).

Here, we have shown that the conversion of O-MAD2 to C-MAD2, which is required for binding CDC20, is the only rate-limiting step in the assembly of the MCC. MAD2 is not a catalyst for the interaction of

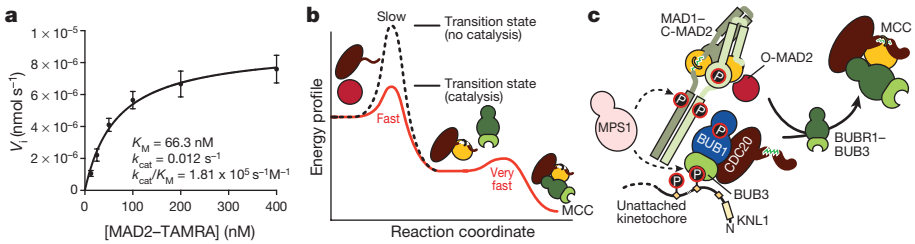

Figure 5 | Role of catalysis in MAD2 activation dynamics. a, Michaelis–Menten kinetics of MCC catalysis. Catalysts were prepared as described in Fig. 2b and used at 5 nM concentration; the concentrations of CDC20 and BUBR1 were 500 nM. Data are mean ± s.e.m. of three independent technical replicates of the experiment. **b**, The catalytic apparatus of the SAC targets the binding of O-MAD2 with CDC20, the rate-limiting step of MCC assembly. Relative energy profiles indicate that the reaction is spontaneous but slow owing to a high activation energy. Catalysis reduces the activation energy, increasing the reaction rate. Incorporation of BUBR1–BUB3 into the MCC is fast and does not require catalysis. **c**, Summary schematic. MPS1 phosphorylates KNL1 to promote kinetochore recruitment of BUB1–BUB3 and MAD1–C-MAD2 to activate it and promote binding to BUB1–BUB3. MAD1–C-MAD2 and BUB1–BUB3 recruit O-MAD2 and CDC20, respectively, catalysing their interaction. The subsequent incorporation of BUBR1–BUB3 drives MCC assembly.

BUBR1 and CDC20, as has been proposed[4,31]; rather, it binds BUBR1 and CDC20 in a stable ternary complex that assembles spontaneously at the cellular concentration of SAC proteins. One implication of this biochemical association is that the disassembly of the MCC requires energy. Several energy-dependent mechanisms of MCC disassembly have been described previously and are shown to operate continuously to disassemble MCC, even when the rate of MCC assembly is at its maximum[32].

We have identified a phosphorylated form of MAD1–C-MAD2 as the crucial catalyst for the accumulation of CDC20–C-MAD2. Omission of MPS1 and usage of a truncated and partly inactive MAD1 construct probably explain why previous studies observed only modest catalytic activation of MAD2 *in vitro*[3] (see Supplementary Information Section F). Our results also indicate that dimerization of O-MAD2 with MAD1–C-MAD2, which was previously shown to be required for SAC signalling[17,33], is essential for catalysis. Two predictions made regarding the MAD2 template model—that MAD1–C-MAD2 is a catalyst and that O-MAD2–C-MAD2 dimerization is required for catalysis[17]—are therefore confirmed here (Fig. 5b, c).

Kinetochores are likely to be required for a robust SAC response, particularly as they increase the local concentration of catalysts, probably favouring their post-translational modification and physical interaction. The role of kinetochores in SAC signalling may be particularly important under stringent conditions, such as when there is only one or a few unattached kinetochores in a cell[34], a point at which the number of MCCs declines and the rate of degradation of APC/C substrates increases considerably[5,35]. The tools we described here may aid the study of this unresolved issue.

Online Content Methods, along with any additional Extended Data display items and Source Data, are available in the online version of the paper; references unique to these sections appear only in the online paper.

Received 21 June 2016; accepted 13 January 2017.
Published online 19 January 2017.

1. Musacchio, A. The molecular biology of spindle assembly checkpoint signaling dynamics. *Curr. Biol.* **25,** R1002–R1018 (2015).
2. Luo, X. *et al.* The Mad2 spindle checkpoint protein has two distinct natively folded states. *Nat. Struct. Mol. Biol.* **11,** 338–345 (2004).
3. Simonetta, M. *et al.* The influence of catalysis on Mad2 activation dynamics. *PLoS Biol.* **7,** e10 (2009).
4. Kulukian, A., Han, J. S. & Cleveland, D. W. Unattached kinetochores catalyze production of an anaphase inhibitor that requires a Mad2 template to prime Cdc20 for BubR1 binding. *Dev. Cell* **16,** 105–117 (2009).
5. Dick, A. E. & Gerlich, D. W. Kinetic framework of spindle assembly checkpoint signalling. *Nat. Cell Biol.* **15,** 1370–1377 (2013).
6. Hagting, A. *et al.* Human securin proteolysis is controlled by the spindle checkpoint and reveals when the APC/C switches from activation by Cdc20 to Cdh1. *J. Cell Biol.* **157,** 1125–1137 (2002).
7. Clute, P. & Pines, J. Temporal and spatial control of cyclin B1 destruction in metaphase. *Nat. Cell Biol.* **1,** 82–87 (1999).
8. Fraschini, R. *et al.* Bub3 interaction with Mad2, Mad3 and Cdc20 is mediated by WD40 repeats and does not require intact kinetochores. *EMBO J.* **20,** 6648–6659 (2001).
9. Sudakin, V., Chan, G. K. & Yen, T. J. Checkpoint inhibition of the APC/C in HeLa cells is mediated by a complex of BUBR1, BUB3, CDC20, and MAD2. *J. Cell Biol.* **154,** 925–936 (2001).
10. Hardwick, K. G., Johnston, R. C., Smith, D. L. & Murray, A. W. *MAD3* encodes a novel component of the spindle checkpoint which interacts with Bub3p, Cdc20p, and Mad2p. *J. Cell Biol.* **148,** 871–882 (2000).
11. Chao, W. C., Kulkarni, K., Zhang, Z., Kong, E. H. & Barford, D. Structure of the mitotic checkpoint complex. *Nature* **484,** 208–213 (2012).
12. Izawa, D. & Pines, J. The mitotic checkpoint complex binds a second CDC20 to inhibit active APC/C. *Nature* **517,** 631–634 (2015).
13. Alfieri, C. *et al.* Molecular basis of APC/C regulation by the spindle assembly checkpoint. *Nature* **536,** 431–436 (2016).
14. Yamaguchi, M. *et al.* Cryo-EM of mitotic checkpoint complex-bound APC/C reveals reciprocal and conformational regulation of ubiquitin ligation. *Mol. Cell* **63,** 593–607 (2016).
15. Luo, X., Tang, Z., Rizo, J. & Yu, H. The Mad2 spindle checkpoint protein undergoes similar major conformational changes upon binding to either Mad1 or Cdc20. *Mol. Cell* **9,** 59–71 (2002).
16. Sironi, L. *et al.* Crystal structure of the tetrameric Mad1–Mad2 core complex: implications of a 'safety belt' binding mechanism for the spindle checkpoint. *EMBO J.* **21,** 2496–2506 (2002).
17. De Antoni, A. *et al.* The Mad1/Mad2 complex as a template for Mad2 activation in the spindle assembly checkpoint. *Curr. Biol.* **15,** 214–225 (2005).
18. Mapelli, M., Massimiliano, L., Santaguida, S. & Musacchio, A. The Mad2 conformational dimer: structure and implications for the spindle assembly checkpoint. *Cell* **131,** 730–743 (2007).
19. Sironi, L. *et al.* Mad2 binding to Mad1 and Cdc20, rather than oligomerization, is required for the spindle checkpoint. *EMBO J.* **20,** 6371–6382 (2001).
20. Santaguida, S., Tighe, A., D'Alise, A. M., Taylor, S. S. & Musacchio, A. Dissecting the role of MPS1 in chromosome biorientation and the spindle checkpoint through the small molecule inhibitor reversine. *J. Cell Biol.* **190,** 73–87 (2010).
21. Baron, A. P. *et al.* Probing the catalytic functions of Bub1 kinase using the small molecule inhibitors BAY-320 and BAY-524. *eLife* **5,** e12187 (2016).
22. Kim, S., Sun, H., Tomchick, D. R., Yu, H. & Luo, X. Structure of human Mad1 C-terminal domain reveals its involvement in kinetochore targeting. *Proc. Natl Acad. Sci. USA* **109,** 6549–6554 (2012).
23. Maldonado, M. & Kapoor, T. M. Constitutive Mad1 targeting to kinetochores uncouples checkpoint signalling from chromosome biorientation. *Nat. Cell Biol.* **13,** 475–482 (2011).
24. Overlack, K. *et al.* A molecular basis for the differential roles of Bub1 and BubR1 in the spindle assembly checkpoint. *eLife* **4,** e05269 (2015).
25. Di Fiore, B. *et al.* The ABBA motif binds APC/C activators and is shared by APC/C substrates and regulators. *Dev. Cell* **32,** 358–372 (2015).
26. Diaz-Martinez, L. A. *et al.* The Cdc20-binding Phe box of the spindle checkpoint protein BubR1 maintains the mitotic checkpoint complex during mitosis. *J. Biol. Chem.* **290,** 2431–2443 (2015).
27. Vleugel, M. *et al.* Dissecting the roles of human BUB1 in the spindle assembly checkpoint. *J. Cell Sci.* **128,** 2975–2982 (2015).
28. London, N. & Biggins, S. Mad1 kinetochore recruitment by Mps1-mediated phosphorylation of Bub1 signals the spindle checkpoint. *Genes Dev.* **28,** 140–152 (2014).
29. Brady, D. M. & Hardwick, K. G. Complex formation between Mad1p, Bub1p and Bub3p is crucial for spindle checkpoint function. *Curr. Biol.* **10,** 675–678 (2000).
30. Moyle, M. W. *et al.* A Bub1–Mad1 interaction targets the Mad1–Mad2 complex to unattached kinetochores to initiate the spindle checkpoint. *J. Cell Biol.* **204,** 647–657 (2014).
31. Han, J. S. *et al.* Catalytic assembly of the mitotic checkpoint inhibitor BubR1–Cdc20 by a Mad2-induced functional switch in Cdc20. *Mol. Cell* **51,** 92–104 (2013).
32. Musacchio, A. & Ciliberto, A. The spindle-assembly checkpoint and the beauty of self-destruction. *Nat. Struct. Mol. Biol.* **19,** 1059–1061 (2012).
33. Mapelli, M. *et al.* Determinants of conformational dimerization of Mad2 and its inhibition by p31comet. *EMBO J.* **25,** 1273–1284 (2006).
34. Rieder, C. L., Cole, R. W., Khodjakov, A. & Sluder, G. The checkpoint delaying anaphase in response to chromosome monoorientation is mediated by an inhibitory signal produced by unattached kinetochores. *J. Cell Biol.* **130,** 941–948 (1995).
35. Collin, P., Nashchekina, O., Walker, R. & Pines, J. The spindle assembly checkpoint works like a rheostat rather than a toggle switch. *Nat. Cell Biol.* **15,** 1378–1385 (2013).

Supplementary Information is available in the online version of the paper.

Acknowledgements We thank T. Kapoor and G. Siemeister for sharing reagents; the J.-M. Peters laboratory for the CDC20 expression vector; H. Ploegh for the Sortase expression vector; Y. Wu for help with construction of FRET probes; O. Durczak for technical assistance; A. Ciliberto for suggestions and comments; and G. Vader and the A.M. laboratory for discussions and reading of the manuscript. A.C.F. acknowledges support by an EMBO long-term fellowship (ALTF 1096-2012) and a Marie Curie Intra-European Fellowship (IEF). A.M. acknowledges funding by the Framework Program 7 Integrated Project MitoSys, the Horizon 2020 ERC agreement RECEPIANCE, and the DFG's Collaborative Research Centre (CRC) 1093.

Author Contributions A.C.F. and A.M. designed experiments and analysed results. A.C.F., M.T., C.B. and S.v.G. set up recombinant expression systems and purified proteins. A.C.F. performed *in vitro* experiments. M.T. performed solid-phase binding assays. S.M. and S.v.G. performed cellular SAC assays. F.M. and T.B. performed mass-spectrometry measurements. A.M. supervised the project. A.C.F. and A.M. wrote the manuscript.

Author Information Reprints and permissions information is available at www.nature.com/reprints. The authors declare no competing financial interests. Readers are welcome to comment on the online version of the paper. Correspondence and requests for materials should be addressed to A.C.F. (alex.faesen@mpi-dortmund.mpg.de) or A.M. (andrea.musacchio@mpi-dortmund.mpg.de).

Reviewer Information *Nature* thanks T. Kapoor, J. Pines and the other anonymous reviewer(s) for their contribution to the peer review of this work.

METHODS

No statistical methods were used to predetermine sample size. The experiments were not randomized and the investigators were not blinded to allocation during experiments and outcome assessment.

Production of recombinant proteins. All recombinant proteins used in this study were of human origin. MAD2 was expressed and purified essential as described previously[18]. All proteins used in this study, except BUBR1 (residues 1–571), were full length. To generate fluorescent BUBR1 and CDC20, we introduced a His-tagged N-terminal mTurquoise2 (ref. 36). Expression of all other protein constructs and mutants was performed in Sf9 (CDC20 and BUB1–BUB3) or TnaO38 insect cells (all other proteins). After infection with virus (at multiplicity of infection 1:50), cultures were grown at 27 °C, collected after 3 days and pellets stored at −20 °C. MAD1–C-MAD2 and BUBR1–BUB3 were cultured by mixing individual viruses, each harbouring individual genes. MPS1 was expressed in the presence of 2 μM Reversine.

Generally, cells were lysed in buffer A (25 mM HEPES (pH 7.5), 300 mM NaCl, 10% glycerol, 2 mM TCEP, 1 mM PMSF). MAD1–C-MAD2 and CDC20 were purified in buffer A with 1,000 and 500 mM NaCl, respectively. Soluble lysate was passed over a 5-ml Ni-NTA column and, after washing with 20 column volumes buffer A, the proteins were eluted by adding 300 mM imidazole to buffer A. Proteins was subsequently gel-filtered on a Superdex S200 16/60 column equilibrated against buffer B (10 mM HEPES (pH 7.5), 150 mM NaCl, 5% glycerol, 2 mM TCEP). All buffers used in the purification of MPS1 were supplemented with 0.2% Triton X-100. Fractions containing purified proteins were concentrated, flash-frozen and stored at −80 °C until use.

TAMRA labelling of O-MAD2. Purified MAD2 was C-terminally labelled using the sortase A transpeptidase enzyme from *Staphylococcus aureus*, which catalyses the cleavage of a short five-amino-acid recognition sequence (LPETG) with the concomitant formation of an amide linkage between an oligoglycine peptide and the target protein[37]. To that end, we mixed 10– 50 μM MAD2–LPETG with 150 μM sortase A and 0.5–1 mM of a TAMRA-conjugated peptide (Gly-Gly-Gly-Gly-Lys–TAMRA; StorkBio). The reactants were mixed in 50 mM Tris-HCl (pH 7.5), 150 mM NaCl and 10 mM $CaCl_2$ and incubated overnight at 4 °C. To purify MAD2 in the open conformation (O-MAD2), the labelling reaction was followed by ion-exchange chromatography (ResQ column, GE Healthcare) to remove the sortase A, excess TAMRA-conjugated peptide and MAD2 in the closed conformation (C-MAD2).

FRET measurements. Fluorimeter scans were performed on a Fluoromax 4 (Jobin Yvon) in a buffer containing fresh 10 mM HEPES (pH 7.5), 150 mM NaCl, 2.5% glycerol, 10 mM β-mercaptoenthanol and 0.05% Triton X-100. Mixtures were excited at 430 nm and the emissions were scanned from 450 to 650 nm. Single-wavelength acceptor-fluorescence measurements were carried out at 583 nm. Mixtures of MAD1–C-MAD2 with BUB1–BUB3 and/or MPS1 were pre-incubated at 1 μM for 30 min at 30 °C. Unless stated otherwise, assays were performed using 100 nM of all proteins (except CDC20, which was added at 500 nM). In all figure panels reporting time-dependent changes in FRET signal of MCC^{S1} and MCC^{S2}, curves report single measurements representative of at least three independent technical replicates.

Kinetic analysis MCC catalysis. To determine the kinetic parameters for catalysis of MCC assembly, we measured initial rates of catalysis of 5 nM 'enzyme' (MAD1–MAD2, BUB1–BUB3 and MPS1, which were pre-activated by incubation at 1 μM for 30 min at 30 °C with 1 mM ATP/$MgCl_2$) against 500 nM CDC20 and BUBR1, while the concentration of O-MAD2–TAMRA was varied. The initial rates of MCC assembly were calculated using a standard of fluorescence emission at 583 nm at known MCC concentrations. The initial rates were subsequently plotted against the concentration of MAD2, and subjected to nonlinear regression fitting using the Michaelis–Menten equation $V = (V_{max} \times [MAD2])/([MAD2] + K_M)$, where V_{max} is the maximal velocity at saturating substrate concentrations and K_M is the Michaelis–Menten constant. The k_{cat} value was derived from the equation $k_{cat} = V_{max}/[E_0]$, where E_0 is the total enzyme concentration. Experimental data were processed using Prism 6 (Graphpad Software, Inc.). Fluorimeter scans were performed on a Fluoromax 4 (Jobin Yvon) in a buffer containing fresh 10 mM HEPES (pH 7.5), 150 mM NaCl, 2.5% glycerol, 10 mM β-mercaptoenthanol and 0.05% Triton X-100. Mixtures were excited at 430 nm and the emissions were measured at 583 nm.

MAD1–C-MAD2 and BUB1–BUB3 pull-down experiments. MBP–MAD1–C-MAD2 (1 μM), BUB1–BUB3 (2 μM), MPS1 (400 nM) and ATP (or variations thereof) were incubated for 1 h at room temperature in 1× kinase buffer (20 mM HEPES (pH 7.5), 50 mM NaCl, 10 mM $MgCl_2$, 0.5 mM EGTA, 2 mM DTE, 0.01% Triton X-100). After incubation with equilibrated amylose beads for 30 min on ice (New England Biolabs), the beads were washed twice with 200 μl wash buffer (50 mM HEPES (pH 7.5), 50 mM NaCl, 0.05% Triton, 10% glycerol, 2 mM DTE). Following this, SDS loading buffer was added (to a final concentration of 62.5 mM Tris pH 6.8, 2% sodium dodecyl sulfate (SDS), 10% glycerol, 0.1 M DTT and 0.01% bromophenol blue), the sample boiled, and samples analysed by western blot.

Mass spectrometry. Liquid chromatography coupled with tandem mass spectrometry (LC–MS/MS) was used to identify phosphorylation sites. Samples were digested with LysC/trypsin and/or GluC and prepared for LC–MS/MS analysis[38]. A total of 100 ng of peptides were separated on a Thermo Scientific EASY-nLC 1000 high-performance liquid chromatography system (Thermo Fisher Scientific, 1 h gradient from 5–60% acetonitrile with 0.1% formic acid) and directly sprayed using a nano-electrospray source in a quadrupole Orbitrap mass spectrometer (Q Exactive, Thermo Fisher Scientific)[39]. The Q Exactive was operated in data-dependent mode acquiring one survey scan and subsequently ten MS/MS scans[40]. The resulting raw files were processed with MaxQuant software (version 1.5.2.18) using a reduced database containing only the proteins of interest and giving phosphorylation on serine, threonine and tyrosine as variable modification[41]. A false-discovery rate cut-off of 1% was applied at the peptide and protein levels and the phosphorylation site decoy fraction.

Cell culture, plasmid transfection, microinjections, immunofluorescence, immunoblotting and imaging. HeLa cells or N-terminal localization and affinity purification peptide (LAP)-tagged LAP–BUB1 HeLa cells (MCB 2334; a gift from A. Hyman) were grown in DMEM (PAN Biotech) supplemented with 10% tetracycline-free FBS (PAN Biotech), L-glutamine (PAN Biotech) and either penicillin and streptomycin or G418 (GIBCO). Cells were grown at 37 °C in the presence of 5% CO_2. CDK1 inhibition, microinjections and live imaging were performed in complemented CO_2-independent medium (GIBCO) at 37 °C. For microinjections, a cDNA segment encoding human CENP-A was cloned in a pcDNA5/FRT/TO-IRES-mCherry vector, a modified version of pcDNA5/FRT/TO (Invitrogen) generated in-house as a C-terminal fusion to mCherry (M. Mattiuzzo and A. De Antoni). Transient transfections of pcDNA5/FRT/TO-IRES-mCherry-CENPA were performed with Lipofectamine 2000 (Invitrogen) according to the manufacturer's instructions and the mCherry–CENPA fusion was expressed by addition of 200 ng/ml doxycycline (Sigma) for 48 h. Where indicated, nocodazole (Sigma) was used at 3.3 μM and RO-3306 (Calbiochem) was used at 9 μM for 18 h. Microinjections were performed using a combination of FemtoJet, InjectMan-NI2 and Femtotip-II, all purchased from Eppendorf. Recombinant CFP–BUBR1–BUB3 complex and TAMRA–MAD2 (or TAMRA) were injected at a concentration of 6 μM and 2 μM, respectively. The number of cells injected, *n*, was: for TAMRA, $n = 2$; for O-MAD2–TAMRA, $n = 9$; for CFP–BUBR1–BUB3, $n = 8$. Live-cell images were taken before injection and 1–10 min after injection.

The plasmid expressing mCherry–MIS12–$MAD1^{WT}$ was a gift from T. Kapoor. The same plasmid background was used to transiently express a synthetically synthesized *MAD1* gene harbouring the various alanine mutations. For this assay, HeLa cells growing on coverslips pre-coated with 15 μg/ml poly-D-lysine (Millipore) were transiently transfected with the mCherry fusion plasmids using Lipofectamine 2000. Thirty hours after transfection, cells were either prepared for immunofluorescence or processed for western blotting analysis. Where indicated, cells were treated with 500 nM Reversine for 2 h before fixation. Cells were then fixed with PBS with 4% paraformaldehyde, followed by permeabilization with PBS/PHEM-Tween 0.3%. The following antibodies were used for immunostaining: anti-α-tubulin (mouse, DM1α, Sigma; 1:500), anti-CREST/anti-centromere antibodies (human, Antibodies Inc.; 1:100). DNA was stained with 0.5 μg/ml DAPI (Serva) and coverslips mounted with Mowiol mounting medium (Calbiochem). For western blotting analysis the following antibodies were used: anti-α-tubulin (DM1α; 1:10,000), anti-MAD1 (in-house-made mouse monoclonal, clone BB3-8/e578-589; 1:100). Imaging for microinjection experiments was performed on a spinning disk confocal microscope of a 3i Marianas system (Intelligent Imaging Innovations) equipped with an Axio Observer Z1 microscope (Zeiss), a CSU-X1 confocal scanner unit (Yokogawa Electric Corporation), Plan-Apochromat 63× or 100×/1.4 NA objectives (Zeiss) and an Orca Flash 4.0 sCMOS Camera (Hamamatsu). Images were acquired as *Z* sections (using Slidebook Software 5.5 from Intelligent Imaging Innovations or using LCS 3D software from Leica) and converted into maximal-intensity-projection TIFF files for illustrative purposes. Imaging for the mCherry fusions experiments was performed on a Deltavision Elite System (GE Healthcare) equipped with an IX-71 inverted microscope (Olympus), a UPlanFLN 40×/1.3 NA objective (Olympus) and a pco.edge sCMOS camera (PCO-TECH Inc.). Images were acquired as *Z* sections (using the softWoRx software from Deltavision) and converted into maximal-intensity-projection TIFF files for illustrative purposes. Quantification of kinetochore signals was performed on unmodified *Z* series images using Imaris 7.3.4 software (Bitplane). Following background subtraction, a ratio for mCherry-MIS12–MAD1/CREST intensity signals was calculated. All ratios were normalized to the mean of

mCherry–MIS12–MAD1^{WT} ratio. The HeLa cell line used in this study was regularly checked for mycoplasma contamination. The cell line was not authenticated.

Data availability statement. All uncropped Coomassie-stained gels and western blots are provided in the Supplementary Information. All other data that support the findings of this study are available from the corresponding author upon request.

36. Goedhart, J. *et al.* Structure-guided evolution of cyan fluorescent proteins towards a quantum yield of 93%. *Nat. Commun.* **3,** 751 (2012).
37. Popp, M. W. & Ploegh, H. L. Making and breaking peptide bonds: protein engineering using sortase. *Angew. Chem. Int. Edn Engl.* **50,** 5024–5032 (2011).
38. Rappsilber, J., Mann, M. & Ishihama, Y. Protocol for micro-purification, enrichment, pre-fractionation and storage of peptides for proteomics using StageTips. *Nat. Protocols* **2,** 1896–1906 (2007).
39. Michalski, A. *et al.* Mass spectrometry-based proteomics using Q Exactive, a high-performance benchtop quadrupole Orbitrap mass spectrometer. *Mol. Cell. Proteomics* **10,** M111.011015 (2011).
40. Olsen, J. V. *et al.* Higher-energy C-trap dissociation for peptide modification analysis. *Nat. Methods* **4,** 709–712 (2007).
41. Cox, J. & Mann, M. MaxQuant enables high peptide identification rates, individualized p.p.b.-range mass accuracies and proteome-wide protein quantification. *Nat. Biotechnol.* **26,** 1367–1372 (2008).
42. Vassilev, L. T. *et al.* Selective small-molecule inhibitor reveals critical mitotic functions of human CDK1. *Proc. Natl Acad. Sci. USA* **103,** 10660–10665 (2006).

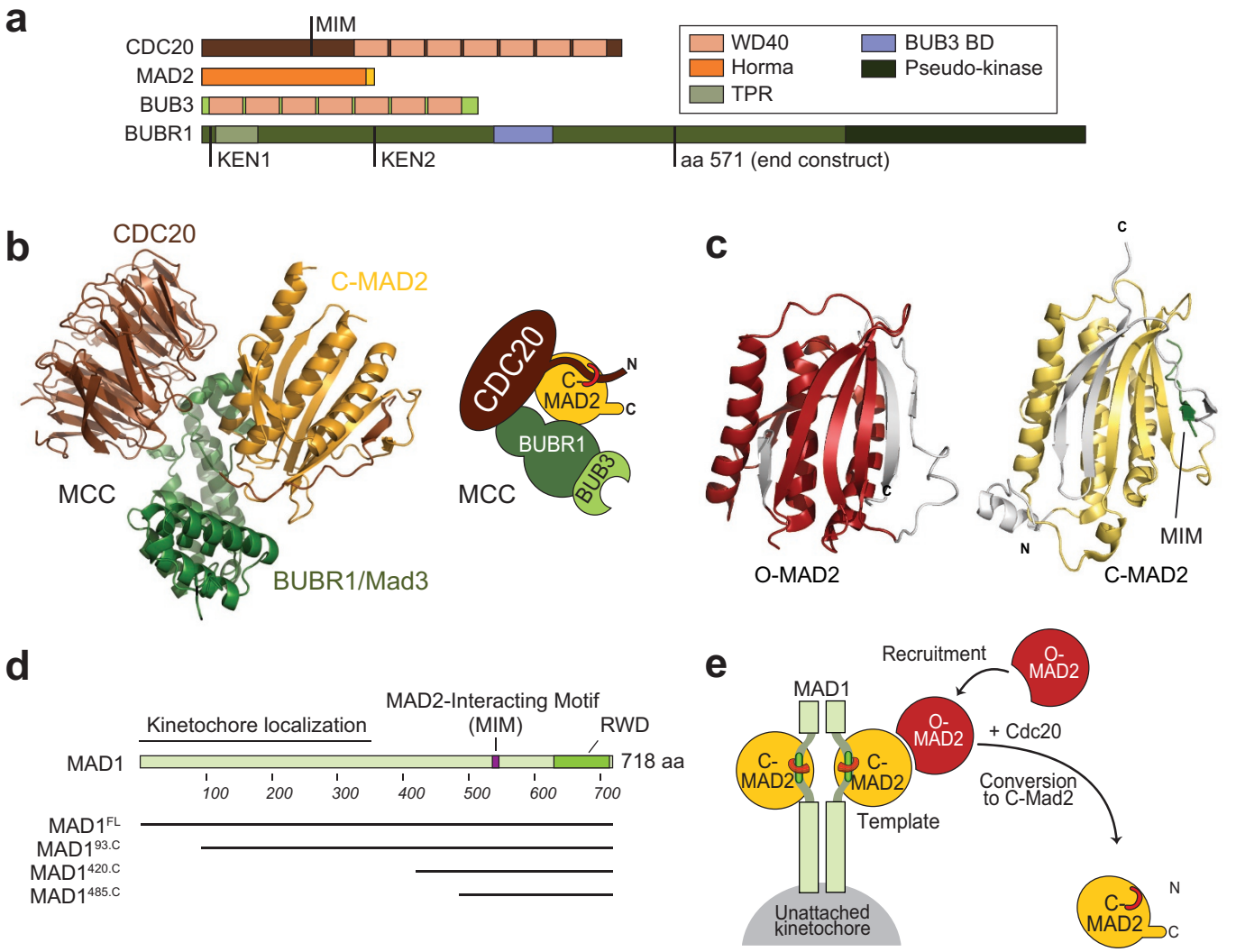

Extended Data Figure 1 | MCC constituents and MAD2-template model. a, Schematic of MCC constituents and their domain structure. **b**, Cartoon model of the crystal structure of the *Schizosaccharomyces pombe* MCC complex[11] (Protein Data Bank accession number: 4AEZ). CDC20 consists mainly of WD40 β-propeller domains, where the N-terminal extension interacts with MAD2 (at the MIM). Mad3 is the yeast orthologue of BUBR1. BUBR1, which is constitutively bound to BUB3, contains many functional motifs and structural domains, a few of which are highlighted in **a**. **c**, Cartoon models of the crystal structures of O-MAD2 and C-MAD2. The HORMA domain of MAD2 exists in two distinct topologies: O-MAD2, when unbound by ligand; and C-MAD2, when bound to the MIMs of MAD1 or CDC20 (refs 15,16). The change in topology is due to relocation of mobile elements of the structure, indicated in grey. **d**, Schematic representation of MAD1 and MAD1-deletion mutants used in this study. **e**, Schematic representation of the MAD2 template model.

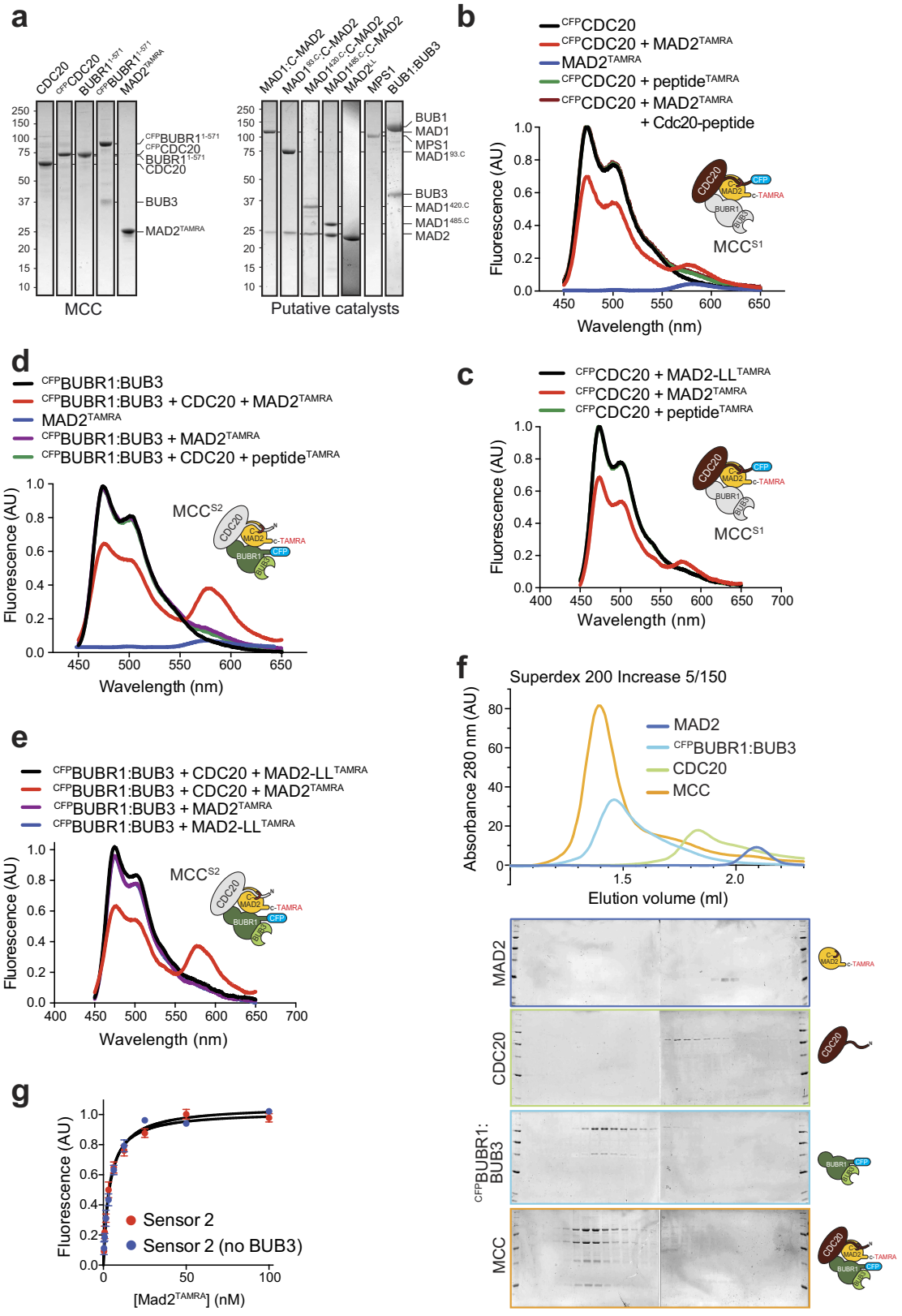

Extended Data Figure 2 | See next page for caption.

Extended Data Figure 2 | Characterizing the MCC using FRET sensors. a, Coomassie-stained SDS–PAGE gel of recombinant proteins used in this study. **b**, Fluorescence emission spectrum of MCC^{S1} excited at 430 nm. The concentration of all proteins is 100 nM, expect for the CDC20 peptide, which was used in large excess (5 μM) in competition reactions. Signals were normalized to peak donor emission at 470 nm. No change in emission was observed in presence of only O-MAD2–TAMRA, or when CFP–CDC20 was measured in isolation (black) or with a TAMRA-labelled peptide (green). The excess of CDC20 peptide competed for MAD2 binding and no FRET was observed (brown). **c**, In an additional control for MCC^{S1}, CFP–CDC20 was tested against TAMRA-labelled 'loopless' (O-MAD2-LL–TAMRA), a MAD2 mutant that is locked in the O-MAD2 conformation and cannot bind CDC20 (ref. 18). Assay conditions were as described in **b**. **d**, MCC formation relies on the presence of CDC20. Fluorescence emission spectra of MCC^{S2} (or parts thereof) excited at 430 nm. No change in emission was observed in the presence of only O-MAD2–TAMRA (no CFP–BUBR1–BUB3, blue) or when CFP–BUBR1–BUB3 was measured in isolation (black), in the presence of O-MAD2–TAMRA (without CDC20, purple), or in the presence of CDC20 and a TAMRA-labelled peptide not conjugated to MAD2 (green). The only condition that led to changes in donor and acceptor emission spectra was when CFP–BUBR1–BUB3, TAMRA–MAD2 and CDC20 were present at the same time (red). FRET efficiency upon complex formation at equilibrium was 35%. The concentration of all proteins was 100 nM. Signals were normalized to peak donor emission at 470 nm. **e**, In an additional control for MCC^{S2}, CFP–BUBR1 was tested in the presence of CDC20 against O-MAD2-LL–TAMRA. Assay conditions were as described in **d**. **f**, Recombinant O-MAD2–TAMRA, CDC20 and CFP–BUBR1–BUB3 form the MCC complex. Size-exclusion chromatography elution profiles of O-MAD2–TAMRA (dark blue trace), CDC20 (green trace), CFP–BUBR1–BUB3 (light blue trace) or all mixed to form the MCC complex (orange trace). The shift in the elution profile indicates complex formation. **g**, BUB3 does not affect MCC^{core} stability. A titration experiment determining the binding isotherms of the MCC complex, using MCC^{S2} in the presence (red) or absence (blue) of BUB3, showed indistinguishable apparent K_d values. Data are mean ± s.e.m. of three independent technical replicates of the experiments.

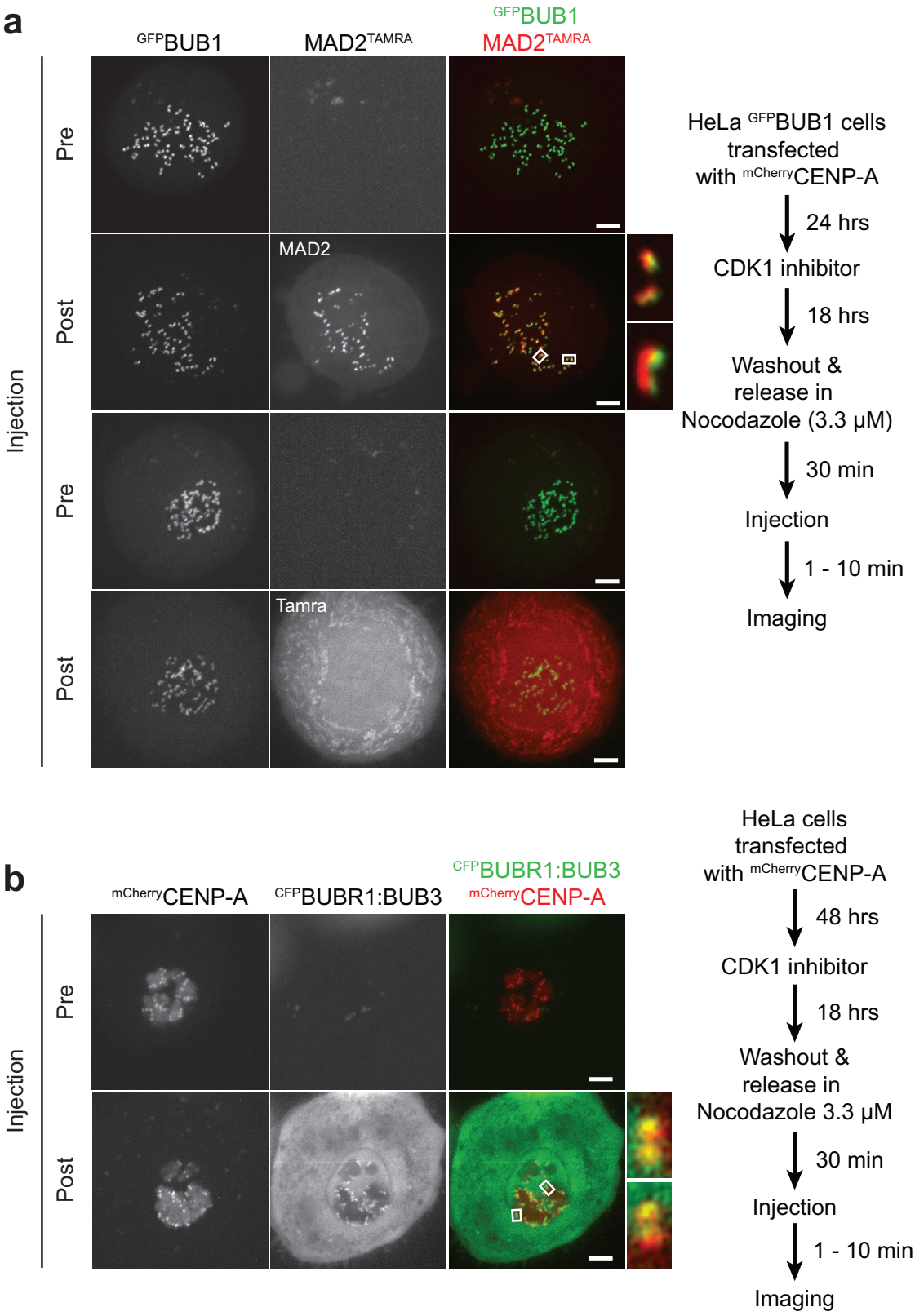

Extended Data Figure 3 | Microinjection of recombinant fluorescent MCC proteins. a, **b**, Recombinant fluorescent MCC proteins injected into mitotic cells localize to kinetochores. HeLa cells constitutively expressing LAP–BUB1 (**a**) or transiently expressing mCherry–CENP-A (**b**) were synchronized in the G2 phase of the cell cycle by treatment with the CDK1 inhibitor RO3306 (ref. 42) and released into mitosis in the presence of nocodazole. Shortly after release, cells were injected with either TAMRA–MAD2 or TAMRA (**a**), or with CFP–BUBR1–BUB3 (**b**). Cells were live-imaged both before (Pre) and after (Post) microinjection. Scale bars, 2 μm. Number of injected cells, *n*, for TAMRA, $n = 2$; for TAMRA–MAD2, $n = 9$; for mTurquoise–BUBR1–BUB3, $n = 8$.

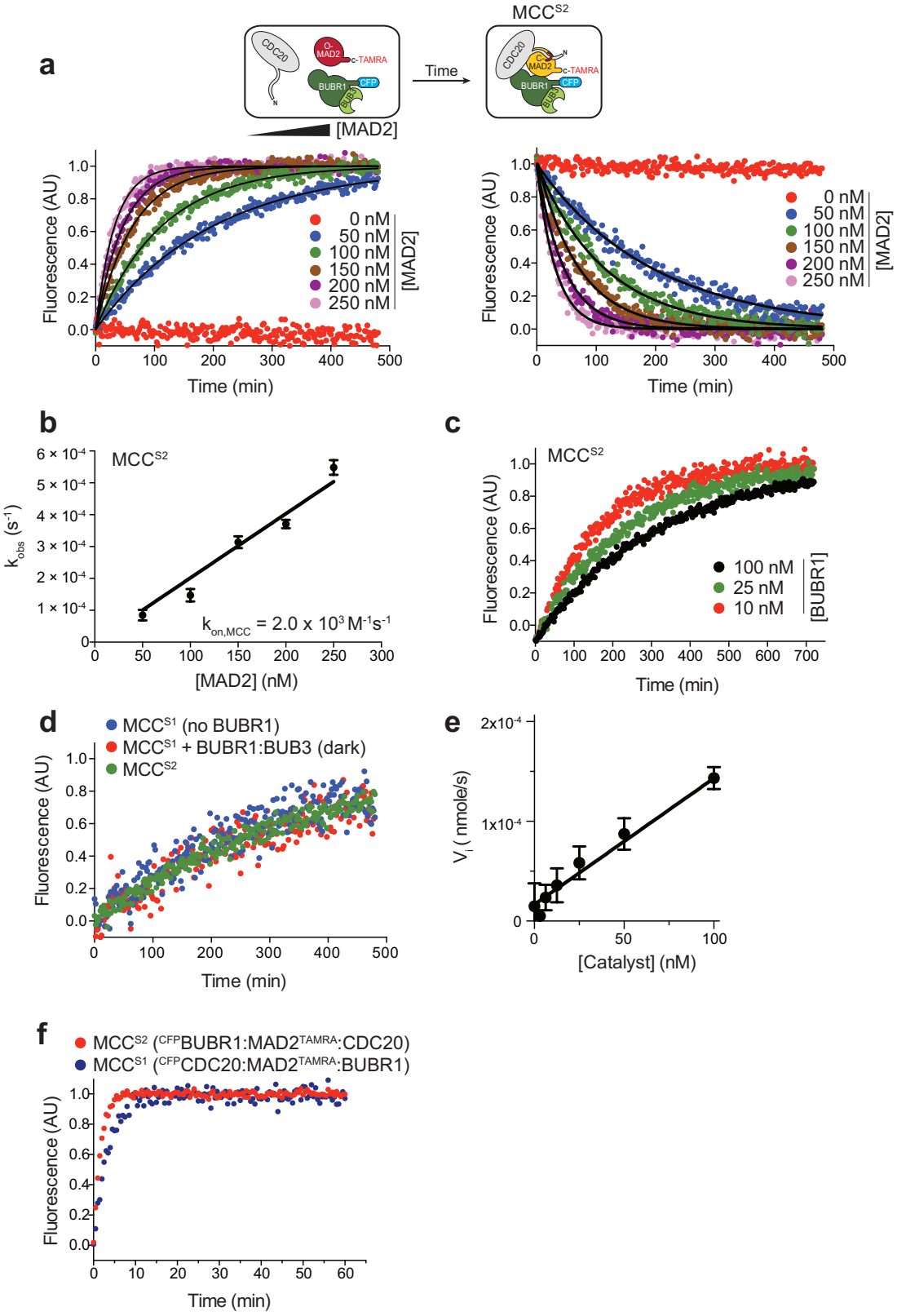

Extended Data Figure 4 | See next page for caption.

Extended Data Figure 4 | MCC assembly kinetics. a, The CDC20–MAD2 complex forms slowly. The time-dependent change of acceptor (left) and donor (right) fluorescence (normalized to values at equilibrium) with 10 nM CFP–BUBR1–BUB3 (see Supplementary Information Section G for details of the effects of BUBR1 concentration on reaction rate of MCC^{S2}) and 500 nM CDC20 with varying concentrations of O-MAD2–TAMRA. Signal changes were fitted to single exponential curves. **b**, After the single-exponential fitting of the curves in **a**, the apparent first order rate constants (k_{obs}) were plotted as a function of MAD2 concentration, with k_{on} being the slope of the resulting curve. These k_{on} values depend on the concentration of BUBR1 (see **c** and Supplementary Information Section G). **c**, MCC assembly assay performed with MCC^{S2} with 100 nM O-MAD2–TAMRA, 500 nM CDC20 and the indicated concentrations of CFP–BUBR1–BUB3. **d**, BUBR1 does not influence the assembly kinetics of the MCC. Monitoring the assembly of CDC20–MAD2 (MCC^{S1}; blue), CDC20–MAD2 with dark BUBR1–BUB3 (MCC^{S1}; red) and BUBR1–MAD2 with dark CDC20 (green) shows indistinguishable rates. **e**, Catalysis rates scale linearly with catalyst concentration. After pre-incubation of the catalyst proteins, MCC assembly was monitored with MCC^{S2} (sensor concentrations were 100 nM, except for CDC20, which was 500 nM) at varying catalyst concentrations. Initial velocity (V_i) signal changes were plotted against catalyst concentration, revealing a linear dependency. **f**, Catalysis of MCC formation could be observed with both FRET sensors. After pre-incubation of MAD1–C-MAD2, BUB1–BUB3 and MPS1 at 1 μM for 30 min, similar catalysis rates were observed with either MCC^{S1} (blue) or MCC^{S2} (red). The assay was performed as described in Fig. 2b, with all proteins at 100 nM. Data are mean ± s.e.m. of three independent technical replicates of the experiments (**b**, **e**).

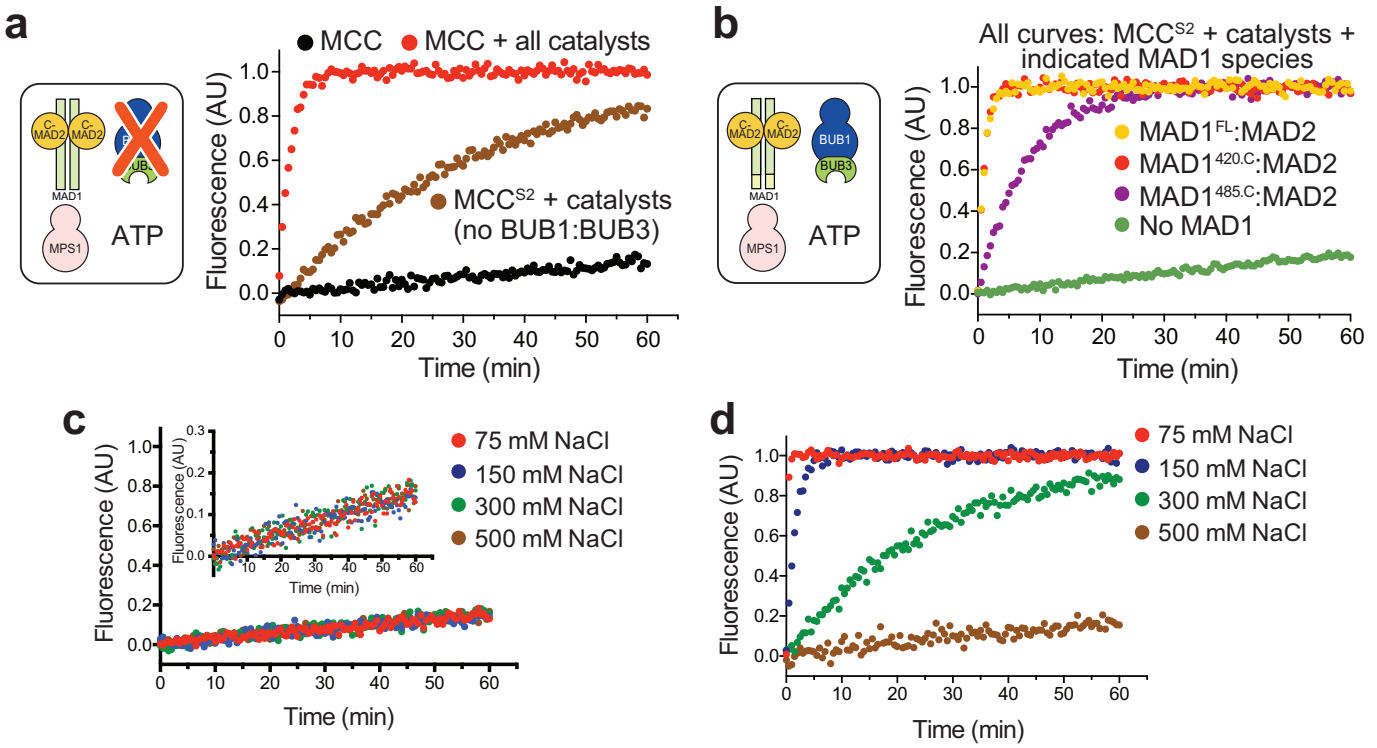

Extended Data Figure 5 | Molecular requirements of catalytic MCC assembly. a, Catalytic MCC assembly requires MAD1–C-MAD2, MPS1, ATP and BUB1–BUB3. MCC assembly was monitored with MCC^{S2}, as described in Fig. 2b, using 100 nM catalysts. Individual components were omitted as indicated. The same control profiles (black and red curves) are shown here and in Fig. 2. **b**, MAD1 with the N-terminal 419 residues deleted ($MAD1^{420\text{-}C}$; red) is a minimal construct capable of full catalysis. A reduction in the catalytic rate was observed with MAD1 with the N-terminal 484 residues deleted ($MAD1^{485\text{-}C}$; purple) compared to full-length MAD1 ($MAD1^{FL}$; yellow) or $MAD1^{420\text{-}C}$. The assay was performed with MCC^{S2} as described in Fig. 2b, using 100 nM catalysts. Catalytic activation is salt-sensitive, probably because high salt inhibits phosphorylation-mediated polar interactions (see **c**, **d**). **c**, **d**, Catalysis is sensitive to salt concentration. MCC assembly was monitored with MCC^{S2}, using 75 mM (red), 150 mM (blue), 300 mM (green) or 500 mM NaCl (brown), in the absence (**c**) or presence (**d**) of catalysts. The assay was performed with MCC^{S2}, as described in Fig. 2b.

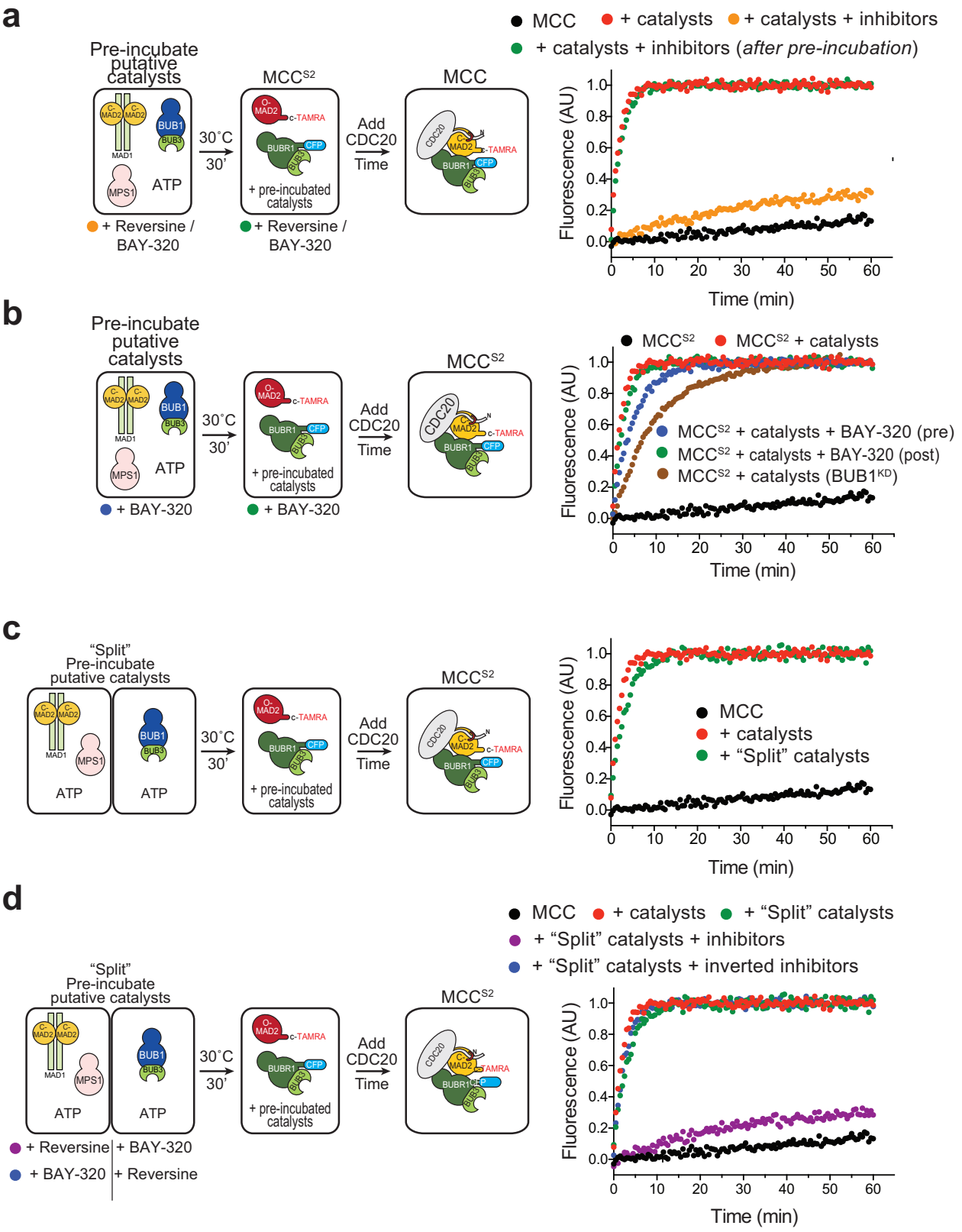

Extended Data Figure 6 | See next page for caption.

Extended Data Figure 6 | Inhibiting catalysis. a, Inhibiting MPS1 and BUB1 during pre-incubation strongly reduces catalysis. Adding both Reversine and BAY-320 to the pre-incubation solution of catalysts strongly reduced the catalysis of MCC formation. Adding the inhibitors after pre-incubation but before addition to the MCC^{S2} components did not affect catalysis. Final concentrations of inhibitors were 50 μM during pre-incubation and 5 μM in the assay. **b**, As in Fig. 4a, but with the BUB1 inhibitor BAY-320 rather than Reversine. BUB1 without functional kinase activity ($BUB1^{KD}$) was used as a control. **c**, Catalysis rates remained unchanged when the pre-incubation of catalyst proteins was 'split' into two reactions (MAD1–C-MAD2 together with MPS1 or BUB1 alone; compare green to red). Assay performed with MCC^{S2}, as described in Fig. 2b, using 100 nM catalysts. **d**, MAD1–C-MAD2 is phosphorylated by MPS1. Catalysis rates remained unchanged when the pre-incubation of catalyst proteins was split into two reactions (MAD1–C-MAD2 together with MPS1 or BUB1 alone; compare green to red). Adding the kinase inhibitors Reversine (targeting MPS1) and BAY-320 (BUB1) to the pre-incubation reaction strongly reduced the rates of catalysis (orange). However, inverting the inhibitors had no effect on the catalysis rates (blue). Assay performed with MCC^{S2}, as described in Fig. 2b, using 100 nM catalysts. Final concentrations of inhibitors are 5 μM in assay (50 μM during pre-incubation).

a

	Phospho (STY) Probabilities	Residue	PEP	Score	
MAD1	QCQQNLDAA**pS**K	Ser142	1.04E-2	49.3	
	ISELQW**pS**VMDQEMR	Ser172	9.91E-4	73.881	
	AILG**pS**YDSELTPAEYSPQLTR	Ser417	1.70E-13	138.96	
	AILGSYDSELTPAEY**pS**PQLTR	**Ser428**	1.73E-42	238.69	
	VHSHSAEMEAQL**pS**QALEELGGQK	Ser457	3.62E-5	44.164	
	SQ**pS**SSAEQSFLFSR	Ser486	1.31E-26	195.46	
	EEAD**pT**LRLK	Thr500	2.20E-11	141.71	
	RALQGDYDQSR**pT**K	Thr540	1.35E-60	237.99	
	VLHMSLNP**pT**(0.861)**pS**(0.139)VAR	Thr550/Ser551	2.64E-11	126.25	
	QRLREDH**pS**QLQAECER	Ser562	1.06E-34	178.56	
	GG**pT**VPADLEAAAASLPSSK	Thr583	8.57E-8	95.223	
	GGTVPADLEAAAASP**pS**(0.718)**pS**(0.266)K	Ser597	1.42E-12	121.84	
	GGTVPADLEAAAASLP**pS**(0.395)**pS**(0.6)K	Ser598	2.08E-5	89.345	
	RQD**pS**IPAFLSSLTLELFSR	**Ser699**	5.99E-12	142.25	RWD
	QDSIPAFLSSLTLELF**pS**RQTVA	**Ser713**	1.62E-54	83.47	RWD
	RQDSIPAFLSSLTLELFSRQ**pT**VA	**Thr716**	5.47E-25	180.51	RWD
MAD2	LR**pS**FTTTIHK	**Ser185**	3.27E-5	61.532	
	VN**pS**MVAYK	**Ser195**	5.44E-14	78.513	

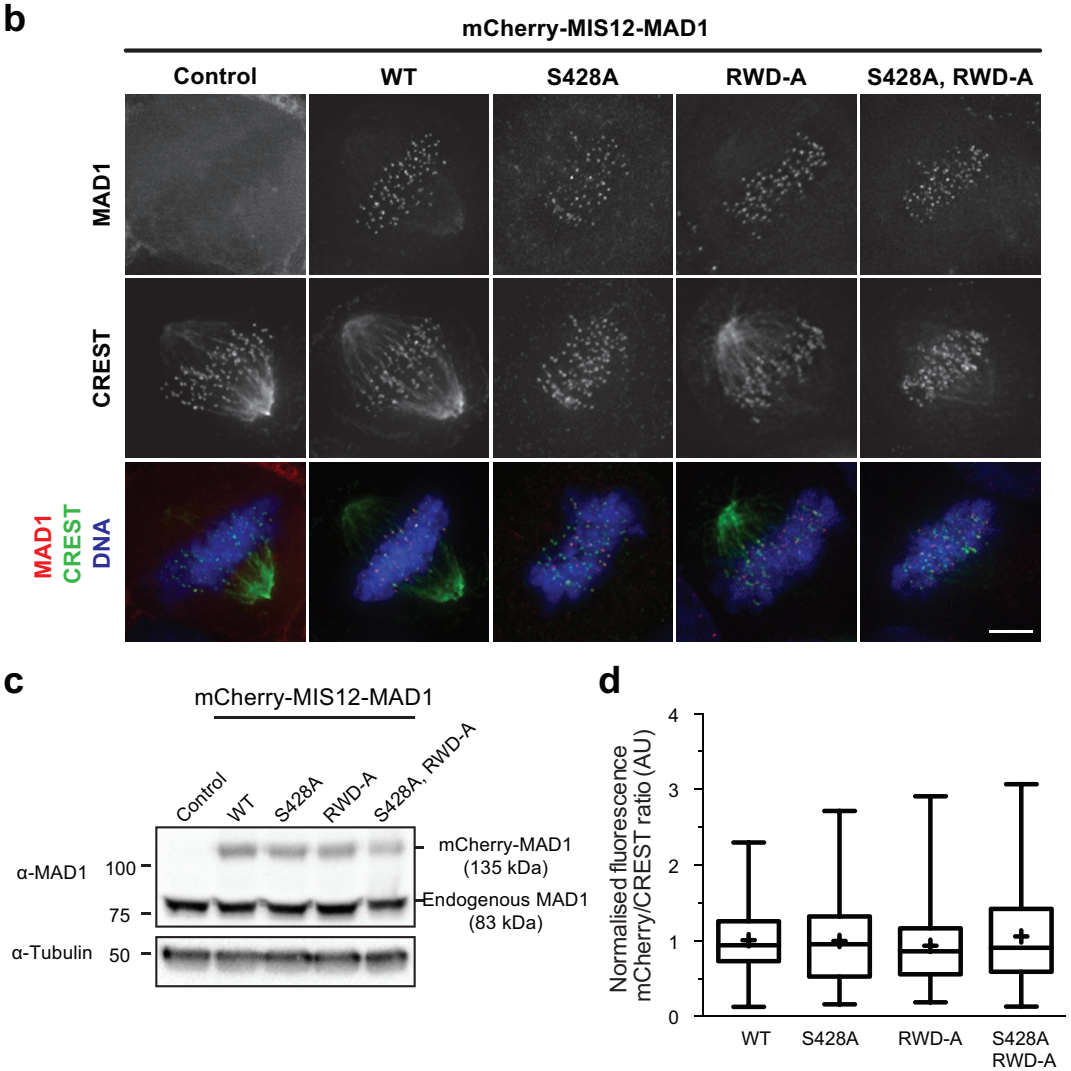

Extended Data Figure 7 | See next page for caption.

Extended Data Figure 7 | MPS1 phosphorylation of MAD1. **a**, Phosphorylation sites of MAD1 by MPS1. The peptide sequence with the phosphorylated residue in bold, the amino acid position within the protein, the *P* value of the posterior error probability for the identified peptide (PEP) and the Andromeda search engine score (score) are shown. Residue numbers in bold indicate phosphorylation sites found in at least two experiments. **b**–**d**, In **b**, HeLa cells were transfected with mCherry (Control), mCherry–MIS12–MAD1^{WT} (WT), mCherry–MIS12–MAD1^{S428A} (S428A), mCherry–MIS12–MAD1$^{RWD\text{-}A}$ (RWD-A) or mCherry–MIS12–MAD1$^{S428A/RWD\text{-}A}$ (S428A, RWD-A) as described and quantified in the legend of Fig. 4c. Shown are mitotic cells, representative of the mitotic population in each cohort (mCherry control, 59 cells; mCherry–MIS12–MAD1^{WT}, 247 cells; mCherry–MIS12–MAD1^{S428A}, 203 cells; mCherry–MIS12–MAD1$^{RWD\text{-}A}$, 83 cells; mCherry–MIS12–MAD1$^{S428A/RWD\text{-}A}$, 91 cells). Following a 30-h transfection with the indicated constructs, cells were fixed and processed for western blotting (**c**) or immunofluorescence (**d** and Fig. 4c). Western blot analysis showed that expression levels of mCherry–MIS12–MAD1 fusions were lower than endogenous MAD1 levels (**c**). Scale bars, 5 μm. Quantification of the kinetochore signal was performed on unmodified *Z* series images. Following background subtraction, a ratio for mCherry–MIS12–MAD1/CREST intensity signals was calculated. All ratios were normalized to the mean of mCherry–MIS12–MAD1^{WT} ratio. Quantifications are based on two independent biological replicates of the experiment, for a total of five cells for each condition, where 254 (mCherry–MIS12–MAD1^{WT}), 143 (mCherry–MIS12–MAD1^{S428A}), 207 (mCherry–MIS12–MAD1$^{RWD\text{-}A}$) or 188 (mCherry–MIS12–MAD1$^{S428A/RWD\text{-}A}$) kinetochores were analysed. Shown is a box-and-whiskers graph, indicating the median, a box with the 25–75th percentile and hinges indicating the upper and lower limits of the data points.

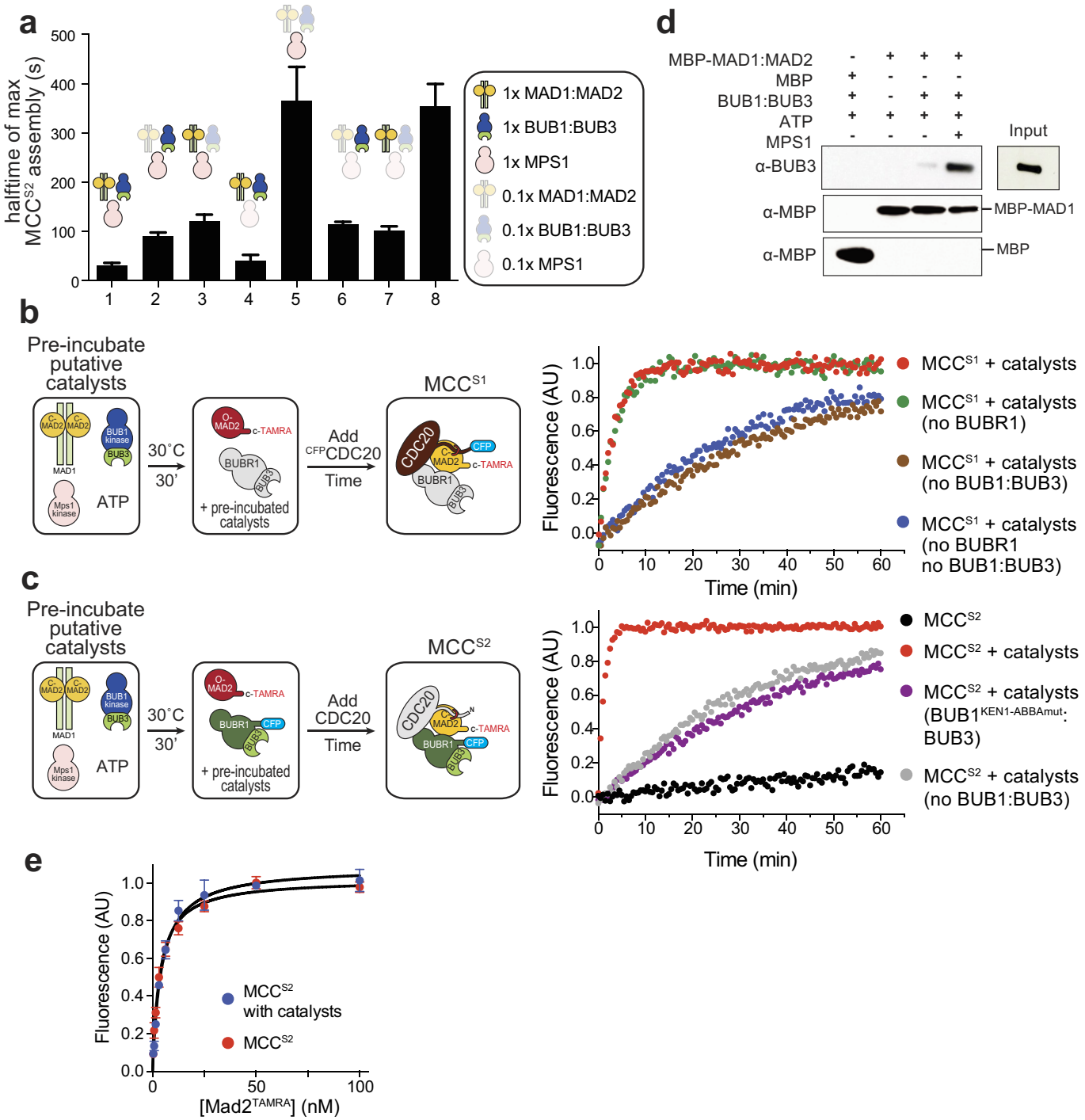

Extended Data Figure 8 | MAD1 and BUB1 interact to combine O-MAD2 and CDC20. a, MAD1–C-MAD2 and BUB1–BUB3 together form the MCC enzyme, while MPS1 suffices in sub-stoichiometric amounts. Lowering the concentration of all catalysts increased the half-life (halftime) tenfold (compare conditions 1 and 8). Lowering individual components reduces rates to intermediate levels for MAD1–C-MAD2 (condition 2) and BUB1–BUB3 (condition 3), but not MPS1 (condition 4). Lowering both MAD1–C-MAD2 and BUB1–BUB3 (condition 5) mimics the reduction of all components (condition 8), whereas reducing MAD1–C-MAD2 or BUB1–BUB3 in combination with MPS1 (conditions 6 and 7, respectively) only resulted in intermediate rates. Assays were performed with MCC^{S2} as described in Fig. 2b, using either 100 nM (1×) or 10 nM (0.1×) catalysts. **b**, Excluding BUBR1 does not affect catalytic rates (green and blue). Assays were performed using MCC^{S1}, all proteins were present at 100 nM. **c**, The interaction between BUB1 and CDC20 enhances binding with MAD2. A BUB1 construct that does not bind CDC20 (the KEN1-ABBA mutant ($BUB1^{KEN1\text{-}ABBAmut}$); purple) yields similar rates as in the absence of BUB1 (grey). Assay performed with MCC^{S2} and as described in Fig. 2b, using 100 nM catalysts. **d**, MAD1–C-MAD2 and BUB1–BUB3 show an ATP-dependent interaction in the presence of MPS1. Pull-down experiment using MBP–MAD1–C-MAD2 as bait. Assay was performed with 1 μM MAD1–C-MAD2, 2 μM BUB1–BUB3 and 400 nM MPS1. **e**, Values of FRET from MCC^{S2} (1 nM CFP–BUBR1 and 500 nM CDC20) after equilibration with or without catalysts (25 nM catalyst concentration). Data are mean ± s.e.m. of three independent technical replicates of the experiment (**b**, **e**).

Structure of the RZZ complex and molecular basis of its interaction with Spindly

Shyamal Mosalaganti,[1]* Jenny Keller,[2]* Anika Altenfeld,[2]* Michael Winzker,[3] Pascaline Rombaut,[4] Michael Saur,[1] Arsen Petrovic,[2] Annemarie Wehenkel,[2] Sabine Wohlgemuth,[2] Franziska Müller,[2] Stefano Maffini,[2] Tanja Bange,[2] Franz Herzog,[4] Herbert Waldmann,[3,5] Stefan Raunser,[1] and Andrea Musacchio[2,6]

[1]Department of Structural Biochemistry, [2]Department of Mechanistic Cell Biology, and [3]Department of Chemical Biology, Max Planck Institute of Molecular Physiology, 44227 Dortmund, Germany
[4]Gene Center, Ludwig-Maximilians-Universität München, 81377 Munich, Germany
[5]Department of Chemistry and Chemical Biology, Technical University Dortmund, 44227 Dortmund, Germany
[6]Centre for Medical Biotechnology, Faculty of Biology, University Duisburg-Essen, 45141 Essen, Germany

Kinetochores are macromolecular assemblies that connect chromosomes to spindle microtubules (MTs) during mitosis. The metazoan-specific ≈800-kD ROD–Zwilch–ZW10 (RZZ) complex builds a fibrous corona that assembles on mitotic kinetochores before MT attachment to promote chromosome alignment and robust spindle assembly checkpoint signaling. In this study, we combine biochemical reconstitutions, single-particle electron cryomicroscopy, cross-linking mass spectrometry, and structural modeling to build a complete model of human RZZ. We find that RZZ is structurally related to self-assembling cytosolic coat scaffolds that mediate membrane cargo trafficking, including Clathrin, Sec13–Sec31, and αβ′ε-COP. We show that Spindly, a dynein adaptor, is related to BicD2 and binds RZZ directly in a farnesylation-dependent but membrane-independent manner. Through a targeted chemical biology approach, we identify ROD as the Spindly farnesyl receptor. Our results suggest that RZZ is dynein's cargo at human kinetochores.

Introduction

Molecular motors such as kinesin and cytoplasmic dynein 1 (hereafter referred to as dynein) hydrolyze ATP to move directionally on microtubules (MTs), actively transporting different cargos to shape the complex spatial organization of eukaryotic cells. Dynein, a member of the AAA family of ATPases, is the major retrograde (MT minus end–directed) motor in eukaryotic cells (Kardon and Vale, 2009; Cianfrocco et al., 2015; Carter et al., 2016). Virtually all functions of dynein also require an accessory subunit called dynactin, as well as a plethora of adaptor proteins that control the recruitment of dynein–dynactin to diversely localized cargos while also activating dynein's motor activity (McKenney et al., 2014; Schlager et al., 2014). Understanding how adaptors bridge dynein–dynactin and cargo is a current challenge of great significance (Kardon and Vale, 2009; Cianfrocco et al., 2015; Carter et al., 2016).

During mitosis in metazoans, dynein is recruited to kinetochores, complex protein assemblies that link chromosomes to spindle MTs. Kinetochores are built on specialized chromosomal loci and consist of chromosome-proximal (inner) and -distal (outer) domains, respectively hosting the 16-subunit constitutive centromere-associated network, which binds directly to chromatin, and the 10-subunit KNL1, MIS12, NDC-80 (KMN) assembly, which binds directly to MTs (Pesenti et al., 2016). Dynein is recruited to an outermost poorly characterized domain of metazoan kinetochores named the fibrous corona, which is clearly visible only before MT attachment (Jokelainen, 1967; Rieder and Alexander, 1990; McEwen et al., 1993; Cooke et al., 1997; Yao et al., 1997; Hoffman et al., 2001; Magidson et al., 2015). Functional attributes of the corona are the expansion of the MT-binding surface of kinetochores into extended crescents, with the purpose of maximizing the likelihood of MT capture (Hoffman et al., 2001; Magidson et al., 2015; Wynne and Funabiki, 2015) and the promotion of spindle assembly checkpoint (SAC) signaling (Basto et al., 2000; Buffin et al., 2005; Kops et al., 2005), which protects genome integrity by

*S. Mosalaganti, J. Keller, and A. Altenfeld contributed equally to this paper.

Correspondence to Stefan Raunser: stefan.raunser@mpi-dortmund.mpg.de; or Andrea Musacchio: andrea.musacchio@mpi-dortmund.mpg.de

S. Mosalaganti's present address is the European Molecular Biology Laboratory, 69117 Heidelberg, Germany.

A. Wehenkel's present address is Institut Pasteur, Unité de Microbiologie Structurale, Centre National de la Recherche Scientifique, UMR3528, Université Paris Diderot, 75724 Paris, France.

Abbreviations used: ACN, acetonitrile; AUC, analytical ultracentrifugation; Fpp, farnesyl pyrophosphate; FRT, FLP recombination target; FSC, Fourier shell correlation; FTase, farnesyl transferase; GDI, guanine–nucleotide dissociation inhibitor; ISAC, iterative stable alignment and clustering; LC, liquid chromatography; MS, mass spectrometry; MT, microtubule; RZZ, ROD–Zwilch–ZW10; SAC, spindle assembly checkpoint; SEC, size-exclusion chromatography; SILAC, stable isotope labeling with amino acid in culture; TCEP, tris(2-carboxyethyl)phosphine; THF, tetrahydrofuran; XL-MS, cross-linking MS.

The Rockefeller University Press $30.00
J. Cell Biol. Vol. 216 No. 4 961–981
https://doi.org/10.1083/jcb.201611060

restricting mitotic exit and sister chromatid separation (anaphase) to cells with bioriented sister chromatids (Musacchio, 2015).

Dynein may not be strictly required for either of these corona functions, but it is crucially involved in corona disassembly (hereafter referred to as "shedding"), which is required to silence the SAC and to promote conversion from lateral to end-on MT attachment. Corona shedding takes place when MTs bind kinetochores, in turn allowing dynein to transport corona and SAC components away from kinetochores (Williams et al., 1996; Howell et al., 2001; Wojcik et al., 2001; Basto et al., 2004; Mische et al., 2008; Varma et al., 2008; Sivaram et al., 2009).

The three-subunit ROD–Zwilch–ZW10 (RZZ) complex (named after the *Drosophila melanogaster* genes *Rough Deal*, *Zwilch*, and *Zeste White 10*; Fig. 1 A) is a primary corona component. Through a poorly understood mechanism, RZZ stabilizes kinetochore localization of the MAD1–MAD2 complex (Buffin et al., 2005; Kops et al., 2005; Matson and Stukenberg, 2014; Caldas et al., 2015; Silió et al., 2015; Zhang et al., 2015). This necessary function of RZZ in SAC signaling terminates with corona shedding, which depletes MAD1–MAD2 from kinetochores, silencing the SAC (Fig. 1 B; Karess, 2005). Importantly, RZZ is also required for kinetochore recruitment of dynein–dynactin, but this additionally requires Spindly, a dynein adaptor whose kinetochore localization also depends on RZZ (Starr et al., 1998; Griffis et al., 2007; Gassmann et al., 2008, 2010; Yamamoto et al., 2008; Chan et al., 2009; Barisic et al., 2010; Cheerambathur et al., 2013). Mutations within a conserved region of Spindly (the Spindly motif) abrogate kinetochore recruitment of dynein–dynactin, effectively blocking corona shedding and SAC silencing (Gassmann et al., 2010).

Spindly recruitment to kinetochores requires the post-translational modification of Cys602 of Spindly with farnesyl, an isoprenoid lipid (Holland et al., 2015; Moudgil et al., 2015). Farnesylation is typically observed in small GTPases of the Ras family, regulators of many signaling and transport functions of eukaryotic cells, where it contributes to the association of GTPases with endomembranes (Wang and Casey, 2016). Precisely how Spindly farnesylation favors its kinetochore recruitment is currently unclear. Similarly to BicD2, another adaptor whose mode of dynein–dynactin binding is better characterized (Chowdhury et al., 2015; Urnavicius et al., 2015), Spindly activates dynein motility in vitro and is predicted to contain extensive coiled-coil segments (McKenney et al., 2014; Schlager et al., 2014; Cianfrocco et al., 2015; Hoogenraad and Akhmanova, 2016).

The structural organization of the RZZ complex and its influence on corona assembly are poorly understood. Previously, we determined the crystal structure of the smallest of the three subunits, Zwilch (Williams et al., 2003), and detected limited sequence similarity of ROD with the Clathrin heavy chain (Çivril et al., 2010). After reconstituting the RZZ complex (Altenfeld et al., 2015), we now report its overall structure by cryo-EM at an approximate resolution of 10 Å. By using the EM density and modeling, we generated a molecular model of the RZZ complex that satisfies several experimental spatial restraints. We now demonstrate a more general structural relatedness of ROD, the largest RZZ subunit, with proteins that oligomerize in proximity of biological membranes, including Clathrin, COPI, and COPII. We show that Spindly binds directly to the RZZ complex and that this requires an interaction of the C-terminal farnesyl moiety of Spindly with the ROD N-terminal region. Our results suggest a possible molecular basis for corona assembly and regulation at human kinetochores and implicate RZZ as dynein's cargo at kinetochores.

Results

Reconstitution and structural analysis of the RZZ complex

We generated recombinant versions of the human RZZ complex and of several RZZ variants (including fluorescently tagged versions and deletion mutants) by baculovirus-driven insect cell expression (Fig. 1 C; see the Expression and purification of RZZ section of Materials and methods; Altenfeld et al., 2015). Sedimentation velocity analytical ultracentrifugation (AUC) of recombinant RZZ showed a single peak with a predicted molecular mass of 813 kD, very close to the theoretical mass of 812 kD calculated by assuming a 2:2:2 stoichiometry, confirming and extending less precise previous measurements (Scaërou et al., 2001; Çivril et al., 2010).

In negative-stain and cryo-EM, RZZ complexes appeared as elongated particles (≈42 nm long and ≈10 nm thick in the other two directions; (Fig. 1, E and F; and Fig. S1, A–D). In agreement with the 2:2:2 stoichiometry of the RZZ complex, a twofold symmetry axis, perpendicular to the long axis of the complex, is clearly discernible. We determined the 3D structure of the RZZ complex at a resolution of 10.4 Å using cryo-EM (Figs. 1 G and S1 C).

Molecular models of RZZ subunits

Probably because of its inherent flexibility (see Video 1), we could not obtain EM reconstructions of the RZZ complex at higher resolution. To facilitate our understanding of the molecular organization of the RZZ complex, we built molecular models of its subunits. The crystal structure of Zwilch has been determined previously (PDB ID 3IF8; Fig. 2 A; Çivril et al., 2010), but no direct structural information on ZW10 and ROD is available. Despite overall limited sequence identity to known structural scaffolds, the programs Phyre and HHpred (Söding et al., 2005; Kelley et al., 2015) generated high-confidence structural models for the majority of ZW10 and ROD (see Table S1 and Fig. 2 [B and C] for summaries). ZW10 is evolutionarily and structurally related to the *S. cerevisiae* proteins Dsl1 and Tip20 (Table S1), subunits of vesicle-tethering complexes consisting of two roughly equally sized helical domains (Tripathi et al., 2009). In line with homology modeling, negative-stain EM and single-particle analysis of ZW10 demonstrated that it consists of two approximately equally sized domains (Fig. 2 D) separated by a flexible linker, as was previously shown for Dsl1 and Tip20 (Tripathi et al., 2009).

Phyre and HHpred identified Sec31, COP1, Sec39, Clathrin, and the nucleoporins Nup155 and Nup145 as high-confidence templates for structural modeling of ROD (Table S1 and Fig. 2 B). A common feature of these proteins is that they self-assemble in oligomeric/polymeric structures at or near cellular membranes. All these proteins share similar overall architectures, consisting of an N-terminal seven-bladed β-propeller domain and an extended α-helical domain built from tandem α-helical hairpins often separated by a structurally variable linker (ter Haar et al., 1998; Fotin et al., 2004; Stagg et al., 2006, 2007; Fath et al., 2007; Brohawn et al., 2008; Lee and Goldberg, 2010). In ROD, the predicted β-propeller domain occupies ≈350 residues from the N terminus and is followed by a predicted helical domain

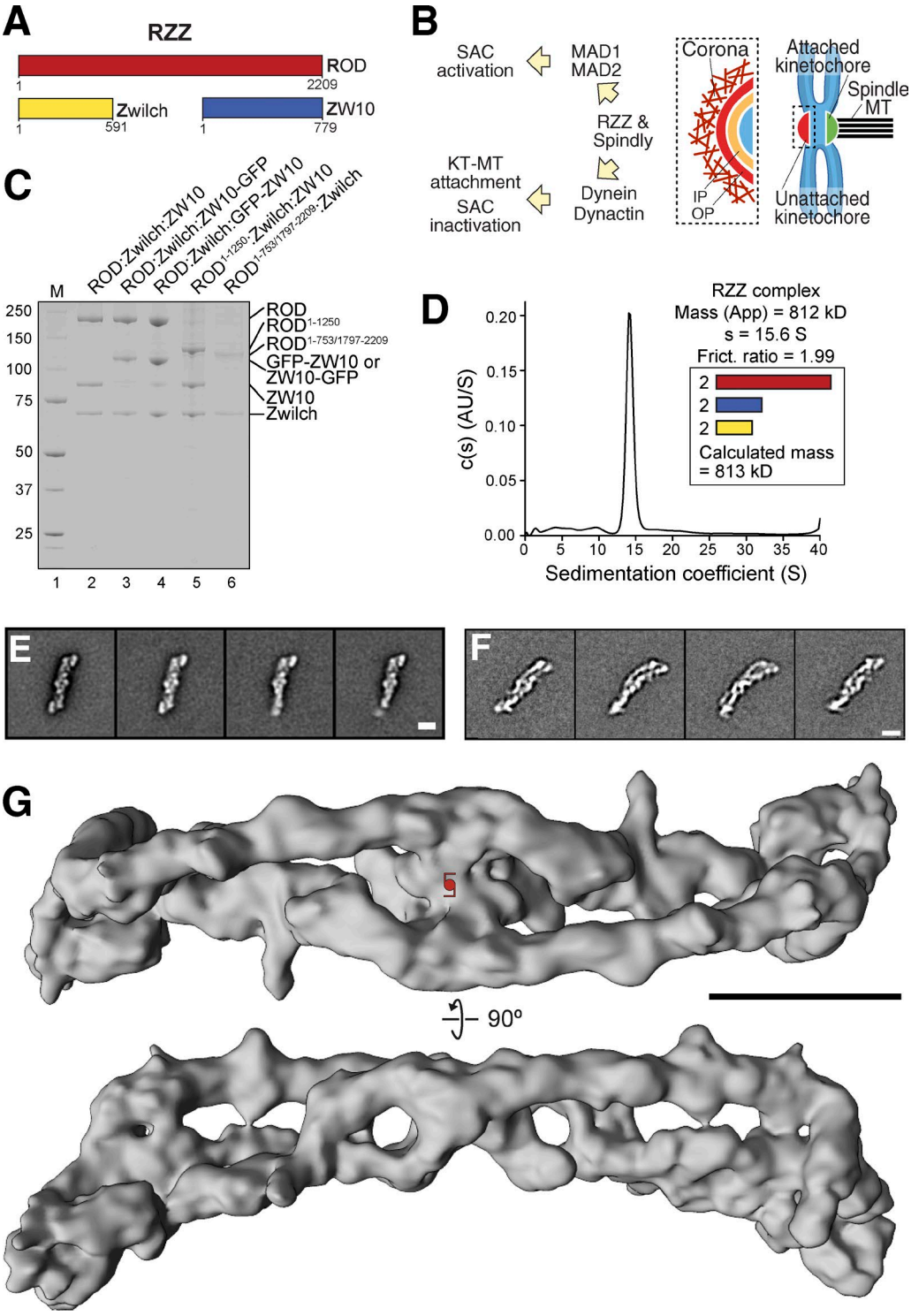

Figure 1. **Reconstitution and structural analysis of the RZZ complex.** (A) Schematic organization of the three RZZ subunits. (B) Biological functions of RZZ and Spindly. IP, inner plate of kinetochore; KT, kinetochore; OP, outer plate of kinetochore. (C) SDS-PAGE analysis of various RZZ complexes used in this paper. M, molecular weight marker. (D) Sedimentation velocity AUC profiles of the recombinant RZZ complex. "Mass (app)" denotes the apparent mass of RZZ derived from the velocity runs; "s" denotes the sedimentation coefficient; "Frict. ratio" is the frictional ratio of the RZZ particle. The calculated molecular mass for a complex containing two copies of each subunit is shown. The sedimentation velocity absorbance profiles and residuals of the fit showing the deviation of the c(*S*) model from the observed signals are shown, for this and other AUC profiles in this paper, in Fig. S1 E. AU, arbitrary units. (E) Typical class averages of negatively stained RZZ complexes. A clear twofold symmetry is evident. (F) Typical class averages of vitrified RZZ complexes. Bars, 10 nm. (G) Cryo-EM 3D reconstruction of the RZZ complex. The complex is ∼42 nm long and 10 nm wide. The position of a twofold symmetry axis is indicated in the top panel. The density maps of RZZ (here) and $R^{1-1,250}ZZ$ (Fig. 4 B) have been deposited into EMDataBank with the accession codes EMD-4103 and EMD-4104, respectively.

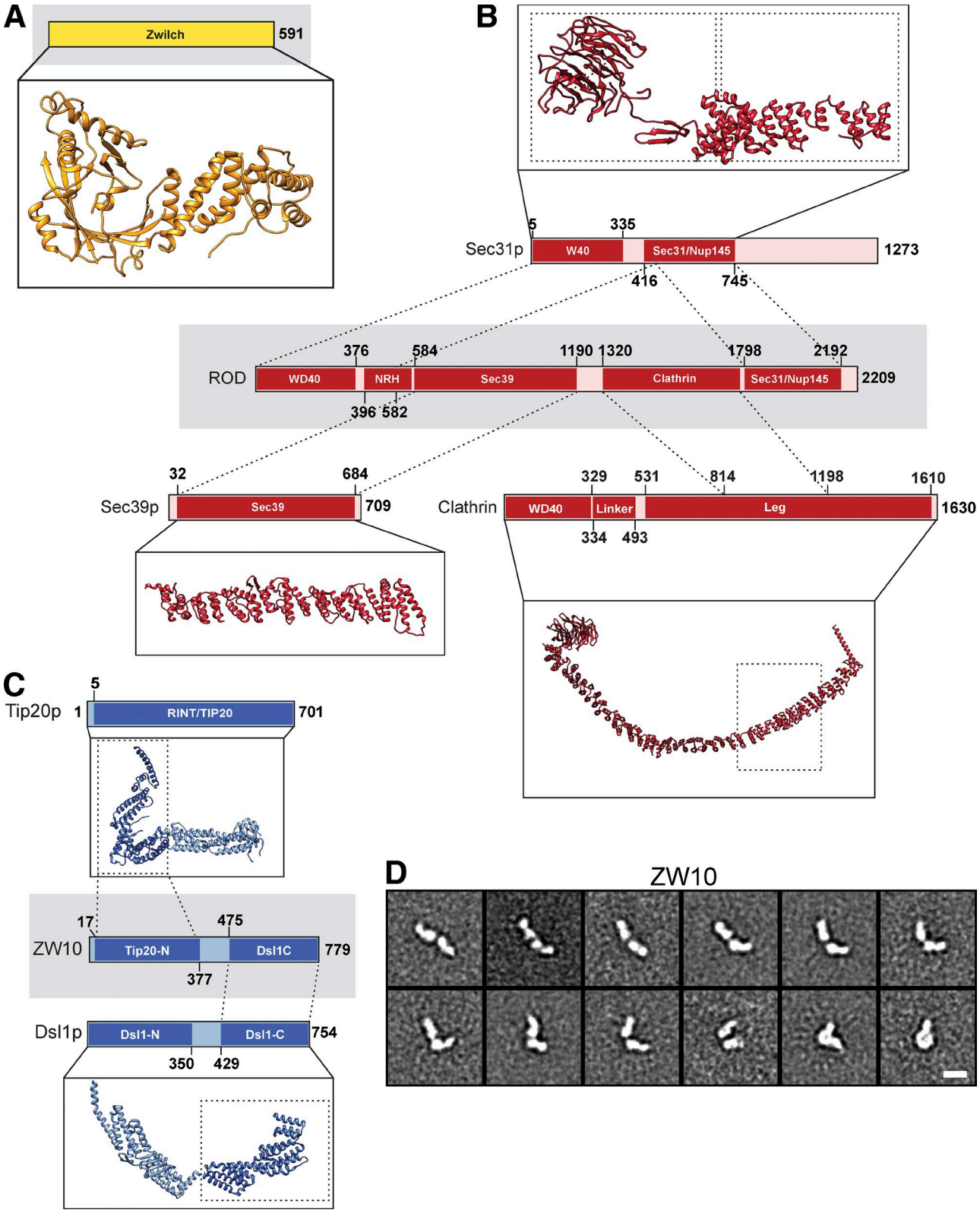

Figure 2. **Summary of modeling.** (A) Cartoon model of Zwilch (PDB ID: 3IF8). (B) Models of ROD were generated by a structure prediction program (I-TASSER). (C) Structures of the yeast homologue of ZW10 (Dsl1p), the N terminus (37–355; PDB ID: 3ETU), and the C terminus (333–684; PDB ID: 3K8P), were used for ZW10. NRH, NAG–ROD homology. (D) Typical negative-stain class averages of ZW10 obtained from ISAC. The averages highlight the inherent flexibility in the sample. Bar, 10 nm.

of ≈1,850 residues, in which a few subdomains are recognizable (Fig. 2 B). ROD was unstable in the absence of other RZZ subunits, and we could not yet address its structure in isolation. However, the results from homology modeling, and especially the observation that models based on tandem α-helical hairpin repeats are consistently predicted along the entire length of ROD after the N-terminal β-propeller, give confidence to the model and strongly suggest that ROD shares common ancestry with these proteins, despite limited overall sequence identity (Table S1).

Building a structural model of the RZZ complex

We used the Fit in Map rigid body fitting tool of program UCSF Chimera (Pettersen et al., 2004) to position experimental or homology models of Zwilch, ZW10, ROD$^{396–1,191}$, and ROD$^{1,319–1,797}$ (see Table S2 for fitting scores and an explanation of fitting procedures). We then manually positioned the homology models for ROD$^{1–376}$ (β-propeller) and ROD$^{1,798–2,189}$ in the residual density. Uninterrupted ribbons of density suggest that ROD spans the entire length of the complex, adopting an antiparallel configuration, with the ROD β-propellers at opposite ends (Fig. 3 A and Video 2). Zwilch fits snugly in the density from which it directly contacts the β-propeller and the C-terminal region of the first and second ROD protomers, respectively, in agreement with previous observations that the N-terminal region of ROD binds Zwilch (Çivril et al., 2010; Cheerambathur et al., 2013). ZW10 is positioned near the middle of the structure and of the twofold axis, where it interacts with the central domain of ROD in agreement with a previous yeast two-hybrid analysis (Scaërou et al., 2001).

Validation of the structural model

At an equivalent resolution, a map calculated from our molecular model of the RZZ complex displayed excellent correlation with the experimental map of the RZZ complex, testifying to the reliability of the model (Fig. 3 B and Table S2). As a further validation strategy, we used disuccinimidyl suberate, a bifunctional cross-linker, to cross-link the primary amines of neighboring lysines in the RZZ complex, and we identified cross-links by mass spectrometry (MS; cross-linking MS [XL-MS]; Herzog et al., 2012). The majority of observed cross-links (listed in Table S3 and displayed schematically in Fig. 3, C–E) were consistent with the organization and physical interactions of RZZ subunits predicted by molecular modeling, confirming the antiparallel organization of ROD as well as interactions of ZW10 with the central domain of ROD and of Zwilch with the N and C termini of ROD. Furthermore, a large majority of observed cross-links were compatible with lysine–lysine distances calculated from the molecular model of RZZ (Table S3), indicating that in spite of limited resolution of the EM map, the model is largely consistent with experimental spatial restraints.

The relative orientation of ZW10 and Zwilch in the model further suggests that they do not interact, or do so weakly. Size-exclusion chromatography (SEC) of individually expressed and purified ZW10 and Zwilch showed that they did not coelute, confirming the prediction (Fig. 4 A). In agreement with the cross-linking and EM data, a recombinant RZZ variant incorporating a ROD deletion mutant lacking the central domain (ROD$^{Δ754–1,796}$; Fig. 1 C, lane 6; shown schematically in Fig. S2 A) was sufficient to bind Zwilch but failed to interact with ZW10 in SEC experiments (Fig. S2 B). Conversely, a ROD deletion mutant consisting of the 1,250 N-terminal residues of ROD (ROD$^{1–1,250}$, shown schematically in Fig. S2 A) was sufficient to bind both Zwilch and ZW10 (Fig. 1 C, lane 5), even if XL-MS predicted the existence of additional interactions of ZW10 with downstream segments of ROD (Fig. 3 D). A negative-stain EM 3D reconstruction of the ROD$^{1–1,250}$–Zwilch–ZW10 (R$^{1–1,250}$ZZ) complex revealed a structure with an overall extension of 26 nm, approximately half that of the full-length RZZ complex (Fig. 4 B, top; and Fig. S2, C and D). The reconstruction is shown together with the portion of the cryo-EM reconstruction of the complete RZZ that corresponds to an RZZ model in which ROD was truncated at residue 1,250 (Fig. 4 B, bottom).

Further validation of the RZZ model included visualization, by gold or antibody labeling, of the N terminus of ROD and of the N and C termini of ZW10 (Fig. 4, C–E), with results that were again in very good agreement with the proposed model (summarized in Fig. 3 F). Thus, we generated a molecular model of the RZZ complex that relies on experimental and high-confidence homology models and that accounts for various spatial restraints derived from EM and cross-linking experiments. Although the RZZ model we have described cannot yet provide atomic detail, it provides a first reference to understanding the topology and general organization of the RZZ complex (Fig. 3 F).

A direct RZZ–Spindly interaction

Recombinant GFP-RZZ (Fig. 1 C, lane 3) brightly decorated kinetochores after injection in HeLa cells, whereas Reversine, a small-molecule inhibitor of the SAC kinase MPS1 (Santaguida et al., 2010), suppressed recruitment (Fig. 5 A). These results further confirm that we have reconstituted a native or near-native recombinant version of RZZ, which can reach its natural destination in the cellular environment.

Because direct binding partners of the RZZ are currently unknown, we incubated mitotic lysates from SILAC (stable isotope labeling with amino acid in culture; Ong et al., 2002)-labeled HeLa cells with recombinant baits consisting of immobilized GFP (negative control) or GFP-RZZ. This identified Spindly as the most prominent binding partner of GFP-RZZ. The kinetochore protein CENP-F was the only other enriched binder identified (Fig. 5 B). Both interactions of GFP-RZZ were strongly reduced in the presence of detergents in the lysis buffer (Fig. 5 C).

Human Spindly is 605 residues and contains extensive coiled-coil segments. The "Spindly motif" (residues 251–267; Fig. 5 D) is required for the interaction with dynein–dynactin, and its mutation prevents the release of MAD1–MAD2 from kinetochores and SAC silencing (Gassmann et al., 2010). Other dynein adaptors, including members of the bicaudal D (BICD) and BICD-related (BICDR) families such as BicD2, also contain several predicted coiled-coil segments (Fig. 5 D). The BicD2 N-terminal region (~270 residues) interacts directly with dynein–dynactin (Urnavicius et al., 2015), and a strongly conserved sequence signature is identified in this region (Hoogenraad and Akhmanova, 2016). Interestingly, we found that Spindly and BicD2 are clearly evolutionarily related, with extensive sequence similarity all along their sequences and a strictly conserved N-terminal signature (Fig. 5 D and Table S4). Thus, Spindly and BicD2 are likely to bind dynein in structurally similar ways, i.e., by engaging their N termini and using their C termini for interactions with cargo.

RZZ interaction with Spindly is direct and requires farnesylation

As Spindly is the most prominent binding partner of GFP-RZZ (Fig. 5, B and C), we asked whether stoichiometric amounts of

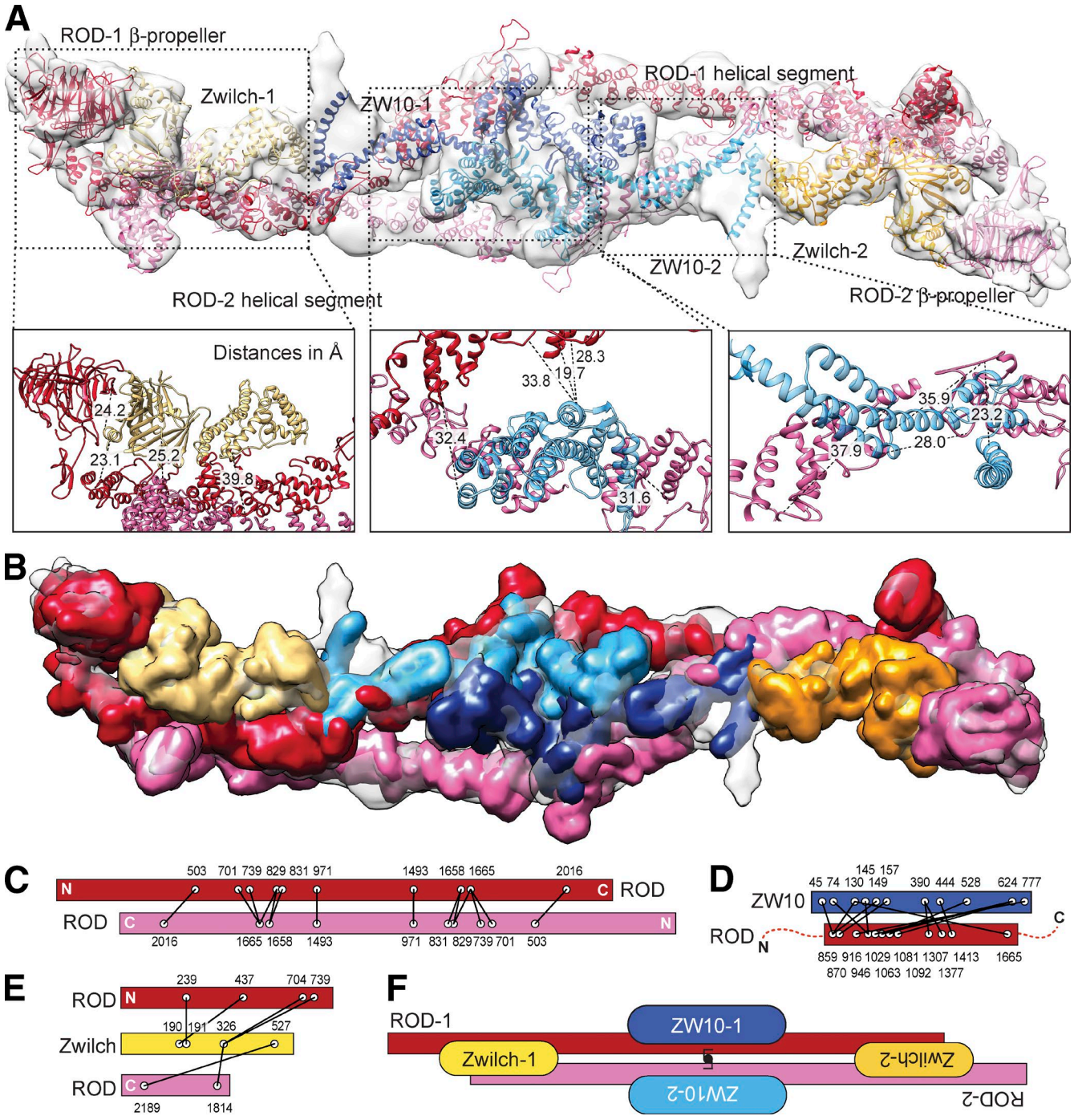

Figure 3. **A molecular model of the RZZ complex.** (A) The molecular model of the RZZ, consisting of a combination of experimental (for Zwilch) or homology models (for ROD and ZW10) of RZZ subunits was fitted in the cryo-EM density. (B) Map calculated from the molecular model at a resolution of 10.4 Å. (C–E) Summary of XL-MS data reporting various classes of intersubunit cross-links (listed in Table S3). (F) Schematic view of the organization of the RZZ complex.

RZZ and Spindly coeluted from an SEC column (Fig. 6 A). A partial shift in the elution volume of Spindly suggested a low-affinity substoichiometric interaction. Because recruitment of Spindly to kinetochores requires farnesylation (Holland et al., 2015; Moudgil et al., 2015), we subjected Spindly to farnesylation in vitro with farnesyl transferase (FTase) and farnesyl pyrophosphate (Fpp) as substrate (Nguyen et al., 2007). By MS, we found Spindly to be homogeneously modified at Cys602 in this reaction (Fig. S3, A and B). Prominent shifts in the SEC elution volumes of both farnesylated Spindly (Spindly^{Farn}) and RZZ demonstrated that Spindly^{Farn} and RZZ bind stoichiometrically, thus identifying Spindly farnesylation as a crucial determinant of the interaction (Fig. 6 A). The modest interaction of Spindly with RZZ observed in the absence of FTase and Fpp is probably caused by a low degree of farnesylation of Spindly upon its expression in insect cells (detected by MS; not depicted). Spindly

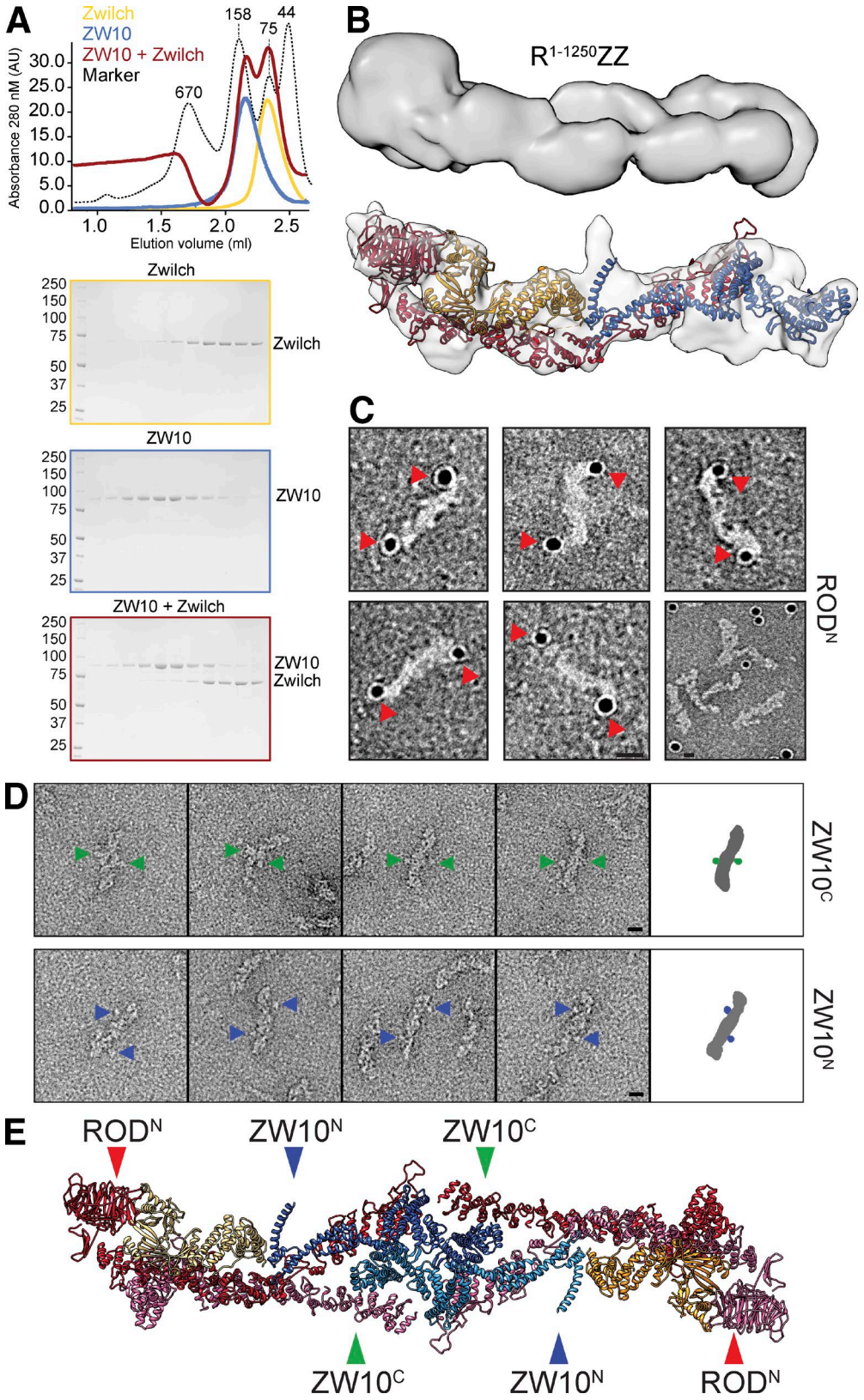

Figure 4. **Validation of the RZZ model.** (A) Elution profiles and SDS-PAGE of SEC experiments on Zwilch, ZW10, or their stoichiometric combination. Molecular mass is indicated in kilodaltons. AU, arbitrary units. (B) Top: 3D reconstruction of the negatively stained ROD$^{1–1,250}$ZZ complex. Bottom: the density corresponding to a model of the ROD$^{1–1,250}$ZZ complex was cut out of the complete RZZ complex for comparison. (C) NiNTA-gold labeling of the N-terminal histidine tag of ROD. The bottom-right panel represents part of a field in which labeling of ROD was performed after proteolytic removal of the His tag. (D) Micrographs of negatively stained GFP-RZZ or ROD–Zwilch–GFP-ZW10 complexes. Bars, 10 nm. (E) Summary of positions identified in experiments in C and D mapped onto the molecular model of RZZ.

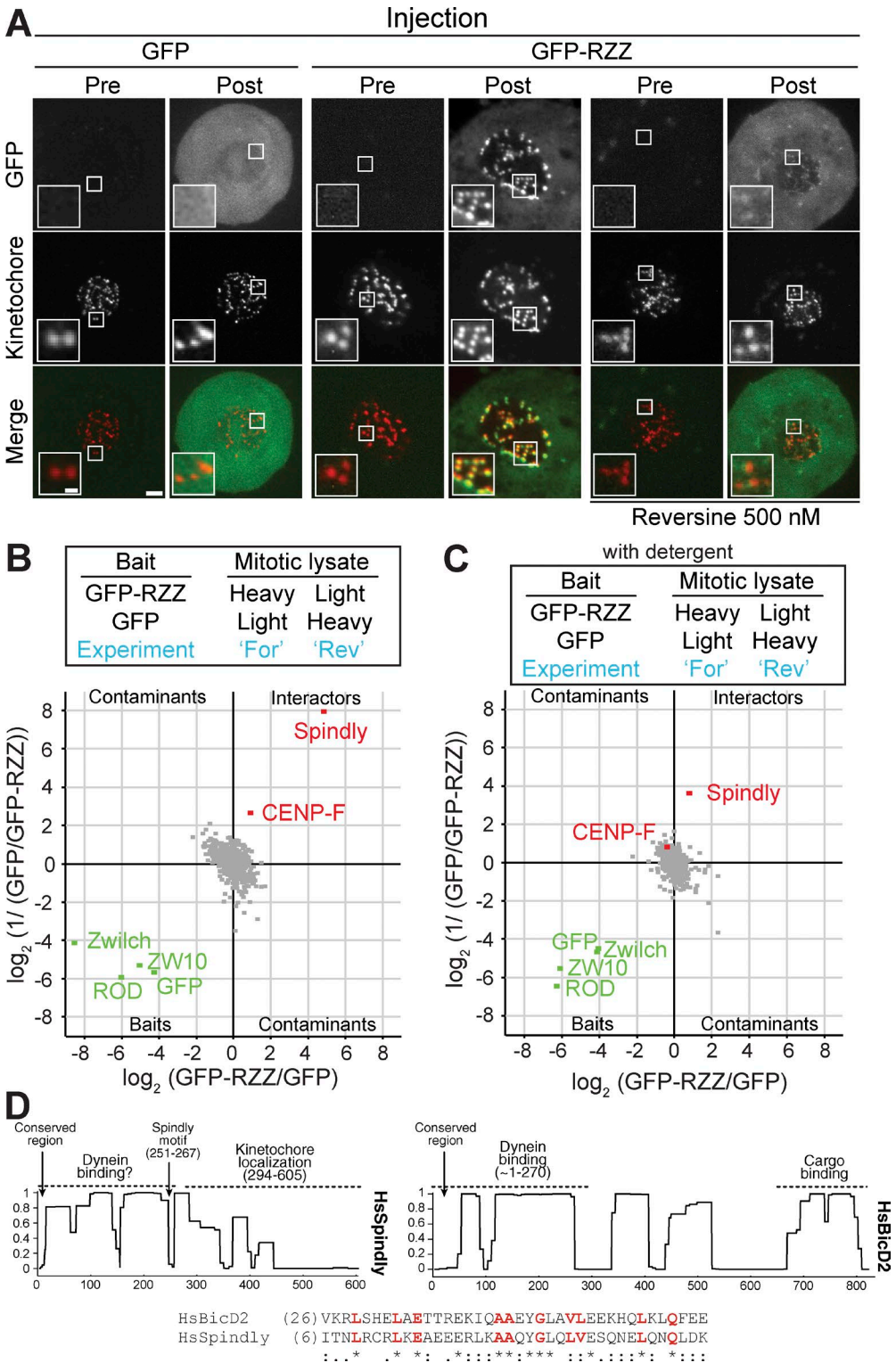

Figure 5. **RZZ interacts with Spindly.** (A) Representative images of the localization of the recombinant GFP-RZZ complex injected in mitotic HeLa cells transiently expressing mCherry-CENPA (to visualize kinetochores). Cells were synchronized in G2 by treatment with the Cdk1 inhibitor RO3306 and released into mitosis in the presence of the indicated drugs. Mitotic cells were live imaged before (Pre) and after (Post) microinjection with recombinant GFP or GFP–RZZ. Bars: (main images) 2 µm; (insets) 0.5 µm. Numbers of cells injected: for GFP, $n = 2$; for GFP-RZZ $n = 8$; for GFP in Reversine-treated cells, $n = 2$ (not depicted); for GFP-RZZ in Reversine-treated cells, $n = 8$. (B and C) Forward (For) and reverse (Rev) SILAC experiments (see the SILAC immunoprecipitation experiments section in Materials and methods) were performed as indicated in the upper part of the figure. Spindly is the most prominent component of the "Interactors" quadrant, which identifies specific binders of the GFP-RZZ complex in comparison with GFP. The experiments were performed in the absence (B) or presence (C) of detergent in lysis buffer. Baits are shown in green, interaction partners in red, and all quantified background proteins in gray. (D) Coiled-coil content of human Spindly and BicD2 predictions obtained with the program COILS (Lupas et al., 1991). Sequence alignment of Spindly and BicD2 shows excellent conservation in Spindly of a highly conserved motif previously identified in BicD2 (Hoogenraad and Akhmanova, 2016). Residues shown in red indicate conservation of signatures within motifs, but sequence conservation is more extensive and extends to the entire dynein-binding domain (not depicted).

and Spindly^{Farn} showed essentially identical elution volumes (Fig. 6 A), suggesting that prenylation does not grossly change the oligomerization or structural organization of Spindly.

XL-MS analysis of the Spindly^{Farn}–RZZ identified multiple contacts between Spindly^{Farn} and ROD but not other RZZ subunits (Fig. 6 B and Table S3, section C). Neither Zwilch nor ZW10 bound Spindly^{Farn} in isolation in SEC experiments (Fig. S2, G and H), whereas the ROD$^{\Delta 1,251\text{-}C}$ZZ complex bound Spindly^{Farn}, confirming a prominent role for ROD and also suggesting that the C-terminal region of ROD is dispensable for Spindly^{Farn} binding (Fig. S2 I). The pattern of cross-links suggests that Spindly projects its C-terminal region (where the farnesyl acceptor residue Cys602 resides) in the direction of the ROD β-propeller. Residues 294–605 of Spindly have been previously identified as the minimal kinetochore recruitment domain (Moudgil et al., 2015), suggesting that farnesylation augments the binding affinity of the interaction but is not its sole determinant. Indeed, RZZ did not bind to a variety of short (<6 residues) farnesylated peptides (unpublished data).

Isolated nonfarnesylated mCherry–Spindly behaved as a monomer in sedimentation velocity AUC experiments (Fig. 6 C). Conversely, the RZZ–Spindly^{Farn} and RZZ–mCherry–Spindly^{Farn} complexes (at a concentration of 5 µM) showed monodisperse samples with very good agreement of the apparent molecular mass with that calculated assuming two copies of each subunit (Fig. 6, D and E). When bound to dynein–dynactin, BicD2 forms a dimeric, parallel coiled-coil (Urnavicius et al., 2015), and we speculate that dimerization on RZZ promotes a similar transition in the N-terminal region of Spindly. Both RZZ–Spindly^{Farn} and RZZ–mCherry–Spindly^{Farn} complexes had slightly increased frictional ratios (i.e., they behaved as more elongated particles) in comparison with the isolated RZZ complex (2.14 and 2.34 against 1.99; Fig. 6, D and E), which likely explains the reduced elution volume of RZZ–Spindly^{Farn} in comparison with RZZ in SEC experiments. Negative-stain EM analysis at low sample concentration did not reveal major structural changes of RZZ–Spindly^{Farn} in comparison with RZZ (Fig. S1 F), suggesting that the increased frictional ratio may be caused by regions of Spindly that do not occupy a fixed position relative to the core of the complex. At higher concentrations (10 and 15 µM), RZZ–mCherry–Spindly^{Farn} complexes sedimented in broader peaks (Fig. 6, F and G), suggesting initial aggregation- or concentration-driven high-order oligomerization.

Mapping the RZZ–Spindly interaction

To begin to shed light on how prenylation contributes to the interaction of the RZZ complex with Spindly, we resorted to a chemical biology approach exploiting pyrophosphate precursors of farnesyl derivatives carrying UV-activatable cross-linking groups (benzophenone 1 [BPP1], benzophenone 2 [BBP2], and diazirine [DPP], shown in Fig. 7 A; Kuhlmann et al., 2002). After applying the first step of the protocol schematized in Fig. 7 B, we found by MS that FTase had efficiently incorporated all three farnesyl derivatives on Spindly (Fig. S3, C–E). The RZZ–Spindly^{Farn} mixes were separated by SEC, and each fraction was exposed to UV. RZZ–Spindly^{Farn} complexes harboring photoactivatable cross-linkers revealed slow-migrating bands in SDS-PAGE gels, suggestive of successful cross-linking. No equivalent bands were observed upon UV treatment of the unmodified RZZ–Spindly^{Farn} complex (Figs. 7 D and S4, A–H). By Western blotting, we determined that the slow-migrating bands contain ROD and Spindly (Figs. 7 D and S4, A–H), suggesting that ROD acts as the receptor for the Spindly farnesyl moiety.

We used MS to identify covalent adducts between Spindly and ROD. Peaks corresponding to (unmodified) photoactivatable cross-linkers conjugated to Cys602 were readily identified in the absence of UV but disappeared when UV was applied to the Spindly–RZZ samples (this is shown for diazirine in Fig. 7, E and F; and for BPP1 and BPP2 in Fig. S4, I–L; tandem MS [MS/MS] fragmentation spectra are shown in Fig. S3, C–H). Correspondingly, new peaks appearing after exposure to UV revealed that all three photoactivatable farnesyl derivatives had become cross-linked with Leu120 in the β-propeller of ROD. Thus, our analysis identifies the β-propeller of ROD as the farnesyl receptor of Spindly.

Discussion

In this study, we have taken advantage of a cryo-EM map, extensive homology modeling, and a comprehensive validation strategy to generate the first structural model of the RZZ complex. ROD, the largest RZZ subunit, is structurally related to proteins that toggle between monomeric and polymeric states, including Clathrin, the αβ'ε-COP (COPI) complex, and the Sec13–Sec31 complex (COPII; Fig. 8 A; Stagg et al., 2007). Underlying the polymerization behavior of these proteins is a common structural design of precursor cage proteins, consisting of an N-terminal β-propeller domain and an extended C-terminal helical domain. The organization of the COPII assembly unit, an inverted dimer of the Sec13–Sec31 complex, with β-propeller domains capping each end, is strongly reminiscent of the dimeric antiparallel arrangement of ROD in RZZ (Stagg et al., 2006, 2007; Fath et al., 2007). These observations make us speculate that RZZ, in analogy to these proteins, may act as the structural precursor of the corona and drive the expansion of the kinetochore into a crescent, as explained in the Introduction (Fig. 8 A). Importantly, there is no evidence at present that the corona exhibits a regular lattice, but this may not be a precondition for its establishment.

If RZZ assembles in higher-order oligomers, is seems likely that kinetochores may be required to limit the process spatially. A speculative working model is that full display of high-order oligomerization by RZZ is only possible after kinetochore recruitment and local activation. Kinetochore-localized mitotic kinases have been implicated in kinetochore expansion and may trigger the self-assembly process to limit it to kinetochores (Wynne and Funabiki, 2015). In the process of cargo-stimulated assembly of coated vesicles, coat units are cytosolic and their self-assembly in cells is strictly controlled by interaction with specific cargo adaptors near membranes (Russell and Stagg, 2010; McMahon and Boucrot, 2011; Jackson, 2014). In view of the structural similarity of the RZZ with Clathrin and COPs, we speculate that kinetochore-localized assembly of the corona bears similarity with processes best known to happen near membranes. The exact mechanism of kinetochore recruitment of the RZZ has not yet been unveiled, but previous studies demonstrated a requirement for the outer kinetochore NDC-80 complex, the main MT receptor (Miller et al., 2008; Chan et al., 2009; Cheerambathur et al., 2013; Samejima et al., 2015). This, however, may also reflect an indirect requirement, as the NDC-80 complex acts as recruitment platform for the MPS1 kinase, whose activity is necessary for

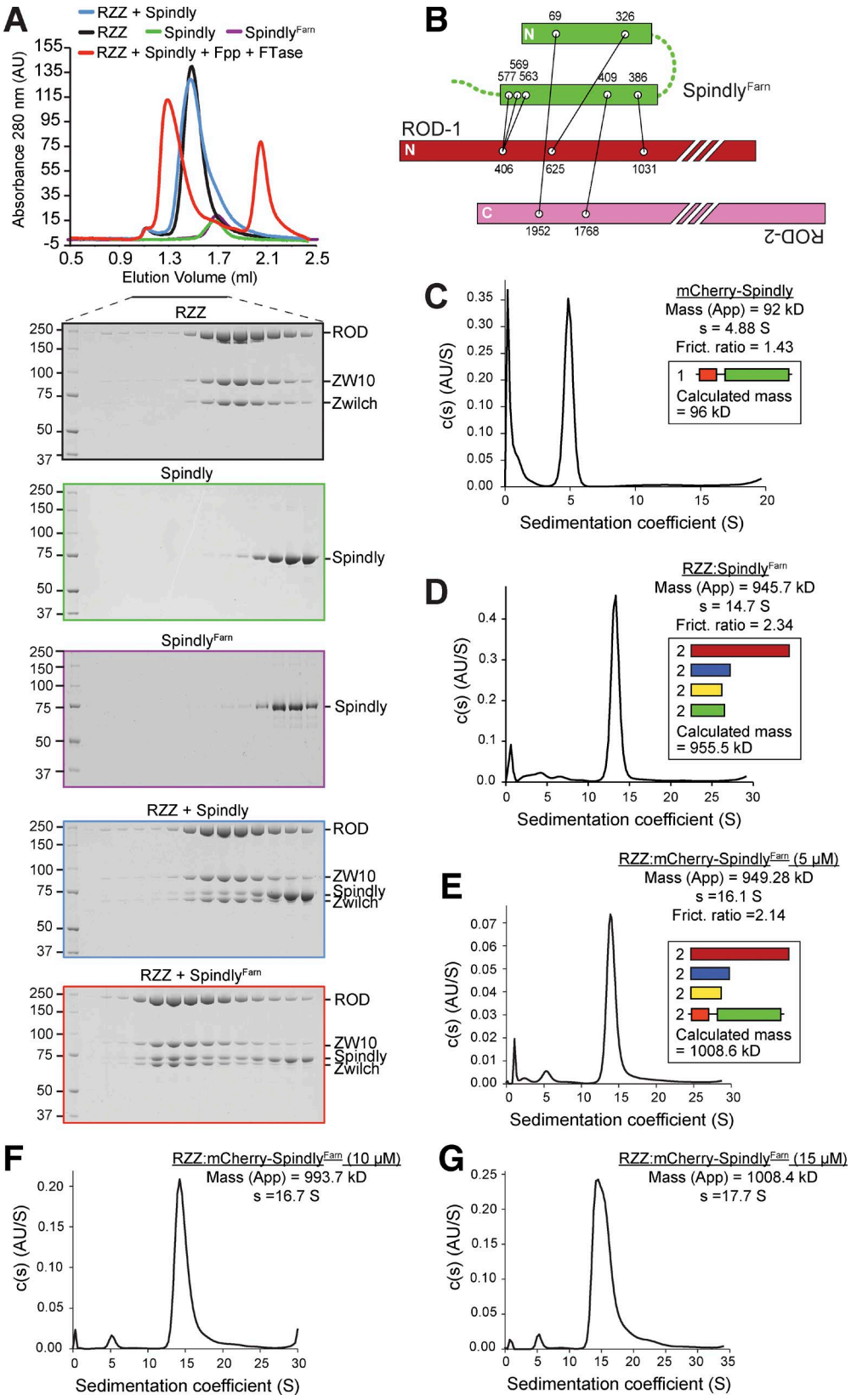

Figure 6. **RZZ interaction with Spindly is direct and requires farnesylation.** (A) Elution profiles and SDS-PAGE analysis of SEC experiments with the indicated proteins. The elution volume of the RZZ–Spindly complex after treatment with FTase and Fpp as substrate shifts significantly, whereas farnesylated Spindly (Spindly^{Farn}) elutes like unmodified Spindly. (B) Summary of XL-MS data reporting ROD–Spindly intersubunit cross-links. (C) Sedimentation velocity AUC profiles of recombinant mCherry-Spindly. The calculated molecular mass for a complex containing two copies of each subunit is shown. (D) Sedimentation velocity AUC profiles of the RZZ–Spindly^{Farn} complex. The calculated molecular mass for a complex containing two copies of each subunit is shown.

RZZ kinetochore recruitment (see, e.g., Martin-Lluesma et al. [2002], Santaguida et al. [2010], and this study). We speculate that once established, the corona, through the oligomeric structure of RZZ, facilitates the formation of multiple cooperative low-affinity interactions that "trap" additional corona proteins (most of which are themselves coiled-coil–rich oligomers, like the MAD1–MAD2 tetramer and the CENP-E and CENP-F dimers; Fig. 8 B). Because the fibrous network of the corona only exists at kinetochores and dissolves rapidly upon cell lysis, this might explain previous difficulties in precisely defining the kinetochore receptors of these proteins. Thus, an important goal of future studies will be the identification of binding partners and regulators of RZZ at kinetochores capable of unleashing its predicted high-order oligomerization potential. We aim to approach this problem by reconstituting corona assembly on artificial kinetochores (Weir et al., 2016).

Recent work reported that Spindly farnesylation is required for kinetochore recruitment and its interaction with the RZZ (Holland et al., 2015; Moudgil et al., 2015). Our results extend these previous findings by showing that the interaction of Spindly with RZZ is direct and requires Spindly farnesylation. Furthermore, by using a chemical biology approach, we mapped the binding site for the Spindly farnesyl group to the ROD β-propeller domain. Thus, ROD is a new example of a very small cohort of isoprenoid-binding proteins that also includes PDEδ, the guanine–nucleotide dissociation inhibitor (GDI) for the small GTPases Rab and Rho, and a 14-3-3 protein (Wang and Casey, 2016). PDEδ has high binding affinity for the isolated isoprenoid moiety (Ismail et al., 2011); RabGDI and RhoGDI require the GTPase domain in addition to the prenyl group for tight binding (Hoffman et al., 2000; Rak et al., 2003); finally, 14-3-3 recognizes a hybrid phosphorylated and prenylated motif in the target RND GTPase (Riou et al., 2013). Our results, combined with the previous observation that the minimal kinetochore-binding region of Spindly comprises the entire second half of Spindly (Moudgil et al., 2015), strongly suggest that the binding affinity of ROD for Spindly results from the combined recognition of the farnesyl group and of an extended interaction interface on Spindly. An interaction of Spindly with the kinetochore and dynein-binding protein CENP-F, FTase, and the MAD1–MAD2 spindle checkpoint complex in cellular lysates has been previously described (Holland et al., 2015). Like Spindly, CENP-F is also farnesylated (Ashar et al., 2000; Hussein and Taylor, 2002), and its identification as a binding partner of RZZ raises the possibility that RZZ acts as a more general receptor for farnesylated proteins.

The evolutionary relationship of Spindly with BicD2, which had escaped previous analyses, suggests that Spindly, like BicD2, binds dynein through its N-terminal domain while interacting with cargo via its C-terminal region (Fig. 8 B). This hypothesis is consistent with the sufficiency of the Spindly C-terminal region in kinetochore binding (Moudgil et al., 2015). In light of our result that Spindly binds RZZ directly and of previous evidence that RZZ is required for recruitment of Spindly to the kinetochore, it can be predicted that the C-terminal region of Spindly is sufficient for an interaction with RZZ. Our identification of ROD as the Spindly farnesyl–binding site is consistent with this prediction. This network of interactions suggests that the RZZ is a dynein cargo at kinetochores, an interpretation that raises the interesting question of whether RZZ augments the relatively modest ability of the Spindly adaptor to turn dynein into a processive motor (McKenney et al., 2014). Our future studies will address these important unresolved mechanistic questions.

Materials and methods

Expression and purification of mCherry–Spindly

Spindly was produced as an mCherry fusion using the biGBac system for baculovirus expression (Weissmann et al., 2016). Specifically, the coding sequence of Spindly was subcloned into the multiple cloning site of pLIB. The mCherry coding sequence was then inserted by PCR at the 5′ end of Spindly. Bacmid was produced from EMBacY cells and subsequently used to transfect Sf9 cells and produce baculovirus. The latter was amplified through three rounds of amplification and used to infect TnaO38 cells (Hashimoto et al., 2012). Cells infected with the mCherry–Spindly virus were cultured for 72 h before harvesting. Cells were resuspended in lysis buffer (50 mM Hepes, pH 8, 250 mM NaCl, 10% glycerol, 20 mM imidazole, and 2 mM tris(2-carboxyethyl) phosphine [TCEP]). Resuspended cells were lysed by sonication in the presence of the protease inhibitor mix HP Plus (Serva), DNaseI (Roche), and 1 mM PMSF before clearance at 100,000 *g* at 4°C for 45 min. The cleared lysate was applied to a 5-ml NiNTA Fast Flow column (GE Healthcare) preequilibrated in lysis buffer. The column was washed with 100 column volumes of lysis buffer, and the bound protein was eluted with lysis buffer supplemented with 300 mM imidazole. The eluate was diluted five times with dilution buffer (50 mM Hepes, pH 8, and 2 mM TCEP) to a final NaCl concentration of 50 mM and applied to a 6-ml Resource Q anion exchange column (GE Healthcare) preequilibrated in buffer A (50 mM Hepes, pH 8, 50 mM NaCl, and 2 mM TCEP). Elution of bound protein was achieved by a linear gradient from 50–400 mM NaCl in 20 column volumes. Relevant fractions were concentrated in 30-kD molecular mass cutoff Amicon concentrators (EMD Millipore) and applied to a Superose6 10/300 column (GE Healthcare) equilibrated in SEC buffer (50 mM Hepes, pH 8, 250 mM NaCl, and 2 mM TCEP). SEC was performed under isocratic conditions at a flow rate of 0.4 ml/min, and the relevant fractions were pooled, concentrated, flash frozen in liquid nitrogen, and stored at −80°C.

Expression and purification of Spindly

Expression of human Spindly was performed with the biGBac system in TnaO38 cells. Lysis of a pellet from 500 ml expression culture was performed by sonication in 100 ml lysis buffer (50 mM Hepes, pH 8.5, 200 mM NaCl, 10% glycerol, 20 mM imidazole, 5 mM β-mercaptoethanol [βMe], 1 mM PMSF, and 1 mM protease inhibitor cocktail [Serva]). The cleared lysate was loaded onto an equilibrated 5-ml HisTrap Fast Flow column (GE Healthcare) using a peristaltic pump (2 ml/min flow rate). The column was washed with 500 ml wash buffer (50 mM Hepes, pH 8.5, 200 mM NaCl, 10% glycerol, 20 mM imidazole, and 5 mM βMe). Elution was performed with wash buffer supplemented with 250 mM imidazole. The 2-ml fractions were analyzed by SDS-PAGE, and those containing Spindly were concentrated up to a volume of 10 ml. The protein solution was diluted five times with buffer A and

(E–G) Sedimentation velocity AUC profiles of the RZZ–mCherry–Spindly^{Farn} at 5, 10, and 15 µM. "Mass (app)" denotes the apparent mass of RZZ derived from the velocity runs; "s" denotes the sedimentation coefficient; "Frict. ratio" is the frictional ratio of the Spindly particle. In E, the calculated molecular mass for a complex containing two copies of each subunit is shown. AU, arbitrary units.

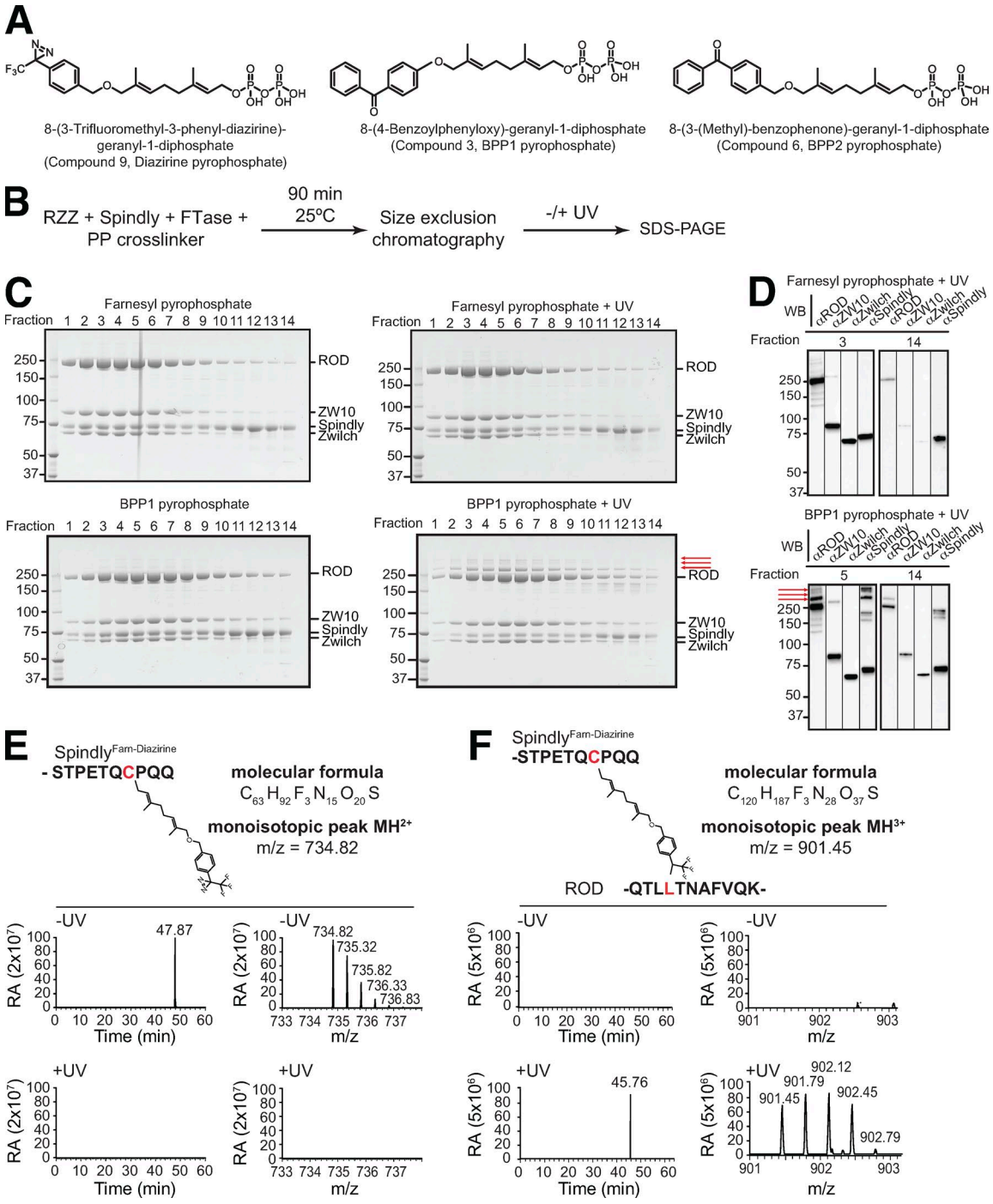

Figure 7. **ROD binds the Spindly farnesyl group.** (A) Chemical structure of Fpp analogues incorporating photoactivatable cross-linking groups. (B) Schematic of the UV-induced RZZ–Spindly^{Farn} cross-linking experiment. PP, pyrophosphate. (C) FTase was incubated with Spindly (also in presence of RZZ) to incorporate farnesyl or a modified farnesyl harboring the cross-linking group BPP1 in Spindly. After separation by SEC, elution fractions were subjected to UV irradiation and visualized by Coomassie staining of SDS-PAGE gels. UV-induced cross-linked bands (the most prominent of which are indicated by red arrows) appear in the sample containing BPP1. Equivalent experiments with BPP2 and diazirine are shown in Fig. S4 (A–H). (D) Western blotting (WB) analysis of the indicated selected fractions (from SDS-PAGE in C) with antibodies against ROD, ZW10, Zwilch, and Spindly. Molecular mass is indicated in kilodaltons. (E and F) MS identifies UV-induced cross-links of Spindly's farnesyl diazirine with residues Leu120 of ROD (shown in red). For each panel, left traces show the chromatographic peak and right traces show the isotopic pattern of the corresponding peptide identified in the MS survey scan. Upper traces represent samples before UV treatment (–UV) and lower traces after UV treatment (+UV). Corresponding MS/MS spectra containing sequence information are shown in Fig. S3 E. Equivalent MS analyses with BPP1 and BPP2 are shown in Fig. S4 (I–L) and MS/MS spectra in Fig. S3 (C and D). RA, relative abundance.

subsequently purified on a Resource Q anion exchange column. Peak fractions were analyzed by SDS-PAGE, and those containing Spindly were concentrated up to 500 µl and applied to a Superose 6 10/300 column. The peak fractions were analyzed by SDS-PAGE, and those containing pure Spindly were concentrated up to 20 mg/ml, flash frozen in liquid nitrogen, and stored at −80°C.

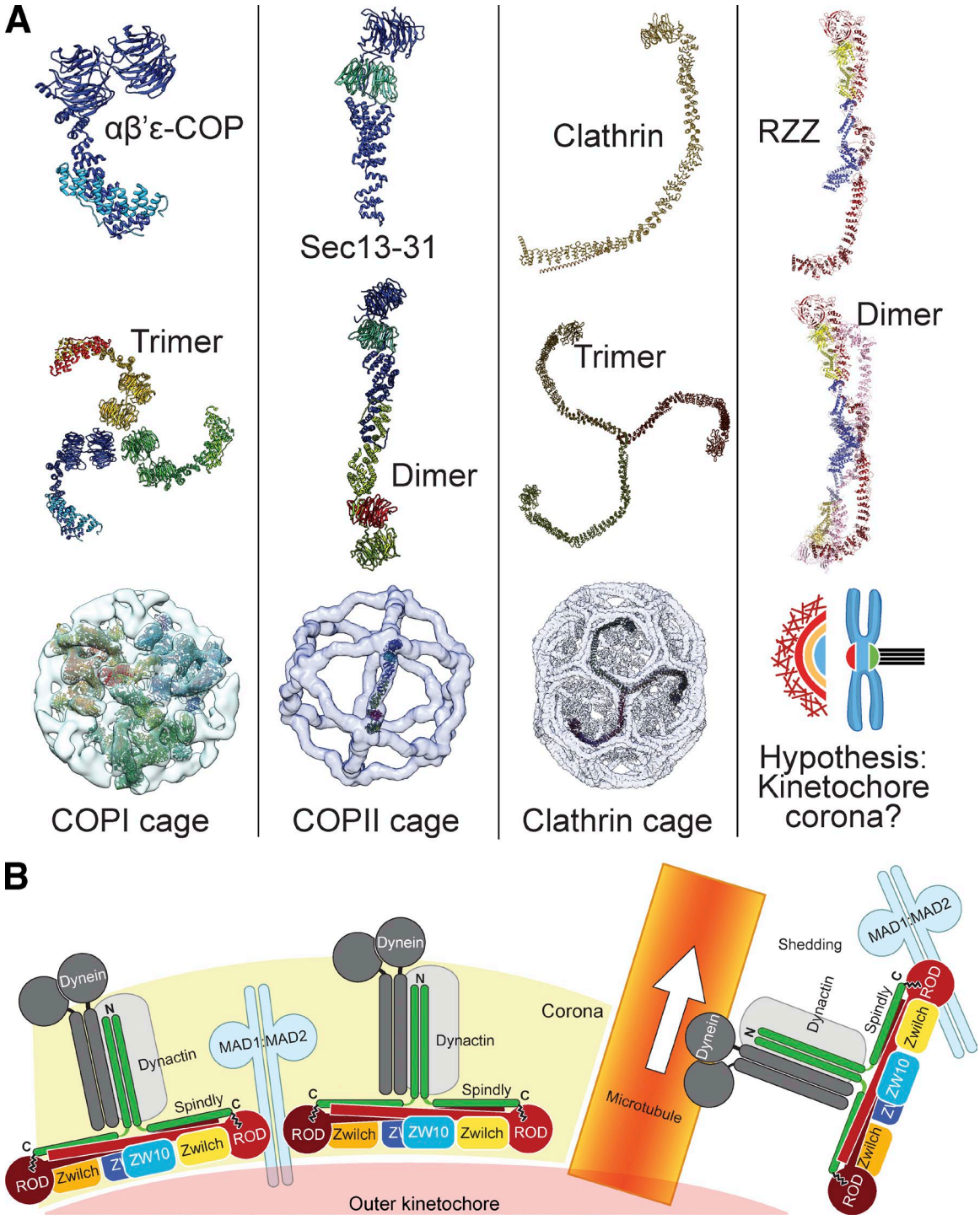

Figure 8. **Comparison of self-assembly properties of coat proteins and implications for RZZ–Spindly.** (A) The units of self-assembly in COPI, COPII, and Clathrin cages are proteins consisting of an N-terminal β-propeller followed by an α-solenoid. These units often form oligomers (e.g., the inverted tetramers of Sec13–31), which further self-assemble to create finite structures like cages. Whether the kinetochore fibrous corona reflects an ordered assembly of RZZ–Spindly complexes is currently unclear. Kinetochores may act to nucleate self-assembly of cytosolic RZZ–Spindly units and to promote the formation of crescents. (B) Summary of interactions and pathways discussed in this paper.

Expression and purification of RZZ

A protocol for the expression of RZZ has been described previously (Altenfeld et al., 2015). For a pellet of 500 ml of expression culture, cell lysis was performed in 100 ml lysis buffer (50 mM Hepes, pH 8.5, 200 mM NaCl, 10% glycerol, 20 mM imidazole, 5 mM βMe, 1 mM PMSF, and 1 mM protease inhibitor cocktail) by sonication. The cleared lysate was loaded onto an equilibrated 5-ml HisTrap Fast Flow column using a peristaltic pump (2 ml/min flow rate). The column was washed with 500 ml wash buffer (50 mM Hepes, pH 8.5, 200 mM NaCl, 10% glycerol, 20 mM imidazole, and 5 mM βMe), and elution was generally performed by an overnight on-column cleavage with Prescission protease at a ratio of 1:10 (protease/target) and in a circulating

buffer volume of 20 ml (15 h, flow rate = 1 ml/min). The eluate was analyzed by SDS-PAGE, concentrated up to a volume of 2 ml, and diluted 1:5 in buffer A (25 mM Hepes, pH 8.5, 25 mM NaCl, and 4 mM TCEP) before loading onto a Resource Q anion exchange column. The diluted sample was loaded onto the column at a flow rate of 1 ml/min and washed (3 column volumes) with buffer A. The buffer was adjusted to a concentration of 50% buffer B (25 mM Hepes, pH 8.5, 1 M NaCl, and 4 mM TCEP) in 20 column volumes. The resulting fractions were pooled and loaded on a Superose 6 10/300 SEC column in SEC buffer (25 mM Hepes, pH 8.5, 250 mM NaCl, and 4 mM TCEP). The eluted RZZ complex was concentrated up to 8–10 mg/ml, flash frozen in liquid nitrogen in aliquots of 20 µl, and then stored at −80°C.

Cell culture, plasmid transfection, microinjections, and imaging

HeLa cells were grown in DMEM (PAN Biotech) supplemented with 10% tetracycline-free FBS (PAN Biotech), penicillin/streptomycin (Gibco), and L-glutamine (PAN Biotech). Cells were grown at 37°C in the presence of 5% CO_2. Cdk1 inhibiton, microinjections, and live imaging were performed in complemented CO_2-independent media (Gibco) at 37°C. A cDNA segment encoding human CENP-A was cloned in a pcDNA5/FLP recombination target/tetracycline operator–internal ribosome entry site–mCherry (pcDNA5/FRT/TO-IRES-mCherry) vector, a modified version of pcDNA5/FRT/TO vector (Invitrogen) generated in house by M. Mattiuzzo and A. De Antoni as a C-terminal fusion to mCherry. Transient transfections of pcDNA5/FRT/TO-IRES-mCherry were performed with Lipofectamine 2000 (Invitrogen) according to the manufacturer's instructions, and the mCherry–CENP-A fusion was expressed by addition of 200 ng/ml doxycycline (Sigma-Aldrich) for 48 h.

Where indicated, nocodazole (Sigma-Aldrich) was used at 3.3 µM, RO-3306 (EMD Millipore) was used at 9 µM for 18 h, MG-132 (EMD Millipore) was used at 10 µM, and Reversine (Cayman Chemical) was used at 500 nM. Microinjections were performed using a combination of FemtoJet, InjectMan-NI2, and Femtotip-II, all purchased from Eppendorf. Recombinant GFP and GFP-RZZ complex were injected at concentrations of 4 µM and 10 µM, respectively. Live-cell images were taken before injection and 1–3 min after injection using the spinning-disk confocal microscopy of a Marianas system (Intelligent Imaging Innovations, Inc.) equipped with an Axio Observer Z1 microscope (ZEISS), a CSU-X1 confocal scanner unit (Yokogawa Electric Corporation), Plan-Apochromat 63× or 100×/1.4 NA objectives (ZEISS), and an Orca Flash 4.0 sCMOS Camera (Hamamatsu Photonics). Images were acquired as Z sections using Slidebook Software (5.5; Intelligent Imaging Innovations, Inc.) or LCS 3D software (Leica Microsystems) and converted into maximal intensity projection TIFF files for illustrative purposes.

FTase α/β

Escherichia coli BL21(DE3)-Codon-plus-RIPL cells containing the pGATEV plasmid encoding the GST fusion of the FTase mutant (W102T/Y154T) were grown in Luria–Bertani medium at 37°C to an OD_{600} of 1. Protein expression was induced by the addition of 0.1 mM IPTG, and cells were incubated at 37°C for 5 h before harvesting. Cells were resuspended in lysis buffer (50 mM Hepes, pH 7.5, 500 mM LiCl, and 2 mM TCEP). Resuspended cells were lysed by sonication in the presence of protease-inhibitor mix HP Plus and 2 mM of PMSF before clearance at 100,000 *g* at 4°C for 45 min. The cleared lysate was applied to a 20-ml GSH4 Fast Flow column (GE Healthcare) pre-equilibrated in lysis buffer. The column was washed with 20 column volumes of lysis buffer, and the bound protein was eluted with 30 ml lysis buffer supplemented with 20 mM glutathione. The GST tag was then cleaved by addition of tobacco etch virus protease to the eluate for 3 h at 4°C. The eluate concentrated in 10-kD molecular mass cut-off Amicon concentrators (EMD Millipore) and was applied to a Superdex200 16/60 column (GE Healthcare) equilibrated in SEC buffer (25 mM Hepes, pH 7.5, 150 mM NaCl, and 2 mM TCEP). SEC was performed under isocratic conditions at a flow rate of 1 ml/min, and the relevant fractions were pooled, concentrated, flash frozen in liquid nitrogen, and stored at −80°C.

In vitro farnesylation and cross-linking reactions

Spindly constructs were incubated with RZZ and FTase for 90 min at 25°C in the reaction buffer (50 mM Hepes, pH 8.0, 250 mM NaCl, 10 mM $MgCl_2$, and 2 mM TCEP) containing Fpp, BPP1 pyrophosphate, BPP2 pyrophosphate, or DPP pyrophosphate. Samples were then loaded onto a Superose 6 5/150 column (GE Healthcare) preequilibrated in the reaction buffer. Eluted fractions containing proteins were then either directly analyzed on SDS-PAGE or exposed to UV (60 min for Fpp, BPP1, and BPP2 and 15 min for DPP) before SDS-PAGE and immunoblotting analysis.

SILAC immunoprecipitation experiments

For SILAC, light cells were grown under normal conditions in DMEM without lysine and arginine and supplemented with 10% FCS and 1% penicillin/streptomycin. FCS was dialyzed against a 10-kD cutoff filter to remove possible residual sources of amino acids and ensure efficient labeling. Heavy labeled cells were grown in medium supplemented with $[^{15}N_2]$,$[^{13}C_6]$lysine and $[^{15}N_4]$,$[^{13}C_6]$arginine. To ensure complete incorporation of labeled amino acids into cellular proteins, cells were passaged at least five times in the corresponding medium. To generate mitotic populations for immunoprecipitation experiments, cells were treated with 330 nM nocodazole for 16 h. Mitotic cells were then harvested by shakeoff and lysed by sonication in lysis buffer (150 mM KCl, 75 mM Hepes, pH 7.5, 1.5 mM EGTA, 1.5 mM $MgCl_2$, 10% glycerol, and 0.075% NP-40) or in lysis buffer without detergents (20 mM Hepes-KOH, pH 7.5, 10 mM KCl, 1 mM $MgCl_2$, 1 mM EGTA, and 1 mM EDTA) supplemented with protease inhibitor cocktail and PhosSTOP phosphatase inhibitors (Roche). Extracts were precleared with a mixture of protein A–Sepharose (CL-4B; GE Healthcare) and protein G–Sepharose (rec-Protein G Sepharose 4B; Invitrogen) for 1 h at 4°C and incubated with GFP-trap beads (3 µl/mg of extract; ChromoTek) presenting GFP-RZZ (2 µg) or GFP (in equimolar amounts) for 15 h at 4°C. After three washing steps, the "light" immunoprecipitate of the reference (GFP alone) was mixed with the "heavy" immunoprecipitate of the bait (GFP-RZZ) in a 1:1 ratio (experiment 1; "For"). In a second experiment with swapped labels, the "heavy" immunoprecipitate of the reference (GFP alone) was mixed with the "light" immunoprecipitate of the bait (GFP-RZZ) in a 1:1 ratio (experiment 2; "Rev"). After two more washes, the respectively combined immunoprecipitates were prepared for analysis by liquid chromatography (LC)–MS/MS.

Sample preparation for MS

Samples of in vitro farnesylated Spindly alone or in complex with RZZ before and after UV treatment were adjusted to a final concentration of 6 M urea and treated with 10 mM DTT and 55 mM chloroacetamide to reduce disulfide bridges. Then, urea was lowered to 4 M, and LysC (129-02541; Wako Pure Chemical Industries) was added for 3 h (protein/enzyme ratio, 50:1). After dilution with 2 vol of 50 mM ammonium bicarbonate, pH 8.3, to a final concentration of 2.0 M urea, peptides were digested overnight at 25°C with sequencing-grade modified trypsin (03708985001; Roche) at a protein/enzyme ratio of 50:1. Resulting peptides were desalted on C18 stage tips (Rappsilber et al., 2007). Approximately 100–200 ng of peptides were injected for every MS run. For GFP/GFP-RZZ pull-downs, 8 M urea was directly applied to the beads, and samples were reduced and alkylated.

Bound proteins were then digested in 4 M urea directly from the beads using LysC for 1 h. Subsequently, urea was further diluted to 2 M with 50 mM ammonium bicarbonate, pH 8.3, and proteins bound to the beads were additionally digested with trypsin for 1 h. Supernatants from LysC and trypsin were further digested for 15 h with trypsin. Samples were purified on C18 stage tips, and half of the sample was injected for every MS run.

LC-MS/MS

Peptides were separated on either an UltiMate 3000 Nano LC system or an EASY-nLC 1000 Nano LC System (Thermo Fisher Scientific). Columns (75-µm inner diameter and 25-cm length) were obtained from New Objective (FS36PF7508-250H363). Peptides were loaded in buffer A (double-distilled H_2O and 0.1% formic acid) and separated with a gradient from 5–60% buffer B (100% acetonitrile [ACN] and 0.1% formic acid) within 50 min (in vitro farnesylation) or 120 min (for pull-downs) at 200 nl/min. The column temperature was set to 40°C. A quadrupole Orbitrap mass spectrometer (Q Exactive or Q Exactive HF; Thermo Fisher Scientific; Scheltema et al., 2014) was directly coupled to the LC via a nanoelectrospray source. The Q Exactive machines were operated in the data-dependent mode after choosing, from one survey scan, the most abundant precursors for sequencing. The survey scan range was set from 300 to 1,650 Th, with a resolution of 70,000 at *m/z* 200 for the Q Exactive and 60,000 at *m/z* 200 for the Q Exactive HF. The target value was set to 3×10^6 and maximum injection time to 20 ms. For sequencing, up to 10 (Q Exactive) or up to 15 (Q Exactive HF) of the most abundant isotope patterns with a charge ≥2 were subjected to higher-energy collisional dissociation with a target value of 1e5. Normalized collision energy was set to 25, and an isolation window of 3 Th for the Q Exactive and 1.4 Th for the Q Exactive HF was used. Resolution for higher-energy collisional dissociation spectra was set to 17,500 at *m/z* 200 with a maximum ion injection time of 120 ms on the Q Exactive and 15,000 at *m/z* 200 with maximum ion injection time of 25 ms on the Q Exactive HF. Dynamic exclusion of sequenced peptides was set to 20 s.

Data analysis

To process MS raw files, MaxQuant software (1.5.2.18) was used (Cox and Mann, 2008). We used the Andromeda search engine, which is integrated into MaxQuant, to search MS/MS spectra. For in vitro samples, we searched against a reduced database containing only Spindly and RZZ. Pull-downs were searched against the human UniProt FAS TA database (version January 2015). Enzyme specificity was set to C-terminal lysine and arginine and up to two miscleavages were allowed. Peptides had to have a minimum length of seven amino acids to be considered hits. For in vitro samples, carbamidomethylation of cysteine, deamidation (NQ), and oxidation of methionine were always set as variable modifications. Farnesylation or farnesyl-like modifications containing the UV-active compounds (diazirine pyrophosphate, BPP1, and BPP2) were set as variable modification on cysteine according to the experiment. To identify UV-induced cross-links between Spindly and RZZ, the mass of the C-terminal peptide of Spindly containing the farnesyl-modified cysteine plus the mass of the different UV-active compounds were given as variable modifications for the database search. In addition, the y3 ion fragment (PQQ; 372.1878 Th) of Spindly was used as diagnostic marker to identify possible cross-links with RZZ subunits. Because the compounds react in a sequence-independent manner with the backbone of amino acids, searches for every amino acid were performed individually to avoid an exponential increase of the database. MS and MS/MS spectra of possible cross-links were carefully inspected manually, and precursors were required to have a charge state of >2. For pull-down experiments, carbamidomethylation of Cys was given as fixed modification. Deamidation (NQ), oxidation of Met, and N-terminal acetylation of proteins were given as variable modifications. A false discovery rate cutoff of 1% was applied at the peptide, protein levels, and the modified site fraction. An initial precursor mass deviation of up to 4.5 ppm and a fragment mass deviation up to 20 ppm were allowed. Precursor ion mass accuracy was improved by time-dependent recalibration algorithms in MaxQuant.

Negative-stain EM

4 µl of the sample was adsorbed for 1 min at 25°C onto freshly glow-discharged carbon-coated grids (G2400C; Agar Scientific). The sample was blotted (no. 4; Whatman), and the grids were subsequently washed with the SEC buffer (respective buffers in which each of the samples was prepared otherwise; Bröcker et al., 2012). All the images for negatively stained specimens were collected on an electron microscope (JEM1400; JEOL) equipped with a LaB6 cathode operated at 120 kV. All the images were collected under low-dose conditions (19 e/Å2) at a magnification of 67,200× on a 4,000 × 4,000 camera (F416; TVIPS).

Image processing of negative stained samples

All micrographs were recorded with a pixel size of 2.32 Å/pixel, unless stated otherwise. Particles were manually selected, aligned, and classified using reference-free alignment and K-means classification procedures implemented in SPARX (Hohn et al., 2007) and EMAN2 (Ludtke, 2010). For the ZW10 dataset, we used the iterative stable alignment and clustering (ISAC) procedure implemented in SPARX, as the K-means classification procedure failed to give well-defined 2D averages (Yang et al., 2012).

For the 3D reconstructions of the RZZ and the miniRZZ complexes, tilt pairs were collected at tilt angles of 55° and 0°, and particle pairs were selected respectively using the e2RCTboxer program in EMAN2. Random conical tilt reconstructions of the tilted particles were calculated from the respective best class average by back projection followed by back projection refinement (Radermacher et al., 1987). The resulting reconstructions were then submitted to several rounds of 3D multireference projection matching against the untilted datasets, respectively, using SPARX. The resolution of the final reconstructions was estimated by the Fourier shell correlation (FSC) criterion of 0.5. Table 1 lists the number of particles and other parameters for the various datasets.

Fitting of homology models in EM densities

Homology models of ROD, ZW10, and the crystallographic structure of Zwilch (PDB ID: 3IF8) were automatically fitted in the density using UCSF Chimera Fit in Map tool. Individual rigid-body fittings were performed using the systematic global search option starting from 10,000 random initial placements of a simulated 10.5-Å map of the proteins within the EM map. The cross-correlation score between the simulated map and the EM map was used as a fitting metric. For each of the placements, local optimization was performed. The best-fitting structures had the best cross-correlation (Table S2) and upon visual examination showed excellent correspondence between the fitted model and the EM map.

Sample preparation for cryo-EM

Holey carbon grids (Quantifoils R2/1; Protochips) were freshly glow discharged (two times on the darker side and once on the lighter side of the grid), and 4 µl of the RZZ was applied. 0.02% (wt/vol) Triton was added to the sample just before its application onto the grid. After 30 s, the sample was manually blotted (no. 4; Whatman) followed by application of another 1.7 µl of the sample that was vitrified by plunging (1-s blotting) into liquid ethane using a Cryoplunge3 (Cp3; Gatan). The humidity was maintained to be ∼90%.

Image processing of the cryo-EM dataset

For optimizing the best conditions, images were collected on an electron microscope (3200FSC; JEOL) equipped with a field-emission gun at an operation voltage of 200 kV and an underfocus range of 1.5–3.5 µm. The omega in-column energy filter of the microscope was used to estimate the best ice conditions (~40–60 nm thickness). A test dataset was collected where the images were recorded manually on an 8,000 × 8,000 CMOS camera (F816; TVIPS) at a pixel size of 1.25 Å/pixel using minimal dose conditions (~20 e^- $Å^{-2}$).

The final dataset was collected on a spherical aberration–corrected transmission electron microscope (Titan Krios; FEI) equipped with an extra-high brightness field emission gun and operated at a voltage of 300 kV at the Netherlands Centre for Electron Nanoscopy (NeCEN), Leiden, Netherlands. Images were recorded on a back-thinned 4,000 × 4,000 direct detection camera (FalconII) under minimal dose conditions using the automatic data collection software EPU (FEI). The images were recorded at a magnification of 122,807×, corresponding to a pixel size of 1.14 Å. We collected seven consecutive frames during each exposure corresponding to a dose of 2.1 e^- $Å^2$ per frame. The frames were collected from 85–475 ms of exposure. A final integrated 1-s image with a total dose of ~38.2 e^- $Å^{-2}$ was also recorded. A total number of 7,575 images with a defocus range of 1.5–3.0 µm were acquired automatically using the EPU software. The frames of the micrographs collected with the Falcon II detector were aligned to each other using the program MotionCorr to reduce beam-induced blurring of the images (Li et al., 2013). All seven frames were used for processing of the data. The defocus of the micrographs was determined using both CTFFIND4 and "sxcter" program (SPARX; Hohn et al., 2007). We excluded micrographs whose relative defocus error and astigmatism angular error as estimated by sxcter was larger than the defocus and astigmatism error percentage. The error is computed as (SD defocus)/defocus*100%. 49,718 particles were manually handpicked using e2boxer. Particle alignment, classification, and 3D reconstruction were performed in SPARX. The dataset was extensively cleaned up by 2D alignment and classification procedure. In brief, the electron density map from the negative-stain reconstruction was low-pass filtered to 70 Å and used as a starting reference. C2 symmetry was applied during refinement. Refinement of orientation parameters and reconstruction was performed where an FSC-based filter was applied to each volume (Scheres and Chen, 2012). The final reconstruction was calculated from 11,666 particles to a mean resolution of 10.4 Å (FSC0.5 Criterion).

Visualization and analysis of EM density

For analysis, visualization, and segmentation of densities, the program Chimera (Pettersen et al., 2004) was used.

Immunoblotting

Samples were diluted in Laemmli sample buffer, boiled at 95°C, resolved on SDS-PAGE with NuPAGE Bis-Tris 4–12% gradient gels (Invitrogen), and transferred onto nitrocellulose membranes (GE Healthcare). The following primary antibodies were used: anti-ROD (mouse monoclonal; clone CB22-1; 1:500), anti-Zwilch (mouse monoclonal; clone CE47-3; 1:500), anti-ZW10 (mouse monoclonal; clone CO-45-2; 1:500), and anti-Spindly (rabbit polyclonal; A301-354A; 1:5,000; Bethyl Laboratories, Inc.). Mice immunized with recombinant full-length RZZ complex were used to generate anti-ROD, anti-ZW10, and anti-Zwilch antibodies. Antibodies were then affinity purified from sera by using immobilized antigens. Antibody productions, purifications, and biochemistry were performed at the Istituto FIRC di Oncologia Molecolare–Instituto Europeo de Oncologia (IFOM-IEO) Campus Biochemistry Unit. Secondary antibodies were anti–mouse and anti–rabbit (working dilutions, 1:10,000; GE Healthcare). After incubation with the ECL Western blotting system (GE Healthcare), images were acquired with the ChemiDoc MP Imaging System (Bio-Rad Laboratories) in 8-bit Tiff format.

AUC

Sedimentation velocity experiments were performed in an analytical ultracentrifuge (Optima XL-A) with epon charcoal-filled double-sector quartz cells and an An-60 Ti rotor (Beckman Coulter). Samples were centrifuged at 203,000 *g* at 20°C, and 500 radial absorbance scans were collected with a time interval of 1 min. Data were analyzed using the SEDFIT software (Brown and Schuck, 2006) in terms of continuous distribution function of sedimentation coefficients (c(S)). The protein partial specific volume was estimated from the amino acid sequence using the program SEDNTERP. Data were plotted using the program GUSSI comprised in the SEDFIT software (Brown and Schuck, 2006). Analysis of Spindly constructs bound to RZZ was performed at 20°C in 50 mM Hepes, pH 8, 250 mM NaCl, and 2 mM TCEP, leading to values of buffer density of 1.01306 g/ml and viscosity of 1.002 cP (centipoise). The values of the partial specific volume of mCherry–Spindly–RZZ and Spindly–RZZ are 0.74268 and 0.74335 ml/g at 20°C, respectively (assuming 1:1 stoichiometry).

Expression and purification of $ROD^{1–1,250}ZZ$ and $ROD^{\Delta754–1,796}$

The expression and purification of $ROD^{1–1,250}ZZ$ was performed almost identically to the RZZ complex by coexpression from individual viruses. Purification was performed within 1 d to limit the effects of reduced stability of the complex. Elution from the NiNTA column was performed by step elution using 250 mM imidazole, and no ion exchange chromatography was performed. To build $ROD^{\Delta754–1,796}$, we fused ROD segments 1–753 and 1,797–2,209 with a $(GGSG)_4$ linker ($ROD^{1–753\text{-}(GGSG)4\text{-}1,797–2,209}$) and subcloned it in the His6-POPIN vector. To assemble a complex with Zwilch, we coinfected TnaO38 cells. Further coinfection with virus for expression of ZW10 did not lead to incorporation of ZW10 in the complex with ROD–Zwilch, indicative of a lack of interaction. For a 500-ml expression culture, cell lysis was performed in 100 ml lysis buffer (50 mM Hepes, pH 8.5, 200 mM

Table 1. **Number of particles and other parameters for the various datasets**

Dataset	Particles	Defocus	Other details
		µm	
RZZ	4,000	−1.5	
RZZ (tilt-pairs, RCT)	1,700	−1.8 and −1.5	Tilted and untilted images were recorded at 55° and 0°, with a nominal negative defocus of 1.8 and 1.5, respectively.
ZW10	10,111	−1.5	
$R^{1–1,250}ZZ$	3,424	−1.5	
$R^{1–1,250}ZZ$ (tilt-pairs, RCT)	1,200	−1.8 and −1.5	Tilted and untilted images were recorded at 55° and 0°, with a nominal negative defocus of 1.8 and 1.5, respectively.

NaCl, 10% glycerol, 20 mM imidazole, 5 mM βMe, 1 mM PMSF, and 1 mM protease inhibitor cocktail) by sonication. The cleared cell lysate was loaded on a HisTrap Fast Flow column previously equilibrated with wash buffer (50 mM Hepes, pH 8.5, 200 mM NaCl, 10% glycerol, 20 mM imidazole, and 5 mM βMe) using a peristaltic pump at 4°C and a flow rate of 2 ml/min, and the column was washed with 500 ml of wash buffer. Elution was performed with 250 mM imidazole added to wash buffer and collecting 1.5-ml fractions. The fractions were analyzed by SDS-PAGE, and those containing $ROD^{\Delta 754–1,796}$–Zwilch were concentrated up to 500 µl and applied to a Superose 6 10/300 column using SEC buffer (25 mM Hepes, pH 8.5, 250 mM NaCl, and 4 mM TCEP). Peak fractions were analyzed by SDS-PAGE, and those containing pure $ROD^{\Delta 754–1,796}$–Zwilch were concentrated up to 5 mg/ml and flash frozen in liquid nitrogen in aliquots of 20 µl and stored at −80°C.

Chemical cross-linking and MS of the RZZ–Spindly complex

Cross-linking of the RZZ–(farnesyl)Spindly complex was performed by mixing 60 µg of the complex (at 0.3 mg/ml) with 450 µM of an equimolar mixture of isotopically light (d_0) and heavy (d_6) labeled disuccinimidyl suberate (Creative Molecules) for 30 min at 37°C or at 4°C for 15 h. The reactions were quenched by adding a final concentration of 100 mM ammonium bicarbonate for 20 min at 37°C. Cross-linked proteins were enzymatically digested, and cross-linked peptides were identified by LC coupled to MS/MS as reported previously (Herzog et al., 2012). In brief, cross-linked proteins were denatured by adding two sample volumes of 8 M urea (Sigma Aldrich) and were reduced by incubating with 5 mM TCEP (Thermo Fisher Scientific) at 35°C for 15 min. Proteins were alkylated with 10 mM iodoacetamide (Sigma Aldrich) for 35 min at room temperature in the dark. Samples were proteolytically digested by incubating with lysyl endopeptidase (1:50, wt/wt; Wako Pure Chemical Industries) for 2 h at 35°C followed by adding trypsin (1:50, wt/wt; Promega) overnight at a final concentration of 1 M urea. Proteolysis was stopped by the addition of 1% (vol/vol) trifluoroacetic acid (Sigma Aldrich). Acidified peptides were purified by reversed-phase chromatography on C18 columns (Sep-Pak; Waters). Eluates were dried and reconstituted in 20 µl of mobile phase (water/ACN/trifluoroacetic acid, 75:25:0.1), and cross-linked peptides were enriched on a Superdex Peptide PC 3.2/30 column (GE Healthcare) at a flow rate of 50 µl/min. Fractions of the cross-linked peptides were analyzed by LC-MS/MS using an LTQ Orbitrap Elite (Thermo Fisher Scientific) instrument. Finally, the cross-link fragment ion spectra were searched, and the peptides were identified by the open source software xQuest (Walzthoeni et al., 2012). False discovery rates were calculated using xProphet, and results were filtered using the following parameters: delta score <0.85, MS1 tolerance window of −4 to 4 ppm and score >22.

Synthesis of photoactivatable compounds

All commercially available compounds were used as provided without further purifications. Chemicals and solvents were purchased from the companies Acros Organics, Alfa Aesar, Sigma-Aldrich, TCI Europe, and Thermo Fisher Scientific. Dry solvents (e.g., tetrahydrofuran [THF] and ACN) were used without further purifications. Dichloromethane was freshly distilled over calcium hydroxide. Analytical thin-layer chromatography was performed on silica gel aluminum plates (Merck) with F254 indicator (Sigma-Aldrich). Compounds were visualized by irradiation with UV light or potassium permanganate staining. Column chromatography was performed using silica gel Acros 60 A. [^{1}H]NMR, [^{13}C]NMR, and [^{31}P]NMR were measured on a DRX-400 (400 MHz), DRW-500 (500 MHz; Bruker), or INOVA 600 (600 MHz; Agilent Technologies) using $CDCl_3$ or 25 mM ND_4OD as solvent and internal standard. The high-resolution mass spectra were recorded on an LTQ Orbitrap mass spectrometer. The preparative HPLC purifications were performed on an Agilent HPLC (1100 series; Agilent Technologies) using a reversed-phase C4 column (NUCLEODUR C4). Method: flowrate 6.0 ml/min from 10% to 100% ACN over 25 min, with 25 mM NH_4OH water as cosolvent.

Synthesis of the photoactivatable probes

Synthesis of 8-hydroxy-geranyl-*t*-butyldimethylsilylether (1). 8-Hydroxy-geranyl-*t*-butyldimethylsilylether 1 was synthesized according to a previous study (Alexander et al., 2009). See Fig. S5 A.

Synthesis of 8-(4-benzoylphenyloxy)-geraniol (2). 8-(4-Benzoylphenyloxy)-geraniol 2 was synthesized according to a previous study (Alexander et al., 2009). See Fig. S5 B.

Synthesis of 8-(4-benzoylphenyloxy)-geranyl-1-diphosphate (3). The compound 2 (104 mg and 0.3 mmol) and PPh_3 (polymer-supported beads; 503.5 mg and 0.86 mmol) were dissolved in CH_2Cl_2 (5 ml) and stirred for 30 min to allow the beads to swell. Afterward, a solution of tetrabromomethane (170.3 mg and 0.5 mmol, in 2 ml CH_2Cl_2) was added, and the mixture was stirred overnight at room temperature. After filtration of the beads, the crude product was extracted with ethyl acetate. The organic phases were combined, and the solvent was removed under reduced pressure. Because of the instability of the allylic bromide, it was directly used without any purification step. See Fig. S5 C.

Therefore, the bromide was dissolved in 6 ml ACN, and $(n\text{-}Bu_4N)_3HP_2O_5$ (714 mg and 0.79 mmol) was added slowly. The reaction was allowed to stir for 3 h, and then the solvent was removed under reduced pressure. An ion-exchange column (AG 50W-X8; Bio-Rad Laboratories) was used to convert the product to its ammonium form. The resin was packed and washed using 3 column volumes of 25 vol% NH_3 in water, followed by an equilibration step with 3 column volumes of 2 vol% propanol in aqueous 25 mM NH_4HCO_3 solution. The dark red residue was dissolved in a minimal volume of solvent and loaded on the column. 3 column volumes of the equilibration solution were applied to the column to convert the product in its ammonium form. Fractions containing the product were combined and lyophilized to dryness. The resulting white powder was purified using preparative HPLC.

Yield: 17%.

[^{1}H]NMR: (600 MHz and 25 mM ND_4OD): δ = 7.85–7.82 (m, 2H), 7.78–7.75 (m, 2H), 7.67–7.62 (m, 2H), 7.13 (m, 2H), 5.69 (t, J = 7.0 Hz, 1H), 5.55 (t, J = 6.5 Hz, 1H), 4.63 (s, 2H), 4.56 (t, J = 6.5 Hz, 2H), 2.30 (t, J = 7.3 Hz, 2H), 2.19 (t, J = 7.6 Hz, 2H), and 1.80 (s, 6H).

[^{13}C]NMR: (150 MHz and 25 mM ND_4OD): δ = 199.51, 162.81, 142.15, 137.36, 133.16, 133.09, 130.67, 130.01, 129.94, 129.42, 128.58, 120.35, 120.29, 114.98, 114.92, 74.31, 62.44, 62.41, 38.35, 25.57, 22.74, 15.74, and 13.15.

[^{31}P]NMR: (243 MHz and 25 mM ND_4OD): δ = −6.33 (d, J = 22.2 Hz) and −10.32 (d, J = 22.2 Hz).

HRMS: calculated exact mass for $C_{23}H_{29}O_9P_2$ m/z 511.1281 [M + H]$^+$; found m/z 511.1288 [M + H]$^+$.

Synthesis of 8-(3-(methyl)-benzophenone)-geranyl-*t*-butyldimethylsilylether (4). The alcohol 1 (300 mg and 1.1 mmol) was slowly added under ice cooling to a solution of NaH (84.3 mg and 2.1 mmol) in THF (15 ml). The mixture was stirred for 30 min under ice cooling before 3-(bromomethyl) benzophenone (580.2 mg and 2.1 mmol) was slowly added. After 2 h at 40°C, the mixture was brought to room temperature and quenched with water (30 ml). The solution was extracted three times with diethyl ether (each 30 ml). Afterward, the combined organic phases were dried over $MgSO_4$. The solvent was removed under reduced pressure and purified using flash chromatography on silica gel (cyclohexane/ethyl acetate). See Fig. S5 D.

Yield: 88%.

R_f: 0.16 (5:1, cyclohexane/ethyl acetate [vol/vol]).

[^{1}H]NMR: (400 MHz and $CDCl_3$): δ = 7.82–7.76 (m, 4H), 7.63–7.55 (m, 1H), 7.53–7.43 (m, 4H), 5.50–5.40 (m, 1H), 5.36–5.26 (m, 1H), 4.53 (d, *J* = 6.6 Hz, 2H), 4.19 (d, *J* = 6.3 Hz, 2H), 3.94 (s, 2H), 2.25–2.01 (m, 4H), 1.70 (s, 3H), 1.64 (s, 3H), 0.90 (s, 9H), and 0.07 (s, 6H).

Synthesis of 8-(3-(methyl)-benzophenone)-geraniol (5). The silylether 4 (517 mg and 1.08 mmol) was dissolved in 5 ml THF. Tetrabutylammoniumfluoride (1.296 ml and 1.3 mmol, 1 M in THF) was added dropwise over 30 min under ice cooling. After 4 h at room temperature, the solution was quenched with brine (20 ml), and the crude product was extracted with diethyl ether (30 ml). The pooled organic phases were dried over $MgSO_4$, and the solvent was removed under reduced pressure. The product was purified using flash chromatography on silica gel (cyclohexane/ethyl acetate). See Fig S5 E.

Yield: 95%.

R_f: 0.18 (2:1, cyclohexane/ethyl acetate [vol/vol]).

[^{1}H]NMR: (500 MHz and $CDCl_3$): δ = 7.82–7.77 (m, 4H), 7.61–7.57 (m, 1H), 7.51–7.43 (m, 4H), 5.45–5.40 (m, 2H), 4.80 (s, 1H), 4.53 (s, 2H), 4.15 (d, *J* = 6.9 Hz, 2H), 3.94 (s, 2H), 2.24–2.06 (m, 4H), 1.70 (s, 3H), and 1.69 (s, 3H).

[^{13}C]NMR: (125 MHz and $CDCl_3$): δ = 196.61, 143.63, 139.30, 137.85, 136.86, 132.49, 132.37, 130.54, 130.38, 130.15, 128.42, 128.40, 128.28, 127.33, 126.54, 123.90, 76.77, 71.00, 59.51, 39.20, 26.09, 16.39, and 14.14.

HRMS: calculated exact mass for $C_{24}H_{29}O_3$ *m/z* 365.2111 (M + H)$^+$; found *m/z* 365.2119 (M + H)$^+$.

Synthesis of 8-(3-(methyl)-benzophenone)-geranyl-1-diphosphate (6). The compound 5 (150 mg and 0.41 mmol) and PPh_3 (polymer-supported beads; 484 mg and 0.82 mmol) were dissolved in CH_2Cl_2 (5 ml) and stirred for 30 min to allow the beads to swell. A solution of tetrabromomethane (164 mg and 0.5 mmol in 2 ml CH_2Cl_2) was added, and the mixture was allowed to stir overnight at room temperature. After filtration of the beads, the crude product was extracted three times with ethyl acetate (each 20 ml). The organic phases were combined and the solvent was removed under reduced pressure. Because of the instability of the allylic bromide, it was directly used without any purification step. See Fig S5 F.

The bromide was dissolved in 6 ml ACN, and then (n-Bu_4N)$_3HP_2O_5$ (680.73 mg and 0.75 mmol) was added slowly. The reaction was allowed to stir for 3 h, and afterward the solvent was removed under reduced pressure. An ion-exchange column (AG 50W-X8; Bio-Rad Laboratories) was used to convert the product to its ammonium form. The resin was packed and washed using 3 column volumes of 25 vol% NH_3, followed by an equilibration step with 3 column volumes of 2 vol% propanol in aqueous 25 mM NH_4HCO_3. The dark red residue was solved in a minimal volume of solvent and loaded on the column. 3 column volumes of equilibration solvent were applied to the column to convert the product in its ammonium form. Fractions containing the product were pooled and lyophilized to dryness. The resulting white powder was purified using preparative HPLC.

Yield: 32%.

[^{1}H]NMR: (600 MHz and 25 mM ND_4OD): δ = 7.93–7.88 (m, 4H), 7.85–7.80 (m, 1H), 7.71–7.62 (m, 4H), 5.62 (t, *J* = 6.7 Hz, 1H), 5.58 (t, *J* = 6.7 Hz, 1H), 4.69 (s, 2H), 4.59–4.54 (m, 2H), 4.11 (s, 2H), 2.32 (t, *J* = 7.1 Hz, 2H), 2.22 (t, *J* = 7.4 Hz, 2H), 1.82 (s, 3H), and 1.78 (s, 3H).

[^{13}C]NMR: (150 MHz and 25 mM ND_4OD): δ = 200.67, 143.53, 142.27, 136.92, 136.36, 133.59, 131.72, 130.72, 130.34, 130.27, 128.65, 128.25, 120.34, 120.28, 76.57, 70.37, 62.39, 38.41, 25.55, 15.66, and 13.31.

[^{31}P]NMR: (243 MHz and 25 mM ND_4OD): δ = −6.35 (d, *J* = 22.3 Hz) and −10.38 (d, *J* = 22.4 Hz).

HRMS: calculated exact mass for $C_{24}H_{31}O_9P_2$ *m/z* 525.1438 (M + H)$^+$; found *m/z* 525.1446 (M + H)$^+$. Calculated exact mass for $C_{24}H_{30}O_9NaP_2$ *m/z* 547.1257 (M + Na)$^+$; found *m/z* 547.1265 (M + Na)$^+$.

Synthesis of 8-(3-trifluoromethyl-3-phenyl-diazirine)-geranyl-*t*-butyldimethylsilylether (7). The alcohol 1 (300 mg and 1.05 mmol) was slowly added under ice cooling to a solution of NaH (51 mg and 2.1 mmol) in THF (7.5 ml). The mixture was stirred for 30 min under ice cooling before the 4-(3-(trifluoromethyl)-3H-diazirin-3-yl)benzyl bromide (589 mg and 2.1 mmol) was slowly added. After 4 h at room temperature, the mixture was brought to room temperature and quenched with water. The solution was extracted three times with diethyl ether (each 20 ml), and the combined organic phases were dried over $MgSO_4$. The solvent was removed under reduced pressure and purified using flash chromatography on silica gel (cyclohexane/ethyl acetate). See Fig. S5 G.

Yield: 81%.

R_f: 0.20 (10:1, cyclohexane/ethyl acetate).

[^{1}H]NMR: (500 MHz and $CDCl_3$): δ = 7.37 (d, *J* = 8.7 Hz, 2H), 7.17 (d, *J* = 7.9 Hz, 2H), 5.40 (d, *J* = 7.0 Hz, 1H), 5.34–5.29 (m, 1H), 4.44 (s, 2H), 4.19 (dd, *J* = 6.3, 0.8 Hz, 2H), 3.88 (s, 2H), 2.22–2.14 (m, 2H), 2.08–2.02 (m, 2H), 1.67 (s, 3H), 1.63 (s, 3H), 0.90 (s, 9H), and 0.06 (s, 6H).

HRMS: calculated exact mass for $C_{25}H_{38}F_3N_2O_2Si$ *m/z* 483.2655 (M + H)$^+$; found *m/z* 483.2649 (M + H)$^+$.

Synthesis of 8-(3-Trifluoromethyl-3-phenyl-diazirine)-geraniol (8). The silylether 7 (320 mg and 0.66 mmol) was dissolved in 6 ml THF. Tetrabutylammoniumfluoride (796 µl and 0.8 mmol, 1 M in THF) was added dropwise over 30 min under ice cooling. After 4 h at room temperature, the solution was quenched with brine (20 ml), and the crude product was extracted with diethyl ether (30 ml). The combined organic phases were dried over $MgSO_4$, and the solvent was removed under reduced pressure. The product was purified using flash chromatography on silica gel (cyclohexane/ethyl acetate). See Fig. S5 H.

Yield: 91%.

R_f: 0.67 (2:1, cyclohexane/ethyl acetate).

[^{1}H]NMR: (500 MHz and $CDCl_3$): δ = 7.37 (d, *J* = 8.5 Hz, 2H), 7.17 (d, *J* = 7.8 Hz, 2H), 5.41 (d, *J* = 7.3 Hz, 2H), 4.44 (s, 2H), 4.15 (d, *J* = 6.7 Hz, 2H), 3.88 (s, 2H), 2.24–2.15 (m, 2H), 2.11–2.04 (m, 2H), 1.68 (d, *J* = 6.9 Hz, 3H), and 1.67 (s, 3H).

HRMS: calculated exact mass for $C_{19}H_{22}F_3N_2O_1$ *m/z* 351.1679 ([M − H_2O] + H)$^+$; found *m/z* 351.1679 ([M − H_2O] + H)$^+$.

Synthesis of 8-(3-trifluoromethyl-3-phenyl-diazirine)-geranyl-1-diphosphate (9). The compound 8 (50 mg and 0.14 mmol) and PPh_3 (polymer-supported beads; 159.68 mg and 0.27 mmol) were dissolved in CH_2Cl_2 (5 ml) and stirred for 30 min to allow the beads to swell. A solution of tetrabromomethane (57 mg and 0.16 mmol in 2 ml CH_2Cl_2) was added, and the mixture was stirred overnight at room temperature. After filtration of the beads, the crude product was extracted with ethyl acetate. The organic phases were combined, and the solvent was removed under reduced pressure. Because of the instability of the allylic bromide, it was directly used without any purification step. See Fig. S5 I.

The bromide was dissolved in 6 ml ACN, and (n-Bu_4N)$_3HP_2O_5$ (332 mg and 0.37 mmol) was added slowly. The reaction was allowed to stir for 3 h, and afterward, the solvent was removed under reduced pressure. An ion-exchange column (AG 50W-X8; Bio-Rad Laboratories) was used to convert the product to its ammonium form. The resin was packed and washed using 3 column volumes of 25 vol% NH_3, followed by an equilibration step with 3 column volumes of 2 vol% propanol in aqueous 25 mM NH_4HCO_3 solution. The dark red residue was solved in a minimal volume of solvent and loaded on the column. 3 column volumes of equilibration solvent were applied to the column

to convert the product in its ammonium form. Fractions containing the product were pooled and lyophilized to dryness. The resulting white powder was purified using preparative HPLC.

Yield: 14%.

[^{1}H]NMR: (600 MHz and 25 mM ND_4OD): δ = 7.54 (s, 2H), 7.39 (s, 2H), 5.56 (s, 2H), 4.57 (s, 2H), 4.53 (s, 2H), 4.04 (s, 2H), 2.34–2.18 (m, 4H), 1.79 (s, 3H), and 1.73 (s, 3H).

[^{13}C]NMR: (150 MHz and 25 mM ND_4OD): δ = 167.02, 165.70, 142.31, 139.57, 131.64, 130.21, 128.94, 128.31, 126.75, 120.25, 76.31, 70.18, 64.25, 62.41, 38.40, 25.52, 23.78, 15.67, and 13.28.

[^{31}P]NMR: (243 MHz and 25 mM ND_4OD): δ = −6.37 (d, J = 21.9 Hz) and −10.37 (d, J = 22.3 Hz).

HRMS: calculated exact mass for $C_{24}H_{31}O_9P_2$ m/z 525.1438 $(M + H)^+$; found m/z 525.1446 $(M + H)^+$. Calculated exact mass for $C_{19}H_{26}O_8N_2F_3P_2$ m/z 529.1111 $(M + H)^+$; found m/z 529.11155 $(M + H)^+$.

Online supplemental material

Fig. S1 shows additional EM data and analyses of the RZZ and RZZ–Spindly complexes as well as sedimentation velocity absorbance profiles associated with experiments shown in Figs. 1 and 6. Fig. S2 shows additional EM and biochemical analyses of different RZZ deletion mutants and SEC analyses of RZZ intersubunit interactions. Fig. S3 shows MS/MS spectra demonstrating incorporation of UV photoactivatable cross-linker farnesyl derivatives on Cys602 as well as MS/MS spectra of their adducts with ROD. Fig. S4 shows additional biochemical and MS analyses of the UV cross-linking experiments. Fig. S5 displays sequences from the Synthesis of the photoactivatable probes section of Materials and methods. Video 1 demonstrates the considerable flexibility of the RZZ complex. Video 2 illustrates the fitting of molecular model into the EM density of the RZZ complex. Table S1 summarizes the strategy to create molecular models of the RZZ subunits. Table S2 summarizes the quality of model fitting experiments. Table S3 summarizes results with bifunctional cross-linkers and MS. Table S4 displays the multiple alignment using fast Fourier transform (MAFFT) of the indicated BicD2 and Spindly sequences.

Acknowledgments

We thank Marta Mattiuzzo and Anna De Antoni for sharing unpublished reagents, and we thank members of our laboratories for helpful discussions.

J. Keller acknowledges support by the European Molecular Biology Organization long-term fellowship ALTF 331-2010. A. Wehenkel acknowledges support by the European Molecular Biology Organization long-term fellowship ALTF 662-2008 and Marie Curie Intra-European Fellowship. A. Musacchio acknowledges funding by the European Research Council Advanced Grant RECEPIANCE (grant 669686) and the Deutsche Forschungsgemeinschaft Collaborative Research Centre (CRC) 1093. F. Herzog is supported by the European Research Council StG MolStruKT (grant 638218) and by the Deutsche Forschungsgemeinschaft (grant GRK1721). S. Raunser gratefully acknowledges the Max Planck Society and the European Council under the European Union's Seventh Framework Programme (FP7/2007–2013; grant 615984).

The authors declare no competing financial interests.

Author contributions: S. Mosalaganti collected EM data and performed EM computational work, and M. Saur additionally contributed to this part of the work. P. Rombaut and F. Herzog performed XL-MS experiments and data analysis. A. Altenfeld, J. Keller, A. Wehenkel, and S. Wohlgemuth expressed and purified RZZ variants and/or Spindly for various experiments and set up the FFase binding assay. A. Petrovic and J. Keller performed and analyzed AUC experiments. M. Winzker synthesized the photoactivatable farnesyl derivatives under supervision of H. Waldmann; J. Keller and S. Wohlgemuth performed UV cross-linking assays with photoactivatable farnesyl derivatives. F. Müller and T. Bange performed MS/MS experiments to identify UV-activated cross-links. S. Maffini carried out RZZ microinjection experiments. J. Keller carried out all the modeling of the RZZ structure. A. Musacchio, S. Raunser, S. Mosalaganti, A. Altenfeld, and J. Keller designed the majority of experiments. S. Raunser coordinated the EM work and wrote sections of the manuscript. A. Musacchio coordinated the team and wrote most of the manuscript.

Submitted: 10 November 2016
Revised: 20 December 2016
Accepted: 23 January 2017

References

Alexander, M., M. Gerauer, M. Pechlivanis, B. Popkirova, R. Dvorsky, L. Brunsveld, H. Waldmann, and J. Kuhlmann. 2009. Mapping the isoprenoid binding pocket of PDEδ by a semisynthetic, photoactivatable N-Ras lipoprotein. *ChemBioChem.* 10:98–108. http://dx.doi.org/10.1002/cbic.200800275

Altenfeld, A., S. Wohlgemuth, A. Wehenkel, I.R. Vetter, and A. Musacchio. 2015. Complex assembly, crystallization and preliminary X-ray crystallographic analysis of the human Rod-Zwilch-ZW10 (RZZ) complex. *Acta Crystallogr. F Struct. Biol. Commun.* 71:438–442. http://dx.doi.org/10.1107/S2053230X15004343

Ashar, H.R., L. James, K. Gray, D. Carr, S. Black, L. Armstrong, W.R. Bishop, and P. Kirschmeier. 2000. Farnesyl transferase inhibitors block the farnesylation of CENP-E and CENP-F and alter the association of CENP-E with the microtubules. *J. Biol. Chem.* 275:30451–30457. http://dx.doi.org/10.1074/jbc.M003469200

Barisic, M., B. Sohm, P. Mikolcevic, C. Wandke, V. Rauch, T. Ringer, M. Hess, G. Bonn, and S. Geley. 2010. Spindly/CCDC99 is required for efficient chromosome congression and mitotic checkpoint regulation. *Mol. Biol. Cell.* 21:1968–1981. http://dx.doi.org/10.1091/mbc.E09-04-0356

Basto, R., R. Gomes, and R.E. Karess. 2000. Rough deal and Zw10 are required for the metaphase checkpoint in *Drosophila*. *Nat. Cell Biol.* 2:939–943. http://dx.doi.org/10.1038/35046592

Basto, R., F. Scaerou, S. Mische, E. Wojcik, C. Lefebvre, R. Gomes, T. Hays, and R. Karess. 2004. In vivo dynamics of the rough deal checkpoint protein during *Drosophila* mitosis. *Curr. Biol.* 14:56–61. http://dx.doi.org/10.1016/j.cub.2003.12.025

Bröcker, C., A. Kuhlee, C. Gatsogiannis, H.J. Balderhaar, C. Hönscher, S. Engelbrecht-Vandré, C. Ungermann, and S. Raunser. 2012. Molecular architecture of the multisubunit homotypic fusion and vacuole protein sorting (HOPS) tethering complex. *Proc. Natl. Acad. Sci. USA.* 109:1991–1996. http://dx.doi.org/10.1073/pnas.1117797109

Brohawn, S.G., N.C. Leksa, E.D. Spear, K.R. Rajashankar, and T.U. Schwartz. 2008. Structural evidence for common ancestry of the nuclear pore complex and vesicle coats. *Science.* 322:1369–1373. http://dx.doi.org/10.1126/science.1165886

Brown, P.H., and P. Schuck. 2006. Macromolecular size-and-shape distributions by sedimentation velocity analytical ultracentrifugation. *Biophys. J.* 90:4651–4661. http://dx.doi.org/10.1529/biophysj.106.081372

Buffin, E., C. Lefebvre, J. Huang, M.E. Gagou, and R.E. Karess. 2005. Recruitment of Mad2 to the kinetochore requires the Rod/Zw10 complex. *Curr. Biol.* 15:856–861. http://dx.doi.org/10.1016/j.cub.2005.03.052

Caldas, G.V., T.R. Lynch, R. Anderson, S. Afreen, D. Varma, and J.G. DeLuca. 2015. The RZZ complex requires the N-terminus of KNL1 to mediate optimal Mad1 kinetochore localization in human cells. *Open Biol.* 5:150160. http://dx.doi.org/10.1098/rsob.150160

Carter, A.P., A.G. Diamant, and L. Urnavicius. 2016. How dynein and dynactin transport cargos: a structural perspective. *Curr. Opin. Struct. Biol.* 37:62–70. http://dx.doi.org/10.1016/j.sbi.2015.12.003

Chan, Y.W., L.L. Fava, A. Uldschmid, M.H. Schmitz, D.W. Gerlich, E.A. Nigg, and A. Santamaria. 2009. Mitotic control of kinetochore-associated dynein and spindle orientation by human Spindly. *J. Cell Biol.* 185:859–874. http://dx.doi.org/10.1083/jcb.200812167

Cheerambathur, D.K., R. Gassmann, B. Cook, K. Oegema, and A. Desai. 2013. Crosstalk between microtubule attachment complexes ensures accurate chromosome segregation. *Science.* 342:1239–1242. http://dx.doi.org/10.1126/science.1246232

Chowdhury, S., S.A. Ketcham, T.A. Schroer, and G.C. Lander. 2015. Structural organization of the dynein-dynactin complex bound to microtubules. *Nat. Struct. Mol. Biol.* 22:345–347. http://dx.doi.org/10.1038/nsmb.2996

Cianfrocco, M.A., M.E. DeSantis, A.E. Leschziner, and S.L. Reck-Peterson. 2015. Mechanism and regulation of cytoplasmic dynein. *Annu. Rev. Cell Dev. Biol.* 31:83–108. http://dx.doi.org/10.1146/annurev-cellbio-100814-125438

Çivril, F., A. Wehenkel, F.M. Giorgi, S. Santaguida, A. Di Fonzo, G. Grigorean, F.D. Ciccarelli, and A. Musacchio. 2010. Structural analysis of the RZZ complex reveals common ancestry with multisubunit vesicle tethering machinery. *Structure.* 18:616–626. http://dx.doi.org/10.1016/j.str.2010.02.014

Cooke, C.A., B. Schaar, T.J. Yen, and W.C. Earnshaw. 1997. Localization of CENP-E in the fibrous corona and outer plate of mammalian kinetochores from prometaphase through anaphase. *Chromosoma.* 106:446–455. http://dx.doi.org/10.1007/s004120050266

Cox, J., and M. Mann. 2008. MaxQuant enables high peptide identification rates, individualized p.p.b.-range mass accuracies and proteome-wide protein quantification. *Nat. Biotechnol.* 26:1367–1372. http://dx.doi.org/10.1038/nbt.1511

Fath, S., J.D. Mancias, X. Bi, and J. Goldberg. 2007. Structure and organization of coat proteins in the COPII cage. *Cell.* 129:1325–1336. http://dx.doi.org/10.1016/j.cell.2007.05.036

Fotin, A., Y. Cheng, P. Sliz, N. Grigorieff, S.C. Harrison, T. Kirchhausen, and T. Walz. 2004. Molecular model for a complete clathrin lattice from electron cryomicroscopy. *Nature.* 432:573–579. http://dx.doi.org/10.1038/nature03079

Gassmann, R., A. Essex, J.S. Hu, P.S. Maddox, F. Motegi, A. Sugimoto, S.M. O'Rourke, B. Bowerman, I. McLeod, J.R. Yates III, et al. 2008. A new mechanism controlling kinetochore-microtubule interactions revealed by comparison of two dynein-targeting components: SPDL-1 and the Rod/Zwilch/Zw10 complex. *Genes Dev.* 22:2385–2399. http://dx.doi.org/10.1101/gad.1687508

Gassmann, R., A.J. Holland, D. Varma, X. Wan, F. Çivril, D.W. Cleveland, K. Oegema, E.D. Salmon, and A. Desai. 2010. Removal of Spindly from microtubule-attached kinetochores controls spindle checkpoint silencing in human cells. *Genes Dev.* 24:957–971. http://dx.doi.org/10.1101/gad.1886810

Griffis, E.R., N. Stuurman, and R.D. Vale. 2007. Spindly, a novel protein essential for silencing the spindle assembly checkpoint, recruits dynein to the kinetochore. *J. Cell Biol.* 177:1005–1015. http://dx.doi.org/10.1083/jcb.200702062

Hashimoto, Y., S. Zhang, S. Zhang, Y.R. Chen, and G.W. Blissard. 2012. Correction: BTI-Tnao38, a new cell line derived from *Trichoplusia ni*, is permissive for AcMNPV infection and produces high levels of recombinant proteins. *BMC Biotechnol.* 12:12. http://dx.doi.org/10.1186/1472-6750-12-12

Herzog, F., A. Kahraman, D. Boehringer, R. Mak, A. Bracher, T. Walzthoeni, A. Leitner, M. Beck, F.U. Hartl, N. Ban, et al. 2012. Structural probing of a protein phosphatase 2A network by chemical cross-linking and mass spectrometry. *Science.* 337:1348–1352. http://dx.doi.org/10.1126/science.1221483

Hoffman, D.B., C.G. Pearson, T.J. Yen, B.J. Howell, and E.D. Salmon. 2001. Microtubule-dependent changes in assembly of microtubule motor proteins and mitotic spindle checkpoint proteins at PtK1 kinetochores. *Mol. Biol. Cell.* 12:1995–2009. http://dx.doi.org/10.1091/mbc.12.7.1995

Hoffman, G.R., N. Nassar, and R.A. Cerione. 2000. Structure of the Rho family GTP-binding protein Cdc42 in complex with the multifunctional regulator RhoGDI. *Cell.* 100:345–356. http://dx.doi.org/10.1016/S0092-8674(00)80670-4

Hohn, M., G. Tang, G. Goodyear, P.R. Baldwin, Z. Huang, P.A. Penczek, C. Yang, R.M. Glaeser, P.D. Adams, and S.J. Ludtke. 2007. SPARX, a new environment for Cryo-EM image processing. *J. Struct. Biol.* 157:47–55. http://dx.doi.org/10.1016/j.jsb.2006.07.003

Holland, A.J., R.M. Reis, S. Niessen, C. Pereira, D.A. Andres, H.P. Spielmann, D.W. Cleveland, A. Desai, and R. Gassmann. 2015. Preventing farnesylation of the dynein adaptor Spindly contributes to the mitotic defects caused by farnesyltransferase inhibitors. *Mol. Biol. Cell.* 26:1845–1856. http://dx.doi.org/10.1091/mbc.E14-11-1560

Hoogenraad, C.C., and A. Akhmanova. 2016. Bicaudal D family of motor adaptors: linking dynein motility to cargo binding. *Trends Cell Biol.* 26:327–340. http://dx.doi.org/10.1016/j.tcb.2016.01.001

Howell, B.J., B.F. McEwen, J.C. Canman, D.B. Hoffman, E.M. Farrar, C.L. Rieder, and E.D. Salmon. 2001. Cytoplasmic dynein/dynactin drives kinetochore protein transport to the spindle poles and has a role in mitotic spindle checkpoint inactivation. *J. Cell Biol.* 155:1159–1172. http://dx.doi.org/10.1083/jcb.200105093

Hussein, D., and S.S. Taylor. 2002. Farnesylation of Cenp-F is required for G2/M progression and degradation after mitosis. *J. Cell Sci.* 115:3403–3414.

Ismail, S.A., Y.X. Chen, A. Rusinova, A. Chandra, M. Bierbaum, L. Gremer, G. Triola, H. Waldmann, P.I. Bastiaens, and A. Wittinghofer. 2011. Arl2-GTP and Arl3-GTP regulate a GDI-like transport system for farnesylated cargo. *Nat. Chem. Biol.* 7:942–949. http://dx.doi.org/10.1038/nchembio.686

Jackson, L.P. 2014. Structure and mechanism of COPI vesicle biogenesis. *Curr. Opin. Cell Biol.* 29:67–73. http://dx.doi.org/10.1016/j.ceb.2014.04.009

Jokelainen, P.T. 1967. The ultrastructure and spatial organization of the metaphase kinetochore in mitotic rat cells. *J. Ultrastruct. Res.* 19:19–44. http://dx.doi.org/10.1016/S0022-5320(67)80058-3

Kardon, J.R., and R.D. Vale. 2009. Regulators of the cytoplasmic dynein motor. *Nat. Rev. Mol. Cell Biol.* 10:854–865. http://dx.doi.org/10.1038/nrm2804

Karess, R. 2005. Rod-Zw10-Zwilch: a key player in the spindle checkpoint. *Trends Cell Biol.* 15:386–392. http://dx.doi.org/10.1016/j.tcb.2005.05.003

Kelley, L.A., S. Mezulis, C.M. Yates, M.N. Wass, and M.J. Sternberg. 2015. The Phyre2 web portal for protein modeling, prediction and analysis. *Nat. Protoc.* 10:845–858. http://dx.doi.org/10.1038/nprot.2015.053

Kops, G.J., Y. Kim, B.A. Weaver, Y. Mao, I. McLeod, J.R. Yates III, M. Tagaya, and D.W. Cleveland. 2005. ZW10 links mitotic checkpoint signaling to the structural kinetochore. *J. Cell Biol.* 169:49–60. http://dx.doi.org/10.1083/jcb.200411118

Kuhlmann, J., A. Tebbe, M. Völkert, M. Wagner, K. Uwai, and H. Waldmann. 2002. Photoactivatable synthetic Ras proteins: "baits" for the identification of plasma-membrane-bound binding partners of Ras. *Angew. Chem. Int. Ed. Engl.* 41:2546–2550. http://dx.doi.org/10.1002/1521-3773(20020715)41:14<2546::AID-ANIE2546>3.0.CO;2-E

Lee, C., and J. Goldberg. 2010. Structure of coatomer cage proteins and the relationship among COPI, COPII, and clathrin vesicle coats. *Cell.* 142:123–132. http://dx.doi.org/10.1016/j.cell.2010.05.030

Li, X., P. Mooney, S. Zheng, C.R. Booth, M.B. Braunfeld, S. Gubbens, D.A. Agard, and Y. Cheng. 2013. Electron counting and beam-induced motion correction enable near-atomic-resolution single-particle cryo-EM. *Nat. Methods.* 10:584–590. http://dx.doi.org/10.1038/nmeth.2472

Ludtke, S.J. 2010. 3-D structures of macromolecules using single-particle analysis in EMAN. *Methods Mol. Biol.* 673:157–173. http://dx.doi.org/10.1007/978-1-60761-842-3_9

Lupas, A., M. Van Dyke, and J. Stock. 1991. Predicting coiled coils from protein sequences. *Science.* 252:1162–1164. http://dx.doi.org/10.1126/science.252.5009.1162

Magidson, V., R. Paul, N. Yang, J.G. Ault, C.B. O'Connell, I. Tikhonenko, B.F. McEwen, A. Mogilner, and A. Khodjakov. 2015. Adaptive changes in the kinetochore architecture facilitate proper spindle assembly. *Nat. Cell Biol.* 17:1134–1144. http://dx.doi.org/10.1038/ncb3223

Martin-Lluesma, S., V.M. Stucke, and E.A. Nigg. 2002. Role of Hec1 in spindle checkpoint signaling and kinetochore recruitment of Mad1/Mad2. *Science.* 297:2267–2270. http://dx.doi.org/10.1126/science.1075596

Matson, D.R., and P.T. Stukenberg. 2014. CENP-I and Aurora B act as a molecular switch that ties RZZ/Mad1 recruitment to kinetochore attachment status. *J. Cell Biol.* 205:541–554. http://dx.doi.org/10.1083/jcb.201307137

McEwen, B.F., J.T. Arena, J. Frank, and C.L. Rieder. 1993. Structure of the colcemid-treated PtK1 kinetochore outer plate as determined by high voltage electron microscopic tomography. *J. Cell Biol.* 120:301–312. http://dx.doi.org/10.1083/jcb.120.2.301

McKenney, R.J., W. Huynh, M.E. Tanenbaum, G. Bhabha, and R.D. Vale. 2014. Activation of cytoplasmic dynein motility by dynactin-cargo adapter complexes. *Science.* 345:337–341. http://dx.doi.org/10.1126/science.1254198

McMahon, H.T., and E. Boucrot. 2011. Molecular mechanism and physiological functions of clathrin-mediated endocytosis. *Nat. Rev. Mol. Cell Biol.* 12:517–533. http://dx.doi.org/10.1038/nrm3151

Miller, S.A., M.L. Johnson, and P.T. Stukenberg. 2008. Kinetochore attachments require an interaction between unstructured tails on microtubules and Ndc80^{Hec1}. *Curr. Biol.* 18:1785–1791. http://dx.doi.org/10.1016/j.cub.2008.11.007

Mische, S., Y. He, L. Ma, M. Li, M. Serr, and T.S. Hays. 2008. Dynein light intermediate chain: an essential subunit that contributes to spindle checkpoint inactivation. *Mol. Biol. Cell.* 19:4918–4929. http://dx.doi.org/10.1091/mbc.E08-05-0483

Moudgil, D.K., N. Westcott, J.K. Famulski, K. Patel, D. Macdonald, H. Hang, and G.K. Chan. 2015. A novel role of farnesylation in targeting a mitotic checkpoint protein, human Spindly, to kinetochores. *J. Cell Biol.* 208:881–896. http://dx.doi.org/10.1083/jcb.201412085

Musacchio, A. 2015. The molecular biology of spindle assembly checkpoint signaling dynamics. *Curr. Biol.* 25:R1002–R1018 (published erratum appears in *Curr. Biol.* 2015. 25:3017). http://dx.doi.org/10.1016/j.cub.2015.08.051

Nguyen, U.T., J. Cramer, J. Gomis, R. Reents, M. Gutierrez-Rodriguez, R.S. Goody, K. Alexandrov, and H. Waldmann. 2007. Exploiting the substrate tolerance of farnesyltransferase for site-selective protein derivatization. *ChemBioChem.* 8:408–423. http://dx.doi.org/10.1002/cbic.200600440

Ong, S.E., B. Blagoev, I. Kratchmarova, D.B. Kristensen, H. Steen, A. Pandey, and M. Mann. 2002. Stable isotope labeling by amino acids in cell culture, SILAC, as a simple and accurate approach to expression proteomics. *Mol. Cell. Proteomics.* 1:376–386. http://dx.doi.org/10.1074/mcp.M200025-MCP200

Pesenti, M.E., J.R. Weir, and A. Musacchio. 2016. Progress in the structural and functional characterization of kinetochores. *Curr. Opin. Struct. Biol.* 37:152–163. http://dx.doi.org/10.1016/j.sbi.2016.03.003

Pettersen, E.F., T.D. Goddard, C.C. Huang, G.S. Couch, D.M. Greenblatt, E.C. Meng, and T.E. Ferrin. 2004. UCSF Chimera--a visualization system for exploratory research and analysis. *J. Comput. Chem.* 25:1605–1612. http://dx.doi.org/10.1002/jcc.20084

Radermacher, M., T. Wagenknecht, A. Verschoor, and J. Frank. 1987. Three-dimensional reconstruction from a single-exposure, random conical tilt series applied to the 50S ribosomal subunit of Escherichia coli. *J. Microsc.* 146:113–136. http://dx.doi.org/10.1111/j.1365-2818.1987.tb01333.x

Rak, A., O. Pylypenko, T. Durek, A. Watzke, S. Kushnir, L. Brunsveld, H. Waldmann, R.S. Goody, and K. Alexandrov. 2003. Structure of Rab GDP-dissociation inhibitor in complex with prenylated YPT1 GTPase. *Science.* 302:646–650. http://dx.doi.org/10.1126/science.1087761

Rappsilber, J., M. Mann, and Y. Ishihama. 2007. Protocol for micro-purification, enrichment, pre-fractionation and storage of peptides for proteomics using StageTips. *Nat. Protoc.* 2:1896–1906. http://dx.doi.org/10.1038/nprot.2007.261

Rieder, C.L., and S.P. Alexander. 1990. Kinetochores are transported poleward along a single astral microtubule during chromosome attachment to the spindle in newt lung cells. *J. Cell Biol.* 110:81–95. http://dx.doi.org/10.1083/jcb.110.1.81

Riou, P., S. Kjær, R. Garg, A. Purkiss, R. George, R.J. Cain, G. Bineva, N. Reymond, B. McColl, A.J. Thompson, et al. 2013. 14-3-3 proteins interact with a hybrid prenyl-phosphorylation motif to inhibit G proteins. *Cell.* 153:640–653 (published erratum appears in *Cell*. 2013. 153:1164). http://dx.doi.org/10.1016/j.cell.2013.03.044

Russell, C., and S.M. Stagg. 2010. New insights into the structural mechanisms of the COPII coat. *Traffic.* 11:303–310. http://dx.doi.org/10.1111/j.1600-0854.2009.01026.x

Samejima, I., C. Spanos, F.L. Alves, T. Hori, M. Perpelescu, J. Zou, J. Rappsilber, T. Fukagawa, and W.C. Earnshaw. 2015. Whole-proteome genetic analysis of dependencies in assembly of a vertebrate kinetochore. *J. Cell Biol.* 211:1141–1156. http://dx.doi.org/10.1083/jcb.201508072

Santaguida, S., A. Tighe, A.M. D'Alise, S.S. Taylor, and A. Musacchio. 2010. Dissecting the role of MPS1 in chromosome biorientation and the spindle checkpoint through the small molecule inhibitor reversine. *J. Cell Biol.* 190:73–87. http://dx.doi.org/10.1083/jcb.201001036

Scaërou, F., D.A. Starr, F. Piano, O. Papoulas, R.E. Karess, and M.L. Goldberg. 2001. The ZW10 and Rough Deal checkpoint proteins function together in a large, evolutionarily conserved complex targeted to the kinetochore. *J. Cell Sci.* 114:3103–3114.

Scheltema, R.A., J.P. Hauschild, O. Lange, D. Hornburg, E. Denisov, E. Damoc, A. Kuehn, A. Makarov, and M. Mann. 2014. The Q Exactive HF, a Benchtop mass spectrometer with a pre-filter, high-performance quadrupole and an ultra-high-field Orbitrap analyzer. *Mol. Cell. Proteomics.* 13:3698–3708. http://dx.doi.org/10.1074/mcp.M114.043489

Scheres, S.H., and S. Chen. 2012. Prevention of overfitting in cryo-EM structure determination. *Nat. Methods.* 9:853–854. http://dx.doi.org/10.1038/nmeth.2115

Schlager, M.A., H.T. Hoang, L. Urnavicius, S.L. Bullock, and A.P. Carter. 2014. In vitro reconstitution of a highly processive recombinant human dynein complex. *EMBO J.* 33:1855–1868. http://dx.doi.org/10.15252/embj.201488792

Silió, V., A.D. McAinsh, and J.B. Millar. 2015. KNL1-Bubs and RZZ Provide Two Separable Pathways for Checkpoint Activation at Human Kinetochores. *Dev. Cell.* 35:600–613. http://dx.doi.org/10.1016/j.devcel.2015.11.012

Sivaram, M.V., T.L. Wadzinski, S.D. Redick, T. Manna, and S.J. Doxsey. 2009. Dynein light intermediate chain 1 is required for progress through the spindle assembly checkpoint. *EMBO J.* 28:902–914. http://dx.doi.org/10.1038/emboj.2009.38

Söding, J., A. Biegert, and A.N. Lupas. 2005. The HHpred interactive server for protein homology detection and structure prediction. *Nucleic Acids Res.* 33:W244–W248. http://dx.doi.org/10.1093/nar/gki408

Stagg, S.M., C. Gürkan, D.M. Fowler, P. LaPointe, T.R. Foss, C.S. Potter, B. Carragher, and W.E. Balch. 2006. Structure of the Sec13/31 COPII coat cage. *Nature.* 439:234–238. http://dx.doi.org/10.1038/nature04339

Stagg, S.M., P. LaPointe, and W.E. Balch. 2007. Structural design of cage and coat scaffolds that direct membrane traffic. *Curr. Opin. Struct. Biol.* 17:221–228. http://dx.doi.org/10.1016/j.sbi.2007.03.010

Starr, D.A., B.C. Williams, T.S. Hays, and M.L. Goldberg. 1998. ZW10 helps recruit dynactin and dynein to the kinetochore. *J. Cell Biol.* 142:763–774. http://dx.doi.org/10.1083/jcb.142.3.763

ter Haar, E., A. Musacchio, S.C. Harrison, and T. Kirchhausen. 1998. Atomic structure of clathrin: a β propeller terminal domain joins an α zigzag linker. *Cell.* 95:563–573. http://dx.doi.org/10.1016/S0092-8674(00)81623-2

Tripathi, A., Y. Ren, P.D. Jeffrey, and F.M. Hughson. 2009. Structural characterization of Tip20p and Dsl1p, subunits of the Dsl1p vesicle tethering complex. *Nat. Struct. Mol. Biol.* 16:114–123. http://dx.doi.org/10.1038/nsmb.1548

Urnavicius, L., K. Zhang, A.G. Diamant, C. Motz, M.A. Schlager, M. Yu, N.A. Patel, C.V. Robinson, and A.P. Carter. 2015. The structure of the dynactin complex and its interaction with dynein. *Science.* 347:1441–1446. http://dx.doi.org/10.1126/science.aaa4080

Varma, D., P. Monzo, S.A. Stehman, and R.B. Vallee. 2008. Direct role of dynein motor in stable kinetochore-microtubule attachment, orientation, and alignment. *J. Cell Biol.* 182:1045–1054. http://dx.doi.org/10.1083/jcb.200710106

Walzthoeni, T., M. Claassen, A. Leitner, F. Herzog, S. Bohn, F. Förster, M. Beck, and R. Aebersold. 2012. False discovery rate estimation for cross-linked peptides identified by mass spectrometry. *Nat. Methods.* 9:901–903. http://dx.doi.org/10.1038/nmeth.2103

Wang, M., and P.J. Casey. 2016. Protein prenylation: unique fats make their mark on biology. *Nat. Rev. Mol. Cell Biol.* 17:110–122. http://dx.doi.org/10.1038/nrm.2015.11

Weir, J.R., A.C. Faesen, K. Klare, A. Petrovic, F. Basilico, J. Fischböck, S. Pentakota, J. Keller, M.E. Pesenti, D. Pan, et al. 2016. Insights from biochemical reconstitution into the architecture of human kinetochores. *Nature.* 537:249–253. http://dx.doi.org/10.1038/nature19333

Weissmann, F., G. Petzold, R. VanderLinden, P.J. Huis in 't Veld, N. Brown, F. Lampert, S. Westermann, H. Stark, B.A. Schulman, and J.-M. Peters. 2016. biGBac enables rapid gene assembly for the expression of large multisubunit protein complexes. *Proc. Natl. Acad. Sci. USA*. 113:E2564–E2569. http://dx.doi.org/10.1073/pnas.1604935113

Williams, B.C., M. Gatti, and M.L. Goldberg. 1996. Bipolar spindle attachments affect redistributions of ZW10, a Drosophila centromere/kinetochore component required for accurate chromosome segregation. *J. Cell Biol.* 134:1127–1140. http://dx.doi.org/10.1083/jcb.134.5.1127

Williams, B.C., Z. Li, S. Liu, E.V. Williams, G. Leung, T.J. Yen, and M.L. Goldberg. 2003. Zwilch, a new component of the ZW10/ROD complex required for kinetochore functions. *Mol. Biol. Cell.* 14:1379–1391. http://dx.doi.org/10.1091/mbc.E02-09-0624

Wojcik, E., R. Basto, M. Serr, F. Scaërou, R. Karess, and T. Hays. 2001. Kinetochore dynein: its dynamics and role in the transport of the Rough deal checkpoint protein. *Nat. Cell Biol.* 3:1001–1007. http://dx.doi.org/10.1038/ncb1101-1001

Wynne, D.J., and H. Funabiki. 2015. Kinetochore function is controlled by a phospho-dependent coexpansion of inner and outer components. *J. Cell Biol.* 210:899–916. http://dx.doi.org/10.1083/jcb.201506020

Yamamoto, T.G., S. Watanabe, A. Essex, and R. Kitagawa. 2008. SPDL-1 functions as a kinetochore receptor for MDF-1 in *Caenorhabditis elegans*. *J. Cell Biol.* 183:187–194. http://dx.doi.org/10.1083/jcb.200805185

Yang, Z., J. Fang, J. Chittuluru, F.J. Asturias, and P.A. Penczek. 2012. Iterative stable alignment and clustering of 2D transmission electron microscope images. *Structure.* 20:237–247. http://dx.doi.org/10.1016/j.str.2011.12.007

Yao, X., K.L. Anderson, and D.W. Cleveland. 1997. The microtubule-dependent motor centromere-associated protein E (CENP-E) is an integral component of kinetochore corona fibers that link centromeres to spindle microtubules. *J. Cell Biol.* 139:435–447. http://dx.doi.org/10.1083/jcb.139.2.435

Zhang, G., T. Lischetti, D.G. Hayward, and J. Nilsson. 2015. Distinct domains in Bub1 localize RZZ and BubR1 to kinetochores to regulate the checkpoint. *Nat. Commun.* 6:7162. http://dx.doi.org/10.1038/ncomms8162

Article

Current Biology

BubR1 Promotes Bub3-Dependent APC/C Inhibition during Spindle Assembly Checkpoint Signaling

Graphical Abstract

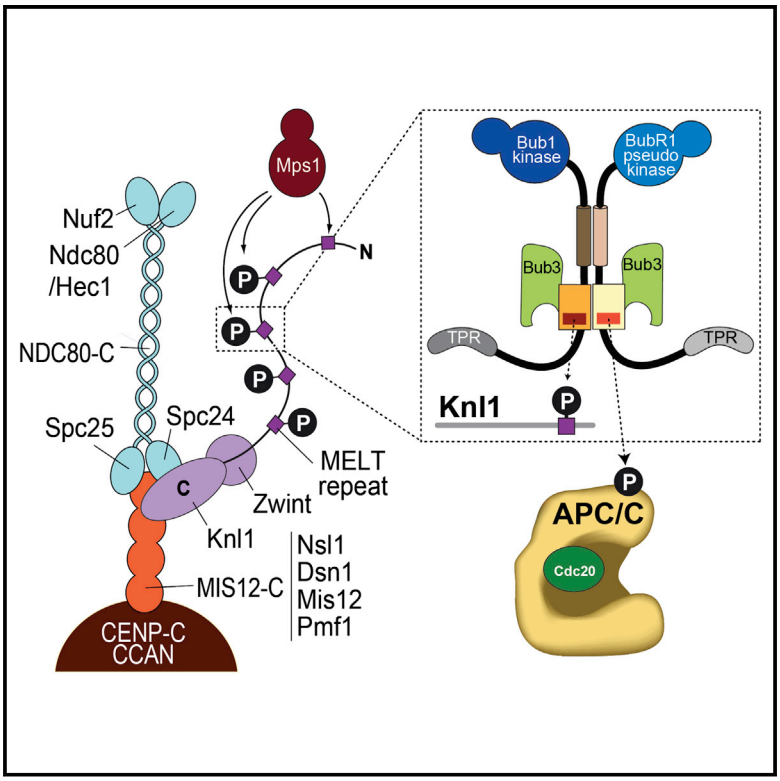

Highlights

- The molecular basis of kinetochore recruitment of Bub1 and BubR1 is dissected
- Bub1 and BubR1 modulate the ability of Bub3 to recognize phosphorylated targets
- A newly identified BubR1 motif targets Bub3 to the anaphase-promoting complex
- The newly identified motif of BubR1 is required for checkpoint signaling

Authors

Katharina Overlack, Tanja Bange, Florian Weissmann, ..., Franziska Müller, Jan-Michael Peters, Andrea Musacchio

Correspondence

andrea.musacchio@mpi-dortmund.mpg.de

In Brief

In spindle assembly checkpoint (SAC) signaling, the phospho-amino acid adaptor Bub3 forms complexes with Bub1 and BubR1 paralogs. Whether Bub3-Bub1 and Bub3-BubR1 bind distinct targets has been unclear. Overlack et al. demonstrate that this is the case and identify a motif in BubR1 that directs Bub3 to the SAC target, the anaphase-promoting complex.

Overlack et al., 2017, Current Biology 27, 2915–2927
October 9, 2017
http://dx.doi.org/10.1016/j.cub.2017.08.033

Current Biology
Article

BubR1 Promotes Bub3-Dependent APC/C Inhibition during Spindle Assembly Checkpoint Signaling

Katharina Overlack,[1] Tanja Bange,[1] Florian Weissmann,[3] Alex C. Faesen,[1] Stefano Maffini,[1] Ivana Primorac,[1,4] Franziska Müller,[1] Jan-Michael Peters,[3] and Andrea Musacchio[1,2,5,*]
[1]Department of Mechanistic Cell Biology, Max Planck Institute of Molecular Physiology, Otto-Hahn-Strasse 11, 44227 Dortmund, Germany
[2]Centre for Medical Biotechnology, Faculty of Biology, University Duisburg-Essen, Universitätsstrasse, 45141 Essen, Germany
[3]Research Institute of Molecular Pathology (IMP), Vienna Biocenter (VBC), Campus-Vienna-Biocenter 1, 1030 Vienna, Austria
[4]Present address: Centre for Medical Biotechnology, Faculty of Biology, University Duisburg-Essen, Universitätsstrasse, 45141 Essen, Germany
[5]Lead Contact
*Correspondence: andrea.musacchio@mpi-dortmund.mpg.de
http://dx.doi.org/10.1016/j.cub.2017.08.033

SUMMARY

The spindle assembly checkpoint (SAC) prevents premature sister chromatid separation during mitosis. Phosphorylation of unattached kinetochores by the Mps1 kinase promotes recruitment of SAC machinery that catalyzes assembly of the SAC effector mitotic checkpoint complex (MCC). The SAC protein Bub3 is a phospho-amino acid adaptor that forms structurally related stable complexes with functionally distinct paralogs named Bub1 and BubR1. A short motif ("loop") of Bub1, but not the equivalent loop of BubR1, enhances binding of Bub3 to kinetochore phospho-targets. Here, we asked whether the BubR1 loop directs Bub3 to different phospho-targets. The BubR1 loop is essential for SAC function and cannot be removed or replaced with the Bub1 loop. BubR1 loop mutants bind Bub3 and are normally incorporated in MCC in vitro but have reduced ability to inhibit the MCC target anaphase-promoting complex (APC/C), suggesting that BubR1:Bub3 recognition and inhibition of APC/C requires phosphorylation. Thus, small sequence differences in Bub1 and BubR1 direct Bub3 to different phosphorylated targets in the SAC signaling cascade.

INTRODUCTION

Bub1 and BubR1 (also known as Mad3 in certain organisms) are paralogous proteins that fulfill different crucial functions in chromosome alignment on the mitotic spindle and in the spindle assembly checkpoint (SAC), a safety mechanism that ensures accurate chromosome segregation during mitosis [1, 2]. Bub1 and BubR1 originated through multiple independent gene-duplication events from a precursor (singleton) surmised to be already present in the hypothetical last eukaryotic common ancestor (LECA). Gene duplication invariably led to sub-functionalization of the resulting gene products [3, 4] (Figure 1A).

The molecular mechanism subtending to sub-functionalization of Bub1 and BubR1 is an active area of research. Bub1 is a Ser/Thr kinase [8] whose kinase activity may be strictly required for chromosome alignment, but not for SAC signaling [9–17]. Bub1 localizes to kinetochores in early prometaphase and is thought to perform its main role in the SAC by acting as a scaffold for the recruitment of downstream checkpoint components, including Mad1, Mad2, BubR1, Bub3, and Cdc20 [11, 14, 18–28]. Bub1 promotes the incorporation of a subset of these proteins, including BubR1, Bub3, Mad2, and Cdc20, into the mitotic checkpoint complex (MCC), the main checkpoint effector, which directly inhibits the ability of the E3 ubiquitin ligase anaphase-promoting complex/cyclosome (APC/C) to promote exit from mitosis [1, 2]. Promotion of MCC formation by Bub1 likely occurs through a direct interaction with a Mad1:Mad2 template that catalyzes MCC assembly [11, 29–35].

Unlike Bub1, BubR1 is an inactive pseudokinase [4]. It contributes directly to the SAC and to APC/C inhibition as a subunit of the MCC (together with Bub3, Cdc20, and Mad2) [36–38]. Two Lys-Glu-Asn (KEN) motifs (also called KEN boxes) in the N-terminal region of BubR1 have been implicated in Cdc20 binding and APC/C inhibition. The first KEN box is essential for stable incorporation of BubR1 in a complex with Cdc20 and Mad2 that represents the core of the MCC [39–43]. The second KEN box promotes binding to a second Cdc20 molecule, possibly when the latter is already bound to the APC/C [44–47]. Both KEN motifs are required for effective APC/C inhibition and SAC function (e.g., see [42]). In addition to its role in SAC activation, BubR1 also contributes to the formation of stable kinetochore-microtubule interactions and SAC silencing through kinetochore recruitment of the phosphatase $PP2A^{B56}$ [48–52].

In human cells, kinetochore localization of Bub1 and BubR1 requires phosphorylation by the SAC kinase Mps1 of so-called Met-Glu-Leu-Thr (MELT) motifs in the outer kinetochore protein Knl1 (also known as Spc105, Spc7, and Casc5) [53–55]. It also requires binding to Bub3, which acts as a targeting adaptor [40, 42, 56–58]. Bub1 and BubR1 bind to Bub3 via conserved Bub3-binding domains (B3BD or GLEBS; Figure 1A) [57, 59]. Bub3, a seven-bladed β propeller, contains an evolutionarily conserved binding pocket that accommodates the phosphorylated Thr residue of the MELT motifs (Figures 1B, S1A, and S1B) [58]. By binding to Bub3, the B3BD of Bub1 is sufficient

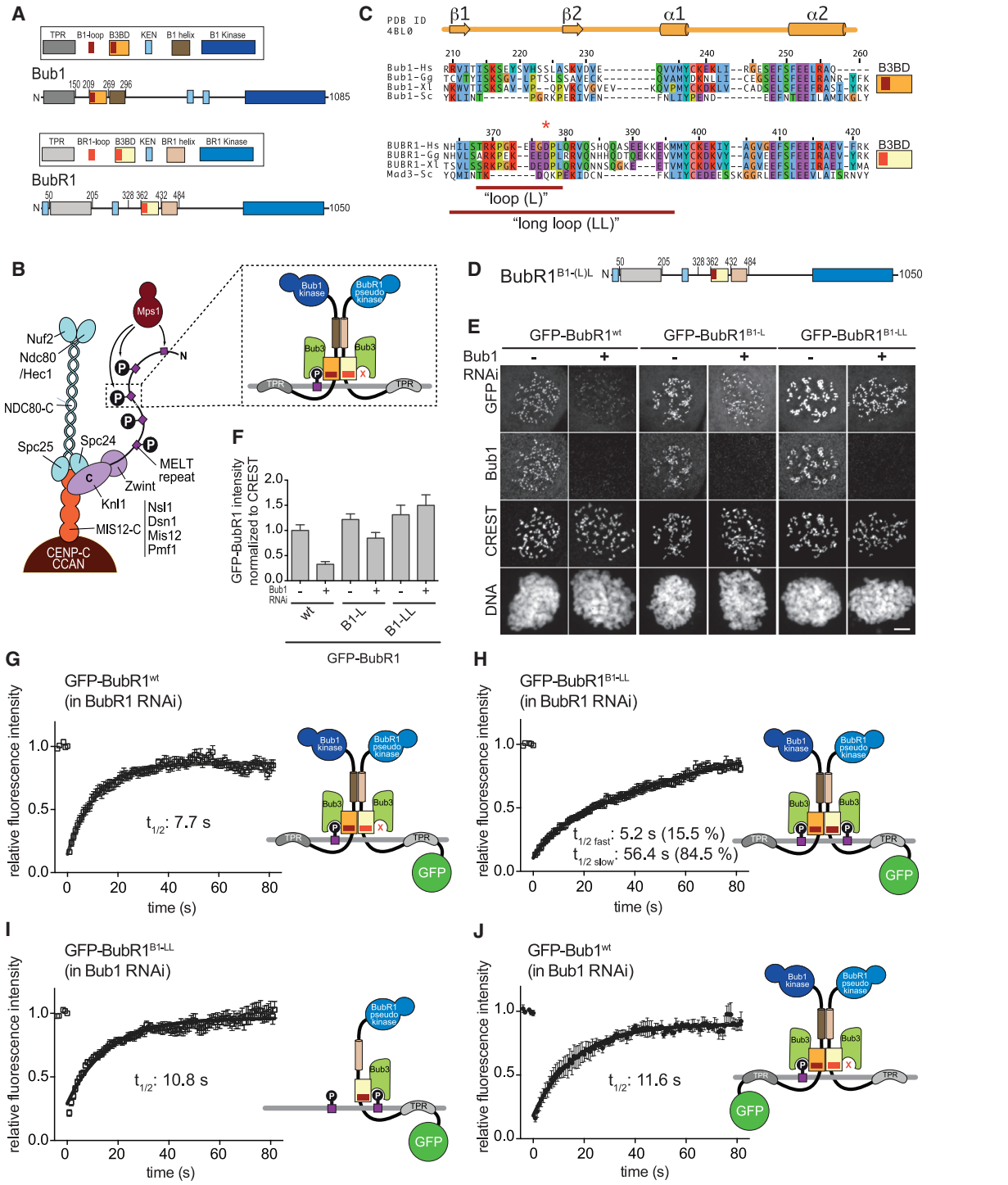

Figure 1. Kinetochore Localization and Turnover of Long BubR1 Loop Mutants in HeLa Cells

(A) Schematic overview of Bub1 and BubR1 domain organization. B1, Bub1; B3BD, Bub3 binding domain; BR1, BubR1; KEN, lysine-glutamate-asparagine motif; TPR, tetratrico peptide repeat.

(B) Schematic depiction of the outer kinetochore (KMN network). MELT repeats in Knl1 are phosphorylated by the checkpoint kinase Mps1 and recruit Bub1:Bub3. Bub1:Bub3 in turn recruits BubR1:Bub3 via a pseudo-symmetric interaction, which involves equivalent segments of Bub1 and BubR1 comprising the B3BD and the C-terminal extension whose first part is predicted to form a helix in both proteins. The presence of Bub3 on both proteins seems to be essential for this interaction. The TPR regions of human Bub1 and BubR1 bind to non-conserved short motifs of Knl1 named KI1 and KI2, respectively [5–7].

(legend continued on next page)

for kinetochore localization in the absence of other Bub1 regions [5, 57]. We recently reported that a short region of the B3BD of Bub1, which we designated as the "loop" (Figures 1C, S1A, and S1B), markedly increases the binding affinity of Bub3 for phosphorylated MELT motifs ($MELT^{P}$) through direct contacts [58, 60]. The loop region in the B3BD of BubR1, on the other hand, is unable to increase the binding affinity of Bub3 for Knl1-$MELT^{P}$ sequences, rendering kinetochore localization of BubR1:Bub3 dependent on additional interactions [5, 60]. We reported that kinetochore-bound Bub1:Bub3 provides these additional interactions [60], thus establishing a clear hierarchy in which Bub1:Bub3 is first directly recruited to the kinetochore via interaction with $MELT^{P}$ motifs, after which BubR1:Bub3 is recruited through a direct interaction with Bub1 (Figure 1B). This model agrees with observations that kinetochore recruitment of Bub1 is independent of BubR1, whereas kinetochore localization of BubR1 depends on Bub1 [11, 12, 21, 56, 60–63]. Hetero-dimerization of Bub1:Bub3 and BubR1:Bub3 requires equivalent domains in Bub1 and BubR1, including the B3BD and a region, directly following the B3BD, predicted to adopt helical conformation. Furthermore, both proteins need to be bound to Bub3 for their effective recruitment to kinetochores (Figure 1B) [60].

The crucial role of the Bub1 loop as enhancer of $MELT^{P}$ binding was emphasized by the fact that grafting the Bub1 loop onto BubR1 promoted Bub1-independent kinetochore recruitment of BubR1 [60]. The observation that this loop swap mutant, however, was unable to support BubR1 SAC function [60] raised the question whether the BubR1 loop performs a specific and so far unidentified function. In this study, we set out to investigate the role of the BubR1 loop in more detail. We demonstrate that the BubR1 loop promotes stable association of the MCC complex with the APC/C.

RESULTS

Definition of Functional Loop Regions of Bub1 and BubR1

The B3BD of Bub1 is sufficient for kinetochore recruitment through Bub3 [5, 57, 60]. In our previous studies, we identified the Bub1 loop region ($Bub1^{L}$) (residues 214–226 within the $Bub1^{B3BD}$; Figures 1A and 1C) as a determinant of kinetochore localization of the Bub1:Bub3 complex and showed that $Bub1^{L}$ enhances the affinity of the interaction of Bub3 for Knl1-$MELT^{P}$ motifs at kinetochores [60]. We also showed that, when grafted onto BubR1, $Bub1^{L}$ promotes Bub1-independent kinetochore recruitment of BubR1. This result agreed with observations in vitro that the equivalent BubR1 loop region ($BubR1^{L}$) (residues 368–379) is unable to promote the interaction of Bub3 with Knl1-$MELT^{P}$ motifs and is therefore functionally distinct from $Bub1^{L}$ [60].

As clarified in Figure S2 (and legend), we discovered that grafting onto BubR1 longer regions of Bub1 (residues 209–235), ranging from the first β sheet (β1) until the beginning of the highly conserved core of the B3BD (Figures 1C and 1D), resulted in more robust kinetochore localization in comparison to that of $BubR1^{B1\text{-}L}$, especially after depletion of endogenous Bub1 (Figures 1E and 1F; to differentiate this longer sequence from that of $Bub1^{L}$, we denote it as "long loop" [$Bub1^{LL}$]). $BubR1^{1–431/B1\text{-}LL}$, which lacks the predicted helical region required for dimerization with Bub1, localized to kinetochores in presence or absence of endogenous Bub1 (Figures S2E and S2F). Thus, the $Bub1^{LL}$ region is sufficient to mediate kinetochore localization when grafted on a dimerization-deficient BubR1 mutant. When we grafted the equivalent region of BubR1 (residues 363–396; $BubR1^{LL}$) onto Bub1 ($Bub1^{BR1\text{-}LL}$), we observed that it impaired kinetochore localization of Bub1 significantly more pervasively than when grafting the shorter $BubR1^{L}$ sequence ($Bub1^{BR1\text{-}L}$) (Figures S2G and S2H). Collectively, these experiments identify the LL regions of Bub1 and BubR1 as crucial determinants of their localization and demonstrate that these sequences impart substantial functional divergence to the Bub1 and BubR1 paralogs.

Kinetochore Turnover of BubR1 Loop Mutants

We investigated the effects of grafting $Bub1^{LL}$ on BubR1 kinetochore turnover. The halftime of kinetochore localization of BubR1 measured by fluorescence recovery after photobleaching (FRAP) is relatively fast ($t_{1/2}$ = 3–20 s) [64, 65]. This rapid turnover of BubR1 likely reflects its dimerization with kinetochore Bub1 and subsequent release, possibly in complex with other MCC subunits. In agreement with the published data [64], we found in FRAP experiments in HeLa cells depleted of endogenous BubR1 that GFP-$BubR1^{WT}$ showed a recovery halftime of 7.7 s (fit with a single exponential curve; Figure 1G; Table S1; the cartoon beside the graph depicts the expected mode of kinetochore localization of the construct).

If grafting of $Bub1^{LL}$ allows $BubR1^{B1\text{-}LL}$ to interact with $MELT^{P}$ in addition to dimerizing with Bub1, substantial increases of its kinetochore residence time might be expected if the two binding modes occurred concomitantly. FRAP curves of the GFP-$BubR1^{B1\text{-}LL}$ mutant were best fitted with a double exponential

(C) Multiple sequence alignments of the B3BDs of Bub1 and BubR1 from four different species: Hs, *Homo sapiens*; Gg, *Gallus gallus*; Xl, *Xenopus laevis*; and Sc, *Saccharomyces cerevisiae*. Mad3 is the budding yeast BubR1 homolog. The initial loop (L) and the long loop (LL) are indicated by the red lines; exact residue numbers are indicated in the main text.

(D) Domain organization of the BubR1 constructs with the Bub1 loop. $BubR1^{B1\text{-}L}$ contains Bub1 residues 214–226; $BubR1^{B1\text{-}LL}$ contains Bub1 residues 209–235.

(E) Representative images of HeLa cells transfected with the indicated GFP-BubR1 constructs showing that GFP-$BubR1^{B1\text{-}LL}$ localizes better to kinetochores than the short loop mutant (B1-L) in presence and absence of endogenous Bub1. In brief, after transfection, cells were depleted of endogenous Bub1 by RNAi, synchronized with a double thymidine block, and arrested in mitosis with nocodazole. The scale bar represents 10 μm.

(F) Quantification of BubR1 kinetochore levels in cells treated as in (E). The graph shows mean intensity from three independent experiments. Error bars represent SEM. Values for $BubR1^{wt}$ in non-depleted cells are set to 1.

(G–J) FRAP analyses of GFP-tagged $BubR1^{wt}$ (G), $BubR1^{B1\text{-}LL}$ (H and I), and GFP-$Bub1^{wt}$ in absence of endogenous BubR1 (G and H) or endogenous Bub1 (I and J). Relevant recovery parameters are shown. The graphs show mean with SEM. The cartoons beside the graphs depict the expected mode of kinetochore localization of each construct.

See also Figures S1–S3.

curve (Figure 1H; Table S1). A minority of GFP-BubR1$^{B1\text{-}LL}$ (15.5%) turned over with a halftime of 5.2 s, likely reflecting single binding events (dimerization with Bub1 or direct binding to MELT^{P} sequences). The majority of GFP-BubR1$^{B1\text{-}LL}$, on the other hand, cycled with a halftime of 56.4 s, indeed suggesting the possibility that the two kinetochore-binding modes, namely the dimerization with Bub1 and the direct interaction of GFP-BubR1$^{B1\text{-}LL}$ with MELT^{P}, occur concomitantly and strongly stabilize GFP-BubR1$^{B1\text{-}LL}$ at kinetochores. GFP-BubR1^{LL} showed higher kinetochore levels than GFP-BubR1^{WT} in cells depleted of endogenous BubR1 (Figures S3A and S3B), as expected given its increased halftime. We note that this is compatible with previous studies showing that only a subset of all MELT^{P} motifs of Knl1 are occupied with Bub1 at any given time [66].

This binding model predicts that depletion of endogenous Bub1 will ablate dimerization, only allowing a single binding mode of GFP-BubR1$^{B1\text{-}LL}$ through MELT^{P} binding. In agreement with this hypothesis, depletion of endogenous Bub1 by RNAi resulted in a recovery curve for GFP-BubR1$^{B1\text{-}LL}$ that could be fitted with a single exponential function with rapid turnover ($t_{1/2}$ = 10.8 s; Figure 1I; Table S1). Like BubR1$^{B1\text{-}LL}$, also Bub1 interacts with kinetochores by binding MELT^{P} sequences, and therefore, it is expected to turn over at kinetochores with a similarly rapid halftime. Whereas previous studies reported that Bub1 turns over relatively slowly at kinetochores [64, 65], our measurements indicate rapid kinetochore turnover of GFP-Bub1^{WT} ($t_{1/2}$ = 11.6 s; Figure 1J; Table S1), very similar to the recovery halftime of GFP-BubR1$^{B1\text{-}LL}$ after Bub1 depletion. Our observations are corroborated by a recent study reporting a recovery halftime of 15 s for kinetochore Bub1 [67].

The Bub1 Loop Cannot Promote the SAC Function of BubR1 In Vivo

Next, we asked whether BubR1$^{B1\text{-}LL}$ was able to rescue SAC signaling in HeLa cells depleted of endogenous BubR1. A BubR1 alanine mutant in the first KEN box (KEN1; Figure 2A) was used as a control for checkpoint deficiency in these experiments [42]. Asynchronous cells entering mitosis in presence of low concentrations of the spindle poison nocodazole arrested robustly in mitosis for several hours, indicative of SAC activation (Figure 2B). Depletion of BubR1 prevented mitotic arrest but could be rescued by expression of a wild-type GFP-BubR1 transgene. On the other hand, BubR1$^{B1\text{-}LL}$ was unable to rescue the deleterious effects on the SAC caused by depletion of endogenous BubR1 to an extent similar to that of the KEN1 box mutant (Figure 2B). Thus, the Bub1^{LL} region cannot functionally replace the equivalent region of BubR1. These findings were corroborated by immunoprecipitation experiments (IPs) of the GFP-BubR1 species, followed by western blotting (WB) to detect MCC and APC/C subunits. This revealed a substantial decrease in the association of GFP-BubR1$^{B1\text{-}LL}$ or GFP-BubR1$^{KEN1/AAA}$ with Mad2 and Cdc20 (but not Bub3, as expected) as well as the APC/C subunits Cdc27, Apc7, and Apc4 (Figure 2C; quantified in Figure S4A). Similar results were obtained when we replaced the sequence of the BubR1 loop with a neutral Gly-Ser-linker sequence (Figures S5A–S5D).

As explained in the previous section, data in Figures 1G–1J suggest that GFP-BubR1$^{B1\text{-}LL}$ dimerizes with Bub1 and also binds to phosphorylated MELT motifs at kinetochores. We hypothesized that the SAC defect following grafting of the Bub1^{LL} region into BubR1 might be caused by increased kinetochore residence of this mutant, which also reflected in a strongly increased interaction with the Knl1 kinetochore receptor (Figure S4A). If rapid kinetochore turnover of BubR1 is required for its efficient incorporation into MCC, tighter kinetochore binding might counteract incorporation into MCC. We therefore asked whether we could rescue the SAC deficiency of the GFP-BubR1$^{B1\text{-}LL}$ mutant by restoring rapid kinetochore turnover.

To test this hypothesis, we designed two constructs expected to reduce the time of kinetochore residence of GFP-BubR1$^{B1\text{-}LL}$ (see Figure 2A for schematics). First, we combined grafting of the Bub1^{LL} region with deletion of the predicted helical region (residues 432–484) involved in BubR1 dimerization with Bub1 (designated as GFP-BubR1$^{B1\text{-}LL/\Delta H}$). GFP-BubR1$^{B1\text{-}LL/\Delta H}$ is expected to localize correctly but exclusively through Bub1^{LL}-mediated recognition of MELT^{P} and not through dimerization. Importantly, deletion of the BubR1 helical region is fully compatible with SAC signaling (see next paragraph). Second, we grafted the entire B3BD and helical region of Bub1 onto GFP-BubR1 (GFP-BubR1$^{B1\text{-}B3BD/B1\text{-}H}$), thus again forcing BubR1 to interact with kinetochores exclusively through MELT^{P} and not through an interaction with Bub1 (because neither Bub1 nor BubR1 can form homodimers).

In agreement with our expectations, and more generally with our model of kinetochore recruitment of Bub1 and BubR1, both GFP-BubR1$^{B1\text{-}B3BD/B1\text{-}H}$ and GFP-BubR1$^{B1\text{-}LL/\Delta H}$ showed robust localization to kinetochores (Figures S4B and S4C), and FRAP analyses of both mutants demonstrated rapid kinetochore turnover (Figures 2D and 2E), with recovery halftimes that were essentially indistinguishable from those of GFP-BubR1^{WT} (Figure 1G; Table S1). Despite normal kinetochore turnover, however, GFP-BubR1$^{B1\text{-}LL/\Delta H}$ was unable to rescue the SAC defect caused by BubR1 depletion (Figure 2F) and was correspondingly unable to form stable complexes with MCC and APC/C subunits in IP experiments (Figure 2G; quantified in Figure S4D). Importantly, GFP-BubR1$^{\Delta H}$ is fully SAC proficient (Figure S4E) [60], strongly suggesting that the SAC defect is caused by Bub1^{LL} grafting. Also, GFP-BubR1$^{B1\text{-}B3BD/B1\text{-}H}$ was unable to rescue the SAC in cells depleted of endogenous BubR1 (Figure S4F). In non-depleted cells, GFP-BubR1$^{B1\text{-}B3BD/B1\text{-}H}$ interacted with BubR1 as expected, but its interaction with MCC and APC/C subunits was reduced (Figure S4G). Collectively, these results indicate that the SAC defect introduced by grafting the Bub1^{LL} region in GFP-BubR1$^{B1\text{-}LL}$ is not due to increased kinetochore residency of this mutant.

The BubR1 Loop Is Required for SAC Function In Vivo

As an alternative explanation for why GFP-BubR1$^{B1\text{-}LL}$ is SAC defective, we considered the hypothesis that the substitution of the BubR1^{LL} region with the Bub1^{LL} region may interfere with the interaction of the BubR1:Bub3 complex with a crucial SAC target. To test this idea, we created two additional BubR1 mutants in which parts of the loop region were deleted (ΔL and ΔLL mutant, corresponding to deletions of residues 368–379 and 363–396, respectively; Figure 3A). GFP-BubR1$^{\Delta L}$ and GFP-BubR1$^{\Delta LL}$ localized to kinetochores at levels that were indistinguishable from those of GFP-BubR1^{WT}, and their

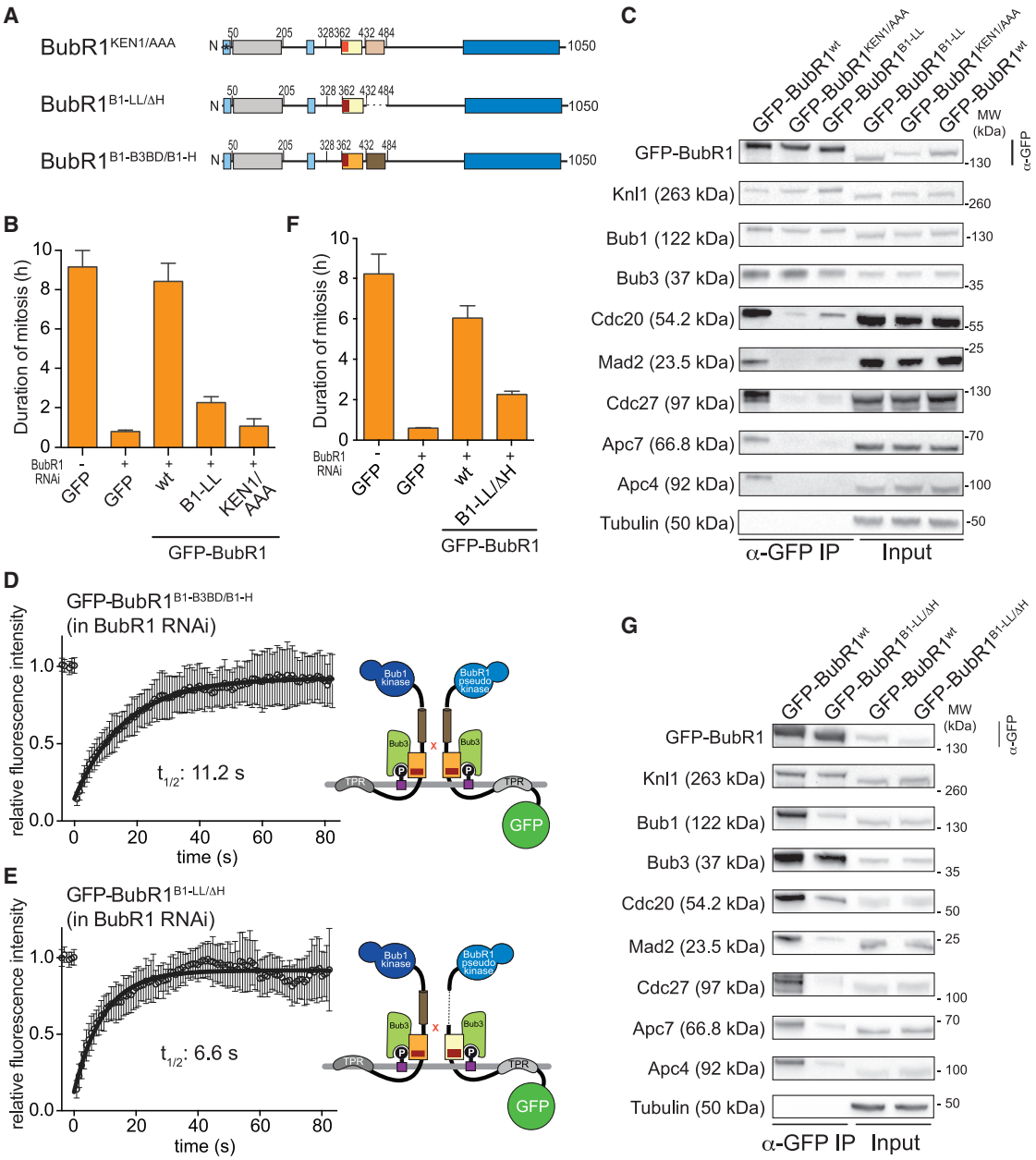

Figure 2. The Bub1 Loop Cannot Promote the SAC Function of BubR1 In Vivo

(A) Domain organization of the BubR1 constructs.

(B and F) Mean duration of mitosis of Flp-In T-REx stable cell lines expressing the indicated GFP-BubR1 constructs in the absence of endogenous BubR1 and in the presence of 50 nM nocodazole. Cell morphology was used to measure entry into and exit from mitosis by time-lapse microscopy ($n > 23$ for BubR1$^{B1\text{-}LL}$ and BubR1$^{KEN1/AAA}$ [B]; $n > 37$ for BubR1$^{B1\text{-}LL/\Delta H}$ [F] per cell line per experiment) from three independent experiments. Error bars depict SEM.

(C and G) Western blot of immunoprecipitates (IPs) from mitotic Flp-In T-REx cell lines expressing the indicated GFP-BubR1 constructs (BubR1$^{B1\text{-}LL}$ and BubR1$^{KEN1/AAA}$ [C]; BubR1$^{B1\text{-}LL/\Delta H}$ [G])showing that the replacement of the BubR1 loop with the Bub1 loop results in strongly impaired APC/C binding. Tubulin was used as loading control.

(D and E) FRAP analyses of GFP-tagged BubR1$^{B1\text{-}B3BD/B1\text{-}H}$ (D) and BubR1$^{B1\text{-}LL/\Delta H}$ (E) in absence of endogenous BubR1. Relevant recovery parameters are shown. The graphs show mean and SD. The cartoons beside the graphs depict the expected mode of kinetochore localization of each construct.

See also Figures S4 and S5 and Table S1.

localization depended on Bub1 (Figures 3B and 3C). In FRAP experiments, GFP-BubR1$^{\Delta LL}$ appeared to have a recovery halftime of 9.9 s (Figure 3D; Table S1), essentially identical to that of GFP-BubR1^{WT} (Figure 1G). These observations are consistent with our model that the BubR1 loop region is not required for kinetochore recruitment [60] (and this study).

Next, we asked whether GFP-BubR1$^{\Delta L}$ and GFP-BubR1$^{\Delta LL}$ were able to support the SAC in cells depleted of endogenous

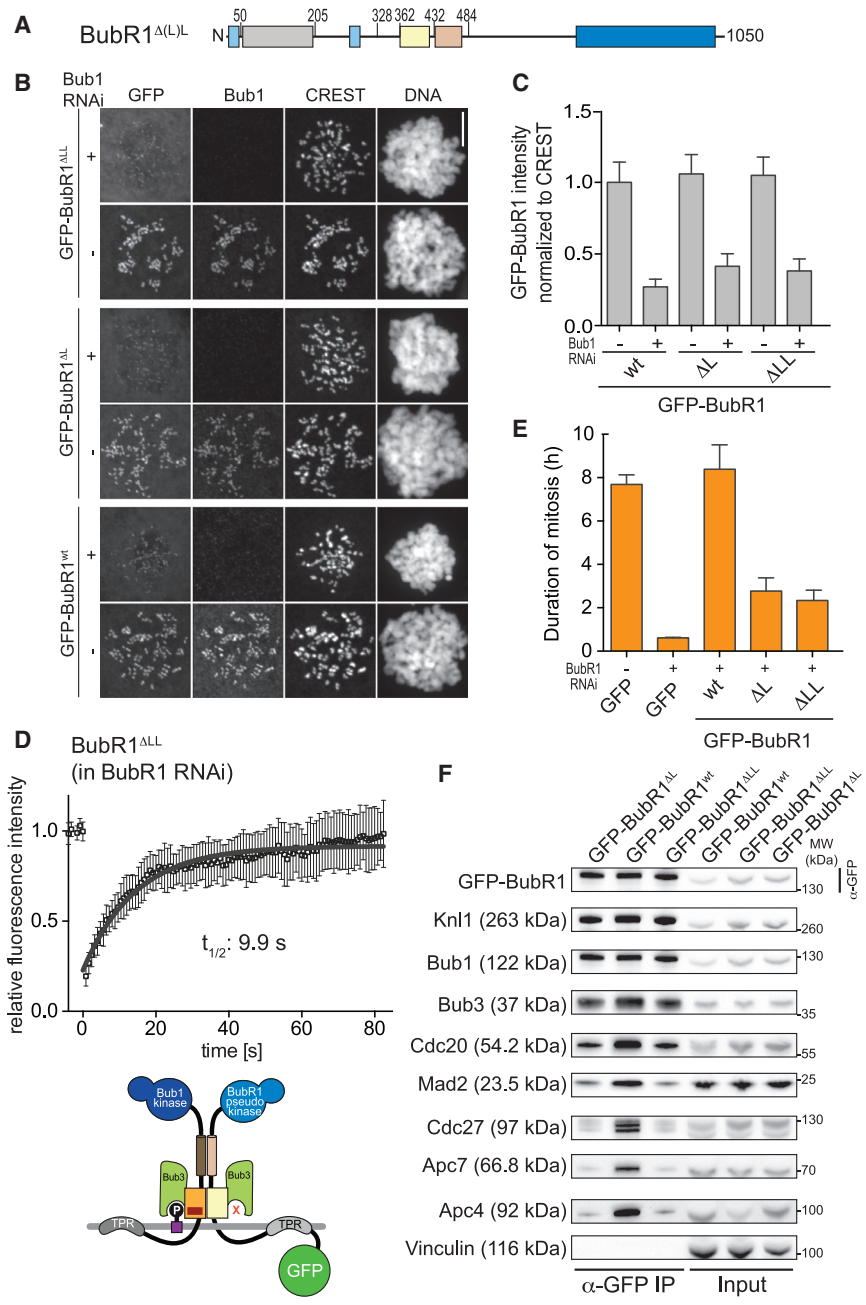

Figure 3. The BubR1 Loop Is Required for SAC Function In Vivo

(A) Domain organization of the BubR1 constructs used. Constructs lacking the short (L) and long loop (LL) versions were created by deleting residues 368–379 or 363–396 of BubR1, respectively.

(B) Representative images of HeLa cells transfected with the indicated GFP-BubR1 constructs in presence or absence of endogenous Bub1, showing that the lack of the loop does not influence kinetochore localization, as expected. Cells were treated as in Figure 1E. The scale bar represents 10 μm.

(C) Quantification of BubR1 kinetochore levels in cells treated as in (B). The graph shows mean intensity from three independent experiments. Error bars represent SEM. Values for $BubR1^{wt}$ in non-depleted cells are set to 1.

(D) FRAP analysis of $BubR1^{\Delta LL}$ in the absence of endogenous BubR1. Relevant recovery parameters are shown. The graph shows mean and SD. The cartoon depicts the expected mode of kinetochore localization of the construct.

(E) Mean duration of mitosis of Flp-In T-REx stable cell lines expressing the indicated GFP-BubR1 constructs in the absence of endogenous BubR1 and in the presence of 50 nM nocodazole. Cell morphology was used to measure entry into and exit from mitosis by time-lapse microscopy ($n > 32$ for $BubR1^{\Delta(L)L}$ per cell line per experiment) from two independent experiments. Error bars depict SEM.

(F) Western blot of IPs from mitotic Flp-In T-REx cell lines expressing the indicated GFP-BubR1 constructs showing that the lack of the BubR1 loop results in strongly impaired APC/C binding. Vinculin was used as loading control.

See also Figure S4 and Table S1.

The BubR1 Loop Promotes APC/C Binding

Collectively, these observations support the idea that the loop region of BubR1 is required for the recognition of crucial SAC target(s). To identify these targets, we used the SILAC (stable isotope labeling with amino acids in cell culture) [68] approach to perform quantitative IP and mass spectrometry identification of proteins bound to minimal reporter constructs in mitotic lysates of HeLa cells. Because the B3BD of Bub1 is sufficient for Bub3 binding and for recognition of Knl1-$MELT^{P}$ repeats [60], we started our analysis with a construct corresponding to $GFP\text{-}BubR1^{B3BD}$ (residues 362–431). We found that several of the APC/C subunits (blue squares, Figure 4A) were specifically enriched in the $GFP\text{-}BubR1^{B3BD}$ precipitates in comparison to those in the GFP control. We validated these interactions by western blotting against the APC/C subunits Cdc27/Apc3, Apc7, and Apc4 on $GFP\text{-}BubR1^{B3BD}$ precipitates (Figure 4B). In reciprocal IP experiments, we detected $GFP\text{-}BubR1^{B3BD}$ in complex with the APC/C subunit Cdc27 (Figure S6A).

BubR1. Both mutants were largely unable to restore the SAC function of BubR1 (Figure 3E). Furthermore, when we combined deletion of the loop with deletion of the helical region ($GFP\text{-}BubR1^{\Delta L/\Delta H}$; Figure S4H), we observed impairment of the SAC (Figure S4E), accompanied by reduced interaction with the APC/C (Figure S4I). In IP experiments, $GFP\text{-}BubR1^{\Delta L}$ and $GFP\text{-}BubR1^{\Delta LL}$ were shown to bind to the MCC subunits Mad2 and Cdc20, although at reduced levels in comparison to $GFP\text{-}BubR1^{WT}$, but were also largely impaired in their ability to interact with the APC/C, likely explaining why these mutants cannot support the SAC (Figure 3F; quantified in Figure S4J).

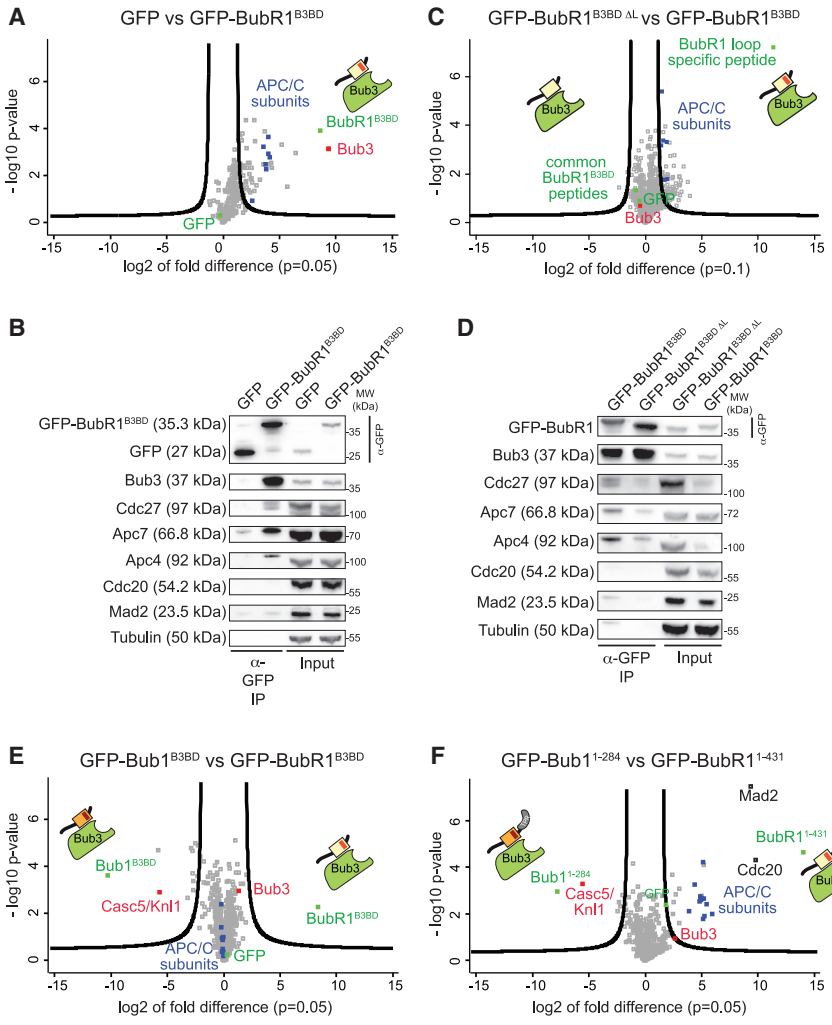

Figure 4. The BubR1 Loop Promotes APC/C Binding

(A and C) Volcano plot showing the results from three independent SILAC experiments using GFP and GFP-BubR1^{B3BD} (residues 362–431) (A) or GFP-BubR1$^{B3BD\ \Delta L}$ and GFP-BubR1^{B3BD} (C) as affinity resins to identify specific interaction partners in mitotic lysates showing that the BubR1 B3BD binds to the APC/C and that this depends on the BubR1 loop. A p value of 0.05 and 0.1 was used as cutoff for significance, respectively.

(B and D) Western blot of IPs from mitotic Flp-In T-REx cell lines expressing the indicated GFP-BubR1 constructs showing that the B3BD of BubR1 is able to pull down APC/C subunits (B) and that this interaction is impaired if the loop is deleted (D). Tubulin was used as loading control.

(E and F) Volcano plot showing the results from two (E) or three (F) independent SILAC experiments using GFP-Bub1^{B3BD} (residues 209–270) and GFP-BubR1^{B3BD} (E) or GFP-Bub1$^{1–284}$ and GFP-BubR1$^{1–431}$ (F) as affinity resins to identify specific interaction partners in mitotic lysates, showing that the BubR1 N-terminal region increases the specificity of the BubR1-APC/C interaction. A p value of 0.05 was used as cutoff for significance.

See also Figures S6 and S7.

Next, we compared the interactome of GFP-BubR1^{B3BD} with and without the loop region (Figure 4C). This showed that APC/C was enriched in precipitates of intact GFP-BubR1^{B3BD}, indicating that the loop promotes binding of the APC/C (Figure 4C). The role of the BubR1 loop on APC/C binding was recapitulated in a GFP-IP experiment followed by western blotting (Figure 4D; quantified in Figure S6B). Collectively, these results indicate that the BubR1 loop promotes an interaction of the GFP-BubR1^{B3BD}:Bub3 complex with the APC/C.

Our results also indicate that the B3BDs of Bub1 and BubR1 direct Bub3 to Knl1 and the APC/C, respectively. To corroborate this idea, we compared precipitates of GFP-Bub1^{B3BD} (residues 209–270) and GFP-BubR1^{B3BD} in another SILAC experiment (Figure 4E). In agreement with the hypothesis, Knl1 was clearly enriched in precipitates of GFP-Bub1^{B3BD}. On the other hand, we did not observe an enrichment of APC/C subunits with GFP-BubR1^{B3BD} in comparison to GFP-Bub1^{B3BD}. Instead, we found APC/C subunits to be strongly enriched in precipitates of both constructs (and therefore appearing in the middle of the volcano plot, together with Bub3). This result suggests that the B3BD of Bub1 can, in principle, interact both with Knl1 and with the APC/C, whereas that of BubR1 can only bind the APC/C.

Based on these observations, we asked whether the presence of longer segments of Bub1 and BubR1 would increase the selectivity for these substrates. GFP-Bub1$^{1–284}$ and GFP-BubR1$^{1–431}$ encompass the entire N-terminal region in addition to the B3BD, including the TPR repeats and, in case of BubR1, also its two KEN boxes, the first of which is essential for binding to Cdc20 and therefore incorporation into the MCC [42] (Figure 1A). In SILAC IP experiments, we observed that GFP-Bub1$^{1–284}$ and GFP-BubR1$^{1–431}$ have exquisite specificity for Knl1 and the APC/C, respectively. Furthermore, we also detected Mad2 and Cdc20 in the BubR1$^{1–431}$ IPs, likely because this BubR1 segment, which contains the KEN boxes, is sufficient for an interaction with these MCC subunits (Figure 4F). Thus, the selectivity of BubR1 for the APC/C results from a combination of factors, including, in addition to the KEN boxes, the BubR1 loop as a direct APC/C binder. This was further confirmed by examining IPs of constructs in which only the loop regions were swapped. GFP-Bub1$^{BR1\text{-}LL}$ and GFP-BubR1$^{B1\text{-}LL}$ were both unable to interact effectively with the APC/C (Figure S7A).

The BubR1 Loop Is Required for APC/C Inhibition In Vitro

We expressed recombinant versions of Bub3 complexes of a BubR1 segment (residues 1–571) that is larger than the minimal segment of BubR1 that can restore SAC function in BubR1-depleted cells [42, 69]. In the same scaffold, we also created the chimeric mutants BubR1$^{B1\text{-}LL}$ and BubR1$^{\Delta LL}$. We then purified the resulting protein complexes to homogeneity. In isolation, BubR1^{WT}:Bub3, BubR1$^{B1\text{-}LL}$:Bub3, and BubR1$^{\Delta LL}$:Bub3 shared

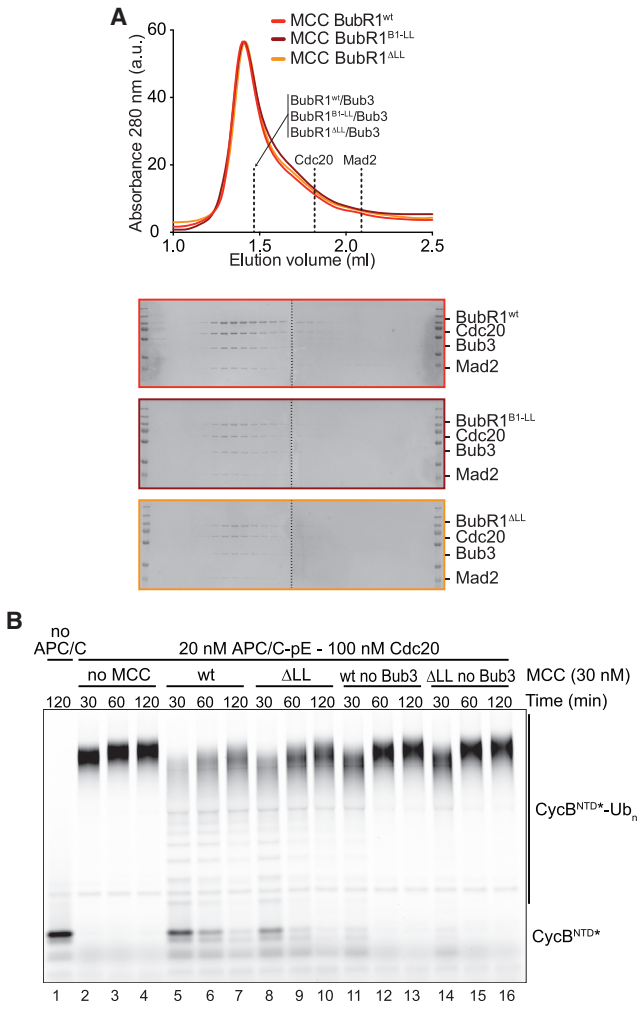

Figure 5. The BubR1 Loop Is Required for APC/C Inhibition In Vitro

(A) BubR1^{wt}:Bub3 as well as the two loop mutants BubR1$^{B1\text{-}LL}$:Bub3 and BubR1$^{\Delta LL}$:Bub3 interact in size exclusion chromatography with the other two MCC components Cdc20 and Mad2. In the chromatogram, the height of elution curves for the three different MCC complexes were rescaled to match that of MCC containing BubR1$^{\Delta LL}$, which emphasizes the remarkable similarity of the elution profiles, an indication that the different MCC complexes are structurally stable and virtually identical. Vertical dashed lines indicate the elution volumes of the individual constituents of the three MCC complexes. The corresponding elution profiles and SDS-PAGE analyses are shown in Figure S7B.

(B) Ubiquitination reactions in the presence of recombinant APC/C-pE (carrying 68 phospho-mimicking mutations) [70] and the fluorescently labeled N-terminal domain of cyclin B were analyzed by SDS-PAGE and fluorescence scanning. MCC containing BubR1$^{\Delta LL}$:Bub3 is less efficient in inhibiting APC/C cyclin B ubiquitination activity in comparison to MCC containing BubR1^{wt}:Bub3. Omitting Bub3 from MCC also reduces APC/C inhibition. NTD, N-terminal domain; Ub, ubiquitin.

See also Figures S6 and S7.

identical retention volumes in size exclusion chromatography experiments, attesting to their stability (Figure S7B). BubR1^{WT}:Bub3, BubR1$^{B1\text{-}LL}$:Bub3, and BubR1$^{\Delta LL}$:Bub3 also formed stoichiometric MCC complexes with Cdc20 and Mad2 with indistinguishable retention volumes (Figures 5A and S7B). We used a recently described in vitro assay to monitor assembly kinetics of MCC complexes containing BubR1$^{B1\text{-}LL}$:Bub3 and BubR1$^{\Delta LL}$:Bub3 [31] and found them to be identical to those of BubR1^{WT}:Bub3 (Figure S6C). Collectively, these observations indicate that the BubR1 loop is dispensable for MCC stability and assembly kinetics.

Therefore, we next tested the ability of MCC containing either BubR1^{WT}:Bub3 or BubR1$^{\Delta LL}$:Bub3 to inhibit APC/C activity in vitro by evaluating ubiquitination of the APC/C substrate cyclin B. For these assays, we used concentrations of MCC (30 nM), APC/C (20 nM), and Cdc20 (100 nM) that are considered physiological [31]. To obtain active APC/C, we used APC/C-pE, an APC/C mutant carrying 68 phosphomimetic mutations that activate APC/C [70]. Wild-type and mutant MCC complexes were allowed to assemble for 15 hr and were purified to homogeneity (Figure S6D). They were then added to APC/C^{Cdc20} (besides being an MCC subunit, Cdc20 also acts as an activator of APC/C), and the cyclin B ubiquitination reaction was initiated by addition of the E1 ubiquitin mix. Under these conditions, we observed near complete ubiquitination of cyclin B already within 30 min (Figure 5B, lanes 2–4). There was substantial inhibition of this reaction upon addition of wild-type MCC, which continued well into the 120 min time point (Figure 5B, lanes 5–7). MCC containing BubR1$^{\Delta LL}$:Bub3, on the other hand, clearly retained partial functionality but inhibited the cyclin B ubiquitination activity of APC/C less efficiently than the wild-type complex (Figure 5B; compare lanes 5–7 with lanes 8–10).

These observations argue that removal of the loop region of BubR1 causes a partial impairment of the ability of MCC to inhibit APC/C. Because our previous studies argue the loop region of Bub1 acts to modulate the binding affinity of Bub3 for phosphorylated MELT repeats [60] and our data so far suggest that this may hold true also for the BubR1 loop, we assembled MCCs with BubR1^{WT} or BubR1$^{\Delta LL}$ that lacked bound Bub3 and purified them to homogeneity. Importantly, the absence of Bub3 did not overtly impair MCC formation or stability (Figure S6D). Both MCC versions lacking Bub3 were less efficient in inhibiting APC/C cyclin B ubiquitination activity than MCC containing BubR1^{WT} bound to Bub3 and showed an even stronger defect than that of MCC containing BubR1$^{\Delta LL}$:Bub3 (Figure 5B, lanes 11–16).

Bub3 Is Required for Robust SAC Signaling

Collectively, these results show that Bub3 plays a role in APC/C inhibition and support the hypothesis that the BubR1 loop contributes to the regulation of this process. To test directly the role of Bub3 in MCC function, we examined the effects on the SAC of expressing BubR1 mutants impaired in their interaction with Bub3. Specifically, we deleted the complete B3BD (BubR1$^{\Delta B3BD}$) or introduced two point mutations in the B3BD that are known to prevent Bub3 binding (BubR1$^{E409K+E413K}$; Figure 6A) [40, 42]. Both mutants were unable to support the SAC in the absence of endogenous BubR1 (Figure 6B). Furthermore, BubR1 mutants defective in Bub3 binding were impaired in binding to APC/C subunits in IPs, similar to the BubR1$^{\Delta LL}$ mutant (Figure 6C; quantified in Figure 6D). Collectively, our data provide a strong indication that Bub3, in complex with BubR1, plays a role in the SAC and that the BubR1 loop region works by modulating the interaction of Bub3 with the APC/C.

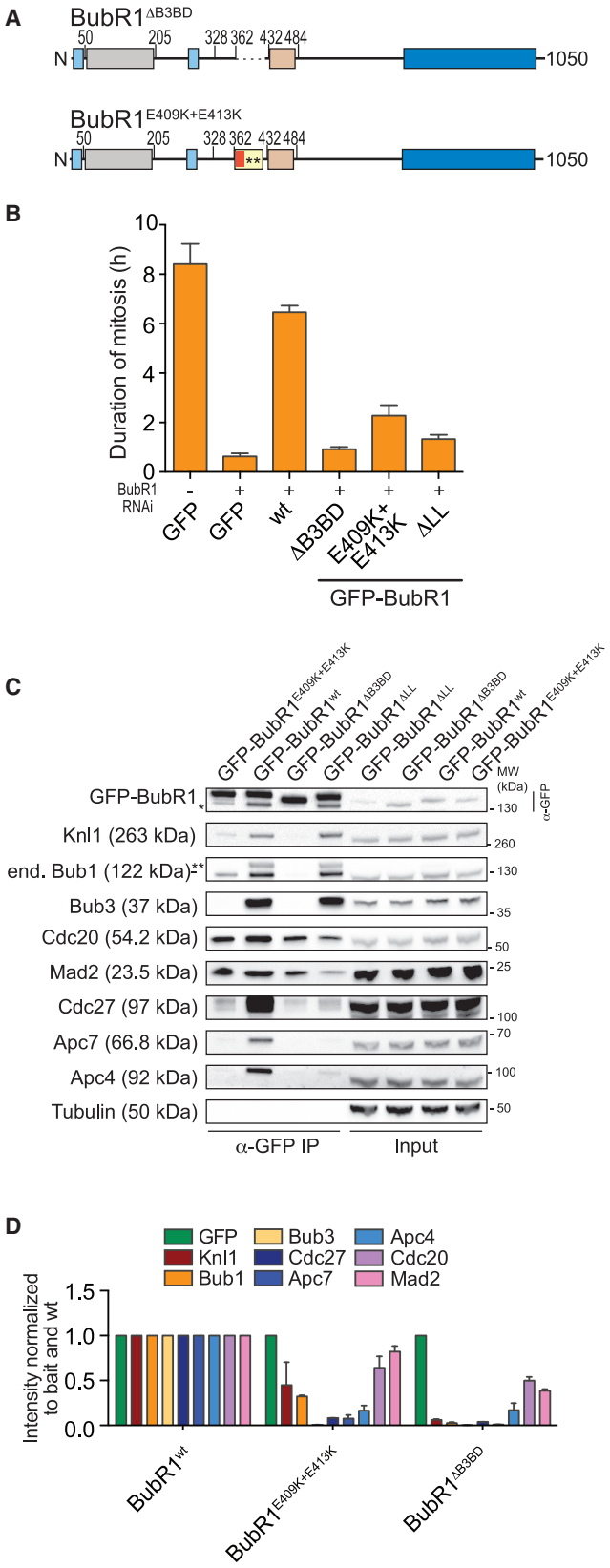

Figure 6. Bub3 Is Required for Robust SAC Signaling

(A) Domain organization of the BubR1 constructs used.

(B) Mean duration of mitosis of Flp-In T-REx stable cell lines expressing the indicated GFP-BubR1 constructs in the absence of endogenous BubR1 and in the presence of 50 nM nocodazole. Cell morphology was used to measure entry into and exit from mitosis by time-lapse microscopy ($n > 55$ per cell line per experiment) from two independent experiments. Error bars depict SEM.

(C) Western blot of IPs from mitotic Flp-In T-REx cell lines expressing the indicated GFP-BubR1 constructs showing a defect especially in binding to APC/C subunits if BubR1 cannot bind to Bub3. Tubulin was used as loading control. *, band resulting from previous incubation with Bub1 antibody; **, unspecific band recognized by the Bub1 antibody.

(D) Quantification of the western blot in Figure 6C. The amounts of co-precipitating proteins were normalized to the amount of GFP-BubR1 bait present in the IPs. Values for GFP-BubR1^{wt} are set to 1. The graph shows mean intensity of two independent experiments. Error bars represent SEM. See also Figure S4.

DISCUSSION

BubR1 is an essential component of the SAC effector, the MCC. Our understanding of the function of BubR1 in the SAC has been greatly facilitated by functional and structural studies on the MCC and of its interaction with APC/C. High-resolution structures of the APC/C^{MCC} complex [43, 46, 47] have offered an ideal framework to understand the molecular basis of the interaction of MCC with the APC/C, including the role of specific BubR1 sequences identified in previous studies [71], such as the KEN1 and KEN2 boxes and the more recently identified ABBA motifs [3, 39, 41–44, 72–77]. The overall picture emerging from these analyses is that a MCC core complex containing one copy each of BubR1, Bub3, Cdc20, and Mad2 binds a second Cdc20 molecule, possibly already bound to the APC/C [2, 44–47]. In the APC/C^{MCC} complex, BubR1 binds extensively to both Cdc20 subunits, stabilizes the interaction of Mad2 with one of the two Cdc20 subunits, and provides extensive contacts with the APC/C that reinforce its interaction with MCC [46, 47].

The SAC role of Bub3, a constitutive binding partner of BubR1 and Bub1, has remained more elusive. In most organisms, Bub3 forms constitutive complexes both with Bub1 and with BubR1 [57]. An exception is *Schizosaccharomyces pombe*, where the BubR1 ortholog Mad3 does not interact with Bub3 [43, 78]. The Bub1 and BubR1 paralogs perform distinct functions and have distinct localization patterns. Ablation of Bub3 affects the function of both paralogs, introducing a significant complication in the interpretation of the resulting mitotic defect. On the other hand, preventing the selective interaction of Bub1 or BubR1 with Bub3 by introducing point mutations in the Bub3 binding domains of Bub1 or BubR1 lends itself to the objection that these mutations, by disrupting an interaction with Bub3, might destabilize MCC or its interaction with the APC/C. To overcome these limitations, we took advantage of our previous structural analysis of the Bub1:Bub3:MELT^{P} ternary complex, which identified Bub3 as a phospho-amino acid adaptor and suggested that a region of Bub1, the loop, contributes to the binding affinity for phosphorylated targets [58]. Modifications of the Bub1 loop predictably alter the function of associated Bub3 [60], providing for the first time a clean handle to distinguish the mitotic functions of Bub1-associated and BubR1-associated Bub3 without a need to ablate Bub3 or its interactions with Bub1 or BubR1. In this study, we have taken advantage of this recent progress to test the role

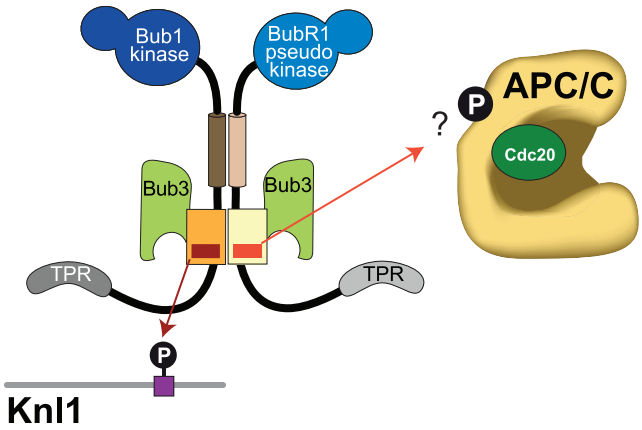

Figure 7. Model for the Differential Functions of the BubR1 and Bub1 Loop

Model showing the different functions of the loops in BubR1 and Bub1. Bub1 and BubR1 form a pseudo-symmetric heterodimer through the B3BDs and the helix as well as through the presence of Bub3. The loops are not involved in this interaction but serve different functions. The Bub1 loop enhances binding of the Bub1:Bub3 complex to Knl1-MELT^{P} motifs, which in turn recruits BubR1:Bub3 to kinetochores. The BubR1 loop, however, is not able to enhance such an interaction of Bub3 with Knl1 but instead seems to promote binding of BubR1:Bub3 to the APC/C. This is required for the SAC function of BubR1. We hypothesize that this interaction could work via modulation of Bub3 and be regulated in a phosphorylation-dependent manner, arguing that the BubR1 loop functions in analogy to the Bub1 loop.

of the BubR1 loop and discovered that it is essential for SAC function. Thus, our analysis identifies another short, crucial sequence determinant of BubR1 function in the SAC response.

Previously, it was proposed that Bub3 acts as a catalytic enhancer of the BubR1:Cdc20 interaction at kinetochores and in the cytosol [77]. The moderate stimulation by Bub3 of MCC-dependent APC/C inhibition was interpreted in light of this possible catalytic effect of Bub3 [77]. This alternative hypothesis, however, is at odds with our recent demonstration that the interaction of Mad2 with Cdc20 is the sole rate-limiting step of MCC assembly [31].

Our interpretation of the role of Bub3 is rather that it contributes, thanks to modulation by the BubR1 loop motif, to the binding affinity of the MCC for the APC/C. Recombinant loop mutants (BubR1$^{B1\text{-}LL}$ and BubR1$^{\Delta LL}$) engaged in stable MCC complexes with Mad2, Cdc20, and Bub3 in vitro, which assembled with rates identical to those observed with wild-type BubR1. Thus, it is unlikely that the SAC defect observed with these mutants reflects a problem in MCC assembly. In vitro cyclin B ubiquitination assays showed that BubR1 lacking the loop is less efficient in inhibiting APC/C than BubR1^{WT}, and this correlates with a loss of APC/C binding affinity in vivo. Two Bub3-binding defective BubR1 mutants (BubR1$^{\Delta B3BD}$ and BubR1$^{E409K+E413K}$) showed the same SAC defect phenotype described for the loop mutants. Their binding to APC/C subunits in coIPs was also impaired.

Phosphorylation of a loop of Apc1 promotes binding of Cdc20 and APC/C activation [70, 79–84]. Similarly, phosphorylation may regulate SAC-dependent inhibition of APC/C. Bub3 is an adaptor protein for phosphorylated motifs, and in complex with Bub1 (through the contribution of the Bub1 loop), it binds to phosphorylated MELT repeats of Knl1 [58, 60]. In analogy to the Bub1 loop, we suspect that the BubR1 loop contributes to the recognition of a phosphorylated motif on the APC/C by Bub3 (Figure 7) [2]. Bub3 (with the help of the BubR1 loop) might be expected to bind sequences related to the MELT^{P} motifs of Knl1. Two such motifs, with sequences MEVT and MELT, exist, respectively, in the Apc4 (residues 116–119) and Apc5 (residues 175–178) subunits of the APC/C, and at least T178^{Apc5} is phosphorylated during mitosis [70]. Furthermore, T178^{Apc5} and S179^{Apc5} are part of the pool of putative phosphomimetic mutations in the APC/C pE sample. We created a new APC/C mutant (APC/C pE-3A; Figure S6D) carrying alanine mutations at T119^{Apc4}, T178^{Apc5}, and S179^{Apc5} and asked whether mutation of these putative Bub3 target motifs in APC/C weakened the sensitivity of APC/C to wild-type MCC, phenocopying the removal of the BubR1 loop. However, APC/C pE-3A remained as sensitive to MCC as APC/C pE, suggesting that phosphorylation of these residues is not important for MCC inhibition or that the penetrance of the phosphomimetic mutations is limited (Figure S6E).

The identification of the relevant phospho-epitopes and of the kinase that generates them is therefore an important priority for future studies. Likely, this will be a challenging task, because the 1.2-MDa APC/C particle is highly phosphorylated in mitosis by several kinases, including Plk1 and Cdk1 [81, 85]. Furthermore, the structural analysis of the APC/C^{MCC} complex offers only limited insight into this specific question, because both Bub3 and the segment of BubR1 that binds to it (the B3BD) were invisible in the structures of APC/C^{MCC} [46, 47].

Our analysis of the role of the BubR1 and Bub1 loop led us to revisit the issue of the molecular basis of kinetochore localization and turnover of Bub1 and BubR1. The main conclusions from this analysis are completely consistent with the model that the B3BD of Bub1 is sufficient for kinetochore localization, whereas that of BubR1 is not. Our analysis tested all major predictions of the model, providing a complete account of the mechanism of Bub1 and BubR1 recruitment to kinetochores. It has recently been proposed that a small autonomous pool of BubR1 can localize to kinetochores in a Bub1-independent fashion to perform its function in the SAC [86]. However, we suspect that this pool of kinetochore BubR1 results from the availability of a high concentration of free MELT^{P} motifs after artificial Bub1 depletion [60, 86]. We show here that BubR1 mutants deprived of the helical domain that mediates robust kinetochore recruitment of BubR1 are SAC proficient and that further mutation of the loop disrupts this SAC function. Finally, the BubR1 loop deletion mutants we have tested localize normally to kinetochores but are entirely SAC defective, clearly showing that the deleterious effects of loop mutations on the SAC are uncorrelated with kinetochore localization of BubR1. In certain organisms, like *C. elegans* and *S. cerevisiae*, the BubR1 ortholog Mad3 may not even be able to localize to kinetochores [62, 87]. The significance of kinetochore recruitment of BubR1 remains therefore an open question for future studies.

In conclusion, our studies illustrate how the divergence of two paralogs resulted in the emergence of motifs that modulate the binding affinity of a phosphopeptide-recognition module to allow binding to distinct binding partners, a vivid example of sub-functionalization. The evolutionary forces that drove the specific sub-functionalization of Bub and Mad proteins, however, remain uncertain [88] and an interesting subject for future studies.

STAR★METHODS

Detailed methods are provided in the online version of this paper and include the following:

- KEY RESOURCES TABLE
- CONTACT FOR REAGENT AND RESOURCE SHARING
- EXPERIMENTAL MODEL AND SUBJECT DETAILS
- METHOD DETAILS
  - Mammalian plasmids
  - Cell culture and transfection
  - Immunoprecipitation and immunoblotting
  - SILAC and mass spectrometry
  - Live cell imaging
  - Fluorescence recovery after photobleaching
  - Immunofluorescence
  - Protein expression and purification
  - Size-exclusion chromatography mobility shift assay
  - MCC assembly kinetics
  - APC/C-mediated ubiquitination assays
- QUANTIFICATION AND STATISTICAL ANALYSES
- DATA AND SOFTWARE AVAILABILITY

SUPPLEMENTAL INFORMATION

Supplemental Information includes seven figures, one table, and one data file and can be found with this article online at http://dx.doi.org/10.1016/j.cub.2017.08.033.

AUTHOR CONTRIBUTIONS

K.O. carried out all cell-biology-based work, including checkpoint assays, immunoprecipitations, immunofluorescence, and data analyses. K.O. and A.C.F. carried out biochemical analyses and experiments with FRET sensor. I.P. contributed unpublished reagents. K.O., F.M., and T.B. carried out SILAC-mass spectrometry experiments. K.O. and S.M. performed and analyzed FRAP experiments. F.W. and J.-M.P. contributed experiments with purified APC/C. K.O. and A.M. conceived the work, prepared the figures, and wrote the paper with contributions from all authors. A.M. coordinated the working team.

ACKNOWLEDGMENTS

We thank the members of the Musacchio laboratory for helpful comments and discussions. A.M. acknowledges funding from the European Research Council (ERC) AdG RECEPIANCE (669686) and the DFG Collaborative Research Centre (CRC) 1093. Research in the lab of J.-M.P. was supported by Boehringer Ingelheim, the Austrian Science Fund (Wittgenstein award Z196-B20) and the Austrian Research Promotion Agency (headquarter grant FFG-852936).

Received: May 5, 2017
Revised: July 16, 2017
Accepted: August 15, 2017
Published: September 21, 2017

REFERENCES

1. Lara-Gonzalez, P., Westhorpe, F.G., and Taylor, S.S. (2012). The spindle assembly checkpoint. Curr. Biol. *22*, R966–R980.
2. Musacchio, A. (2015). The molecular biology of spindle assembly checkpoint signaling dynamics. Curr. Biol. *25*, R1002–R1018.
3. Tromer, E., Bade, D., Snel, B., and Kops, G.J. (2016). Phylogenomics-guided discovery of a novel conserved cassette of short linear motifs in BubR1 essential for the spindle checkpoint. Open Biol. *6*, 160315.
4. Suijkerbuijk, S.J., van Dam, T.J., Karagöz, G.E., von Castelmur, E., Hubner, N.C., Duarte, A.M., Vleugel, M., Perrakis, A., Rüdiger, S.G., Snel, B., and Kops, G.J. (2012). The vertebrate mitotic checkpoint protein BUBR1 is an unusual pseudokinase. Dev. Cell *22*, 1321–1329.
5. Krenn, V., Wehenkel, A., Li, X., Santaguida, S., and Musacchio, A. (2012). Structural analysis reveals features of the spindle checkpoint kinase Bub1-kinetochore subunit Knl1 interaction. J. Cell Biol. *196*, 451–467.
6. Kiyomitsu, T., Obuse, C., and Yanagida, M. (2007). Human Blinkin/AF15q14 is required for chromosome alignment and the mitotic checkpoint through direct interaction with Bub1 and BubR1. Dev. Cell *13*, 663–676.
7. Krenn, V., Overlack, K., Primorac, I., van Gerwen, S., and Musacchio, A. (2014). KI motifs of human Knl1 enhance assembly of comprehensive spindle checkpoint complexes around MELT repeats. Curr Biol. *24*, 29–39.
8. Kang, J., Yang, M., Li, B., Qi, W., Zhang, C., Shokat, K.M., Tomchick, D.R., Machius, M., and Yu, H. (2008). Structure and substrate recruitment of the human spindle checkpoint kinase Bub1. Mol. Cell *32*, 394–405.
9. Fernius, J., and Hardwick, K.G. (2007). Bub1 kinase targets Sgo1 to ensure efficient chromosome biorientation in budding yeast mitosis. PLoS Genet. *3*, e213.
10. Kawashima, S.A., Yamagishi, Y., Honda, T., Ishiguro, K., and Watanabe, Y. (2010). Phosphorylation of H2A by Bub1 prevents chromosomal instability through localizing shugoshin. Science *327*, 172–177.
11. Klebig, C., Korinth, D., and Meraldi, P. (2009). Bub1 regulates chromosome segregation in a kinetochore-independent manner. J. Cell Biol. *185*, 841–858.
12. Perera, D., Tilston, V., Hopwood, J.A., Barchi, M., Boot-Handford, R.P., and Taylor, S.S. (2007). Bub1 maintains centromeric cohesion by activation of the spindle checkpoint. Dev. Cell *13*, 566–579.
13. Ricke, R.M., Jeganathan, K.B., Malureanu, L., Harrison, A.M., and van Deursen, J.M. (2012). Bub1 kinase activity drives error correction and mitotic checkpoint control but not tumor suppression. J. Cell Biol. *199*, 931–949.
14. Sharp-Baker, H., and Chen, R.H. (2001). Spindle checkpoint protein Bub1 is required for kinetochore localization of Mad1, Mad2, Bub3, and CENP-E, independently of its kinase activity. J. Cell Biol. *153*, 1239–1250.
15. Liu, H., Rankin, S., and Yu, H. (2013). Phosphorylation-enabled binding of SGO1-PP2A to cohesin protects sororin and centromeric cohesion during mitosis. Nat. Cell Biol. *15*, 40–49.
16. Liu, H., Jia, L., and Yu, H. (2013). Phospho-H2A and cohesin specify distinct tension-regulated Sgo1 pools at kinetochores and inner centromeres. Curr. Biol. *23*, 1927–1933.
17. Yamagishi, Y., Honda, T., Tanno, Y., and Watanabe, Y. (2010). Two histone marks establish the inner centromere and chromosome bi-orientation. Science *330*, 239–243.
18. Boyarchuk, Y., Salic, A., Dasso, M., and Arnaoutov, A. (2007). Bub1 is essential for assembly of the functional inner centromere. J. Cell Biol. *176*, 919–928.
19. Brady, D.M., and Hardwick, K.G. (2000). Complex formation between Mad1p, Bub1p and Bub3p is crucial for spindle checkpoint function. Curr. Biol. *10*, 675–678.
20. Chen, R.H. (2002). BubR1 is essential for kinetochore localization of other spindle checkpoint proteins and its phosphorylation requires Mad1. J. Cell Biol. *158*, 487–496.
21. Johnson, V.L., Scott, M.I., Holt, S.V., Hussein, D., and Taylor, S.S. (2004). Bub1 is required for kinetochore localization of BubR1, Cenp-E, Cenp-F and Mad2, and chromosome congression. J. Cell Sci. *117*, 1577–1589.
22. Meraldi, P., and Sorger, P.K. (2005). A dual role for Bub1 in the spindle checkpoint and chromosome congression. EMBO J. *24*, 1621–1633.
23. Rischitor, P.E., May, K.M., and Hardwick, K.G. (2007). Bub1 is a fission yeast kinetochore scaffold protein, and is sufficient to recruit other spindle checkpoint proteins to ectopic sites on chromosomes. PLoS ONE *2*, e1342.

24. Vigneron, S., Prieto, S., Bernis, C., Labbé, J.C., Castro, A., and Lorca, T. (2004). Kinetochore localization of spindle checkpoint proteins: who controls whom? Mol. Biol. Cell *15*, 4584–4596.

25. Kruse, T., Larsen, M.S., Sedgwick, G.G., Sigurdsson, J.O., Streicher, W., Olsen, J.V., and Nilsson, J. (2014). A direct role of Mad1 in the spindle assembly checkpoint beyond Mad2 kinetochore recruitment. EMBO Rep. *15*, 282–290.

26. Heinrich, S., Sewart, K., Windecker, H., Langegger, M., Schmidt, N., Hustedt, N., and Hauf, S. (2014). Mad1 contribution to spindle assembly checkpoint signalling goes beyond presenting Mad2 at kinetochores. EMBO Rep. *15*, 291–298.

27. Han, J.S., Holland, A.J., Fachinetti, D., Kulukian, A., Cetin, B., and Cleveland, D.W. (2013). Catalytic assembly of the mitotic checkpoint inhibitor BubR1-Cdc20 by a Mad2-induced functional switch in Cdc20. Mol. Cell *51*, 92–104.

28. Mora-Santos, M.D., Hervas-Aguilar, A., Sewart, K., Lancaster, T.C., Meadows, J.C., and Millar, J.B. (2016). Bub3-Bub1 binding to Spc7/KNL1 toggles the spindle checkpoint switch by licensing the interaction of Bub1 with Mad1-Mad2. Curr. Biol. *26*, 2642–2650.

29. London, N., and Biggins, S. (2014). Mad1 kinetochore recruitment by Mps1-mediated phosphorylation of Bub1 signals the spindle checkpoint. Genes Dev. *28*, 140–152.

30. De Antoni, A., Pearson, C.G., Cimini, D., Canman, J.C., Sala, V., Nezi, L., Mapelli, M., Sironi, L., Faretta, M., Salmon, E.D., and Musacchio, A. (2005). The Mad1/Mad2 complex as a template for Mad2 activation in the spindle assembly checkpoint. Curr. Biol. *15*, 214–225.

31. Faesen, A.C., Thanasoula, M., Maffini, S., Breit, C., Müller, F., van Gerwen, S., Bange, T., and Musacchio, A. (2017). Basis of catalytic assembly of the mitotic checkpoint complex. Nature *542*, 498–502.

32. Ji, Z., Gao, H., Jia, L., Li, B., and Yu, H. (2017). A sequential multi-target Mps1 phosphorylation cascade promotes spindle checkpoint signaling. eLife *6*, e22513.

33. Overlack, K., Krenn, V., and Musacchio, A. (2014). When Mad met Bub. EMBO Rep. *15*, 326–328.

34. Yuan, I., Leontiou, I., Amin, P., May, K.M., Soper Ní Chafraidh, S., Zlámalová, E., and Hardwick, K.G. (2017). Generation of a spindle checkpoint arrest from synthetic signaling assemblies. Curr. Biol. *27*, 137–143.

35. Moyle, M.W., Kim, T., Hattersley, N., Espeut, J., Cheerambathur, D.K., Oegema, K., and Desai, A. (2014). A Bub1-Mad1 interaction targets the Mad1-Mad2 complex to unattached kinetochores to initiate the spindle checkpoint. J. Cell Biol. *204*, 647–657.

36. Hardwick, K.G., Johnston, R.C., Smith, D.L., and Murray, A.W. (2000). MAD3 encodes a novel component of the spindle checkpoint which interacts with Bub3p, Cdc20p, and Mad2p. J. Cell Biol. *148*, 871–882.

37. Sudakin, V., Chan, G.K., and Yen, T.J. (2001). Checkpoint inhibition of the APC/C in HeLa cells is mediated by a complex of BUBR1, BUB3, CDC20, and MAD2. J. Cell Biol. *154*, 925–936.

38. Fraschini, R., Beretta, A., Sironi, L., Musacchio, A., Lucchini, G., and Piatti, S. (2001). Bub3 interaction with Mad2, Mad3 and Cdc20 is mediated by WD40 repeats and does not require intact kinetochores. EMBO J. *20*, 6648–6659.

39. Burton, J.L., and Solomon, M.J. (2007). Mad3p, a pseudosubstrate inhibitor of APCCdc20 in the spindle assembly checkpoint. Genes Dev. *21*, 655–667.

40. Elowe, S., Dulla, K., Uldschmid, A., Li, X., Dou, Z., and Nigg, E.A. (2010). Uncoupling of the spindle-checkpoint and chromosome-congression functions of BubR1. J. Cell Sci. *123*, 84–94.

41. King, E.M., van der Sar, S.J., and Hardwick, K.G. (2007). Mad3 KEN boxes mediate both Cdc20 and Mad3 turnover, and are critical for the spindle checkpoint. PLoS ONE *2*, e342.

42. Lara-Gonzalez, P., Scott, M.I., Diez, M., Sen, O., and Taylor, S.S. (2011). BubR1 blocks substrate recruitment to the APC/C in a KEN-box-dependent manner. J. Cell Sci. *124*, 4332–4345.

43. Chao, W.C., Kulkarni, K., Zhang, Z., Kong, E.H., and Barford, D. (2012). Structure of the mitotic checkpoint complex. Nature *484*, 208–213.

44. Izawa, D., and Pines, J. (2015). The mitotic checkpoint complex binds a second CDC20 to inhibit active APC/C. Nature *517*, 631–634.

45. Primorac, I., and Musacchio, A. (2013). Panta rhei: the APC/C at steady state. J. Cell Biol. *201*, 177–189.

46. Alfieri, C., Chang, L., Zhang, Z., Yang, J., Maslen, S., Skehel, M., and Barford, D. (2016). Molecular basis of APC/C regulation by the spindle assembly checkpoint. Nature *536*, 431–436.

47. Yamaguchi, M., VanderLinden, R., Weissmann, F., Qiao, R., Dube, P., Brown, N.G., Haselbach, D., Zhang, W., Sidhu, S.S., Peters, J.M., et al. (2016). Cryo-EM of mitotic checkpoint complex-bound APC/C reveals reciprocal and conformational regulation of ubiquitin ligation. Mol. Cell *63*, 593–607.

48. Foley, E.A., Maldonado, M., and Kapoor, T.M. (2011). Formation of stable attachments between kinetochores and microtubules depends on the B56-PP2A phosphatase. Nat. Cell Biol. *13*, 1265–1271.

49. Kruse, T., Zhang, G., Larsen, M.S., Lischetti, T., Streicher, W., Kragh Nielsen, T., Bjørn, S.P., and Nilsson, J. (2013). Direct binding between BubR1 and B56-PP2A phosphatase complexes regulate mitotic progression. J. Cell Sci. *126*, 1086–1092.

50. Suijkerbuijk, S.J., Vleugel, M., Teixeira, A., and Kops, G.J. (2012). Integration of kinase and phosphatase activities by BUBR1 ensures formation of stable kinetochore-microtubule attachments. Dev. Cell *23*, 745–755.

51. Xu, P., Raetz, E.A., Kitagawa, M., Virshup, D.M., and Lee, S.H. (2013). BUBR1 recruits PP2A via the B56 family of targeting subunits to promote chromosome congression. Biol. Open *2*, 479–486.

52. Espert, A., Uluocak, P., Bastos, R.N., Mangat, D., Graab, P., and Gruneberg, U. (2014). PP2A-B56 opposes Mps1 phosphorylation of Knl1 and thereby promotes spindle assembly checkpoint silencing. J. Cell Biol. *206*, 833–842.

53. Shepperd, L.A., Meadows, J.C., Sochaj, A.M., Lancaster, T.C., Zou, J., Buttrick, G.J., Rappsilber, J., Hardwick, K.G., and Millar, J.B. (2012). Phosphodependent recruitment of Bub1 and Bub3 to Spc7/KNL1 by Mph1 kinase maintains the spindle checkpoint. Curr. Biol. *22*, 891–899.

54. London, N., Ceto, S., Ranish, J.A., and Biggins, S. (2012). Phosphoregulation of Spc105 by Mps1 and PP1 regulates Bub1 localization to kinetochores. Curr. Biol. *22*, 900–906.

55. Yamagishi, Y., Yang, C.H., Tanno, Y., and Watanabe, Y. (2012). MPS1/Mph1 phosphorylates the kinetochore protein KNL1/Spc7 to recruit SAC components. Nat. Cell Biol. *14*, 746–752.

56. Logarinho, E., Resende, T., Torres, C., and Bousbaa, H. (2008). The human spindle assembly checkpoint protein Bub3 is required for the establishment of efficient kinetochore-microtubule attachments. Mol. Biol. Cell *19*, 1798–1813.

57. Taylor, S.S., Ha, E., and McKeon, F. (1998). The human homologue of Bub3 is required for kinetochore localization of Bub1 and a Mad3/Bub1-related protein kinase. J. Cell Biol. *142*, 1–11.

58. Primorac, I., Weir, J.R., Chiroli, E., Gross, F., Hoffmann, I., van Gerwen, S., Ciliberto, A., and Musacchio, A. (2013). Bub3 reads phosphorylated MELT repeats to promote spindle assembly checkpoint signaling. eLife *2*, e01030.

59. Larsen, N.A., Al-Bassam, J., Wei, R.R., and Harrison, S.C. (2007). Structural analysis of Bub3 interactions in the mitotic spindle checkpoint. Proc. Natl. Acad. Sci. USA *104*, 1201–1206.

60. Overlack, K., Primorac, I., Vleugel, M., Krenn, V., Maffini, S., Hoffmann, I., Kops, G.J., and Musacchio, A. (2015). A molecular basis for the differential roles of Bub1 and BubR1 in the spindle assembly checkpoint. eLife *4*, e05269.

61. Vanoosthuyse, V., Valsdottir, R., Javerzat, J.P., and Hardwick, K.G. (2004). Kinetochore targeting of fission yeast Mad and Bub proteins is essential for spindle checkpoint function but not for all chromosome segregation roles of Bub1p. Mol. Cell. Biol. *24*, 9786–9801.

62. Gillett, E.S., Espelin, C.W., and Sorger, P.K. (2004). Spindle checkpoint proteins and chromosome-microtubule attachment in budding yeast. J. Cell Biol. *164*, 535–546.

63. Millband, D.N., and Hardwick, K.G. (2002). Fission yeast Mad3p is required for Mad2p to inhibit the anaphase-promoting complex and localizes to kinetochores in a Bub1p-, Bub3p-, and Mph1p-dependent manner. Mol. Cell. Biol. *22*, 2728–2742.

64. Howell, B.J., Moree, B., Farrar, E.M., Stewart, S., Fang, G., and Salmon, E.D. (2004). Spindle checkpoint protein dynamics at kinetochores in living cells. Curr. Biol. *14*, 953–964.

65. Shah, J.V., Botvinick, E., Bonday, Z., Furnari, F., Berns, M., and Cleveland, D.W. (2004). Dynamics of centromere and kinetochore proteins; implications for checkpoint signaling and silencing. Curr. Biol. *14*, 942–952.

66. Vleugel, M., Omerzu, M., Groenewold, V., Hadders, M.A., Lens, S.M., and Kops, G.J. (2015). Sequential multisite phospho-regulation of KNL1-BUB3 interfaces at mitotic kinetochores. Mol. Cell *57*, 824–835.

67. Asghar, A., Lajeunesse, A., Dulla, K., Combes, G., Thebault, P., Nigg, E.A., and Elowe, S. (2015). Bub1 autophosphorylation feeds back to regulate kinetochore docking and promote localized substrate phosphorylation. Nat. Commun. *6*, 8364.

68. Ong, S.E., Blagoev, B., Kratchmarova, I., Kristensen, D.B., Steen, H., Pandey, A., and Mann, M. (2002). Stable isotope labeling by amino acids in cell culture, SILAC, as a simple and accurate approach to expression proteomics. Mol. Cell. Proteomics *1*, 376–386.

69. Malureanu, L.A., Jeganathan, K.B., Hamada, M., Wasilewski, L., Davenport, J., and van Deursen, J.M. (2009). BubR1 N terminus acts as a soluble inhibitor of cyclin B degradation by APC/C(Cdc20) in interphase. Dev. Cell *16*, 118–131.

70. Qiao, R., Weissmann, F., Yamaguchi, M., Brown, N.G., VanderLinden, R., Imre, R., Jarvis, M.A., Brunner, M.R., Davidson, I.F., Litos, G., et al. (2016). Mechanism of APC/CCDC20 activation by mitotic phosphorylation. Proc. Natl. Acad. Sci. USA *113*, E2570–E2578.

71. Davey, N.E., and Morgan, D.O. (2016). Building a regulatory network with short linear sequence motifs: lessons from the degrons of the anaphase-promoting complex. Mol. Cell *64*, 12–23.

72. Lu, D., Hsiao, J.Y., Davey, N.E., Van Voorhis, V.A., Foster, S.A., Tang, C., and Morgan, D.O. (2014). Multiple mechanisms determine the order of APC/C substrate degradation in mitosis. J. Cell Biol. *207*, 23–39.

73. Diaz-Martinez, L.A., Tian, W., Li, B., Warrington, R., Jia, L., Brautigam, C.A., Luo, X., and Yu, H. (2015). The Cdc20-binding Phe box of the spindle checkpoint protein BubR1 maintains the mitotic checkpoint complex during mitosis. J. Biol. Chem. *290*, 2431–2443.

74. Di Fiore, B., Davey, N.E., Hagting, A., Izawa, D., Mansfeld, J., Gibson, T.J., and Pines, J. (2015). The ABBA motif binds APC/C activators and is shared by APC/C substrates and regulators. Dev. Cell *32*, 358–372.

75. Di Fiore, B., Wurzenberger, C., Davey, N.E., and Pines, J. (2016). The mitotic checkpoint complex requires an evolutionary conserved cassette to bind and inhibit active APC/C. Mol. Cell *64*, 1144–1153.

76. Lischetti, T., Zhang, G., Sedgwick, G.G., Bolanos-Garcia, V.M., and Nilsson, J. (2014). The internal Cdc20 binding site in BubR1 facilitates both spindle assembly checkpoint signalling and silencing. Nat. Commun. *5*, 5563.

77. Han, J.S., Vitre, B., Fachinetti, D., and Cleveland, D.W. (2014). Bimodal activation of BubR1 by Bub3 sustains mitotic checkpoint signaling. Proc. Natl. Acad. Sci. USA *111*, E4185–E4193.

78. Sczaniecka, M., Feoktistova, A., May, K.M., Chen, J.S., Blyth, J., Gould, K.L., and Hardwick, K.G. (2008). The spindle checkpoint functions of Mad3 and Mad2 depend on a Mad3 KEN box-mediated interaction with Cdc20-anaphase-promoting complex (APC/C). J. Biol. Chem. *283*, 23039–23047.

79. Fujimitsu, K., Grimaldi, M., and Yamano, H. (2016). Cyclin-dependent kinase 1-dependent activation of APC/C ubiquitin ligase. Science *352*, 1121–1124.

80. Zhang, S., Chang, L., Alfieri, C., Zhang, Z., Yang, J., Maslen, S., Skehel, M., and Barford, D. (2016). Molecular mechanism of APC/C activation by mitotic phosphorylation. Nature *533*, 260–264.

81. Kraft, C., Herzog, F., Gieffers, C., Mechtler, K., Hagting, A., Pines, J., and Peters, J.M. (2003). Mitotic regulation of the human anaphase-promoting complex by phosphorylation. EMBO J. *22*, 6598–6609.

82. Kramer, E.R., Scheuringer, N., Podtelejnikov, A.V., Mann, M., and Peters, J.M. (2000). Mitotic regulation of the APC activator proteins CDC20 and CDH1. Mol. Biol. Cell *11*, 1555–1569.

83. Golan, A., Yudkovsky, Y., and Hershko, A. (2002). The cyclin-ubiquitin ligase activity of cyclosome/APC is jointly activated by protein kinases Cdk1-cyclin B and Plk. J. Biol. Chem. *277*, 15552–15557.

84. Shteinberg, M., Protopopov, Y., Listovsky, T., Brandeis, M., and Hershko, A. (1999). Phosphorylation of the cyclosome is required for its stimulation by Fizzy/cdc20. Biochem. Biophys. Res. Commun. *260*, 193–198.

85. Herzog, F., Mechtler, K., and Peters, J.M. (2005). Identification of cell cycle-dependent phosphorylation sites on the anaphase-promoting complex/cyclosome by mass spectrometry. Methods Enzymol. *398*, 231–245.

86. Zhang, G., Mendez, B.L., Sedgwick, G.G., and Nilsson, J. (2016). Two functionally distinct kinetochore pools of BubR1 ensure accurate chromosome segregation. Nat. Commun. *7*, 12256.

87. Essex, A., Dammermann, A., Lewellyn, L., Oegema, K., and Desai, A. (2009). Systematic analysis in *Caenorhabditis elegans* reveals that the spindle checkpoint is composed of two largely independent branches. Mol. Biol. Cell *20*, 1252–1267.

88. Nguyen Ba, A.N., Strome, B., Osman, S., Legere, E.A., Zarin, T., and Moses, A.M. (2017). Parallel reorganization of protein function in the spindle checkpoint pathway through evolutionary paths in the fitness landscape that appear neutral in laboratory experiments. PLoS Genet. *13*, e1006735.

89. Hashimoto, Y., Zhang, S., Zhang, S., Chen, Y.R., and Blissard, G.W. (2012). Correction: BTI-Tnao38, a new cell line derived from Trichoplusia ni, is permissive for AcMNPV infection and produces high levels of recombinant proteins. BMC Biotechnol. *12*, 12.

90. Cox, J., and Mann, M. (2008). MaxQuant enables high peptide identification rates, individualized p.p.b.-range mass accuracies and proteome-wide protein quantification. Nat. Biotechnol. *26*, 1367–1372.

91. Tyanova, S., Temu, T., Sinitcyn, P., Carlson, A., Hein, M.Y., Geiger, T., Mann, M., and Cox, J. (2016). The Perseus computational platform for comprehensive analysis of (prote)omics data. Nat. Methods *13*, 731–740.

92. Liu, H., and Naismith, J.H. (2008). An efficient one-step site-directed deletion, insertion, single and multiple-site plasmid mutagenesis protocol. BMC Biotechnol. *8*, 91.

93. Ong, S.E., and Mann, M. (2005). Mass spectrometry-based proteomics turns quantitative. Nat. Chem. Biol. *1*, 252–262.

94. Olsen, J.V., Macek, B., Lange, O., Makarov, A., Horning, S., and Mann, M. (2007). Higher-energy C-trap dissociation for peptide modification analysis. Nat. Methods *4*, 709–712.

95. Maddox, P.S., Bloom, K.S., and Salmon, E.D. (2000). The polarity and dynamics of microtubule assembly in the budding yeast Saccharomyces cerevisiae. Nat. Cell Biol. *2*, 36–41.

96. Chen, D., and Huang, S. (2001). Nucleolar components involved in ribosome biogenesis cycle between the nucleolus and nucleoplasm in interphase cells. J. Cell Biol. *153*, 169–176.

97. Trowitzsch, S., Bieniossek, C., Nie, Y., Garzoni, F., and Berger, I. (2010). New baculovirus expression tools for recombinant protein complex production. J. Struct. Biol. *172*, 45–54.

STAR★METHODS

KEY RESOURCES TABLE

REAGENT or RESOURCE	SOURCE	IDENTIFIER
Antibodies		
rabbit polyclonal anti-GFP	generated in-house	N/A
rabbit polyclonal anti-Knl1-N	generated in-house	#SI0787
rabbit polyclonal anti-Bub1	Abcam	Cat#ab9000
mouse monoclonal anti-BubR1	BD Transduction lab	Cat#612503
sheep polyclonal anti-BubR1	Stephen S. Taylor, University of Manchester [89]	N/A
mouse monoclonal anti-Bub3	BD Transduction lab	Cat#611731
mouse monoclonal anti-Tubulin	Sigma	Cat#T9026
rabbit polyclonal anti-Apc7	generated in-house	#SI0651
goat polyclonal anti-Apc4	Santa Cruz	Cat#sc21414
mouse monoclonal anti-Cdc20	Santa Cruz	Cat#sc5296
mouse monoclonal anti-Mad2	generated in-house	#AS55-A12
mouse monoclonal anti-Cdc27	BD Transduction lab	Cat#610455
mouse monoclonal anti-Vinculin	Sigma	Cat#V9131
sheep anti-mouse HRP	Amersham	Cat#NXA931-1ML
donkey anti-rabbit HRP	Amersham	Cat#NXA934-1ML
human anti-centromere (CREST)	Antibodies Inc.	Cat#15-234-0001
donkey anti-goat HRP	Santa Cruz	Cat#sc2020
Protein G HRP	Life Technologies	Cat#P21041
mouse monoclonal anti-Bub1	Abcam	Cat#ab54893
goat anti-human Alexa Fluor-647	Invitrogen	Cat#A-21445
goat anti-mouse Rhodamine Red	Jackson ImmunoResearch	Cat#115-295-003
Chemicals, Peptides, and Recombinant Proteins		
APC/C-pE	Jan-Michael Peters lab [70]	N/A
APC/C-pE-3A	this paper	N/A
Uba1	Jan-Michael Peters lab [70]	N/A
UbcH10	Jan-Michael Peters lab [70]	N/A
Ube2S	Jan-Michael Peters lab [70]	N/A
CycB-NTD	Jan-Michael Peters lab [70]	N/A
Ubiquitin	Enzo Life Sciences Inc.	Cat#BML-UW8795-0005
BubR1 1-571 wt/Bub3	Andrea Musacchio lab [31]	N/A
BubR1 1-571 wt	Andrea Musacchio lab [31]	N/A
BubR1 1-571 B1-LL/Bub3	this paper	N/A
BubR1 1-571 ΔLL/Bub3	this paper	N/A
BubR1 1-571 ΔLL	this paper	N/A
Cdc20	Andrea Musacchio lab [31]	N/A
Mad2	Andrea Musacchio lab [31]	N/A
Lysyl Endopeptidase	Wako	Cat#125-05061
Glu-C Endopeptidase	Promega	Cat#V1651
Protease-inhibitor mix HP Plus	Serva	Cat#39107
PhosSTOP phosphatase inhibitors	Roche	Cat#04906845001
Zeocin	Invitrogen	Cat#R25001
Doxycycline	Sigma	Cat#D9891; CAS:24390-14-5
Nocodazole	Sigma	Cat#M1404; CAS:31430-18-9
DAPI	Serva	Cat#:18860.01

(*Continued on next page*)

Continued

REAGENT or RESOURCE	SOURCE	IDENTIFIER
Poly-L-Lysine	Sigma	Cat#:P4832; CAS:25988-63-0
CO2-independent medium	GIBCO	Cat#18045_054
Thymidine	Sigma	Cat#T1895
Lipofectamine2000	Invitrogen	Cat#11668-019
X-treme Gene	Roche	Cat#06365809001
Poly-D-Lysine	Millipore	Cat#A-003-E
Mowiol	Calbiochem	Cat#475904
SILAC DMEM	PAA	Cat#E15-086
dialyzed serum	PAA	Cat#A11-107
Arg-0	Sigma	Cat#A6969; CAS:1119-34-2
Lys-0	Sigma	Cat#L8662; CAS:657-27-2
Arg-10	Silantes	Cat#201604102
Lys-8	Silantes	Cat#211604102
Urea	Sigma	Cat#U6504; CAS: 57-13-6
Acetonitrile	Fluka	Cat#34967; CAS: 75-05-8
Trypsin	Promega	Cat#V5113
Ammonium Bicarbonate (Ambic)	Fluka	Cat#C990X98; CAS: 1066-33-7
trifluoroacetic acid (TFA)	Sigma	Lot#RB228879; CAS: 76-05-1
iodoacetamide	Sigma	Cat#I6125; CAS: 144-48-9
Experimental Models: Cell Lines		
Trichoplusia ni: BTI-Tnao38	Garry W. Blissard Lab	N/A
S. frugiperda: Sf9 cells in Sf900^{TM} III SFM	Thermo Fisher	Cat#12659017
Human: HeLa, female Cervix Adenocarcinoma Cells	ATCC	Cat#CCL-2^{TM}
Human: Flp-In T-Rex HeLa	Stephen S. Taylor, University of Manchester	N/A
Human: Flp-In T-Rex HeLa GFP	Andrea Musacchio lab [60]	N/A
Human: Flp-In T-Rex HeLa Bub1 wt	Andrea Musacchio lab [60]	N/A
Human: Flp-In T-Rex HeLa Bub1 B3BD	Andrea Musacchio lab [60]	N/A
Human: Flp-In T-Rex HeLa BubR1 wt	Andrea Musacchio lab [60]	N/A
Human: Flp-In T-Rex HeLa BubR1 B1-L	Andrea Musacchio lab [60]	N/A
Human: Flp-In T-Rex HeLa BubR1 B1-LL	this paper	N/A
Human: Flp-In T-Rex HeLa BubR1 B1-LL/ΔH	this paper	N/A
Human: Flp-In T-Rex HeLa BubR1 B1-B3BD/B1-H	this paper	N/A
Human: Flp-In T-Rex HeLa BubR1 KEN1/AAA	this paper	N/A
Human: Flp-In T-Rex HeLa BubR1 ΔL	this paper	N/A
Human: Flp-In T-Rex HeLa BubR1 ΔLL	this paper	N/A
Human: Flp-In T-Rex HeLa BubR1 B3BD	Andrea Musacchio lab [60]	N/A
Human: Flp-In T-Rex HeLa BubR1 B3BD ΔL	this paper	N/A
Human: Flp-In T-Rex HeLa Bub1 1-284	this paper	N/A
Human: Flp-In T-Rex HeLa BubR1 1-431	this paper	N/A
Human: Flp-In T-Rex HeLa BubR1 ΔB3BD	this paper	N/A
Human: Flp-In T-Rex HeLa BubR1 E409K+E413K	Andrea Musacchio lab [60]	N/A
Human: Flp-In T-Rex HeLa BubR1 ΔH	Andrea Musacchio lab [60]	N/A
Human: Flp-In T-Rex HeLa BubR1 ΔL/ΔH	this paper	N/A
Experimental Models: Organisms/Strains		
E.coli:One Shot OmniMAX 2 T1R Chemically Competent Cells	Thermo Fisher	Cat#C854003

(*Continued on next page*)

Continued

REAGENT or RESOURCE	SOURCE	IDENTIFIER
Oligonucleotides		
siRNA Bub1: 5′-GGUUGCCAACACAAGUUCU-3′	Dharmacon, custom made	N/A
siRNAi BubR1: 5′-CGGGCAUUUGAAUAUGAAA-3′	Dharmacon, custom made	N/A
Recombinant DNA		
MultiBac	Geneva Biotech	N/A
pCDNA 5/FRT/TO plasmid	Invitrogen	Cat#V6520-20
pCDNA5/FRT/TO-EGFP-IRES	Andrea Musacchio lab [5]	N/A
pCDNA5/FRT/TO-EGFP-Bub1 wt	Andrea Musacchio lab [5]	N/A
pCDNA5/FRT/TO-EGFP-BubR1 wt	Andrea Musacchio lab [5]	N/A
pCDNA5/FRT/TO-EGFP-BubR1 B1-LL	this paper	N/A
pCDNA5/FRT/TO-EGFP-BubR1 B1-L	Andrea Musacchio lab [60]	N/A
pCDNA5/FRT/TO-EGFP-BubR1 KEN1/AAA	this paper	N/A
pCDNA5/FRT/TO-EGFP-BubR1 B1-LL/ΔH	this paper	N/A
pCDNA5/FRT/TO-EGFP-BubR1 B1-B3BD/B1-H	this paper	N/A
pCDNA5/FRT/TO-EGFP-BubR1 ΔLL	this paper	N/A
pCDNA5/FRT/TO-EGFP-BubR1 ΔL	this paper	N/A
pCDNA5/FRT/TO-EGFP-BubR1 B3BD	Andrea Musacchio lab [60]	N/A
pCDNA5/FRT/TO-EGFP-Bub1 B3BD	Andrea Musacchio lab [5]	N/A
pCDNA5/FRT/TO-EGFP-BubR1 B3BD ΔL	this paper	N/A
pCDNA5/FRT/TO-EGFP-Bub1 1-284	Andrea Musacchio lab [5]	N/A
pCDNA5/FRT/TO-EGFP-BubR1 1-431	Andrea Musacchio lab [60]	N/A
pCDNA5/FRT/TO-EGFP-BubR1 ΔB3BD	this paper	N/A
pCDNA5/FRT/TO-EGFP-BubR1 E409K+E413K	Andrea Musacchio lab [60]	N/A
pCDNA5/FRT/TO-EGFP-BubR1 ΔH	Andrea Musacchio lab [60]	N/A
pCDNA5/FRT/TO-EGFP-BubR1 B1-L/ΔH	this paper	N/A
pCDNA5/FRT/TO-EGFP-BubR1 1-431 B1-L	this paper	N/A
pCDNA5/FRT/TO-EGFP-BubR1 1-431 B1-LL	this paper	N/A
pCDNA5/FRT/TO-EGFP-Bub1 BR1-L	Andrea Musacchio lab [60]	N/A
pCDNA5/FRT/TO-EGFP-Bub1 BR1-LL	this paper	N/A
pCDNA5/FRT/TO-EGFP-BubR1 ΔL/ΔH	this paper	N/A
Software and Algorithms		
ImageJ 1.46 r	NIH	https://imagej.nih.gov/ij/
Imaris 7.3.4 32-bit	Bitplane	http://www.bitplane.com/imaris
GraphPad Prism 6.0	GraphPad software	http://www.graphpad.com
Illustrator CS5.1, version 15.1.0	Adobe	http://www.adobe.com
Photoshop CS5.1, version 12.1	Adobe	http://www.adobe.com
MaxQuant, version 1.5.2.18	[90]	http://www.coxdocs.org/doku.php?id=maxquant:start
Perseus, version 1.5.1.5	[91]	http://www.coxdocs.org/doku.php?id=perseus:start
Other		
Roti®garose Protein A beads	Roth	Cat#1278.1
Protein G affinity resin	Amintra	Cat#APG0005
GFP-Trap_A	ChromoTek	Cat#gta-20
ECL Prime western blotting system	GE Healthcare	Cat#RPN 2232
Amicon concentrators (10K/30K)	Millipore	Cat#UFC901024;UFC903024
Nitrocellulose membrane	GE Healthcare	Cat#10600001
Mowiol mounting media	Calbiochem	Cat#475904
4%–12% NuPAGE Bis-Tris gels	Life Technologies	Cat#NP0321BOX

(*Continued on next page*)

Continued

REAGENT or RESOURCE	SOURCE	IDENTIFIER
His Trap FF (5ml)	GE Healthcare	Cat#17-5255-01
Superdex 200 Increase 5/150 GL	GE Healthcare	Cat#28-9909-45
Superdex 200 16/60	GE Healthcare	Cat#28989335
Sep-Pak C18 Vac Cartridge, 50 mg Sorbent	Waters	Cat#WAT054955
24-well μ-plate	ibidi	Cat#82406
35 mm glass bottom μ-dishes	ibidi	Cat#81158
Rotilabo® syringe filters	Roth	Cat#P820.1

CONTACT FOR REAGENT AND RESOURCE SHARING

Further information and requests for reagents may be directed to and will be fulfilled by Andrea Musacchio (andrea.musacchio@mpi-dortmund.mpg.de).

EXPERIMENTAL MODEL AND SUBJECT DETAILS

cDNAs used for expression of recombinant proteins were either of human origin, or generated synthetically based on human sequences. HeLa (female Cervix Adenocarcinoma) cells were grown in DMEM (PAN Biotech) supplemented with 10% FBS, penicillin and streptomycin and 2 mM L-glutamine. Cells were grown in a humidified atmosphere of 37°C and 5% CO_2.

METHOD DETAILS

Mammalian plasmids

Plasmids were derived from the pCDNA5/FRT/TO-EGFP-IRES, a previously modified version [5] of the pCDNA5/FRT/TO vector (Invitrogen). To create N-terminally tagged EGFP Bub1 and BubR1 truncation constructs, Bub1 and BubR1 sequences were obtained by PCR amplification from the previously generated pCDNA5/FRT/TO-EGFP-Bub1-IRES and pCDNA5/FRT/TO-EGFP-BubR1-IRES vector, respectively [5] and subcloned in frame with the GFP-tag. Mutations and deletions within the Bub1 and BubR1 constructs were generated by standard site-directed mutagenesis or by a mutagenesis protocol [92]. All Bub1 constructs were RNAi resistant [6]. BubR1-expressing constructs were made siRNA-resistant by changing the sequence targeted by the RNAi oligos to 'AACGTGCCTTCGAGTACGAGA'. pCDNA5/FRT/TO-based plasmids were used for generation of stable cell lines, as well as for transient transfection. All plasmids were verified by sequencing.

Cell culture and transfection

HeLa cells were grown in DMEM (PAN Biotech) supplemented with 10% FBS (Clontech), penicillin and streptomycin (GIBCO) and 2 mM L-glutamine (PAN Biotech). For all plasmid transfections of HeLa cells X-tremeGENE transfection agent (Roche) was used at a 3:1 ratio with plasmid DNA. Flp-In T-REx HeLa cells used to generate stable doxycycline-inducible cell lines were a gift from S.S. Taylor (University of Manchester, Manchester, England, UK). Flp-In T-REx host cell lines were maintained in DMEM with 10% tetracycline-free FBS (Clontech) supplemented with 50 μg/ml Zeocin (Invitrogen). Flp-In T-REx HeLa expression cell lines were generated as previously described [5]. Briefly, Flp-In T-Rex HeLa host cells were cotransfected with a ratio of 9:1 (w/w) pOG44:pcDNA5/FRT/TO expression plasmid using X-tremeGene transfection agent (Roche). 48 hr after transfection, Flp-In T-Rex HeLa expression cell lines were put under selection for two weeks in DMEM with 10% tetracycline-free FBS (Invitrogen) supplemented with 250 μg/ml Hygromycin (Roche) and 5 μg/ml Blasticidin (ICN Chemicals). The resulting foci were pooled and tested for expression. Gene expression was induced by addition of 0.05-0.5 μg/ml doxycycline (Sigma) for 24 hr. siBUB1 (GE Healthcare Dharmacon; 5′-GGUUGCCAACACAAGUUCU-3′) or siBUBR1 (GE Healthcare Dharmacon; 5′-CGGGCAUUUGAAUAUGAAA-3′) duplexes were transfected with Lipofectamine 2000 (Invitrogen) at 50 nM for 24 hr.

For experiments in HeLa cells, cells were synchronized with a double thymidine arrest 5 hr after transfection with siRNA duplexes. In brief, after washing the cells with PBS they were treated with thymidine for 16 hr and then released into fresh medium. 3 hr after the release, 50 nM siRNA duplexes were transfected for a second time. 5 hr after transfection, cells were treated with thymidine for 16 hr and afterward released in fresh medium. Thymidine (Sigma-Aldrich) was used at 2 mM. Unless differently specified, nocodazole (Sigma-Aldrich) was used at 3.3 μM.

Immunoprecipitation and immunoblotting

To generate mitotic populations for immunoprecipitation experiments, cells were treated with 330 nM nocodazole for 16 hr. Mitotic cells were then harvested by shake off and lysed in lysis buffer [150 mM KCl, 75 mM HEPES, pH 7.5, 1.5 mM EGTA, 1.5 mM $MgCl_2$, 10% glycerol, and 0.075% NP-40 supplemented with protease inhibitor cocktail (Serva) and PhosSTOP phosphatase inhibitors (Roche)]. Extracts were precleared using a mixture of protein A–agarose (Roti®garose Protein A beads; Roth) and protein G-agarose

(Protein G affinity resin; Amintra) beads for 1 hr at 4°C. Subsequently, extracts were incubated with GFP-Traps (ChromoTek; 3 μl/mg of extract) for 3 hr at 4°C. Immunoprecipitates were washed with lysis buffer and resuspended in sample buffer, boiled, and analyzed by SDS-PAGE and western blotting using 4%–12% gradient gels (NuPAGE® Bis-Tris Gels, Life technologies). For Cdc27 IPs, cells were lysed in lysis buffer (described above) and extracts were precleared with protein G-agarose beads for 1 hr at 4°C. Afterward, extracts were incubated with 1.5 ug/mg of the anti-Cdc27 primary antibody (mouse monoclonal, BD) for 2 hr at 4°C. Subsequently, protein G-agarose beads were added for 4 hr at 4°C. Immunoprecipitates were washed with a mild wash buffer (lysis buffer without salt) and analyzed as described above. The following antibodies were used: anti-GFP (in house made rabbit polyclonal antibody; 1:1000-3000), anti-Knl1-N (in house made rabbit polyclonal SI0787 antibody; 1:1000), anti-Bub1 (rabbit polyclonal; Abcam; 1:5000), anti-BubR1 (mouse monoclonal; BD; 1:1000), anti-BubR1 (sheep polyclonal, 1:500, a gift from S. S. Taylor (University of Manchester, Manchester, England, UK)), anti-Bub3 (mouse monoclonal; BD; 1:1000), anti-Tubulin (mouse monoclonal; Sigma; 1:8000), anti-Apc7 (in house made rabbit polyclonal antibody SI0651, 1:500), anti-Apc4 (goat polyclonal, Santa-Cruz, 1:100), anti-Cdc20 (mouse monoclonal, Santa Cruz, 1:500), anti-Mad2 (in house made mouse monoclonal antibody, clone AS55-A12, 1:500), anti-Cdc27 (mouse monoclonal, BD; 1:1000-3000), anti-Vinculin (mouse monoclonal, Sigma, 1:20000). Secondary antibodies were anti–mouse (Amersham), anti-goat (Santa-Cruz) and anti–rabbit (Amersham) affinity-purified with horseradish peroxidase conjugate (working dilution 1:10000) or Protein G with horseradish peroxidase conjugate (Life technologies) (working dilution 1:8000). After incubation with ECL western blotting system (GE Healthcare), images were acquired with the ChemiDoc™ MP Imaging System (BioRad) in 16-bit TIFF format. Images were cropped and converted to 8-bit using ImageJ software (NIH). Brightness and contrast were adjusted using Photoshop CS5 (Adobe). Unmodified 16-bit TIFF images were used for quantification with ImageJ software. Measurements were graphed with Excel (Microsoft) and GraphPad Prism version 6.0 for Mac OS X (GraphPad Software).

SILAC and mass spectrometry

For labeling, cells were cultivated for five passages in specialized SILAC medium (DMEM, E15-086, PAA; dialyzed serum, A11-107, PAA) supplemented with either "light" arginine and lysine (referred to as Arg-0 and Lys-0, A6969 and L8662, Sigma) or "heavy" arginine ($^{13}C_6{}^{15}N_4$) and lysine ($^{13}C_6{}^{15}N_2$) (referred to as Arg-10 and Lys-8) [68, 93]. Afterward, cells were synchronized in prometaphase by the addition of 330 nM nocodazole for 16 hr and harvested by mitotic shake off. During the following anti-GFP IP (described in immunoprecipitation and immunoblotting) the washing steps were performed in a mild wash buffer (75 mM HEPES, pH 7.5, 1.5 mM EGTA, 1.5 mM $MgCl_2$, 10% glycerol) to preserve potentially weak interactions. IPs were usually performed in duplicates swapping the labels (called FOR and REV) and repeated three times to be able to perform statistical analyses of the results. The corresponding heavy and light samples of the forward and reverse experiment were mixed in the last washing step. Afterward, samples were processed for mass spectroscopy. Briefly, samples were reduced, alkylated, digested directly on the beads with LysC/Trypsin and desalted/concentrated on C18-reversed phase stage tips. Samples were then separated on a Thermo Fisher Scientific™ EASY-nLC 1000 HPLC system using a two hour gradient from 5%–60% with 0.1% formic acid and directly sprayed via a nanoelectrospray ion source (Proxeon Biosystems, now Thermo Fisher Scientific) in a quadrupole Orbitrap mass spectrometer (Q Exactive™, Thermo Fisher Scientific). The Q Exactive™ was operated in a data dependent mode acquiring one survey scan and subsequently ten MS/MS scans [94]. Data were analyzed with the quantitative proteomics software MaxQuant (version 1.5.2.18) [90] and further processed in Perseus (version 1.5.1.5) [91]. Contaminants and reverse hits were removed from the protein lists. For t tests and volcano plots, proteins were further filtered to be quantified in at least 2 out of 3 replicates.

Live cell imaging

Cells were plated on a 24-well μ-Plate (Ibidi®). Drugs were diluted in CO_2 Independent Medium (GIBCO®) and added to the cells 1 hr before filming. Cells were imaged every 20 to 30 min in a heated chamber (37°C) on a 3i Marianas system (Intelligent Imaging Innovations Inc.) equipped with Axio Observer Z1 microscope (Zeiss), Plan-Apochromat 40x/1.4NA oil objective, M27 with DIC III Prism (Zeiss), Orca Flash 4.0 sCMOS Camera (Hamamatsu) and controlled by Slidebook Software 6.0 (Intelligent Imaging Innovations Inc). For cells expressing the GFP-BubR1 proteins, only cells in which kinetochores were visible (or that were GFP-positive - for constructs that do not localize to kinetochores) were considered for the analysis.

Fluorescence recovery after photobleaching

For FRAP experiments cells were grown in 35 mm glass bottom μ-dishes (Ibidi®). Experiments were performed in the presence of 3.3 μM nocodazole, the presence of the GFP-tagged wild-type or mutant fusionprotein and in the absence of the endogenous protein. Cells were imaged on a 3i Marianas system (Intelligent Imaging Innovations Inc., described above) using a 100x/1.4NA Oil Objective (Zeiss). Photobleaching was performed as described previously [95]. Briefly, individual kinetochores were bleached with 100% laser power of an Argon-488 laser line. Images were binned 2x2 to increase signal-over-camera noise. At each time point a z stack consisting of 3 sections at 0.27 μm intervals was acquired. The GFP-signal was imaged for 5 time frames before photobleaching. After opening the laser shutter for 5 ms, cells were imaged by time-lapse microscopy, taking a z series every 0.8 s for a total duration of 2 min with an exposure time of 125 ms. Images were converted into maximal intensity projections and exported as 16-bit TIFF files. Measurements of fluorescence intensity were made on the 16-bit maximal intensity projections using ImageJ. Apart from the bleached KT, a non-bleached KT from the same nucleus and a region of the same size outside of the cell were also measured. Afterward, measurements were exported into excel. The relative fluorescence intensity was calculated as $RFI = (F_{ROI}(t)/F_{BG}(t)) / (F_{ROI}(t_0)/F_{BG}(t_0))$, as also described in [96], to correct for background intensity and for photobleaching that occurred during image

acquisition. $F_{ROI}(t)$ is the intensity of the bleached KT at different time points after bleaching, $F_{BG}(t)$ is the intensity of the control non-bleached KT at the corresponding time points. $F_{ROI}(t_0)$ is the average intensity of the bleached KT before bleaching, $F_{BG}(t_0)$ is the average intensity of the control non-bleached KT before bleaching. A baseline value, calculated from the region outside of the cell, was subtracted from all values before entering the values into the formula shown above. The final data were analyzed using Graph Pad Prism 6.0. Between 5 and 20 cells from at least two independent experiments were analyzed for each investigated construct.

Immunofluorescence

HeLa cells and Flp-In T-REx HeLa cells were grown on coverslips precoated with poly-D-Lysine (Millipore, 15 μg/ml) and poly-L-Lysine (Sigma), respectively. For the experiments with HeLa cells, cells were synchronized with a double thymidine block and after release from that arrested in prometaphase by the addition of 330 nM nocodazole for 3 hr. For all other experiments, asynchronously growing cells were arrested in prometaphase by the addition of nocodazole for 3-4 hr and fixed using 4% paraformaldehyde. Cells were stained for Bub1 (mouse, ab54893, 1:400) and CREST/anti-centromere antibodies (Antibodies, Inc., 1:100), diluted in 2% BSA-PBS for 1.5 hr. Goat anti–human Alexa Fluor 647 (Invitrogen) and goat anti–mouse RRX (Jackson ImmunoResearch Laboratories, Inc.) were used as secondary antibodies. DNA was stained with 0.5 μg/ml DAPI (Serva) and coverslips were mounted with Mowiol mounting media (Calbiochem). Cells were imaged at room temperature using a spinning disk confocal device on the 3i Marianas system equipped with an Axio Observer Z1 microscope (Zeiss), a CSU-X1 confocal scanner unit (Yokogawa Electric Corporation), Plan-Apochromat 63x or 100x/1.4NA Oil Objectives (Zeiss) and Orca Flash 4.0 sCMOS Camera (Hamamatsu). Images were acquired as z sections at 0.27 μm. Images were converted into maximal intensity projections, exported, and converted into 8-bit. Quantification of kinetochore signals was performed on unmodified 16-bit z series images using Imaris 7.3.4 32-bit software (Bitplane). After background subtraction, all signals were normalized to CREST. At least 307 kinetochores were analyzed per condition. Measurements were exported in Excel (Microsoft) and graphed with GraphPad Prism 6.0 (GraphPad Software).

Protein expression and purification

Sequences coding for H6-mTurquoise-BubR1$^{1\text{-}571\text{-}\Delta LL}$ and H6-mTurquoise-BubR1$^{1\text{-}571\text{-}B1\text{-}LL}$ were sub-cloned into pFLMultiBac vectors and baculoviruses were generated [97]. Expression of H6-mTurquoise-BubR1$^{1\text{-}571}$, the BubR1 mutant constructs, untagged Bub3, and Mps1 was performed in TnaO38 insect cells. Expression of H6-3xMyc-and BUB1:BUB3 was carried out in Sf9 cells. Expression of H6-Mad2 was carried out in *Escherichia coli* [97]. After infection with virus (1:50), cultures were grown at 27°C degrees and harvested after three days, and pellets stored at −20°C. MAD1:C-MAD2 and BUBR1:BUB3 were cultured by mixing individual viruses, each harboring individual genes. MPS1 was expressed in the presence of 2 μM Reversine. Insect cells were harvested by centrifugation at 750 g for 12 min in a Sorvall RC3BP+ (Thermo Scientific) centrifuge with Rotor H6000A. The pellet was resuspended in PBS, centrifuged at 500 g for 5 min, the supernatant was discarded and the pellet was stored at −20°C.

Generally, the cell pellet from 1 l of insect cell culture volume was re-suspended in 250 mL lysis buffer (25 mM HEPES pH 7.5, 300 mM NaCl, 5% glycerol, 10 mM imidazole, 1 mM TCEP, 1 mM PMSF). Cdc20 was purified in lysis buffer with 500 mM NaCl. Cells were lysed by sonication and centrifuged at 108000 g (Rotor JA30.50, Avanti-J30I, Beckman Coulter) for 30 min at 4°C. The supernatant was filtered through 0.8 μm Rotilabo® syringe filters (Carl Roth GmbH). The proteins were isolated from the cleared lysate on a 5 mL HisTrap FF affinity column (GE Healthcare). Peak fractions were pooled, concentrated, and further purified in gelfiltration buffer (10 mM HEPES pH 7.5, 150 mM NaCl, 5% glycerol, 1 mM TCEP) by size exclusion chromatography on a S200 16/60 column (GE Healthcare). Peak fractions were pooled, concentrated to typically 3 to 5 mg/ml, flash frozen and stored at −80°C until use.

For the purification of recombinant MCC complexes, individual purified MCC components were mixed to obtain 250 μg of MCC and incubated at 4°C over night. Afterward, gelfiltration was performed using a Superdex 200 increase 5/150 column (GE Healthcare) equilibrated against a buffer containing 20 mM HEPES pH 7.5, 200 mM NaCl and 2 mM DTT. Peak fractions were pooled, concentrated flash frozen and stored at −80°C.

Size-exclusion chromatography mobility shift assay

Proteins tested for interactions were diluted to a final concentration of 5 μM in 50 μl reactions in binding buffer (10 mM HEPES pH 7.5, 150 mM NaCl, 5% glycerol, 1 mM TCEP, 1 mM $MgCl_2$) and incubated at 4°C over night. Complex formation was analyzed by size exclusion chromatography on a Superdex 200 increase 5/150 column (GE Healthcare). Eluates were analyzed by SDS-PAGE and Coomassie staining.

MCC assembly kinetics

The assay was performed precisely as described [31]. Fluorimeter scans were performed on a Fluoromax 4 (Jobin Yvon) in a buffer containing fresh 10 mM HEPES (pH 7.5), 150 mM NaCl, 2.5% glycerol, 10 mM beta-mercaptoenthanol and 0.05% Triton X-100. Mixtures were excited at 430 nm and the emissions were scanned from 450 to 650 nm. Single wavelength acceptor fluorescence measurements were carried out at 583 nm. Mixtures of MAD1:C-MAD2 with BUB1:BUB3 and/or MPS1 were pre-incubated at 1 μM for 30 min at 30 degrees. Assays were performed using 100 nM of all proteins, except CDC20, which was added at 500 nM. Curves reporting time-dependent changes in FRET signal report single measurements representative of at least three independent technical replicates.

APC/C-mediated ubiquitination assays

To measure the activity of APC/C, its ability to form poly-ubiquitin chains on its substrate Cyclin B was analyzed. Recombinant APC/C-pE, containing 68 phospho-mimicking mutations [70], was used as mimic of mitotic APC/C. APC/C-pE (20 nM) and Cdc20 (100 nM) were part of a mastermix with 500 nM $CycB^{NTD*}$, 500 nM UbcH10, 500 nM Ube2S, 2.5 mM MgATP and 0.5 mg/ml BSA. This was aliquoted and mixed with recombinant MCC versions (30 nM) on ice. Reactions were equilibrated to room temperature for 10 min and afterward started by the addition of the Uba1 (100 nM)/Ub (100 μM) mix. After 30, 60 and 120 min reactions were stopped by the addition of SDS sample buffer. Samples were analyzed by SDS-PAGE and fluorescence scanning.

QUANTIFICATION AND STATISTICAL ANALYSES

For FRAP experiments, statistical analysis is described in the Figure legends, in the Method Details, and in Table S1. For kinetochore localization experiments and checkpoint assays, quantification and statistical analysis (mean ± SEM) are described in the figure legends. Quantification and statistical analysis of immunoprecipitation experiments (mean ± SEM) are described in the figure legends. Analysis of SILAC data is described in the Methods details.

DATA AND SOFTWARE AVAILABILITY

The full list of interacting proteins identified in the SILAC experiments is available with the online version of the paper as Data S1.